CONTEMPORARY MODELS IN ECTODERMAL ORGAN DEVELOPMENT, MAINTENANCE AND REGENERATION

EDITED BY: Isabelle Miletich, Abigail Saffron Tucker and Maisa Hanna-Maija Seppala

PUBLISHED IN: Frontiers in Physiology

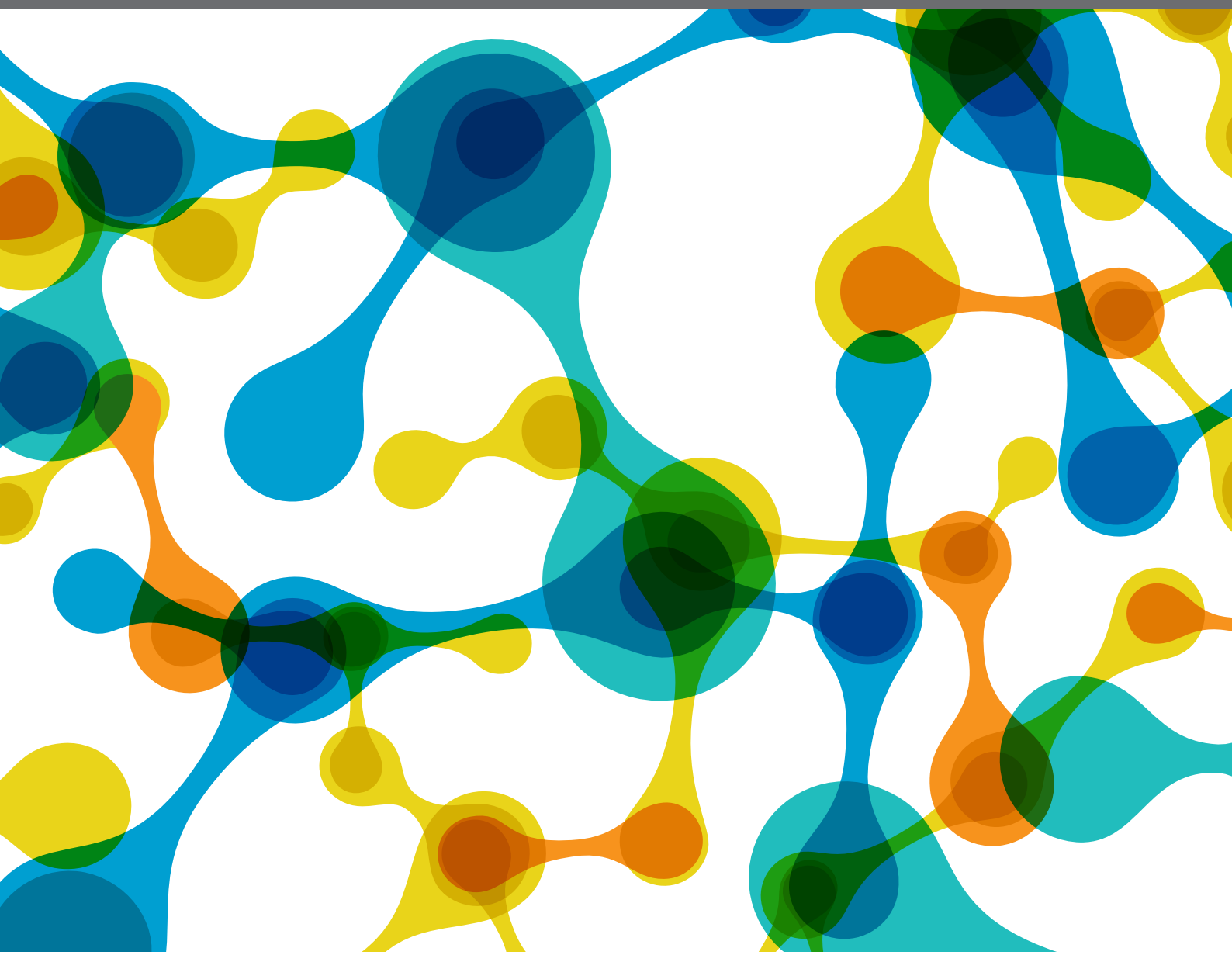

frontiers Research Topics

ISSN 1664-8714
ISBN 978-2-88971-628-9
DOI 10.3389/978-2-88971-628-9

About Frontiers

Frontiers is more than just an open-access publisher of scholarly articles: it is a pioneering approach to the world of academia, radically improving the way scholarly research is managed. The grand vision of Frontiers is a world where all people have an equal opportunity to seek, share and generate knowledge. Frontiers provides immediate and permanent online open access to all its publications, but this alone is not enough to realize our grand goals.

Frontiers Journal Series

The Frontiers Journal Series is a multi-tier and interdisciplinary set of open-access, online journals, promising a paradigm shift from the current review, selection and dissemination processes in academic publishing. All Frontiers journals are driven by researchers for researchers; therefore, they constitute a service to the scholarly community. At the same time, the Frontiers Journal Series operates on a revolutionary invention, the tiered publishing system, initially addressing specific communities of scholars, and gradually climbing up to broader public understanding, thus serving the interests of the lay society, too.

Dedication to Quality

Each Frontiers article is a landmark of the highest quality, thanks to genuinely collaborative interactions between authors and review editors, who include some of the world's best academicians. Research must be certified by peers before entering a stream of knowledge that may eventually reach the public - and shape society; therefore, Frontiers only applies the most rigorous and unbiased reviews.
Frontiers revolutionizes research publishing by freely delivering the most outstanding research, evaluated with no bias from both the academic and social point of view. By applying the most advanced information technologies, Frontiers is catapulting scholarly publishing into a new generation.

What are Frontiers Research Topics?

Frontiers Research Topics are very popular trademarks of the Frontiers Journals Series: they are collections of at least ten articles, all centered on a particular subject. With their unique mix of varied contributions from Original Research to Review Articles, Frontiers Research Topics unify the most influential researchers, the latest key findings and historical advances in a hot research area! Find out more on how to host your own Frontiers Research Topic or contribute to one as an author by contacting the Frontiers Editorial Office: frontiersin.org/about/contact

CONTEMPORARY MODELS IN ECTODERMAL ORGAN DEVELOPMENT, MAINTENANCE AND REGENERATION

Topic Editors:
Isabelle Miletich, King's College London, United Kingdom
Abigail Saffron Tucker, King's College London, United Kingdom
Maisa Hanna-Maija Seppala, King's College London, United Kingdom

Citation: Miletich, I., Tucker, A. S., Seppala, M. H.-M., eds. (2021). Contemporary Models in Ectodermal Organ Development, Maintenance and Regeneration. Lausanne: Frontiers Media SA. doi: 10.3389/978-2-88971-628-9

Table of Contents

frontiers in Physiology

EDITORIAL
published: 24 September 2021
doi: 10.3389/fphys.2021.758271

Editorial: Contemporary Models in Ectodermal Organ Development, Maintenance and Regeneration

Abigail Saffron Tucker and Maisa Hanna-Maija Seppala*

Centre for Craniofacial and Regenerative Biology, King's College London, Guy's Hospital, London, United Kingdom

Keywords: ectodermal organ, development, tooth, gland, palate, tongue

Editorial on the Research Topic

Contemporary Models in Ectodermal Organ Development, Maintenance and Regeneration

This Research Topic stems from the 2019 Tooth Morphogenesis and Development (TMD) Meeting held in Oxford, UK. The topic expands the interactions and discussions initiated during the meeting, and acts as a snapshot of the current research in ectodermal organs, particularly those of the head. Ectodermal organs, include tooth, glands, and hair, are essential for physiological functions such as feeding, maintenance of normal body temperature and homeostasis of microenvironments. Development of these organs is extensively studied and forms the basis of many ectodermal organ regeneration strategies. The topic includes 14 papers focused on ectodermal organ development in the craniofacial region, and the impact of defects in development on these structures. The papers straddle three main areas: tooth/oral, palate, and gland development.

Papers on tooth development spanned early epithelial thickening to later differentiation and maturation of the dental tissues (**Figure 1**). Qiu et al. investigate the development of the dental lamina (DL) during human embryonic and foetal development, focusing on its association with the adjacent vestibular lamina (VL). The paper highlights the close relationship of the VL and DL and confirms in culture the linked origin of the two laminas in the lower incisor region. The paper then goes on to look at the mechanisms used to generate the oral vestibule (cheek/lip furrow) by a process involving epithelial differentiation, differential proliferation and ultimately cell death to create the furrow. Ultimately this research can be used to understand the mechanisms underlying defects in vestibule formation, as observed in syndromes such as Ellis-van Creveld syndrome.

Sánchez et al. move to morphogenesis of the tooth and highlight the role of hyaluronan in controlling both tooth shape and number, suggesting a trade-off between the two. While the function of proteins has been widely studied in the tooth, very little research has looked at the role of carbohydrates. Hyaluronan is an important structural component of the extracellular matrix and has been shown to coordinate processes such as cell shape, proliferation and migration in other organs. Here, Sanchez shows that inhibition of HA synthesis in the mouse molar led to changes in cell orientation and shape, leading to larger but fewer molars. Carbohydrates can therefore provide instructive information to control important cell decisions.

Keeping to the theme of tooth number, Brink et al. investigate whether removal of a replacing tooth (second generation) impacted formation of the rest of the dental lamina and the stem cell population that has been hypothesised to reside there. For this they utilised the polyphodont (continuously replacing) gecko as a model. The dental lamina holds the generations of replacement teeth together, like beads on a necklace. Surgical removal of the second unerupted tooth, therefore, disrupted this link. Calcein and Xylenol orange dyes were used to chart the return of replacement teeth,

OPEN ACCESS

Edited by:
Thimios Mitsiadis,
University of Zurich, Switzerland

Reviewed by:
Thomas G. H. Diekwisch,
Texas A&M University, United States
Natalina Quarto,
University of Naples Federico II, Italy

****Correspondence:***
Abigail Saffron Tucker
abigail.tucker@kcl.ac.uk

Specialty section:
This article was submitted to Craniofacial Biology and Dental Research, a section of the journal Frontiers in Physiology

Received: *13 August 2021*
Accepted: *27 August 2021*
Published: *24 September 2021*

Citation:
Tucker AS and Seppala MH-M (2021) Editorial: Contemporary Models in Ectodermal Organ Development, Maintenance and Regeneration. Front. Physiol. 12:758271. doi: 10.3389/fphys.2021.758271

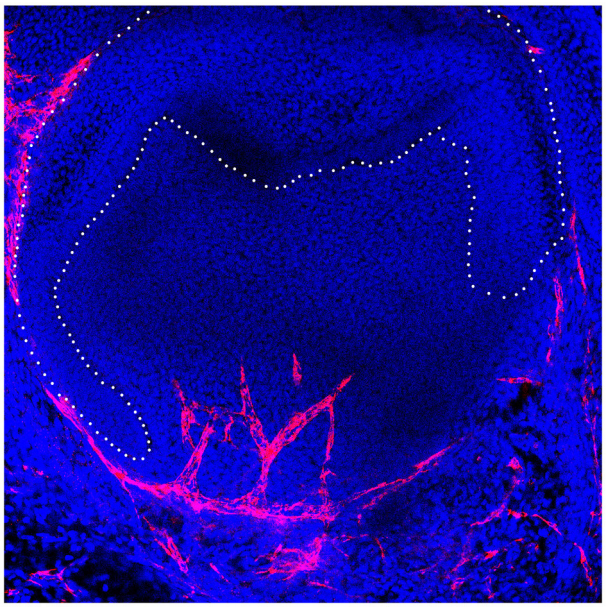

FIGURE 1 | Developing murine tooth germ with invading vasculature in red.

while BrDU pulse chase experiments, followed the location of label retaining cells in the lamina. Interestingly they show that tooth replacement patterns recovered within 3 months, highlighting the regenerative potential of the gecko dentition. Overall, the study confirms that the dental lamina contains a source of dental stem cells but also that this structure contains the information to correctly pattern newly initiating teeth.

Said et al. investigate the role of the circadian clock in regulation of enamel thickness and mineralisation focusing on the connexion between amelogenesis and calcium signalling. Individuals with mutations in STIM 1, a component of the store operated calcium entry (SOCE) signalling pathway, have hypomineralised enamel characterised as amelogenesis imperfecta (AI). To understand the underlying mechanisms, the authors showed that loss of STIM1 specifically in ameloblasts in conditional knockout mice led to changes in circadian activator and inhibitor genes. These changes in the circadian clock were hypothesised to contribute to the enamel defects observed in STIM1-mediated AI.

Keeping with ameloblasts, Ruspita et al. investigated the control of amelogenesis by the *Msx2-Sp6-Follistain* pathway. Mutations in either *MSX2* or *SP6* lead to AI, with mutant mice showing similar defects in enamel. Here the authors show that these genes work in the same pathway, with overlapping expression in secretory ameloblasts, and both inhibiting *follistatin* expression in dental epithelial cell lines. Transient transfection of *Msx2* lead to an upregulation of *Sp6* and downregulation of *Follistatin*, with ChIP confirming the binding of Msx2 to the *Sp6* promotor. Together these experiments unpick the complex transcriptional networks at play during amelogenesis and help to further explain the mechanisms underlying AI.

Malik et al. turn to mineralisation of the tooth and the interplay between morphogenesis and differentiation. Here they show that Bone morphogenetic protein 7 (Bmp7) was important for controlling the onset of mineralisation in the mouse molar, with a delay in mineralisation observed in conditional mutants at birth. Unlike *Bmp2*, which is known to affect odontoblast polarity, loss of *Bmp7* in the neural crest derived mesenchyme led to a loss of Wnt signalling in the overlying pre-ameloblasts. *Bmp6* was also upregulated, suggesting some compensation mechanisms at play. The delay in initiation affected the shape of the final cusps, linking changes in differentiation to changes in shape.

On the clinical side, the link between Wnt signalling and non-syndromic tooth agenesis (NSTA) was further strengthened by analysis of Thai individuals by Kanchanasevee et al.. Tooth agenesis is one of the most common orodental anomalies, and mutations in *WNT10A* and the *EDA* signalling pathway have previously been highlighted as causing defects in early tooth development. Here novel variants in both *WNT10a* and *EDARADD*, the intracellular adapter for the *EDA* pathway, were discovered, enhancing our knowledge of how specific variants can impact tooth development.

The Eda pathway was also studied by Jia et al. who investigated the interaction between *Eda* and *Pax9*. Both genes in patients cause selective tooth agenesis, and here the authors show that compound mouse mutants have specific loss of the lower incisors, with higher incidence of loss of the third molar. Loss of the incisors was associated with downregulation of *Fibroblast growth factor (Fgf)3* and *Sonic Hedgehog* signalling, with defects evident from the bud to cap stage and arrest thereafter. Overall, this paper highlights the interaction between *Eda* and *Pax9*, working together to control odontogenesis.

Continuing the theme of Wnt signalling in ectodermal organs, Eliason et al. investigate the interaction between *Lef1*, a key downstream readout of canonical Wnt signalling and the microRNA miR-26b. Overexpression of miR-26b mimicked the ectodermal phenotype of *Lef1* null mice, while it rescued the defects in *Lef1* overexpression mice. This paper shows the key role that microRNAs play in regulating signalling pathways, and, in the case of the tooth, in regulating the stem cell niche.

Jumping from the tooth to the neighbouring tongue, Zhang et al. investigate the formation of the circumvallate papilla (CVP). This papilla, found at the back of the tongue, houses the von Ebner's glands, and has a high density of tastebuds, and complex folded shape. How this shape is created from a placodal thickening was investigated by looking at the dynamics of actomyosin dependent constriction. Using an elegant explant culture system, they show that morphogenesis is driven by epithelial cell constriction, dependent on focal adhesion kinase, with *Shh* signalling coordinating the process. Recombination between epithelium and mesenchyme tongue tissue highlighted the role of *Fgf10* in driving the invagination of the CVP epithelium.

The creation of complex shapes from simple epithelial thickenings at the cell level was a central focus of the review from Mogollón and Ahtiainen. Here they follow how live imaging can be used to track cell level decisions, and the latest advances

in technology and culture that allow resolution at the cell level. These include the use of fluorescent reporter mice combined with confocal microscopy and highlight how live imaging advances in hair follicles have been recently applied to tooth placodes, with promise for use in other ectodermal organs.

Two papers in this Research Topic shed light on the delicate mechanisms of primary and secondary palate fusion and disappearance of the epithelial palatal seam. Yamamoto et al. explore the previously less well-known mechanisms of primary and secondary palate fusion and specifically observed the epithelial cell behaviours using palatal explant cultures of K-14-GFP mice. SEM analysis of time-lapse observations of these mice revealed that some of the epithelial behaviours of the primary palate, such as rostral extrusion and apoptosis in the presumptive fusion site with the secondary palate, happen independently without any contact with the secondary palate. In contrast, they did not identify any cellular migration that results in mesenchymal exposure during secondary palate development.

Ohki et al. investigate the molecular control of soft palate development and identified that TGF-β and SHH regulate expression of the extracellular matrix glycoprotein, Tenascin-C (TNC). TNC is required for morphological changes of the palatal shelves and its unique expression in the posterior part of the palatal shelves appeared to rely specifically on the epithelial activity of Tgf-β. Agreeing with this, TNC levels were diminished when TGF-β type II receptor was conditionally removed from the palatal epithelial cells. SHH also increased the expression of TNC mRNA and protein in palatal mesenchymal cells, providing further understanding of the aetiology of facial clefts.

Finally, moving to the eye, Liu et al. investigate the molecular changes associated with primary dry eye in the Aquaporin 5 null mouse. These mice develop spontaneous dry eye due to defects in the epithelial cells of the lacrimal gland. Using a transcriptomic approach, the authors identified molecular changes in the mutant glands, focusing on differentially expressed circular RNAs. The molecular changes highlighted a potential role for phagosomes in the pathogenesis of dry eye disease, suggesting new treatment options for this condition.

Overall, this Research Topic highlighted the flexible approaches used to understand ectodermal organ development, providing mechanistic insight into how defects in ectodermal organs occur and suggesting novel avenues for future treatments.

AUTHOR CONTRIBUTIONS

All authors listed have made a substantial, direct and intellectual contribution to the work, and approved it for publication.

Conflict of Interest: The authors declare that the research was conducted in the absence of any commercial or financial relationships that could be construed as a potential conflict of interest.

Publisher's Note: All claims expressed in this article are solely those of the authors and do not necessarily represent those of their affiliated organizations, or those of the publisher, the editors and the reviewers. Any product that may be evaluated in this article, or claim that may be made by its manufacturer, is not guaranteed or endorsed by the publisher.

frontiers in Physiology

ORIGINAL RESEARCH
published: 04 June 2020
doi: 10.3389/fphys.2020.00532

Transforming Growth Factor-Beta and Sonic Hedgehog Signaling in Palatal Epithelium Regulate Tenascin-C Expression in Palatal Mesenchyme During Soft Palate Development

Shirabe Ohki[1], Kyoko Oka[1,2], Kayoko Ogata[2,3], Shigeru Okuhara[4], Mihoko Rikitake[1], Masako Toda-Nakamura[1], Shougo Tamura[1], Masao Ozaki[1], Sachiko Iseki[4] and Takayoshi Sakai[5]*

[1] Section of Pediatric Dentistry, Department of Oral Growth and Development, Fukuoka Dental College, Fukuoka, Japan, [2] Oral Medicine Research Center, Fukuoka Dental College, Fukuoka, Japan, [3] Section of Functional Structure, Department of Morphological Biology, Fukuoka Dental College, Fukuoka, Japan, [4] Section of Molecular Craniofacial Embryology, Graduate School of Dental and Medical Sciences, Tokyo Medical and Dental University, Tokyo, Japan, [5] Department of Oral-Facial Disorders, Osaka University Graduate School of Dentistry, Osaka, Japan

OPEN ACCESS

Edited by:
Abigail Saffron Tucker, King's College London, United Kingdom

Reviewed by:
Yang Chai, University of Southern California, United States
Daniel Graf, University of Alberta, Canada

***Correspondence:**
Kyoko Oka
okak@college.fdcnet.ac.jp

Specialty section:
This article was submitted to Craniofacial Biology and Dental Research, a section of the journal Frontiers in Physiology

Received: *03 March 2020*
Accepted: *30 April 2020*
Published: *04 June 2020*

Citation:
Ohki S, Oka K, Ogata K, Okuhara S, Rikitake M, Toda-Nakamura M, Tamura S, Ozaki M, Iseki S and Sakai T (2020) Transforming Growth Factor-Beta and Sonic Hedgehog Signaling in Palatal Epithelium Regulate Tenascin-C Expression in Palatal Mesenchyme During Soft Palate Development. Front. Physiol. 11:532. doi: 10.3389/fphys.2020.00532

During palatogenesis, the palatal shelves first grow vertically on either side of the tongue before changing their direction of growth to horizontal. The extracellular matrix (ECM) plays an important role in these dynamic changes in palatal shelf morphology. Tenascin-C (TNC) is an ECM glycoprotein that shows unique expression in the posterior part of the palatal shelf, but little is known about the regulation of TNC expression. Since transforming growth factor-beta-3 (TGF-β3) and sonic hedgehog (SHH) signaling are known to play important roles in palatogenesis, we investigated whether TGF-β3 and SHH are involved in the regulation of TNC expression in the developing palate. TGF-β3 increased the expression of TNC mRNA and protein in primary mouse embryonic palatal mesenchymal cells (MEPM) obtained from palatal mesenchyme dissected at embryonic day 13.5–14.0. Interestingly, immunohistochemistry experiments revealed that TNC expression was diminished in *K14-cre*;*Tgfbr2*$^{fl/fl}$ mice that lack the TGF-β type II receptor in palatal epithelial cells and exhibit cleft soft palate, whereas TNC expression was maintained in *Wnt1-cre*;*Tgfbr2*$^{fl/fl}$ mice that lack the TGF-β type II receptor in palatal mesenchymal cells and exhibit a complete cleft palate. SHH also increased the expression of TNC mRNA and protein in MEPM cells. However, although TGF-β3 up-regulated TNC mRNA and protein expression in O9-1 cells (a cranial neural crest cell line), SHH did not. Furthermore, TGF-β inhibited the expression of osteoblastic differentiation markers (osterix and alkaline phosphatase) and induced the expression of fibroblastic markers (fibronectin and periostin) in O9-1 cells, whereas SHH did not affect the expression of osteoblastic and fibroblastic markers in O9-1 cells. However, immunohistochemistry experiments showed that TNC expression was diminished in the posterior palatal shelves of *Shh*$^{-/+}$;*MFCS4*$^{+/-}$ mice, which have deficient SHH signaling in the posterior palatal epithelium. Taken together, our findings support the proposal that TGF-β and SHH signaling in palatal epithelium co-ordinate the expression of TNC in the posterior palatal mesenchyme through a paracrine mechanism. This

signal cascade may work in the later stage of palatogenesis when cranial neural crest cells have differentiated into fibroblast-like cells. The spatiotemporal regulation of ECM-related proteins by TGF-β and SHH signaling may contribute not only to tissue construction but also to cell differentiation or determination along the anterior–posterior axis of the palatal shelves.

Keywords: soft palate, palatogenesis, tumor growth factor-beta, tenascin-C, sonic hedgehog

INTRODUCTION

Cleft palate is one of the most common craniofacial birth defects in humans. Multidisciplinary research into palatal development has yielded important insights into the mechanisms underlying cleft palate (Li et al., 2017). However, the causes of partial clefts, especially cleft soft palate and submucous cleft palate, remain incompletely understood.

The palatal shelf starts to form on embryonic day 11.5 (E11.5). The mesenchymal tissue of the palatal shelf is mostly composed of cranial neural crest-derived cells that are divided into distinct regions along their anterior–posterior axis (Chai et al., 2000; Oka et al., 2012; Smith et al., 2012). The cranial neural crest-derived mesenchymal cells give rise to the bony hard palate in the anterior and middle parts and to the connective tissue of the soft palate in the posterior part. Previously we reported that transforming growth factor-beta (TGF-β) induces the co-expression of type I collagen and periostin in the region of the posterior palatal mesenchyme that forms the palatine aponeurosis, an important structure for palatine muscle formation (Oka et al., 2012). TGF-β signaling is widely recognized as playing an important role in the synthesis, deposition and regulation of the extracellular matrix (ECM) (Yun et al., 2019). During palatogenesis, the pattern of ECM expression along the anterior–posterior axis may regulate and support osteoblastic or fibroblastic differentiation of cranial neural crest-derived mesenchymal cells.

Numerous growth factors, including TGF-β, have been implicated in the development of cleft palate (Li et al., 2017). TGF-β ligands and receptors are ubiquitously expressed in palatal epithelium and mesenchyme, but their roles differ between the epithelium and mesenchyme along the anterior–posterior axis (Iwata et al., 2011). Furthermore, mutations of individual TGF-β ligands and receptors in mice lead to distinctive types of cleft palate caused by different mechanisms. For example, it has been reported that TGF-β signaling regulates cell proliferation in palatal mesenchyme and that loss of the TGF-β type II receptor in palatal mesenchyme leads to a complete cleft palate (Ito et al., 2003). On the other hand, TGF-β signaling in palatal epithelium regulates palatal adhesion and epithelial seam degradation for fusion of the palatal shelves. TGF-β3 is characteristically expressed in the medial edge epithelium located at the adhesive region of each palatal shelf (Taya et al., 1999). Interestingly, loss of the TGF-β type I and II receptors in palatal epithelium leads to a partial cleft in the posterior region (Dudas et al., 2006; Xu et al., 2006). This latter finding raises the possibility that TGF-β signaling in palatal epithelium is involved not only in epithelial seam degradation but also in the formation of the posterior palatal region. Therefore, we have been interested in exploring the influence of palatal TGF-β signaling on ECM expression patterns during epithelial–mesenchymal interactions.

The sonic hedgehog (SHH) signaling pathway plays a crucial role in embryogenesis and is involved in epithelial–mesenchymal interactions (Bitgood and McMahon, 1995). SHH is also thought to be important for palatal development. For example, SHH was shown to regulate palatal shelf morphogenesis (Rice et al., 2006). Furthermore, SHH signaling was found to modulate palatal growth through epithelial–mesenchymal interactions, whereby alterations in the expressions of transcription factors in the palatal mesenchyme influenced the proliferation of palatal epithelial cells (Lan and Jiang, 2009). Notably, SHH has been implicated in the regulation of palatal fusion by TGF-β3 (Sasaki et al., 2007), and abnormal SHH signaling in mice is associated with cleft palate (Hammond et al., 2018; Li et al., 2018).

Tenascins are a family of large oligomeric ECM glycoproteins comprising four members in vertebrates (-C, -R, -X, and -W). All tenascin subunits are composed of an N-terminal domain, a variable number of tandem epidermal growth factor and fibronectin type III repeats, and a fibrinogen homology domain at the C-terminus (Chiquet-Ehrismann and Chiquet, 2003; Chiquet-Ehrismann and Tucker, 2011). Among the tenascin family, tenascin-C (TNC) is widely expressed in mesenchymal tissue at sites of epithelial–mesenchymal interactions and around motile cells, including neural crest cells and migrating neuroblasts and glial precursors (Chiquet-Ehrismann et al., 2014). It has been reported that TNC is expressed in palatal mesenchyme during palatogenesis (Chiquet et al., 2016; Li et al., 2017; Paiva et al., 2019). However, the mechanisms regulating this characteristic expression of TNC during palatogenesis have not been elucidated.

Here, we show that TNC expression in the palatal mesenchyme is regulated by both TGF-β and SHH signaling in the palatal epithelium. However, the regulation of TNC expression by these signaling pathways differs and depends on the developmental stage of the palatal mesenchyme. Spatiotemporal regulation of TNC expression in the palatal mesenchyme by TGF-β and SHH in the palatal epithelium might be critical for the characteristic development of the hard and soft palate.

MATERIALS AND METHODS

Animals

All procedures for animal care were reviewed and approved by the Animal Experiment Committee of Fukuoka Dental College, Fukuoka, Japan (nos. 17012 and 18005). ICR mice (Kyudo

Co., Tosu, Japan) were used for immunohistochemical analyses and cell culture experiments. Male mice carrying the K14-Cre allele and Wnt1-Cre allele were crossed with *Tgfbr2*$^{fl/fl}$ females to generate *K14-Cre*;*Tgfbr2*$^{fl/fl}$ mice, which lack the TGF-β type II receptor in palatal epithelial cells, and *Wnt1-Cre*;*Tgfbr2*$^{fl/fl}$ mice, which lack the TGF-β type II receptor in palatal mesenchymal cells (Chytil et al., 2002; Ito et al., 2003; Andl et al., 2004). In compound heterozygous *Shh*$^{-/+}$;*MFCS4*$^{+/-}$ mice (Amano et al., 2009; Sagai et al., 2009), the *MFCS4* long-distance Shh enhancer is deleted on one allele, whereas the *Shh* gene remains intact on the same allele, resulting in reduced levels of SHH. To achieve *Shh* deletion at specific developmental stages, *pCag-CreERTM*;*Shh*$^{flox/+}$ mice were mated with *Shh*$^{flox/+}$ mice (Dassule et al., 2000; Hayashi and McMahon, 2002), and pregnant mice were administered tamoxifen by intraperitoneal injection (75 mg/kg, equivalent to 3 mg per 40 g body weight) at the appropriate developmental stage. For the experiments, comparisons were made between each of the above mutants and wild-type littermates.

Palatal Development Stages

We selected the developmental stages for analysis on the basis of previous reports (Oka et al., 2012; Higa et al., 2016). The palatal shelves are evident on either side of the tongue at E13.5 and are elevated above the tongue at around E14.0. Palatal mesenchymal cells undergo proliferation rather than differentiation during E13.5–14.0, and at this stage it is difficult to distinguish between the hard and soft palate. At E14.5, the bone matrix of the maxilla of the hard palate and the sphenoid bone of the soft palate (which represent characteristic components of each palate) are detectable in histological section. After E14.5, each of the neural crest cell-derived osteogenic and fibrogenic components of the hard and soft palates is clearly identifiable in histological section. The skeletal muscle cells that originate from mesoderm-derived cells do not exist in the palatal shelves of mice (Grimaldi et al., 2015). Thus, palatal mesenchymal cells before E15.5 are mainly derived from cranial neural crest cells.

Immunohistochemistry

Immunohistochemistry was performed on palatal tissues obtained from mice at embryonic stages E13.5 to E15.5. The tissues were fixed with 10% neutral buffered formalin or 4% paraformaldehyde in phosphate-buffered saline, dehydrated in graded ethanol solutions, embedded in paraffin, and cut into 6-μm sections for immunostaining. The primary antibodies used were rat anti-TNC monoclonal antibody (1:100 dilution; MAB2138, R&D Systems, Minneapolis, MN, United States) and rabbit anti-cytokeratin broad-spectrum screening polyclonal antibody (1:200 dilution; Z0622, Dako Cytomation, Carpinteria, CA, United States), and these were applied for 1 h at room temperature. The secondary antibodies used were Alexa Fluor® 488 anti-rabbit immunoglobulin G (IgG), Alexa Fluor® 594 goat anti-rat IgG, and biotin-conjugated goat anti-rat IgG H&L (Abcam, Tokyo, Japan). The nuclei were counterstained with DAPI (4′,6-diamidino-2-phenylindole), which was present in the mounting medium (Vectashield, Vector Laboratories, Burlingame, CA, United States) or Methyl Green (Merck Millipore, Darmstadt, Hessen, Germany). Specimens treated with biotin-conjugated secondary antibody were sensitized using streptavidin peroxidase (Vector Laboratories) and visualized using a diaminobenzidine kit (Nichirei Biosciences Inc., Tokyo, Japan). The specimens were observed using a fluorescence microscope (BZ9000; Keyence, Osaka, Japan).

Real-Time Polymerase Chain Reaction (PCR)

Palatal shelves were dissected from ICR mouse embryos at E13.5, E14.5, and E15.5 and divided into anterior and posterior portions. The position of the border between the anterior and posterior portions of the palatal shelf was defined with reference to a 3D reconstruction of the mouse embryo provided by NIH FaceBase[1]. Using morphologic observations, it was straightforward to distinguish the much smaller posterior portion of the palatal shelf from the anterior portion in the secondary palate. In addition, visualization of the developing rugae under a stereomicroscope from E14.5 also helped to define the border between the anterior and posterior portions. RNA was isolated from tissue using TRIzol reagent (Thermo Fisher Scientific, Tokyo, Japan) and extracted from cells using the RNeasy® Mini kit (Qiagen, Valencia, CA, United States). cDNA was synthesized using PrimeScript® II Reverse Transcriptase (Takara, Otsu, Japan). After mixing each cDNA with SsoAdvanced™ Universal SYBR® Green Supermix (Bio-Rad, Hercules, CA, United States), amplification was performed in a CFX96™ Real-Time System (Bio-Rad). Primer sequences for the genes investigated are shown in **Table 1**. Results were standardized to the expression of the glyceraldehyde 3-phosphate dehydrogenase gene (*Gapdh*), and fold differences in the expression of each gene were calculated according to the ΔΔCT method with normalization to *Gapdh*.

Cell Cultures

Mouse embryonic palatal mesenchymal (MEPM) cells were isolated from secondary palatal shelves dissected from ICR mouse embryos at E13.5–14.0. The MEPM cells were a mixture of cells obtained from the anterior and posterior portions of the palatal shelves. MEPM cells were cultured in Dulbecco's Modified Eagle Medium/Nutrient Mixture F-12 (DMEM/F12; Gibco, Thermo Fisher Scientific) containing 10% fetal bovine serum (FBS; Gibco, Thermo Fisher Scientific) and 1% penicillin-streptomycin (Roche Diagnostics, Berlin, Germany). For stability, the medium was changed to FBS-free DMEM (Gibco, Thermo Fisher Scientific) containing 50 ng/mL recombinant human TGF-β3 (PeproTech, London, United Kingdom) or 100 ng/mL SHH (R&D Systems) for 0, 24, or 48 h. In some experiments, the cells were pre-treated with 10 μM SB203580 (a p38 inhibitor; Adipogen Life Sciences, San Diego, CA, United States) or 1.0 μM SIS3 (a Smad3 inhibitor; Cayman Chemical Company, Ann Arbor, MI, United States) for 24 h prior to the addition of TGF-β3.

O9-1 cells (Merck Millipore) were derived from mass cultures of Wnt1-Cre/R26R-GFP reporter-expressing cranial neural crest cells from E8.5 mouse embryos. O9-1 cells were seeded on a dish coated with Matrigel™ (Thermo Fisher Scientific)

[1]https://www.facebase.org/mouseanatomy/

TABLE 1 | Primers used for real-time polymerase chain reaction.

Gene	Primer sequences	
	Forward	**Reverse**
Glyceraldehyde 3-phosphate dehydrogenase (*Gapdh*)	5′–TGTGTCCGTCGTGGATCTGA–3′	5′–TTGCTGTTGAAGTCGCAGGAG–3′
Tenascin C (*Tnc*)	5′– GGAGCAAGCTGATCCAAACCA –3′	5′-CCAGTGCTTGAGTCTTGTCACCA-3′
Fibronectin (*Fn*)	5′–GTGGTCATTTCAGATGCGATTCA–3′	5′–ATTCCCGAGGCATGTGCAG–3′
Periostin (*Postn*)	5′–CAGTTGGAAATGATCAGCTCTTGG–3′	5′–CAATTTGGATCTTCGTCATTGCAG–3′
Type I collagen (*Col1*)	5′–GGGTCCCTCGACTCCTACA–3′	5′–TGTGTGCGATGACGTGCAAT–3′
Runt-related transcription factor-2 (*Runx2*)	5′–GCCCAGGCGTATTTCAGA–3′	5′–TGCCTGGCTCTTCTTACTGAG–3′
Osterix (*Osx*)	5′–GAAAGGAGGCACAAAGAAG–3′	5′–CACCAAGGAGTAGGTGTGTT–3′
Alkaline phosphatase (*Alp*)	5′–ATCTTTGGTCTGGCTCCCATG–3′	5′–TTTCCCGTTCACCGTCCAC–3′

and cultured in Complete ES Cell Medium containing 15% fetal bovine serum, mouse leukemia inhibitory factor (mLIF; Merck Millipore) and 25 ng/mL recombinant human basic fibroblast growth factor (rhbFGF; Kaken Pharmaceutical Co., Ltd, Tokyo, Japan). For stability, the medium was changed to FBS-free Minimum Essential Medium-α (Wako Pure Chemical Corporation, Osaka, Japan) containing 10 ng/mL recombinant human TGF-β3 (PeproTech) or 100 ng/mL SHH (R&D Systems) for 0, 24, or 48 h.

Enzyme-Linked Immunosorbent Assay (ELISA)

The concentration of TNC in the medium bathing cultured cells was measured using an ELISA kit (27767; IBL, Fujioka, Japan). Dilute samples of culture medium were added to 96-well plates and incubated for 1 h at 37°C. Horseradish peroxidase-conjugated mouse anti-TNC monoclonal antibody (clone 4F10TT, IBL, Fujioka, Japan) was added to each well and incubated for 30 min at 4°C. Substrate solution was then added to each well, and the mixture was incubated for 30 min at room temperature. Subsequently, stop solution was added to each well, and the level of TNC was determined with a microplate reader at 450 nm (ImmunoMini NJ-2300; NJ InterMed, Tokyo, Japan).

Statistical Analysis

Data are presented as the mean ± standard deviation. Comparisons between groups were made using the Mann–Whitney *U* test. A P-value < 0.05 was considered significant.

RESULTS

TNC Is Expressed More Strongly in the Posterior Palatal Shelves Than Tenascin-W (TNW) or Tenascin-X (TNX) During Palatal Development

Real-time PCR was used to investigate the mRNA expressions of TNC, TNX, and TNW in the anterior and posterior palatal shelves at three time points (E13.5, E14.5, and E15.5) during palatal development. The mRNA expression of TNC in the palatal shelves was greater than that of TNX or TNW (**Figure 1A**). Furthermore, TNC mRNA expression was significantly higher in the posterior palate than in the anterior palate at E15.5 (**Figure 1A**). Immunohistochemistry experiments were performed to examine the expression of TNC protein in the posterior palate. TNC was widely expressed in the palatal mesenchyme and underneath the palatal epithelium (**Figure 1B**). Evaluation of the immunostaining intensity along the anterior–posterior axis of the palatal shelves revealed a higher level of TNC expression in the posterior portion than in the middle or mid-posterior regions, and this trend was particularly evident at the later developmental stages of palatogenesis (E14.5 and E15.5; **Figure 1B**). Therefore, the immunohistologic observations support the results of the real-time PCR experiments.

TGF-β3 and SHH Induce TNC Expression in MEPM Cells *in vitro*

Based on our observation of strong TNC expression in the posterior palatal shelves, we speculated that TNC may play an important role in the development of the soft palate. Since TGF-β3 mutations are associated with cleft palate and bifid uvula in humans (Bertoli-Avella et al., 2015), we hypothesized that TGF-β regulates the expression of TNC in palatal mesenchyme. In cultured MEPM cells, TGF-β3 increased the expression of TNC mRNA and the secretion of TNC protein at 24 h and 48 h (**Figures 2A,B**). These effects of TGF-β3 were prevented by inhibitors of Smad3 or p38, which are known mediators of TGF-β signaling during palatal development (**Figures 2C,D**) (Iwata et al., 2011). Since it has been reported that the expression of SHH in palatal epithelium is diminished in mice deficient in TGF-β3 (Sasaki et al., 2007; Ozturk et al., 2013), we also hypothesized that SHH regulates the expression of TNC mRNA in palatal mesenchyme. SHH also enhanced the expression of TNC mRNA and secretion of TNC protein by MEPM cells at 48 h (**Figures 2E,F**).

Loss of TGF-β Signaling in the Palatal Epithelium Reduces TNC Expression in the Palatal Mesenchyme

Since the above findings support the possibility that TNC expression is regulated by TGF-β signaling and plays an important role in soft palate development, we performed immunohistochemistry experiments to evaluate TNC expression

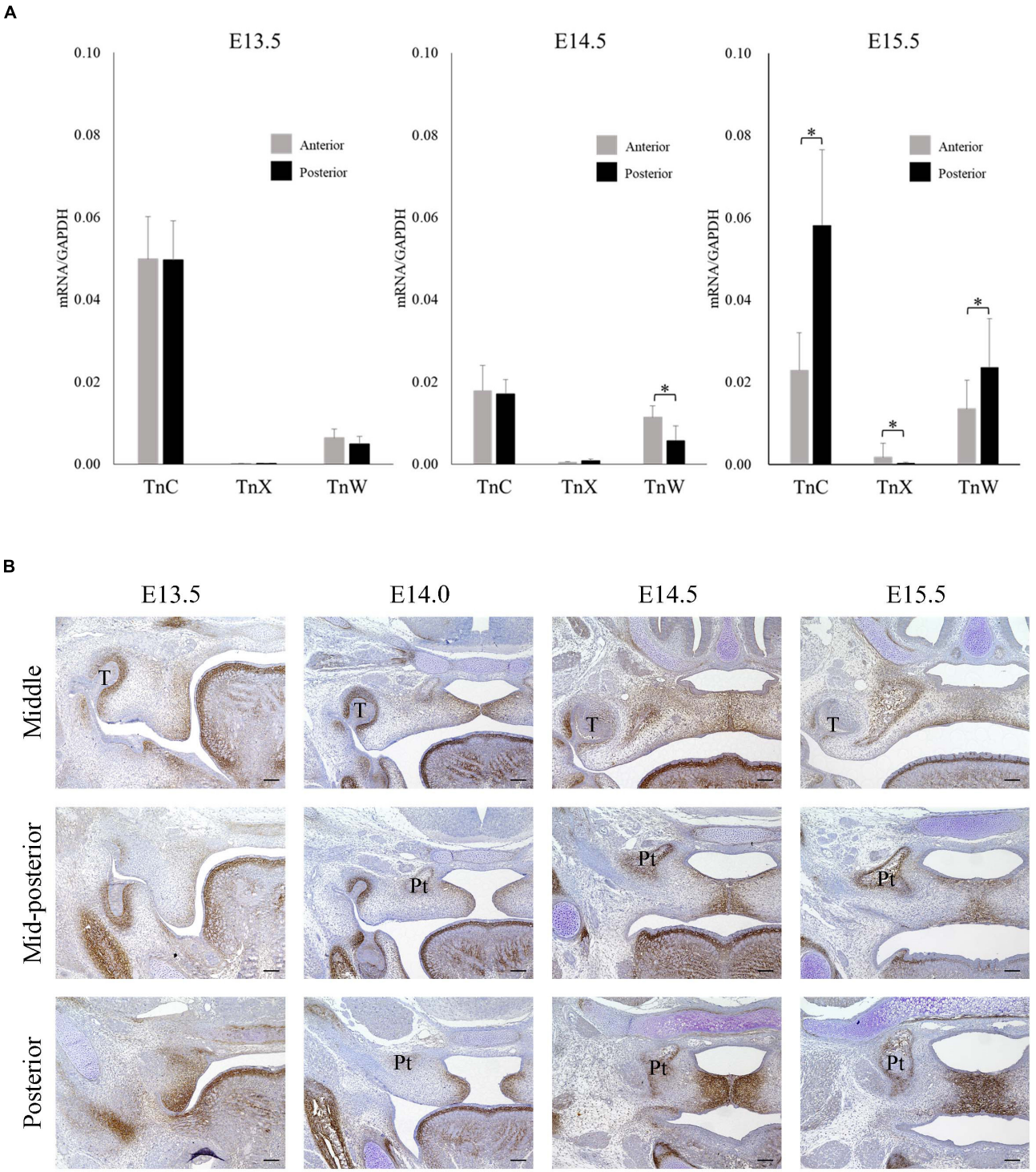

FIGURE 1 | Tenascin C expression during palatal development in mice between embryonic day 13.5 (E13.5) and E15.5. **(A)** The mRNA expressions of tenascin-C (TNC), tenascin-X (TNX), and tenascin-W (TNW) in the anterior and posterior palatal shelves at E13.5, E14.5, and E15.5 (real-time polymerase chain reaction). The mRNA expression of TNC was greater than that of TNX or TNW and significantly higher in the posterior palate than in the anterior palate at E15.5. Data are presented as the mean ± standard deviation ($n = 6$). The mRNA expressions were normalized to that of glyceraldehyde 3-phosphate dehydrogenase (GAPDH). $^*P < 0.05$. **(B)** Immunofluorescence staining of TNC protein in the middle, mid-posterior and posterior regions of the palatal shelves at E13.5, E14.0, E14.5, and E15.5. Stronger TnC expression was observed in the posterior palatal shelves than in the middle or mid-posterior regions, particularly at the later developmental stages. T, tooth germ; Pt, pterygoid process. Bar = 100 μm.

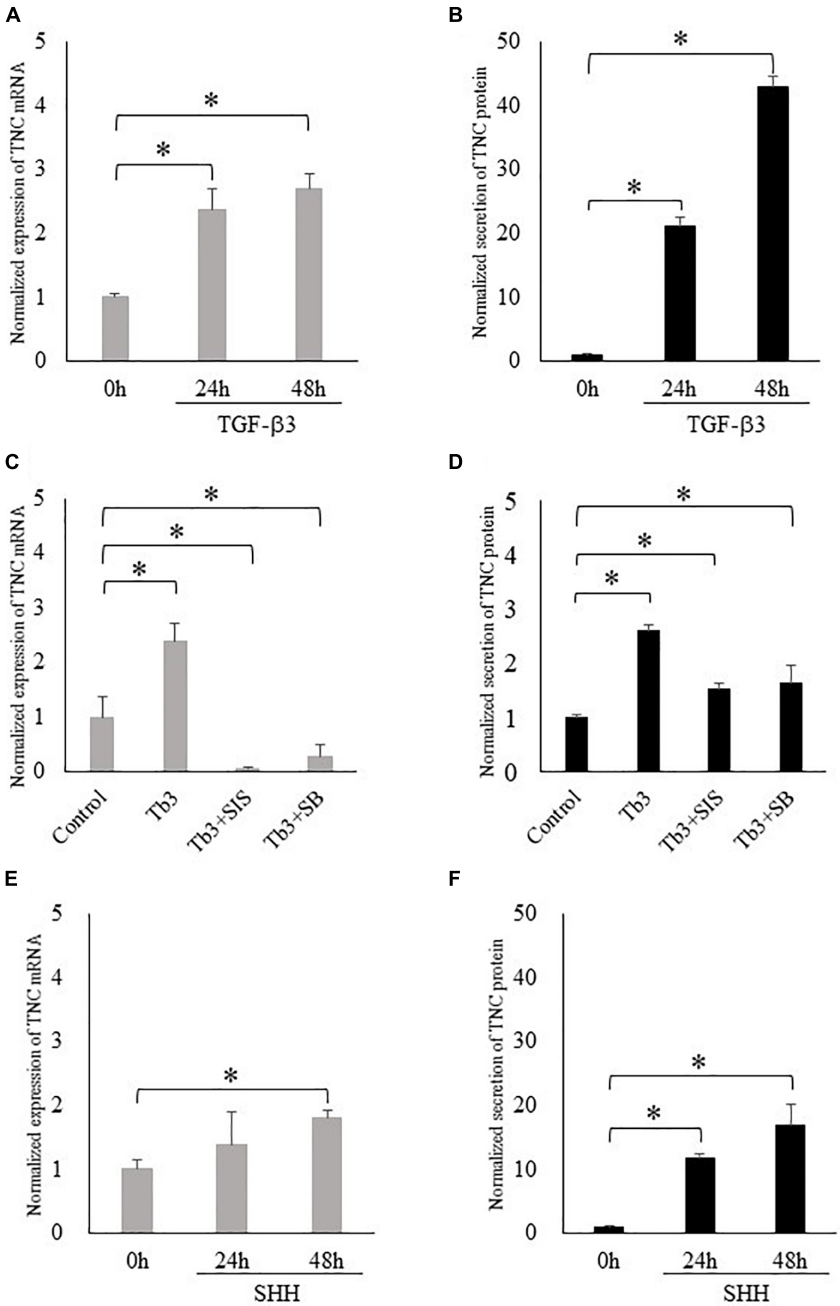

FIGURE 2 | Transforming growth factor-beta-3 (TGF-β3) and sonic hedgehog (SHH) increase the expression of tenascin-C (TNC) in mouse embryonic palatal mesenchymal (MEPM) cells (embryonic day 13.5–14.0). **(A,C,E)** The mRNA expression of tenascin-C (TNC) measured using real-time polymerase chain reaction. **(B,D,F)** The amount of TNC protein secreted into the culture medium measured by enzyme-linked immunosorbent assay. TGF-β3 increased the expression of TNC mRNA **(A)** and the secretion of TNC protein **(B)** by MEPM cells at 24 h and 48 h. **(C,D)** These effects of TGF-β3 (Tb3) were inhibited by a Smad3 inhibitor (Tb3 + SIS) and a p38 inhibitor (Tb3 + SB). SHH also enhanced the expression of TNC mRNA **(E)** and the secretion of TNC protein **(F)** by MEPM cells. Data are expressed as the mean ± standard deviation ($n = 4$) and were normalized to the 0 h or control values. $^*P < 0.05$.

in *Tgfbr2* conditional knockout mice that exhibit cleft palate. Interestingly, TNC expression was dramatically reduced in *K14-cre*;*Tgfbr2*$^{fl/fl}$ mice that lack the TGF-β type II receptor in palatal epithelial cells but not decreased in *Wnt1-cre*;*Tgfbr2*$^{fl/fl}$ mice that lack the TGF-β type II receptor in palatal mesenchymal cells (**Figure 3**). To facilitate orientation, **Supplementary Figure S1** presents lower-magnification images of HE-stained sections adjacent to those shown in **Figure 3**. *K14-cre*; *Tgfbr2*$^{fl/fl}$ mice exhibit a cleft soft palate caused by a defect in the disappearance of the medial edge epithelium (Xu et al.,

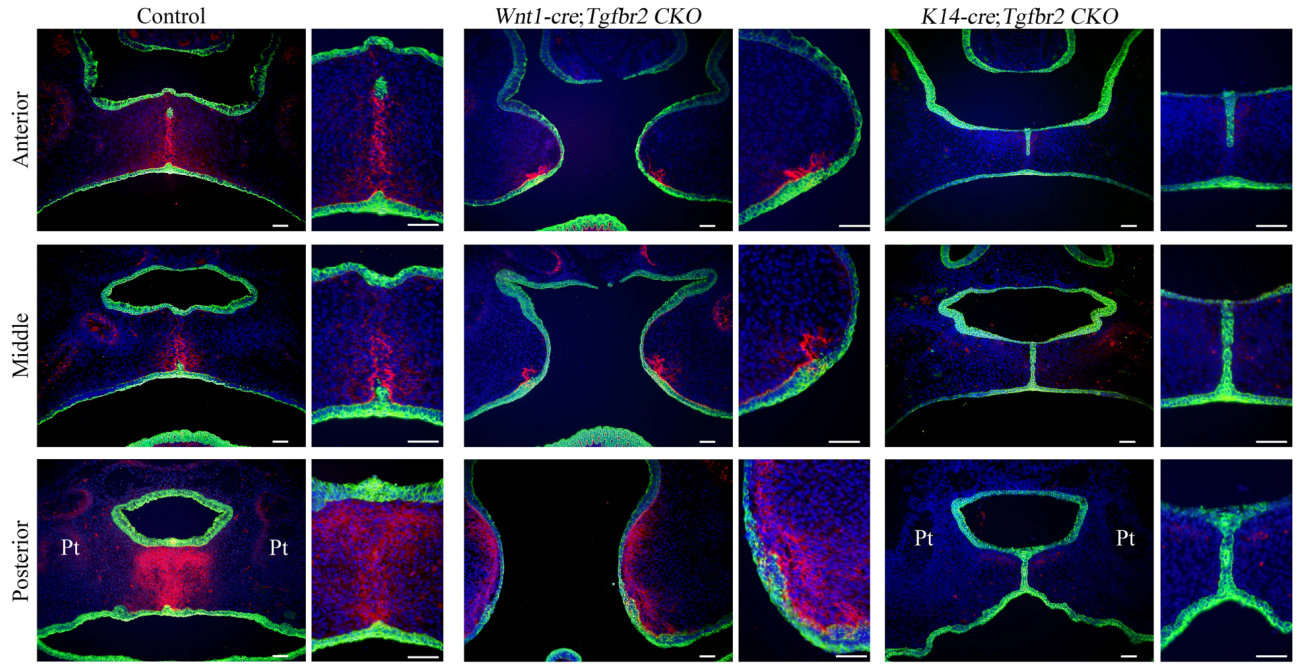

FIGURE 3 | Disruption of transforming growth factor-beta (TGF-β) signaling in the palatal epithelium reduces tenascin-C (TNC) expression in the palatal mesenchyme. The images show TNC (pink) and K14 (green) expression during palatal development in control mice, *Wnt1-cre*;*Tgfbr2*$^{fl/fl}$ mice (which lack the TGF-β type II receptor in palatal mesenchymal cells) and *K14-cre*;*Tgfbr2*$^{fl/fl}$ mice (which lack the TGF-β type II receptor in palatal epithelial cells) at embryonic day 15.5. Each narrow image is an enlarged view of part of the wider image to its left. Cell nuclei were stained blue with 4′,6-diamidino-2-phenylindole (DAPI). Pt, pterygoid process. Bar = 50 μm.

2006). These observations indicate that TGF-β signaling in the palatal epithelium plays an important role in the paracrine regulation of TNC expression in palatal mesenchyme. We also confirmed that *Tgfb3* mutant mice, which exhibit cleft palate because of a loss of TGF-β3 in the palatal epithelium, also lacked TNC expression in the palatal mesenchyme (data not shown).

The Effect of TGF-β and SHH in a Cranial Neural Crest Cell Line

During palatogenesis, TGF-β3 is expressed continuously in the medial edge epithelium along the entire anterior–posterior axis of the palate. By contrast, SHH does not show continuous expression; instead, SHH is found in the palatal rugae of the anterior hard palate during early palatal development and then expressed at a later stage in the posterior soft palate (Welsh and O'Brien, 2009). The differences in the spatiotemporal patterns of TGF-β3 and SHH expression in the palatal epithelium cannot explain the characteristic expression of TNC in the posterior region. Therefore, we investigated the functional significance of TGF-β and SHH signaling to palatal mesenchymal cells during palatogenesis, not only in terms of TNC expression but also with regard to cell differentiation or fate. O9-1 cells (a cranial neural crest cell line) were first cultured with medium containing mLIF and rhbFGF to prevent progression of differentiation and then challenged with TGF-β3 or SHH. TGF-β3 was found to induce the expression of TNC mRNA in O9-1 cells (real-time PCR; **Figure 4A**) and enhance the secretion of TNC protein by these cells (ELISA; **Figure 4B**). Surprisingly, SHH did not stimulate TNC mRNA expression (**Figure 4A**) or TNC protein secretion (**Figure 4B**) in O9-1 cells.

TGF-β Signaling Promotes Fibroblastic Differentiation and Inhibits Osteoblastic Differentiation of Cranial Neural Crest Cells

Because SHH was able to induce TNC expression in MEPM cells but not O9-1 cells, we hypothesized that the regulation of TNC expression by SHH signaling might depend on cell type. Visual inspection of the O9-1 cells revealed a morphologic change to a fibroblastic appearance after stimulation for 24 h with TGF-β3, whereas no obvious alteration in cell shape was observed after challenge with SHH. Real-time PCR demonstrated that O9-1 cells showed upregulation of fibroblastic markers, including fibronectin (**Figure 5A**) and periostin (**Figure 5B**), and downregulation of osteogenic markers, including osterix (**Figure 5E**) and alkaline phosphatase (**Figure 5F**), after stimulation with TGF-β3 for 24 h or 48 h. Interestingly, administration of SHH for 24 h or 48 h was without effect on fibroblastic and osteogenic marker expression (**Figure 5**). The above findings suggest that TGF-β3 can induce O9-1 cells to differentiate into fibroblastic cells, whereas SHH does not affect the differentiation of immature mesenchymal cells in the palatal shelves.

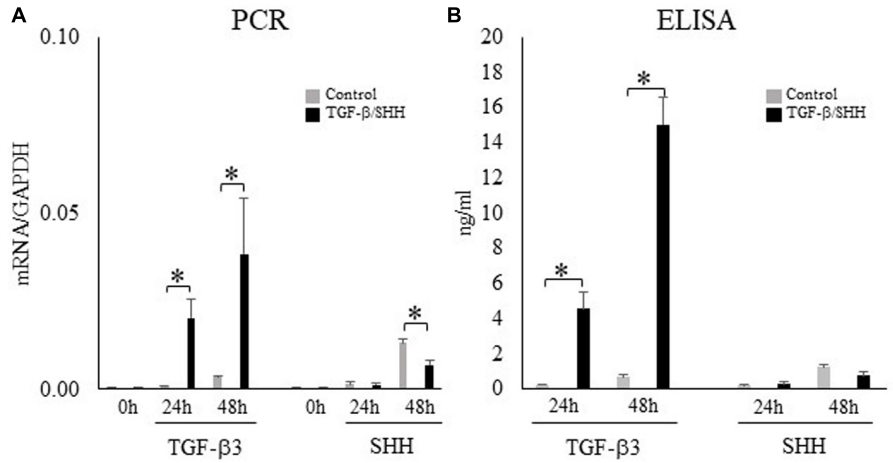

FIGURE 4 | Transforming growth factor-beta-3 (TGF-β3) but not sonic hedgehog (SHH) stimulates the expression of tenascin-C (TNC) mRNA and protein in O9-1 cells. **(A)** The mRNA expression of TNC in O9-1 cells cultured with or without TGF-β3 or SHH for 0 h, 24 h or 48 h (real-time polymerase chain reaction). The mRNA expressions were normalized to that of glyceraldehyde 3-phosphate dehydrogenase (GAPDH). **(B)** Secretion of TNC protein by O9-1 cells cultured with or without TGF-β3 or SHH for 24 h or 48 h (enzyme-linked immunosorbent assay). Data are expressed as the mean ± standard deviation ($n = 4$). *$P < 0.05$.

Loss of SHH Signaling in the Posterior Region of the Palatal Epithelium Leads to Decreased TNC Expression in the Posterior Palatal Mesenchyme

In view of the differing responses of O9-1 cells to TGF-β3 and SHH, we compared TNC expression in the posterior region of the palatal mesenchyme between SHH-deficient mice and wild-type mice. SHH expression in the palatal epithelium is restricted to the area of the rugae (Welsh and O'Brien, 2009; Xu et al., 2016). Remarkably, SHH expression in the posterior palatal epithelium is delayed compared with the middle portion because of restricted regulation by the SHH enhancer, MFCS4, in the posterior part of the palate and oropharyngeal region (Sagai et al., 2009). Therefore, we prepared compound heterozygous mice ($Shh^{-/+}$;$MFCS4^{+/-}$) in which SHH was only deleted in the posterior palatal shelves. Immunohistochemistry experiments demonstrated that TNC expression in the posterior region of the palatal shelf of $Shh^{-/+}$;$MFCS4^{+/-}$ mice was slightly reduced at E13.5 and completely lost at E15.0 (**Figure 6**). By contrast, TNC expression was detected in the anterior region of the palatal shelf of $Shh^{-/+}$;$MFCS4^{+/-}$ mice at both E13.5 and E15.0 (**Figure 6**). These results indicate that TNC expression in the posterior palatal mesenchyme is regulated by SHH signaling.

DISCUSSION

Recent progress in palatogenesis research has provided important insights into the genes responsible for cleft palate, and there has been particular interest in the role of spatiotemporal signaling between the anterior and posterior axis (Li et al., 2017). The NIH FaceBase consortium has produced a comprehensive review of the transcription factors, growth factors and receptors that are specifically expressed in the palatal region (Potter and Potter, 2015). Nevertheless, there are various types of cleft palate, and the mechanisms underlying submucous cleft palate and partial cleft palate remain incompletely understood.

Mutations of the genes encoding TGF-β ligands, Smads and their receptors have been reported as candidate mechanisms for cleft soft palate or bifid uvula in humans (Bertoli-Avella et al., 2015). Although TGF-β signaling is recognized to have particular significance in the posterior palatal mesenchyme, TGF-β3 is expressed continuously throughout the entire palatal epithelium (Taya et al., 1999). Furthermore, we have reported that Smad2 and Smad3, which are transcriptional factors involved in TGF-β signaling, are also activated in the palatal epithelium throughout the entire anterior–posterior axis (Higa et al., 2016). However, the phenotype of mice with conditional knockout of the TGF-β type I receptor (*K14-cre*;$Tgfbr1^{fl/fl}$) and TGF-β type II receptor (*K14-cre*;$Tgfbr2^{fl/fl}$) in the palatal epithelium is partial cleft of the posterior palatal shelves, with no developmental abnormality of the anterior portion. This apparent discrepancy raises the possibility that signaling between the palatal epithelium and mesenchyme varies along the anterior–posterior axis. In palatal mesenchyme, many growth factors and transcriptional factors show differential expression along the anterior–posterior axis, and this is considered important for the development of the palate (Smith et al., 2012). However, the role of ECM proteins along the anterior–posterior axis has not been characterized previously. TGF-β is known as an important regulator of ECM production. Therefore, we investigated how the expression pattern of an ECM component (TNC) was influenced by TGF-β signaling and how this was related to cell fate, which is relevant to the formation of bone in the anterior palate and connective tissue in the posterior palate.

TNC confers 'anti-adhesive' properties to the ECM and plays an important role in embryonic morphogenesis and tissue repair during wound healing. TNC exhibits characteristic expression in the posterior end of the palatal shelves during palatogenesis.

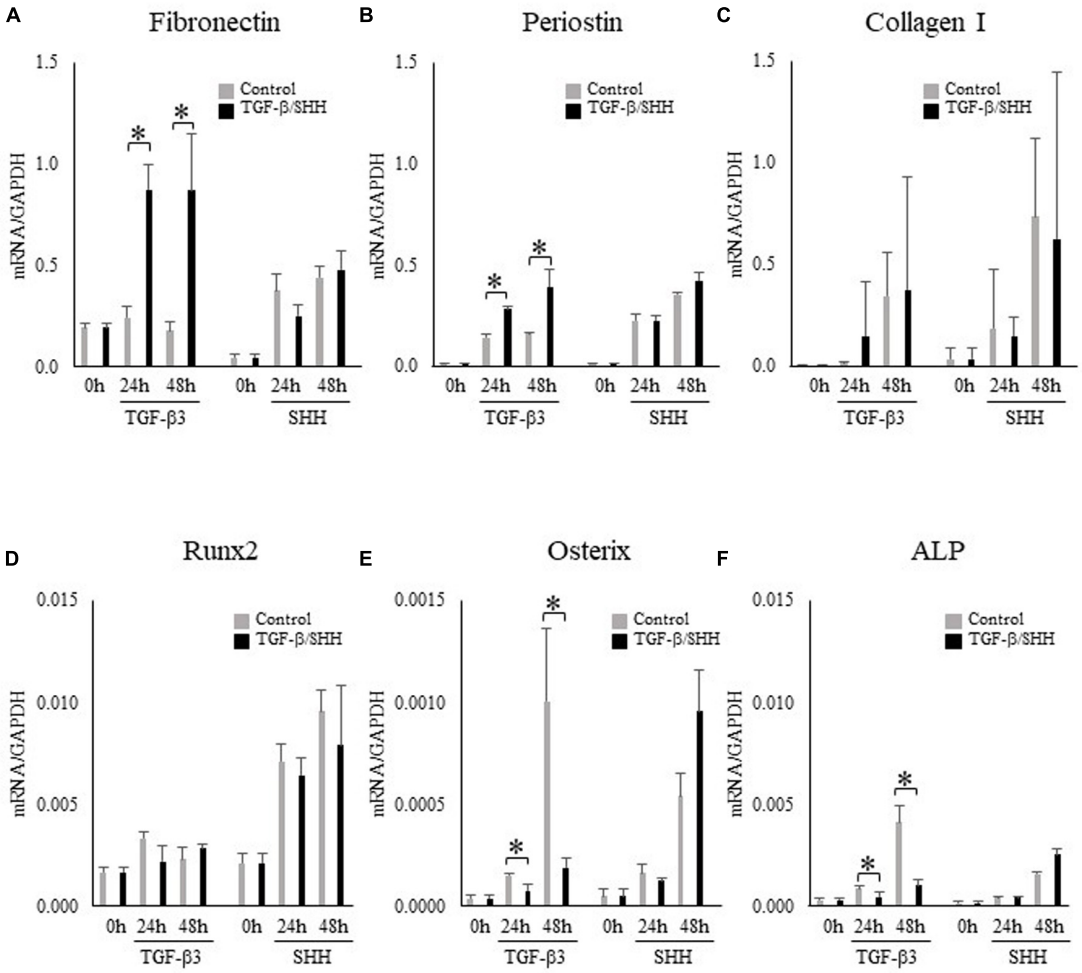

FIGURE 5 | Effects of transforming growth factor-beta-3 (TGF-β3) and sonic hedgehog (SHH) on the expression of fibroblastic and osteoblastic cell markers in O9-1 cells. **(A–C)** The mRNA expressions of the fibroblastic cell markers, fibronectin **(A)**, periostin **(B)** and type I collagen **(C)** in O9-1 cells. **(D–F)** The mRNA expressions of the osteoblastic cell markers Runx2 **(D)**, osterix **(E)** and alkaline phosphatase (ALP) **(F)** in O9-1 cells. The mRNA expressions were normalized to that of glyceraldehyde 3-phosphate dehydrogenase (GAPDH). Data are expressed as the mean ± standard deviation ($n = 4$). $^*P < 0.05$.

In the present study, we demonstrated that TGF-β3 upregulated TNC expression in primary MEPM cells and O9-1 cells, both of which are derived from the cranial neural crest. It has been reported that a binding element in the proximal region of the TNC promoter mediates the responsiveness to TGF-β, which involves Smad3/4, Sp1, Ets1, and CBP/p300 (Jinnin et al., 2004). The present study investigated the direct transcriptional regulation of TNC expression by TGF-β. However, somewhat unexpectedly, we found that TNC expression was dramatically reduced in *K14-cre*;*Tgfbr2*$^{fl/fl}$ mice (which lack the TGF-β type II receptor in palatal epithelial cells) but not decreased in *Wnt1-cre*;*Tgfbr2*$^{fl/fl}$ mice (which lack the TGF-β type II receptor in palatal mesenchymal cells). Iwata et al. (2012) showed that loss of the TGF-β type II receptor in the palatal mesenchyme led to upregulation of the expression of TGF-β2 and acceleration of a non-canonical TGF-β signaling pathway via a TGF-β type I/III receptor complex. We speculate that TNC expression in *Wnt1-cre*;*Tgfbr2*$^{fl/fl}$ mice may have been maintained by this non-canonical TGF-β signaling pathway. Since *K14-cre*;*Tgfbr2*$^{fl/fl}$ mice exhibit partial cleft of the posterior palate, this suggests that the development of the anterior hard palatal mesenchyme is not affected by the loss of TNC expression caused by defective TGF-β signaling in the palatal epithelium.

Paracrine regulation of TNC expression in the posterior palatal mesenchyme by TGF-β in the posterior palatal epithelium requires the secretion of a TGF-β-regulated factor from the epithelium that targets genes in the mesenchyme. Therefore, we explored the possible role of SHH signaling in palatal epithelium (Welsh and O'Brien, 2009; Lee et al., 2011), since the expression of SHH in palatal rugae is diminished in mice deficient in TGF-β3 (Sasaki et al., 2007; Ozturk et al., 2013). Interestingly, we found that SHH induced TNC expression in primary cells from embryonic palatal mesenchyme (MEPM cells) but not in O9-1 cells, which are undifferentiated cranial neural crest cells. Since the primary MEPM cells were harvested on E13.5–E14.0, they would have been a complex population of cells such as

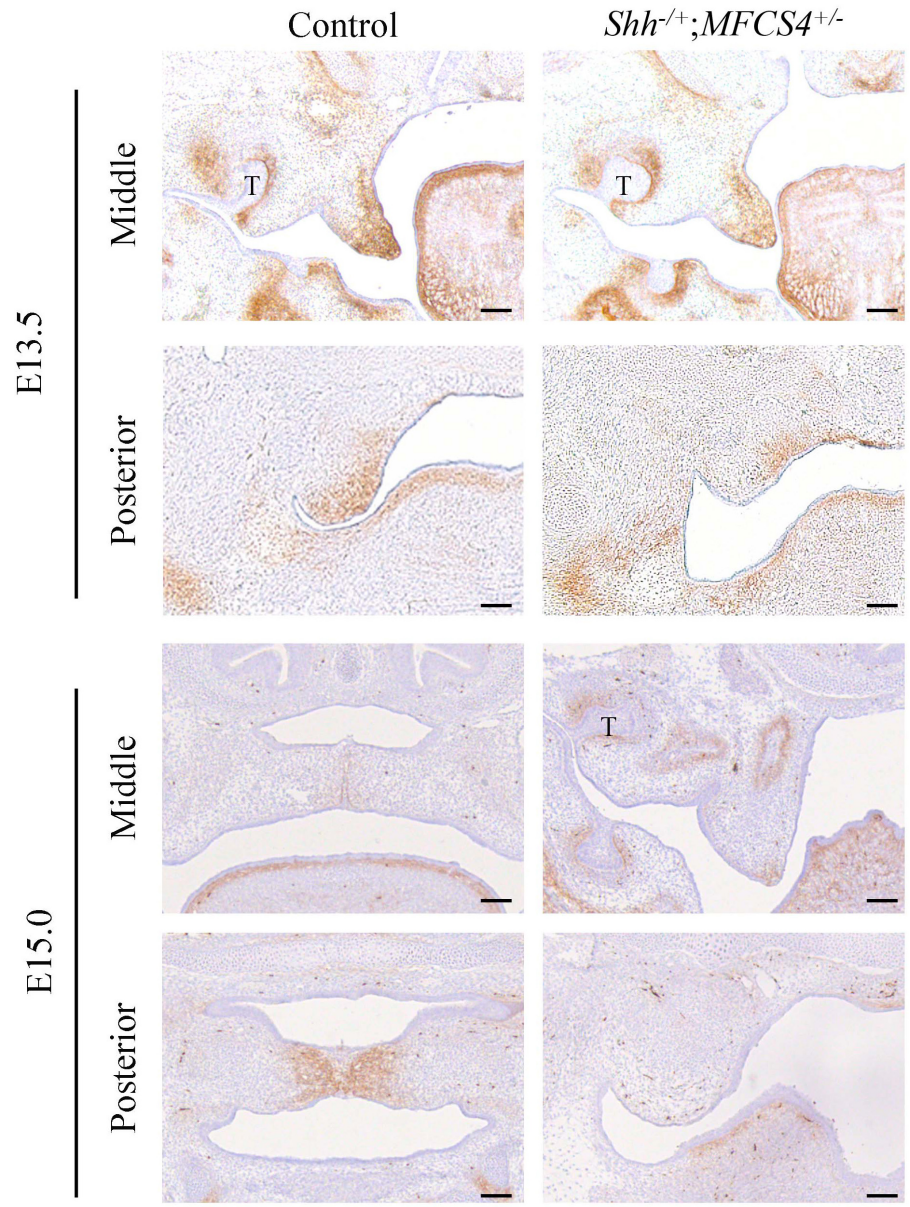

FIGURE 6 | Tenascin-C (TNC) expression during palatal development in *Shh*$^{-/+}$;*MFCS4*$^{+/-}$ mice. The expression of TNC in the anterior and posterior palatal shelves at embryonic day 13.5 (E13.5) and E15.0 was evaluated using immunohistochemistry techniques. T, tooth germ. Bar = 100 μm.

osteogenic and fibrogenic progenitors. We speculate that SHH induces TNC expression in fibrogenic cells but not immature cells. This would explain the lack of effect of SHH on TNC expression in O9-1 cells, which were maintained as immature cells before stimulation with SHH. Furthermore, SHH had no effect on the expression of osteoblastic and fibroblastic markers in O9-1 cells. Based on the above observations, we suggest that SHH does not influence the determination of cell fate during the early embryonic developmental stage but can do so in palatal mesenchyme at a later developmental stage. The above findings are also consistent with the lack of TNC expression in *Shh*$^{-/+}$;*MFCS4*$^{+/-}$ mice, which have delayed expression of SHH in the posterior region of the palatal shelves as compared with the anterior and middle regions (Sagai et al., 2009). We generated these compound heterozygous mice to avoid early embryonic lethality, utilizing the fact that MFCS4, an enhancer of SHH, is expressed only in the region of the soft palate. Interestingly, homozygous MFCS4 mutant mice have soft palates that are shortened in length (Sagai et al., 2009), indicating that deficiency of SHH in the posterior palatal epithelium impairs the growth of the soft palate but does not affect palatal fusion. The regulation of TNC expression by SHH signaling in the posterior soft portion during the later stages of palatogenesis may also affect the development of the palatal muscles via actions

on myofibrogenic cells. More recently, Li et al. (2018) reported that *K14-cre*;*R26SmoM2* mice with constitutive activation of SHH signaling in the palatal epithelium exhibit a submucous cleft palate. The authors suggested that constitutive activation of hedgehog signaling resulted in dysfunction of the p63/Irf6 regulatory loop that is necessary for the disappearance of the medial edge epithelium during fusion of the palatal shelves. However, the study of Li et al. (2018) did not consider the role of SHH signaling in palatal mesenchyme.

The Foxf2 transcriptional factor is a downstream target of SHH expression in palatal epithelium, which in turn is regulated by FGF-10 expressed by palatal mesenchyme. Furthermore, $Foxf2^{-/-}$ mice show downregulated expression of TGF-β ligands and TNC as well as reduced phosphorylation of Smad2/3 (Nik et al., 2016). We have also confirmed that TGF-β3 is expressed in the posterior palatal epithelium in $Shh^{-/+}$;$MFCS4^{+/-}$ mice using *in situ* hybridization experiments (data not shown). We initially considered that SHH may be a downstream target of TGF-β3 in palatal epithelium for regulation of TNC expression. However, we found that *pCag-CreERTM*;$Shh^{fl/fl}$ mice exhibit decreased TGF-β3 expression in skeletal muscle and reduced phosphorylation of Smad2/3 (Okuhara et al., 2019). This raises the possibility that both TGF-β3 and SHH act as major mediators of epithelial–mesenchymal cross-talk during palatogenesis, with this signaling loop regulating proliferation, migration and ECM deposition in the palatal mesenchyme. Even partial collapse of this signaling loop would impair normal palatogenesis, and the regulation of this loop may be more sensitive to disturbance in the posterior palatal epithelium.

Soft palate development is thought to involve many different growth factors including Wnt and FGF (Janeckova et al., 2019). It has been reported that Wnt-β-catenin signaling is disrupted in $Tgfbr2^{fl/fl}$;*K14-Cre* mice by the upregulated expression of Dickkopf-related protein-1 (Dkk1) and Dkk4 (Iwata et al., 2014) and that Wnt5a induces the expression of TNC in osteogenic cells (Morgan et al., 2011). Based on the above reports, it is possible that osteoblastic and fibroblastic cell differentiation may involve competition between Wnt and TGF signaling through TNC expression.

On the other hand, Rice et al. (2014) have shown that FGF-10 is expressed in the palatal mesenchyme and that exogenous FGF-10 induces SHH expression in the palatal epithelium in wild-type but not $Fgfr2b^{-/-}$ mutant mice. Furthermore, $Fgf10^{-/-}$ and $Fgfr2b^{-/-}$ mutant mice show altered patterns of TGF-β3 and SHH expression in the palatal epithelium (Alappat et al., 2005; Rice et al., 2014). Since FGF receptor-2b is expressed in palatal epithelium, epithelial–mesenchymal interactions may involve FGF-10–SHH–TNC signaling in addition to the TGF-β3–SHH–TNC pathway described in the present study.

TNC functions as an adhesion-modulating ECM protein that inhibits the adhesive effects of fibronectin (Chiquet-Ehrismann and Chiquet, 2003). Fibronectin is expressed ubiquitously in palatal mesenchyme (Tang et al., 2015). The orientation/alignment of fibronectin fibers during palatal development is important for morphologic changes in the palatal shelves such as the elevation process. The anti-adhesive function of TNC in fibronectin-expressing regions might play a role in the regulation of cell migration or aggregation that contributes to the changes in palatal shelf morphology. The initial studies of TNC-knockout mice did not report any obvious developmental abnormalities such as cleft palate (Saga et al., 1992; Forsberg et al., 1996), suggesting the existence of mechanisms that compensate for the loss of TNC. In the present study, we also detected TNW expression in the palatal shelves (**Figure 1A**). Therefore, TNW might be one candidate that compensates for a lack of TNC during palatal development. Furthermore, we also speculate that the orientation of the palatal muscles might be disrupted in TNC-knockout mice. Additionally, TNC function is required for recovery from pathologic events such as wounds, fibrosis or inflammation (Tamaoki et al., 2005). In future, TNC may be an important biomaterial for use in reconstruction of the soft palate using regenerative medicine techniques. Further studies are needed to clarify the role of TNC in posterior palatogenesis.

DATA AVAILABILITY STATEMENT

The datasets generated for this study are available on request to the corresponding author.

ETHICS STATEMENT

The animal study was reviewed and approved by Animal Experiment Committee of Fukuoka Dental College, Fukuoka, Japan (nos. 17012 and 18005).

AUTHOR CONTRIBUTIONS

KOk contributed to the conception and design of the study SOh, KOg, SOk, MT-N, ST, and MR contributed to data acquisition. MO, SI, and TS contributed to the analysis and interpretation of the results. KOk contributed to the writing of the manuscript. All authors read and approved the submitted version.

FUNDING

This study was supported in part by Grant in-Aid for KIBAN C (No. 18K09849 to KOk) from the Japan Society for the Promotion of Science (JSPS).

ACKNOWLEDGMENTS

We thank Prof. Yang Chai and Prof. Toshihiko Shiroishi for kindly providing us with *Wnt1-Cre*; $Tgfbr2^{fl/fl}$, *K14-Cre*; $Tgfbr2^{fl/fl}$, and $Shh^{-/+}$; $MFCS4^{+/-}$ mice. We thank www.oxmedcomms.com for writing assistance.

SUPPLEMENTARY MATERIAL

The Supplementary Material for this article can be found online at: https://www.frontiersin.org/articles/10.3389/fphys.2020.00532/full#supplementary-material

REFERENCES

Alappat, S. R., Zhang, Z., Suzuki, K., Zhang, X., Liu, H., Jiang, R., et al. (2005). The cellular and molecular etiology of the cleft secondary palate in Fgf10 mutant mice. *Dev. Biol.* 277, 102–113. doi: 10.1016/j.ydbio.2004.09.010

Amano, T., Sagai, T., Tanabe, H., Mizushina, Y., Nakazawa, H., and Shiroishi, T. (2009). Chromosomal dynamics at the Shh locus: limb bud-specific differential regulation of competence and active transcription. *Dev. Cell* 16, 47–57. doi: 10.1016/j.devcel.2008.11.011

Andl, T., Ahn, K., Kairo, A., Chu, E. Y., Wine-Lee, L., Reddy, S. T., et al. (2004). Epithelial Bmpr1a regulates differentiation and proliferation in postnatal hair follicles and is essential for tooth development. *Development* 131, 2257–2268. doi: 10.1242/dev.01125

Bertoli-Avella, A. M., Gillis, E., Morisaki, H., Verhagen, J. M. A., de Graaf, B. M., van de Beek, G., et al. (2015). Mutations in a TGF-βeta ligand, TGFB3, cause syndromic aortic aneurysms and dissections. *J. Am. Coll. Cardiol.* 65, 1324–1336. doi: 10.1016/j.jacc.2015.01.040

Bitgood, M. J., and McMahon, A. P. (1995). Hedgehog and Bmp genes are coexpressed at many diverse sites of cell-cell interaction in the mouse embryo. *Dev. Biol.* 172, 126–138. doi: 10.1006/dbio.1995.0010

Chai, Y., Jiang, X., Ito, Y., Bringas, P. Jr., Han, J., Rowitch, D. H., et al. (2000). Fate of the mammalian cranial neural crest during tooth and mandibular morphogenesis. *Development* 127, 1671–1679.

Chiquet, M., Blumer, S., Angelini, M., Mitsiadis, T. A., and Katsaros, C. (2016). Mesenchymal remodeling during palatal shelf elevation revealed by extracellular matrix and F-Actin expression patterns. *Front. Physiol.* 7:392. doi: 10.3389/fphys.2016.00392

Chiquet-Ehrismann, R., and Chiquet, M. (2003). Tenascins: regulation and putative functions during pathological stress. *J. Pathol.* 200, 488–499. doi: 10.1002/path.1415

Chiquet-Ehrismann, R., Orend, G., Chiquet, M., Tucker, R. P., and Midwood, K. S. (2014). Tenascins in stem cell niches. *Matrix Biol.* 37, 112–123. doi: 10.1016/j.matbio.2014.01.007

Chiquet-Ehrismann, R., and Tucker, R. P. (2011). Tenascins and the importance of adhesion modulation. *Cold Spring Harb. Perspect. Biol.* 3:a004960. doi: 10.1101/cshperspect.a004960

Chytil, A., Magnuson, M. A., Wright, C. V., and Moses, H. L. (2002). Conditional inactivation of the TGF-βeta type II receptor using Cre:Lox. *Genesis* 32, 73–75. doi: 10.1002/gene.10046

Dassule, H. R., Lewis, P., Bei, M., Maas, R., and McMahon, A. P. (2000). Sonic hedgehog regulates growth and morphogenesis of the tooth. *Development* 127, 4775–4785.

Dudas, M., Kim, J., Li, W. Y., Nagy, A., Larsson, J., Karlsson, S., et al. (2006). Epithelial and ectomesenchymal role of the type I TGF-βeta receptor ALK5 during facial morphogenesis and palatal fusion. *Dev. Biol.* 296, 298–314. doi: 10.1016/j.ydbio.2006.05.030

Forsberg, E., Hirsch, E., Frohlich, L., Meyer, M., Ekblom, P., Aszodi, A., et al. (1996). Skin wounds and severed nerves heal normally in mice lacking tenascin-C. *Proc. Natl. Acad. Sci. U.S.A.* 93, 6594–6599. doi: 10.1073/pnas.93.13.6594

Grimaldi, A., Parada, C., and Chai, Y. (2015). A comprehensive study of soft palate development in mice. *PLoS One* 10:e0145018. doi: 10.1371/journal.pone.0145018

Hammond, N. L., Brookes, K. J., and Dixon, M. J. (2018). Ectopic hedgehog signaling causes cleft palate and defective osteogenesis. *J. Dent. Res.* 97, 1485–1493. doi: 10.1177/0022034518785336

Hayashi, S., and McMahon, A. P. (2002). Efficient recombination in diverse tissues by a tamoxifen-inducible form of Cre: a tool for temporally regulated gene activation/inactivation in the mouse. *Dev. Biol.* 244, 305–318. doi: 10.1006/dbio.2002.0597

Higa, A., Oka, K., Kira-Tatsuoka, M., Tamura, S., Itaya, S., Toda, M., et al. (2016). Intracellular signaling pathway activation via TGF-β differs in the anterior and posterior axis during palatal development. *J. Hard Tissue Biol.* 25, 195–204. doi: 10.2485/jhtb.25.195

Ito, Y., Yeo, J. Y., Chytil, A., Han, J., Bringas, P. Jr., Nakajima, A., et al. (2003). Conditional inactivation of Tgfbr2 in cranial neural crest causes cleft palate and calvaria defects. *Development* 130, 5269–5280. doi: 10.1242/dev.00708

Iwata, J., Hacia, J. G., Suzuki, A., Sanchez-Lara, P. A., Urata, M., and Chai, Y. (2012). Modulation of noncanonical TGF-βeta signaling prevents cleft palate in Tgfbr2 mutant mice. *J. Clin. Invest.* 122, 873–885. doi: 10.1172/JCI61498

Iwata, J., Parada, C., and Chai, Y. (2011). The mechanism of TGF-βeta signaling during palate development. *Oral Dis.* 17, 733–744. doi: 10.1111/j.1601-0825.2011.01806.x

Iwata, J., Suzuki, A., Yokota, T., Ho, T. V., Pelikan, R., Urata, M., et al. (2014). TGFβ regulates epithelial-mesenchymal interactions through WNT signaling activity to control muscle development in the soft palate. *Development* 141, 909–917. doi: 10.1242/dev.103093

Janeckova, E., Feng, J., Li, J., Rodriguez, G., and Chai, Y. (2019). Dynamic activation of Wnt, Fgf, and Hh signaling during soft palate development. *PLoS One* 14:e0223879. doi: 10.1371/journal.pone.0223879

Jinnin, M., Ihn, H., Asano, Y., Yamane, K., Trojanowska, M., and Tamaki, K. (2004). Tenascin-C upregulation by transforming growth factor-beta in human dermal fibroblasts involves Smad3, Sp1, and Ets1. *Oncogene* 23, 1656–1667. doi: 10.1038/sj.onc.1207064

Lan, Y., and Jiang, R. (2009). Sonic hedgehog signaling regulates reciprocal epithelial-mesenchymal interactions controlling palatal outgrowth. *Development* 136, 1387–1396. doi: 10.1242/dev.028167

Lee, J. M., Miyazawa, S., Shin, J. O., Kwon, H. J., Kang, D. W., Choi, B. J., et al. (2011). Shh signaling is essential for rugae morphogenesis in mice. *Histochem. Cell Biol.* 136, 663–675. doi: 10.1007/s00418-011-0870-7

Li, C., Lan, Y., and Jiang, R. (2017). Molecular and cellular mechanisms of palate development. *J. Dent. Res.* 96, 1184–1191. doi: 10.1177/0022034517703580

Li, J., Yuan, Y., He, J., Feng, J., Han, X., Jing, J., et al. (2018). Constitutive activation of hedgehog signaling adversely affects epithelial cell fate during palatal fusion. *Dev. Biol.* 441, 191–203. doi: 10.1016/j.ydbio.2018.07.003

Morgan, J. M., Wong, A., Yellowley, C. E., and Genetos, D. C. (2011). Regulation of tenascin expression in bone. *J. Cell. Biochem.* 112, 3354–3363. doi: 10.1002/jcb.23265

Nik, A. M., Johansson, J. A., Ghiami, M., Reyahi, A., and Carlsson, P. (2016). Foxf2 is required for secondary palate development and Tgfbeta signaling in palatal shelf mesenchyme. *Dev. Biol.* 415, 14–23. doi: 10.1016/j.ydbio.2016.05.013

Oka, K., Honda, M. J., Tsuruga, E., Hatakeyama, Y., Isokawa, K., and Sawa, Y. (2012). Roles of collagen and periostin expression by cranial neural crest cells during soft palate development. *J. Histochem. Cytochem.* 60, 57–68. doi: 10.1369/0022155411427059

Okuhara, S., Birjandi, A. A., Adel Al-Lami, H., Sagai, T., Amano, T., Shiroishi, T., et al. (2019). Temporospatial sonic hedgehog signalling is essential for neural crest-dependent patterning of the intrinsic tongue musculature. *Development* 146:dev180075. doi: 10.1242/dev.180075

Ozturk, F., Li, Y., Zhu, X., Guda, C., and Nawshad, A. (2013). Systematic analysis of palatal transcriptome to identify cleft palate genes within TGFbeta3-knockout mice alleles: RNA-Seq analysis of TGFbeta3 Mice. *BMC Genomics* 14:113. doi: 10.1186/1471-2164-14-113

Paiva, K. B. S., Maas, C. S., Dos Santos, P. M., Granjeiro, J. M., and Letra, A. (2019). Extracellular matrix composition and remodeling: current perspectives on secondary palate formation, cleft lip/palate, and palatal reconstruction. *Front. Cell Dev. Biol.* 7:340. doi: 10.3389/fcell.2019.00340

Potter, A. S., and Potter, S. S. (2015). Molecular anatomy of palate development. *PLoS One* 10:e0132662. doi: 10.1371/journal.pone.0132662

Rice, R., Connor, E., and Rice, D. P. (2006). Expression patterns of Hedgehog signalling pathway members during mouse palate development. *Gene Expr. Patterns* 6, 206–212. doi: 10.1016/j.modgep.2005.06.005

Rice, R., Spencer-Dene, B., Connor, E. C., Gritli-Linde, A., McMahon, A. P., Dickson, C., et al. (2014). Disruption of Fgf10/Fgfr2b-coordinated epithelial-mesenchymal interactions causes cleft palate. *J. Clin. Invest.* 113, 1692–1700. doi: 10.1172/JCI20384

Saga, Y., Yagi, T., Ikawa, Y., Sakakura, T., and Aizawa, S. (1992). Mice develop normally without tenascin. *Genes Dev.* 6, 1821–1831. doi: 10.1101/gad.6.10.1821

Sagai, T., Amano, T., Tamura, M., Mizushina, Y., Sumiyama, K., and Shiroishi, T. (2009). A cluster of three long-range enhancers directs regional Shh expression in the epithelial linings. *Development* 136, 1665–1674. doi: 10.1242/dev.032714

Sasaki, Y., O'Kane, S., Dixon, J., Dixon, M. J., and Ferguson, M. W. (2007). Temporal and spatial expression of Pax9 and Sonic hedgehog during development of normal mouse palates and cleft palates in TGF-βeta3 null embryos. *Arch. Oral Biol.* 52, 260–267. doi: 10.1016/j.archoralbio.2006.09.012

Smith, T. M., Lozanoff, S., Iyyanar, P. P., and Nazarali, A. J. (2012). Molecular signaling along the anterior-posterior axis of early palate development. *Front. Physiol.* 3:488. doi: 10.3389/fphys.2012.00488

Tamaoki, M., Imanaka-Yoshida, K., Yokoyama, K., Nishioka, T., Inada, H., Hiroe, M., et al. (2005). Tenascin-C regulates recruitment of myofibroblasts during tissue repair after myocardial injury. *Am. J. Pathol.* 167, 71–80. doi: 10.1016/S0002-9440(10)62954-9

Tang, Q., Li, L., Jin, C., Lee, J. M., and Jung, H. S. (2015). Role of region-distinctive expression of Rac1 in regulating fibronectin arrangement during palatal shelf elevation. *Cell Tissue Res.* 361, 857–868. doi: 10.1007/s00441-015-2169-9

Taya, Y., O'Kane, S., and Ferguson, M. W. (1999). Pathogenesis of cleft palate in TGF-βeta3 knockout mice. *Development* 126, 3869–3879.

Welsh, I. C., and O'Brien, T. P. (2009). Signaling integration in the rugae growth zone directs sequential SHH signaling center formation during the rostral outgrowth of the palate. *Dev. Biol.* 336, 53–67. doi: 10.1016/j.ydbio.2009.09.028

Xu, J., Liu, H., Lan, Y., Aronow, B. J., Kalinichenko, V. V., and Jiang, R. (2016). A Shh-Foxf-Fgf18-Shh molecular circuit regulating palate development. *PLoS Genet.* 12:e1005769. doi: 10.1371/journal.pgen.1005769

Xu, X., Han, J., Ito, Y., Bringas, P. Jr., Urata, M. M., and Chai, Y. (2006). Cell autonomous requirement for Tgfbr2 in the disappearance of medial edge epithelium during palatal fusion. *Dev. Biol.* 297, 238–248. doi: 10.1016/j.ydbio.2006.05.014

Yun, S. M., Kim, S. H., and Kim, E. H. (2019). The molecular mechanism of transforming growth factor-beta signaling for intestinal fibrosis: a mini-review. *Front. Pharmacol.* 10:162. doi: 10.3389/fphar.2019.00162

Conflict of Interest: The authors declare that the research was conducted in the absence of any commercial or financial relationships that could be construed as a potential conflict of interest.

frontiers in Physiology

ORIGINAL RESEARCH
published: 03 July 2020
doi: 10.3389/fphys.2020.00698

Mesenchymal Bmp7 Controls Onset of Tooth Mineralization: A Novel Way to Regulate Molar Cusp Shape

*Zeba Malik[1], Daniela M. Roth[1], Farah Eaton[1], Jessica M. Theodor[2] and Daniel Graf[1,3]**

[1] School of Dentistry, Faculty of Medicine and Dentistry, University of Alberta, Edmonton, AB, Canada, [2] Department of Biological Sciences, University of Calgary, Calgary, AB, Canada, [3] Department of Medical Genetics, Faculty of Medicine and Dentistry, University of Alberta, Edmonton, AB, Canada

OPEN ACCESS

Edited by:
Abigail Saffron Tucker, King's College London, United Kingdom

Reviewed by:
Paul Sharpe, King's College London, United Kingdom
Yiping Chen, Tulane University, United States

***Correspondence:**
Daniel Graf
dgraf@ualberta.ca

Specialty section:
This article was submitted to Craniofacial Biology and Dental Research, a section of the journal Frontiers in Physiology

Received: *20 April 2020*
Accepted: *28 May 2020*
Published: *03 July 2020*

Citation:
Malik Z, Roth DM, Eaton F, Theodor JM and Graf D (2020) Mesenchymal Bmp7 Controls Onset of Tooth Mineralization: A Novel Way to Regulate Molar Cusp Shape. Front. Physiol. 11:698. doi: 10.3389/fphys.2020.00698

Investigating the molecular basis for tooth shape variation provides an important glimpse into the evolution of tooth function. We recently showed that loss of mesenchymal BMP7 is sufficient to alter morphology and function of the toothrow. Here we report on the underlying mechanism. Expression of mesenchymal Bmp7 is observed at sites where mineralization is initiated, in tooth cusps of developing molars. Neural crest-specific deletion of *Bmp7* ($Bmp7^{ncko}$) resulted in a complete lack of dentin/enamel formation at birth, the time when mineralization is normally initiated in the upper molars, similar to what was observed in $Bmp2^{ncko}$ mice. Unlike loss of *Bmp2*, loss of *Bmp7* did not affect odontoblast polarization and did not significantly alter the levels of pSmad1/5/8, but almost completely abolished canonical Wnt signaling in (pre)-ameloblasts. Tooth mineralization resumed with a 48-h delay allowing for additional mesenchymal proliferation. Enamel volume was still reduced at P4 and P8, but was comparable in erupted teeth, which were broader and had altered cusp shapes. Tooth eruption was also delayed. Overall, enamel appeared inconspicuous, although some structural changes along with reduced mineral density could be observed. Loss of Bmp7 led to an increase in mesenchymal Bmp6 suggesting an interplay between Bmp6 and Bmp7 in the regulation of mineralization initiation. Our findings show that regulation of the onset of tooth mineralization is a hitherto unsuspected mechanism controlling tooth shape variation. Initiation of tooth mineralization is regulated by a complex epithelial-mesenchymal Bmp/Wnt-signaling network to which Bmp7 contributes. This network is separate and independent of the Bmp2-signaling network regulating odontoblast cell polarization. From an evolutionary perspective, addition of Bmp7 as initiator of tooth mineralization might be akin to an upgrade of an existing computer operating system. While not essential, it provides obviously sufficient advantage warranting its evolutionary incorporation.

Keywords: tooth mineralization, bone morphogenetic protein, signaling, epithelial–mesenchymal interaction, mouse genetics, gene expression

INTRODUCTION

Enamel and dentin formation, the two major mineralized compartments of the tooth, are regulated by intricate signaling events between the different hard tissue-forming cells, ameloblasts and odontoblasts. Although changes to these signaling events may result in disturbed or poor quality mineralized structures (Kim and Simmer, 2007; Coxon et al., 2012), dental hard tissue formation is remarkably robust. Patterning of molar cusps precedes their mineralization, which is initiated at the tip of a cusp (Simmer et al., 2010). Variations in mineralization and molar cusp shape contribute to dental diversity and functionality and thus provide important parameters for understanding ecological processes that drive evolution (Jernvall and Jung, 2000; Salazar-Ciudad and Jernvall, 2002; Kavanagh et al., 2007; Ungar, 2009).

The outer dentin surface is specified by the interface between the epithelium and mesenchyme which becomes the dentino–enamel junction in developing crown. Enamel crown formation on the outer dentin surface starts with the onset of biomineralization at the future cusp tips defined by growth parameters (Salazar-Ciudad and Jernvall, 2002, 2010; Simmer et al., 2010). A better understanding of how crown growth is regulated would be essential in defining evolutionary crown morphology in hominoids (Dean and Reid, 2001). Epithelial enamel knots direct folding of the inner enamel epithelium by producing diffusible molecules that inhibit new knots nearby and initiate them only in the zones outside the previously initiated cusps (Jernvall, 2000). The primary enamel knot occurs at the tip of the first cusp and directs the formation of secondary or tertiary enamel knots before the tooth starts to mineralize (Jernvall, 2000; Luukko et al., 2003). Studies over the past two decades have focused on enamel knot activation and silencing in defining multicuspid molar formation.

Members of the bone morphogenetic protein (Bmp) family are evolutionarily conserved signaling molecules belonging to the Tgfβ family. They can be grouped into several subfamilies and might function as homo- or heterodimers to control a multitude of developmental processes including craniofacial development (Graf et al., 2016; Kim et al., 2019; Wisotzkey and Newfeld, 2020). Various Bmps are expressed at all stages of tooth development (Aberg et al., 1997). They are found in enamel knots that control cusp formation and are critical components of reciprocal epithelial–mesenchymal signaling events that coordinate early tooth mineralization (Wang et al., 2004; Malik et al., 2018; Meguro et al., 2019). For instance, Bmp2 is expressed in odontoblasts at onset of tooth mineralization, where it coordinates odontoblast polarization to ensure ordered dentin deposition. Loss of mesenchymal Bmp2 results in a dentinogenesis imperfecta-like phenotype (Malik et al., 2018). Various Bmps are often expressed in close vicinity, lending support to the notion that they might be redundant or function as heterodimers. In addition to Bmp2, Bmp7 is also expressed in the cusp and in odontoblasts at the onset of tooth mineralization (Aberg et al., 1997). However, neural crest-specific deletion of *Bmp7*, which includes mesenchymal dental pulp cells, leads to the formation of wider teeth and the appearance of extra cusps with no apparent effect on mineralization (Zurowski et al., 2018). These changes in tooth morphology have functional consequences and implications for mammalian dental evolution (Zurowski et al., 2018). These divergent phenotypes suggest that Bmp2 and Bmp7, although likely expressed in close spatial and temporal vicinity, act largely independent. Here we use early tooth mineralization as a unique system to address redundancy and independence of these two Bmps. We find that loss of Bmp7 results in a delay of tooth mineralization and tooth eruption. We explore the molecular/cellular mechanisms that underlie this mineralization delay as well as the formation of wider/extra cusps in Bmp7-deficient molars. We find that these independent roles of Bmp2 and Bmp7 are characterized by the differential use of downstream signaling pathways. Whereas Bmp2 coordinates tooth mineralization, Bmp7 acts to initiate tooth mineralization.

MATERIALS AND METHODS

Animals

Animal experiments were approved by the Research Ethics office of the University of Alberta (Animal Use and Care Committee protocol AUP1149) in compliance with guidelines by the Canadian Council of Animal Care. Mouse lines were backcrossed more than 10 generations to the C57Bl/6J background. $Bmp7^{fl/fl}$ mice (Zouvelou et al., 2009a) were crossed to Wnt1-Cre mice [Tg(Wnt1-cre)11Rth] for neural crest-specific deletion of *Bmp7* (subsequently referred to as $Bmp7^{ncko}$). *Bmp7* expression was detected using Bmp7lacZ reporter mice (Godin et al., 1998). Mice were PCR-genotyped with DNA obtained from tissue biopsies as described (Zouvelou et al., 2009b; Segklia et al., 2012).

Micro-Computed Tomography (μCT) Analysis

MicroCT scans were obtained using a MILabs μCT (Milabs, Utrecht, Netherlands) at the School of Dentistry, University of Alberta. For live scanning, mice were anesthetized using isoflurane. For scans from post-mortem, dissected tissues, samples were fixed in 4% paraformaldehyde (PFA) for 24 h, washed, and stored in PBS prior to scanning. Scans were acquired in a mouse bed holder using the ultra-focused setting with following parameters: voxel size = 10 μm; voltage = 50 kV; current = 0.24 mA; and exposure time = 75 ms. Scans were reconstructed at a voxel size of 25 μm or smaller and analyzed using the AVIZO 3D software (Life Technologies, version 2019.1). To determine the total mineral volume of enamel or dentin, a manual segmentation was performed using appropriate gray level values corresponding to the single mineralized tissues (enamel, dentin, bone). Mineral density was determined using Hounsfield units.

Tissue Preparation and Histology

Control and mutant embryonic heads or isolated adult mandibles were fixed in 4% PFA. Samples were decalcified

using 0.5M EDTA solution for 1 day (newborn heads) to 4 weeks before processing for paraffin embedding. Paraffin blocks were cut on a type '820' Spencer microtome at 5–7 microns and stored at room temperature until use. For histological analysis, sections were placed in an oven at 60°C for 30 min, de-paraffinized in xylol, rehydrated in a decreasing ethanol gradient followed by staining with hematoxylin and eosin (H&E), immunohistochemistry (IHC), or immunofluorescence (IF).

Immunohistochemistry (IHC) and Immunofluorescence (IF)

Tissue sections were boiled in 10 mM sodium citrate buffer (pH 6) for 1 min in a microwave and allowed to cool to room temperature to facilitate antigen retrieval. Sections were blocked with 1% BSA + 0.5% Tween in PBS. Primary antibodies were incubated overnight at 4°C in blocking solution in a humidified chamber. Details of primary and secondary antibodies and dilutions used are summarized in **Supplementary Table S1**.

LacZ Staining

LacZ staining was performed as described previously (Zouvelou et al., 2009a). Alternatively, mice were directly perfused with lacZ staining solution; mandibles were dissected, stained, fixed, and processed as described above.

Scanning Electron Microscopy (SEM)

For backscatter scanning electron microscopy (SEM) imaging, mandibles were dissected, fixed in 4% PFA for 2 days, washed, and dehydrated in series of ascending grades of alcohol and embedded in sagittal orientation in Technovit 7200 VLC. Sections were prepared for imaging using a cutting and grinding system (Wolff et al., 2010). Processing of samples and imaging was performed by electron microscopic facility staff at the Institute of Oral Biology, University of Zurich.

RNA Extraction and Quantitative Real-Time PCR (qRT-PCR)

Tooth germs from newborn (postnatal day 0, P0) control or $Bmp7^{ncko}$ pups were dissected and immediately processed for extraction of total RNA using Thermo Scientific RNA extraction kit (#K0731). cDNA was transcribed from 0.5 to 1 μg RNA using Thermo Scientific cDNA kit (#K1620). Quantitative RT-PCR was performed with 5–10 ng cDNA/reaction using appropriate primer pairs (see **Supplementary Table S2**) and a SYBR green-based amplification kit (SsoAdvanced™ Universal SYBR® Green Supermix-Biorad) on a BioRad C1000 Touch Thermal Cycler. Relative expression was determined in relation to the housekeeping gene 36B4 using the ddCt method (Schmittgen et al., 2000). Analysis was performed on triplicate samples, and data shown are representative from at least three independent biological repeats.

Statistical Analysis

RT-PCR and quantitative data are presented as mean ± SD. Analysis between groups was performed using an unpaired Student's *t*-test using Microsoft Excel. A P-value < 0.01 was considered to be statistically significant. For RT-qPCR analysis, groups were performed in triplicates. Number of biological repeats of each independent experiment is denoted as n.

RESULTS

Bmp7 Is Expressed in Differentiating Odontoblasts and a Subset of Ameloblasts at Early Mineralization Stages

Previous studies reported that Bmp7 is expressed in dental epithelium (placode, enamel knot) at early stages of tooth development, but shifts to the dental mesenchyme around the time tooth mineralization is initiated (Aberg et al., 1997; Helder et al., 1998; Zouvelou et al., 2009b). We confirmed this shift using *Bmp7*LacZ reporter mice. At E16.5, *Bmp7* expression was restricted to the enamel knot in the epithelium, and at E18.5, expression in both mesenchyme and epithelium was hardly detectable (**Supplementary Figure S1**). At P0, when the upper first molar is in its early mineralization stages, *Bmp7* expression was restricted to differentiating odontoblasts at the tip of cusps or mesenchymal cells in their vicinity (**Figures 1A,A'**). Expression was also observed in a subset of ameloblasts in vicinity to *Bmp7*-positive odontoblasts (**Figures 1A,A"**). This mesenchymal expression in the 1st molar was variable and transient and was not observed at P2. At this stage, *Bmp7* expression was noted in the sequentially differentiating odontoblasts of the 2nd molar (**Figures 1B,B'**). To note, ameloblasts expressing *Bmp7* were found at the non-secretory side of the cusp evident by lack of mineral matrix and flattened morphology (**Figure 1B'** arrows). At P6, no *Bmp7* expression was observed in odontoblasts (**Figure 1C**). At P14, expression was variable (**Figures 1D,E**), with expression being noted in odontoblasts in more lateral regions of the 1st/2nd molar and the 3rd molar.

Neural Crest-Specific Deletion of Bmp7 Results in Delayed Tooth Mineralization

Deletion of *Bmp7* in the dental mesenchyme resulted in a lack of mineralization at P0, similar to what is seen with the deletion of *Bmp2* (Malik et al., 2018). Odontoblasts and ameloblasts appeared less mature, and in particular, ameloblasts were less polarized. Hardly any mineral matrix deposition was evident when compared to control molar cusp (**Figures 2A,E**, arrows). At P2, the dentin and enamel mineral matrix deposition had progressed in molar cusps of control mice (**Figure 2B**, arrow). Mice lacking Bmp7 still showed little evidence of mineral matrix deposition (**Figure 2F**, arrow). However, by P6, mineralization could be observed in mutant teeth. Polarized ameloblasts and odontoblasts were evident along with a defined dentin and enamel matrix (**Figures 2C,G**).

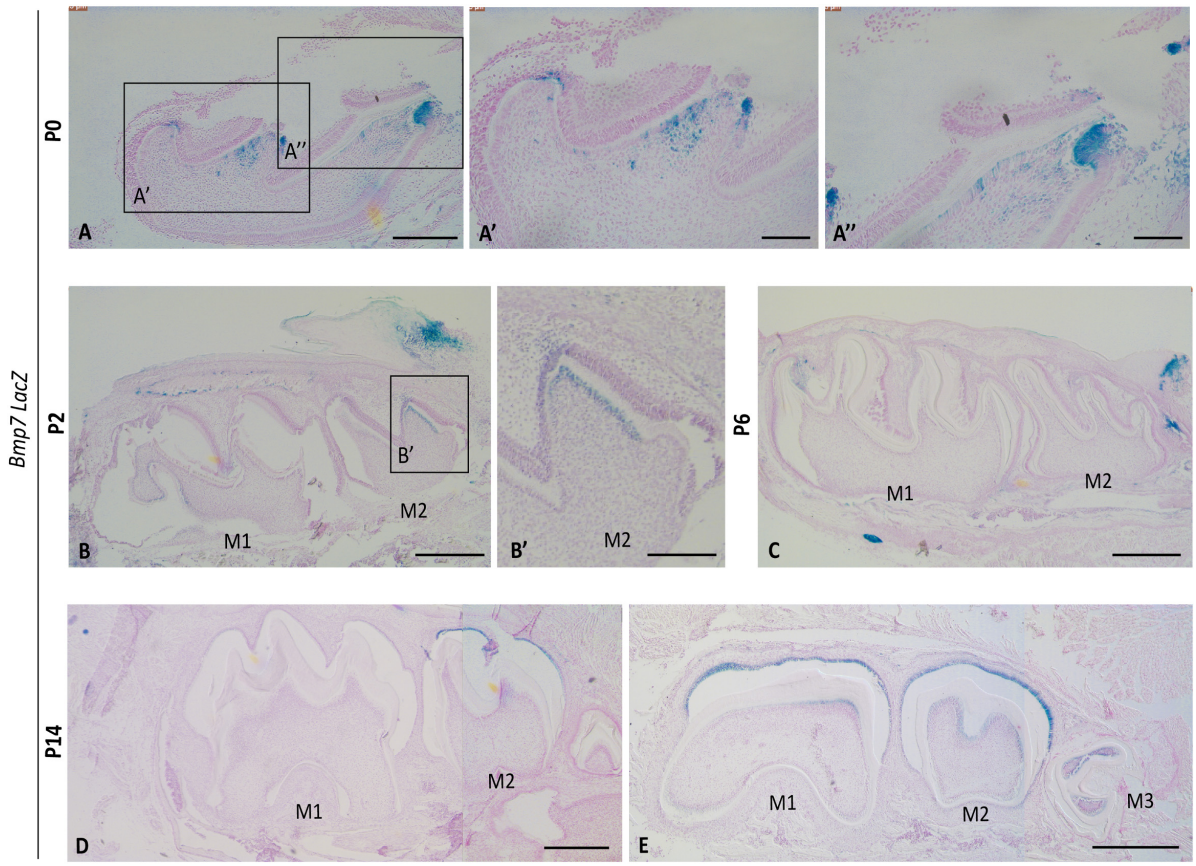

FIGURE 1 | *Bmp7* expression in odontoblasts correlates with onset of mineralization. Sagittal sections of molars from *Bmp7*LacZ reporter mice **(A)** at P0 Bmp7 is expressed in a subset of odontoblasts at the crown region in the cusps of the 1st maxillary molar. **(A',A")** Magnified view of **(A)**. **(B)** At P2 *Bmp7* expression is restricted to the 2nd molar and is not visibly noticed in 1st mandibular molars. **(B')** Magnified view of 2nd molars shown in **(B)**. **(C)** At P6 expression is lost in both 1st and 2nd molars. **(D,E)** At P14 *Bmp7* expression is dynamic and Bmp7 appears in the 3rd molar and is re-expressed in some lateral areas of the 1st/2nd molars. Expression of Bmp7 in ameloblasts is dynamic and can be observed at various stages. Scale bars: **(A–E)**: 250 μm, **(A')**: 100 μm, **(A",B')**: 50 μm.

Overall appearance was fairly similar to control molars. At P8, maturation of the mineral matrix progressed in both control and mutant molars and a distinction between pre-dentin and mature dentin was evident (**Figures 2D,H**). To assess whether mineralization was objectively reduced at P8, we performed volume quantification of the mineralized tooth structures from microCT scans at P4 and P8. The volume was reduced in the mutant at both stages. Furthermore, mutant enamel showed reduced radiolucency at P8 (**Figures 2I–M**). These findings indicate that Bmp7 is involved in regulating the onset of tooth mineralization.

Reduction or loss of Bmp7 results in slightly enlarged, broader teeth (Saito et al., 2016; Zurowski et al., 2018). To explore if the delay in mineralization initiation resulted in additional cell proliferation in the cusp areas, we assessed cell proliferation in relation to mesenchymal Bmp7-lacZ expression. In a P0 wild-type control tooth, mesenchymal proliferation had ceased in cusp areas showing morphological features consistent with the onset of mineralization (odontoblast polarization), but continued in less mature, lateral cusp areas (**Figure 3A**). Correlating proliferation to *Bmp7* expression, areas showing Bmp7-lacZ staining were generally devoid of proliferating cells, whereas proliferation could be detected in adjacent lacZ-negative areas (**Figure 3B**). Deletion of mesenchymal Bmp7 resulted in persistent mesenchymal proliferation in areas where mineralization was delayed at P0 (**Figure 3C**). This suggests that delaying mineralization allows for additional mesenchymal proliferation expected to affect overall tooth size and leading to minor cusp shape variations, as observed in mice deficient for mesenchymal *Bmp7* (Zurowski et al., 2018).

Bmp7 Controls Onset of Tooth Mineralization

We next confirmed whether the apparent delay in tooth mineralization was reflected on the molecular level by delayed expression of enamel and dentin matrix proteins. As shown in **Figure 4**, expression of both Amelogenin (Amlx) and Dentin sialoprotein (Dsp) was delayed by around 48 h in Bmp7-mutant teeth. In contrast to control teeth, where Amlx expression originated at the tip of the cusp, Amlx was completely absent in P0 Bmp7-mutant teeth (**Figures 4A,E**); 48 h later, at P2, when Amlx expression extended further down along the mineralization

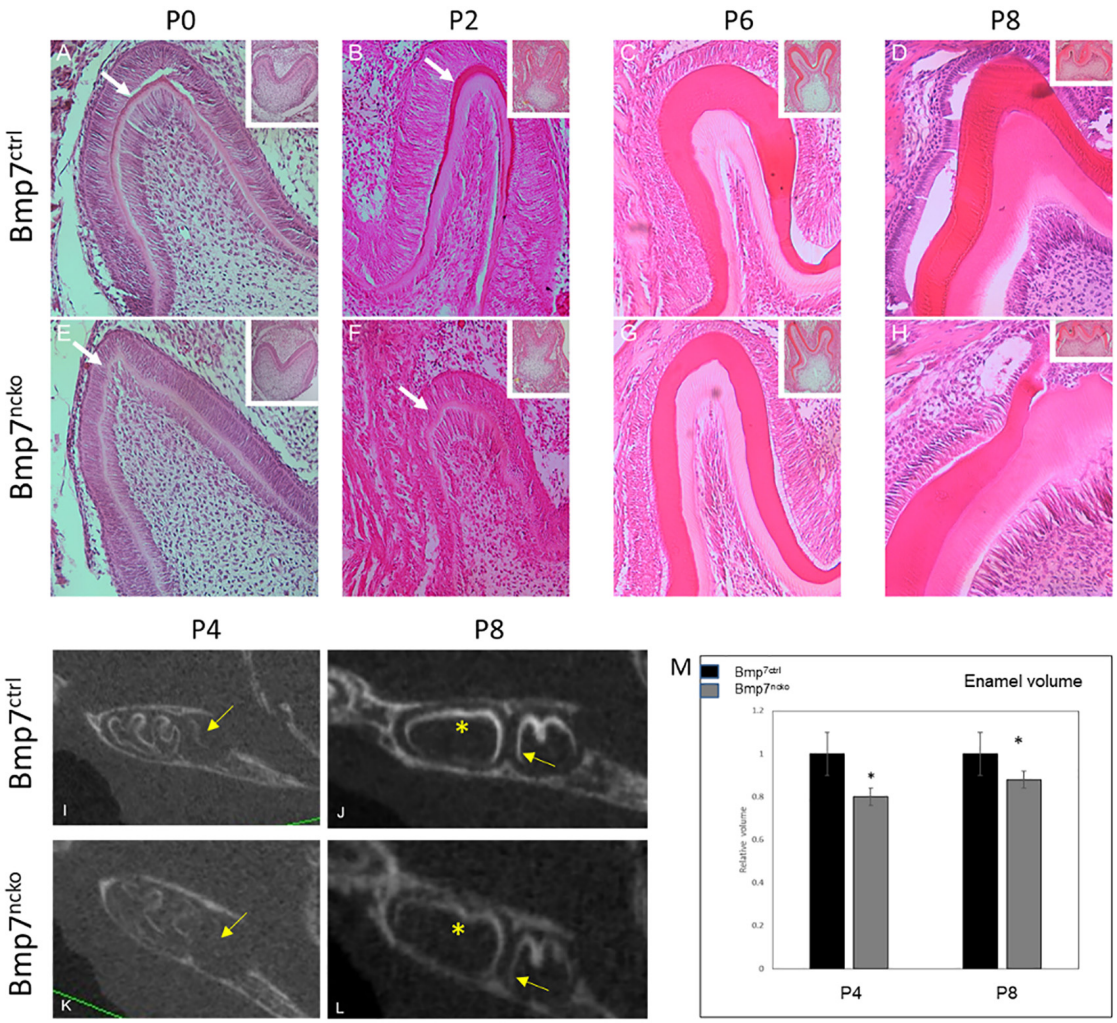

FIGURE 2 | Loss of mesenchymal Bmp7 leads to a delay in tooth mineralization. **(A–H)** H&E stained frontal sections from 1st mandibular molars of control **(A–D)** and Bmp7^{ncko} mutant mice **(E–H)** at P0 **(A,E)**, P2 **(B,F)**, P6 **(C,G)**, and P8 **(D,H)** show an initial delay of onset of tooth mineralization. At P0, maturation and organization of ameloblasts and odontoblasts appears delayed with little or no deposition of mineral matrix. At later stages dentin and enamel are formed. **(I–L)** Sagittal ortho-slices from microCT scans at P4 **(I,K)** and P8 **(J,L)** of control **(I–J)** and Bmp7^{ncko} mutant mice **(K,L)** showing delayed mineralization. Note lack of mineralization at P4 and delayed mineralization at P8 in the 2nd molar in Bmp7^{ncko} (arrows) and reduced mineral density (star). **(M)** Quantification of tooth mineralization from microCT scans at P4 and P8 show that differences persist until at least P8. *$p < = 0.05$.

front in control teeth, some initial Amlx expression was now observed at the tip of the cusp in mutant teeth (**Figures 4B,F**). At subsequent stages (P6 and P8), Amlx expression became weaker at the tip of the cusps, where the most mature enamel would be found, but remained apparent more in cervical and in intercuspal areas in control teeth (**Figures 4C,D**). In the mutant, these local differences in Amlx expression were less apparent at P6. Expression toward cervical appeared to progress faster, while expression at the cusp tip remained (**Figure 4G**). At P8, expression between control and mutant teeth was comparable (**Figures 4D,H**). Similarly, Dsp expression was delayed by 48 h in Bmp7-mutant teeth. At P0, Dsp was expressed in control teeth in odontoblasts (**Figure 4I**, yellow arrowheads) and pre-ameloblasts (**Figure 4I**, red arrow) as expected. In contrast, Dsp was completely absent from mutant teeth (**Figure 4M**). At P2, Dsp expression in control teeth became more restricted to odontoblasts (**Figure 4J**, yellow arrowheads), whereas mutant teeth just started weakly expressing Dsp (**Figure 4N**). At P6 and P8, Dsp expression became largely comparable, although expression appeared to be less homogeneous in Bmp7 mutant teeth (**Figures 4O,P**, yellow arrowheads) when compared to the control (**Figures 4K,L**, yellow arrowhead). These findings establish that Bmp7 controls onset of tooth mineralization.

Bmp7 Controls the Balance Between Canonical and Non-canonical Wnt Signaling

Bmp2 signals to pre-ameloblasts via Bmp-specific Smad1/5/8 signaling, which in turn regulates expression of the Wnt

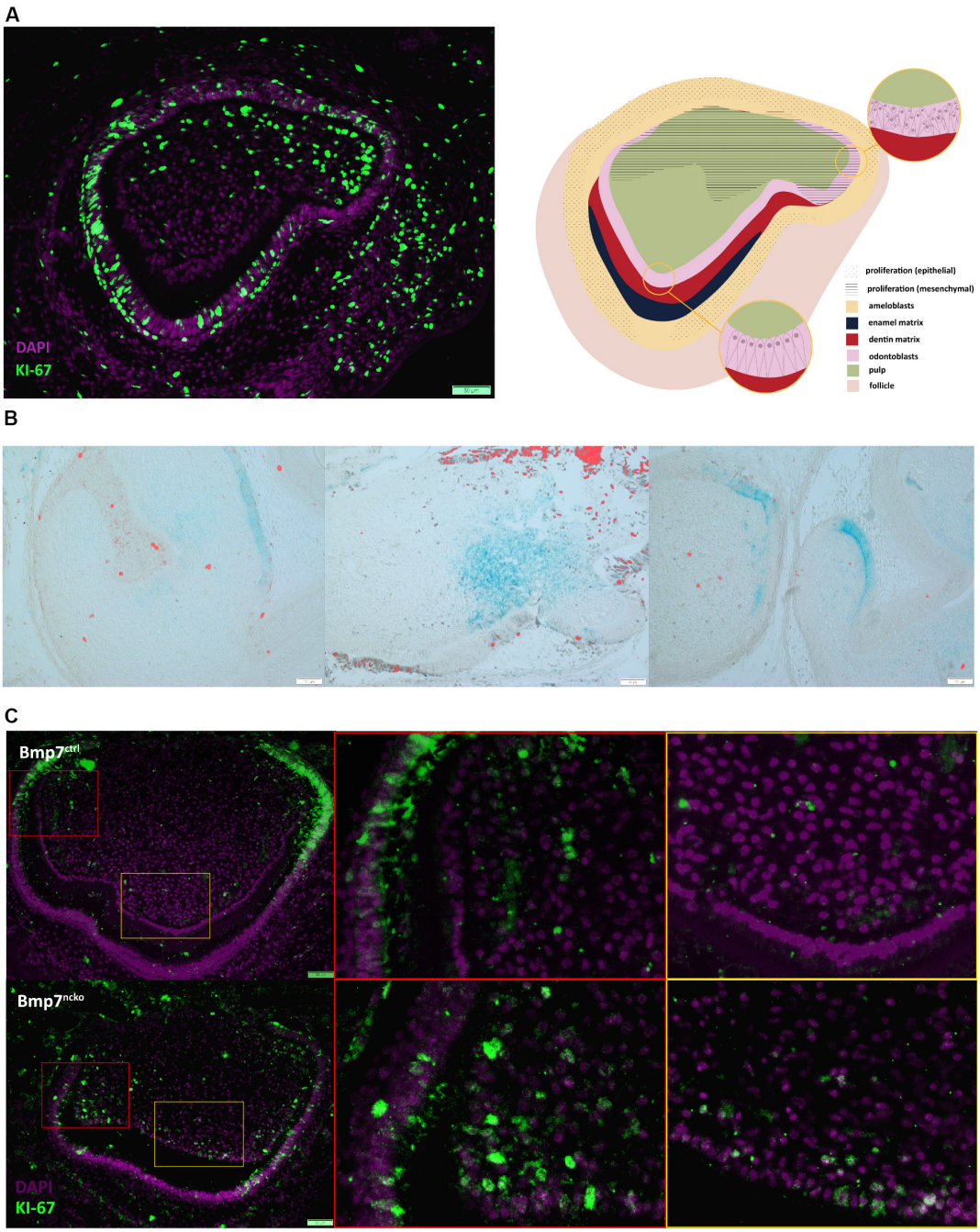

FIGURE 3 | *Bmp7* expression is associated with termination of proliferation. **(A)** (left panel) Frontal section of a P0 molar stained for Ki67 (green) to identify cell proliferation counterstained with DAPI (purple). Note mesenchymal proliferation has ceased in the cusp with polarized odontoblasts, whereas mesenchymal proliferation continues in the more immature, lateral cusp. (Right panel) Schematic representation of panel to the left. **(B)** *Bmp7*LacZ staining in relation to Ki67 indicates that areas with mesenchymal Bmp7 are non-proliferating. **(C)** Frontal sections of P0 Bmp7 control or mutant molars showing that loss of Bmp7 is associated with persistent mesenchymal proliferation in the cusp area including odontoblasts (orange boxes) and loss of epithelial proliferation toward cervical (red boxes). Scale bars: 50 μm.

antagonists Sost and Dkk1 and odontoblast polarization (Malik et al., 2018). Loss of Bmp7 had no obvious effect on pSmad1/5/8 in the tooth epithelium (**Figures 5A,F**) indicating that Bmp7 might not engage canonical Bmp signaling or might only make a minor contribution to it. However, loss of Bmp7 led to an almost complete loss of canonical Wnt-signaling as seen by the very strong reduction of non-phosphorylated β-catenin in the epithelium of mutant teeth (**Figures 5B,G**).

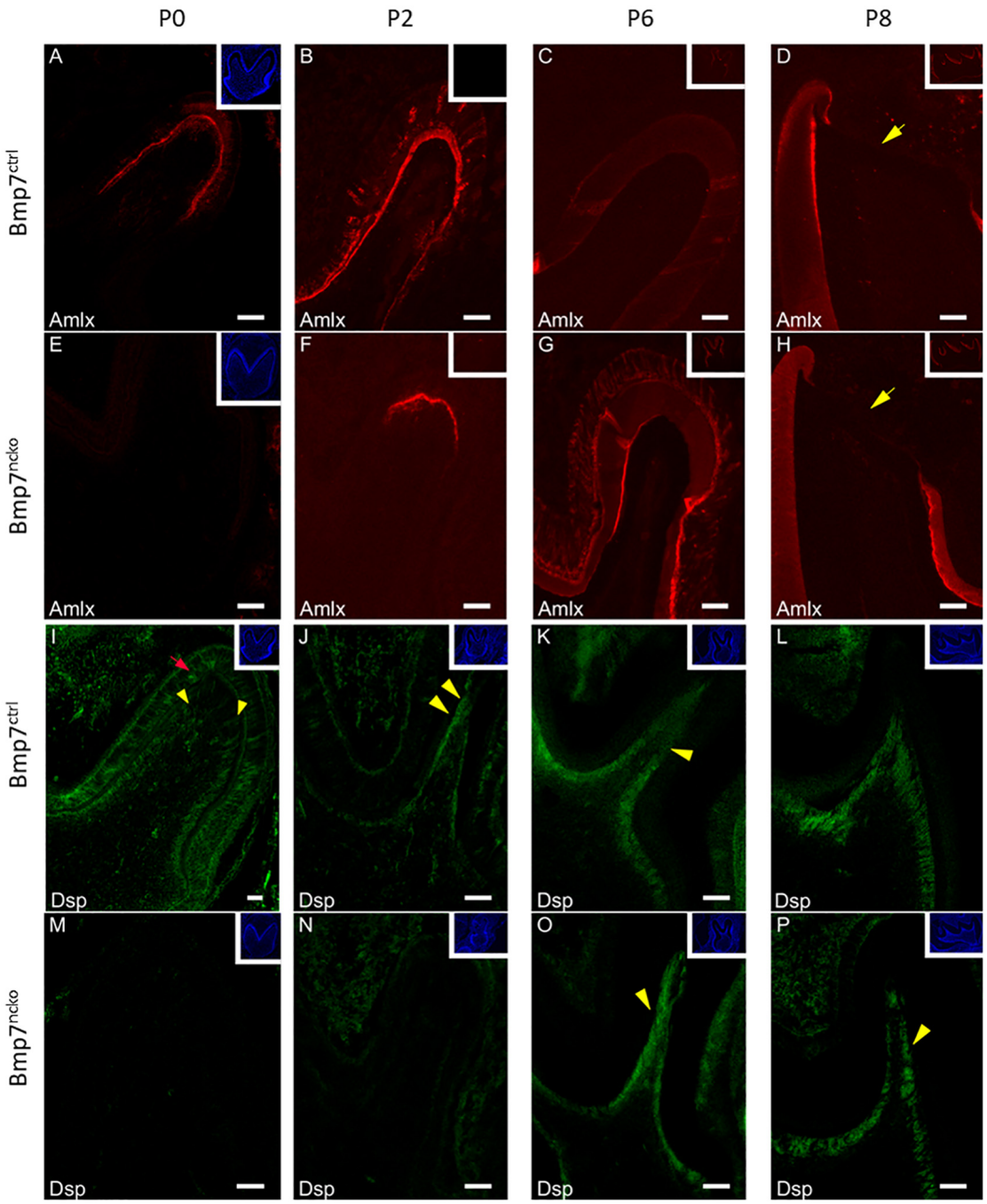

FIGURE 4 | Bmp7 controls onset of dentin and enamel formation. Frontal sections of mandibular 1st molars at P0 **(A,E,I,M) (A–H)**, P2 **(B,F,J,N)**, P6 **(C,G,K,O)**, and P8 **(D,H,L,P)** from Bmp7 control **(A–D,I–L)** and Bmp7^{ncko} mice **(E–H,M–P)** stained for Amelogenin (Amlx) or Dentin sialoprotein (Dsp). For better orientation, DAPI stained sections are shown in the insert in the top left corner with the exception of **(C,D,G,H)**, where Amlx staining is shown. At P0 Amlx is absent and induction at tip of the cusp can be seen at P2 **(A,B,E,F)**. Overall expression pattern is conserved in the mutant evidenced by the presence of enamel-free zones [**(D,H)**, yellow arrow heads]. Similarly, Dsp expression is not initiated before P2 in the mutant **(N)**, while present in odontoblasts in control teeth from P0 onward [**(I,J)**, yellow arrowheads] or pre-ameloblasts (red arrow). Dsp expression at DN6 and DN8 **(K,L,O,P)** is comparable, although patchier staining can be observed in mutant teeth (yellow arrowheads).

Loss of Bmp7 had no effect on the expression of the Wnt antagonists Dkk1 and Sost, but a lack of Dkk1 polarization was noted (**Figures 5C,D,H,I**). Expression of the Wnt-antagonist Frzb was unaffected and was expressed both in the control and mutant at the tip of the molar cusps (**Figures 5E,J**). We next assessed components of the Bmp and Wnt signaling

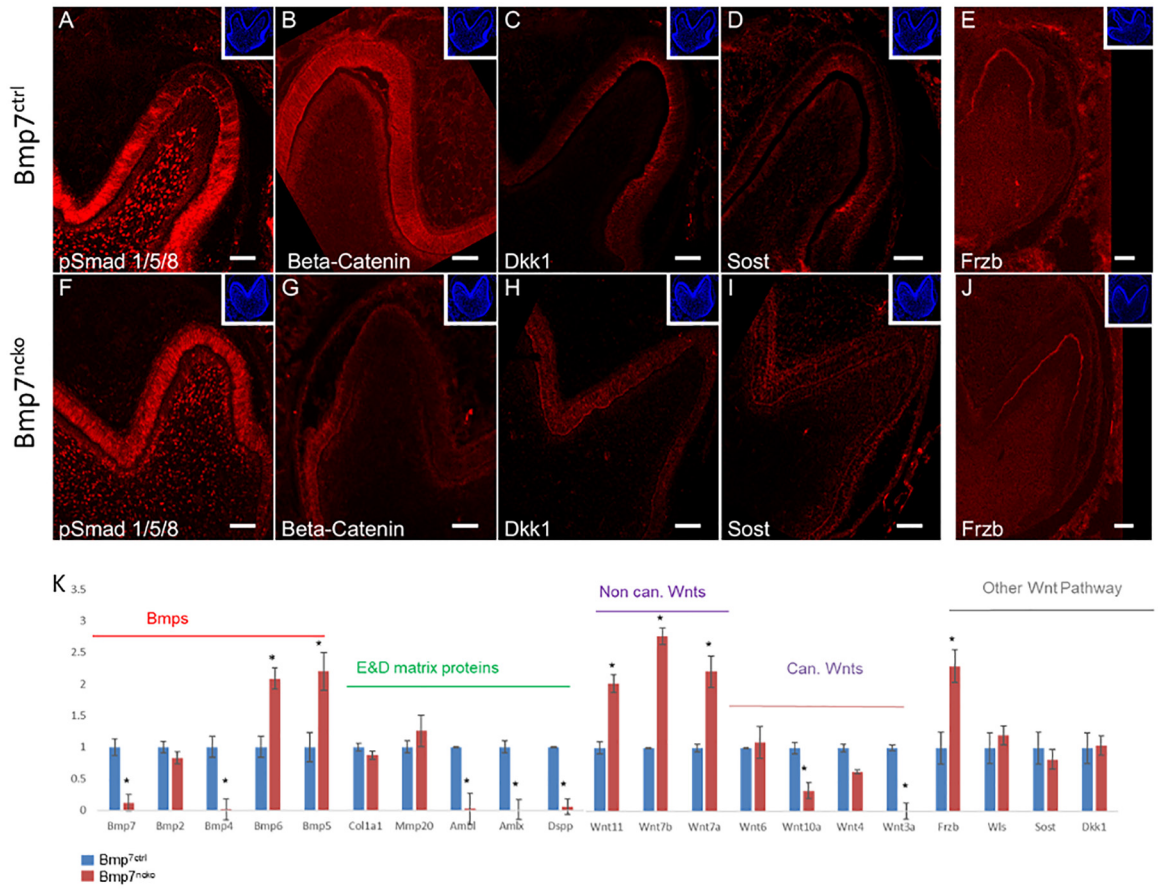

FIGURE 5 | Bmp7 engages non-Smad1/5/8 signaling and controls the balance of canonical/non-canonical Wnt signaling. **(A–J)** Frontal sections of mandibular 1st molars from Bmp7 control **(A–E)** and Bmp7^{ncko} mice **(F–J)** at P0 stained for pSmad1/5/8 [Smad-dependent Bmp signaling, **(A,F)**], non-phosphorylated β-catenin [canonical Wnt signaling, **(B,G)**], Wnt antagonists Dkk1 **(C,H)**, Sost **(D,I)**, and Frzb **(E,J)**. Note persistence of pSmad1/5/8 in Bmp7^{ncko} teeth **(F)**, almost complete loss of non-phosphorylated β-catenin in the epithelium **(G)**, loss of polarization of Dkk1 **(H)**, and persistent expression of Frzb **(J)**. **(K)** RT-qPCR from RNA isolated from dissected 1st molars from Bmp7 control (blue) and Bmp7^{ncko} mice (red) showing changes to Bmp and Wnt signaling as well as selected enamel and dentin matrix genes. Note: lack of *Bmp4* expression and upregulation of *Bmp5* and *Bmp6,* downregulation of several canonical Wnt ligands (Wnts3a, 4, 10a) and up-regulation of non-canonical Wnts7a, 7b, 11, as well as lack of *Dspp, Amlx, Ambl* expression in Bmp7-mutant teeth. $^{*}p < = 0.05$.

pathways by RT-qPCR, as Bmp signaling is known to coordinate Wnt signaling during early tooth development (Itasaki and Hoppler, 2010) and loss of Bmp7 had an obvious effect on canonical Wnt signaling. As expected, expression of *Bmp7* was strongly reduced in mutant teeth. Expression of *Bmp2* was not affected, *Bmp4* was almost completely abolished, whereas both *Bmp5* and *Bmp6* were increased. *Bmp2, 6*, and *7* are predominantly expressed in odontoblasts, whereas *Bmp4* and *5* show predominant epithelial expression (**Supplementary Figure S2**). We next tested for the expression of several Wnt ligands known to be expressed during tooth development (Sarkar and Sharpe, 1999; Suomalainen and Thesleff, 2010). The non-canonical Wnts *11, 7a, 7b* (Wnt/Ca^{2+} and planar cell polarity signaling pathways) were all upregulated in Bmp7-mutant teeth, whereas several canonical Wnts engaging in β-catenin signaling were downregulated or almost absent (*Wnt3a, 4, 10)* (**Figure 4K**). Expression of *Dkk1, Sost* and *Wls* were unchanged, whereas *Frzb* was upregulated at the gene expression level (**Figure 5K**). We also tested several genes involved in the formation of the dentin or enamel matrix. *Col1* and *Mmp20* were unchanged in mutant teeth; however, the dentin-specific *Dentinsialophosphoprotein (Dspp)* and enamel-specific *Ameloblastin (Ambl)* and *Amelogenin (Amlx)* genes failed to be induced in Bmp7-mutant teeth (**Figure 4K**). This establishes that Bmp7 contributes to the complex, reciprocal mesenchymal–epithelial cross-talk to control the initiation of tooth mineralization.

Initial Mineralization Delay Is Observed in All Molars and Results in Delayed Tooth Eruption

We next tested whether tooth maturation was also delayed in the other molars and whether such a delay would be reflected in delayed tooth eruption. As can be seen on sagittal representations of μCT of P14 and P21 teeth, there was a clear delay in the

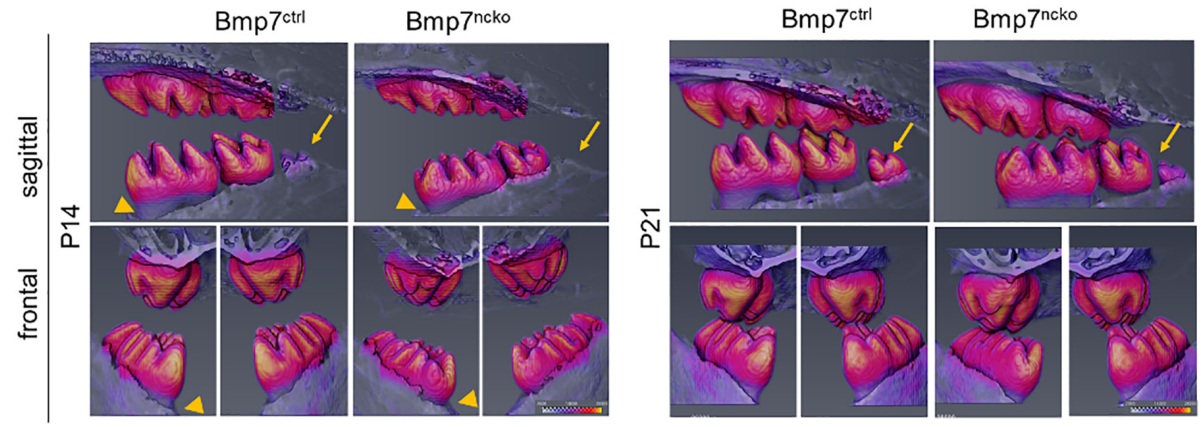

FIGURE 6 | Delay in mineralization of 1st molar delays tooth eruption and maturation of the 3rd molar. μCT scans from P14 control and mutant mice reveal a delay in tooth eruption (arrowhead), a difference that is not evident at P21. The development of the 3rd molar is also delayed (arrows) evident as smaller size and reduced mineralization. Areas of highest radiodensity are also reduced in mutant teeth, as seen by less yellow in some of the cusps. This effect is also seen at P21.

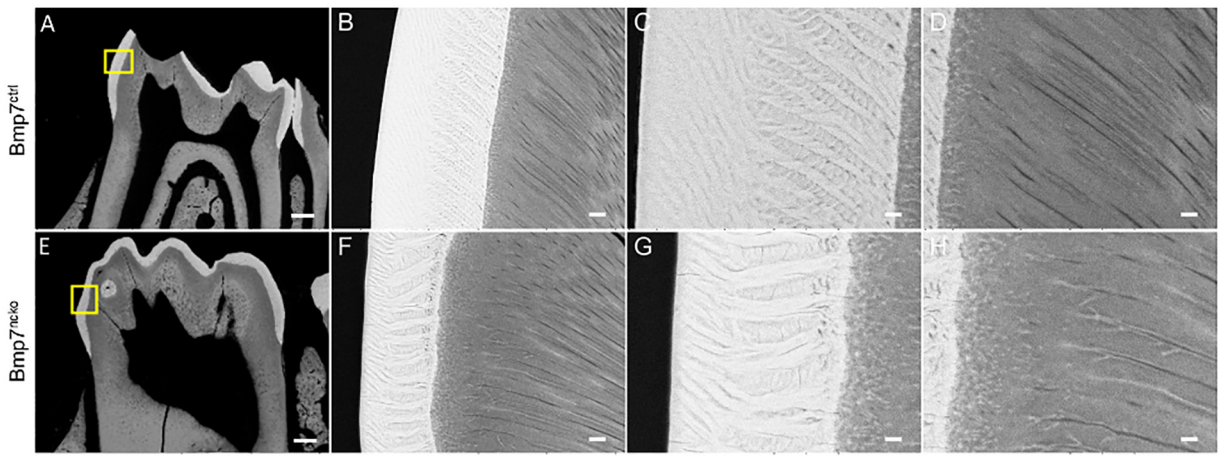

FIGURE 7 | Loss of Bmp7 causes variations in enamel and dentin appearance. **(A,E)** Back scatter electron microscopy images of control and mutant P14 1st mandibular molars showing no gross anatomical differences in enamel/dentin structure. **(B–D,F–H)** High resolution view of control **(B,C,D)** and mutant **(F,G,H)** crowns suggests minor variations in organization of enamel and dentin bundles and the enamel–dentin junction. Scale bars: **(A,E)**: 200 μm; **(B,F,G)**: 12.5 μm; **(C,G,H)**: 5 μm.

maturation of the 3rd molar (**Figure 5**, arrows). Eruption of the 1st and 2nd molars was also delayed at P14 (**Figure 6**, arrowheads); however, this difference was less evident at P21. Furthermore, the radiodensity of control and mutant teeth appeared to be slightly different. Control teeth showed larger areas with the highest mineral density (**Figure 6**, yellow areas on cusps). This indicates that a delay in onset of tooth mineralization is reflected in an overall delay in dental age. Back scatter SEM analysis of adult control and mutant teeth revealed that loss of Bmp7 does not cause major changes to the mineralized structures (**Figures 7A,E**). The apparent loss of enamel free zones in the mutant tooth is not a general phenotypic feature, but because a more lateral tooth section was analyzed. Analysis of high power images showed differences in the orientation and thickness of enamel ribbons (**Figures 7B,C,F,G**). Dentinal tubules appeared also to be slightly altered, in particular in the region of the dentino–enamel junction (**Figures 7D,H**). This indicates that the changes to tooth mineralization caused by loss of Bmp7 are subtle and may not be clinically obvious.

DISCUSSION

A reduction in Bmp7 or loss of mesenchymal Bmp7 results in subtle changes to tooth size and cusp morphology and orientation, as well as the formation of extra cusps on the first upper and lower molars (Saito et al., 2016; Zurowski et al., 2018). Changes in attrition facets of Bmp7-mutant toothrows indicate concomitant changes in chewing behavior (Zurowski et al., 2018). Such changes could provide an advantage for accessing different

food resources and thus contribute to niche diversification. Bmp signaling has long been proposed to contribute to the morphoregulation of teeth (Plikus et al., 2005), and expression patterns of various Bmps in tooth cusps support this notion (Meguro et al., 2019). Formation of molar cusps has been attributed to enamel knots, epithelial signaling centers that form at the tip of the cusp to coordinate proliferation and cytodifferentiation (Jernvall, 2000; Luukko et al., 2003). Lack of mesenchymal Bmp7 could either alter the distribution and timing of secondary/tertiary enamel knots or affect differential growth at the dentino–enamel junction, or both. Former would explain the appearance of additional cusps, and the latter occurs at the site where the main shape of the tooth is determined (Jernvall, 2000). Bmp7 expression correlated with lack of cell proliferation, and loss of Bmp7 resulted in continued proliferation in molar cusps providing an explanation for the larger tooth and wider cusp shape. As mineralization is not simultaneously initiated in all cusps, the increased duration in mesenchymal proliferation could allow for normally "hidden," uninvolved secondary/tertiary enamel knots to become relevant. This could lead to the formation of additional cusps, in line with the finding that the temporal pattern of odontoblast terminal differentiation differs from enamel knot formation (Lisi et al., 2003). As the initiation of tooth mineralization goes in hand with an obligatory termination of odontoblast proliferation, controlling the time of mineralization onset provides an elegant means to fine-tune tooth size and cusp shape appearance.

Loss of mesenchymal Bmp7 results in an approximately 2-day delay in tooth mineralization. Thus, onset of tooth mineralization underlies an independent molecular control like other developmental events. It is not simply the consequence of a linear progression of a pre-determined developmental program. Loss of Bmp7 does not appear to alter the ordered sequence of tooth mineralization. Expression of Amlx and Dsp is still initiated at the tip of cusp and continues toward cervical as in control teeth. Although some cellular properties appear to be altered, such as lack of ameloblast polarization, the overall patterning of the cusp appears not to be changed. Frzb is still expressed at the molar cusp. This suggests that the morphological patterning, presumably driven by enamel knots, is not strictly dependent on concomitant cytodifferentiation of odontoblasts and ameloblasts, in line with earlier observations (Lisi et al., 2003).

The delay in mineralization is evident in all teeth investigated. First, the regulated temporal appearance of Bmp7 in pre-osteoblasts/osteoblasts just prior to the onset of mineralization is observed in all molars. Second, delayed mineralization of all molars was observed. Third, in the continuously growing incisor, the mineralization front was shifted to anterior (data not shown). Thus, the molecular control of tooth mineralization appears to be conserved within a toothrow and between different types of teeth. Apart from the reported morphological changes, the crowns of $Bmp7^{ncko}$ teeth appear otherwise inconspicuous (Zurowski et al., 2018). However, local differences in maximal radiodensity were apparent and high resolution electron microscopy revealed additional minor differences in the appearance of enamel ribbons and the intercalation at the dentino–enamel junction. These discrete differences in mineralization could themselves contribute to altered wear facets in addition to the morphological differences (Zurowski et al., 2018). Thus, timing the onset of tooth mineralization is a novel parameter contributing to dental variation. It was somewhat surprising that the delay in mineralization would still be reflected by a delay in tooth eruption. One possibility is that the time of tooth eruption is directly linked to the onset of mineralization; however, it might be more plausible that mesenchymal Bmp7 in the pulp or alveolar bone has additional not yet understood functions that directly or indirectly affect tooth eruption. It is of interest to point toward the clonal appearance of Bmp7-positive cells observed in the first molar. This is reminiscent of nerve-associated glia cells that migrate and integrate into the odontoblast front (Kaukua et al., 2014). Whether Bmp7 can indeed be associated with the migration of such late migrating odontoblast precursors cells requires further validation. It certainly provides an interesting hypothesis to integrate molecular regulation of tooth mineralization with dental evolution.

Several members of the Bmp family are expressed in odontoblast/ameloblasts around the time of tooth mineralization. We have previously shown that mesenchymal Bmp2 is required for directed deposition of the dentin matrix (Malik et al., 2018). Bmp2 is expressed concomitantly with Bmp7 at the onset of tooth mineralization. As summarized in **Figure 8**, Bmp2 engages in a mesenchymal-epithelial crosstalk, polarizes odontoblasts and signals ameloblasts in a Smad1/5/8-dependent manner to downregulate the expression of Dkk1 and Sost. This in turn enables canonical Wnt signaling important for the induction of Dsp expression in odontoblasts (Yamashiro et al., 2007). In contrast, Bmp7 either only makes a minor contribution to pSmad1/5/8 signaling - there is some residual pSmad1/5/8 activity in Bmp2-mutant teeth (Malik et al., 2018) – or it engages non-canonical Bmp signaling to directly or indirectly control canonical Wnt signaling in ameloblasts. Non-canonical Bmp signaling pathways include Mapk, Pi3K, and Tak signaling mediated via p38, pJun, or NFκB (Jun et al., 2010; Huang et al., 2014; Rodríguez-Carballo et al., 2016; Cui et al., 2019). None of those pathways is specific to Bmp signaling and all those pathways can be engaged by non-canonical WNT signaling. Signaling could occur in odontoblasts – its absence leading to delayed odontoblast maturation - or ameloblasts. While expression of canonical Wnt ligands is suppressed in Bmp7-mutant teeth, those engaged in non-canonical Wnt signaling (Tamura and Nemoto, 2016) are increased, complicating the detailed molecular dissection. Bmp7 could also affect canonical Wnt signaling directly. Expression of the β-catenin transcriptional partner Lef1 is controlled by Bmp7 in the dentate gyrus (Choe et al., 2013). Lef1 is under direct transcriptional control of Bmp4 (Armenteros et al., 2018), and Bmp4 expression was strongly reduced in Bmp7-mutant teeth. Overall, our data indicate that Bmp2 and Bmp7 are independently required to coordinate canonical Wnt signaling in odontoblasts. Our data furthermore indicate that canonical/non-canonical Wnt signaling serve different roles in the specification and differentiation of the molar cusp, reminiscent of Bmp/Wnt crosstalk during early tooth development (Yuan et al., 2015).

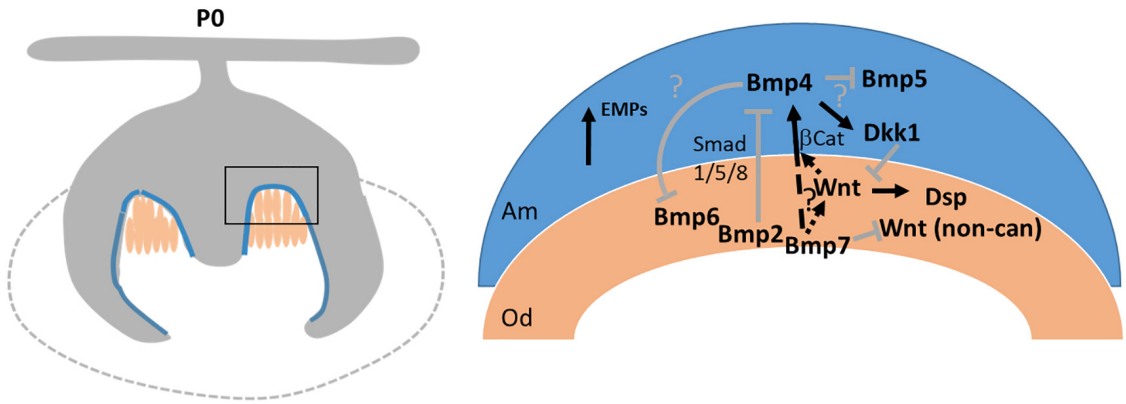

FIGURE 8 | Schematic representation of how BMP signaling regulates the initial stages of tooth mineralization. **(Left)** Schematic of a molar at onset of mineralization. Blue: ameloblasts/pre-ameloblasts. Peach: odontoblasts. **(Right)** Intricate Bmp and Wnt signaling networks coordinate initiation of mineralization by engaging in multiple reciprocal mesenchymal-epithelial signaling events. Bmp7 signals independent of Bmp2 to regulate the balance between canonical/non-canonical Wnt signaling, induction of Bmp4 in ameloblasts, and polarization of Dkk1. Bmp6 expression is increased in the absence of Bmp7. Bmp2 is required for polarization of odontoblasts and downregulation of Dkk1 expression (Malik et al., 2018). Bmp4 expression in pre-ameloblasts/ameloblasts is increased in the absence of Bmp2. Loss of Bmp7 does not affect Bmp2 expression.

In addition to Bmp2 and Bmp7, several other Bmps are expressed in odontoblasts/ameloblasts around the time of onset of mineralization. Bmp6 is also predominantly expressed in the mesenchyme, and its expression increases in the absence of Bmp7. Bmp4 and Bmp5 are both expressed in the epithelium. Because of overlapping expression and promiscuous receptor binding, there might be functional redundancy, but combinatorial signaling or signaling as heterodimers is also considered (Yadin et al., 2016; Antebi et al., 2017; Kim et al., 2019). The Bmp family can be subdivided into several subfamilies. Bmp2 and Bmp4 are orthologs of *Drosophila* Decapentaplegic (Dpp), whereas Bmps 5/6/7/8 are orthologs of 60A or Glass-bottom-boat (Gbb) (Newfeld et al., 1999). Their evolutionary conservation argues against a general functional redundancy. In line with this, Bmp2 and Bmp7 exert very different and independent functions during early tooth mineralization mediated through differential engagement of downstream signaling events as shown here and previously (Malik et al., 2018). Loss of Bmp2 but not Bmp7 leads to an almost complete loss of pSMAD1/5/8 signaling in pre-ameloblasts, upregulation of BMP4 in the epithelium, persistence of polarized epithelial Dkk1, and upregulation of Sost in mesenchyme and epithelium. Loss of either signal results in the reduction of mesenchymal Wnt signaling activity, but only Bmp7 leads to an almost complete loss of canonical β-catenin signaling in pre-ameloblasts. The enamel/dentin phenotype in Bmp2 and Bmp7 mutants is also very different: whereas loss of mesenchymal Bmp2 leads to a dentinogenesis imperfecta-like phenotype, loss of mesenchymal Bmp7 shows only mild, inconspicuous changes to mineralization. Thus, heterodimer signaling does not make a major contribution as has recently been suggested for other developmental systems (Kim et al., 2019). A similar interplay between Bmps of the two subgroups might also take place in early ameloblasts, where concomitant expression of Bmp4 and Bmp5 was observed. Of interest, both Bmp2 and Bmp7 appear to regulate the expression of those two Bmps. Clearly, Bmp7 is an important factor controlling the induction of mineralization. However, mineralization also occurs in the absence of Bmp7. Mesenchymal Bmp6 was increased in the absence of Bmp7. We speculate that mesenchymal Bmp6 might play a similar role as Bmp7 and both can be used to fine-tune the timing of mineralization. It is tempting to speculate that Bmp7 might have taken over a more ancient role of Bmp6 to initiate tooth mineralization. For this to be the case, one would predict differential binding affinities of these two Bmps for either their cognate receptor or a regulatory Bmp antagonist. However, given the complexity of cusp shapes, state of mineralization (enamel, enamel-free zones), different timing of mineralization, it is equally likely that Bmp7 does not control mineralization in every single cusp and other molecular signals such as Bmp6 are also involved.

In summary, our findings show that regulation of onset of tooth mineralization is a hitherto unsuspected mechanism controlling tooth shape variation. Initiation of tooth mineralization is regulated by a complex epithelial–mesenchymal Bmp/Wnt-signaling network involving mesenchymal Bmp7. This network is separate and independent of the Bmp2-signaling network regulating odontoblast cell polarization. This unexpected complexity not only illustrates the multitude of cellular events required for tooth mineralization but also brings into question how successful the application of individual Bmp or Wnt signaling molecules can be to control odontoblast differentiation or initiate dentin repair. From an evolutionary perspective, addition of Bmp7 as initiator of tooth mineralization might be akin to an upgrade of an existing computer operating system. While not essential, it provides obviously sufficient advantage warranting its evolutionary incorporation. This notion provides an important and novel angle on the well-established

concepts of gene redundancy and robustness of biological processes (Wagner, 2008): If biological processes evolve over time through addition of a novel functional layer while not completely removing the previous one, then what appears like redundancy might actually constitute reversion to a previous version of the same process.

DATA AVAILABILITY STATEMENT

The raw data supporting the conclusions of this article will be made available by the authors, without undue reservation.

ETHICS STATEMENT

The animal study was reviewed and approved by the Research Ethics office of the University of Alberta (Animal Use and Care Committee protocol AUP1149).

AUTHOR CONTRIBUTIONS

ZM performed the experiments, analyzed the results, and wrote the manuscript. FE performed the experiments and analyzed the results. JT analyzed the results and edited the manuscript. DG conceived the study, performed the experiments, analyzed the results, wrote and edited the manuscript. All authors contributed to the article and approved the submitted version.

FUNDING

This work was supported by the Natural Science and Engineering Research Council of Canada (RGPIN-2014-06311), the Swiss National Science Foundation (grant no. 31003A_135530), and start-up funds from the School of Dentistry, University of Alberta (all to DG).

ACKNOWLEDGMENTS

The authors would like to acknowledge the excellent technical assistance of Jacqueline Hofmann-Lobsiger (Institute for Oral Biology, University of Zurich) for the SEM studies.

SUPPLEMENTARY MATERIAL

The Supplementary Material for this article can be found online at: https://www.frontiersin.org/articles/10.3389/fphys.2020.00698/full#supplementary-material

REFERENCES

Aberg, T., Wozney, J., and Thesleff, I. (1997). Expression patterns of bone morphogenetic proteins (Bmps) in the developing mouse tooth suggest roles in morphogenesis and cell differentiation. *Dev. Dyn.* 210, 383–396. doi: 10.1002/(sici)1097-0177(199712)210:4<383::aid-aja3>3.0.co;2-c

Antebi, Y. E., Linton, J. M., Klumpe, H., Bintu, B., Gong, M., Su, C., et al. (2017). Combinatorial signal perception in the BMP pathway. *Cell* 1184.e24–1196.e24. doi: 10.1016/j.cell.2017.08.015

Armenteros, T., Andreu, Z., Hortigüela, R., Lie, D. C., and Mira, H. (2018). BMP and WNT signalling cooperate through LEF1 in the neuronal specification of adult hippocampal neural stem and progenitor cells. *Sci. Rep.* 8:9241. doi: 10.1038/s41598-018-27581-0

Choe, Y., Kozlova, A., Graf, D., and Pleasure, S. J. (2013). Bone morphogenic protein signaling is a major determinant of dentate development. *J. Neurosci.* 33, 6766–6775. doi: 10.1523/JNEUROSCI.0128-13.2013

Coxon, T. L., Brook, A. H., Barron, M. J., and Smith, R. N. (2012). Phenotype-genotype correlations in mouse models of amelogenesis imperfecta caused by Amelx and Enam mutations. *Cells Tissues Organs.* 196, 420–430. doi: 10.1159/000336440

Cui, Y., Zhang, F., Jia, Y., Sun, L., Chen, M., Wu, S., et al. (2019). The BMP antagonist, SOSTDC1, restrains gastric cancer progression via inactivation of c-Jun signaling. *Am J Cancer Res.* 9, 2331–2348.

Dean, M. C., and Reid, D. J. (2001). Perikymata spacing and distribution on hominid anterior teeth. *Am. J. Phys. Anthropol.* 116, 209–215. doi: 10.1002/ajpa.1116

Godin, R. E., Takaesu, N. T., Robertson, E. J., and Dudley, A. T. (1998). Regulation of BMP7 expression during kidney development. *Development* 125, 3473–3482.

Graf, D., Malik, Z., Hayano, S., and Mishina, Y. (2016). Common mechanisms in development and disease: BMP signaling in craniofacial development. *Cytokine Growth. Factor. Rev.* 27, 129–139. doi: 10.1016/j.cytogfr.2015.11.004

Helder, M. N., Karg, H., Bervoets, T. J., Vukicevic, S., Burger, E. H., D'Souza, R. N., et al. (1998). Bone morphogenetic protein-7 (osteogenic protein-1, OP-1) and tooth development. *J. Dent. Res.* 77, 545–554. doi: 10.1177/00220345980770040701

Huang, R.-L., Yuan, Y., Tu, J., Zou, G.-M., and Li, Q. (2014). Opposing TNF-α/IL-1β- and BMP-2-activated MAPK signaling pathways converge on Runx2 to regulate BMP-2-induced osteoblastic differentiation. *Cell Death Dis.* 5:e1187. doi: 10.1038/cddis.2014.101

Itasaki, N., and Hoppler, S. (2010). Crosstalk between Wnt and bone morphogenic protein signaling: a turbulent relationship. *Dev. Dyn.* 239, 16–33. doi: 10.1002/dvdy.22009

Jernvall, J. (2000). Linking development with generation of novelty in mammalian teeth. *Proc. Natl. Acad. Sci. U.S.A.* 97, 2641–2645. doi: 10.1073/pnas.050586297

Jernvall, J., and Jung, H. S. (2000). Genotype, phenotype, and developmental biology of molar tooth characters. *Am. J. Phys. Anthropol. Suppl.* 31, 171–190. doi: 10.1002/1096-8644(2000)43:31%2B<171::aid-ajpa6>3.0.co;2-3

Jun, J. H., Yoon, W.-J., Seo, S.-B., Woo, K.-M., Kim, G.-S., Ryoo, H.-M., et al. (2010). BMP2-activated Erk/MAP kinase stabilizes Runx2 by increasing p300 levels and histone acetyltransferase activity. *J. Biol. Chem.* 285, 36410–36419. doi: 10.1074/jbc.M110.142307

Kaukua, N., Shahidi, M. K., Konstantinidou, C., Dyachuk, V., Kaucka, M., Furlan, A., et al. (2014). Glial origin of mesenchymal stem cells in a tooth model system. *Nature* 513, 551–554. doi: 10.1038/nature13536

Kavanagh, K. D., Evans, A. R., and Jernvall, J. (2007). Predicting evolutionary patterns of mammalian teeth from development. *Nature* 449, 427–432. doi: 10.1038/nature06153

Kim, H.-S., Neugebauer, J., McKnite, A., Tilak, A., and Christian, J. L. (2019). BMP7 functions predominantly as a heterodimer with BMP2 or BMP4 during mammalian embryogenesis. *eLife* 8:e48872. doi: 10.7554/eLife.48872

Kim, J.-W., and Simmer, J. P. (2007). Hereditary dentin defects. *J. Dent. Res.* 86, 392–399. doi: 10.1177/154405910708600502

Lisi, S., Peterková, R., Peterka, M., Vonesch, J. L., Ruch, J. V., and Lesot, H. (2003). Tooth morphogenesis and pattern of odontoblast differentiation. *Connect. Tissue Res.* 44(Suppl. 1), 167–170. doi: 10.1080/03008200390152278

Luukko, K., Løes, S., Furmanek, T., Fjeld, K., Kvinnsland, I. H., and Kettunen, P. (2003). Identification of a novel putative signaling center, the tertiary enamel knot in the postnatal mouse molar tooth. *Mech. Dev.* 120, 270–276. doi: 10.1016/s0925-4773(02)00458-6

Malik, Z., Alexiou, M., Hallgrimsson, B., Economides, A. N., Luder, H. U., and Graf, D. (2018). Bone morphogenetic protein 2 coordinates early tooth mineralization. *J. Dent. Res.* 97, 835–843. doi: 10.1177/0022034518758044

Meguro, F., Porntaveetus, T., Kawasaki, M., Kawasaki, K., Yamada, A., Kakihara, Y., et al. (2019). Bmp signaling in molar cusp formation. *Gene Expr. Patterns* 32, 67–71. doi: 10.1016/j.gep.2019.04.002

Newfeld, S. J., Wisotzkey, R. G., and Kumar, S. (1999). Molecular evolution of a developmental pathway: phylogenetic analyses of transforming growth factor-beta family ligands, receptors and Smad signal transducers. *Genetics* 152, 783–795.

Plikus, M. V., Zeichner-David, M., Mayer, J.-A., Reyna, J., Bringas, P., Thewissen, J. G. M., et al. (2005). Morphoregulation of teeth: modulating the number, size, shape and differentiation by tuning Bmp activity. *Evol. Dev.* 7, 440–457. doi: 10.1111/j.1525-142X.2005.05048.x

Rodríguez-Carballo, E., Gámez, B., and Ventura, F. (2016). p38 MAPK signaling in osteoblast differentiation. *Front. Cell Dev. Biol.* 4:40. doi: 10.3389/fcell.2016.00040

Saito, K., Takahashi, K., Asahara, M., Kiso, H., Togo, Y., Tsukamoto, H., et al. (2016). Effects of Usag-1 and Bmp7 deficiencies on murine tooth morphogenesis. *BMC Dev. Biol.* 16:14. doi: 10.1186/s12861-016-0117-x

Salazar-Ciudad, I., and Jernvall, J. (2002). A gene network model accounting for development and evolution of mammalian teeth. *Proc. Natl. Acad. Sci. U.S.A.* 99, 8116–8120. doi: 10.1073/pnas.132069499

Salazar-Ciudad, I., and Jernvall, J. (2010). A computational model of teeth and the developmental origins of morphological variation. *Nature* 464, 583–586. doi: 10.1038/nature08838

Sarkar, L., and Sharpe, P. T. (1999). Expression of Wnt signalling pathway genes during tooth development. *Mech. Dev.* 85, 197–200. doi: 10.1016/s0925-4773(99)00095-7

Schmittgen, T. D., Zakrajsek, B. A., Mills, A. G., Gorn, V., Singer, M. J., and Reed, M. W. (2000). Quantitative reverse transcription-polymerase chain reaction to study mRNA decay: comparison of endpoint and real-time methods. *Anal. Biochem.* 285, 194–204. doi: 10.1006/abio.2000.4753

Segklia, A., Seuntjens, E., Elkouris, M., Tsalavos, S., Stappers, E., Mitsiadis, T. A., et al. (2012). Bmp7 regulates the survival, proliferation, and neurogenic properties of neural progenitor cells during corticogenesis in the mouse. *PLoS One* 7:e34088. doi: 10.1371/journal.pone.0034088

Simmer, J. P., Papagerakis, P., Smith, C. E., Fisher, D. C., Rountrey, A. N., Zheng, L., et al. (2010). Regulation of dental enamel shape and hardness. *J. Dent. Res.* 89, 1024–1038. doi: 10.1177/0022034510375829

Suomalainen, M., and Thesleff, I. (2010). Patterns of Wnt pathway activity in the mouse incisor indicate absence of Wnt/beta-catenin signaling in the epithelial stem cells. *Dev. Dyn.* 239, 364–372. doi: 10.1002/dvdy.22106

Tamura, M., and Nemoto, E. (2016). Role of the Wnt signaling molecules in the tooth. *Jpn. Dent. Sci. Rev.* 52, 75–83. doi: 10.1016/j.jdsr.2016.04.001

Ungar, P. S. (2009). Tooth form and function: insights into adaptation through the analysis of dental microwear. *Front. Oral. Biol.* 13:38–43. doi: 10.1159/000242388

Wagner, A. (2008). Gene duplications, robustness and evolutionary innovations. *BioEssays* 30, 367–373. doi: 10.1002/bies.20728

Wang, X.-P., Suomalainen, M., Jorgez, C. J., Matzuk, M. M., Werner, S., and Thesleff, I. (2004). Follistatin regulates enamel patterning in mouse incisors by asymmetrically inhibiting BMP signaling and ameloblast differentiation. *Dev. Cell* 7, 719–730. doi: 10.1016/j.devcel.2004.09.012

Wisotzkey, R. G., and Newfeld, S. J. (2020). TGF-β prodomain alignments reveal unexpected cysteine conservation consistent with phylogenetic predictions of cross-subfamily heterodimerization. *Genetics* 214, 447–465. doi: 10.1534/genetics.119.302255

Wolff, A., Koch, M. J., Benzinger, S., van Waes, H., Wolf, N. I., Boltshauser, E., et al. (2010). Rare dental peculiarities associated with the hypomyelinating leukoencephalopathy 4H syndrome/ADDH. *Pediatr. Dent.* 32, 386–392.

Yadin, D., Knaus, P., and Mueller, T. D. (2016). Structural insights into BMP receptors: specificity, activation and inhibition. *Cytokine Growth. Factor. Rev.* 27, 13–34. doi: 10.1016/j.cytogfr.2015.11.005

Yamashiro, T., Zheng, L., Shitaku, Y., Saito, M., Tsubakimoto, T., Takada, K., et al. (2007). Wnt10a regulates dentin sialophosphoprotein mRNA expression and possibly links odontoblast differentiation and tooth morphogenesis. *Differentiation* 75, 452–462. doi: 10.1111/j.1432-0436.2006.00150.x

Yuan, G., Yang, G., Zheng, Y., Zhu, X., Chen, Z., Zhang, Z., et al. (2015). The non-canonical BMP and Wnt/β-catenin signaling pathways orchestrate early tooth development. *Development* 142, 128–139. doi: 10.1242/dev.117887

Zouvelou, V., Luder, H.-U., Mitsiadis, T. A., and Graf, D. (2009a). Deletion of BMP7 affects the development of bones, teeth, and other ectodermal appendages of the orofacial complex. *J. Exp. Zool. B Mol. Dev. Evol.* 312B, 361–374. doi: 10.1002/jez.b.21262

Zouvelou, V., Passa, O., Segklia, K., Tsalavos, S., Valenzuela, D. M., Economides, A. N., et al. (2009b). Generation and functional characterization of mice with a conditional BMP7 allele. *Int. J. Dev. Biol.* 53, 597–603. doi: 10.1387/ijdb.082648vz

Zurowski, C., Jamniczky, H., Graf, D., and Theodor, J. (2018). Deletion/loss of bone morphogenetic protein 7 changes tooth morphology and function inMus musculus:implications for dental evolution in mammals. *R. Soc. Open Sci.* 5:170761. doi: 10.1098/rsos.170761

Conflict of Interest: The authors declare that the research was conducted in the absence of any commercial or financial relationships that could be construed as a potential conflict of interest.

frontiers in Physiology

ORIGINAL RESEARCH
published: 14 July 2020
doi: 10.3389/fphys.2020.00780

Ectodermal Organ Development Is Regulated by a *microRNA-26b-Lef-1-Wnt* Signaling Axis

*Steve Eliason[1,2], Thad Sharp[1,2], Mason Sweat[1,2], Yan Y. Sweat[1,2] and Brad A. Amendt[1,2,3]**

[1] Department of Anatomy and Cell Biology, The University of Iowa, Iowa City, IA, United States, [2] Craniofacial Anomalies Research Center, The University of Iowa, Iowa City, IA, United States, [3] Iowa Institute for Oral Health Research, The University of Iowa, Iowa City, IA, United States

The developmental role of *Lef-1* in ectodermal organs has been characterized using *Lef-1* murine knockout models. We generated a *Lef-1* conditional over-expression (COEL) mouse to determine the role of *Lef-1* expression in epithelial structures at later stages of development after endogenous expression switches to the mesenchyme. *Lef-1* over expression (OE) in the oral epithelium creates a new dental epithelial stem cell niche that significantly increases incisor growth. These data indicate that *Lef-1* expression is switched off in the dental epithelial at early stages to maintain the stem cell niche and regulate incisor growth. Bioinformatics analyses indicated that *miR-26b* expression increased coinciding with decreased *Lef-1* expression in the dental epithelium. We generated a murine model over-expressing *miR-26b* that targets endogenous *Lef-1* expression and *Lef-1*-related developmental mechanisms. *miR-26b* OE mice have ectodermal organ defects including a lack of incisors, molars, and hair similar to the *Lef-1* null mice. *miR-26b* OE rescues the *Lef-1* OE phenotype demonstrating a critical genetic and developmental role for *miR-26b* in the temporal and spatial expression of *Lef-1* in epithelial tissues. *Lef-1* expression regulates Wnt signaling and Wnt target genes as well as cell proliferation mechanisms, while *miR-26b* OE reduced the levels of Wnt target gene expression. The extra stem cell compartment in the *COEL* mice expressed *Lef-1* suggesting that *Lef-1* is a stem cell factor, which was absent in the *miR-26b OE/COEL* rescue mice. This is the first demonstration of a microRNA OE mouse model that has ectodermal organ defects. These findings demonstrate that the levels of *Lef-1* are critical for development and establish a role for *miR-26b* in the regulation of ectodermal organ development through the control of *Lef-1* expression and an endogenous stem cell niche.

Keywords: *microRNA-26b*, *Lef-1*, Wnt signaling, ectodermal organ, stem cells, *miR-26b* mouse models

OPEN ACCESS

Edited by:
Maisa Hanna-Maija Seppala, King's College London, United Kingdom

Reviewed by:
Zhi Chen, Wuhan University, China
Andrew Jheon, University of California, San Francisco, United States
Xiao Li, University of California, San Diego, United States

***Correspondence:**
Brad A. Amendt
brad-amendt@uiowa.edu

Specialty section:
This article was submitted to Craniofacial Biology and Dental Research, a section of the journal Frontiers in Physiology

Received: *13 April 2020*
Accepted: *15 June 2020*
Published: *14 July 2020*

Citation:
Eliason S, Sharp T, Sweat M, Sweat YY and Amendt BA (2020) Ectodermal Organ Development Is Regulated by a microRNA-26b-Lef-1-Wnt Signaling Axis. Front. Physiol. 11:780. doi: 10.3389/fphys.2020.00780

INTRODUCTION

MicroRNAs (miRs) play an important role in the development of craniofacial structures. A conditional craniofacial specific knockdown of miRs lead to specific tooth defects and growth defects. An oral epithelial specific $Pitx2^{Cre}$ crossed to a *Dicer1 floxed* mouse demonstrated that teeth developed abnormally when *Dicer1* expression was ablated in the oral epithelium (Cao et al., 2010). One of the mature miRs expressed and deleted by $Pitx2^{Cre}/Dicer1^{Flox/Flox}$ in the murine craniofacial region was *miR-26b* (Cao et al., 2010).

miR-26b expression is widespread in different tissues at different stages of development. Established roles have been determined for *miR-26b* in tissue/organ growth and several cancer models (Zhang et al., 2010; Gao et al., 2011) and we have reported that *miR-26b* can act as a tumor suppressor in a colon cancer model (Zhang et al., 2014). In the pituitary, *miR-26b* directly binds the *3′UTR* of the Lymphoid enhancer-binding factor 1 gene (*Lef-1) in vitro* and *in vivo* and regulation of *Lef-1* may promote Pit-1 lineage differentiation during pituitary development (Zhang et al., 2010). A direct role for *miR-26b* in ectodermal organ development has not been reported.

Lef-1 plays a critical role in organ, craniofacial and tooth development. The Lef-1 protein shares homology with HMG family proteins and has been shown to act as a transcription factor (Travis et al., 1991). *Lef-1* is required for the development of multiple organ systems, including hair and tooth development and its role in Wnt signaling has been established (Travis et al., 1991; Van Genderen et al., 1994). In the developing tooth bud, *Lef-1* is expressed in the oral and dental epithelium at embryonic day E10.5, followed by a transition to mostly mesenchymal expression in the developing tooth bud starting at E14.5 (Kratochwil et al., 1996; Sasaki et al., 2005; Sun et al., 2016). The *Lef-1* general knockout has tooth developmental defects and a complete arrest of molar and incisor development at the late bud stage, but earlier stages of tooth development appear normal (Van Genderen et al., 1994). In addition, growth defects, abnormal hair/fur, and a kink in the tail have been described in the *Lef-1* null mice. *Lef-1* has been shown to be important for the regulation of *Fgf4* expression and over-expression of *FGF4* can rescue the late stage tooth bud delay in *Lef-1*$^{-/-}$ mice and FGF activation is thought to induce interactions between the dental epithelium and the dental mesenchyme (Kratochwil et al., 1996). Interestingly, in the murine epidermis and hair follicles, *Lef-1* establishes stem and progenitor cell compartments (Reya and Clevers, 2005; Huang and Qin, 2010; Petersson et al., 2011).

The transcription factor *Sox2* is required for the development of several endodermal tissues, including the trachea (Xie et al., 2014), stomach and gut (Que et al., 2007), and ectodermal tissues including the anterior pituitary (Jayakody et al., 2012), lens epithelium (Taranova et al., 2006), tongue epithelium (Balaguer et al., 2011) and hair follicles (Clavel et al., 2012). We have recently shown that conditional inactivation of *Sox2* leads to lower incisor arrest at E16.5 and abnormal dental development due to decreased stem cell proliferation (Sun et al., 2016). *Sox2* and *Lef-1* epithelial expression domains are juxtaposed in the murine oral epithelium and dental placode (Sun et al., 2016). Interestingly, ablation of either *Sox2* or *Lef-1* results in arrested tooth development at early developmental stages (Van Genderen et al., 1994; Kratochwil et al., 1996; Sun et al., 2016).

To define the role of *Lef-1* during embryonic development we used a conditional over-expression (COEL) of *Lef-1* (*COEL*) murine model to determine if dental epithelial specific over-expression would affect craniofacial and dental development (Sun et al., 2016). The ectopic over-expression of *Lef-1* in the epithelium leads to alterations in the labial cervical loop (LaCL) morphology and enhanced incisor growth, altered regulation of *Sox2*, enhanced proliferation, altered *Amelogenin* expression and the regulation of Wnt associated gene expression. In addition, we created a *EF1a* promoter-*miR-26b* transgenic over-expression mouse (*miR-26b* OE) to establish the role of *miR-26b* in craniofacial and tooth development. The *miR-26b OE* mouse shows growth defects, abnormal hair/fur, a crook in the tail and a complete lack of molar or incisor development, all phenotypes that are shared by the *Lef-1* knockout mouse (Van Genderen et al., 1994). Furthermore, we mated the *miR-26b OE* mice with the *COEL* mice and were able to rescue the *COEL* incisor growth phenotype. These studies demonstrate that *Lef-1* expression levels are critical for incisor growth. The correct *Lef-1* dosage is required because ablation of epithelial *Lef-1* causes tooth development to arrest at E14.5 and that an increase in epithelial *Lef-1* results in an expanded dental epithelial stem cell (DESC) niche and over-grown incisors. These finding correlate with increased levels of *miR-26b* in the dental epithelium after E14.5 at which stage *Lef-1* is normally decreased to allow for normal tooth development. Thus, our research demonstrates that; (1) precise *Lef-1* levels are critical for tooth development; (2) *miR-26b* is an important regulator of *Lef-1* in tooth development; (3) *Lef-1/miR-26b* work together to regulate the Wnt response required for normal tooth development, growth and maintenance; and (4) *miR-26b* expression in the dental stem cell niche after E14.5 reduces *Lef-1* expression required to maintain the stem cell niche and normal incisor growth.

MATERIALS AND METHODS

Mouse Lines and Embryonic Staging

Mice were housed and experiments performed according to the Office of Animal Resources guidelines at the University of Iowa.

TABLE 1 | A list of the primers used for genotyping and qPCR.

Genotype primers:
Cre: GCATTACCGGTCGATGCAACGAGTGATG GAGTGAACGAACCTGGTCGAAA TCAGTGC
Lef-1 cKI: TGAGGCGGAAGTTCCTATTCT GGCGGATCACAAGCAATAAT
Lef-1 WT: TCCCAAAGTCGCTCTGAGTT GGCGGATCACAAGCAATAAT
Mir26bTg+: TCAAGCCTCAGACAGTGGTTC AGTAATGGAGAACAGGCTGG
RT primers
Lef-1: TCACTGTCAGGCGACACTTC ATGAGGTCTTTTGGGCTCCT
Sox2: ATGCACAACTCGGAGATCAG TGAGCGTCTTGGTTTTCCG
Pitx2: CTGGAAGCCACTTTCCAGAG AAGCCATTCTTGCACAGCTC
Actb: GCCTTCCTTCTTGGGTATG ACCACCAGACAGCACTGTG
Axin2: ATGAGTAGCGCCGTGTTAGTG GGGCATAGGTTTGGTGGACT
Fgf7: TGGGCACTATATCTCTAGCTTGC GGGTGCGACAGAACAGTCT
Wnt5a: CAACTGGCAGGACTTTCTCAA CCTTCTCCAATGTACTGCATGTG
Tcf7: ACGAGCTGATCCCCTTCCA CAGGGACGACTTGACCTCAT
Lef1: GCCACCGATGAGATGATCCC TTGATGTCGGCTAAGTCGCC
Bmp4: ATTCCTGGTAACCGAATGCTG CCGGTCTCAGGTATCAAACTAGC
Nanog: CACAGTTTGCCTAGTTCTGAGG GCAAGAATAGTTCTCGGGATGAA
Pou5f1: AGAGGATCACCTTGGGGTACA CGAAGCGACAGATGGTGGTC
Mmp2: TGTCTTGCGTCTGACACTGC CTCCTTTGGGCTAGGTATCTCT
Fgf8: AGAGCCTGGTGACGGATCA CTTCCAAAAGTATCGGTCTCCAC
Ccnd2: GAGTGGGAACTGGTAGTGTTG CGCACAGAGCGATGAAGGT
miR-26b: TTCAAGTAATTCAGGATAGGTT Qiagen Univ rev

The *Lef-1 COEL* mouse line was generated by inserting *Lef-1* downstream of a CAAG promoter and a floxed transcription stop signal (Sun et al., 2016). The *miR-26b* transgenic mouse was derived by insertion of an *EF1a* promoter-*miR-26b-5p* (61 bp) construct into mice by pronuclear injection. After backcrossing to C57BL/6 mice multiple times, the location of the insertion was determined by genomic sequencing. The $Pitx2^{Cre}$ mouse used in this study has been described previously (Liu et al., 2003). Each mouse line derived was crossed to a C57BL/6 background. For embryonic staging experiments, the observed vaginal plug date of the female was designated as E0.5. Embryos were collected on the required date, and genomic DNA was isolated from a portion of the embryonic or neonatal material (usually the tail) for genotyping. The genotyping primers for all the mouse lines are listed in **Table 1**.

Plasmid Constructs and Reporter Assays

Lef-1 promoter luciferase and *pSil-miR-26b* constructs were previously described (Amen et al., 2007; Zhang et al., 2014). We used our recently described plasmid-based microRNA inhibitor system (PMIS) to generate a specific *PMIS-miR-26b* inhibitor (Cao et al., 2016). The luciferase TOP flash and FOP flash reporter constructs were purchased from EMD/Millipore (Burlington, MA, United States). Luciferase assays were done as previously described (Sun et al., 2016).

Immunohistochemistry, Immunofluorescence, and Histology

Mouse embryos and tissue morphology was examined by Hematoxylin and Eosin staining procedure as done previously (Sun et al., 2016). Primary antibodies against Lef-1 (Cell signaling, Danvers, MA, United States), Myc (Santa Cruz, Dallas, TX, United States), Ki67 (Abcam, Cambridge, MA, United States), Sox2 (Abcam, Cambridge, MA, United States), and Amelogenin (Santa Cruz, Dallas, TX, United States) were then added to the sections. Incubation with primary antibody occurred overnight at 4°C. The slides were treated with FITC (Alexa-488)- or Texas Red (Alexa-555)-conjugated

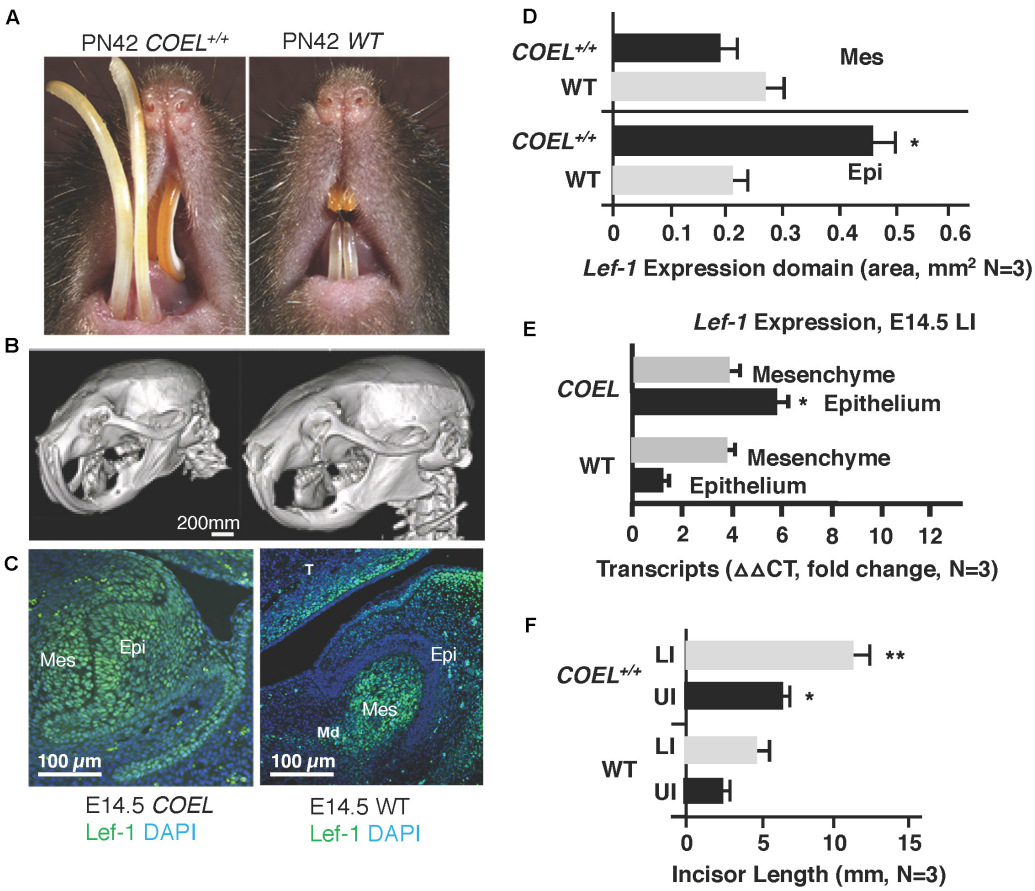

FIGURE 1 | *Lef-1* conditional over-expression in the dental epithelium increases murine incisor growth. **(A)** The conditional over-expression of *Lef-1* (*COEL*) 42-day old (PN42) mice have an incisor overgrowth phenotype compared to WT mice. **(B)** μCT images to PN42 COEL mice show overgrown incisors and cranial bone defects. **(C)** Lef-1 expression by immunofluorescence shows Lef-1 ectopically expressed in the E14.5 dental epithelium of the COEL vs. WT (mesenchyme, Mes; epithelium, Epi). **(D)** Quantitation of the E14.5 *Lef-1* expression domains (mesenchyme, Mes; epithelium, Epi) from **(C)**. Three images, including the image in **(C)** were used to calculate expression domains. qPCR of *Lef-1* transcripts from the mesenchyme and epithelial tissues of E14.5 dissected tooth germs and isolated RNA, $N = 3$. **(F)** Incisor length measurements (mm) from the PN42 mice in **(A)**, $N = 3$. $^{*}p < 0.05$, $^{**}p < 0.01$.

Secondary antibody and then were incubated for 30 min at room temperature for detection (Invitrogen, Carlsbad, CA, United States). Nuclear counterstaining was performed using DAPI-containing mounting solution. Pictures were taken under confocal microscope Zeiss 700 and photo preparation done on adobe photoshop. For some sections, photos were quantitated for fluorescence intensity using ImageJ.

Imaging and Microcomputed Tomography (μCT)

Mouse skulls from three experimental and control animals were scanned with a Siemens Inveon Micro-CT/PET scanner using 60 kVp and 500 mA with a voxel size of 30 μm. Reconstructed images were imported using Osirx DICOM software. Mouse heads were prepared by overnight fixation at 4°C, followed by storage in 70% EtOH. Scans directed across the anterior-posterior plane produced 2D images which were matched between animals using topology markers such as the molar.

RNA Isolation and Quantitative Real-Time PCR Gene Expression Analysis

RNA was isolated from dissected mouse tissues (mouse mandibles or dissected dental epithelium and mesenchyme tissues from the tooth germ) using RNA easy and miRNA easy kits (Qiagen, Carlsbad, CA, United States) and validated on agarose gels for purity, and qualitative assessment using rRNA bands to ensure minimal degradation. Nanodrop analysis gave precise concentration and cDNAs were generated by a mix of oligo DT and random hexamers and RT polymerase. cDNA quality was accessed by qPCR analysis to ensure consistency and melt curves and sequencing of qPCR products ensured the specificity of our probes. Experiments were done in triplicate and independent cDNAs were used to perform qPCR. ΔΔCT values were calculated and used to determine fold changes. qPCR primers are listed in **Table 1**.

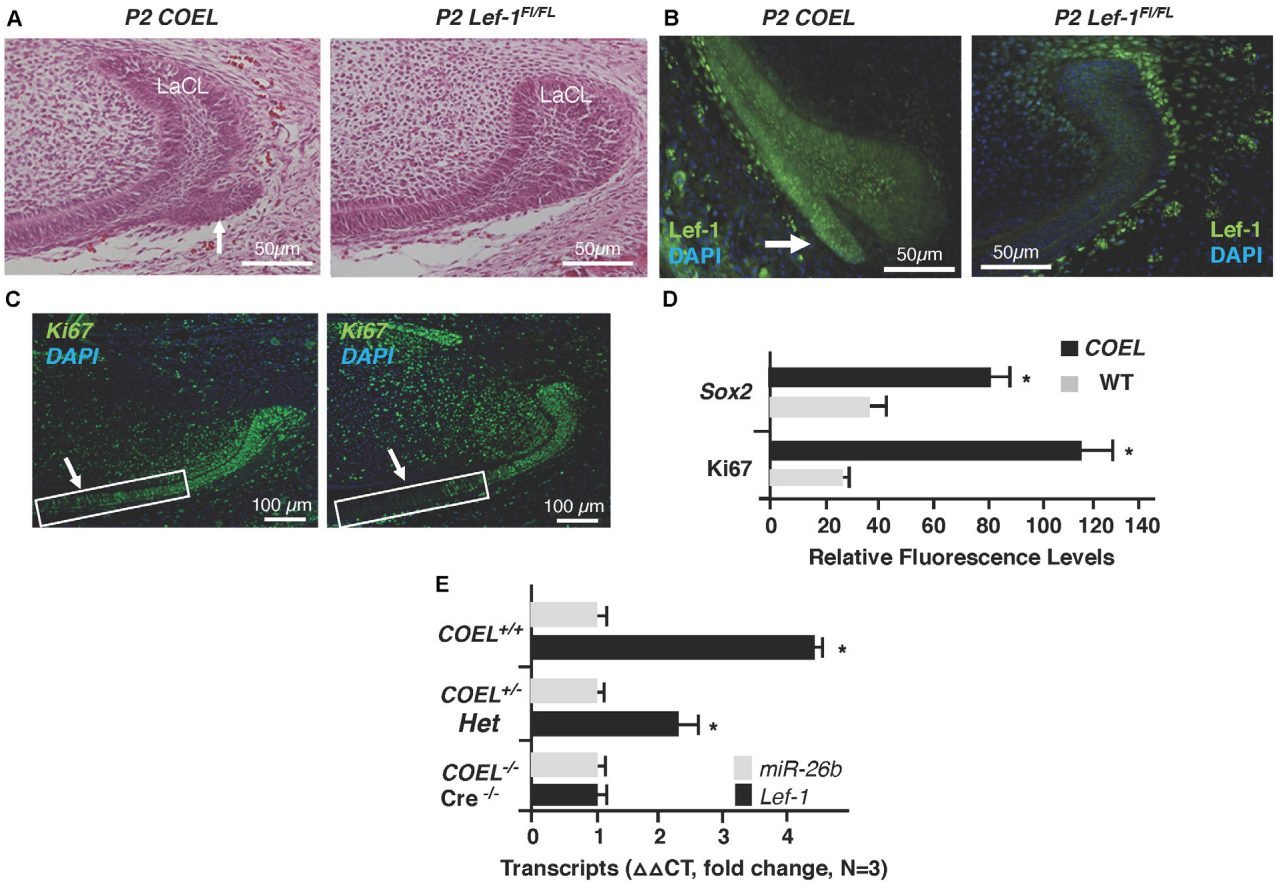

FIGURE 2 | *Lef-1* over-expression creates an extra stem cell niche and increases cell proliferation in the lower incisor. **(A)** H&E staining of P2 sagittal sections of the mouse lower incisor showing the extra stem cell niche formed in the *COEL* mouse (white arrow). **(B)** Lef-1 is highly expressed in the new stem cell compartment of P2 *COEL* mice (white arrow). **(C)** Ki67 expression show by immunofluorescence was increased in the P2 *COEL* mice. **(D)** Sox2 and Ki67 positive cells were quantitated by ImageJ in *COEL* and WT mandibles. **(E)** *Lef-1* expression from P0 mandibles was increased in *COEL* mice with two copies of the transgene ($COEL^{+/+}$) compared to one copy of *Lef-1* cDNA ($COEL^{\pm}$) and WT or Cre negative mice, $N = 3$. *miR-26b* expression is not regulated by *Lef-1*. Labial cervical loop, LaCL. *$p < 0.05$.

Wnt Array

Tissue was dissected from the mandibular region of a P0/P1 mouse and RNA was isolated as described (Sun et al., 2016). Using a Primer PCR Wnt signaling array (Bio-Rad, Hercules, CA, United States) cDNA from a WT or *miR-26b* overexpression mouse were compared according to the manufacture recommendations. RT primer probes were generated against genes that showed a twofold increase or decrease in the Biorad Wnt array plate and independently verified by qPCR.

Statistical Analysis

For each condition, a minimum of three experiments was performed and error bars were presented as the ±SEM. An independent two-tailed *t*-test was used to determine the significance of differences between *WT*, *COEL*, *miR-26b*, and *COEL/miR-26b* groups.

RESULTS

Conditional Overexpression of *Lef-1* in the Oral and Dental Epithelium Results in Formation of an Extra Stem Cell Niche

Lef-1 conditional knock-in (*Lef-1*^{cKI}) mice were crossed with *Pitx2*^{Cre} mice to drive the over-expression of *Lef-1* in the dental and oral epithelium at E10.5. *Pitx2*^{Cre}/*Lef-1*^{cKI} or COEL of Lef-1 mice have a striking incisor over-growth phenotype, not due

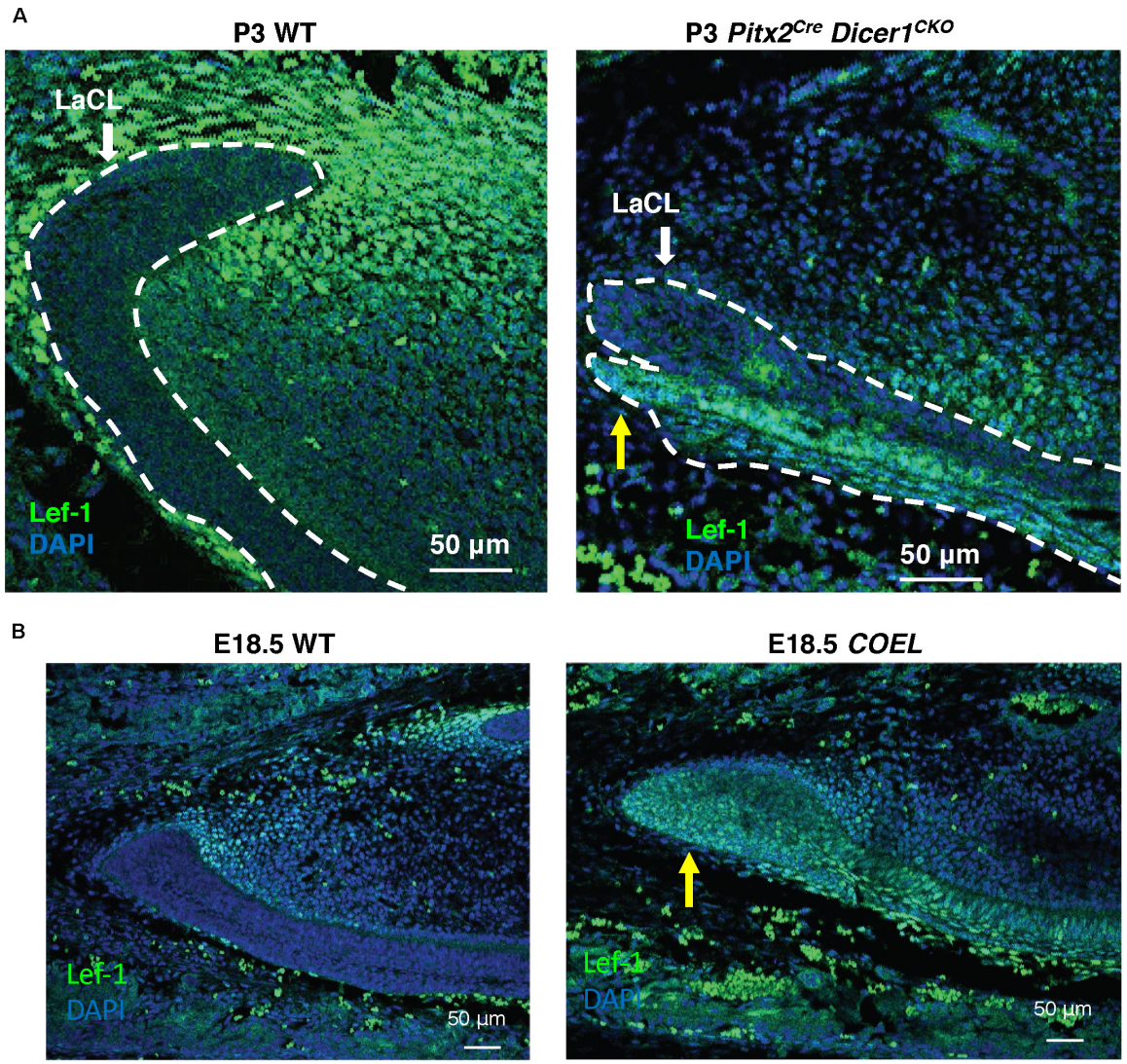

FIGURE 3 | *Lef-1* expression was increased in the *Dicer1*^{cKO} incisor forming a new stem cell niche like *COEL* mice. **(A)** Lef-1 expression in sagittal sections of *Pitx2*^{Cre}/*Dicer1*^{cKO} P3 lower incisors. Low levels of Lef-1 expression in P3 WT epithelium were observed and increased Lef-1 expression was found in the branched stem cell niche of the P3 *Dicer1*^{cKO} mice (yellow arrow). **(B)** Lef-1 expression in the lower incisor of the E18.5 *COEL* lower incisor (yellow arrow). Labial cervical loop, LaCL.

to malocclusions as the phenotype is observed in 100% of the mice (**Figures 1A,B** uCT images). The *COEL* mice have shorter nasal bone, snout length, frontal bone length, parietal bone length, cranial base length, cranial base angle, and ramus height (measurements not shown). However, the mandibular length is increased over WT mice. The *COEL* mandible is characterized by a reduced coronoid process and angular processes. There is also a general thinning or porosity in the region of the angular process (**Figure 1B**).

Lef-1 expression remains in the tooth bud/oral epithelium during embryonic stages E14.5 in *COEL* embryos but is mostly mesenchymal in E14.5 WT embryos (**Figure 1C**). Lef-1 expression levels from IF sections were quantitated for fluorescence intensity (FI) and shown in **Figure 1D** (E14.5). *Lef-1* transcripts were quantitated in E14.5 dental mesenchyme and epithelium from WT and *COEL* embryos. As expected *Lef-1* transcripts increased in the epithelium of *COEL* embryos compared to WT (**Figure 1E**). Incisor length was measured and recorded in adult *COEL* mice compared to WT mice and show a large increase in overall length (**Figure 1F**). These data demonstrate ectopic expression of *Lef-1* in the oral epithelia after E14.5 correlating with dental and craniofacial growth defects.

In a previous report we documented a new stem cell compartment located in the LaCL of *COEL* mice (**Figure 2A**; Sun et al., 2016). This extra stem cell niche is created by the over-expression of *Lef-1* and contains high levels of Lef-1 expression (**Figure 2B**). Cell proliferation as measured by Ki67 staining was expanded in the P2 *COEL* transient amplifying cells and indicative of rapidly growing incisors (**Figures 2C,D**). Furthermore, Sox2 expression was significantly increased in the lower incisor LaCL (**Figure 2D**) (Sox2 staining shown in Sun et al., 2016). *Lef-1* transcripts in the mandible of *COEL* mice with one copy of the *Lef-1* cDNA transgene ($COEL^{\pm}$) and two copies of *Lef-1* cDNA ($COEL^{+/+}$) are increased proportionally (**Figure 2E**). Thus, ectopic *Lef-1* expression in the dental epithelium after E14.5 (when endogenous *Lef-1* expression transitions to the dental mesenchyme) results in an expanded stem cell niche and increased epithelial cell proliferation. Interestingly, the new stem cell compartment does not contain Ki67 positive cells.

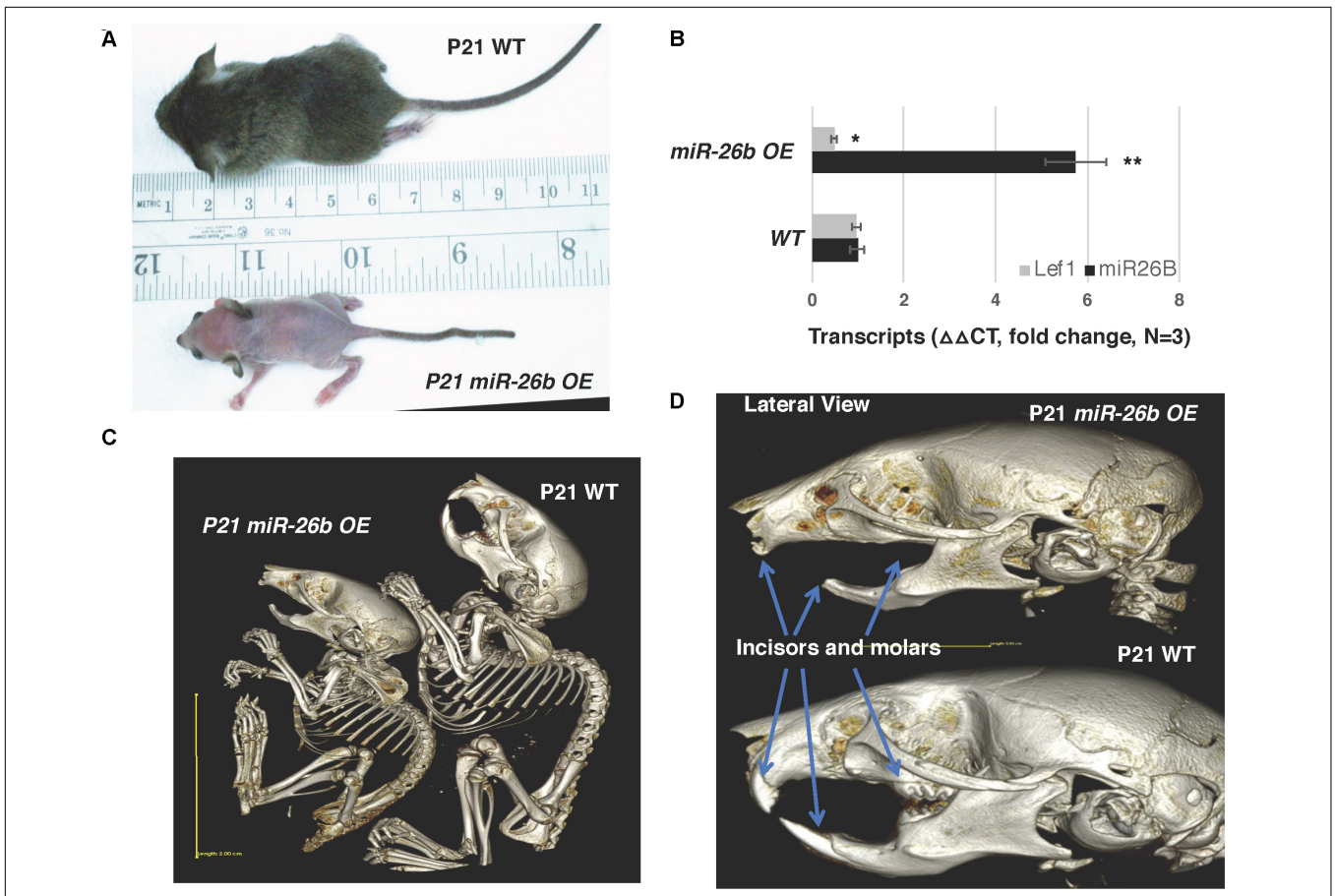

FIGURE 4 | *miR-26b OE* mice have defects in ectodermal organ development. **(A)** *miR-26b* over-expression (OE) mice are small, have a loss of hair and a crooked tail like *Lef-1* knockout mice. **(B)** *miR-26b* is over-expressed in the *miR-26b OE* mouse mandible with a decrease in *Lef-1* transcripts shown by qPCR. **(C)** μCT whole body images of the P21 *miR-26b OE* and WT mice. **(D)** μCT head images showing a lack of incisors and molars and bone defects in the P21 *miR-26b* mice compared to WT. $^{*}p < 0.05$; $^{**}p < 0.01$.

We began studying the function of miRs during tooth development by conditionally knocking out *Dicer1* using the $Pitx2^{Cre}$ and found these mice had multiple enamel-free incisors (Cao et al., 2010). The complete ablation of mature miRs in these mice resulted in branched incisors caused by the formation of extra stem cell niches (Cao et al., 2010), similar to the *COEL* mice. We hypothesized that this might result from ectopic *Lef-1* expression in the mutant LaCL and thus assayed for Lef-1 expression in P3 $Pitx2^{Cre/}Dicer1^{CKO}$ mice. Indeed, like in the *COEL* mice, Lef-1 expression was associated with the formation of an additional stem cell niche (**Figure 3A**, yellow arrow). This extra niche was used to create a branched incisor (Cao et al., 2010). The E18.5 *COEL* embryos also show increased Lef-1 expression in a similar region of the LaCL producing a new stem cell niche compartment (**Figure 3B**, yellow arrow). These results show that miRs are controlling the organization of the stem cell niche by regulating *Lef-1* expression.

The *miR-26b* Over-Expression Mice Have Craniofacial Defects That Phenocopy *Lef-1* Knockout Mice

We have shown that *miR-26b* directly targets *Lef-1* and represses colon cancer cell proliferation (Zhang et al., 2014). Furthermore, *miR-26b* represses the expression of the *Lef-1* target genes *cyclin D1* and *cMyc* (Zhang et al., 2014). To determine miR expression profiles, we analyzed the dental mesenchyme and epithelial tissues from P0 and E14.5 mice and embryos, respectively. We identified several miRs that were differentially expressed in the epithelial tissue compared to mesenchyme (Cao et al., 2010). *miR-26b* was not highly expressed prior to E14.5 in the dental epithelium at a time when *Lef-1* expression was transitioning to the mesenchyme. However, *miR-26b* expression was increased after E14.5 in the dental epithelium, which may act to decrease *Lef-1* expression at this stage (Cao et al., 2010).

The *miR-26b* transgenic over-expression (OE) mouse has an incomplete penetrance. $miR\text{-}26b^{Tg\pm}$ (Het) mice are mostly normal, but under-represented in live births and late embryonic stages, and most of the double transgenic $miR\text{-}26b^{Tg+/Tg+}$ mice die early in embryonic development, before E14.5. However, some mice are born and live to weaning date, but then cannot process solid food. These mice are small, with a lack of fur, and a very defined crook in the tail (**Figure 4A**). Interestingly, these mice resemble the *Lef-1* general knockout mice (Van Genderen et al., 1994). *miR-26b* expression is increased and endogenous *Lef-1* transcripts are decreased in the *miR-26b OE* mice (**Figure 4B**).

These mice lack teeth, including molars and incisors, shown by uCT imaging (**Figures 4C,D**). Full body uCT images reveal skeletal and bone defects in P21 mice (**Figures 4C,D**). The cranial base and cranial breath measurements are essentially identical in the *miR-26b OE* mice. However, the *miR-26b OE* mice have a shorter nasal bone, snout, frontal bone, parietal bone, cranial breath, and cranial base length compared to WT mice (measurements not shown). The cranial base angle and ramus height are also decreased in the *miR-26b OE* mice compared to WT mice. In contrast to the *COEL* mice, the *miR-26B OE* mice have a decreased mandibular length compared to WT mice (measurements not shown).

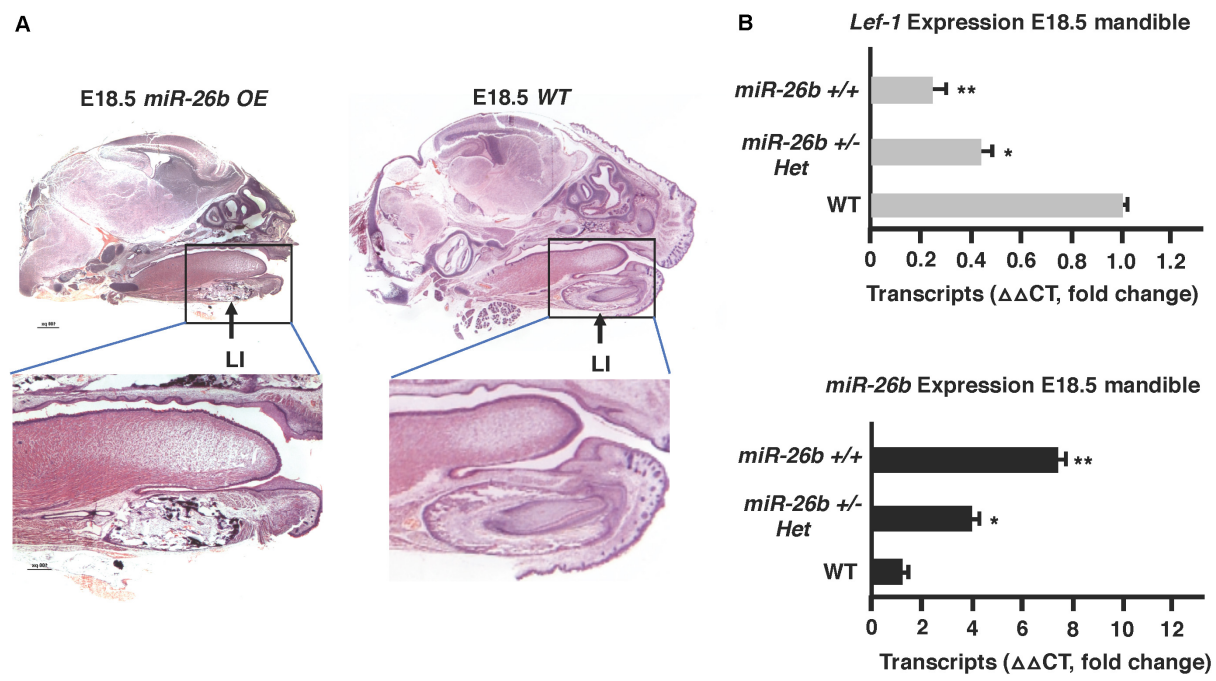

FIGURE 5 | Tooth development is arrested in the *miR-26b OE* embryo. **(A)** Sagittal sections and H&E staining of the E18.5 *miR-26b OE* and WT heads. The boxed region is magnified to show a lack of a lower incisor tooth germ formation. **(B)** *miR-26b* expression correlates with decreased *Lef-1* expression in the mandibles of the mice in **(A)** by qPCR ($N = 3$, $^{*}p < 0.05$, $^{**}p < 0.01$).

miR-26b OE Inhibits *Lef-1* Expression and Arrests Tooth Development

The μCT images show that the *miR-26b OE* P21 mice do not have incisors or molars. *miR-26b OE* embryos were harvested, sectioned and H&E stained to examine tooth development at an earlier stage. The lower and upper incisors and molar tooth germs were completely absent at E18.5 (**Figure 5A**). We show a dose response for *miR-26b* expression and *Lef-1* expression. In mice with one copy of the *miR-26b* transgene, *Lef-1* expression is decreased approximately 50% (**Figure 5B**). In mice with two copies of *miR-26b* we show that *Lef-1* expression is further decreased and the E18.5 *miR-26b OE* embryos shown without tooth germs have two copies of the *miR-26b* transgene (**Figures 5A,B**). These data demonstrate that *miR-26b* is a potent regulator of tooth and cranial bone development.

The Wnt Signaling Effectors and Pathway Are Regulated by *miR-26b*

Lef-1 is known to play a role in Wnt signaling and transcriptional activation. We tested for the possibility that reductions in *Lef-1* expression levels would cause alterations in Wnt signaling. Wnt signaling in the *miR-26b OE* mouse was analyzed by isolating RNA and using a Bio-Rad Wnt signaling array. There were reductions in 10 of the 80 Wnt target genes, including *Fgf7/8* and *Bmp4* and an increase in several genes involved in stemness, such as *Nanog* and *Pou5F1* (**Figures 6A,B**). These results were verified by qPCR from P0 mandible tissue. The *COEL* mouse showed upregulation of *Fgf7/8* and *Bmp4* by qPCR (**Figure 6C**). Lef-1 regulates several key Wnt targets and Wnt signaling genes are upregulated by OE of *Lef-1* and reduced by OE of *miR-26b* (**Figure 6C**). We further demonstrate the effect of *Lef-1* and *miR-26b* transcriptional regulation using the Topflash

A

BioRad Wnt Array Genes	*miR-26b* OE >2X decrease N=1	qPCR N=3
AXIN2	2.51672	2.127407072
FGF7	2.41	1.933813306
ETS	2.317413	NT
PITX2	2.263874725	1.851947111
FGF20	2.25174	NT
SOX2	2.21735511	1.798313
WNT5A	2.2175	2.002655654
TCF7	2.13	0.733233502
LEF1	2.117784	2.159051881
DPP10	2.068085952	NT
BMP4	2.11778	2.455392549

B

BioRad Wnt Array Genes	*miR-26b* OE >2X increase N=1	qPCR N=3
NANOG	7.10623803	2.99426722
POU5F1	3.91502501	1.9321221
ACTB	2.472645	2.134731
MMP2	6.04931791	3.59355201
FN1	4.27674443	NT
EGR1	2.78955328	NT

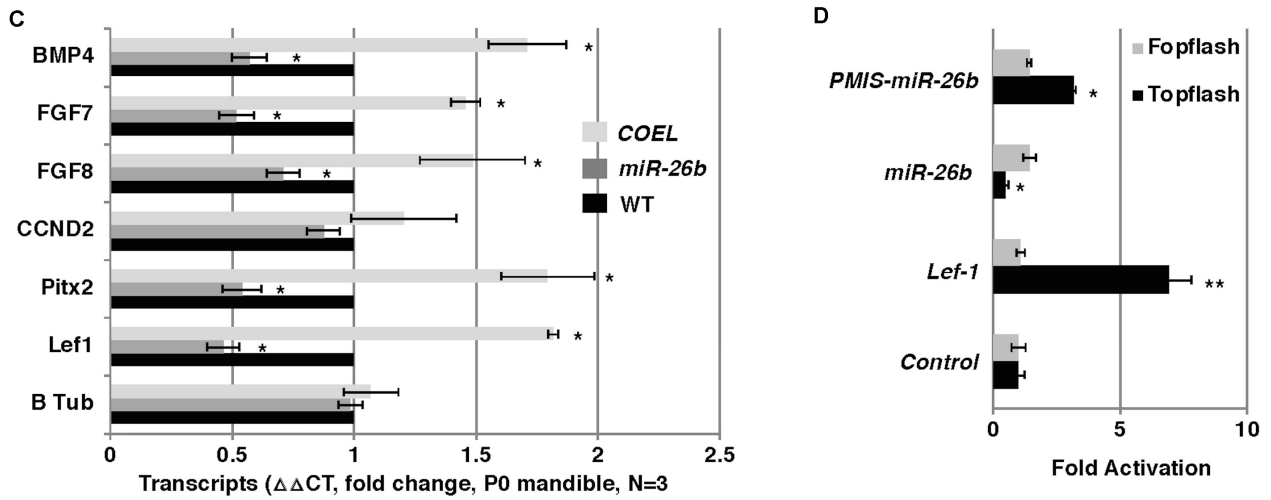

FIGURE 6 | Wnt responsive genes are regulated by *miR-26b*. **(A)** Wnt PCR array was used to probe for Wnt genes regulated by *miR-26b*. Specific genes are shown that were decreased in the *miR-26b OE* mouse, $N = 1$. The genes were validated by qPCR ($N = 3$). **(B)** Wnt array genes that were increased in *miR-26b OE* mice ($N = 1$) and validated by qPCR. **(C)** Selected genes were assayed by qPCR from RNA isolated from P0 mandibles of *COEL*, *miR-26b OE*, and WT mice, $N = 3$. **(D)** *Lef-1* cDNA, *miR-26b*, and *PMIS-miR-26b* plasmid DNAs were transfected into HEK 293 cells with either Topflash or Fopflash luciferase reporter constructs. Luciferase activity was recorded and expressed as fold activation compared to controls without *Lef-1*, *miR-26b,* or *PMIS-miR-26b* expression ($N = 3$, $^{*}p < 0.05$, $^{**}p < 0.01$).

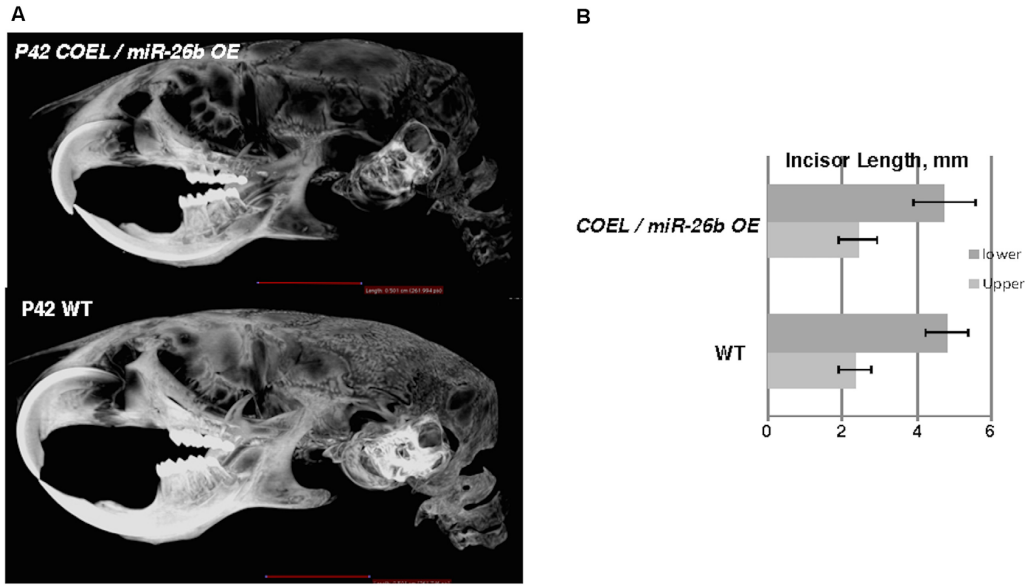

FIGURE 7 | *miR-26b OE* rescues the *COEL* phenotype. **(A)** μCT head images of PN42 *COEL/miR-26b OE* rescue mice and WT mice. **(B)** Incisor length measurements demonstrate that the length of rescue mice incisors are similar in length to WT mice, *N* = 3.

luciferase reporter (Zhang et al., 2011). A *Lef-1* cDNA, a *miR-26b* construct and an inhibitor of endogenous *miR-26b* (*PMIS-miR-26b*) were transfected into HEK293 cells with the Topflash or Fopflash control reporter constructs. As expected Lef-1 activated the Topflash reporter but did not activate the Fopflash control reporter (**Figure 6D**). *miR-26b* expression inhibited the Topflash reporter, which contains 7 *Lef-1* binding elements, but has no effect on the control Fopflash reporter (**Figure 6D**). When endogenous *miR-26b* was inhibited using the *PMIS-miR-26b* construct the Topflash reporter was activated due to increased endogenous *Lef-1* activity (**Figure 6D**). Together these data show that *miR-26b* is regulating the Wnt signaling pathway through the regulation of *Lef-1* expression.

miR-26b OE Rescues the *COEL* Phenotype

The over-expression of *miR-26b* phenocopied *Lef-1*$^{-/-}$ mice and regulated *Lef-1* expression *in vivo*. We hypothesized that crossing the *miR-26b OE* mice with *COEL* mice might result in a rescue of the tooth phenotype. Indeed, these mice (*COEL/miR-26b OE*) resulted in 100% penetrance of the rescued phenotype as all mice had normal tooth development. The μCT images show the restoration of the incisors and molars (**Figure 7A**). The measurements of the P42 *COEL/miR-26b OE* lower incisor length were similar as observed in P42 WT mice (**Figure 7B**). Overall growth defects were not corrected (data not shown) as the mice continue to be smaller than wild-type littermates. Also, OE of *Lef-1* corrected the lethality and tooth defects in the *miR-26b OE* mouse strain. While liter sizes were small, we obtained Mendelian frequencies of all genotypes when crossing the *COEL* and *miR-26b OE* strains and no mice were born with defects in incisors or molar growth.

We show representative P42 mice with *COEL*, control and *COEL/miR-26b OE* rescue mice phenotypes (**Figure 8A**). For comparison, separate μCT images of these phenotypes are shown to contrast the tooth and cranial bone phenotypes (**Figure 8B**). We sectioned P0 mice to determine if *miR-26b* OE could correct the defects of the LaCL and the developmental defects in the *COEL* mouse. The LaCL morphology was mostly restored to the WT structure in the *COEL/miR-26b OE* mouse (**Figure 8C**). The altered Ki67 and *Amelogenin* expression shown in the *COEL* mice were corrected in the rescue mice and similar to the wild-type control (**Figure 8C**). Furthermore, *Lef-1* expression in the rescue mice was similar to WT mice (**Figure 8D**). These data demonstrate a genetic association between the *COEL* and *miR-26b OE* murine phenotypes. Furthermore, we show that *miR-26b* specifically regulates *Lef-1* and that *Lef-1* is a major target of *miR-26b* during craniofacial and tooth development. Specifically, we have identified a *Lef-1* dosage effect required for normal tooth development and craniofacial development modulated by *miR-26b*.

DISCUSSION

Stem cells derived from stem cell niches contribute to the regeneration of mature tissue types in many different organs, including the trachea, lungs and teeth, amongst others (Harada et al., 1999; Tummers and Thesleff, 2003; Chistiakov, 2010; Juuri et al., 2012; Sun et al., 2016). These niches are formed in developing embryos, and must be maintained throughout life by symmetric cellular divisions that produce daughter pluripotent stem cells (Morrison, 2008). Another equally important behavior of the cells in a stem cell niche is the production of differentiated daughter cells by asymmetric cell division, which then take

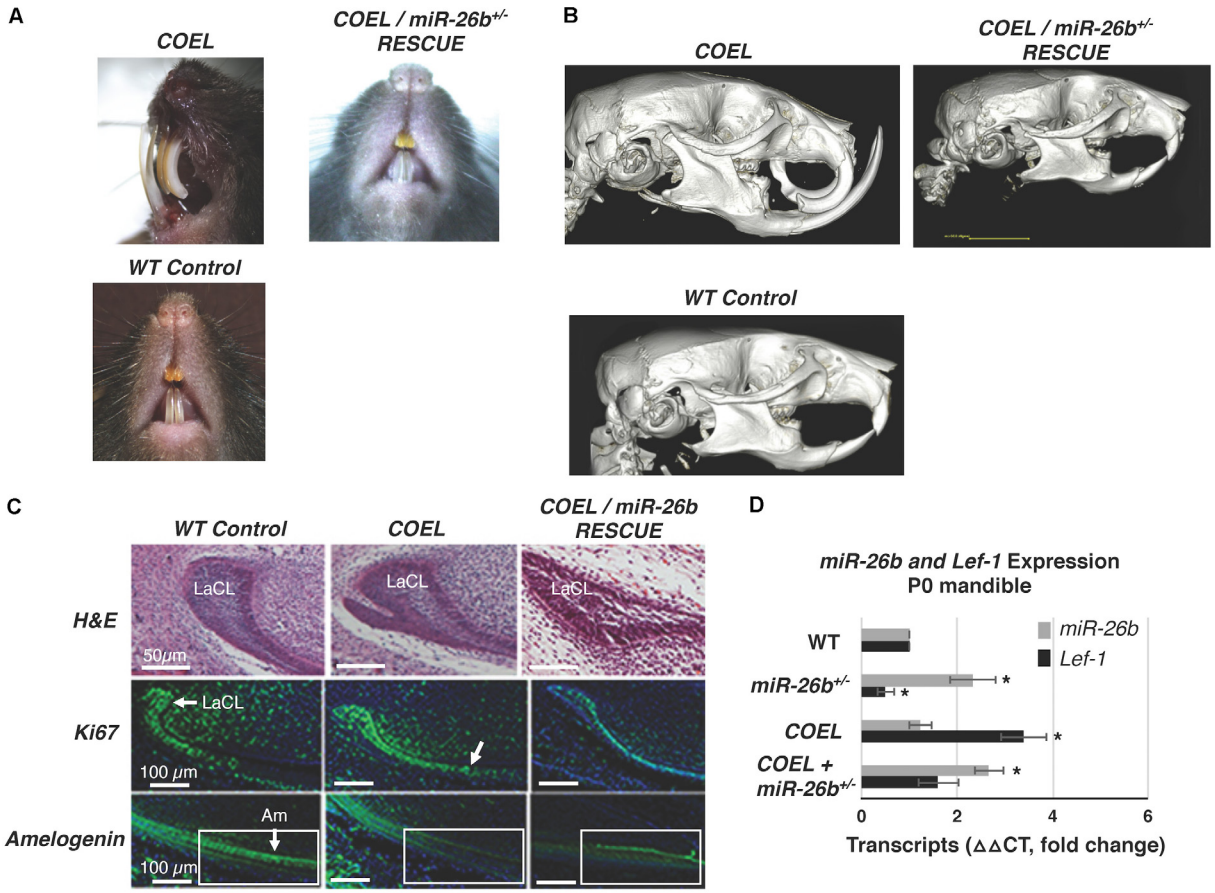

FIGURE 8 | Comparison of the *COEL*, *COEL/miR-26b* rescue and WT mice demonstrating normal incisor development in the rescued mice. **(A)** Mice heads with incisor phenotypes are shown, **(B)** μCT head images comparing the *COEL*, *COEL/miR-26b* rescue, and *Cre* negative control mice bone and tooth development. **(C)** Sagittal sections of P2 lower incisors of the three mice showing the *COEL* extra stem cell compartment and rescue by *miR-26b*, H&E staining; Ki67 staining shows that cell proliferation in the rescue mice is similar to WT mice; and Amelogenin expression is similar in the rescue mice as observed in WT mice. The boxed region is shown for comparison. **(D)** P0 mandibles were processed for RNA and analyzed for *Lef-1* and *miR-26b* expression from WT, *COEL*, and *COEL miR-26b*$^{\pm}$ mice. ($N = 3$, $^{*}p < 0.05$). Labial cervical loop, LaCL; Ameloblasts, Am.

the place of damaged cells in regenerative organs, in order to allow the organ to continue to function (Knoblich, 2008). How these behaviors are regulated is an important question for stem cell biologists, who seek to ultimately apply stem cell therapies to a host of diseases in which the ability of the body to sustain the production of cell types required for normal function becomes impaired. Currently, much is known about the transcriptional programs that maintain a stem like state (Young, 2011). However, more work is required to investigate how cells can turn off these stem cell programs in order to differentiate. Historically, transcription factors have been thought of as the key determinants of cell state (Iwafuchi-Doi and Zaret, 2016). Recently, however, miRs have become appreciated as playing a role in stem cell differentiation (Schwamborn, 2009). The ability to co-opt miR expression to reprogram and control the differentiation of naive cells into different cell types is an important tool required to create artificial organs and repair diseased tissues, saving millions of lives and public dollars.

Several miR families have been implicated in tooth development by our group and others. *miR-26b* is of interest because it is highly expressed during specific stages of tooth development. We found its expression was absent from the oral epithelium and DESCs of the LaCL in the lower murine incisor prior to E14.5, when *Lef-1* is expressed. However, *miR-26b* is highly expressed at later stages in all dental epithelial tissues, including the LaCL indicating that it may play a functional role in DESC differentiation. The *COEL* mouse was generated to understand the function of tissue specific *Lef-1* expression and demonstrates that *Lef-1* regulates DESC proliferation. While Lef-1 is known to control stem cell self-renewal and stem cell compartments in the epidermis and hair follicles, we show it is also required for the formation of a DESC niche. Interestingly, the *miR-26b* OE mouse completely inhibits tooth development by targeting *Lef-1* expression, demonstrating a critical role for *miR-26b* during embryonic development. These are two new mouse models that will allow us to understand the genetic and functional activities of both *Lef-1* and *miR-26b*.

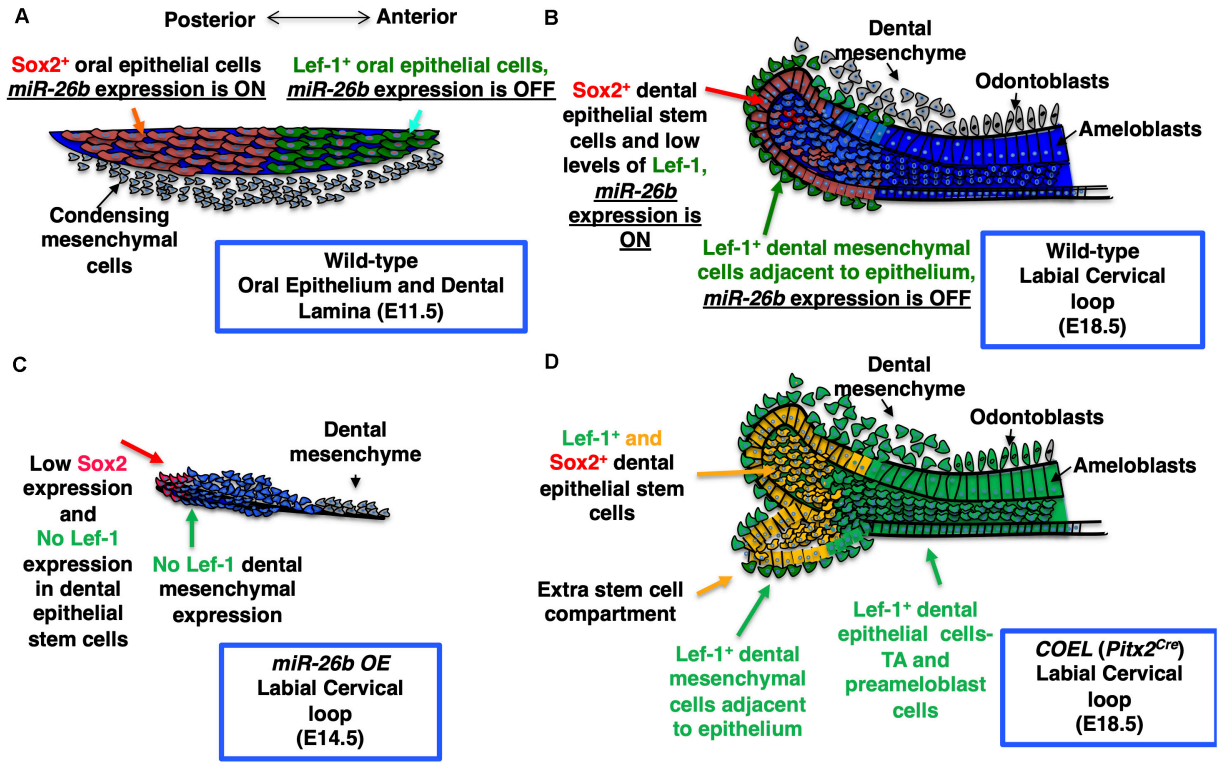

FIGURE 9 | Model for the role of *miR-26b* and *Lef-1* in the lower incisor during development. **(A)** The normal expression of *Sox2* and *Lef-1* during E11.5 dental placode development. **(B)** The normal lower incisor development at E18.5 showing the WT labial cervical loop (LaCL), *Sox2* and *Lef-1* expression and *miR-26b* expression domains. **(C)** *miR-26b OE* inhibits tooth bud development with no Lef-1 and reduced Sox2 expression at E14.5 in the LaCL. **(D)** An extra stem cell compartment is formed in the E18.5 *COEL* LaCL expressing *Sox2* and *Lef-1* and the dental epithelial cells express *Lef-1* causing an increase in dental epithelial cell proliferation and increased incisor growth. TA refers to the Transient Amplifying Cells.

Lef-1 in Tooth Development

Previous studies have shown that *Lef-1* is regulated by FGF signaling and is required for early tooth development (Kratochwil et al., 1996, 2002; Sasaki et al., 2005). *Lef-1* deficiency results in arrested tooth morphogenesis at the late bud stage (Van Genderen et al., 1994), and that *Lef-1* is required only transiently in the dental epithelium for tooth development (Kratochwil et al., 1996). *Lef-1* expression is shifted to mesenchymal cells/tissues surrounding the epithelium at the bud stage, although low levels of *Lef-1* expression remain in the dental epithelium (Kratochwil et al., 1996; Sasaki et al., 2005). A developmental mechanism for this transition was recently shown using the *COEL* mice thus, Lef-1 expression after E14.5 in the dental epithelium creates a new LaCL stem cell niche and abnormal "tusk-like" incisors (Sun et al., 2016). Furthermore, over-expression of *Lef-1* partially rescued tooth arrest in $Sox2^{cKO}$ embryos (Sun et al., 2016). Both *Sox2* and *Lef-1* are markers of early craniofacial development and are expressed in the oral and dental epithelium (Sasaki et al., 2005; Juuri et al., 2012, 2013; Zhang et al., 2012; Sun et al., 2016). These data demonstrated that *Lef-1* can partially replace *Sox2* as a potential stem cell factor to both initiate and maintain the lower incisor LaCL stem cell niche.

In this report, we show that the new LaCL stem cell compartment highly expresses *Lef-1* and that this new compartment does not contain actively dividing cells, whereas cell proliferation is increased in the transient amplifying cells. The new stem cell compartment contains quiescence cells that are partitioned adjacent to the LaCL and these cells may provide progeny to the outer enamel epithelium and the stratum intermedium cell layers as well as the inner enamel epithelium. Interestingly, the new stem cell compartment does not form until birth or shortly before, suggesting that continued *Lef-1* expression in the dental epithelium contributes to stem cell development but not maintenance. The rapid growth of the *COEL* incisors may indicate that the new stem cell niche provides an additional progenitor cell source that contributes to increased cell proliferation in both the outer and inner enamel epithelial cell layers. We are currently exploring *Lef-1*-mediated cell reprogramming and tissue/tooth regeneration as Lef-1 may act as a master transcription factor for tooth development.

These data provide a molecular mechanism for why *Lef-1* expression is required for early formation of the LaCL epithelial stem cell niche. In normal incisor development *Lef-1* expression is decreased in the dental epithelium at E14.5 and *Lef-1* expression transitions to the dental mesenchyme. It is well established that the odontogenic potential shifts from the

dental epithelium after E12.5 to the mesenchyme during early murine tooth development (Zhang et al., 2005). Interestingly, COEL of *Lef-1* in the mesenchyme also results in an incisor overgrowth phenotype (unpublished data). *Lef-1* may be playing an essential role in this transition. As *Lef-1* expression increases in the dental mesenchyme this correlates with the odontogenic potential shift to the mesenchyme. Furthermore, we have shown that *Lef-1* over-expression in the LaCL results in an increase in *Sox2* expression in the new stem cell compartment (Sun et al., 2016). Therefore, *Lef-1* may act as an initial stem cell factor during ectodermal organ development to set up specific cell fates and regulate gene expression required for the maintenance and compartmentalization of the dental stem cell niche.

The Role of MicroRNAs in Tooth Development and Regulation of *Lef-1* Expression

The conditional inactivation of the microRNA processing gene, *Dicer1*, resulted in tooth defects including, extra teeth, branched teeth, abnormal tooth shape, and loss of enamel due to impaired ameloblast differentiation (Cao et al., 2010; Michon et al., 2010). However, ablating all mature miRs from the dental epithelium offered clues as to the actions of miRs but did not identify which specific miRs were involved in the early process of tooth development. We isolated dental epithelial tissues and profiled them for miR expression and found that *miR-26b* was also differentially expressed in the dental epithelium (Cao et al., 2010). Prior to E14.5 *miR-26b* is not expressed in the LaCL stem cell niche, however after E14.5 *miR-26b* expression is increased and its expression in the epithelium remains until birth. *miR-26b* expression is inversely correlated with *Lef-1* expression in the developing tooth.

The role of *miR-26b* during development was unknown until this report, as no mouse models were generated and more importantly nothing is known about the role of *miR-26b* in dental stem cell proliferation and tooth morphogenesis. Murine *miR-26b* is expressed on chromosome 1 and is an intragenic miR and has been reported to be involved in multiple cancers. We have previously shown that *miR-26b* directly targets *Lef-1* and regulates cell proliferation through the *Lef-1* target genes *Cyclin D1* and *cMyc* (Zhang et al., 2014). When we checked our $Pitx2^{Cre}$/*Dicer1* conditional knockout mice for *Lef-1* expression, we found increased *Lef-1* expression (Cao et al., 2010) and it was also associated with the extra stem cell compartment we identified in the $Dicer1^{cKO}$ embryos.

miR-26b Over-Expression Inhibits *Lef-1* Expression and Results in Ectodermal Organ Defects

Because *miR-26b* targets *Lef-1* expression and Lef-1 is a critical factor for early tooth development we asked if *miR-26b* over-expression affected tooth development. The ectopic expression of *miR-26b* occurs early in development using a *EF1a* promoter to over-express *miR-26b* in all tissues. We show that *miR-26b OE* mice have arrested tooth development. Therefore, during tooth development the epithelial expression of *Lef-1* is inhibited prior to its expression in the mesenchyme by ectopic expression of *miR-26b*. The effect of over-expressing *miR-26b* demonstrates its role during embryonic development is to regulate *Lef-1*, as most of the mouse defects are associated with tissues that require *Lef-1* for normal development. Therefore, *miR-26b* only regulates specific tissues and the genes required for *Lef-1*-dependent developmental processes. The *miR-26b OE* mice have a loss of both molars and incisors as well as a loss of hair and other defects associated with *Lef-1* deletion in mice. Interestingly, other defects such as cranial bone defects or decreased growth of bones could be affected by mesenchymal *miR-26b* expression or by affecting pituitary development. We have shown that *miR-26b* targets *Lef-1*, which modulates Pituitary Transcription Factor 1 (Pit-1) expression (Zhang et al., 2010). A similar mechanism occurs in the pituitary where *miR-26b* regulates *Pit-1* expression by inhibiting *Lef-1* expression to promote *Pit-1* lineage differentiation during pituitary development. Curiously, in the $Pitx2^{Cre}$/$Dicer1^{cKO}$ mutant pituitary we also reported an abnormal branching phenotype of the pituitary with a loss of mature miRs (Zhang et al., 2010). We postulated that *miR-26b* was targeting the Wnt pathway for pituitary development. In this report, we show that *miR-26b OE* in the mandible reduced the expression of multiple Wnt target genes and upregulated several stemness genes. Thus, in normal development *miR-26b* inhibits *Lef-1* expression to allow for cell differentiation and inhibit proliferation. These data demonstrate a unique role for *miR-26b* in ectodermal organ development by regulating *Lef-1* expression in a temporal and spatial manner to ensure stem cell niche maintenance and cell differentiation. We propose a model for *Lef-1* and *miR-26b* function during incisor development (**Figure 9**).

miR-26b Over-Expression Rescues the *COEL* Phenotype

A previous report demonstrated that exogenous Fgfs were able to rescue the phenotype of *Lef-1* mutant teeth (Kratochwil et al., 2002). We demonstrate that *miR-26b OE* rescues the *COEL* phenotype and results in normal tooth development. Because our *COEL* mouse model uses a *Lef-1* cDNA construct it is not regulated by *miR-26b* however, endogenous *Lef-1* expression can be inhibited allowing us to differentially regulate *Lef-1* expression and rescue *Lef-1 OE* phenotypes by inhibiting endogenous *Lef-1*. These unique transgenic mouse models demonstrate an effective *Lef-1* dosage requirement for ectodermal organ development. Thus, *miR-26b* over-expression only targets endogenous *Lef-1* expression, because it targets the 3′UTR of *Lef-1*. Whereas the *COEL* mouse conditionally expresses a cDNA lacking the *Lef-1* 3′UTR and is not regulated by *miR-26b*. Therefore, the rescue is due to normal levels of *Lef-1* cDNA expression, because *miR-26b* inhibits the endogenous *Lef-1* expression in the *COEL/miR-26b* mouse. These experiments show that *Lef-1* expression is tightly regulated for normal ectodermal development. It is interesting that the rescue mice have an overall growth phenotype suggesting that not all defects are affected by this rescue. More research is required to understand the role of *miR-26b* and *Lef-1* during development of multiple organs and tissues.

DATA AVAILABILITY STATEMENT

The raw data supporting the conclusions of this article will be made available by the authors, without undue reservation.

ETHICS STATEMENT

The animal study was reviewed and approved by Institutional Animal Care and Use Committee (IACUC). Mice were housed and experiments performed according to the Office of Animal Resources guidelines at the University of Iowa.

AUTHOR CONTRIBUTIONS

SE performed the experiments, analyzed the data, prepared the manuscript, and contributed to the design of the study. TS and YS performed the experiments and analyzed the data. MS collected and analyzed the data. BA contributed to the design of the study, data interpretation, and acquisition, and prepared the manuscript. All authors contributed to the article and approved the submitted version.

FUNDING

The following NIH grant mechanisms contributed to this work: NIH R43DE027569, NIH R01DE026433, NIH R03EB025873, NIH R21DE025328, and NIH 5T90DE023520-07.

ACKNOWLEDGMENTS

We thank members of the Amendt and Cao labs and Liu Hong for helpful discussions. We also thank the DSHB maintained by the University of Iowa for several antibodies used in the study and the Roy J. Carver Trust for funding the uCT scanner.

REFERENCES

Amen, M., Liu, X., Vadlamudi, U., Elizondo, G., Diamond, E., Engelhardt, J. F., et al. (2007). PITX2 and ß-catenin interactions regulate Lef-1 isoform expression. *Mol. Cell. Biol.* 27, 7560–7573. doi: 10.1128/mcb.00315-07

Balaguer, F., Moreira, L., Lozano, J. J., Link, A., Ramirez, G., Shen, Y., et al. (2011). Colorectal cancers with microsatellite instability display unique miRNA profiles. *Clin. Cancer Res.* 17, 6239–6249. doi: 10.1158/1078-0432.ccr-11-1424

Cao, H., Wang, J., Li, X., Florez, S., Huang, Z., Venugopalan, S. R., et al. (2010). MicroRNAs play a critical role in tooth development. *J. Dent Res.* 89, 779–784. doi: 10.1177/0022034510369304

Cao, H., Yu, W., Li, X., Wang, J., Gao, S., Holton, N. E., et al. (2016). A new plasmid-based microRNA inhibitor system that inhibits microRNA families in transgenic mice and cells: a potential new therapeutic reagent. *Gene Therapy* 23:527. doi: 10.1038/gt.2016.22

Chistiakov, D. A. (2010). Endogenous and exogenous stem cells: a role in lung repair and use in airway tissue engineering and transplantation. *J. Biomed. Sci.* 17:92. doi: 10.1186/1423-0127-1117-1192

Clavel, C., Grisanti, L., Zemla, R., Rezza, A., Barros, R., Sennett, R., et al. (2012). Sox2 in the dermal papilla niche controls hair growth by fine-tuning BMP signaling in differentiating hair shaft progenitors. *Dev. Cell* 23, 981–994. doi: 10.1016/j.devcel.2012.10.013

Gao, J., Yang, T., Han, J., Yan, K., Qiu, X., Zhou, Y., et al. (2011). MicroRNA expression during osteogenic differentiation of human multipotent mesenchymal stromal cells from bone marrow. *J. Cell. Biochem.* 112, 1844–1856. doi: 10.1002/jcb.23106

Harada, H., Kettumen, P., Jung, H.-S., Mustonen, T., Wang, Y. A., and Thesleff, I. (1999). Localization of putative stem cells in dental epithelium and their association with notch and FGF signaling. *J. Cell Biol.* 147, 105–120. doi: 10.1083/jcb.147.1.105

Huang, C., and Qin, D. (2010). Role of Lef1 in sustaining self-renewal in mouse embryonic stem cells. *J. Genet. Genomics* 37, 441–449. doi: 10.1016/s1673-8527(09)60063-1

Iwafuchi-Doi, M., and Zaret, K. S. (2016). Cell fate control by pioneer transcription factors. *Development* 143, 1833–1837. doi: 10.1242/dev.133900

Jayakody, S. A., Andoniadou, C. L., Gaston-Massuet, C., Signore, M., Cariboni, A., Bouloux, P. M., et al. (2012). SOX2 regulates the hypothalamic-pituitary axis at multiple levels. *J. Clin. Invest.* 122, 3635–3646. doi: 10.1172/jci64311

Juuri, E., Jussila, M., Seidel, K., Holmes, S., Wu, P., Richman, J., et al. (2013). Sox2 marks epithelial competence to generate teeth in mammals and reptiles. *Development* 140, 1424–1432. doi: 10.1242/dev.089599

Juuri, E., Saito, K., Ahtiainen, L., Seidel, K., Tummers, M., Hochedlinger, K., et al. (2012). Sox2+ stem cells contribute to all epithelial lineages of the tooth via Sfrp5+ progenitors. *Dev. Cell* 23, 317–328. doi: 10.1016/j.devcel.2012.05.012

Knoblich, J. A. (2008). Mechanisms of asymmetric stem cell division. *Cell* 132, 583–597. doi: 10.1016/j.cell.2008.02.007

Kratochwil, K., Dull, M., Farinas, I., Galceran, J., and Grosschedl, R. (1996). Lef1 expression is activated by BMP-4 and regulates inductive tissue interactions in tooth and hair development. *Genes Dev.* 10, 1382–1394. doi: 10.1101/gad.10.11.1382

Kratochwil, K., Galceran, J., Tontsch, S., Roth, W., and Grosschedl, R. (2002). FGF4, a direct target of LEF1 and Wnt signaling, can rescue the arrest of tooth organogenesis in Lef1(-/-) mice. *Genes Dev.* 16, 3173–3185. doi: 10.1101/gad.1035602

Liu, W., Selever, J., Lu, M. F., and Martin, J. F. (2003). Genetic dissection of *Pitx2* in craniofacial development uncovers new functions in branchial arch morphogenesis, late aspects of tooth morphogenesis and cell migration. *Development* 130, 6375–6385. doi: 10.1242/dev.00849

Michon, F., Tummers, M., Kyyronen, M., Frilander, M. J., and Thesleff, I. (2010). Tooth morphogenesis and ameloblast differentiation are regulated by micro-RNAs. *Dev. Biol.* 340, 355–368. doi: 10.1016/j.ydbio.2010.01.019

Morrison, S. J. (2008). Stem cells and niches: mechanisms that promote stem cell maintenance throughout life. *Cell* 132, 598–611. doi: 10.1016/j.cell.2008.01.038

Petersson, M., Brylka, H., Kraus, A., John, S., Rappl, G., Schettina, P., et al. (2011). TCF/Lef1 activity controls establishment of diverse stem and progenitor cell compartments in mouse epidermis. *EMBO J.* 30, 3004–3018. doi: 10.1038/emboj.2011.199

Que, J., Okubo, T., Goldenring, J. R., Nam, K. T., Kurotani, R., Morrisey, E. E., et al. (2007). Multiple dose-dependent roles for Sox2 in the patterning and differentiation of anterior foregut endoderm. *Development* 134, 2521–2531. doi: 10.1242/dev.003855

Reya, T., and Clevers, H. (2005). Wnt signalling in stem cells and cancer. *Nature* 434, 843–850. doi: 10.1038/nature03319

Sasaki, T., Ito, Y., Xu, X., Han, J., Bringas, J., Maeda, P. T., et al. (2005). LEF1 is a critical epithelial survival factor during tooth morphogenesis. *Dev. Biol.* 278, 130–143. doi: 10.1016/j.ydbio.2004.10.021

Schwamborn, J. C. (2009). The TRIM-NHL Protein TRIM32 activates MicroRNAs and prevents self-renewal in mouse neural progenitors. *Cell* 136, 913–925. doi: 10.1016/j.cell.2008.12.024

Sun, Z., Yu, W., Navarro, M. S., Sweat, M., Eliason, S., Sharp, T., et al. (2016). Sox2 and Lef-1 interact with Pitx2 to regulate incisor development and stem cell renewal. *Development* 143, 4115–4126. doi: 10.1242/dev.138883

Taranova, O. V., Magness, S. T., Fagan, B. M., Wu, Y., Surzenko, N., Hutton, S. R., et al. (2006). SOX2 is a dose-dependent regualtor of retinal neural progenitor competence. *Genes Dev.* 20, 1187–1202. doi: 10.1101/gad.1407906

Travis, A., Amsterdam, A., Belanger, C., and Grosschedl, R. (1991). LEF-1, a gene encoding a lymphoid-specific protein with an HMG domain, regulates T-cell receptor a enhancer function. *Genes Dev.* 5, 880–894. doi: 10.1101/gad.5.5.880

Tummers, M., and Thesleff, I. (2003). Root or crown: a developmental choice orchestrated by the differential regulation of the epithelial stem cell niche in the tooth of two rodent species. *Development* 130, 1049–1057. doi: 10.1242/dev.00332

Van Genderen, C., Okamura, R. M., Farinas, I., Quo, R.-G., Parslow, T. G., Bruhn, L., et al. (1994). Development of several organs that require inductive epithelial-mesenchymal interactions is impared in LEF-1-deficient mice. *Genes Dev.* 8, 2691–2703. doi: 10.1101/gad.8.22.2691

Xie, W., Lynch, T. J., Liu, X., Tyler, S. R., Yu, S., Zhou, X., et al. (2014). Sox2 modulates Lef-1 expression during airway submucosal gland development. *Am. J. Physiol. Lung Cell Mol. Physiol.* 306, L645–L660.

Young, R. A. (2011). Control of the embryonic stem cell state. *Cell* 144, 940–954. doi: 10.1016/j.cell.2011.01.032

Zhang, L., Yuan, G., Liu, H., Lin, H., Wan, C., and Chen, Z. (2012). Expression pattern of Sox2 during mouse tooth development. *Gene Expr. Patterns* 12, 273–281. doi: 10.1016/j.gep.2012.07.001

Zhang, Y. D., Chen, Z., Song, Y. Q., Liu, C., and Chen, Y. (2005). Making a tooth: growth factors, transcription factors and stem cells. *Cell Res.* 15, 301–316. doi: 10.1038/sj.cr.7290299

Zhang, Z., Florez, S., Gutierrez-Hartmann, A., Martin, J. F., and Amendt, B. A. (2010). MicroRNAs regulate pituitary development, and microRNA 26b specifically targets lymphoid enhancer factor 1 (Lef-1), which modulates pituitary transcription factor 1 (Pit-1) expression. *J. Biol. Chem.* 285, 34718–34728. doi: 10.1074/jbc.m110.126441

Zhang, Z., Kim, K., Li, X., Moreno, M., Sharp, T., Goodheart, M. J., et al. (2014). MicroRNA-26b represses colon cancer cell proliferation by inhibiting lymphoid enhancer factor 1 expression. *Mol. Cancer Ther.* 13, 1942–1951. doi: 10.1158/1535-7163.mct-13-1000

Zhang, Z., Wlodarczyk, B. J., Niederreither, K., Venugopalan, S., Florez, S., Finnell, R. H., et al. (2011). Fuz regulates craniofacial development through tissue specific responses to signaling factors. *PLoS One* 6:e24608. doi: 10.1371/journal.pone.0024608

Conflict of Interest: The authors declare that the research was conducted in the absence of any commercial or financial relationships that could be construed as a potential conflict of interest.

frontiers in Physiology

REVIEW
published: 16 July 2020
doi: 10.3389/fphys.2020.00818

Live Tissue Imaging Sheds Light on Cell Level Events During Ectodermal Organ Development

*Isabel Mogollón and Laura Ahtiainen**

Cell and Tissue Dynamics Research Program, Institute of Biotechnology/Helsinki Institute of Life Science, University of Helsinki, Helsinki, Finland

Embryonic development of ectodermal organs involves a very dynamic range of cellular events and, therefore, requires advanced techniques to visualize them. Ectodermal organogenesis proceeds in well-defined sequential stages mediated by tissue interactions. Different ectodermal organs feature shared morphological characteristics, which are regulated by conserved and reiterative signaling pathways. A wealth of genetic information on the expression patterns and interactions of specific signaling pathways has accumulated over the years. However, the conventional developmental biology methods have mainly relied on two-dimensional tissue histological analyses at fixed time points limiting the possibilities to follow the processes in real time on a single cell resolution. This has complicated the interpretation of cause and effect relationships and mechanisms of the successive events. Whole-mount tissue live imaging approaches are now revealing how reshaping of the epithelial sheet for the initial placodal thickening, budding morphogenesis and beyond, involve coordinated four dimensional changes in cell shapes, well-orchestrated cell movements and specific cell proliferation and apoptosis patterns. It is becoming evident that the interpretation of the reiterative morphogenic signals takes place dynamically at the cellular level. Depending on the context, location, and timing they drive different cell fate choices and cellular interactions regulating a pattern of behaviors that ultimately defines organ shapes and sizes. Here we review how new tissue models, advances in 3D and live tissue imaging techniques have brought new understanding on the cell level behaviors that contribute to the highly dynamic stages of morphogenesis in teeth, hair and related ectodermal organs during development, and in dysplasia contexts.

Keywords: ectodermal, imaging, whole-mount, explant culture, embryonic development, cell cycle, cell migration, cell shape

OPEN ACCESS

Edited by:
Abigail Saffron Tucker, King's College London, United Kingdom

Reviewed by:
Marcia Gaete, Pontificia Universidad Católica de Chile, Chile
Lisa L. Sandell, University of Louisville, United States

***Correspondence:**
Laura Ahtiainen
laura.ahtiainen@helsinki.fi

Specialty section:
This article was submitted to Craniofacial Biology and Dental Research, a section of the journal Frontiers in Physiology

Received: *20 April 2020*
Accepted: *18 June 2020*
Published: *16 July 2020*

Citation:
Mogollón I and Ahtiainen L (2020) Live Tissue Imaging Sheds Light on Cell Level Events During Ectodermal Organ Development. Front. Physiol. 11:818. doi: 10.3389/fphys.2020.00818

ECTODERMAL ORGANS, A VERSATILE PLATFORM FOR STUDYING ORGANOGENESIS ON A CELLULAR LEVEL

Ectodermal organs arise during embryonic development from the outer layer of the embryo. These organs include teeth, hair follicles, and glands such as mammary, sweat, and salivary glands. This group of organs serve a wide array of different functions from cutting and chewing food, to secretion of saliva or milk, or protection from the elements with hair or feathers. Some of the ectodermal organs have the capacity to constantly grow and renew throughout the lifetime,

such as the hairs and the cutting front incisor teeth of mice. Whereas some develop during embryogenesis, but go through extensive re-modification in the adult, such as the mammary gland during lactation. Some ectodermal organs do not maintain a stem cell niche and have lost the renewal capacity. These include the molar teeth of the mouse that develop in the embryonic stages, but then mineralize and erupt after birth and do not grow after that. Unlike humans, that have two sets of teeth the deciduous and permanent teeth, mice only have one. Because of shared developmental features, but also this variety in structure and function, ectodermal organs provide a versatile multifaceted platform to study regulation of embryonic tissue patterning and remodeling in a cell level resolution; the morphogenesis from a flat epithelial sheet to intricate tooth cusp and hair growth patterns and complex ductal branching trees in the glands.

The initial stages of ectodermal organogenesis are very similar in the different organs: They all start out as a simple thickening of the epithelium. Through progressive differentiation and inductive interactions between the epithelium and underlying mesenchyme, they mature into highly differentiated functional organs. The ectodermal organs have for several decades served as model organs of choice to study mechanisms of mammalian embryonic development with respect to tissue interactions and genetic regulation (Jernvall and Thesleff, 2000; Pispa and Thesleff, 2003; Biggs and Mikkola, 2014). The well characterized shared regulatory pathways include Hedgehog, Wnt, Fibroblast growth factor, Ectodysplasin and Bone morphogenetic protein family members (Jernvall and Thesleff, 2000; Biggs and Mikkola, 2014). In recent years, with significant help from emerging new microscopy techniques, the cell level events and interactions within the different tissue compartments are beginning to be understood in detail. These have been challenging to investigate with conventional developmental biology techniques, and also because of the shortage of appropriate reporters to follow the dynamic cellular events in intact tissue. Especially research in the early development of hair follicles (**Figure 1**) and teeth (**Figure 2**) using fluorescent transgenic reporter mouse models have paved the way: These studies have led to methodological advances, and identification of hallmark behavioral signatures in specific cell populations and their contribution to morphogenesis. Understanding the delicate balance between proliferative growth, controlled differentiation and cell cycle exit, apoptotic silencing, adhesion remodeling, and cell movement patterns regulated by specific signaling cues in these model organs are shedding light on the fundamental mechanisms of embryonic development.

ECTODERMAL ORGANS ARE EMERGING AS EXCELLENT MODELS FOR LIVE MICROSCOPY TO REVEAL CELLULAR BEHAVIORS SHAPING THE DEVELOPING TISSUE

Despite shared morphological characteristics and conserved signaling in ectodermal organs (Jernvall and Thesleff, 2000; Biggs and Mikkola, 2014), it is now becoming evident that signaling cues are interpreted into diverse cellular behaviors depending on the context, location, and timing, thereby defining different organ shapes and sizes. Embryonic development proceeds in a dynamic sequence and to properly understand the causalities in the constantly changing system it is necessary to follow the constituents in real time. In recent years, advances in imaging techniques have permitted the field to move from the conventional two dimensional section views to truly three-dimensional (3D) volume and surface data sets and, with live tissue imaging, adding a temporal dimension to the 3D data (4D imaging). These advances together have started to bring new understanding of the cell level behaviors that contribute to the sequential stages of morphogenesis (Sharir and Klein, 2016). Real time visualization of these events is now increasing the understanding of the highly dynamic nature of these processes.

Embryonic ectodermal organs are emerging as models well suited for studies with imaging approaches as well, for several reasons: The development proceeds in morphologically well-defined sequential stages, shared by the different organs, mediated by tissue interactions, and regulated by increasingly well-characterized genetic regulatory pathways (Jernvall and Thesleff, 2000; Biggs and Mikkola, 2014). Transgenic mouse disease models and spontaneous natural mutants, with defects that arrest or alter organogenesis at specific stages, have been widely utilized in ectodermal research. Therefore, the knowledge on specific pathways and their targets and how they can be manipulated genetically is available. Particularly useful is also the pharmacological or mechanical manipulation of cultured explants, together with careful staging of the samples, providing accurate control over the timing of the manipulations (Munne et al., 2009; Närhi and Thesleff, 2010; Ahtiainen et al., 2014; Prochazka et al., 2015; Li J. et al., 2016; Panousopoulou and Green, 2016; Cetera et al., 2018). Finally, the ectodermal organs develop in the surface of the embryo and tissues are highly accessible to imaging with methods that maintain the integrity of the tissue environment.

CULTURING ECTODERMAL ORGANS TO MAINTAIN THE PHYSIOLOGICAL ENVIRONMENT DURING LIVE IMAGING

The *in vitro* whole-mount culturing of tissue explants allows the monitoring of growth and morphogenesis throughout specific stages of organ development. Several approaches have been taken to culture embryonic ectodermal tissues for live imaging: the selection of a specific method depends on tissue type, tissue developmental stage, the time span of the process that is being visualized and the available microscopy setups. The advantage of culturing tissues in whole-mount is preservation of an intact environment closely resembling the physiological growth conditions. In the classical Trowell-type organ culture, tissue explants are cultured at the liquid-gas interface on filter membrane supported by a grid (Trowell, 1959). This culture technique supports normal developmental processes

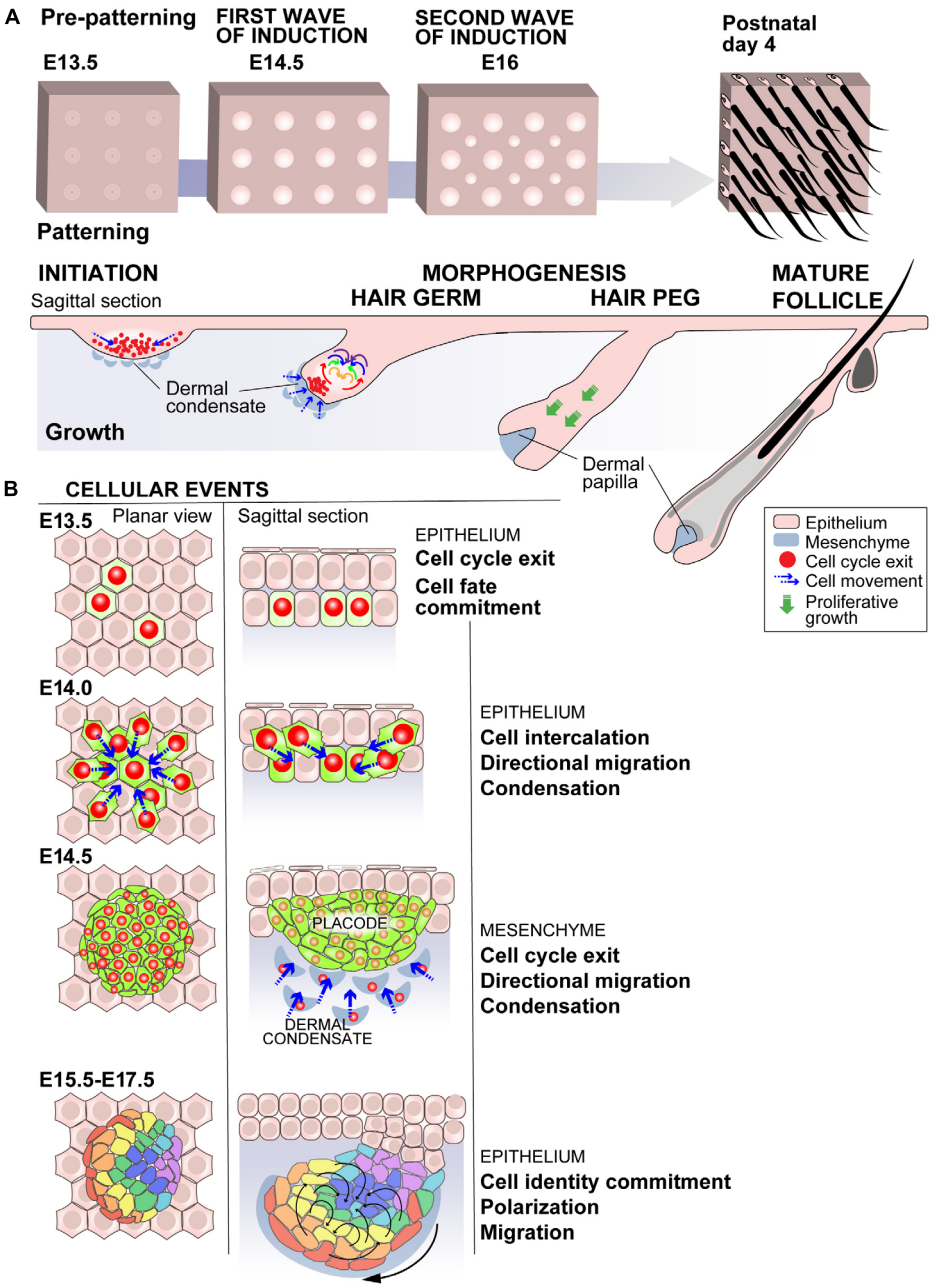

FIGURE 1 | Mammalian early embryonic hair development, a model for cellular mechanisms driving ectodermal organogenesis. **(A)** Mice have four different hair types that arise in three successive waves of hair follicle induction. The first wave of embryonic development of hair follicles in the mouse back skin starts with the establishment of a pre-pattern around embryonic day 13.5 (E13.5) creating the spacing of the hair follicles by a reaction-diffusion type signaling system. At E14.5 the initial thickening of the epidermis, the epithelial placode, is induced by a signal from the mesenchymal compartment the dermis. The epithelium of the hair germ polarizes, and at the same time mesenchymal cells start forming a dermal condensate. The epithelium then buds by cell proliferation invaginating into the dermis to form the hair peg and the condensed mesenchyme engulfed by the epithelium becomes the dermal papilla. This is followed by further differentiation in a mature hair follicle. The second wave of hair morphogenesis takes place around E16–E17 and third at E18- postnatal day 1 (P1) with specific molecular patterning mechanisms for each. The mature hair follicle cycles producing new hairs throughout the adult life. **(B)** The hair has been one of first ectodermal model organs in which live imaging approaches have brought understanding of the cellular dynamics of the morphogenesis and patterning especially in the early stages of morphogenesis: during the first wave of hair follicle induction the cellular events start with a cell fate commitment and cell cycle exit in the prospective placode cells at E13.5. These cells then intercalate and migrate centripetally to condense into a placode thickening at E14.5. The placode signals to the mesenchymal compartment and the dermal cells commit to dermal condensate fate, exit the cell cycle and migrate to form the dermal condensate. The epithelial compartment concomitantly polarizes. The cellular mechanisms of hair follicle polarization have been studied during the second wave of hair follicle induction (E15.5–E17.5). The polarization takes place through planar cell polarity mediated mechanisms and the cells acquire specific fates and collectively actively redistribute into a polarized structure (Duverger and Morasso, 2009; Ahtiainen et al., 2014; Biggs and Mikkola, 2014; Biggs et al., 2018; Cetera et al., 2018).

in a variety organs in different developmental stages and can be used both for whole-mount tissues or organotypic cultures of dissected tissues and thick sections (Grobstein, 1953; Saxen et al., 1976; Nogawa and Takahashi, 1991; Sahlberg et al., 2002; Cho et al., 2007; Munne et al., 2009, 2010). The classical whole mount tissue Trowell culturing method has been used for live imaging to understand the cellular dynamics of early incisor development in the embryonic mouse mandible and the hair follicle placode and dermal condensate induction in embryonic mouse back skin (Ahtiainen et al., 2014; Ahtiainen et al., 2016; Biggs et al., 2018). Embryonic ectodermal whole mount tissues can also be cultured for live imaging submerged in culture medium mechanically stabilized in the bottom of transparent culture dish. This has been used in the context of early tooth induction where initiation stage (embryonic day E11.5) mandible explants were maintained in a sealed glass bottom dish (Prochazka et al., 2015). For live imaging study of hair follicle development, whole mount back skins (E16.5), during the second wave of hair follicle induction were imaged in an inverted conformation, stabilized between a piece of agarose gel on the dermal side and a transparent gas permeable membrane, forming the bottom of the culture dish, on the epidermal side (Cetera et al., 2018).

The potential challenges with these whole-mount culturing methods include (1) the flattening and spreading of the tissue when removed from the embryo and maintained in culture (2) a slight lag in development caused by culturing (3) increase in apoptotic cells and/or reduction of physiological cell proliferation and increased cell cycle exit especially affecting the superficial layers of the tissue. These issues not only concern the Trowell method, but also the submerged inverted culture as also in this setup tissue needs to be stabilized physically for imaging. It is possible that the artificial distortion caused by the culturing can affect organization of the tissue and possibly also alter cell migration trajectories. All of these effects can be controlled, at least to an extent, by carefully comparing live imaging to the *in vivo* situation with directly fixed tissues of comparable developmental stages.

Especially in later developmental stages, beyond bud stage in the teeth (13.5) and after E16.5 in the back skin, tissue thickness and opaqueness cause limitations to whole-mount imaging. To circumvent this, dissected organs and thick section cultures have been utilized in a variety of setups. In the context of live imaging of molar teeth, from late bud and cap stages (E13.5), Morita et al. (2016) utilized thick frontal slices dissected with needles, containing the central region of the developing tooth and cultured the organ submerged in a drop of collagen. Thick section cultures of molar teeth have been used extensively to study tooth development (Sahlberg et al., 2002; Cho et al., 2007; Munne et al., 2009; Alfaqeeh and Tucker, 2013). In this setup tooth frontal tissue slices (200 μm) are cut with a McIlwain Tissue Chopper (Alfaqeeh and Tucker, 2013). In studies utilizing this method of culturing for live imaging, slices have either been fixed to the bottom of the plate and immobilized using a fragment of coverslip or cultured in a Trowel-type setup (Li J. et al., 2016; Panousopoulou and Green, 2016; Yamada et al., 2019) (**Figure 3**).

MICROSCOPY SETUPS FOR EMBRYONIC ECTODERMAL TISSUE IMAGING

For live imaging, tissue cultures are maintained in a humidified, temperature and pH controlled microscopy chamber that allows non-intrusive confocal fluorescence imaging of the tissue. It is also possible to manipulate specific cellular functions and pathways by adding soluble regulatory molecules or pharmacological inhibitors to the culture medium and follow the effects of cellular behaviors in real time. Live imaging of whole-mount ectodermal organs has been done with an upright microscope setup with an air interface objective or in the inverted conformation with either an air interface objective or water/oil immersion objectives (Ahtiainen et al., 2014, 2016; Biggs et al., 2018; Cetera et al., 2018). The advantages of air interface objectives is the long free working distance allowing accommodation of the tissue and supporting grid/filter or in the inverted setup a gas permeable translucent membrane dish. This type of objective does not suffer from multiple refraction index mismatches, which reduces imaging resolution when imaging live tissues maintained in culture medium with oil/glycerol immersion lenses. However, air interface objectives typically have a low numerical aperture with a restricted light acceptance cone and thus limitations in the light-gathering ability, and suffer from light reflection in the tissue interface and out-of-focus light limiting the achievable resolution (Spencer et al., 2007). Therefore, these imaging setups are best suited for applications where there is high intensity fluorescence signal from the reporters, good signal to background ratio and a need to cover large areas of tissue.

Confocal laser excitation setups that have been used for live imaging of whole mount tissue explant cultures feature either laser scanning or spinning disk confocal microscopes (Ahtiainen et al., 2014, 2016; Prochazka et al., 2015; Morita et al., 2016; Panousopoulou and Green, 2016; Biggs et al., 2018; Cetera et al., 2018). The advantage of a spinning disk confocal is the high acquisition speed. This minimizes the scanning time and with reduced phototoxicity allows acquisition of long time lapses. Laser point scanning excitation on the other hand offers in many cases better depth of imaging, true confocality and is compatible with a weaker fluorescence signal. A disadvantage of spinning disk confocal systems is that the theoretical confocality is somewhat reduced compared to laser scanning systems as some out-of-focus light is transmitted to the camera through closely adjacent pinholes (Conchello and Lichtman, 1994).

Imaging parameters depend on specific sample requirements. These include (1) tissue type in respect to culturing system compatibility, and tissue thickness, tissue opacity and level of inherent autofluorescence, (2) specific fluorescence signal intensity from the fluorescent reporters and signal to noise ratio, (3) length of time lapse, (4) analysis type. In most cases

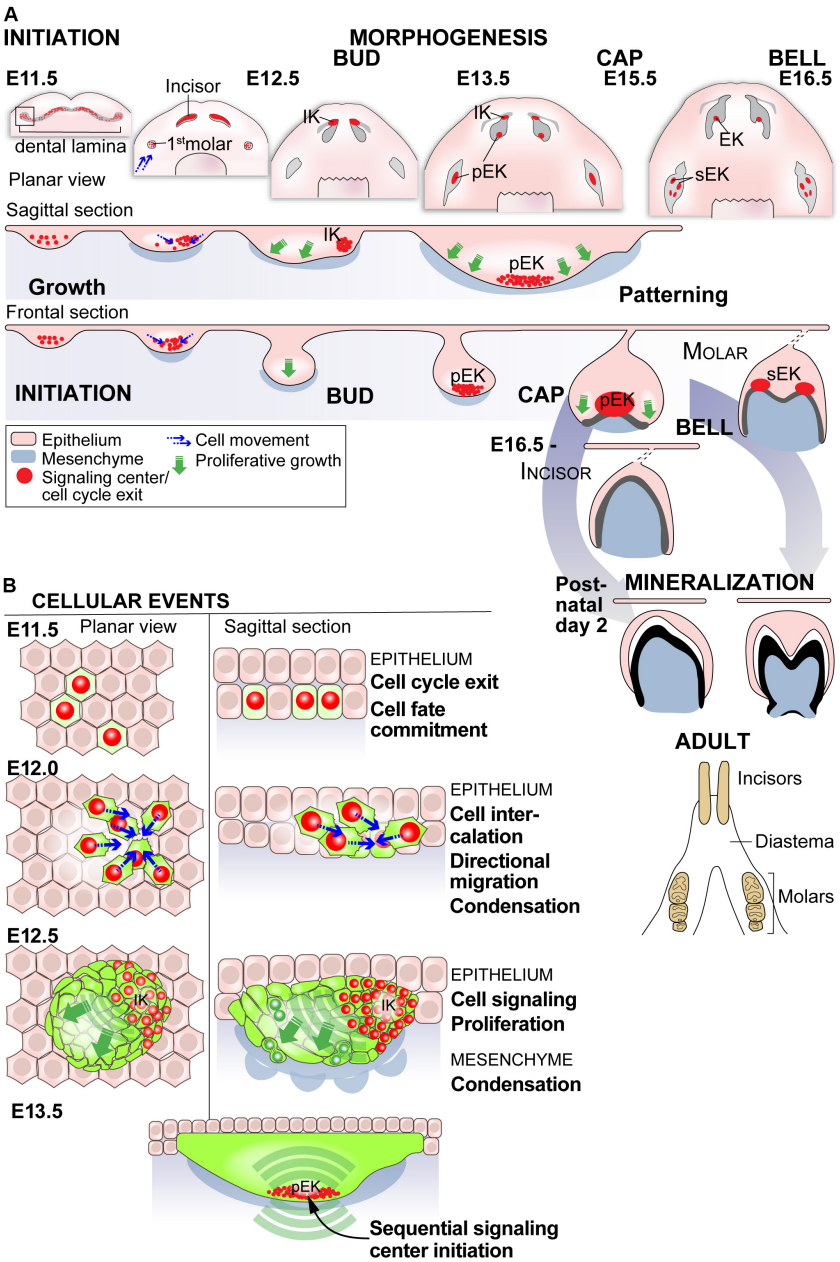

FIGURE 2 | Embryonic development of mouse teeth is governed by specialized signaling centers. **(A)** The embryonic development of mouse teeth in the lower jaw, the mandible, initiates at E11 with a continuous epithelial thickening called the dental lamina. In teeth the initial inductive signal is thought come from the epithelial compartment. The dental lamina resolves into separate placodes for the incisor and molar teeth. A group of cells in the placode acquire a signaling center fate, forming a specialized cluster of cells that signal to the neighboring cells to induce proliferative growth for budding (E12.5). This initiation knot (IK) signaling center is followed by successive signaling centers that use the same signaling pathways reiteratively. The first of these is called the primary enamel knot (pEK) that arises in the bud stage in both incisor and molar teeth. In the following cap stage the epithelium surrounding the signaling center extends deeper into the mesenchyme. Until the stage the development proceeds in a similar way in incisors and molars. The pEK is followed by secondary enamel knots (sEK), but only in the molar tooth, that regulate the epithelial folding into cusp patterns. The first molar is followed by two more molars developing sequentially posteriorly to the first one. In the mouse mandible the incisors and molars have a toothless diastema region in between. The teeth go through differentiation, hard tissue mineralization and erupt postnatally. The incisors continue to grow through the lifetime of the animal, whereas the molars do not grow after complete mineralization. **(B)** The cellular events driving tooth morphogenesis share features with the hair follicle, but there is also differences. The initial epithelial specification into placodes includes cell cycle exit and active cell condensation in both. In the hair follicle the whole placode seems to act as a signaling center, while in teeth a subpopulation of epithelial cells show the hallmarks of the signaling center behavioral signature including specific marker expression, cell cycle exit and active migration for condensation. The epithelial specification is accompanied by mesenchymal condensation also in teeth. The successive epithelial signaling centers, receiving inductive signals from the mesenchyme, shape the developing tooth by controlled ligand distribution driving specific proliferative growth patterns and are ultimately silenced by apoptosis (Jernvall and Thesleff, 2012; Prochazka et al., 2015; Ahtiainen et al., 2016; Morita et al., 2016; Panousopoulou and Green, 2016).

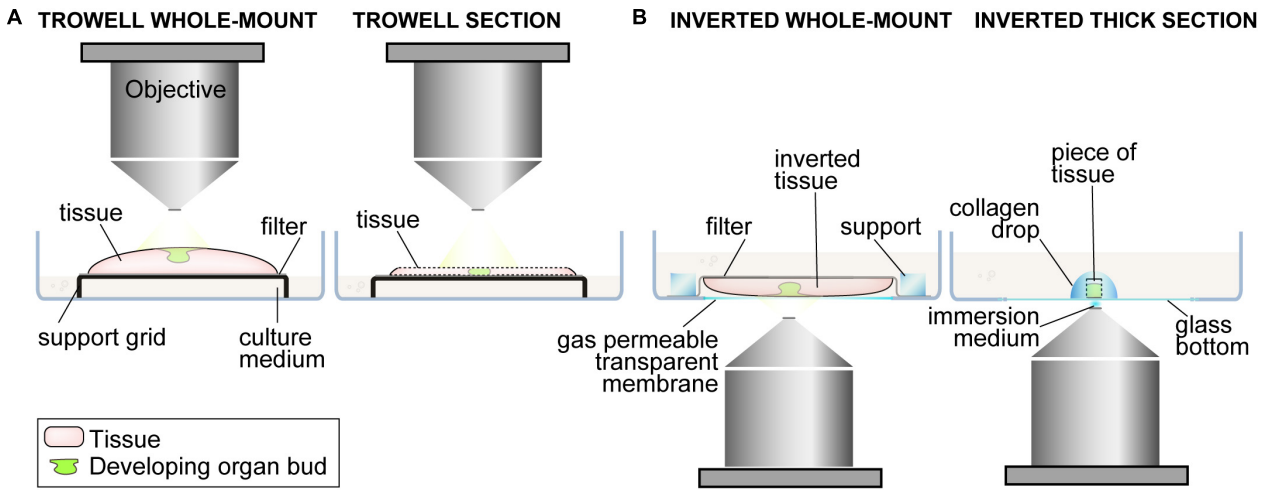

FIGURE 3 | Culturing methods for live tissue whole mount imaging. A schematic representation of culturing setups that have been used for ectodermal live tissue whole mount imaging. **(A)** In the Trowell-type whole-mount setup the tissue, such as the whole embryonic mandible or back skin, is maintained in the interface of air and culturing medium on a filter supported by a grid. The tissue is oriented with the epithelium side upward. This culturing setup allows free gas exchange and maintains the physiologically intact tissue environment. Imaging is done with a upright microscope setup with an air interface objective in an environment controlled chamber. This imaging and culturing setup can also be used with thick tissue sections that are useful especially in later developmental stages when the tissue becomes thicker and/or less transparent and it gives high resolution information in the cross-sectional *z*-axis. **(B)** Tissues can also be cultured for imaging submerged in the culture medium. In this setup the whole-mount tissue is mechanically fixed in place with the epithelium side facing the bottom of the culture dish. The gas exchange and imaging with a inverted microscope setup takes place through a gas permeable optically transparent membrane in the bottom of the dish. The developing organ bud can also be dissected out of the tissue and maintained and imaged similarly.

the maximum theoretical resolution has to be compromised with suboptimal sampling in order not to disturb physiological processes and to avoid phototoxicity by extended illumination. Images are acquired as z-stacks, with a sampling frequency in practice roughly a half of the theoretical resolution stated by the Nyquist Sampling Theorem. This translates to 2–5 μm optical sections depending on the analysis target and tissue type (Ahtiainen et al., 2014, 2016; Morita et al., 2016; Biggs et al., 2018; Cetera et al., 2018). Reported stack sampling frequency varies between 5 and 30 min. Optimization depends on sample features. For example detection of multiple fluorophores and/or thick tissues and large areas takes a longer acquisition time decreasing the achievable practical sampling frequency (Pawley, 2006).

FLUORESCENT MOUSE REPORTER MODELS FOR TISSUE IMAGING

Several types of fluorescent reporter models, depending on the application both constitutive and inducible, have been used individually or in combination for live ectodermal tissue imaging (summarized in **Table 1**). These models can be divided into three, partially overlapping, categories: indicators of cellular behaviors, cell identity/fate, signaling activity. Examples of reporters for cellular behaviors include reporters to visualize cell divisions such as the R26-H2B-EGFP model (Hadjantonakis and Papaioannou, 2004) and the ubiquitinoylation oscillator based fluorescent (Fucci) cell cycle reporters that allow direct real-time follow-up of the progress of the cell cycle in individual cells with a nuclear, dynamically color changing, fluorescent signal (Sakaue-Sawano et al., 2008; Mort et al., 2014). These reporters have also been used to follow cell movements with live imaging. Fluorescent inducible cell membrane bound reporters such as the $R26R^{mT/mG}$ (Muzumdar et al., 2007) and $R26R^{Confetti}$ (Snippert et al., 2010) allow visualization of tissue type, cell shape changes, lineage tracing, and scarce labeling approaches tracking of individual cells. The signaling reporter TCF/Lef:H2B-GFP (Ferrer-Vaquer et al., 2010) is a sensitive fluorescent reporter of canonical Wnt signaling activation and is based on tandem transcription factor binding sites driving expression of the H2B-EGFP fusion protein. Examples of fluorescent reporters for cell identity are the $Shh^{GFP-Cre}$ (Harfe et al., 2004) reporter visualizing signaling center identity, Sox2-GFP for hair follicle dermal condensate cells (Biggs et al., 2018) and keratin 17-GFP to visualize the ectodermal organ epithelium (Bianchi et al., 2005; Ahtiainen et al., 2014).

TISSUE MANIPULATION IN EMBRYONIC WHOLE MOUNT TISSUE IMAGING

Physical Manipulation

Physical manipulation of a live tissue whole-mount ectodermal organ culture visualized by microscopy, has so far been reported in mouse whole mount back skin cultures with specific laser ablation followed by 24 h culture (Cetera et al., 2018), while Panousopoulou and Green (2016) report the immediate effects of microsurgical manipulation in molar tooth thick section culture.

Cetera et al. (2018) used laser ablation, with a pulsed IR laser, with E15.5 dorsal skin explants expressing ubiquitous membrane-Tomato to test if signals from the mesenchymal dermal condensate are required to maintain cell fate asymmetry in the epithelium in the post-polarization stage hair follicle. Tissues were imaged and cultured in an inverted setup with a 40×/1.0 N.A. water immersion objective. Ablated follicles showed a loss in asymmetry with even expression of cell fate markers, indicating that the maintenance of cell fates requires mesenchymal signals with active repression of stem cell progenitor fate. Tissue welfare and was verified by imaging the tissue immediately after ablation and after culturing.

Panousopoulou and Green (2016) took a different, short term, approach and explored properties of physical tension in the epithelium and basal membrane in slice cultures of placode/early bud stage tooth tissue. They explored mechanisms of epithelial invagination by visualizing immediate effects of microsurgical manipulation. In this experimental setup they made a cut into the epithelium with a needle, directly adjacent to the tooth initiating epithelial thickening. They measured nuclear deformation, and observed tissue shape immediately after the cut, and tissue recoil in the presence or absence of inhibitors of actin dynamics. The frontal slices were maintained immobilized in a bottom of a culture plate and imaging done with a stereoscopic zoom microscope with a real-time viewing (RTV) camera optimized for lowlight time lapse applications. Images were acquired with high frequency every 5sek in a 2 min time window. The condition of the tissue was confirmed form DAPI and fluorescently labeled phalloidin stained tissue after live imaging.

Modulation of Signaling Pathway Activity

To dissect the molecular mechanisms of ectodermal organogenesis, modulation of signaling pathway activity in the context of live tissue imaging, has been done with administration of pharmacological inhibitors/activators and recombinant proteins, applied either directly into the culture medium or in slowly releasing beads. Prochazka et al. (2015) studied intraepithelial cell migration in the developing mandible. They observed, with whole mount live tissue imaging, a group of fibroblast growth factor 8 (Fgf8)-expressing progenitor cells close to the mandible hinge and followed the actively migrating descendants of these progenitors. The epithelial cell flow was directed anteriorly toward, the initiator of molar tooth

TABLE 1 | Fluorescent mouse reporter models for live tissue imaging of ectodermal embryogenesis.

	Mouse model	Characteristics*	Application in ectodermal embryonic research	Live tissue imaging reference
Cell behavior	Fucci (1st generation)	Dynamic cell cycle indicator Ubiquitinylation oscillators emit nuclear red fluorescence in G_1/G_0 phase and transition to green fluorescence in $S/G_2/M$ phases[1]	Cell cycle, migration Hair follicle, incisor and molar teeth	Ahtiainen et al., 2014, 2016; Morita et al., 2016; Biggs et al., 2018
	R26Fucci2aR	Dynamic cell cycle indicator Bicistronic, inducible[2]	Cell cycle, migration Hair follicle	Biggs et al., 2018
	R26-H2B-EGFP	Visualization of mitoses Histone 2B-GFP fusion protein[3]	Cell division Molar tooth	Morita et al., 2016
	$R26R^{mT/mG}$	Constitutive red membrane fluorescence, inducible green membrane fluorescence[4]	Cell shape, movement and lineage tracing Molar tooth, hair follicle	Prochazka et al., 2015; Panousopoulou and Green, 2016; Cetera et al., 2018
	$R26R^{Confetti}$	Inducible random multicolor membrane fluorescence[5]	Lineage tracing Molar tooth	Prochazka et al., 2015
	LifeAct	Fluorescent actin labeling[6]	Cytoskeletal dynamics Molar tooth	Prochazka et al., 2015
	K14EGFP/Actb	Fluorescent actin labeling, under keratin 14 promoter[7]	Cytoskeletal dynamics Molar tooth	Prochazka et al., 2015
Cell signaling	TCF/Lef:H2B-GFP	Active canonical Wnt signaling, nuclear fluorescence[8]	Signaling activity, cell identity, movement Molar and incisor teeth	Ahtiainen et al., 2016
Cell identity	$Shh^{GFP-Cre}$	Cytoplasmic GFP expression consistent with the endogenous *Shh* locus[9]	Hair follicle placode cell subpopulation	Cetera et al., 2018
	Sox2-GFP	Cytoplasmic GFP expression consistent with the endogenous *Sox2* locus[10]	Hair follicle dermal condensate	Biggs et al., 2018
	K17-GFP	Cytoplasmic GFP expression consistent with the endogenous *keratin 17* locus[11]	Ectodermal organ epithelium Hair follicle, incisor teeth	Ahtiainen et al., 2014, 2016
	E-cadherin-mCFP	Cytoplasmic CFP expression consistent with the endogenous *E-cadherin* locus[12]	Ectodermal organ epithelium Molar tooth	Prochazka et al., 2015

**References to mouse models: [1](Sakaue-Sawano et al., 2008), [2](Mort et al., 2014), [3](Hadjantonakis and Papaioannou, 2004)(#006069, Jackson Laboratories), [4](Muzumdar et al., 2007) (#007576, Jackson), [5](Snippert et al., 2010) (#013731, Jackson), [6](Vaezi et al., 2002), [7](Riedl et al., 2010), [8](Ferrer-Vaquer et al., 2010) (#013752, Jackson), [9](Harfe et al., 2004) (#005622, Jackson), [10](D'Amour and Gage, 2003) (#017592, Jackson), [11](Bianchi et al., 2005) (#023965, Jackson), [12](Snippert et al., 2010) (#016933, Jackson).*

development, the Sonic hedgehog (*Shh*) expressing molar placode. To dissect the regulation of this cell movement by different signaling pathways they used pharmacological inhibitors in the culture medium. A wide variety of often redundant Fgf ligands and receptors are expressed during mouse tooth development. Therefore, they used a broad-spectrum inhibitor of FGF signaling the MEK/ERK pathway inhibitor SU5402. Shh signaling was modulated by inhibition with cyclopamine, an inhibitor of smoothened, an ubiquitously expressed transducer of Shh signaling, or by applying a recombinant Shh releasing bead. Live tracking of cell movement showed that inhibition of Fgf signaling impeded cell movement while Shh modulation disrupted movement directionality and cell convergence in this context.

Fgf dependent cellular behaviors have also been studied in hair follicle development. Biggs et al. (2018) studied the cellular mechanisms in the early stages of the mesenchymal dermal papilla formation and the contribution of the dermal condensate specific growth factor Fgf20. They followed normal mesenchymal cell movement patterns during dermal condensate formation with live whole mount imaging of embryonic back skin cultures. They showed that directed migration of fibroblasts drives the condensate formation. This study did not directly address the effects of Fgf modulation on the movement patterns with live imaging. However, they treated explants with both pharmacological inhibitors and recombinant protein bead approaches and observed the effects on cell condensation in fixed tissues. They confirmed the specificity of SU5402 of inhibition: the inhibitor induced a similar stripy hair patterning phenotype to the *Fgf20* mouse mutants (Huh et al., 2013). SU5425 inhibits VEGFR2 and PDGFRB receptors in addition to FGFR1, but blocking these with other specific inhibitors did not block DC formation. FGF20 releasing beads on the other hand, induced DC condensation in explants and cell culture scratch wound and transwell migration assays lead the authors to propose a chemokinetic role for Fgf20 in the DC context.

Ahtiainen et al. (2014) studied the cellular mechanisms in the initial stages of development of the hair follicle epithelial compartment by whole mount live tissue imaging together with the modulation of ectodysplasin/NF-κB and Wnt/β-catenin pathways. They applied pathway activity stimulating recombinant proteins to the culture medium and followed the effect on cell movement and proliferation. The Eda receptor becomes focally upregulated in developing hair placode and offers the responsive specificity to the ligand in this system (Headon and Overbeek, 1999; Laurikkala et al., 2002). Stimulation of the explants with both recombinant Eda and the global canonical Wnt inducer Wnt3a together with a signaling cofactor Rspo2 lead to increased cell cycle exit and increased area of the organ primordium similarly as in the epithelial overexpression mutant of Eda (K14-Eda) (Mustonen et al., 2003). Overactivation of both pathways resulted in increased overall cell motility together with reduced directionality disrupting the centripetal migration for condensation and proper development of the organ.

Pharmacological Perturbation of Specific Cell Behaviors

Perturbation of specific cell behaviors with carefully timed application of pharmacological inhibitors onto cultured tissues, a method conventionally used in cell biology research in cell culture, can be an precise tool to dissect cell level developmental sequences. Inhibitors applied to cultures affect the whole tissue and do not have the specificity of genetic approaches, where a specific disruption can be targeted to a tissue compartment or group of cells. These limitation in compartment specificity have to be taken into account by employing proper controls and with careful interpretation of the results. Despite this, pharmacological perturbations also have several advantages. Administration into cultures permits accurate control over dosing ranges. Imaging of reporters allows both a very specific developmental stage timing in ectodermal organs for these *ex vivo* treatments and follow-up of both morphogenic and cell level immediate and long term behavioral spatiotemporal effects. Cell motility and shape changes are important cell behaviors in several steps of ectodermal organ morphogenesis. Both depend on cytoskeletal dynamics. The disruption of these has been reported in both development of the hair follicle and teeth with specific small molecule inhibitors, including a myosin II inhibitor blebbistatin, selective Rho kinase inhibitor Y-27632, or toxins such as Latrunculin A (actin polymerization), Jasplakinolide (F-actin capping) (Ahtiainen et al., 2014, 2016; Prochazka et al., 2015; Panousopoulou and Green, 2016; Cetera et al., 2018). Some studies have utilized disruption of cell adhesion in the molar tooth with calcium chelator EGTA (for E-cadherin) or specific inhibitor PF-573228 (for focal adhesion kinase) (Panousopoulou and Green, 2016; Yamada et al., 2019). Also cell proliferation has been targeted: Inhibition of cell proliferation with a DNA polymerase inhibitor aphidicolin in the embryonic back skin did not abrogate hair placode formation or bud-to-cap transition in molar tooth sections, leading to the interpretation that these events do not depend on cell proliferation (Ahtiainen et al., 2014; Yamada et al., 2019).

CELL BEHAVIOR ANALYSES IN TISSUE IMAGING

Advancements in live tissue imaging techniques are bringing forth a multitude of cell level behaviors and cell population dynamics, within tissue compartments of ectodermal organs. These could not be studied with conventional methods in fixed tissues and 2D sections. Recent research has shown that cell movements are crucial in the morphogenesis and they can only be studied with live imaging. There are different modes of cell movement found in ectodermal organs: these range from long distance large scale rearrangements to local migration within the organ primordia and timescales of days to just minutes. Depending on the specific cell population, movements can vary from directional to random, and homogenous to variable. These patterns depend on the signaling milieu and spatial interactions.

A variety of analyses have been used to dissect the movement patterns in developing ectodermal organs (**Table 2**). Directionality of cell movement is defined by follow-up of individual cells within the tissue in time and three dimensions and analysis of track orientation (directionality, angle), straightness, length, and persistence. Centripetal cell movement, a specific type of directional movement toward a center point of a circular area, can be identified by measuring escape angles. Cell migration can occur over long distances or in confined areas. An example of a long distance cell flow is the intraepithelial cell migration from a distal progenitor pool to frontal parts of the mandible toward the molar initiating region (Prochazka et al., 2015).

Local and directional migration takes place when signaling center cells condense during early tooth development (Ahtiainen et al., 2016). Hair follicle initiating epithelial placode cells and mesenchymal condensate forming cells move centripetally and condense (Ahtiainen et al., 2014; Biggs et al., 2018). Local random cell movements have been described in proliferative tooth bud populations and interplacodal cells in the mouse back skin (Ahtiainen et al., 2014, 2016; Biggs et al., 2018). Local cell rearrangements such as cell convergence, polarization and cell intercalation have been shown in molar teeth and hair follicles in the early stages of organ development (Panousopoulou and Green, 2016; Cetera et al., 2018). Chemokinetic and chemotactic cues direct cell movements and shape changes during epithelial and mesenchymal condensation (Ahtiainen et al., 2014, 2016; Prochazka et al., 2015; Biggs et al., 2018).

Lineage tracing with fluorescent reporters in whole mount tissue culture offers a single cell level resolution, with much higher accuracy than what can be achieved with many conventional methods (Prochazka et al., 2015). Live visualization of cell cycle reporters enables the study of the continuum of relationships among different cell populations in time and space (**Table 2**).

Large scale analysis of differential proliferation patterns have been done to study dynamic transitions in molar epithelium shape (Morita et al., 2016). Local tracking of individual cells within the organ primordium showed that proliferation is an important mechanism driving tooth budding morphogenesis (Ahtiainen et al., 2014, 2016). In contrast, epithelial signaling center cells in incisor teeth, the hair placode and the mesenchymal dermal condensate cells in the hair exited the cell cycle (Ahtiainen et al., 2016). A summary of analyses of different cell behavior classes with references to ectodermal organ systems is presented in **Table 2**.

IMAGING EARLY HAIR FOLLICLE DEVELOPMENT REVEALS CELLULAR PROCESSES IN EARLY ECTODERMAL ORGANOGENESIS

Early Hair Development a Success in Ectodermal Live Imaging Analyses

One of the first model organs showing success in imaging cellular dynamics in early embryonic ectodermal organogenesis has been the hair follicle. The development of the hair follicle takes place in defined stages from the initial epidermal placode thickening that signals to induce the condensation of dermal cells. These together form the hair germ that invaginates through epidermal proliferation (Sennett and Rendl, 2012). Embryonic development of the mouse coat hair takes place in three waves, with specific molecular patterning mechanisms for each, giving rise to the different hair types present in mouse (reviewed in Duverger and Morasso, 2009; Biggs and Mikkola, 2014). The spacing of hair follicles is postulated to be regulated by a reaction-diffusion system, while orientation of hair follicles is driven by planar cell polarity (Sick et al., 2006; Wang et al., 2006). Live-imaging studies on whole mount embryonic back skin have revealed the cellular behaviors contributing to initial steps of the first wave of hair placode epithelial morphogenesis, crucial steps in the formation of

TABLE 2 | Cell behavior analyses in live tissue imaging of ectodermal embryogenesis.

Cell behavior	Measure	Analysis	References
Migration			Ahtiainen et al., 2014, 2016; Prochazka et al., 2015; Morita et al., 2016; Panousopoulou and Green, 2016; Biggs et al., 2018; Cetera et al., 2018
Distance	Track length, net displacement	Movement pattern	
Velocity	Velocity, net velocity	Velocity and variation	
Directionality	Movement angle, track straightness	Orientation, escape angle, directional persistence, variation	
Rearrangement			Panousopoulou and Green, 2016; Cetera et al., 2018
Intercalation	Relative position	Cell intercalation	
Convergence		Convergence, collective migration	
Cell shape			Ahtiainen et al., 2014, 2016; Prochazka et al., 2015; Panousopoulou and Green, 2016; Biggs et al., 2018
Cell size/shape	Cell size, dimensions	Isotropic/anisotropic change	
Density	Cell density	Cell compaction	
Cell adhesion	Junction position/angle	Junction rearrangement	Cetera et al., 2018
Lineage progression	Clonality	Lineage tracing	Prochazka et al., 2015
Cell cycle			Ahtiainen et al., 2014, 2016; Morita et al., 2016; Biggs et al., 2018
Phase	G_1/G_0; $S/G_2/M$	Number of cells/ratio/position	
Cell division	Number, orientation	Stratification, growth rate	

the dermal condensate in the first wave hair germ (Ahtiainen et al., 2014; Biggs et al., 2018). Live imaging has also been used to study the cellular mechanisms of polarization in the hair follicle during the second wave of hair follicle induction (Cetera et al., 2018).

The cellular mechanisms contributing to the first wave of hair placode induction remained elusive for a long time due to lack of techniques and appropriate reporters to follow the dynamic events on a single cell level in live tissue. The cellular events were first approached, by live imaging in the epithelial context, during the establishment of hair placodes at E13.75. The study (Ahtiainen et al., 2014) utilized embryonic Trowell-type culture of whole-mount back skins and upright laser scanning confocal microscopy of the keratin 14-GFP reporter to visualize the epithelial invagination and quantitative analysis with a fluorescent ubiquitination–based cell cycle indicator (Fucci) mouse to distinguish stages of the cell cycle *in vivo* (Bianchi et al., 2005; Sakaue-Sawano et al., 2008). Prior to this study the interpretation of the cellular mechanisms contributing to hair placode formation, based on expression and histological studies, was very static: basal keratinocytes had been proposed to enlarge and orient vertically to form the thickening (Sengel, 1976) and the contribution of cell proliferation in the early stage prior to downgrowth was unclear. Surprisingly in light of previous hypotheses, live imaging showed that the hair placode is a very dynamic structure featuring cell cycle exit, active cell compaction, and directional centripetal migration. Pharmacological manipulation by inhibition of actin remodeling suppressed placode formation, including specific marker expression and epithelial thickening formation completely. Live imaging together with stimulation of key regulatory pathways, ectodysplasin/NF-κB and Wnt/β-catenin, with application of recombinant proteins to whole mount tissue culture medium showed increased cell motility, suppressed proliferation and induced placodal cell fate. These findings linked cell fate choices and morphogenetic events.

Biggs et al. (2018) later used the same imaging setup to explore the mechanisms of cell condensation in the hair mesenchymal compartment. They studied the dermal condensate, which is the precursor to the dermal papilla, a mesenchymal regulator of hair cycling in the mature organ. A mouse mutant model had shown that the dermal condensate is dependent on Fgf20 as lack of the growth factor resulted in the loss of dermal condensation while the epithelial compartment was able to form placodes (Huh et al., 2013). In the study Biggs et al. (2018) explored how the fibroblasts in the developing skin are regulated by the epithelium derived fibroblast growth factor 20 (Fgf20) from the initial stages of condensation. They combined a transcriptomic approach (RNA sequencing) and live imaging to show that condensation takes place via Fgf20 primed cell cycle exit and cell motility leading to cell aggregation. They imaged the emerging dermal condensate cells from E13.75 for 13 h and used a Sox2-GFP reporter to mark dermal condensate fate and utilized the G_0/G_1 cell cycle phase Fucci reporter for cell cycle analysis and cell tracking. They showed with live imaging that the mesenchymal fibroblasts exit the cell cycle and directional centripetal migration of these cells drives the condensate formation.

In the study Cetera et al. (2018) explored mechanisms of epithelial planar cell polarity that define the cell organization and cell fate asymmetry in the invaginating hair bud utilizing whole mount back skin cultures imaged with a spinning disk confocal. The authors used cell tracking with fluorescent reporters, genetic knock out models for *Shh* and planar cell polarity (PCP) components, pharmacological inhibitors and mechanical laser ablation of the dermal condensate. Imaging Shh-Cre driven GFP together with membrane bound fluorescent reporter, at E17.5 during the second wave of hair induction in the back skin, they showed that, again unexpectedly, the polarization of the follicles took place through collective cell movement. The patterns of cell movement were defined by Shh signaling spatially patterning progenitor fates, together with planar cell polarity, and established cell fate asymmetry. Coordinated movement of the epidermal cells induced mesenchymal displacement and the asymmetrical epithelial polarization was further maintained by signaling from these cells. This study showed that spatial cell patterning and polarity within the developing organ can drive collective cell behavior for morphological and cell fate asymmetry.

These studies are prime examples of how ectodermal organ whole-mount tissue culture combined with live imaging analyses of individual cell level behaviors, brings completely new understanding on the mechanisms of embryonic morphogenesis that has not been possible to achieve with conventional developmental biology methods. Imaging approaches have revealed a completely new level of dynamics in the developing skin: The crucial contribution of cell fate changes, coupled to cell behaviors including cell cycle exit and intricately orchestrated cell movement patterns are necessary for the proper progression on morphogenesis and ultimately organogenesis.

NEW UNDERSTANDING OF THE CELLULAR BASIS OF TOOTH DEVELOPMENT WITH LIVE IMAGING

Mouse Teeth as a Model to Study Development With Whole Mount Tissue Imaging

Many of the conventional developmental biology methods that have been used to study the molecular regulation of tooth development rely on static, often 2D, snapshots of the developing tissue. Yet ectodermal organogenesis proceeds in a three-dimensional and dynamic sequence. Following the individual constituents with imaging methods in real time now offers an unprecedented view on the developmental mechanisms and cellular relationships in tooth development. A large part of the understanding of tooth development has come from mouse mutants and studies have mostly focused later stages of development the bud stage and beyond. Whole-mount live imaging approaches are now revealing the cellular mechanisms of initiation and very early tooth organogenesis that have previously remained elusive.

In mice, teeth initiate at embryonic day (E) 11 with a continuous epithelial thickening called the dental lamina. It resolves into separate thickenings, the tooth placodes. At E12.5 the epithelium invaginates forming a bud together with mesenchymal condensation followed by epithelial folding in cap stage (E13.5–E14.5), bell stage and finally hard tissue mineralization (Thesleff, 2016). Mice have two different tooth types: the large ever-growing incisors and multicuspid molars. These are separated by a toothless diastema in between. Tooth morphogenesis is regulated by signaling centers, specialized groups of cells that organize embryonic organogenesis. The best characterized signaling centers in teeth are the enamel knots (EKs). The EKs secrete signals that determine tooth size and shape beyond bud stage. The incisors have only one EK and in molar teeth the EKs arise sequentially. The first, primary EK (pEK), is followed by successive EKs that determine the cusp pattern (Jernvall and Thesleff, 2000).

Whole Mount Tissue Imaging Reveals an Initiation Knot Signaling Center Regulating Early Incisor Development

Expression of shared molecular markers in tooth placodes and in EKs had suggested the presence of a signaling center regulating tooth development prior to bud stage (Dassule and McMahon, 1998; Jernvall and Thesleff, 2000; Hovorakova et al., 2011). This was first studied with a combination of whole-mount mandible explant cultures and live imaging in the mouse incisor (Ahtiainen et al., 2016) in a similar imaging setup the authors previously utilized in the context of the hair placode (Ahtiainen et al., 2014). This study explored the cellular mechanisms of tooth budding morphogenesis using fluorescent cell identity and cell cycle reporters. The bright and specific fluorescence from the reporters enabled the follow-up of the process for the first time on a cell level resolution in intact tissue. Live imaging, using the Fucci cell cycle reporter, showed that a group of cells within the incisor placode exited the cell cycle. It was specifically these cells that expressed signaling center markers and were identified as a signaling center regulating tooth initiation and therefore called the initiation knot (IK). Whole-mount live tissue microscopy follow-up of the IK cells confirmed that IK cells did not re-enter the cell cycle during budding morphogenesis. Instead, epithelial invagination took place through cell proliferation in the adjacent lingual side cells while the IK was retained close to the epithelial surface. Incisor IK cells exited the cell cycle similarly as in hair placodes, albeit in the hair the whole placode acts as signaling center that is later positioned in the tip of the proliferating invaginating bud (Ahtiainen et al., 2014; Ouspenskaia et al., 2016). Another shared characteristic revealed by tissue imaging approaches was condensation of the signaling cells via active cell migration. The orientation of migration patterns was somewhat different: centripetal and rotational in hair placodes (Ahtiainen et al., 2014; Cetera et al., 2018) versus distal to mesial in the incisor. This suggests either differences in factors and signaling pattern distribution mediating directionality of the movement and/or differences in timing in mesenchymal-epithelial interactions and tissue polarization. Despite these variations cell condensation through active movement is part of the behavioral signature of signaling centers and may be necessary for controlled ligand distribution. Physical condensation has also been shown to cause transcriptional changes for cell differentiation: a study in tooth mesenchyme primary cell cultures showed that physical compression caused transcriptional changes and tooth specific cell differentiation (Mammoto et al., 2011). In another study co-cultures of dental epithelial and mesenchymal cells showed that condensation is necessary for signaling center function (Li C. Y. et al., 2016).

Whole Mount Tissue Imaging Brings Clarity to the Debate Over Competing Hypothesis Over the Control of Initial Stages of Tooth Development

Previous studies utilizing 3D reconstructions of histological sections had interpreted the signaling center marker pattern, with two temporally distinct expression domains, as evidence of transient rudimentary teeth preceding the actual incisor bud (Prochazka et al., 2010; Hovorakova et al., 2011). Using an epithelium specific fluorescent reporter (keratin 17 GFP) and the Fucci cell cycle reporter (Bianchi et al., 2005; Sakaue-Sawano et al., 2008) to identify signaling center cells, Ahtiainen et al. (2016) showed that both expression domains are part of the same incisor bud. The second important question addressed by this study with live tissue imaging was the relationship of the IK and EK cells. For this purpose, the Fucci reporter was used together with a canonical Wnt signaling reporter [TCF/Lef:H2B-GFP (Ferrer-Vaquer et al., 2010)] to visualize signaling center cells. IK cells were followed until the emergence of the EK revealing that the two signaling centers formed in separate parts of the same bud and were clonally distinct. This was later confirmed by a conventional lineage tracing approach (Du et al., 2017).

The classical view of tooth development, largely based on molecular studies, states that each placode gives rise to a respective functional tooth (Jernvall and Thesleff, 2000). Incisor initiation appeared to follow the classical view in which the placode and successive, clonally distinct, signaling centers regulate morphogenesis driving proliferation for elongation and invagination of the bud (Ahtiainen et al., 2016; Du et al., 2017). The initiation, positioning and invagination of the molar tooth seemed more complicated: Depending on the experimental setup studies lead to seemingly contrasting interpretations about the contributing cellular mechanisms. Histological studies with carefully staged embryos had led to the interpretation that transient epithelial thickenings in the diastema, anterior to the first molars, would be remnants from vestigial rudimentary teeth lost during mouse evolution (Prochazka et al., 2010; Hovorakova et al., 2011, 2013). On the other hand, a study using whole mount mandible cultures and live imaging to explore the mechanisms of the first molar development and positioning (Prochazka et al., 2015), had reported intraepithelial migration along the mesiodistal axis toward the site of molar initiation, the *Shh* expressing placode. Studies in cultured molar sections highlighted epithelial stratification enriched in the

placode through vertical cell divisions and short term imaging revealed convergent migration and intercalation of suprabasal cells shaping emerging buds (Li J. et al., 2016; Panousopoulou and Green, 2016). Long term live imaging starting form bud stage up to bell stage cultures of dissected molar teeth (omitting the most mesial and distal parts), and quantification of cell trajectories, divisions and 3D growth landmarks in the epithelium highlighted the importance of differential cell proliferation (Morita et al., 2016). Proliferation in bud to cap transition was similarly highlighted in *in silico* simulations of morphogenesis (Marin-Riera et al., 2018), whereas experimental work on section cultures emphasized cell shape changes over differential proliferation (Yamada et al., 2019).

Especially in the molar, studies with different experimental conditions and approaches seemed to highlight different aspects of the contributing cell behaviors. This is likely reflective of several factors: variable contribution of physical forces including differential adhesion and tissue mechanical properties; the spatial signaling milieu with proper proximo-distal, lingual-labial and vertical (epithelium-to-mesenchyme) signaling gradients; presence/absence of the contributing cell populations.

Contribution of Cell Proliferation to Tooth Development – A Cell Behavior Sensitive to the Experimental Environment Complicates Interpretations

The exact contribution and timing of cell proliferation to tooth morphogenesis during the initial invagination, and later in bud-to cap transition, has been debated; based on studies in whole mount and section models interpretations have varied. The study by Li J. et al. (2016) used cultured molar frontal sections and pharmacological manipulation of Shh and Fgf signaling. This experimental setup highlighted epithelial stratification in early invagination over cell proliferation. This culturing technique preserves the milieu for epithelial to mesenchymal interactions, but disrupts signaling gradients within the epithelial plane especially affecting planar signaling within the epithelium in the mesiodistal axis. Later whole mount live imaging studies using the Fucci cell cycle reporter showed, that in the incisor, while the placode cells exited the cell cycle and condensed, invagination and bud elongation happened through cell proliferation (Ahtiainen et al., 2016). In the every early developmental stages the signaling, signaling center condensation, and IK driven cell proliferation likely depend largely on planar signaling within the epithelium while signaling depends more on the epithelium-mesenchyme axis at the following developmental stages. Molar frontal slice cultures compromise the mesiodistal axis and omit the mesial IK, likely to affect more morphogenetic events involving these.

In comparison to cultured tissue sections, whole mount tissue culture in many cases better preserves physiological conditions by maintaining tissue interactions, associated signaling, and maintaining physical forces within the tissue. Whole mount tissue imaging studies in later stages of development are, however, limited by tissue size and opacity. The work by Morita et al. (2016) used an intermediate organotypic model of molar tooth development to study the contribution cell proliferation to tissue deformations defining tooth shape in bud-to cap and cap-to-bell stages. In this model the developing tooth was dissected out of the mandible with the very anterior and posterior parts of the tooth germs cut off, but still preserving the middle part of the organ architecture. All cells were tracked with the aid of nuclear GFP-labeled histone 2B (H2B) and the authors quantified cell trajectories, orientations of cell divisions and 3D growth landmarks. With these techniques they showed how spatiotemporal patterns of growth, division, and motility are systematically regulated during epithelial deformation from bud stage up to bell stage. This study highlighted cell proliferation as the main driving force for tissue growth. This idea was supported by a *in silico* modeling study in the same developmental stage (Marin-Riera et al., 2018) and also consistent with findings in the earlier stages of tooth morphogenesis (Ahtiainen et al., 2016). There has also since been a contradicting report in cultured sections (Yamada et al., 2019) suggesting a secondary role for proliferation and emphasizing differential anisometric cell shape changes as the principal mechanism in epithelial deformation. Taken together, some cell behaviors in embryonic ectodermal organogenesis seem to be more sensitive to specific experimental conditions and this should be taken into account when making interpretations.

CONCLUDING REMARKS

The embryonic development and morphogenesis of ectodermal tissues is coordinated by signaling networks that drive intricate programs of interactive cell behaviors within and between tissue types. 4D imaging of the tissue, in physiologically intact configurations for specific processes, is bringing mechanistic understanding on how the molecular networks control cell level actions in the constantly changing dynamic chain of events. Tightly spatiotemporally regulated processes of cell movement, differentiation, proliferation, adhesion, polarization, and apoptotic cell death shape these organs from a simple thickening of the epithelium to highly diverse functional organs.

A lot of the pioneering work in this field especially in the early stages of organ development, that we have reviewed here, has been done in the developing mouse hair follicle and teeth. The mammary gland is also emerging as organ of choice for developmental imaging studies. While emphasis has been more in the branching morphogenesis of this organ, and also another branching ectodermal organ the salivary gland, it will be of interest to see if the early stages of development in these organs follow a similar program of cell behaviors established by live imaging approaches in teeth and hair.

The fundamental understanding of the molecular basis of ectodermal development comes from mouse mutants. It will be of interest to deeper address the cell level impacts in these mutant models with imaging approaches. Especially of interest is the combination of mutant models crossed with fluorescent reporter models and analyzed with new transcriptomic analyses that are

applied to whole tissues, such as the spatial genomic analysis method (SGA) described by Lignell and Kerosuo (2019). This will allow correlation of cell behavior and molecular regulation in the developing tissue with high sensitivity even of low expression levels targets. Moreover, the method allows prediction of gene relationships within individual cells. This is promising for bringing detailed understanding of the single cell level regulation of behaviors in different interacting cell populations. Accumulating data from new high throughput transcriptomics studies on different stages of ectodermal organ development will serve as a driving force for new hypotheses on the cell level mechanisms and regulation, that can be further functionally tested with live imaging approaches.

AUTHOR CONTRIBUTIONS

IM and LA contributed to conceptualization, writing, review, and editing the text. LA contributed to acquisition and supervision. Both authors contributed to the article and approved the submitted version.

FUNDING

The work was financially supported by the Academy of Finland, the Sigrid Jusélius Foundation, Finnish Cultural Foundation, Finnish Doctoral Programme in Oral Sciences, and Helsinki Institute of Life Sciences.

REFERENCES

Ahtiainen, L., Lefebvre, S., Lindfors, P. H., Renvoise, E., Shirokova, V., Vartiainen, M. K., et al. (2014). Directional cell migration, but not proliferation, drives hair placode morphogenesis. *Dev. Cell* 28, 588–602. doi: 10.1016/j.devcel.2014.02.003

Ahtiainen, L., Uski, I., Thesleff, I., and Mikkola, M. L. (2016). Early epithelial signaling center governs tooth budding morphogenesis. *J. Cell Biol.* 214, 753–767. doi: 10.1083/jcb.201512074

Alfaqeeh, S. A., and Tucker, A. S. (2013). The slice culture method for following development of tooth germs in explant culture. *J. Vis. Exp.* 2013: e50824.

Bianchi, N., DePianto, D., McGowan, K., Gu, C., and Coulombe, P. A. (2005). Exploiting the keratin 17 gene promoter to visualize live cells in epithelial appendages of mice. *Mol. Cell. Biol.* 25, 7249–7259. doi: 10.1128/mcb.25.16.7249-7259.2005

Biggs, L. C., Mäkelä, O. J., Myllymäki, S.-M., Roy, R. D., Närhi, K., Pispa, J., et al. (2018). Hair follicle dermal condensation forms via Fgf20 primed cell cycle exit, cell motility, and aggregation. *eLife* 7:e36468.

Biggs, L. C., and Mikkola, M. L. (2014). Early inductive events in ectodermal appendage morphogenesis. *Sem. Cell Dev. Biol.* 2, 11–21. doi: 10.1016/j.semcdb.2014.01.007

Cetera, M., Leybova, L., Joyce, B., and Devenport, D. (2018). Counter-rotational cell flows drive morphological and cell fate asymmetries in mammalian hair follicles. *Nat. Cell Biol.* 20, 541–552. doi: 10.1038/s41556-018-0082-7

Cho, S. W., Lee, H. A., Cai, J., Lee, M. J., Kim, J. Y., Ohshima, H., et al. (2007). The primary enamel knot determines the position of the first buccal cusp in developing mice molars. *Differentiation* 75, 441–451. doi: 10.1111/j.1432-0436.2006.00153.x

Conchello, J. W., and Lichtman, J. A. (1994). Theoretical analysis of a rotating-disk partially confocal scanning microscope. *Appl. Opt.* 33, 585–596.

D'Amour, K. A., and Gage, F. H. (2003). Genetic and functional differences between multipotent neural and pluripotent embryonic stem cells. *Proc. Natl. Acad. Sci. U.S.A.* 100, 11866–11872. doi: 10.1073/pnas.1834200100

Dassule, H. R., and McMahon, A. P. (1998). Analysis of epithelial-mesenchymal interactions in the initial morphogenesis of the mammalian tooth. *Dev. Biol.* 202, 215–227. doi: 10.1006/dbio.1998.8992

Du, W., Hu, J. K., Du, W., and Klein, O. D. (2017). Lineage tracing of epithelial cells in developing teeth reveals two strategies for building signaling centers. *J. Biol. Chem.* 292, 15062–15069. doi: 10.1074/jbc.m117.785923

Duverger, O., and Morasso, M. I. (2009). Epidermal patterning and induction of different hair types during mouse embryonic development. *Birth Defects Res. C Embryo Today* 87, 263–272. doi: 10.1002/bdrc.20158

Ferrer-Vaquer, A., Piliszek, A., Tian, G., Aho, R. J., Dufort, D., and Hadjantonakis, A.-K. (2010). A sensitive and bright single-cell resolution live imaging reporter of Wnt/ss-catenin signaling in the mouse. *BMC Dev. Biol.* 10:121. doi: 10.1186/1471-213X-10-121

Grobstein, C. (1953). Inductive epitheliomesenchymal interaction in cultured organ rudiments of the mouse. *Science* 118, 52–55. doi: 10.1126/science.118.3054.52

Hadjantonakis, A.-K., and Papaioannou, V. E. (2004). Dynamic in vivo imaging and cell tracking using a histone fluorescent protein fusion in mice. *BMC Biotechnol.* 4:33. doi: 10.1186/1472-6750-4-33

Harfe, B. D., Scherz, P. J., Nissim, S., Tian, H., McMahon, A. P. and Tabin, C. J. (2004). Evidence for an expansion-based temporal Shh gradient in specifying vertebrate digit identities. *Cell* 118, 517–528. doi: 10.1016/j.cell.2004.07.024

Headon, D. J., and Overbeek, P. A. (1999). Involvement of a novel Tnf receptor homologue in hair follicle induction. *Nat. Genet.* 22, 370–374. doi: 10.1038/11943

Hovorakova, M., Prochazka, J., Lesot, H., Smrckova, L., Churava, S., Boran, T., et al. (2011). Shh expression in a rudimentary tooth offers new insights into development of the mouse incisor. *J. Exp. Zool. B Mol. Dev. Evol.* 316, 347–358. doi: 10.1002/jez.b.21408

Hovorakova, M., Smrckova, L., Lesot, H., Lochovska, K., Peterka, M., and Peterkova, R. (2013). Sequential Shh expression in the development of the mouse upper functional incisor. *J. Exp. Zool. B Mol. Dev. Evol.* 320, 455–464.

Huh, S. H., Närhi, K., Lindfors, P. H., Häärä, O., Yang, L., Ornitz, D. M., et al. (2013). Fgf20 governs formation of primary and secondary dermal condensations in developing hair follicles. *Genes Dev.* 27, 450–458. doi: 10.1101/gad.198945.112

Jernvall, J., and Thesleff, I. (2000). Reiterative signaling and patterning during mammalian tooth morphogenesis. *Mech. Dev.* 92, 19–29. doi: 10.1016/s0925-4773(99)00322-6

Jernvall, J., and Thesleff, I. (2012). Tooth shape formation and tooth renewal: evolving with the same signals. *Development* 139, 3487–3497. doi: 10.1242/dev.085084

Laurikkala, J., Pispa, J., Jung, H. S., Nieminen, P., Mikkola, M., Wang, X., et al. (2002). Regulation of hair follicle development by the TNF signal ectodysplasin and its receptor Edar. *Development* 129, 2541–2553.

Li, C. Y., Hu, J., Lu, H., Lan, J., Du, W., Galicia, N., et al. (2016). alphaE-catenin inhibits YAP/TAZ activity to regulate signalling centre formation during tooth development. *Nat. Commun.* 7:12133.

Li, J., Chatzeli, L., Panousopoulou, E., Tucker, A. S., and Green, J. B. (2016). Epithelial stratification and placode invagination are separable functions in early morphogenesis of the molar tooth. *Development* 143, 670–681. doi: 10.1242/dev.130187

Lignell, A., and Kerosuo, L. (2019). Spatial genomic analysis: a multiplexed transcriptional profiling method that reveals subpopulations of cells within intact tissues. *Methods Mol. Biol.* 2002, 151–163. doi: 10.1007/7651_2018_188

Mammoto, T., Mammoto, A., Torisawa, Y. S., Tat, T., Gibbs, A., Derda, R., et al. (2011). Mechanochemical control of mesenchymal condensation and embryonic tooth organ formation. *Dev. Cell* 21, 758–769. doi: 10.1016/j.devcel.2011.07.006

Marin-Riera, M., Moustakas-Verho, J., Savriama, Y., and Jernvall, J. (2018). Differential tissue growth and cell adhesion alone drive early tooth

morphogenesis: an ex vivo and in silico study. *PLoS Comput. Biol.* 14:e1005981. doi: 10.1371/journal.pcbi.1005981

Morita, R., Kihira, M., Nakatsu, Y., Nomoto, Y., Ogawa, M., Ohashi, K., et al. (2016). Coordination of cellular dynamics contributes to tooth epithelium deformations. *PLoS One* 11:e0161336. doi: 10.1371/journal.pone.0161336

Mort, R. L., Ford, M. J., Sakaue-Sawano, A., Lindstrom, N. O., Casadio, A., Douglas, A. T., et al. (2014). Fucci2a: a bicistronic cell cycle reporter that allows Cre mediated tissue specific expression in mice. *Cell Cycle* 13, 2681–2696. doi: 10.4161/15384101.2015.945381

Munne, P. M., Felszeghy, S., Jussila, M., Suomalainen, M., Thesleff, I., and Jernvall, J. (2010). Splitting placodes: effects of bone morphogenetic protein and Activin on the patterning and identity of mouse incisors. *Evol. Dev.* 12, 383–392. doi: 10.1111/j.1525-142x.2010.00425.x

Munne, P. M., Tummers, M., Järvinen, E., Thesleff, I., and Jernvall, J. (2009). Tinkering with the inductive mesenchyme: Sostdc1 uncovers the role of dental mesenchyme in limiting tooth induction. *Development* 136, 393–402. doi: 10.1242/dev.025064

Mustonen, T., Pispa, J., Mikkola, M. L., Pummila, M., Kangas, A. T., Pakkasjarvi, L., et al. (2003). Stimulation of ectodermal organ development by ectodysplasin-A1. *Dev. Biol.* 259, 123–136. doi: 10.1016/s0012-1606(03)00157-x

Muzumdar, M. D., Tasic, B., Miyamichi, K., Li, L., and Luo, L. (2007). A global double-fluorescent Cre reporter mouse. *Genesis* 45, 593–605. doi: 10.1002/dvg.20335

Närhi, K., and Thesleff, I. (2010). Explant culture of embryonic craniofacial tissues: analyzing effects of signaling molecules on gene expression. *Methods Mol. Biol.* 666, 253–267. doi: 10.1007/978-1-60761-820-1_16

Nogawa, H., and Takahashi, Y. (1991). Substitution for mesenchyme by basement-membrane-like substratum and epidermal growth factor in inducing branching morphogenesis of mouse salivary epithelium. *Development* 112, 855–861.

Ouspenskaia, T., Matos, I., Mertz, A. F., Fiore, V. F., and Fuchs, E. (2016). WNT-SHH antagonism specifies and expands stem cells prior to niche formation. *Cell* 164, 156–169. doi: 10.1016/j.cell.2015.11.058

Panousopoulou, E., and Green, J. B. (2016). Invagination of ectodermal placodes is driven by cell intercalation-mediated contraction of the suprabasal tissue canopy. *PLoS Biol.* 14:e1002405. doi: 10.1371/journal.pbio.1002405

Pawley, J. B. (2006). "Points, Pixels and Gray Levels: Digitizing Image Data," in *Handbook of Biology Confocal Microscopy*, 3rd Edn, Chap. 4, ed. J. B. Pawley (New York, NY: Springer), 59–79. doi: 10.1007/978-0-387-45524-2_4

Pispa, J., and Thesleff, I. (2003). Mechanisms of ectodermal organogenesis. *Dev. Biol.* 262, 195–205. doi: 10.1016/s0012-1606(03)00325-7

Prochazka, J., Pantalacci, S., Churava, S., Rothova, M., Lambert, A., Lesot, H., et al. (2010). Patterning by heritage in mouse molar row development. *Proc. Natl. Acad. Sci. U.S.A.* 107, 15497–15502. doi: 10.1073/pnas.1002784107

Prochazka, J., Prochazkova, M., Du, W., Spoutil, F., Tureckova, J., Hoch, R., et al. (2015). Migration of founder epithelial cells drives proper molar tooth positioning and morphogenesis. *Dev. Cell* 35, 713–724. doi: 10.1016/j.devcel.2015.11.025

Riedl, J., Flynn, K. C., Raducanu, A., Gartner, F., Beck, G., Bosl, M., et al. (2010). Lifeact mice for studying F-actin dynamics. *Nat. Methods* 7, 168–169. doi: 10.1038/nmeth0310-168

Sahlberg, C., Mustonen, T., and Thesleff, I. (2002). Explant cultures of embryonic epithelium. analysis of mesenchymal signals. *Methods Mol. Biol.* 188, 373–382. doi: 10.1385/1-59259-185-x:373

Sakaue-Sawano, A., Kurokawa, H., Morimura, T., Hanyu, A., Hama, H., Osawa, H., et al. (2008). Visualizing spatiotemporal dynamics of multicellular cell-cycle progression. *Cell* 132, 487–498. doi: 10.1016/j.cell.2007.12.033

Saxen, L., Lehtonen, E., Karkinen-Jaaskelainen, M., Nordling, S., and Wartiovaara, J. (1976). Are morphogenetic tissue interactions mediated by transmissible signal substances or through cell contacts? *Nature* 259, 662–663. doi: 10.1038/259662a0

Sengel, P. (1976). *Morphogenesis of Skin*. Cambridge: Cambridge University Press.

Sennett, R., and Rendl, M. (2012). Mesenchymal-epithelial interactions during hair follicle morphogenesis and cycling. *Sem. Cell Dev. Biol.* 23, 917–927. doi: 10.1016/j.semcdb.2012.08.011

Sharir, A., and Klein, O. D. (2016). Watching a deep dive: live imaging provides lessons about tooth invagination. *J. Cell Biol.* 214, 645–647. doi: 10.1083/jcb.201608088

Sick, S., Reinker, S., Timmer, J., and Schlake, T. (2006). WNT and DKK determine hair follicle spacing through a reaction-diffusion mechanism. *Science* 314, 1447–1450. doi: 10.1126/science.1130088

Snippert, H. J., Van Der Flier, L. G., Sato, T., Van Es, J. H., Van Den Born, M., Kroon-Veenboer, C., et al. (2010). Intestinal crypt homeostasis results from neutral competition between symmetrically dividing Lgr5 stem cells. *Cell* 143, 134–144. doi: 10.1016/j.cell.2010.09.016

Spencer, L., Shorte, P., Friedrich, M., and Frischknecht, R. (2007). *Imaging Cellular and Molecular Biological Functions*. Berlin: Springer Science & Business Media.

Thesleff, I. (2016). "The developmental anatomy of teeth," in *Kaufman's Atlas of Mouse Development Supplement*, eds R. Baldock, J. Bard, D.R. Davidson, and G. Morriss-Kay (Amsterdam: Elsevier), 231–238. doi: 10.1016/b978-0-12-800043-4.00018-x

Trowell, O. A. (1959). The culture of mature organs in a synthetic medium. *Exp. Cell Res.* 16, 118–147. doi: 10.1016/0014-4827(59)90201-0

Vaezi, A., Bauer, C., Vasioukhin, V., and Fuchs, E. (2002). Actin cable dynamics and Rho/Rock orchestrate a polarized cytoskeletal architecture in the early steps of assembling a stratified epithelium. *Dev. Cell* 3, 367–381. doi: 10.1016/s1534-5807(02)00259-9

Wang, Y., Badea, T., and Nathans, J. (2006). Order from disorder: Self-organization in mammalian hair patterning. *Proc. Natl. Acad. Sci. U.S.A.* 103, 19800–19805. doi: 10.1073/pnas.0609712104

Yamada, S., Lav, R., Li, J., Tucker, A. S., and Green, J. B. A. (2019). Molar bud-to-cap transition is proliferation independent. *J. Dent Res.* 98, 1253–1261. doi: 10.1177/0022034519869307

Conflict of Interest: The authors declare that the research was conducted in the absence of any commercial or financial relationships that could be construed as a potential conflict of interest.

frontiers in Physiology

ORIGINAL RESEARCH
published: 16 July 2020
doi: 10.3389/fphys.2020.00753

Development of the Vestibular Lamina in Human Embryos: Morphogenesis and Vestibule Formation

*Tengyang Qiu[1], Tathyane H. N. Teshima[1], Maria Hovorakova[2,3] and Abigail S. Tucker[1,3]**

[1]Centre for Craniofacial and Regenerative Biology, Faculty of Dentistry, Oral and Craniofacial Sciences, King's College London, London, United Kingdom, [2]Institute of Histology and Embryology, First Faculty of Medicine, Charles University in Prague, Prague, Czechia, [3]Institute of Experimental Medicine, Czech Academy of Sciences, Prague, Czechia

The vestibular lamina (VL) is a transient developmental structure that forms the lip furrow, creating a gap between the lips/cheeks and teeth (oral vestibule). Surprisingly, little is known about the development of the VL and its relationship to the adjacent dental lamina (DL), which forms the teeth. In some congenital disorders, such as Ellis-van Creveld (EVC) syndrome, development of the VL is disrupted and multiple supernumerary frenula form, physically linking the lips and teeth. Here, we assess the normal development of the VL in human embryos from 6.5 (CS19) to 13 weeks of development, showing the close relationship between the VL and DL, from initiation to differentiation. In the anterior lower region, the two structures arise from the same epithelial thickening. The VL then undergoes complex morphogenetic changes during development, forming a branched structure that separates to create the vestibule. Changing expression of keratins highlight the differentiation patterns in the VL, with fissure formation linked to the onset of filaggrin. Apoptosis is involved in removal of the central portion of the VL to create a broad furrow between the future cheek and gum. This research forms an essential base to further explore developmental defects in this part of the oral cavity.

Keywords: dental pathologies, keratin, epithelial differentiation, apoptosis, oral mucosa, human development

OPEN ACCESS

Edited by:
Ophir D. Klein, University of California, San Francisco, United States

Reviewed by:
Gareth John Fraser, University of Florida, United States
Heather L. Szabo-Rogers, University of Pittsburgh, United States
Jimmy Hu, University of California, Los Angeles, United States

****Correspondence:***
Abigail S. Tucker
abigail.tucker@kcl.ac.uk

Specialty section:
This article was submitted to Craniofacial Biology and Dental Research, a section of the journal Frontiers in Physiology

Received: *17 April 2020*
Accepted: *11 June 2020*
Published: *16 July 2020*

Citation:
Qiu T, Teshima THN, Hovorakova M and Tucker AS (2020) Development of the Vestibular Lamina in Human Embryos: Morphogenesis and Vestibule Formation. Front. Physiol. 11:753. doi: 10.3389/fphys.2020.00753

INTRODUCTION

The vestibular lamina (VL) or lip furrow band is an embryonic structure that forms the oral vestibule (vestibulum oris), the gap in between the teeth and cheeks and lips. The oral vestibule has been proposed to have evolved to aid suckling, and as such is assumed to be a structure unique to mammals and the evolution of lactation. The VL develops labially/buccally to the dental lamina (DL), which forms the dentition of the jaw. These two laminas have been suggested to originate from a common oral epithelial thickening, which subdivides into the two laminas in the mouse (Peterková, 1985). The thickening of the oral epithelium occurs approximately during the 6th week in human embryos, with a single lamina suggested to split to form two diverticula (Bolk, 1921). However, two independently forming laminas have also been described, with the VL forming before or after the DL (Schour, 1929; Tonge, 1969; Nery et al., 1970). The various theories are summarized in Hovorakova et al. (2005). Tooth buds along the DL progress through bud, cap, and bell stages (Tucker and Sharpe, 2004), while the neighboring VL opens up to create a cleft separating the lips and checks from the dental arch between

the 12th and 14th week (Coslet and Cohen, 1969). Although the VL and DL have a very close early relationship, the VL is largely ignored in odontogenetic studies.

Originally the relationship between the human embryonic VL and DL was represented in a classical "horseshoe-shape," with the VL running in parallel on the outside of the DL. This view was based on histological sections of the upper jaw, where the VL appeared continuous throughout the jaw. Interestingly, however, when viewed in 3D, the human VL is clearly discontinuous, integrating with the DL at distinct points along the jaw, and is therefore a much more complex structure than initially proposed (**Figures 1A, 2A**; Hovorakova et al., 2005, 2007). The complex relationship of the VL and DL in different parts of the jaw probably explains the different accounts of their development, and it appears likely that, at least in the anterior region of the human lower jaw, the VL and DL do share a common origin (Bolk, 1921; Hovorakova et al., 2007). This common origin of the VL and DL is supported by the discovery that both laminas in the anterior area form from a common Shh expressing domain in mice (Hovorakova et al., 2016).

The VL has been described in sheep, mouse, humans, and voles (Pavlikova et al., 1999; Hovorakova et al., 2005, 2016; Witter et al., 2005). Across species, clear anatomical differences are evident along the jaw. For example, in the mouse the VL is very prominent in the anterior lower jaw, while it is almost absent in the anterior upper jaw. The mouse and vole have very thin VLs, while the sheep and human have very thick multi-layered VLs. Such differences are likely to lead to differences in morphology of the final oral cavity and may reflect differences in diet.

The early VL has similarities to other embryonic structures that have a close relationship to the teeth across vertebrates. For example, in reptiles the DL shares a common origin with the adjacent forming dental glands (Vonk et al., 2008; Tucker, 2010). Here, a single epithelial thickening appears to divide to form the DL and a gland, similar to the process described for the VL and DL (Kochva, 1965). Both the VL of mammals and

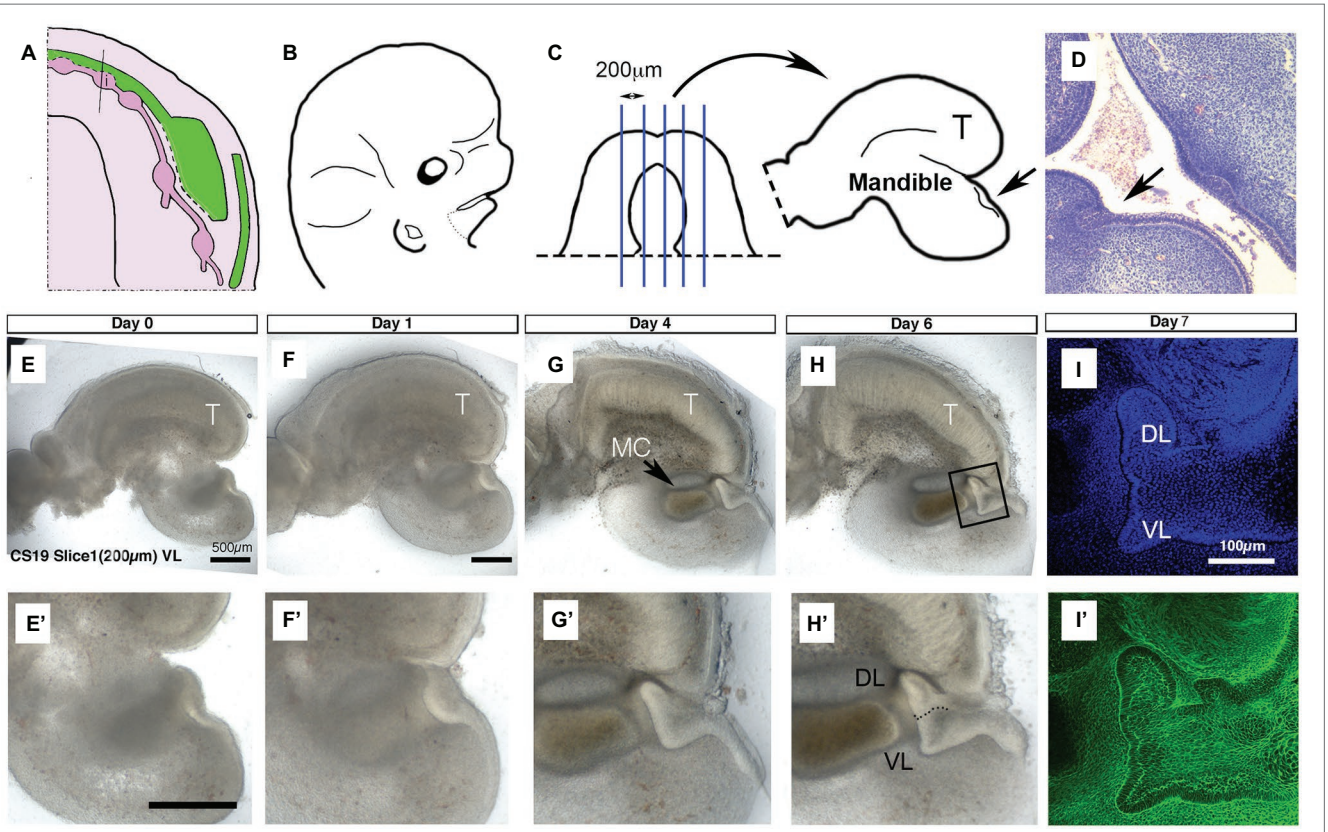

FIGURE 1 | United development of the vestibular lamina (VL) and dental lamina (DL) in the anterior mandible. **(A)** Schematic of the developing VL (green) and DL (pink) during human embryonic lower jaw development. Line through deciduous incisor (i) tooth germ indicates the plane of dissection for culture. **(B)** Schematic of head at CS19 (46 days). Dots indicate dissection of lower jaw. **(C)** Schematic of dissected lower jaw, with blue lines indicating chopping planes to create sagittal live slices. Medial slices contain tongue (T) and single thickening for the DL/VL (arrow). **(D)** Histology section through an embryonic head at 6 weeks. Arrow points to single thickening for the DL/VL. **(E–H)** Developing live sagittal slices of a CS19 mandible. **(E'–H')** Close up of developing VL/DL area shown in **(E–H)**. **(E,E')** Day 0. A single epithelial thickening is evident under the tongue (T). **(F,F')** Day 1. **(G,G')** Day 4. Meckel's cartilage (MC) has condensed and differentiated during the culture period. The tongue (T) has started to fuse with the mandible underneath as an artifact of the culture system. **(H,H')** Day 6. **(I,I')** Day 7 slice fixed and processed for immunofluorescence. Boxed inset in **(H)** shows equivalent regions highlighted in **(I,I')**. **(I)** DAPI, **(I')** Phalloidin stain highlighting F-actin. Schematic in **(A)** based on data in the literature (Hovorakova et al., 2005, 2007). Scale bar in **(E,E',F)** = 500 μm, same scale in **(G,H)** and **(F'–H')**. Scale bar in **(I)** = 100 μm, same scale in **(I')**. VL, vestibular lamina; DL, dental lamina; T, tongue; MC, Meckel's cartilage.

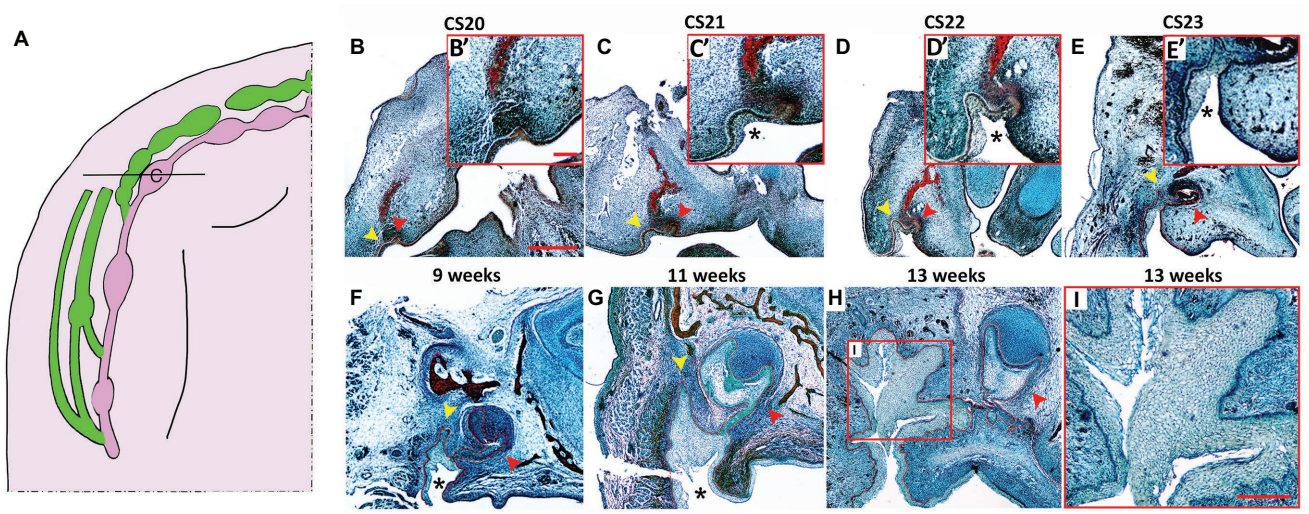

FIGURE 2 | Histological development of the VL and DL in the upper canine region. **(A)** Schematic of the developing VL (green) and DL (pink) during human embryonic upper jaw development. Line through deciduous canine (c) tooth germ indicates the position of the sections in **(B–I)**. **(B–I)** Frontal sections human embryo and fetal tissue stained with a trichrome stain (Alcian blue, Alizarin red, and haematoxylin). **(B)** CS20, **(C)** CS21, **(D)** CS22, **(E)** CS23, **(F)** 9 weeks, **(G)** 11 weeks, **(H,I)** 13 weeks. High power view of VL/DL shown in red inset **(B'–E')**. Boxed area in **(H)** shown in **(I)**. DL and VL outlined by red dashed lines in **(B–H)**. Schematic in **(A)** based on data in the literature (Hovorakova et al., 2005, 2007). Yellow arrowheads indicate forming VL. Red arrowheads indicate forming DL. * = cheek furrow or labio-tectal furrow, which forms from CS21 at the canine. Scale bar in **(B)** = 500 μm, same scale in **(C–H)**. Scale bar in inset **(B')** = 125 μm, same scale in insets **(C',D',E')**. Scale bar in **(I)** = 250 μm.

the dental gland primordium of reptiles form on the outside of the DL and potentially evolved from an outer tooth row from a common amniote ancestor (Hovorakova et al., 2020). This theory is supported by the existence of tooth-germ like bulges that transiently form in the upper VL (**Figure 2A**) and by the high incidence of odontomas and other dental pathologies in the oral vestibule (Hovorakova et al., 2020). In animal models, the VL has the potential to form tooth-like odontomas when signaling in this tissue is perturbed. In mice, supernumerary teeth have been reported to form in the VL region after overexpression of the Wnt pathway in adenomatous polyposis coli conditional knockouts (Wang et al., 2009) and after stabilization of β-catenin in $Sox2^{+}$ positive cells (Popa et al., 2019). The close developmental and evolutionary relationship between the VL and DL may, therefore, explain some of these pathologies.

In addition, the VL is one of the most affected oral tissues in Ellis-van Creveld (EVC) syndrome patients, where defects disrupt the VL development and lead to fusion of the upper lip to the gingiva with multiple frenula (Sasalawad et al., 2013). However, little is known about the development of the VL. We therefore investigated the development of the VL and DL in human embryos and assessed the mechanisms of fissure formation in the vestibular epithelium as the oral vestibule forms. We used organ culture, histology, and immunofluorescence to study the VL development at different stages of human embryos. We have observed that the VL and DL have a very close relationship. We show the complex structure of the VL during development and highlight the roles of epithelial differentiation, proliferation, and apoptosis in the opening of the VL in human embryos. These findings can help our understanding of the normal development of the VL and shed light on the complex relationships between the VL and DL during development, which is crucial for the further exploration of developmental VL defects.

MATERIALS AND METHODS

Human embryos/fetuses were provided by the Human Developmental Biology Resource (HDBR; Project 200504: Characterizing the development of the oral vestibular lamina). Eight stages of human development were examined to study the development of the VL. Samples included CS19 (46 days), CS20 (49 days), CS21 (51 days), CS22 (53 days), CS23 (56 days), 9, 11, and 13 weeks stages. N = 1–2 freshly fixed samples for immunofluorescence were analyzed at each stage (total N = 8). HDBR samples were compared with a larger archival histology collection from the Department of Teratology, IEM, CAS, Prague compiled from the 1960's to the 1980's (recently deposited at First Medical Faculty, Charles University, Prague; N = 53 in total ranging from CS17 to 9 weeks). The stages in the study were selected as they span the period from the initiation of the VL and DL to fissure formation in the VL (Coslet and Cohen, 1969; Hovorakova et al., 2005).

Slice Culture

The lower jaw was isolated from one CS19 and one CS20 human embryo and chopped sagittally at a cutting distance of 200 μm using a McIlwain tissue chopper (Alfaqeeh and Tucker, 2013). A clear DL/VL bud was only evident in the CS19 specimen, so this was used for further analysis for this project. Selected slices from the lower jaw were placed on permeable

membranes (BD) over culture medium [DMEM-Advanced Dulbecco Modified Eagle Medium F12, (Invitrogen); 1% GlutaMAX (Invitrogen); and 1% penicillin-streptomycin solution (10,000 units penicillin and 10 mg streptomycin/ml; Sigma-Aldrich)]. Slices (N = 3 from CS19) were photographed by using a Leica dissecting microscope at day 0 of culture, to record the morphology, and then incubated in 5% CO_2 at 37°C with the culture medium changed every 2–3 days. Slices were photographed at regular intervals for 7 days before fixation in 4% paraformaldehyde (PFA).

Tissue Processing and Histology

The upper jaws of heads were dissected from human embryos (CS20, CS21, CS22, CS23, 9, 11, and 13 weeks) and fixed in 4% PFA. Calcified tissues were decalcified in 0.5 M ethylenediaminetetraacetic acid (EDTA) in PBS. After decalcification, samples were dehydrated in an increasing ethanol concentration and permeated in xylene. Samples were then embedded in paraffin and cut in 10 µm serial sections by Microtome Leica RM2245. One of the sections in the series was stained with trichrome staining (Sirrus red, Alcian blue, and hematoxylin). Stained slides were observed under the Nikon Eclipse 80i light microscope, and images were taken by the attached Nikon Digital Sight DS-Fi1 camera.

Immunofluorescence

Wax embedded serial sections of the VL were de-waxed, rehydrated, and transferred into the citric acid (pH = 6) in 92°C water bath for antigen retrieval. The antibody blocking solution consists of PBS, 0.05% Tween20, 10% goat serum, and 1% bovine serum albumin (1% = 1 g/100 µl). The slides were then incubated with rabbit keratin 14 (K14; 1:200; Covance #905501), mouse keratin 10 (K10; 1:300; Abcam #ab76318), rabbit keratin 5 (K5; 1:300; Covance #PRB-160P), rabbit fillagrin (Cambridge Bioscience #HPA030188), rabbit proliferating cell nuclear antigen (PCNA; Abcam #ab193965), and rabbit Cleaved Caspase-3 (1:200, Cell Signaling #9579) overnight at 4°C. For immunofluorescence, sections were incubated in Alexa Fluor™ donkey anti-mouse 488 (1:500; Invitrogen #A11001), Alexa Fluor™ donkey anti-rabbit 488 (1:500; Abcam ab150073), and Alexa Fluor™ donkey anti-rabbit 568 (1:500; Invitrogen #A10042) for 2 h at RT. Sections were mounted with Fluoroshield™ with DAPI (Sigma-Aldrich #SLBV4269) and imaged with a Leica TCS SP5 confocal microscope or Zeiss ApoTome. To test each antibody, controls were performed where the primary antibodies had been omitted in order to confirm specific staining. Each antibody was repeated at least twice, at different timepoints, using serial sections. To aid comparison, the color of filaggrin was changed to green from red on the ApoTome (13 weeks) or in photoshop (11 weeks), while the K5 was changed on the ApoTome from red to blue.

For wholemount immunofluorescence, explant culture slices were fixed in 4% PFA for 30 min at RT. Samples were permeabilized with PBS Triton 0.5% (PBT) at RT for 1 h, followed by trypsinization for 5 min on ice and incubation in blocking solution for 2 h. After blocking, slices were incubated in Alexa Fluor Phalloidin 488 (Invitrogen; 1:50) and DAPI (1:1,000; Sigma) overnight at 4°C. After washing in PBS, cultures were mounted in glycerol and analyzed by a Leica TCS SP5 confocal microscope.

RESULTS

The Human VL and DL Bud Off From a Single Epithelial Thickening

It has been suggested from 3D reconstructions of histology sections that the human VL and DL are derived from a common oral epithelium in the lower lip region (**Figure 1A**; Hovorakova et al., 2007). To follow the development of these two laminas during development, we made live slices through the dissected mandible of a human embryo at the placode stage (CS19: 6.5 weeks; **Figures 1B,C**; N = 1 embryo). Slices were sectioned in the sagittal plane, and medial slices that contained an epithelial thickening under the developing tongue were selected (N = 3 slices). A single thickening was observed at CS19 (**Figures 1E,E'**), similar to that observed in histology sections through this region of the jaw (**Figure 1D**). The thickening in culture became more pronounced after a day in culture (**Figures 1F,F'**). The thickening extended into the underlying mesenchyme, with a lip of epithelial cells elongating toward the tongue after 4 days (**Figures 1G,G'**). The epithelium divided into two protrusions after 6 days in culture forming the VL and DL (**Figures 1H,H'**). At day 7, a clear bifurcation of the epithelium into a tooth bud and a wider VL was observed when imaged by confocal, with phalloidin staining (green) used to highlight the cell morphology (**Figures 1I,I'**). This confirms the histology findings that, at least in the anterior region of the lower jaw, the human VL and DL form from a single placode and are therefore directly associated with each other.

The Morphology of the Human VL Increases in Complexity During Development

To further investigate the development of the VL and DL in human embryos, we studied the development of VL and DL at embryonic CS20, CS21, CS22, CS23, 9, 11, and 13 weeks. This time period spans the period from defined VL and DL thickenings to proposed formation of the fissure in the VL to create the oral vestibule (Coslet and Cohen, 1969). The relationship between the VL and DL is very complex across the jaw with large variations depending on the A-P position (summarized in **Figures 1A, 2A**). In order to follow how the VL and DL co-develop, we therefore focused on a single region in the jaw. For this, we selected the deciduous canine area of the maxilla. The upper canine and VL are very closely associated in 3D reconstructions (**Figure 2A**), and the VL in this region appears particularly complex in shape (Bolk, 1921, data not shown), thus providing an intriguing area to study further. The primary canine primordia at these stages develop from an oral epithelial thickening at CS20 (**Figures 2B,B'**), bud stage at CS21 (**Figures 2C,C'**) and CS22 (**Figures 2D,D'**), to cap stage at CS23 (**Figures 2E,E'**) and 9 weeks (**Figure 2F**), to a bell stage at 11 (**Figure 2G**) and 13 weeks (**Figure 2H**). At CS20, the VL was visible as a slight thickening on the buccal side of the tooth

germ, forming a prominent thickening by CS21 (**Figures 2B–C'**). By CS22, the whole VL/DL region had invaginated inward to sit within a groove (**Figures 2D,D'**). This groove has previously been described as the labio-tectal furrow and the cheek furrow (Bolk, 1921; Hovorakova et al., 2005). The cheek furrow deepened as the VL/DL developed, with the cap stage canine tooth connected to the VL (**Figures 2E,F**). A narrow fissure in the VL started to form at 11 weeks, extending up from the base of the furrow (**Figure 2G**). By 13 weeks, several fissures had formed that split the VL into a branched structure, with the DL extending from the lingual side of the VL (**Figures 2H,I**).

Epithelial Differentiation Highlights Labial-Lingual Differences in Structure of the VL and May Trigger Furrow Formation

Skin epidermal differentiation occurs in layers from the basal cell layer, where the basal cells sit on the basement membrane adjacent to the surrounding mesenchymal cells, to the superficial cornified layer. K5 and K14 are expressed in more undifferentiated/basal cells; while K10 is expressed in the middle spinous layer with filaggrin expressed in the overlying granular layer (Lee et al., 1999; Coolen et al., 2010). We therefore utilized K5, K14, K10, and filaggrin as markers to investigate the differentiation state of the VL from CS23 to 13 weeks. The expression of various keratins have previously been followed in the human oral mucosa, with expression of K10 in the VL, but not DL, shown at 11 weeks (Pelissier et al., 1992). Where, it was suggested that the boundary between the K10 positive and negative cells in the VL might indicate the site of future fissure formation (Pelissier et al., 1992). At CS23, the buccal oral epithelium within the labio-tectal furrow expressed K5, with very limited expression of K10 and a patchy expression of K14 in the basal epithelial cells, highlighting the undifferentiated state of the epithelium at this stage (**Figures 3A–C**). By 9 weeks, more K10 expressing cells were evident lying in a suprabasal layer on top of the K14 basal layer, with K5 still expressed in most cells (**Figures 3D–F**). By 11 weeks, expression of K10 had spread up into the VL extending from the labio-tectal furrow (**Figure 3G**). Expression was concentrated on the buccal side and was largely absent from the lingual side (**Figures 3G,H,J**), agreeing with the results of Pelissier et al. (1992). The cells of the VL near to the basal lamina and the DL expressed K14 at this stage (**Figure 3G**). The cells in the center of the VL did not express K14, with scattered expression of K10, indicating that the center was more differentiated than the edges (**Figure 3G**). On the buccal side near the oral epithelium, K14 was mainly restricted to the basal layer, with K5 expressed more widely and K10 expressed in a suprabasal layer, with some overlap of expression in the intermediate area between K14 and K10 (**Figures 3H,I**). On the lingual side, the expression of K14 and K5 were similar but with minimal K10, highlighting that the two sides of the lamina appear to differentiate asynchronously (**Figures 3J,K**).

The strong expression of K10 on the buccal side of the VL was maintained at 13 weeks but more K10 positive cells were now found throughout the rest of the lamina (**Figures 4A,B,D**). The expression of K5 reduced, particularly on the buccal side, where expression was mainly restricted to the cells of the basal lamina, overlapping with K14 (**Figures 4C,E**). Some cells again co-expressed K14 and K10, indicating a change in differentiation state (**Figure 4B**). At 13 weeks, a number of fissures had developed in the VL (as seen in **Figure 2H**). To understand how these fissures formed, we looked at expression of filaggrin. Filaggrin has previously been reported as turning on at 22–24 weeks in the interfollicular epidermis and granular layer of the skin, with expression at 14 weeks in developing hair follicles (Dale et al., 1985; Lee et al., 1999). At 13 weeks, filaggrin was strongly expressed in the cells lining the developing fissures (**Figures 4F–J**). As filaggrin expression in keratinocytes results in loss of cell-cell adhesion (Presland et al., 2001), filaggrin upregulation in the VL might trigger fissure formation. To investigate this further, we analyzed filaggrin expression at 11 weeks (**Figures 4K–N**). As at 13 weeks, in areas where fissures had already started to form, filaggrin was expressed (**Figures 4K–M**). Interestingly, however, diffuse expression was also evident in the middle of the VL in regions where fissure formation was yet to initiate (**Figure 4N**), highlighting that filaggrin might be playing a role in fissure initiation. Filaggrin expression in keratinocytes results in decreased proliferation (Presland et al., 2001) and increased susceptibility to apoptosis (Kuechle et al., 2000). Given the links with proliferation and apoptosis, we next investigated how these processes were altered during fissure formation during VL development.

Cells at the Center of the VL Do Not Proliferate and Undergo Cell Death

To investigate proliferation levels, we utilized PCNA as a marker for the S phase of cell proliferation (Dietrich, 1993). At 13 weeks, proliferating cells were generally found associated with the basal layer next to the basal lamina (**Figures 5A,C,D**). Fewer positive cells were observed moving away from the basal lamina (**Figures 5C,D**), with no positive cells in the center (**Figures 5A,B**). Cell death has previously been investigated during the development of the vole VL (Witter et al., 2005). A few scattered apoptotic bodies were evident in the forming VL at E13.5 and E14.5 in the vole, in contrast to high levels in the forming EKs in the DL, suggesting that cell death only played a minor role at these stages (Witter et al., 2005). A lack of degenerating cells in the VL was also described during formation of the furrow in human fetal samples (Coslet and Cohen, 1969), although others have reported localized cellular atrophy as the cause of the split (Bolk, 1921; West, 1924). We utilized Caspase-3 as a marker for apoptosis and correlated to the presence of apoptotic bodies, as identified by condensed nuclei. As in the vole, very few Caspase positive cells were observed at early stages of VL formation (9 and 11 weeks; **Figures 5E–J**). The few positive cells, corresponded to apoptotic bodies, confirming that the cells were undergoing programmed cell death (**Figures 5G,J**). At 13 weeks, there were no positive cells associated with the forming fissures (**Figures 5K–N**); however, a large number of positive cells were found in the V-shaped epithelial tissue at the center of the VL (**Figures 5O–Q2**). Cell death, therefore, appears to play a role in removal of the tissue lying in between the forming fissures but did not play a role in the formation of the fissures themselves.

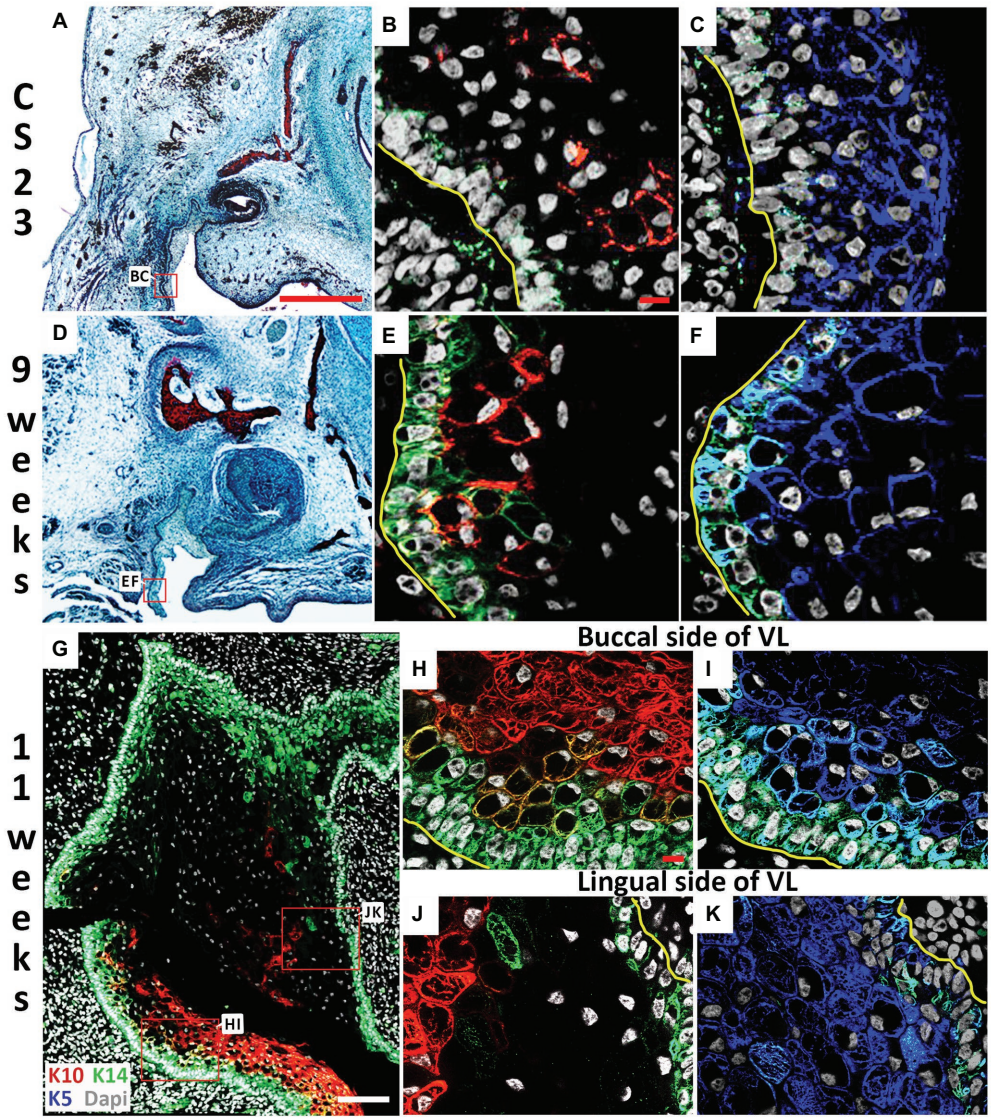

FIGURE 3 | Lingual/buccal differences in VL epithelium. **(A,D)** Histological frontal sections through the upper canine. **(B,C,E–K)** Immunofluorescence. DAPI shows nuclei in white. **(A–C)** CS23. Box in **(A)** highlights regions in **(B,C)**. The buccal side of the cheek furrow comprises cells with **(B)** limited Keratin 14 (K14; Green) and Keratin 10 (K10; red), and **(C)** high levels of Keratin 5 (K5; blue). **(D–F)** 9 weeks. Box in **(D)** highlights regions in **(E,F)**. The buccal side of the cheek furrow comprises cells with **(E)** robust K14 in the basal layer (Green), with K10 turning on in the overlying suprabasal layer (red), and **(F)** high levels of K5 (blue). **(G–K)** 11 weeks. Box in **(G)** highlights regions in **(J,K)**. **(G)** K14 (green) is robustly expressed around the edges of the VL, with K10 (red) observed at high levels mainly on the buccal side only. **(H–K)** High power of the buccal side **(H,I)** and lingual **(J,K)** side of the VL comparing the expression of K5 (blue) and K14 (green) in the basal layer and overlying layer, and K10 (red) in the suprabasal layer. Yellow lines outline the basement membrane separating the epithelial and mesenchymal cells in **(B,C,E,F,H–K)**. Scale bars in **(A)** = 500 μm, same scale in **(D)**. Scales bars in **(B,H)** = 10 μm, same scale in **(C,E,F,I–K)**. Scale bar in **(G)** = 100 μm.

DISCUSSION

A Single Origin of the Anterior VL and DL During Human Development

The DL and VL have a very close relationship during development. In the maxillary canine region, the DL is physically attached to the VL at all stages investigated. In the lower anterior region, our culture experiments confirm that a single epithelial thickening gives rise to both the VL and the DL. Due to the rarity of the material, culture was only attempted for one embryo at CS19 but the results agree with findings indicated from 3D reconstruction of human sections and from lineage tracing in the mouse (Hovorakova et al., 2007, 2016). Although we confirm this dual origin for the lower anterior oral region, the relationship between the DL and VL is dynamic throughout the jaw (**Figures 1A, 2A**). This heterogeneity explains the differing results from papers that have investigated different regions of the jaw (Bolk, 1921; Schour, 1929; Tonge, 1969). We, therefore, suggest that a single thickening, which subsequently divides into the DL and VL, forms in the anterior region, while distinct DL and VL thickenings

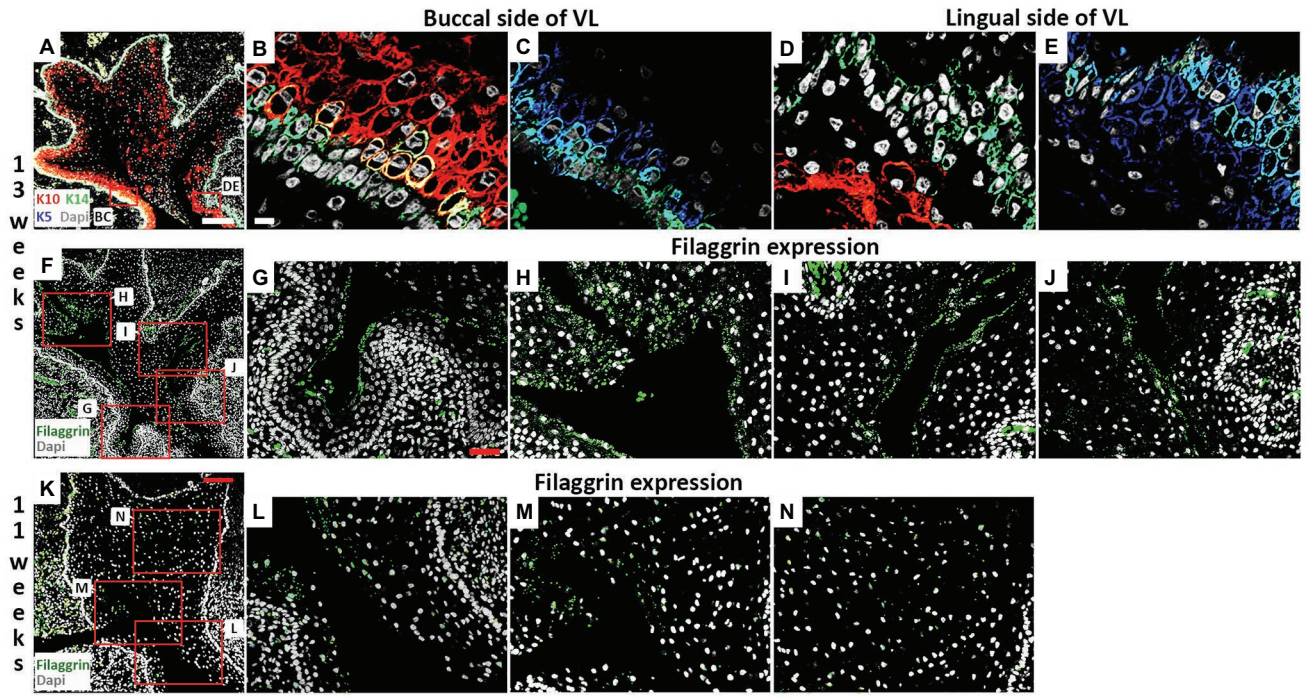

FIGURE 4 | Filaggrin expression is associated with fissure formation in the VL. **(A–J)** Frontal sections through the canine VL at 13 weeks. DAPI shows nuclei in white. **(A)** Branching structure of VL. Boxes in **(A)** highlights regions in **(B–E)**. **(A–E)** K10 (red), K5 (blue), K14 (green). **(B,C)** On the buccal side, K14 is largely limited to the basal layer, with a wider expression of K5, and K10 at high levels in the overlying layer. **(D,E)** On the lingual side, K10 levels remain low, with a less organized layer of K14. **(F–J)** Filaggrin (green) lines the forming fissures at 13 weeks. **(F)** Branching structure of VL. Boxes in **(F)** highlights different parts of the VL in **(G–J)**. **(K–N)** Frontal sections through the canine VL at 11 weeks. DAPI shows nuclei in white. **(K)** VL with evidence of a main fissure running through the structure. Filaggrin (Green). Boxes in **(K)** highlights regions in **(L–N)**. Scale bar in **(A)** = 200 μm, same scale in **(F)**. Scale bar in **(B)** = 10 μm, same scale in **(C–E)**. Scale bar in **(G)** = 50 μm, same scale in **(H–J,L–N)**. Scale bar in **(K)** = 100 μm.

arise more posteriorly. Whether this is a feature across mammals, will be an interesting area for future investigation.

The DL is closely associated with a number of developing structures across vertebrates. In the mouse, a single thickened epithelium has been proposed to be the primordium for the DL, VL, and the rugae of the palate (Peterková, 1985). Similarly, in reptiles the DL and the neighboring dental gland have been suggested to form from a single placode (Vonk et al., 2008; Tucker, 2010). A close relationship between the DL and the neighboring taste bud primordium has also been suggested in the shark and rays, with cells from the taste buds contributing to the cells of the lamina during embryonic development (Martin et al., 2016). The DL should therefore not be thought of in isolation but together with its neighboring epithelial organs. What signals govern the decision to form a VL or DL is an interesting future question. Mistakes in such a process might lead to the VL taking on a DL fate, as in the case when tooth pathologies form in the region of the vestibule (Hovorakova et al., 2020).

The Lingual and Labial/Buccal Sides of the VL Have Different Differentiation Patterns

The VL forms as a block of epithelium which then divides to create the vestibule. Here, we show that the canine VL is not divided by formation of a single fissure but by the development of numerous fissures that split the VL into several pieces. The epithelial cells on the labial/buccal side differentiate earlier, with the expression of the suprabasal marker K10, while this marker was only weakly expressed on the lingual side by 13 weeks when the fissures are apparent. Differences in keratin patterns between the mucosa on either side of the vestibule have also been observed in adult tissue, suggesting that these developmental differences are maintained throughout life (Verlach et al., 2017). It has been proposed that the lingual and labial/buccal sides are divided along the line of the K10 positive and negative expressing cells (Pelissier et al., 1992). There appears to be a slight oversimplification given that many fissures form and do not follow the lines of K10 expression. However, the fissures were lined with the terminal marker filaggrin, with filaggrin expression evident before fissure formation at 11 weeks. Filaggrin has been shown to have a role in cell adhesion (Presland et al., 2001). In epithelial cells, over expressing filaggrin, two desmosome proteins, desmoplakin, and plakoglobin, were lost at the cell interfaces and the cells detached from their neighbors (Presland et al., 2001). The upregulation of filaggrin in the VL, prior to any evidence of a fissure, may therefore lead to the cells at the center losing their adhesion, with the consequence that gaps would appear between the cells, creating the fissures. This is a particularly interesting hypothesis, given that filaggrin expression is observed extremely early in the VL, several weeks before its described upregulation

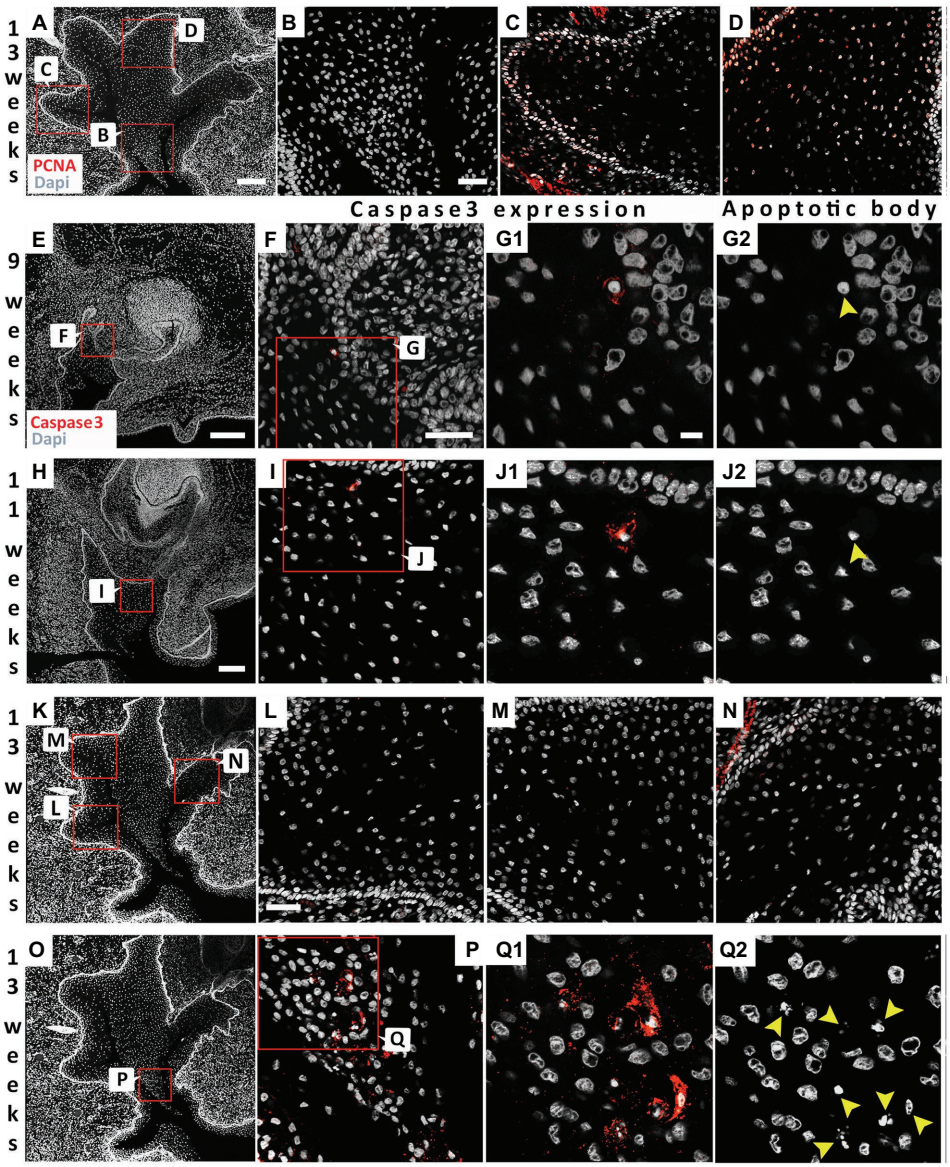

FIGURE 5 | Differential proliferation and apoptosis to remove the central cells to create the vestibule. **(A)** 13 weeks VL. DAPI shows nuclei in white. Boxes in **(A)** highlights regions in **(B–D)**. **(B–D)** PCNA (red). **(B)** Absence of proliferating cells at the center of the VL. **(C,D)** Proliferating cells in the more basal cells at the edges of the VL. **(E–Q2)** Analysis of program cell death. **(F,G1,I,J1,L–N,P,Q1)** activated Caspase-3 immuno (red). **(G2,J2,Q2)** same sections as in **(G1,J1,Q1)** showing the presence of apototic bodies (yellow arrowheads). **(E–G2)** 9 weeks. **(E)** 9 weeks VL. DAPI shows nuclei in white. Box in **(E)** highlights regions in **(F–G2)**. **(H–J2)** 11 weeks. **(H)** 11 weeks VL. DAPI shows nuclei in white. Box in **(H)** highlights regions in **(I–J2)**. **(K–Q2)** 13 weeks. **(K)** 13 weeks VL. DAPI shows nuclei in white. Boxes in **(K)** highlights regions in **(L–N)**. Box in **(O)** highlights regions in **(P–Q2)**. Scale bar in **(A)** = 200 μm, Scale Bar in **(B)** = 50 μm, same scale in **(C,D)**. Scale bar in **(E,H)** = 200 μm, same scale in **(K,O)** as for **(H)**. Scale bar in **(F)** = 50 μm, same scale in **(I)**. Scale bar in **(G1)** = 10 μm, same scale in **(G2,J1,J2,Q1,Q2)**. **(G1)** = 10 μm, same scale in **(G2,J1,J2,Q1,Q2)**. Scale bar in **(L)** = 50 μm, same scale in **(M,N)**.

in forming hair follicles and its expression in fetal skin (Dale et al., 1985; Lee et al., 1999). Division of the VL based on changes in cell adhesion agrees with the hypothesis suggested by Coslet and Cohen (1969) based on cell morphology in histological sections. The upregulation of filaggrin and differentiation of the VL cells agreed with the restriction of proliferation to the more basal parts of the structure. Failure in formation of these fissures along the VL would be predicted to result in the formation of frenulum, with tissue permanently linking the dental arch and lips/cheeks, as observed in EVC syndrome (Sasalawad et al., 2013). EVC syndrome is associated with defects in primary cilia and the Shh signaling pathway (Caparrós-Martín et al., 2013; Nakatomi et al., 2013), suggesting that this pathway may have an important role in development of the VL. In mice, the DL and VL form from a Shh positive placode but then Shh turns off in the VL (Hovorakova et al., 2016). Shh, therefore does not appear to be associated with later development of the VL.

Apoptosis Plays a Role in Removing Tissue From the VL but Not in Fissure Formation

During formation of the fissures, we did not see any evidence of programmed cell death, as evidenced by expression of activated Caspase-3 or of apoptotic bodies. Fissure formation is therefore unlikely to be triggered by death of cells at the center of each fissure, but rather by changes in cell-cell interactions. Several fissures were formed in the VL at the canine, creating a V-shaped wedge of cells at the middle of the VL. It is here that high levels of apoptosis were observed. Removal of the cells in the middle of the VL, created by formation of the fissures, therefore does appear to be dependent on cell death. Cell death in this region would help to broaden the developing vestibule, creating a more pronounced division between the dental arch and surrounding cheeks and lips.

Overall, we show that the DL and VL develop in close association, with the VL as a transient structure, having a perhaps surprisingly complex development. New understanding of development can shed light on dental pathologies associated with the vestibule, and to congenital defects in this region.

DATA AVAILABILITY STATEMENT

The raw data supporting the conclusions of this article will be made available by the authors, without undue reservation.

ETHICS STATEMENT

The studies involving human embryonic and fetal tissue were reviewed and approved by the Human Developmental Biology Resource under the approval of the National Research Ethics Service.

AUTHOR CONTRIBUTIONS

MH and AT conceived the idea. TQ performed the histology and immunohistochemistry. TT performed the explant culture experiments. AT and TQ wrote the manuscript. All authors contributed to the article and approved the submitted version.

FUNDING

This work was supported by the Grant Agency of the Czech Republic (18-04859S to MH and AT). TQ was funded by the China Scholarship Council as part of a PhD studentship at KCL. The human embryonic and fetal material in this paper was provided by the Human Developmental Biology Resource (www.hdbr.org), which is jointly funded by the Medical Research Council and Wellcome Trust (grant #099175/Z/12/Z).

REFERENCES

Alfaqeeh, S. A., and Tucker, A. S. (2013). The slice culture method for following development of tooth germs in explant culture. *J. Vis. Exp.* 81:e50824. doi: 10.3791/50824

Bolk, L. (1921). Odontological essays. *J. Anat.* 57, 55–75.

Caparrós-Martín, J. A., Valencia, M., Reytor, E., Pacheco, M., Fernandez, M., Perez-Aytes, A., et al. (2013). The ceiliary EVC/EVC2 complex interacts with smo and controls hedgehog pathway activity in chondrocytes by regulating Sufu/Gli3 dissociation and Gli3 trafficking in primary cilia. *Hum. Mol. Genet.* 22, 124–139. doi: 10.1093/hmg/dds409

Coolen, N. A., Schouten, K. C. W. M., Middelkoop, E., and Ulrich, M. M. W. (2010). Comparison between human fetal and adult skin. *Arch. Dermatol. Res.* 302, 47–55. doi: 10.1007/s00403-009-0989-8

Coslet, J. G., and Cohen, D. W. (1969). Observations on the development of the vestibular trough in the human fetus part I. The anterior portion of the mouth. *J. Periodontol.* 40, 320–329. doi: 10.1902/jop.1969.40.6.320

Dale, B. A., Holbrook, K. A., Kimball, J. R., Hoff, M., and Sun, T. T. (1985). Expression of epidermal keratins and filaggrin during human fetal skin development. *J. Cell Biol.* 101, 1257–1269. doi: 10.1083/jcb.101.4.1257

Dietrich, D. R. (1993). Toxicological and pathological applications of proliferating cell nuclear antigen (PCNA), a novel endogenous marker for cell proliferation. *Crit. Rev. Toxicol.* 23, 77–109. doi: 10.3109/10408449309104075

Hovorakova, M., Lesot, H., Peterka, M., and Peterkova, R. (2005). The developmental relationship between the deciduous dentition and the oral vestibule in human embryos. *Anat. Embryol.* 209, 303–313. doi: 10.1007/s00429-004-0441-y

Hovorakova, M., Lesot, H., Vonesch, J. -L., Peterka, M., and Peterkova, R. (2007). Early development of the lower deciduous dentition and oral vestibule in human embryos. *Eur. J. Oral Sci.* 115, 280–287. doi: 10.1111/j.1600-0722.2007.00464.x

Hovorakova, M., Lochovska, K., Zahradnicek, O., Tibenska, K. D., Dornhoferova, M., Horakova-Smrckova, L., et al. (2016). One odontogenic cell-population contributes to the development of the mouse incisors and of the oral vestibule. *PLoS One* 11:e0162523. doi: 10.1371/journal.pone.0162523

Hovorakova, M., Zahradnicek, O., Bartos, M., Hurnik, P., Stransky, J., Stembirek, J., et al. (2020). Reawakening of ancestral dental potential as a mechanism to explain dental pathologies. *Integr. Comp. Biol*. icaa053. doi: 10.1093/icb/icaa053

Kochva, E. (1965). The development of the venom gland in the opisthoglyph snake *Telescopus fallax* with remarks on *Thamnophis sirtalis*. *Copeia* 1965, 147–154. doi: 10.2307/1440716

Kuechle, M. K., Presland, R. B., Lewis, S. P., Fleckman, P., and Dale, B. A. (2000). Inducible expression of filaggrin increases keratinocyte susceptibility to apoptotic cell death. *Cell Death Differ.* 7, 566–573. doi: 10.1038/sj.cdd.4400687

Lee, S. C., Lee, J. B., Kook, J. P., Seo, J. J., Nam, K. I., Park, S. S., et al. (1999). Expression of differentiation markers during fetal skin development in humans: immunohistochemical studies on the precursor proteins forming the cornified cell envelope. *J. Invest. Dermatol.* 112, 882–886. doi: 10.1046/j.1523-1747.1999.00602.x

Martin, K. J., Rasch, L. J., Cooper, R. L., Metscher, B. D., Johanson, Z., and Fraser, G. J. (2016). Sox2+ progenitors in sharks link taste development with the evolution of regenerative teeth from denticles. *Proc. Natl. Acad. Sci. U. S. A.* 113, 14769-14774. doi: 10.1073/pnas.1612354113

Nakatomi, M., Hovorakova, M., Gritli-Linde, A., Blair, H. J., MacArthur, K., Peterka, M., et al. (2013). Evc regulates a symmetrical response to Shh signaling in molar development. *J. Dent. Res.* 92, 222–228. doi: 10.1177/0022034512471826

Nery, E. B., Kraus, B. S., and Croup, M. (1970). Timing and topography of early human tooth development. *Arch. Oral Biol.* 15, 1315–1326. doi: 10.1016/0003-9969(70)90020-8

Pavlikova, H., Witter, K., and Misek, I. (1999). Primordium of the upper vestibulum oris in the domestic sheep. *Acta Vet. Brno* 68, 175–178. doi: 10.2754/avb199968030175

Pelissier, A., Ouhayoun, J. P., Sawaf, M. H., and Forest, N. (1992). Changes in cytokeratin expression during the development of the human oral mucosa. *J. Periodontal Res.* 27, 588–598. doi: 10.1111/j.1600-0765.1992.tb01741.x

Peterková, R. (1985). The common developmental origin and phylogenetic aspects of teeth, rugae palatinae, and fornix vestibuli oris in the mouse. *J. Craniofac. Genet. Dev. Biol.* 5, 89–104.

Popa, E. M., Buchtova, M., and Tucker, A. S. (2019). Revitalising the rudimentary replacement dentition in the mouse. *Development* 146:dev171363. doi: 10.1242/dev.171363

Presland, R. B., Kuechle, M. K., Lewis, S. P., Fleckman, P., and Dale, B. A. (2001). Regulated expression of human filaggrin in keratinocytes results in cytoskeletal disruption, loss of cell-cell adhesion, and cell cycle arrest. *Exp. Cell Res.* 270, 199–213. doi: 10.1006/excr.2001.5348

Sasalawad, S. S., Hugar, S. M., Poonacha, K. S., and Mallikarjuna, R. (2013). Ellis-van Creveld syndrome. *BMJ Case Rep.* 2013:bcr2013009463. doi: 10.1136/bcr-2013-009463

Schour, I. (1929). Early human tooth development, with special reference to the relationship between the dental lamina and the lip-furrow band. *J. Dent. Res.* 9, 699–717. doi: 10.1177/00220345290090050801

Tonge, C. H. (1969). The time-structure relationship to tooth development in human embryogenesis. *J. Dent. Res.* 48, 745–752.

Tucker, A. S. (2010). "Salivary gland adaptations: Modification of the glands for novel uses" in *Salivary glands.* eds. A.S., Tucker and I., Miletich (Basel: Karger), 21–31.

Tucker, A., and Sharpe, P. (2004). The cutting-edge of mammalian development: how the embryo makes teeth. *Nat. Rev. Genet.* 5, 499–508. doi: 10.1038/nrg1380

Verlach, J., Foltan, R., Vlk, M., Szabo, P., and Smetana, K. (2017). Phenotypic chacterisation of oral mucosa: what is normal? *J. Oral Pathol. Med.* 46, 834–839. doi: 10.1111/jop.12556

Vonk, F. J., Admiraal, J. F., Jackson, K., Reshef, R., de Bakker, M. A. G., Vanderschoot, K., et al. (2008). Evolutionary origin and development of snake fangs. *Nature* 454, 630–633. doi: 10.1038/nature07178

Wang, X. P., O'Connell, D. J., Lund, J. J., Saadi, I., Kuraguchi, M., Turbe-Doan, A., et al. (2009). Apc inhibition of Wnt signaling regulates supernumerary tooth formation during embryogenesis and throughout adulthood. *Development* 136, 1939–1949. doi: 10.1242/dev.033803

West, C. M. (1924). The development of the gums and their relationship to the deciduous teeth in the human fetus. *Contr. Embroyol. Carnegie Inst.* 16, 25–45.

Witter, K., Pavlikova, H., Matulova, P., and Misek, I. (2005). Relationship between vestibular lamina, dental lamina, and the developing oral vestibule in the upper jaw of the field vole (*Microtus agrestis*, Rodentia). *J. Morphol.* 265, 264–270. doi: 10.1002/jmor.10356

Conflict of Interest: The authors declare that the research was conducted in the absence of any commercial or financial relationships that could be construed as a potential conflict of interest.

frontiers in Physiology

ORIGINAL RESEARCH
published: 31 July 2020
doi: 10.3389/fphys.2020.00936

Action of Actomyosin Contraction With *Shh* Modulation Drive Epithelial Folding in the Circumvallate Papilla

*Sushan Zhang†, Jong-Min Lee†, Adpaikar Anish Ashok and Han-Sung Jung**

Division in Anatomy and Developmental Biology, Department of Oral Biology, Brain Korea 21 PLUS Project, Taste Research Center, College of Dentistry, Yonsei University, Seoul, South Korea

The mouse tongue possesses three types of gustatory papillae: large circumvallate papillae (CVP), foliate papillae (FOP) and fungiform papillae (FFP). Although CVP is the largest papilla and contain a high density of taste buds, little is known about CVP development. Their transition from placode to dome-shape is particularly ambiguous. Understanding this phase is crucial since dome-shaped morphology is essential for proper localization of the imminent nerve fibers and taste buds. Here, we report actomyosin-dependent apical and basal constriction of epithelial cells during dynamic epithelial folding. Furthermore, actomyosin-dependent basal constriction requires focal adhesion kinase to guide dome-shape formation. Sonic hedgehog (Shh) is closely associated with the differentiation or survival of the neurons in CVP ganglion and cytoskeletal alteration in trench epithelial cells which regulate CVP morphogenesis. Our results demonstrate the CVP morphogenesis mechanism from placode to dome-shape by actomyosin-dependent cell shape change and suggest roles that Shh may play in trench and stromal core formation during CVP development.

Keywords: circumvallate papilla, sonic hedgehog, epithelial folding, actomyosin, focal adhesion kinase

OPEN ACCESS

Edited by:
Maisa Hanna-Maija Seppala, King's College London, United Kingdom

Reviewed by:
Linda April Barlow, University of Colorado, School of Medicine, United States
Jeffrey Hildebrand, University of Pittsburgh, United States

****Correspondence:***
Han-Sung Jung
hsj8076@gmail.com

† These authors have contributed equally to this work

Specialty section:
This article was submitted to Craniofacial Biology and Dental Research, a section of the journal Frontiers in Physiology

Received: *17 April 2020*
Accepted: *13 July 2020*
Published: *31 July 2020*

Citation:
Zhang S, Lee J-M, Ashok AA and Jung H-S (2020) Action of Actomyosin Contraction With Shh Modulation Drive Epithelial Folding in the Circumvallate Papilla. Front. Physiol. 11:936. doi: 10.3389/fphys.2020.00936

INTRODUCTION

Circumvallate papillae (CVP) are located on the dorsal surface of the posterior tongue in mammals (Jitpukdeebodintra et al., 2003; Chandrashekar et al., 2006; Barlow and Klein, 2015). Despite the importance of CVP as the largest gustatory papilla and that possess a high density of taste buds, our understanding of its cellular development is imperfect. Recently, molecular regulation of FFP development have substantially been revealed. Previous studies showed that Shh, Bmps, and Wnts regulate FFP patterning and morphogenesis in early stages. However, the functions that these genes play in CVP development have not been fully investigated (Hall et al., 2003; Mistretta et al., 2003; Liu et al., 2004, 2007; Zhou et al., 2006; Iwatsuki et al., 2007; Beites et al., 2009).

Previously, various genes associated with CVP defects have been reported. Mesenchymal Fgf10 is essential for the maintenance of Lgr5/Sox2-positive CVP epithelial progenitor cells, which is consistent with the absence of CVP structures in Fgf10-/- mice (Petersen et al., 2011; Zhang et al., 2018). In *Pax9*$^{-/-}$ mice, trench formation in CVP and FOP is retarded (Kist et al., 2014). Morphological abnormalities of CVP have been observed in *Six1*$^{-/-}$*Six4*$^{-/-}$, *Ripply3*$^{-/-}$ and *Tbx1*$^{-/-}$ mice correlated with glossopharyngeal nerve innervation failure. These abnormalities

correlated with glossopharyngeal nerve innervation failure suggest a potential relationship between innervation and morphogenesis (Guth, 1957; Suzuki et al., 2011; Okubo and Takada, 2015). Although correlations were recorded, no single gene has been identified as the direct regulator of the morphological change from placode to dome-shape. Nor did the prior investigations into this transition yield a working hypothesis for the responsible mechanism (Petersen et al., 2011).

The placode to dome-shape transition is based on epithelial folding, including invagination and evagination (Pearl et al., 2017). Invagination has been studied in various organs such as teeth and salivary glands (Jaskoll et al., 2004; Li et al., 2016; Panousopoulou and Green, 2016). However, the invagination mechanisms, including apical constriction and basal relaxation, are strictly applicable to the monolayer epithelial folding seen in neural tubes and lenses (Sai and Ladher, 2008; Sawyer et al., 2010; Martin and Goldstein, 2014; Pearl et al., 2017). Conversely, the CVP placode is composed of multiple layers of epithelial cells at E12.5. The transition from dental placode to tooth bud is an example of a multilayered epithelial folding. It has been explained using the suprabasal intercalation model, which is applicable to the development of other ectoderm-derived organs. Invagination in the suprabasal intercalation model is led by parallel suprabasal cells intercalation with region-specific E-cadherin (Panousopoulou and Green, 2016; Pearl et al., 2017). However, according to E-cadherin expressing cells and their cell orientation, both parallel suprabasal cells and region-specific E-cadherin were absent in the CVP placode. Because monolayered and multilayered epithelial folding models could not explain invagination in CVP, we analyzed each cell shape during early CVP development that potentially lead to morphological changes by epithelial folding (Pearl et al., 2017). Most of the previously reported epithelial folding was influenced by cell shape changes, especially actomyosin-dependent apical/basal constriction (Pearl et al., 2017). In this study, we confirmed that both apical and basal constriction during epithelial folding in developing CVP were actomyosin-dependent. Invagination is necessary for various organogenesis phenomena, however, genes responsible for regulating invagination have not been reported for CVP. Previous studies have reported that Shh regulates invagination during the transition from dental placode to tooth bud through changes in the epithelial cell shape. Similar to what is exhibited in dental epithelium, Shh is continuously expressed in CVP epithelium from E12.5 through adulthood (Mistretta et al., 2003; Iwatsuki et al., 2007; Kim et al., 2009). Reduced Shh expression, which led to impaired trench formation in *Pax9*$^{-/-}$ mice, indicates a potential correlation between epithelial Shh and CVP morphogenesis (Kist et al., 2014). However, morphological defects in CVP has not been reported in Shh pathway-inhibited embryonic tongue cultures (Hall et al., 1999, 2003; Mistretta et al., 2003; Liu et al., 2004; Iwatsuki et al., 2007).

In this study, basal constriction-dependent evagination was observed in the dome-shaped region of the developing CVP. Focal adhesion kinase (FAK) was necessary for basal constriction in outward epithelial folding (evagination) and for proper adherence to the underlying extracellular matrix. This mechanism is highly conserved and established in both the midbrain-hindbrain boundary and the developing tooth germ (Gutzman et al., 2008, 2018; Yamada et al., 2019).

The CVP placode to dome-shape transition happens simultaneously with innervation (Jitpukdeebodintra et al., 2003; Petersen et al., 2011; Kist et al., 2014). Nerve fibers of gustatory nerve enter the developing tongue mesenchyme at E12.0 and reach the tongue epithelium at E13.5 As the gustatory nerve innervates CVP, glial cells in the glossopharyngeal nerve are derived from neural crest cells (NCCs) and neurons in the glossopharyngeal nerve are derived from epibranchial placode-originated neuroblasts. Previous studies indicated that the underlying mesenchyme of CVP is NCCs-derived (Liu et al., 2012). Moreover, nerve fibers in the underlying mesenchyme of CVP were stained by PGP9.5 according to our results. The population of neuroblasts was further confirmed by expression of Neurogenin-2, an essential transcription factor for neuronal development in the glossopharyngeal nerve (Fode et al., 1998; Harlow and Barlow, 2007; Okubo and Takada, 2015; Fan et al., 2019).

The underlying mechanisms of dome-shape and trench formation in developing CVP were investigated in this study. The epithelial folding responsible for the dome and trench formations was actomyosin-dependent. Moreover, basal constriction requiring FAK led to evagination in the dome-shape region. Disruption of trench formation and stromal core morphology was observed after inhibition of Shh pathway by Cyclopamine. Invagination in the trench region was regulated by Shh through modulating apical constriction. Moreover, Shh was found impacted in stromal core formation by regulating differentiation or survival of neurons in CVP ganglion.

MATERIALS AND METHODS

All experiments were performed according to the guidelines of the Intramural Animal Use and Care Committee of the College of Dentistry, Yonsei University.

Animals

Adult ICR mice were housed in a temperature-controlled room (22°C) under artificial illumination and 55% relative humidity with access to food and water *ad libitum*. Embryos were obtained from time-mated pregnant mice. E0 was the day when the presence of a vaginal plug was confirmed. Embryos at each developmental stage (E12.5, E13.0, E13.5) were used in this study.

In situ Hybridization

In situ hybridization of tongues was performed as previously described (Kim et al., 2009). Embryonic tongues were dissected and fixed in 4% paraformaldehyde (PFA), dehydrated in methanol at -20°C. After rehydration, tissue went through proteinase K treatment and subsequent 0.25%glutaraldehyde in 4%PFA, then prehybridized in hybridization solution at 68°C for 2 h and hybridized with Digoxigenin-labeled RNA probes for overnight at 68–70°C. Mouse complementary *shh/ptch1*-inserted plasmids were used for synthesizing probes.

In vitro Organ Culture

The tongue was isolated from E12.5 mouse embryos and cultured on a 1.0 μm Nucleapore Track-Etch Membrane (Whatman, Pittsburg, PA, United States) in the medium at 37°C and 5%CO_2 for 48 h using culture method reported by Trowell. The culture medium (DMEM, Invitrogen, United States) was supplemented with 10% fetal bovine serum (FBS) (Invitrogen, United States) and 1% penicillin/streptomycin and was renewed every 24 h.

Histology and Immunofluorescence

Samples were fixed in 4% paraformaldehyde and processed until paraffin using standard procedures. Sections (4 μm) were prepared for hematoxylin/eosin staining and immunostaining. After citrate buffer (pH 6.0), Specimens were blocked using 1% goat serum or 5% bovine serum albumin in PBS, incubated with antibodies against endothelin receptor B (1:50, Abcam, United Kingdom), PGP9.5 (1:100, Abcam, United Kingdom), fibronectin (1:100, BD Bioscience, United States), E-cadherin (1:100, R&D Systems, United States), phosphomyosin light chain II (1:50, Cell Signaling Technology, United States), β-catenin (1:100, Santa Cruz, United States), and ZO-1 (1:100, Invitrogen, United States). Sequentially incubate with a secondary antibody (1:200, Invitrogen, United States) and stained with DAPI to visualize nuclei. All specimens were observed by confocal microscopy (YOKOGAWA CQ1, Japan). At least 10 mice were examined in each experiment.

Inhibitor Treatment

The medium was supplemented with 3μg/ml Blebbistatin, myosin II phosphorylation inhibitor (Sigma Aldrich, United States); 0.75 μM PF-573228, FAK inhibitor (Cayman Chemicals, United States), and 20 μM Cyclopamine, Smoothened inhibitor (Toronto Research Chemicals, Canada). The above chemicals were dissolved in Dimethyl Sulfoxide (DMSO; Sigma Aldrich, United States) for stock until use. Vehicle (DMSO)-treated tongues from the same littermates were used as controls. To minimize effects other than cytoskeleton, drug treatments were performed for the first 24 h.

Tissue Recombination

Tongues were dissected from E13.5 mouse embryos and kept in ice-cold PBS. Tissue was cut into approximately 200 μm-thick slices use microtome blades. After 60-min incubation in 2.2 U/ml Dispase II (neutral protease, grade II) at 37°C, the epithelium and mesenchyme of CVP were manually separated by forceps and washed in basal medium containing 10% FBS. After 1 h/3 h of standard culture, the epithelium was transferred to PBS and photographed. At least 12 embryos were examined for this experiment.

Recombination Experiment and Bead Implantation

E12.5 embryonic tongues were dissected and incubated in 2.2 U/ml Dispase II for 50 min at 37°C and washed in basal medium containing 10% FBS. Tongue epithelium and mesenchyme were gently separated in cold medium. The epithelium was placed 180° rotated anterior-posterior. Heparin beads (100–200 mesh; Sigma Aldrich, United States) soaked with 100 μg/ml FGF10 protein (6224-FG-02S; R&D Systems, United States) were implanted between the recombined CVP epithelium and non-CVP mesenchyme at E12.5 and cultured for 48 h as in both groups. The CVP epithelium and underlying mesenchyme combined at original as control. Specimens from 4 embryos were examined for each group.

Cellular Analysis

400X z-stack images of β-catenin-stained epithelial cells in developing CVP were measured and analyzed by Fiji (Schindelin et al., 2012). Category of cells with contact with basal lamina (basal cells), without contact (suprabasal cells). The maximum cross-sectional area of cells was measured to avoid artifacts. Basal width: width of cell attachment to the basal lamina, apical width: perpendicular to the cell long axis at the apical 20% site. Apical/basal ratio = apical width/basal width. Width/length ratio = width/length. The angle between the cell long axis and its projection into the flanking epithelium plane was measured. Parallel (0°–30°, 150°–180°), oblique (30°–60°, 120°–150°) and vertical (60°–120°) were used for categorize angles (Panousopoulou and Green, 2016; Yamada et al., 2019). 120 cells were counted for each analysis from 3 different specimens for each stage (n = 120). Significance was assessed by the t test. Data were expressed as the mean ± SD.

RESULTS

Epithelial Folding Involves Cytoskeletal Alteration

The multilayered CVP placode and monolayered non-CVP epithelium were observed in E12.5 mouse tongue (**Figure 1A**). At E13.0, CVP epithelium started to fold outward at the medial region of the placode and a low cell density region was observed in the underlying mesenchyme (**Figure 1B**). Dome-shaped formations and lateral trenches were formed at E13.5 with monolayered or pseudostratified CVP epithelium and stromal core (**Figure 1C**). The enteric nervous system precursor marker (Baynash et al., 1994; Hosoda et al., 1994), endothelin receptor B (ETB), was located in both the lateral tongue mesenchyme at E12.5 (**Figure 1D**) and the underlying mesenchyme of CVP placode at E13.0 specifically (**Figure 1E**). ETB was intensively localized in the stromal core at E13.5 (**Figure 1F**). Similarly, neuronal marker PGP9.5 was detected in the tongue mesenchyme distant from CVP at E12.5 (**Figure 1G**). PGP9.5 was observed underneath the mesenchyme of CVP at E13.0 (**Figure 1H**). At stage E13.5, PGP9.5 was detected in the stromal core (**Figure 1I**). Furthermore, ETB and PGP9.5 were co-localized at E13.0 (**Supplementary Figure S1A**). Moreover, neural cell adhesion molecule (NCAM) was detected in the nerve endings and cell bodies inside the stromal core at E13.5. A previous study reported that NCAM is detected in nerves innervated the adult CVP (**Supplementary Figure S1B**) (Nosrat et al., 2012). Fibronectin was markedly downregulated within the ETB located region at E13.0 (**Figure 1K**, arrowhead,

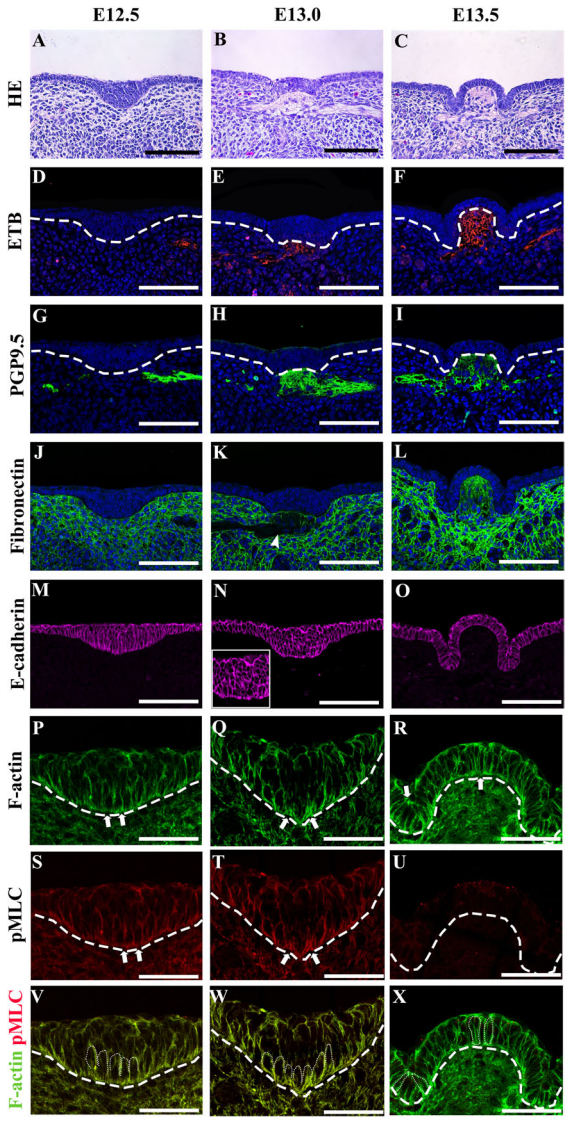

FIGURE 1 | (A) The circumvallate papilla (CVP) epithelium at E12.5 is a stratified placode, while non-CVP epithelium is monolayered. **(B)** At E13.0, epithelium started to fold outward at the medial region of the placode. A low cell density region is observed in the underlying mesenchyme at E13.0. **(C)** Dome-shape and lateral trenches are observed with monolayered or pseudostratified CVP epithelium at E13.5. **(D,E)** Endothelin receptor B (ETB) is located in the lateral tongue mesenchyme at E12.5 and underlying mesenchyme of CVP at E13.0. **(F)** ETB is detected in the stromal core of CVP at E13.5. **(G,H)** Protein gene product 9.5 (PGP9.5) is located in the lateral tongue mesenchyme at E12.5 and the underlying mesenchyme of CVP at E13.0. **(I)** The stromal core of CVP is marked by PGP9.5 at E13.5. **(J)** Fibronectin is located throughout the tongue mesenchyme at E12.5. **(K)** Fibronectin density is relatively low in the presence of neuroblasts (marked by ETB) at E13.0 (according to S1C) (arrowhead). **(L)** Fibronectin localization in the stromal core is relatively weaker than the surrounding mesenchyme at E13.5. **(M)** E-cadherin is located throughout the entire epithelium at E12.5. **(N)** E-cadherin is relatively enriched in basal and suprabasal cells of placodes at E13.0. **(O)** At E13.5, slight enrichment of E-cadherin is found in suprabasal cells. **(P)** F-actin accumulation is detected at the basal site of basal cells at E12.5. **(Q)** At E13.0, F-actin strongly accumulates at the basal site of basal cells in the medial region of CVP placode. **(R)** F-actin is enriched at the basal *(Continued)*

FIGURE 1 | Continued
site in the dome-shape region and at the apical site of the trench region epithelial cells at E13.5. **(S,T)** Phosphomyosin light chain II (pMLC) is enriched at the basal site of basal cells at E12.5 and strictly accumulated at the basal site of the medial region at E13.0. **(U)** pMLC is weakly detected in CVP epithelium at E13.5. **(V–X)** pMLC is co-accumulated with F-actin at E12.5 and E13.0 but not E13.5. Scale bar = 100 μm in panels **(A–O)**, 50 μm in panels **(P–X)**. Arrows indicate the cells which go through apical and basal constriction. Arrowhead indicates the low-density region of fibronectin localization. Thick dotted lines mark the border between developing tongue epithelium and mesenchyme. Thin dotted lines indicate individual cell shapes which go through apical and basal constriction.

Supplementary Figure S1C). At E13.5, fibronectin was more weakly displayed in the stromal core than in the surrounding mesenchyme (**Figure 1L**). E-cadherin located throughout the tongue epithelium, including CVP at E12.5 (**Figure 1M**). At E13.0, no significant difference of E-cadherin was observed when compared to E12.5 (**Figure 1N**). At E13.5, slightly prominent E-cadherin localization was observed in peridermal cells (**Figure 1O**). F-actin accumulated slightly at the basal site of basal cells at E12.5 (**Figure 1P**). Specifically, F-actin was strongly accumulated at the basal site of the medial region of the placode at E13.0 (**Figure 1Q**). Also, F-actin was slightly enriched at the apical site of the trench region as well as the basal portion of dome-shape region at E13.5 (**Figure 1R**). The F-actin intensity differences between the apical and basal site of epithelial cells were confirmed (**Table 1**). pMLC was enriched basally in basal cells at E12.5 and E13.0 (**Figures 1S,T**). pMLC enrichment was not detected in CVP epithelium at E13.5 (**Figure 1U**). Interestingly, F-actin and pMLC co-accumulated in developing CVP epithelium (**Figures 1V–X**) at E12.5 and E13.0 but not E13.5, which suggested that active actomyosin contraction occurred during CVP morphogenesis. Proliferative and apoptotic cells were not detected in CVP epithelium; proliferative cells were observed in the non-CVP epithelium and tongue mesenchyme including CVP mesenchyme from E12.5 to E13.5 (**Supplementary Figures S1D–I**). Neurogenin2, a neuroblast marker, was expressed in the underlying mesenchyme of CVP from E12.5 to E13.0, similar to ETB and PGP9.5 localization (**Supplementary Figures S1J,K**). These results indicated that the neuronal components supposed to be the neurons of the CVP ganglion and nerve fibers of gustatory neurons (Fode et al., 1998; Okubo and Takada, 2015).

Cell Shape Changes Following Epithelial Folding

Basal cells were colored black while suprabasal cells were colored red in cell shape drawing based on β-catenin staining (Meng and Takeichi, 2009) (**Figures 2A–C,A'–C'**). At E12.5, epithelial cells in CVP were columnar (**Figures 2A,A'**). The medial region was designated as "M," the hinge region as "H" and lateral as "L." At E13.0, basal constriction occurred in basal cells while suprabasal cells became oval-shaped in the medial region. Cells remained columnar in the lateral region (**Figures 2B,B'**). At E13.5, basal cells in both the lateral and medial regions became columnar with

TABLE 1 | Fluorescent intensity of F-actin between apical and basal site of epithelial cells.

	Stages groups	Apical intensity basal intensity of F-actin
Not defined	E12.5	0.99 ± 0.093
Medial	El3.0	0.85 ± 0.112
	El3.5	0.99 ± 0.099
	Control	0.89 ± 0.105
	Blebbistatin	1.01 ± 0.104
	PF-573228	0.97 ± 0.114
Lateral	E13.0	1.21 ± 0.120
	E13.5	1.18 ± 0.112
	Control	1.27 ± 0.095
	Cyclopamine	0.97 ± 0.110

<1 indicates apical site weaker than basal site. ≈1 indicates no significant difference is observed. >1 indicates apical site stronger than basal site.

basal constriction, while hinge cells were with apical constriction (**Figures 2C,C'**).

To understand whether cell shape changes result in epithelial folding, we measured the apical and basal widths of basal cells (apical/basal ratio = apical width/basal width indicated aw-aw'/b-b') (**Figure 2D**). At E12.5, all basal cells were columnar with apical/basal ratio ≈1 (**Figures 2A,A',D'**). At E13.0, the apical/basal ratio of mediobasal cells increased (>1), due to the basal width reduction (**Figures 2B,B',D'**). At E13.5, basal cells were categorized by the apical/basal ratio into two groups: cells in the hinge region with apical constriction (<1) and cells in the medial and lateral regions with basal constriction (>1) (**Figures 2C,C',D'**). To understand whether cell elongation had occurred, the width/length ratio (b-b'/a-a') was calculated (**Figures 2E,E'**). At E12.5, suprabasal cells were mostly elongated (width/length ratio ≈0.5) (**Figures 2A,A',E'**). However, suprabasal cells in the medial region became oval-shaped at E13.0 (≈1) while those in the lateral region remained elongated (≈0.5) (**Figures 2B,B',E'**). Overlaying the novel placode-to-invagination mechanism with the suprabasal intercalation model requires the existence of suprabasal elongated cells positioned in the direction parallel to the basal lamina to generate force for invagination (Panousopoulou and Green, 2016). To investigate whether suprabasal intercalation occurs in the placode to dome-shape transition, the orientations of suprabasal cells at E12.5 and E13.0 were measured (**Figures 2F,F'**). The angles of suprabasal cells (long axis) to the plane of the flanking epithelia were all in the vertical-to-oblique range (i.e., 45°–135°) at E12.5 (80°–100°) and E13.0 (70°–110°). Each suprabasal cell was not parallel to the plane of the flanking epithelium (**Figure 2F'**). Thus, suprabasal intercalation did not occur; the force of invagination could not be generated.

Actomyosin-Dependent Cellular Morphology

In order to examine whether epithelial folding is mechanically independent of the underlying mesenchyme, the CVP epithelium was separated from the mesenchyme at E13.5. Detached CVP epithelium maintained its original structure after in vitro culture for 1 and 3 h; this revealed that the mesenchyme was not mechanically required (**Figures 3A,B**). To determine whether epithelial folding depends on epithelial cells, reverse recombination was performed at E12.5 for 48 h. As we have shown previously, the CVP epithelium and non-CVP mesenchyme recombination group showed an absence of CVP structure. For rescue experiment, FGF10-soaked beads were implanted in the recombinant CVP epithelium and non-CVP mesenchyme for the maintenance of Lgr5-positive epithelial cells (Zhang et al., 2018). Epithelial folding was observed when CVP epithelium and the mesenchyme were recombined (**Figure 3C**), but absent when non-CVP epithelium was recombined with CVP mesenchyme (**Figure 3D**). To further clarify the role of CVP mesenchyme in epithelial folding, CVP epithelium, and non-CVP mesenchyme were recombined with FGF10-soaked beads. Epithelial folding morphology was similar to that seen in CVP epithelium and mesenchyme recombination, indicating that epithelial folding might be dependent on epithelial cell shape changes (**Figure 3D'**). Blebbistatin binds to the ATPase intermediate with ADP and phosphate bound to the active site and slows down the subsequent phosphorylation of myosin light chain II (Kovács et al., 2004). PF-573228 works as an FAK phosphorylation inhibitor on Tyr^{397} (Slack-Davis et al., 2007). Blebbistatin and PF-573228 were introduced to reveal the roles of actomyosin contraction and FAK in CVP morphogenesis. In tongue from E12.5 cultured for 48 h, the control group with vehicle (DMSO) developed into a dome-shape similar to that seen at stage E13.5 in vivo (**Figure 3E**). In the Blebbistatin-treated group, the epithelium remained stratified while both invagination and evagination were disrupted (**Figure 3F**). In the PF-573228-treated group, even invagination was reduced; shallow trenches were observed. However, evagination was arrested and CVP placodes were observed in the dome-shaped region (**Figure 3G**). F-actin accumulated at the basal site of mediobasal cells (arrow) and the apical site of laterobasal cells (arrowhead) in control (**Figure 3H**). F-actin accumulation in basal sites of medial cells was reduced after Blebbistatin treatment (**Figure 3I**, arrow). In the PF-573228-treated group, F-actin accumulation remained at the apical site in the trench region (arrowhead), but the basal accumulation in mediobasal cells was completely diminished (**Figure 3J**). The differences in F-actin intensity between apical and basal sites of basal cells were evident in the control group, but diminished after treatment with Blebbistatin and PF-573228 (**Table 1**). β-catenin staining showed that cells in both dome-shaped and trench regions were elongated in the control group (**Figures 3K,K'**). In the Blebbistatin-treated group, basal constriction was reduced in the dome-shaped region. In the trench region, cells remained oval-shaped instead of elongated (**Figures 3L,L'**). The shapes of basal cells in trenches were similar to those of the control after PF-573228 treatment, but basal cells in the medial region remained apical-constricted or columnar (**Figures 3M,M'**). These results indicated that actomyosin contraction is necessary for apical/basal constriction of epithelial cells. Thus, subsequent epithelial folding was disrupted after Blebbistatin treatment.

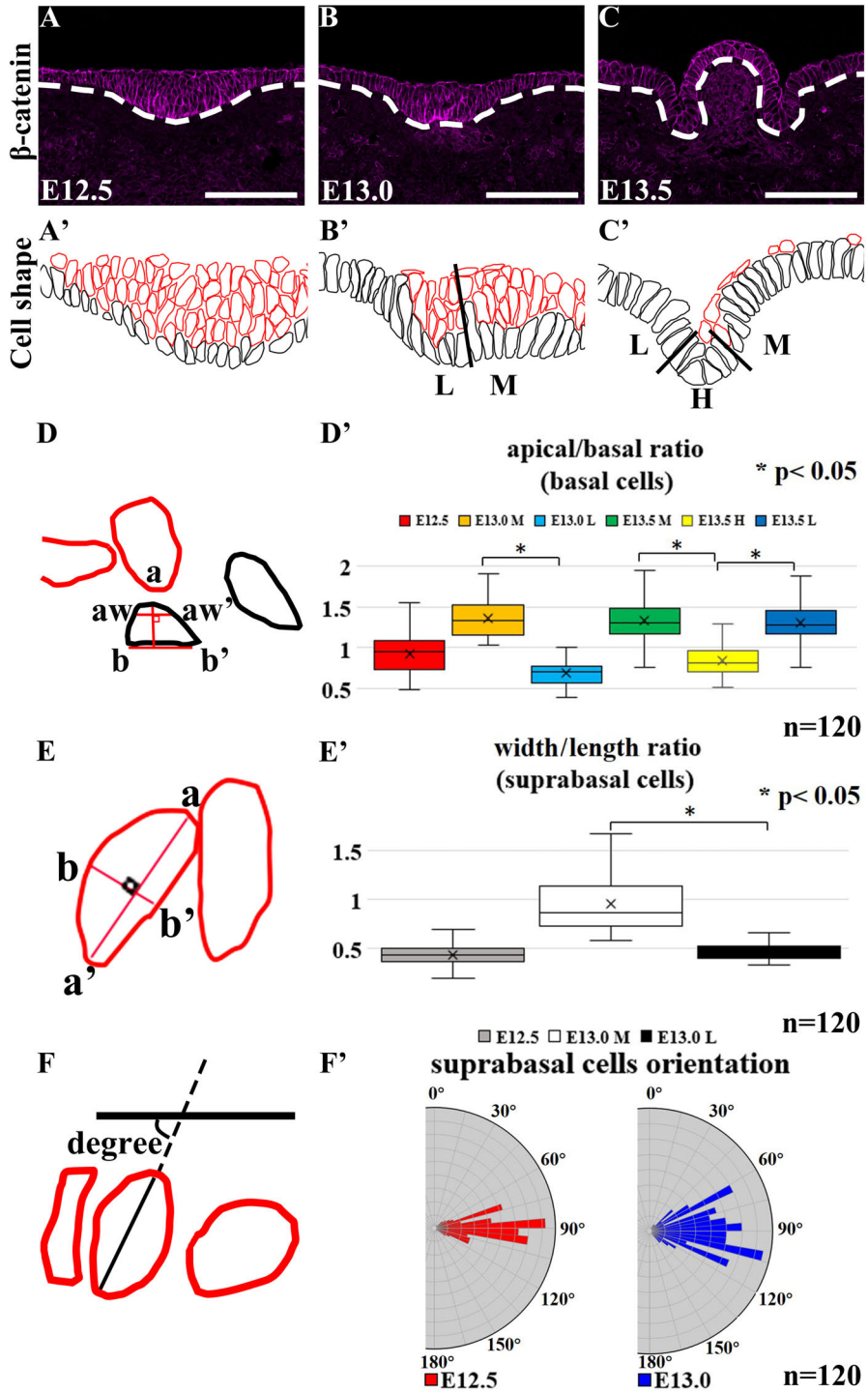

FIGURE 2 | (A'–C',D–F) Black-colored are basal cells while red-colored are suprabasal cells. **(A,A')** Basal and suprabasal cells in CVP are columnar at E12.5. In medial region "M," basal cells become constricted at the basal site, while suprabasal cells become oval-shaped at E13.0. **(B,B')** Epithelial cells in the lateral region "L" of the CVP remain columnar. **(C,C')** Cells in the medial and lateral regions become columnar with basal constrictions at E13.5. Cells in the hinge region "H" of CVP show apical constriction at E13.5. **(A,A',D')** At E12.5, all basal cells were columnar. **(B,B',D')** At E13.0, mediobasal cells become basal constricted, while laterobasal cells are relatively columnar. **(C,C',D')** At E13.5, basal constriction is found in basal cells in the medial and lateral regions, while hinge region cells show strong apical constriction. **(A,A',B,B',E')** At E12.5, all suprabasal cells are elongated, but suprabasal cells in the medial region become oval-shaped at E13.0; suprabasal cells in the lateral region remain elongated. **(F,F')** The angles between the suprabasal cell long axis to the plane of flanking epithelium are 80°–100° at E12.5 and 70°–110° at E13.0 in vertical-to-oblique range (45°–135°). Scale bar = 100 μm. White dotted lines mark the border between the developing tongue epithelium and mesenchyme. n = 120 cells (from three different littermates for each stage). $^*P < 0.05$.

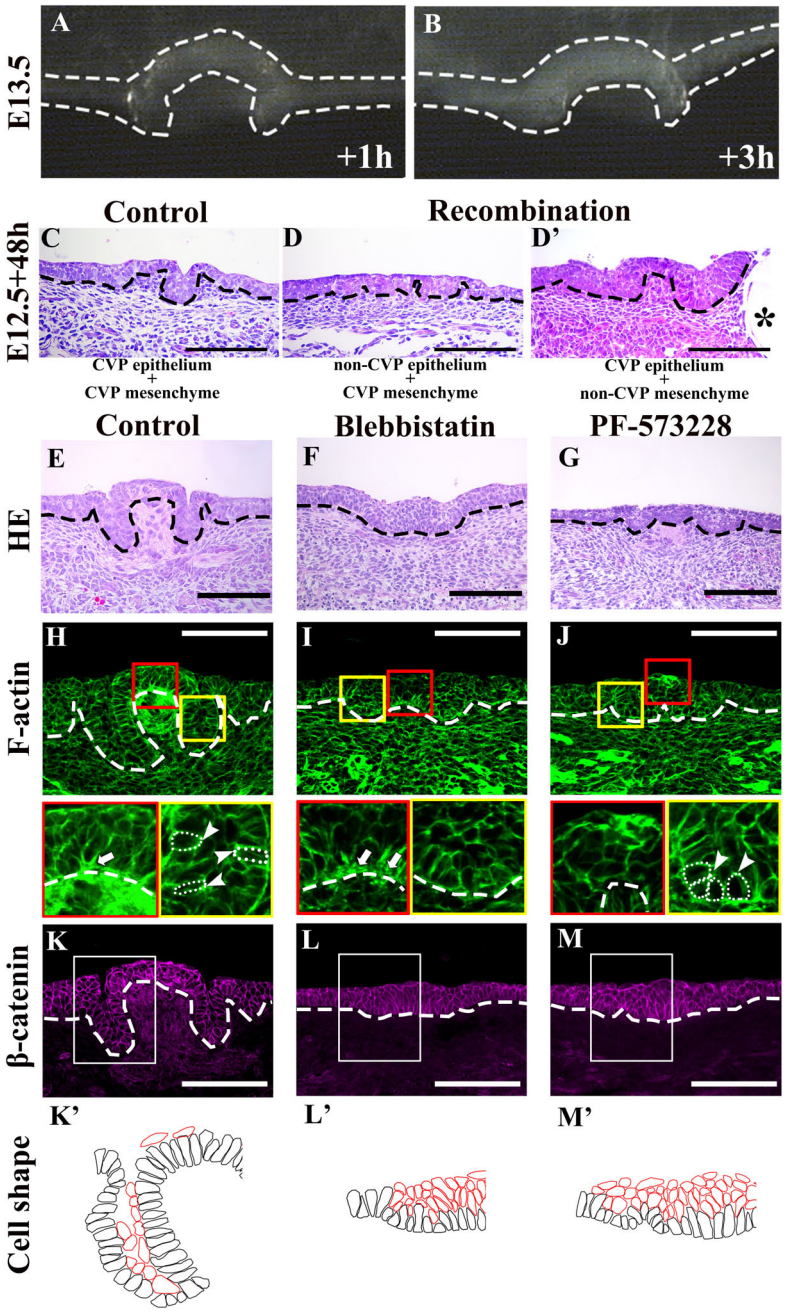

FIGURE 3 | (A,B) Original dome-shaped and trenches of the detached CVP epithelium retain their own structure after 1 and 3 h of in vitro culture at E13.5. **(C)** After recombination at E12.5 with the CVP epithelium and CVP mesenchyme, dome-shaped and trench structures are observed after 48 h culture. **(D)** Epithelial folding is not observed in the recombination of non-CVP epithelium and CVP mesenchyme group. **(D')** Similar epithelial folding is found in the recombination of CVP epithelium and non-CVP mesenchyme with FGF10-soaked bead. The asterisk indicates the FGF10-soaked beads for the maintenance of Lgr5-positive epithelial stem cells in CVP (Zhang et al., 2018). **(E)** E12.5 + 48 h cultured control group CVP morphology is similar to E13.5 in vivo. **(F)** The Blebbistatin-treated group shows disrupted invagination and evagination, and the CVP epithelium remains stratified. **(G)** The PF-573228-treated group shows shallow trenches and CVP placode in the dome-shape region are observed. **(H)** Basal F-actin accumulation at the dome-shaped region and apical accumulation of F-actin at the trench region are observed in control (arrow and arrowhead; compared to **Figure 1R**). **(I)** In the Blebbistatin-treated group, both basal accumulation (arrow) and apical F-actin accumulation are reduced. **(J)** In the PF-573228-treated group, apical accumulation of F-actin exists in the trench region (arrowhead), but basal F-actin accumulation is not observed. **(K,K')** Most basal cells are elongated in the control group, similar to those at E13.5 in vivo. **(L,L')** Mediobasal cells show disrupted basal constriction and cells in the trench region remain oval-shape in the Blebbistatin-treated group. **(M,M')** In the PF-573228-treated group, basal cell shape in the trench region are similar to the control. Basal cells in the dome-shape region are columnar with apical constriction instead of basally constriction. Scale bar = 100 μm. Arrowheads indicate the apical accumulation of F-actin. Arrows indicate basal accumulation of F-actin. Thick dotted lines mark the border between developing tongue epithelium and mesenchyme. Asterisks indicate FGF10 soaked beads. Thin white dotted circles indicate individual cell shape which goes through apical/basal constriction.

Moreover, basal constriction in the medial region was highly dependent on FAK.

Shh Regulates Trench and Stromal Core Formation

To investigate the roles of Shh and Ptch1 on epithelial folding and stromal core formation, we examined Shh and Ptch1 expression patterns in developing CVP. Shh was expressed in the CVP placode at E12.5 and the apical region of the dome-shaped epithelium at E13.0 and E13.5 (**Figures 4A–C**). Ptch1 was expressed in the lateral region of the placode in non-CVP epithelium and the underlying mesenchyme at E12.5 (**Figure 4F**). At E13.0, Ptch1 was faintly expressed in the CVP epithelium (**Figure 4G**). Strong Ptch1 expression was found within the trench region epithelium and the stromal core at E13.5 (**Figure 4H**). Similar to the localization of ETB expression, neuronal components were also marked by Ptch1 from E12.5 to E13.5 (**Figures 4F–H**). To understand Shh pathway function in CVP morphogenesis, Cyclopamine was introduced into an in vitro culture for 48 h. Similar to CVP at E13.5, Shh was expressed in the apical region of the dome-shaped epithelium in both control and Cyclopamine-treated groups (**Figures 4D,E**). Both in control and Cyclopamine-treated groups, Ptch1 expression was detected within the apical region of the CVP epithelium and detected more weakly in

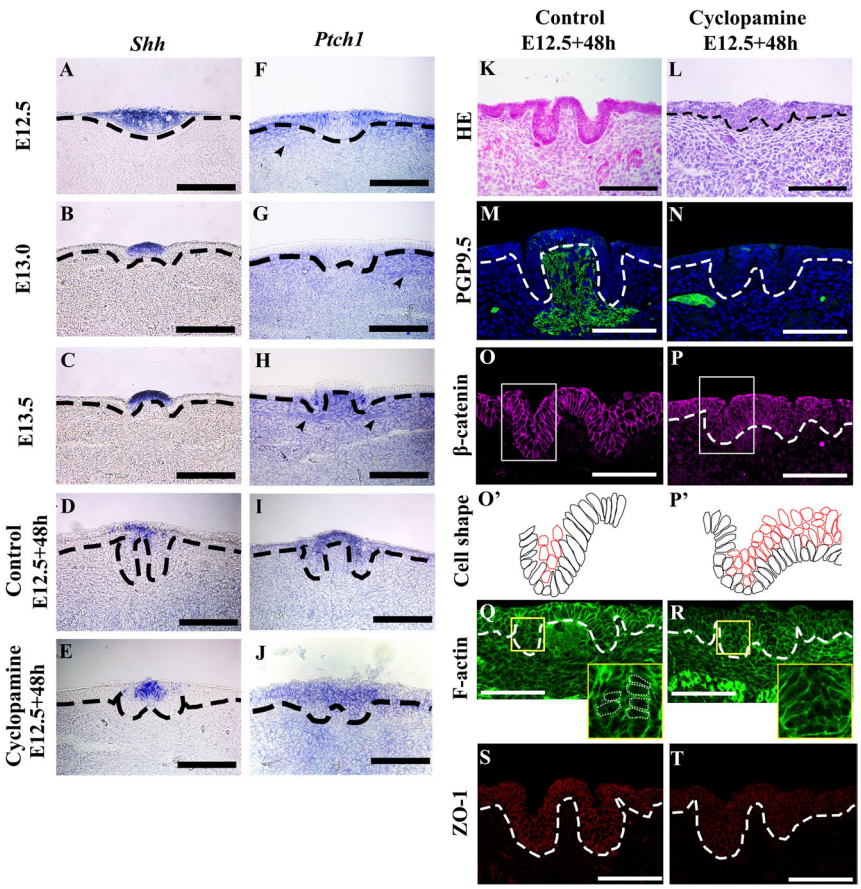

FIGURE 4 | (A) Sonic hedgehog (Shh) expression is observed in the whole CVP placode at E12.5. **(B,C)** Shh expression is detected in the apical region of the dome-shape epithelium at E13.0 and E13.5. **(D,E)** In the E12.5 + 48 h cultured control group and Cyclopamine-treated group, expression patterns of Shh are similar to E13.5 CVP in vivo. **(F)** At E12.5, Ptch1 is expressed in the lateral region of the CVP placode, non-CVP epithelium, and underlying mesenchyme. **(G)** The expression of Ptch1 is weakly detected in CVP at E13.0 compared to at E12.5. **(H)** Epithelial cells in the trench region and stromal core show a strong expression of Ptch1 at E13.5. **(F–H)** The arrowheads indicate Ptch1-positive neuronal components from E12.5 to E13.5. **(I,J)** In the E12.5 + 48 h cultured control and Cyclopamine-treated groups, Ptch1 is strongly expressed in the apical region of the dome-shape compared to the non-CVP epithelium. **(K,L)** Compared to the control group, the Cyclopamine-treated group has abnormal trenches and a stratified CVP epithelium with disrupted stromal core. **(M,N)** The stromal core in the Cyclopamine-treated group shows the absence of PGP9.5-positive neuronal components while strong localization is observed in control group. **(O,P,O',P')** β-catenin staining shows that mediobasal cells in the dome-shaped region show basal constriction in both control and Cyclopamine-treated group. Cells in the trench region are not elongated but remain oval-shape in the Cyclopamine-treated group. Suprabasal cells remain in the Cyclopamine-treated group. **(Q,R)** Phalloidin staining shows that the apical accumulation of F-actin in trench region is reduced after the Cyclopamine treatment while basal accumulation of F-actin in dome-shape region is similar as control. **(S,T)** Tight junction protein 1 (ZO-1) is strongly located in epithelial cells in the control group, but reduced in the Cyclopamine-treated group. Scale bar = 100 μm. Arrowheads indicate neuronal components. Thick dotted lines mark the border between developing tongue epithelium and mesenchyme. Thin dotted circles indicate individual cell shape which goes through apical/basal constriction.

the trench region (**Figures 4I,J**). Moreover, Cyclopamine-treated groups showed defects in trench formation within the stratified epithelium and exhibited disrupted stromal cores (**Figure 4L**) compared to the control (**Figure 4K**). PGP9.5-positive neuronal components were absent in the stromal core after Cyclopamine treatment, which compared starkly to strong PGP9.5 localization in the control group (**Figures 4M,N**). Mediobasal cells showed basal constriction in the dome-shaped region of both the control and Cyclopamine-treated groups. Cells in the trench region were oval-shaped, not columnar, while trench formation was disrupted after Cyclopamine treatment (**Figures 4O,P,O',P'**). According to the Blebbistatin-inhibited actomyosin contraction in the trench region, we hypothesized that trench formation is regulated via cytoskeletal alteration through Shh and its downstream signaling. F-actin accumulation was detected at the basal site of mediobasal cells in both control and Cyclopamine-treated groups (**Figures 4Q,R**). However, apical accumulation of F-actin in the trench region was reduced after Cyclopamine treatment (Yellow panels in **Figures 4Q,R**), which corresponds with disrupted cell shape changes in trench epithelial cells (**Figures 4P,P'**). The differences in F-actin intensity between apical and basal sites of trench regions were disrupted in the Cyclopamine-treated group (**Table 1**). ZO-1 strongly localized within the epithelial cells in the control group (**Figure 4S**). Conversely, ZO-1 was reduced in the Cyclopamine-treated group (**Figure 4T**). These results indicated that Shh signaling regulated trench formation through actomyosin-dependent apical constriction. Finally, stromal core formation was affected by Shh the modulating survival or differentiation of neurons in CVP ganglion.

This study demonstrated that the transition of CVP from placode to dome-shape required actomyosin-dependent epithelial folding invagination and evagination. Moreover, the occurrence of evagination in the dome-shaped formations required FAK for basal constriction Trench and stromal core formations were interrupted as a result of inhibited Shh pathway. In the process of invagination during the formation of trenches, a correlation was demonstrated between the presence of Shh and apical constriction of trench epithelial cells. Furthermore, the differentiation or survival of neurons in CVP ganglion might be impacted by epithelial Shh in the formation of stromal core.

DISCUSSION

This study demonstrated that CVP placode to dome-shape transition required actomyosin-dependent epithelial folding including invagination and evagination. Moreover, evagination in dome-shape formation required FAK for basal constriction. Trench and stromal core formation were interrupted after inhibition of Shh pathway by Cyclopamine. Furthermore, epithelial *Shh* also showed impact in stromal core formation of developing CVP.

Previously, multiple epithelial folding mechanisms have been reported, including actions on both monolayered and multilayered epithelium (Sai and Ladher, 2008; Sawyer et al., 2010; Martin and Goldstein, 2014; Li et al., 2016; Panousopoulou and Green, 2016; Pearl et al., 2017). Multilayered CVP placodes lack parallel-oriented suprabasal cells with specific E-cadherin localization. The morphology indicated that previously considered epithelial folding mechanisms were not responsible for the transitions in developing CVP (Panousopoulou and Green, 2016; Pearl et al., 2017). Therefore, we analyzed cell shape changes to investigate the underlying mechanisms of epithelial folding (Pearl et al., 2017). Cell shape analysis indicated that basal constriction occurred in the evagination region and apical constriction occurred in the invagination region (**Figure 2D'**). F-actin and pMLC staining in developing CVP (**Figures 1S–X**) corresponded with the co-accumulation of F-actin and pMLC observed in basal and apical constriction sites. This indicated that cell shape changes might depend on actomyosin. To further confirm whether cell shape changes are actomyosin-dependent, actomyosin was inhibited by Blebbistatin and epithelial folding was sufficiently disrupted (**Figures 3F,I,L,L'**).

Since both evagination and invagination were instigated by different types of cell shape changes (basal and apical constriction) and were actomyosin-dependent, we investigated whether the previously reported actomyosin-dependent mechanisms applied in the case of dome-shape formation. Outward folding activated by actomyosin-dependent basal constriction has been found FAK-dependent in the formation of the midbrain-hindbrain boundary (Gutzman et al., 2008, 2018). Recently, it has also been demonstrated that this mechanism is conserved in the bud-to-cap transition in tooth development, which suggested that evagination in developing CVP might be controlled by similar mechanisms (Yamada et al., 2019). We showed that inhibition of FAK was sufficient to arrest basal constriction and subsequent evagination and indicated that FAK-dependent basal constriction is involved in the formation

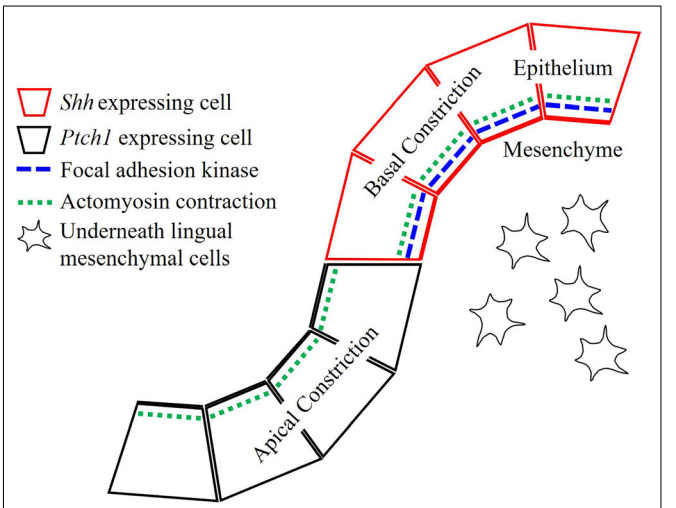

FIGURE 5 | Actomyosin contraction is essential for both dome-shape and trench formation. Actomyosin-dependent basal constriction in the dome-shape region requires focal adhesion kinase. Epithelial Shh regulates cytoskeletal alteration in the trench formation and differentiation or survival of neurons in stromal core of CVP.

of dome-shaped CVP (**Figures 3G,J,M,M'**). This result suggested that the factors involved in the midbrain-hindbrain boundary and tooth bud-to-cap transition might be active in developing CVP (Gutzman et al., 2008; Pearl et al., 2017; Yamada et al., 2019).

We further investigated factors with the potential to regulate apical constriction. Previously research indicates that Shh could play a large regulatory role in CVP morphogenesis. Shh was continuously expressed from the placode stage through the dome-shaped stage in developing CVP (Li et al., 2016). *Shh* was continuously expressed from the placode stage through the dome-shaped stage in developing CVP (Hall et al., 1999, 2003; Liu et al., 2004; Lee et al., 2006; Iwatsuki et al., 2007). Inhibition experiments of Shh have been conducted previously, but morphological defects within CVP has not been reported (Hall et al., 1999, 2003; Liu et al., 2004; Lee et al., 2006; Iwatsuki et al., 2007; Kim et al., 2009). To pinpoint the impact of Shh, we conducted the experiments herein. Based on our results, inhibition of Shh pathway disrupted both trench and stromal core formation in developing CVP (**Figures 4L,N,P**). The abnormal trenches (**Figure 4L**) after inhibition of Shh pathway were similar to the Cyclopamine-treated tooth placodes and hair placodes with cell intercalation defects (Ahtiainen et al., 2014; Li et al., 2016). Disrupted apical accumulation of F-actin in the Cyclopamine-treated CVP indicated that the morphological defect was caused by the interrupted cytoskeletal alteration (**Figure 4R**). Since Ptch1 was expressed at the lateral region of the placode at E13.0 and trench epithelium at E13.5 (**Figures 4G,H**), Shh expressed at the apical region of CVP epithelium possesses a potential regulatory role in cytoskeletal alteration in trench epithelial cells and subsequent trench formation. Support for this hypothesis comes concurrently from the impaired trench formation by the reduction of Shh expression in *Pax9*$^{-/-}$ mice (Kist et al., 2014). Moreover, ZO-1 has been reported to bind directly to F-actin and determine epithelial polarity (Itoh et al., 1997; Fanning et al., 1998; Odenwald et al., 2017). ZO-1 was reduced in CVP trench epithelial cells after Cyclopamine treatment during CVP morphogenesis.

A disrupted stromal core lacking neuronal components was observed after Cyclopamine treatment (**Figure 4N**). Epithelial Shh has been reported as a regulator of neuron formation through its modulation of cell migration in the development of the enteric nervous system (Baynash et al., 1994; Hosoda et al., 1994; Nagy et al., 2016). We observed that the neuronal components in the stromal core were marked by ETB, an enteric nervous system marker, as well as PGP9.5 (**Figures 1D–F**). In addition to this finding, Neurogenin2 was expressed in the underlying mesenchyme (**Supplementary Figures S1J–K**), which marks neuroblasts (Fode et al., 1998; Okubo and Takada, 2015; Fan et al., 2019). *Shh* supposed to involve in stromal core formation via the regulation of neuroblasts- and NCCs-derived cell.

Previous studies reported that cell migration regulated by Shh occurs through a Gli-Smoothened pathway-independent mechanism (Testaz et al., 2001; Nagy et al., 2016). Though neuroblasts and NCCs-derived cells in the stromal core were Ptch1 positive (**Figures 4F–H**), Gli1, Gli2, and Gli3 expression were not detected in the stromal core of CVP from E12.5 to E13.5 (data not shown). The absence of Gli1, Gli2 and Gli3 indicated that the Gli-Smoothened pathway might not be involved in the stromal core formation from E12.5 to E13.5.

In summary, the epithelial folding seen in the transition from placode to dome-shape was actomyosin-dependent (**Figure 5**). FAK-dependent basal constriction in the medial region led to evagination, which formed the dome-shape. Shh-guided apical constriction in the lateral region led trenches to form via invagination. Moreover, stromal core formation is also under regulation of Shh pathway.

DATA AVAILABILITY STATEMENT

The raw data supporting the conclusions of this article will be made available by the authors, without undue reservation.

ETHICS STATEMENT

The animal study was reviewed and approved by the Intramural Animal Use and Care Committee of the College of Dentistry, Yonsei University.

AUTHOR CONTRIBUTIONS

SZ, J-ML, and H-SJ designed and performed the experiments and analysis. AA performed the analysis of data. All authors contributed to manuscript revision, read and approved the submitted version.

FUNDING

This work was supported by the National Research Foundation of Korea (NRF) Grant funded by the Korea Government (MSIP) (NRF-2016R1A5A2008630) and (NRF-2019R1A2C3005294).

SUPPLEMENTARY MATERIAL

The Supplementary Material for this article can be found online at: https://www.frontiersin.org/articles/10.3389/fphys.2020.00936/full#supplementary-material

FIGURE S1 | (A) The neuronal marker PGP9.5 and enteric nervous system precursor marker endothelin receptor B (ETB) are co-localized in the underlying mesenchyme of CVP at E13.0. **(B)** NCAM is located in the stromal core of CVP at E13.5. **(C)** Fibronectin is weakly detected in ETB located underlying mesenchyme of CVP at E13.0. **(D)** At E12.5, Ki67-positive proliferating cells are absent in the CVP placode. **(E)** Ki67-positive cells retain in flanking non-CVP epithelium but reduce in the CVP mesenchyme at E13.0. At E13.5, proliferative cells appear in the trench region but not in the dome-shaped region epithelium. **(F)** Ki67-positive cells are located in the stromal core of CVP at E13.5. **(G–I)** There is no apoptotic cell in developing CVP epithelium and mesenchyme from E12.5 to E13.5 (Lee et al.). There is no apoptotic cell in developing CVP epithelium and mesenchyme from E12.5 to E13.5 (Lee et al.). **(J,K)** Neurogenin2 is expressed in neuronal components located in the underlying mesenchyme of developing CVP at E12.5 and E13.0. Scale bar = 100 μm. White/black dotted lines mark the border between developing tongue epithelium and mesenchyme. Arrowheads indicates neuronal components.

REFERENCES

Ahtiainen, L., Lefebvre, S., Lindfors, P. H., Renvoisé, E., Shirokova, V., Vartiainen, M. K., et al. (2014). Directional cell migration, but not proliferation, drives hair placode morphogenesis. *Dev. Cell* 28, 588–602. doi: 10.1016/j.devcel.2014.02.003

Barlow, L. A., and Klein, O. D. (2015). Developing and regenerating a sense of taste. *Curr. Top. Dev. Biol.* 111, 401–419. doi: 10.1016/bs.ctdb.2014.11.012

Baynash, A. G., Hosoda, K., Giaid, A., Richardson, J. A., Emoto, N., Hammer, R. E., et al. (1994). Interaction of endothelin-3 with endothelin-B receptor is essential for development of epidermal melanocytes and enteric neurons. *Cell* 79, 1277–1285. doi: 10.1016/0092-8674(94)90018-3

Beites, C. L., Hollenbeck, P. L., Kim, J., Lovell-Badge, R., Lander, A. D., and Calof, A. L. (2009). Follistatin modulates a BMP autoregulatory loop to control the size and patterning of sensory domains in the developing tongue. *Development* 136, 2187–2197. doi: 10.1242/dev.030544

Chandrashekar, J., Hoon, M. A., Ryba, N. J., and Zuker, C. S. (2006). The receptors and cells for mammalian taste. *Nature* 444, 288–294. doi: 10.1038/nature05401

Fan, D., Chettouh, Z., Consalez, G. G., and Brunet, J. F. (2019). Taste bud formation depends on taste nerves. *eLife* 8:e49226. doi: 10.7554/eLife.49226

Fanning, A. S., Jameson, B. J., Jesaitis, L. A., and Anderson, J. M. (1998). The tight junction protein ZO-1 establishes a link between the transmembrane protein occludin and the actin cytoskeleton. *J. Biol. Chem.* 273, 29745–29753. doi: 10.1074/jbc.273.45.29745

Fode, C., Gradwohl, G., Morin, X., Dierich, A., LeMeur, M., Goridis, C., et al. (1998). The bHLH protein NEUROGENIN 2 is a determination factor for epibranchial placode–derived sensory neurons. *Neuron* 20, 483–494. doi: 10.1016/s0896-6273(00)80989-7

Guth, L. (1957). The effects of glossopharyngeal nerve transection on the circumvallate papilla of the rat. *Anat. Rec.* 128, 715–731. doi: 10.1002/ar.1091280406

Gutzman, J. H., Graeden, E., Brachmann, I., Yamazoe, S., Chen, J. K., and Sive, H. (2018). Basal constriction during midbrain–hindbrain boundary morphogenesis is mediated by Wnt5b and focal adhesion kinase. *Biol. Open* 7:bio034520. doi: 10.1242/bio.034520

Gutzman, J. H., Graeden, E. G., Lowery, L. A., Holley, H. S., and Sive, H. (2008). Formation of the zebrafish midbrain–hindbrain boundary constriction requires laminin-dependent basal constriction. *Mech. Dev.* 125, 974–983. doi: 10.1016/j.mod.2008.07.004

Hall, J. M., Bell, M. L., and Finger, T. E. (2003). Disruption of sonic hedgehog signaling alters growth and patterning of lingual taste papillae. *Dev. Biol.* 255, 263–277. doi: 10.1016/s0012-1606(02)00048-9

Hall, J. M., Hooper, J. E., and Finger, T. E. (1999). Expression of sonic hedgehog, patched, and Gli1 in developing taste papillae of the mouse. *J. Comp. Neurol.* 406, 143–155. doi: 10.1002/(sici)1096-9861(19990405)406:2<143::aid-cne1>3.0.co;2-x

Harlow, D. E., and Barlow, L. A. (2007). Embryonic origin of gustatory cranial sensory neurons. *Dev. Biol.* 310, 317–328. doi: 10.1016/j.ydbio.2007.07.042

Hosoda, K., Hammer, R. E., Richardson, J. A., Baynash, A. G., Cheung, J. C., Giaid, A., et al. (1994). Targeted and natural (piebald-lethal) mutations of endothelin-B receptor gene produce megacolon associated with spotted coat color in mice. *Cell* 79, 1267–1276. doi: 10.1016/0092-8674(94)90017-5

Itoh, M., Nagafuchi, A., Moroi, S., and Tsukita, S. (1997). Involvement of ZO-1 in cadherin-based cell adhesion through its direct binding to α catenin and actin filaments. *J. Cell Biol.* 138, 181–192. doi: 10.1083/jcb.138.1.181

Iwatsuki, K., Liu, H.-X., Grónder, A., Singer, M. A., Lane, T. F., Grosschedl, R., et al. (2007). Wnt signaling interacts with Shh to regulate taste papilla development. *Proc. Natl. Acad. Sci. U.S.A.* 104, 2253–2258. doi: 10.1073/pnas.0607399104

Jaskoll, T., Leo, T., Witcher, D., Ormestad, M., Astorga, J., Bringas, P. Jr., et al. (2004). Sonic hedgehog signaling plays an essential role during embryonic salivary gland epithelial branching morphogenesis. *Dev. Dyn.* 229, 722–732. doi: 10.1002/dvdy.10472

Jitpukdeebodintra, S., Chai, Y., and Snead, M. L. (2003). Developmental patterning of the circumvallate papilla. *Int. J. Dev. Biol.* 46, 755–763.

Kim, J. Y., Lee, M. J., Cho, K. W., Lee, J. M., Kim, Y. J., Kim, J. Y., et al. (2009). Shh and ROCK1 modulate the dynamic epithelial morphogenesis in circumvallate papilla development. *Dev. Biol.* 325, 273–280. doi: 10.1016/j.ydbio.2008.10.034

Kist, R., Watson, M., Crosier, M., Robinson, M., Fuchs, J., Reichelt, J., et al. (2014). The formation of endoderm-derived taste sensory organs requires a Pax9-dependent expansion of embryonic taste bud progenitor cells. *PLoS Genet.* 10:e1004709. doi: 10.1371/journal.pgen.1004709

Kovács, M., Tóth, J., Hetényi, C., Málnási-Csizmadia, A., and Sellers, J. R. (2004). Mechanism of blebbistatin inhibition of myosin II. *J. Biol. Chem.* 279, 35557–35563. doi: 10.1074/jbc.m405319200

Lee, M.-J., Kim, J.-Y., Lee, S.-I., Sasaki, H., Lunny, D. P., Lane, E. B., et al. (2006). Association of Shh and Ptc with keratin localization in the initiation of the formation of circumvallate papilla and von Ebner's gland. *Cell Tissue Res.* 325:253. doi: 10.1007/s00441-006-0160-1

Li, J., Chatzeli, L., Panousopoulou, E., Tucker, A. S., and Green, J. B. (2016). Epithelial stratification and placode invagination are separable functions in early morphogenesis of the molar tooth. *Development* 143, 670–681. doi: 10.1242/dev.130187

Liu, F., Thirumangalathu, S., Gallant, N. M., Yang, S. H., Stoick-Cooper, C. L., Reddy, S. T., et al. (2007). Wnt-β-catenin signaling initiates taste papilla development. *Nat. Genet.* 39:106. doi: 10.1038/ng1932

Liu, H. X., Komatsu, Y., Mishina, Y., and Mistretta, C. M. (2012). Neural crest contribution to lingual mesenchyme, epithelium and developing taste papillae and taste buds. *Dev. Biol.* 368, 294–303. doi: 10.1016/j.ydbio.2012.05.028

Liu, H.-X., MacCallum, D. K., Edwards, C., Gaffield, W., and Mistretta, C. M. (2004). Sonic hedgehog exerts distinct, stage-specific effects on tongue and taste papilla development. *Dev. Biol.* 276, 280–300. doi: 10.1016/j.ydbio.2004.07.042

Martin, A. C., and Goldstein, B. (2014). Apical constriction: themes and variations on a cellular mechanism driving morphogenesis. *Development* 141, 1987–1998. doi: 10.1242/dev.102228

Meng, W., and Takeichi, M. (2009). Adherens junction: molecular architecture and regulation. *Cold Spring Harb. Perspect. Biol.* 1:a002899. doi: 10.1101/cshperspect.a002899

Mistretta, C. M., Liu, H.-X., Gaffield, W., and MacCallum, D. K. (2003). Cyclopamine and jervine in embryonic rat tongue cultures demonstrate a role for Shh signaling in taste papilla development and patterning: fungiform papillae double in number and form in novel locations in dorsal lingual epithelium. *Dev. Biol.* 254, 1–18. doi: 10.1016/s0012-1606(02)00014-3

Nagy, N., Barad, C., Graham, H. K., Hotta, R., Cheng, L. S., Fejszak, N., et al. (2016). Sonic hedgehog controls enteric nervous system development by patterning the extracellular matrix. *Development* 143, 264–275. doi: 10.1242/dev.128132

Nosrat, I. V., Margolskee, R. F., and Nosrat, C. A. (2012). Targeted taste cell-specific overexpression of brain-derived neurotrophic factor in adult taste buds elevates phosphorylated TrkB protein levels in taste cells, increases taste bud size, and promotes gustatory innervation. *J. Biol. Chem.* 287, 16791–16800. doi: 10.1074/jbc.m111.328476

Odenwald, M. A., Choi, W., Buckley, A., Shashikanth, N., Joseph, N. E., Wang, Y., et al. (2017). ZO-1 interactions with F-actin and occludin direct epithelial polarization and single lumen specification in 3D culture. *J. Cell Sci.* 130, 243–259. doi: 10.1242/jcs.188185

Okubo, T., and Takada, S. (2015). Pharyngeal arch deficiencies affect taste bud development in the circumvallate papilla with aberrant glossopharyngeal nerve formation. *Dev. Dyn.* 244, 874–887. doi: 10.1002/dvdy.24289

Panousopoulou, E., and Green, J. B. (2016). Invagination of ectodermal placodes is driven by cell intercalation-mediated contraction of the suprabasal tissue canopy. *PLoS Biol.* 14:e1002405. doi: 10.1371/journal.pbio.1002405

Pearl, E. J., Li, J., and Green, J. B. (2017). Cellular systems for epithelial invagination. *Philos. Trans. R. Soc. Lond. B Biol. Sci.* 372:20150526. doi: 10.1098/rstb.2015.0526

Petersen, C. I., Jheon, A. H., Mostowfi, P., Charles, C., Ching, S., Thirumangalathu, S., et al. (2011). FGF signaling regulates the number of posterior taste papillae by controlling progenitor field size. *PLoS Genet.* 7:e1002098. doi: 10.1371/journal.pgen.1002098

Sai, X., and Ladher, R. K. (2008). FGF signaling regulates cytoskeletal remodeling during epithelial morphogenesis. *Curr. Biol.* 18, 976–981. doi: 10.1016/j.cub.2008.05.049

Sawyer, J. M., Harrell, J. R., Shemer, G., Sullivan-Brown, J., Roh-Johnson, M., and Goldstein, B. (2010). Apical constriction: a cell shape change that can drive morphogenesis. *Dev. Biol.* 341, 5–19. doi: 10.1016/j.ydbio.2009.09.009

Schindelin, J., Arganda-Carreras, I., Frise, E., Kaynig, V., Longair, M., Pietzsch, T., et al. (2012). Fiji: an open-source platform for biological-image analysis. *Nat. Methods* 9:676. doi: 10.1038/nmeth.2019

Slack-Davis, J. K., Martin, K. H., Tilghman, R. W., Iwanicki, M., Ung, E. J., Autry, C., et al. (2007). Cellular characterization of a novel focal adhesion kinase inhibitor. *J. Biol. Chem.* 282, 14845–14852.

Suzuki, Y., Ikeda, K., and Kawakami, K. (2011). Development of gustatory papillae in the absence of Six1 and Six4. *J. Anat.* 219, 710–721. doi: 10.1111/j.1469-7580.2011.01435.x

Testaz, S., Jarov, A., Williams, K. P., Ling, L. E., Koteliansky, V. E., Fournier-Thibault, C., et al. (2001). Sonic hedgehog restricts adhesion and migration of neural crest cells independently of the Patched-Smoothened-Gli signaling pathway. *Proc. Natl. Acad. Sci. U.S.A.* 98, 12521–12526. doi: 10.1073/pnas.221108698

Yamada, S., Lav, R., Li, J., Tucker, A. S., and Green, J. B. A. (2019). Molar Bud-to-Cap Transition Is Proliferation Independent. *J. Dent. Res.* 98, 1253–1261. doi: 10.1177/0022034519869307

Zhang, S., Choi, H. S., Jung, H.-S., and Lee, J.-M. (2018). FGF10 is required for circumvallate papilla morphogenesis by maintaining Lgr5 activity. *Front. Physiol.* 9:1192. doi: 10.3389/fphys.2018.01192

Zhou, Y., Liu, H.-X., and Mistretta, C. M. (2006). Bone morphogenetic proteins and noggin: inhibiting and inducing fungiform taste papilla development. *Dev. Biol.* 297, 198–213. doi: 10.1016/j.ydbio.2006.05.022

Conflict of Interest: The authors declare that the research was conducted in the absence of any commercial or financial relationships that could be construed as a potential conflict of interest.

frontiers in Physiology

BRIEF RESEARCH REPORT
published: 31 July 2020
doi: 10.3389/fphys.2020.00920

Calcium Sets the Clock in Ameloblasts

*Raed Said[1,2], Liubov Lobanova[2], Silvana Papagerakis[3] and Petros Papagerakis[1,2]**

[1] Department of Anatomy, Physiology and Pharmacology, College of Medicine, University of Saskatchewan, Saskatoon, SK, Canada, [2] College of Dentistry, University of Saskatchewan, Saskatoon, SK, Canada, [3] Department of Surgery, College of Medicine, University of Saskatchewan, Saskatoon, SK, Canada

Background: Stromal interaction molecule 1 (*STIM1*) is one of the main components of the store operated Ca^{2+} entry (SOCE) signaling pathway. Individuals with mutated *STIM1* present severely hypomineralized enamel characterized as amelogenesis imperfecta (AI) but the downstream molecular mechanisms involved remain unclear. Circadian clock signaling plays a key role in regulating the enamel thickness and mineralization, but the effects of *STIM1*-mediated AI on circadian clock are unknown.

Objectives: The aim of this study is to examine the potential links between SOCE and the circadian clock during amelogenesis.

Methods: We have generated mice with ameloblast-specific deletion of *Stim1* (*Stim1*$^{fl/fl}$/Amelx-iCre$^{+/+}$, *Stim1* cKO) and analyzed circadian gene expression profile in *Stim1 cKO* compared to control (*Stim1*$^{fl/fl}$/Amelx-iCre$^{-/-}$) using ameloblast micro-dissection and RNA micro-array of 84 circadian genes. Expression level changes were validated by qRT-PCR and immunohistochemistry.

Results: *Stim1* deletion has resulted in significant upregulation of the core circadian activator gene Brain and Muscle Aryl Hydrocarbon Receptor Nuclear Translocation 1 (*Bmal1*) and downregulation of the circadian inhibitor Period 2 (*Per2*). Our analyses also revealed that SOCE disruption results in dysregulation of two additional circadian regulators; p38α mitogen-activated protein kinase (MAPK14) and transforming growth factor-beta1 (TGF-β1). Both MAPK14 and TGF-β1 pathways are known to play major roles in enamel secretion and their dysregulation has been previously implicated in the development of AI phenotype.

Conclusion: These data indicate that disruption of SOCE significantly affects the ameloblasts molecular circadian clock, suggesting that alteration of the circadian clock may be partly involved in the development of *STIM1*-mediated AI.

Keywords: ameloblast, enamel, STIM1, calcium, store operated Ca^{2+} channels, circadian clock, amelogenesis, amelogenesis imperfecta

OPEN ACCESS

Edited by:
Maisa Hanna-Maija Seppala, King's College London, United Kingdom

Reviewed by:
Marianna Bei, Harvard Medical School, United States
Javier Catón, Universidad Complutense de Madrid, Spain

****Correspondence:***
Petros Papagerakis
petros.papagerakis@usask.ca

Specialty section:
This article was submitted to Craniofacial Biology and Dental Research, a section of the journal Frontiers in Physiology

Received: *14 April 2020*
Accepted: *09 July 2020*
Published: *31 July 2020*

Citation:
Said R, Lobanova L, Papagerakis S and Papagerakis P (2020) Calcium Sets the Clock in Ameloblasts. Front. Physiol. 11:920. doi: 10.3389/fphys.2020.00920

INTRODUCTION

Calcium plays a pivotal role in enamel mineralization, yet the exact mechanisms involved in Ca^{2+} transport and the roles of Ca^{2+} signaling in regulating ameloblast functions during amelogenesis remain unclear (Berdal et al., 1995; Bailleul-Forestier et al., 1996; Nurbaeva et al., 2017). Initially, Ca^{2+} influx into ameloblasts was thought to occur passively via paracellular diffusion (Bawden, 1989). However, several subsequent reports have shown that Ca^{2+} transport occurs principally transcellularly and mainly through high capacity intracellular stores in endoplasmic reticulum (ER) (Hubbard, 2000; Lacruz et al., 2012b; Nurbaeva et al., 2015a,b, 2017). This mode of transport is termed Store-operated Ca^{2+} entry (SOCE) and is mainly mediated by the ER transmembrane proteins Stromal interaction molecule 1 and 2 (STIM1 and STIM2) and the highly selective plasma membrane (PM) calcium release activated channels (CRAC) (Prakriya and Lewis, 2015; Lacruz, 2017). STIM1 and STIM2 serve as intracellular (i) [Ca^{2+}] sensors, while CRAC protein 1, 2 and 3 (ORAI1, 2, and 3) are transmembrane proteins that form the pores of the CRAC channels and serve as a highly selective filter during Ca^{2+} entry from the circulation to the ameloblasts (Lacruz, 2017; Fahrner et al., 2018). Upon Ca^{2+} depletion from the ER, STIM1 binds to ORAI to facilitate Ca^{2+} entry and activate Ca^{2+} -dependent signal transduction. It must be noted that STIM2 is usually present at lower levels than STIM1, and that ORAI2 and ORAI3 activation results in a lower Ca^{2+} intake compared with ORAI1 (Hoth and Niemeyer, 2013). The importance of SOCE in regulating calcium transport during enamel mineralization is clearly reflected in the fact that patients with mutations in either STIM1 or ORAI1 have severe dental enamel defects, characterized as hypocalcified Amelogenesis Imperfecta (AI) (Eckstein and Lacruz, 2018; Feske, 2019). Moreover, several *in vivo* and *in vitro* studies have shown that SOCE components are robustly expressed by ameloblasts and served as key modulators of ameloblast's differentiation and function (Nurbaeva et al., 2015a,b; Zheng et al., 2015; Eckstein et al., 2017; Furukawa et al., 2017; Said et al., 2019).

It is well established that Ca^{2+} may act as a second messenger with a broad role in regulating gene expression *via* orchestrating several major signaling pathways (Tonelli et al., 2012). One of the main molecular systems essential for amelogenesis is the circadian clock (Athanassiou-Papaefthymiou et al., 2011). Circadian clock is an intracellular mechanism that regulates gene and protein expression levels oscillations over a 24-h period (Adeola et al., 2019). These circadian genetic rhythms are directly controlled by a complex system of body clocks, which entails a central or master clock located in the hypothalamic suprachiasmatic nucleus (SCN) and several subordinate peripheral clocks located in multiple tissues including in ameloblasts (Adeola et al., 2019). At the molecular level, circadian rhythms are maintained *via* the differential expression of several transcription factors called clock genes (Partch et al., 2014; Takahashi, 2017). The main mammalian clock genes include Circadian Locomotor Output Cycles Kaput (Clock), Brain and Muscle Aryl Hydrocarbon Receptor Nuclear Translocation (Arntl or Bmal1), Period 1 (Per1), Period 2 (Per2), Period 3 (Per3), and Cryptochromes (Cry1) and Cry2 (Partch et al., 2014). Clock genes interact with each other in an intricate manner and form perpetual autoregulatory transcription translation feedback loops (TTFLs) that control the rhythmic expression of several clock-controlled genes (CCG) to create 24-h repetitive expression patterns necessary for normal functions in several physiological processes (Takahashi, 2017). TTFLs are affected directly by extracellular events whose actions are transduced intracellularly by second messengers such as calcium and cAMP (Honma and Honma, 2003; Hastings et al., 2018). In mammalian tissues, several studies showed that calcium can act directly on TTFLs via the calcium/cAMP-dependent transcription factor (CREB) (O'Neill and Reddy, 2012; Herzog et al., 2017). In the mouse SCN, it was shown that blocking calcium influx and lowering i[Ca^{2+}] had abolished the rhythmic expression of *Per1* (Lundkvist et al., 2005). In addition, the amplitude of *Per1* and *Per2* expression was significantly decreased by voltage-gated Ca^{2+} channel antagonists (Lundkvist et al., 2005). On the other hand, it must be noted that i[Ca^{2+}] and cAMP levels oscillate in a circadian manner in the SCN neurons (O'Neill and Reddy, 2012). Thus, it has been suggested that cAMP and Ca^{2+} signaling may not only contribute in regulating timekeeping, but also that they are regulated by the cellular clock (i.e., Ca^{2+} and cAMP signaling is both output from, as well as input into the core clock pathway) (Palacios-Muñoz and Ewer, 2018).

The periodical nature of enamel secretion and the synchronized sequential pattern of ameloblast differentiation and mineralization strongly suggest that the process of amelogenesis is under circadian regulation (Papagerakis et al., 2014). Moreover, several publications from our group and others showed that this time-related control of ameloblasts activities may be orchestrated by the differential expression of circadian clock proteins during the distinct stages of enamel formation (Simmer et al., 2010; Athanassiou-Papaefthymiou et al., 2011; Lacruz et al., 2012a; Zheng et al., 2013, 2014). However, the molecular mechanisms involved in regulating the circadian clock during amelogenesis remain largely unexplored. In this study, we aimed to investigate the effects of calcium disruption on the ameloblasts molecular clock *in vivo* using a unique *Stim1*$^{fl/fl}$/Amelx-iCre$^{+/+}$ (*Stim1* cKO) model (Said et al., 2019). The significant impact of Ca^{2+} and circadian clock in ameloblasts makes amelogenesis an excellent model system for deciphering the mechanistic links that may exist between intracellular calcium dynamics and molecular circadian clock. Indeed, our analysis showed that *Stim1* ablation in ameloblasts results in significant dysregulation of the ameloblasts' circadian clock. More specifically, we found that loss of *Stim1* results in significant upregulation of the master circadian clock gene *Bmal1* and down regulation of its antagonist, *Per2*. We also found that targeting *Stim1* leads to significant changes of several other circadian regulators, including the p38α mitogen-activated protein kinase (MAPK14) and transforming growth factor-beta1 (TGF-β1). Both MAPK14 and TGF-β1 pathways are known to play a key role in tooth

morphogenesis and enamel secretion, and their dysregulation has been previously implicated in the development of AI phenotype. Our data strongly suggest that SOCE affects the molecular circadian clock in ameloblast, which could be one of the downstream pathways involved in the development of *Stim1*-mediated AI.

MATERIALS AND METHODS

Animals

Stim1 cKO generation and characterization were previously described (Said et al., 2019). Animals were housed in a pathogen-free facility in the Lab Animal Service Unit (LASU) at the University of Saskatchewan and all procedures for this study were authorized by the University Animal Care Committee (UACC) under an approved protocol (#20170014). All mice were housed under standard laboratory conditions in light-dark (LD) 12:12 conditions, normal room temperature, with *ad libitum* access to food and water. Genotypes were determined by tail biopsy and conventional polymerase chain reaction (PCR). The mice were humanely culled at postnatal day 14 (P14).

PCR Arrays

Enamel organ and secretory ameloblasts were micro-dissected from 2-week-old incisors in the left hemimandibles as previously described (Houari et al., 2018) and used for RNA extraction. RNA from *Stim1* cKO and control animals was extracted using the RNeasy MiniKit (Qiagen). cDNA was made using RT2 First Strand Kit (Qiagen). The cDNA was used on the real-time RT^2 Profiler PCR Array (QIAGEN, Cat. no. PAMM-153Z) in combination with RT^2 SYBR Green qPCR Mastermix (Cat. no. 330529). CT values were exported to an Excel file to create a table of CT values. This table was then uploaded onto the data analysis web portal at http://www.qiagen.com/genelobe. Samples were assigned to controls and test groups. CT values were normalized based on a manual selection of two reference genes (HKG), B-actin (*Actb*) and Glyceraldehyde 3-phosphate dehydrogenase (*Gapdh*). The CT cut-off was set to 35. The data analysis web portal calculated fold change/regulation using ΔΔCT method, in which ΔCT is calculated between gene of interest (GOI) and an average of reference genes (HKG), followed by delta-delta CT (ΔΔCT) calculations [ΔCT (Test Group)– ΔCT (Control Group)]. Fold Change was then calculated using $2^{\wedge}(-\Delta\Delta CT)$ formula. The data analysis web portal also plots scatter plot, volcano plot, clustergram, and heat map. DAVID software tool was used to analyze the examined genes (Huang et al., 2009).

qRT-PCR

RNA was extracted with the RNeasy MiniKit (Qiagen) from *Stim1* cKO and control mice ($Stim1^{fl/fl}$/Amelx-$iCre^{-/-}$) (n = 5 per genotype). After cDNA synthesis, the gene expression of *Bmal1*, *Clock*, *Per1 & 2*, *Cry 1&2*, *Mapk14*, *Tgf*-β*1*, Signal Transducer, and Activator of Transcription 5A (*Stat5a*), F-Box and Leucine Rich Repeat Protein (*Fbxl*) 3, RAR-related orphan receptor alpha (*Rora*), Nuclear Receptor Subfamily 1 Group D Member 1 (*NR1D1*), was assessed by quantitative PCR (qRT-PCR) with the $2^{\wedge}(-\Delta\Delta Ct)$ method. *Gapdh* was used as the reference gene. All primer sequences are included (**Supplementary Table 1**).

Statistics

All data are presented as mean ± standard deviation (SD). Student's *t*-test was used to compare the gene expression. For the PCR profiler assays, fold-change values greater than 2 or less than 0.5 were considered differentially expressed. The *P*-values were calculated based on a Student's *t*-test of the replicate $2^{\wedge}(-\Delta\Delta Ct)$ values for each gene in the control and *Stim1* cKO groups; P-value < 0.05 was considered significant.

Immunohistochemistry

The right hemimandibles were sectioned in a sagittal plane and immunostained to assess BMAL1, PER2, and *STIM1* protein cellular and tissue localization with a rabbit anti-PER2 antibody (1:200, LS-C2836; LifeSpan Biosciences), a rabbit anti-BMAL1 (1:250, NB100-2288; Novus Biologicals) and a rabbit anti-STIM1 (1:200, LSC34692; LSBio).

RESULTS

The Circadian Profile of Ameloblasts Changes Significantly After *Stim1* Deletion

We first assessed the effect of *Stim1* ablation on ameloblasts' circadian clock signaling by performing a validated circadian pathway PCR RNA microarray analysis. This analysis enabled us to evaluate the mRNA levels of 84 different genes in the circadian network. Gene Ontology and KEGG pathway analysis in the DAVID software (Huang et al., 2009) showed that the examined genes function in several essential signaling pathways including many calcium dependent ones (**Figure 1A**). Compared to control, we found that fourteen circadian genes were significantly differentially expressed ($P < 0.05$) in *Stim1* cKO ameloblasts with at least a twofold differential expression compared to control (**Figures 1B,C**, **Supplementary Table 2**, and **Supplementary Datasheet 1**). Specifically, we found that *Stim1* disruption had led to significant changes in the expression levels of several key clock genes that form the circadian loops, including *Bmal1*, *Per2*, *Fbxl3*, *Ror-a*, *and Ror-c*, which strongly indicates that SOCE may influence the ameloblast circadian clock system. The most significant changes were observed in *Bmal1 and Per2* expression, as *Bmal1* expression was greatly upregulated while *Per2* was greatly downregulated in *Stim1* cKO ameloblasts. We also found that *Stim1* knock out resulted in significant changes in the expression levels of circadian regulators that are also known to be involved in regulating amelogenesis throughout its different stages whether it is during early craniofacial development (Transcription Factor AP-2 Alpha, *Tfap2a*), tooth morphogenesis and early enamel secretion (*Mapk14*), or enamel maturation and mineralization (*Tgf-* β1). Additionally, the RNA profile revealed that SOCE disruption altered the expression of other circadian transcription factors including, the nuclear receptor subfamily 2 group F

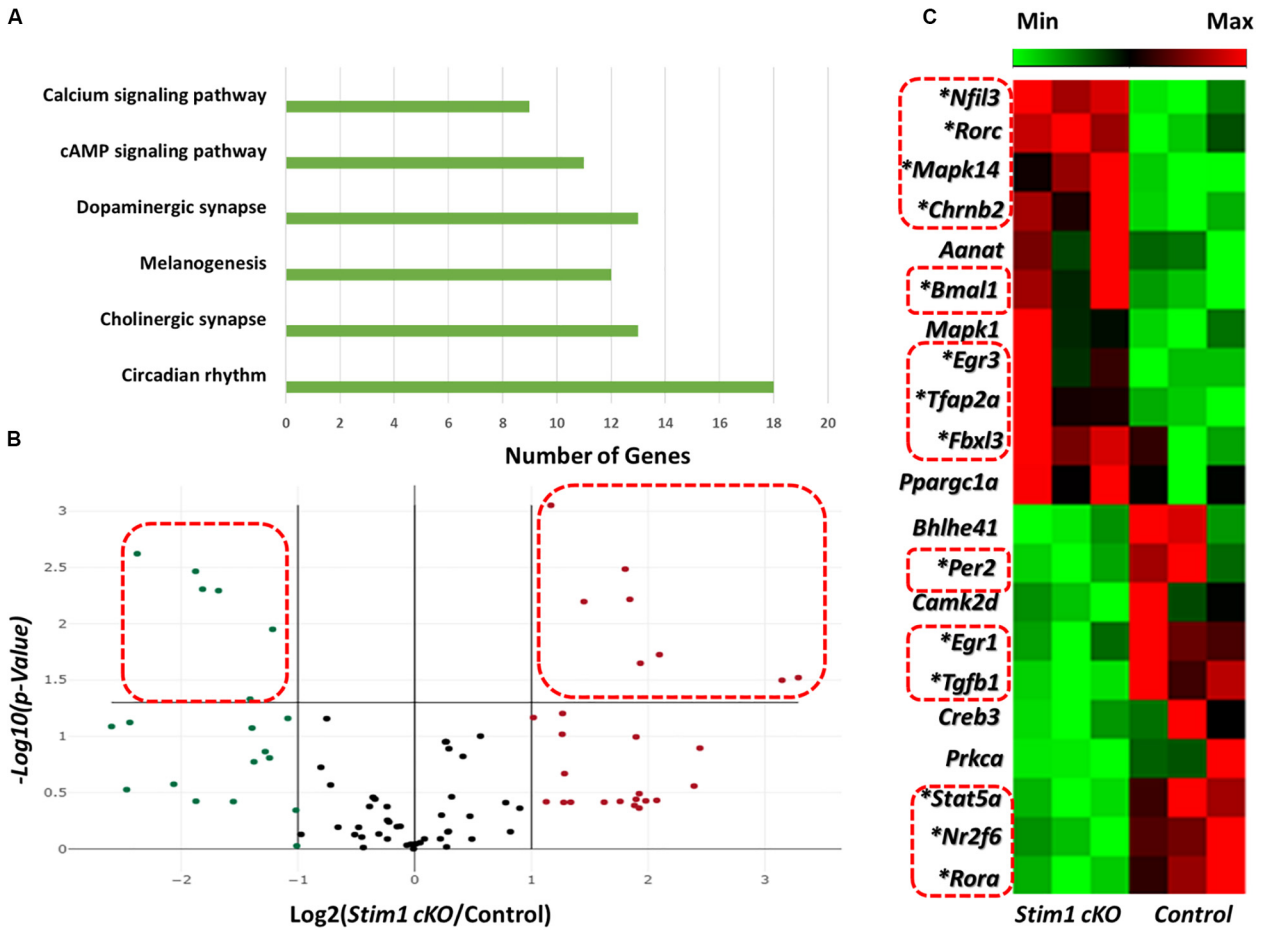

FIGURE 1 | Effects of *Stim1* KO on the gene expression profiles in ameloblasts. The expression change of 84 genes in ameloblasts from *Stim1* cKO and control mice was performed by real-time PCR based array analysis. **(A)** A bar diagram showing the functional clustering of the examined genes in the 6 most enriched signal transduction pathways according to the Gene Ontology and KEGG pathway analysis performed by the DAVID software **(B)** A volcano plot for the examined genes in total, black dots indicates genes with unchanged gene expression in Stim 1 cKO versus control; the genes with at least two fold change [(i.e., Log2 (*Stim1 cKO*/Control) > 1 or < −1] were represented as red dots for the upregulated genes and in green dots for the downregulated genes; the genes were deemed to be significantly differentially expressed if presented with at least two fold change and a *P*-value < 0.05 [i.e., $-\text{Log}_{10}$(*P*-Value) > 1.305, represented by the dots within the dashed red rectangles]. **(C)** A cluster heatmap showing the expression changes in some of the examined genes in *Stim1* cKO ameloblasts against the control group. A total of 14 genes were found to be significantly differentially expressed in *Stim1* cKO ameloblasts compared to the control group (*P* < 0.05, labeled by asterisks and within dashed red rectangles).

member 6 (NR2F6) and early growth response proteins 1 & 3 (EGR1, EGR3).

Validation of *Stim1* Deletion Effects on the Ameloblasts Circadian Clock

We further validated these substantial changes in the circadian clock gene expression by qRT-PCR analysis in which we first assessed the differences in the mRNA levels of 8 core clock genes (**Figures 2A,B**). Similar to profiler RNA micro-array analysis, the qRT-PCR analysis showed that *Bmal1* was greatly upregulated in *Stim1* cKO mice while both *Per2* and *Ror-a* were significantly downregulated. In addition to examining the core circadian genes we further assessed the changes of four additional circadian clock related genes of interest (**Figure 2C**). Similar to the profiler RNA micro-array pathway analysis, the qRT-PCR analysis showed that loss of *Stim1* function in ameloblasts significantly alters the expression pattern of *Tgf-β1* (downregulated) and *Mapk14* (upregulated) and *Fbxl3* (upregulated). It must be noted however, that contrary to the profiler assay analysis results, no significant changes were detected in the *Stat5a* gene.

Examining the Clock Proteins in *Stim1* cKO Ameloblasts

Immunohistochemical analysis using specific antibodies against BMAL1, PER2, and STIM1 was performed in order to further validate the RNA data reported above and to confirm *Stim1* deletion in ameloblasts. Our data clearly showed that in *Stim1* cKO ameloblasts BMAL1 proteins levels were much higher compared to control (**Figure 3A**). The PER2 expression levels were clearly downregulated overall, although PER2 expression

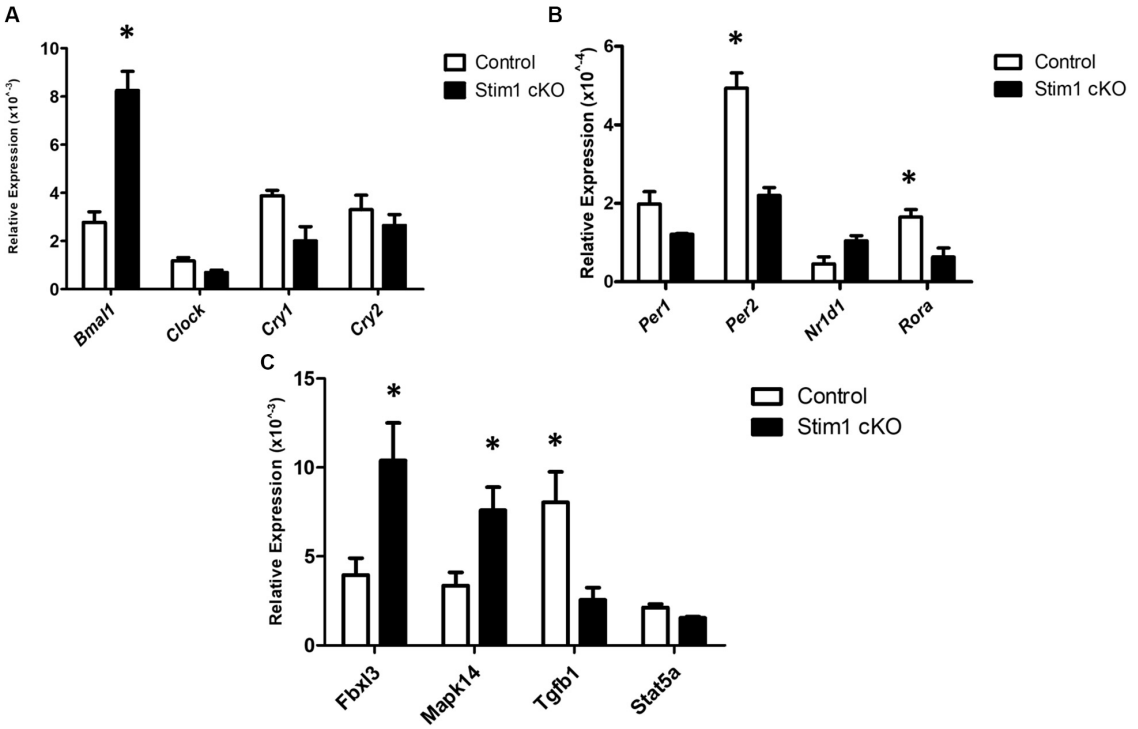

FIGURE 2 | The validation for selected candidate genes by qRT-PCR **(A–C)**. Data showed the relative mRNA fold changes of candidate genes in *Stim1* cKO groups versus the control groups ($n = 5$ per genotype). All experiments were performed in triplicates ($^*P < 0.05$).

pattern was quite peculiar as it appears to be expressed strongly in some ameloblasts nuclei and very weakly in others (**Figure 3B**, stars). This heterogeneity of PER2 localization in *Stim1* cKO ameloblasts may be attributed to posttranslational modifications including abnormal protein sequestering and degradation. Finally, our data here clearly showed that PER2 protein is mainly located in the nucleus (**Figure 3B** arrows) while BMAL1 is concentrated in the apical cytoplasm (**Figure 3A**, arrows). We previously reported the alternating pattern of these BMAL1 and PER2 localizations, where BMAL1 is cytoplasmic in the morning (8:00 AM) and translocates into the nucleus at night (8:00 PM) (Zheng et al., 2014). All mice for the current study were euthanized at 1:00 PM which may explain the differential localization between PER2 and BMAL1 in our data. Finally, only a very weak STIM1 signal can be detected in *Stim1* cKO ameloblasts, which confirms the validity of our experimental model (**Figure 3C**).

DISCUSSION

In this study we investigated the possible links between two important molecular regulators of amelogenesis, SOCE and the circadian clock. Using the *Stim1* cKO model, we demonstrated that enamel specific disruption of SOCE had profound effects on the ameloblasts' circadian gene profile as *Stim1*-deficient ameloblasts showed an altered expression of several key clock genes including *Bmal1*, *Per2*, *Ror-a*, and *Fbxl3*. Furthermore, our analyses demonstrated that SOCE disruption affected the expression levels of other circadian regulators that are known to be involved in regulating tooth morphogenesis and ameloblasts differentiation, such as p38 MAPK and TGF- β1. Collectively, these data strongly implicate SOCE as a vital modulator of the ameloblasts' circadian clock. To the best of our knowledge, this is the first study to show evidence of a direct interplay between circadian clock and calcium signaling in ameloblasts.

Our PCR RNA array, qRT-PCR, and IHC analyses of core clock genes revealed that *Stim1* knockdown had significantly affected the expression of the core circadian genes *Bmal1* (upregulated) and *Per2* (downregulated). Both genes serve as essential components of the autoregulatory mammalian clock gene network. BMAL1 protein heterodimerizes in the cytoplasm with the other circadian activator CLOCK (or NPAS2 in neurons) and then translocate into the nucleus where they enhance the expression of their repressors PER 1&2 and CRY 1&2 *via* binding to an E-box sequence in their promoter region (Ye et al., 2014). Subsequently, PER and CRY proteins multimerize with another core circadian regulator, casein kinase I δ in the cytoplasm and enter the nucleus to inhibit the activity of BMAL1/CLOCK complexes (St. John et al., 2014). Both genes are involved in the circadian regulation of several physiological (e.g., bone metabolism) and pathological processes (e.g., development of cancer) (Adeola et al., 2019; Janjiæ and Agis, 2019). In enamel, we have previously demonstrated that both *Bmal1* and *Per2* are robustly expressed by pre-ameloblast and differentiating ameloblasts in both human and mice embryonic

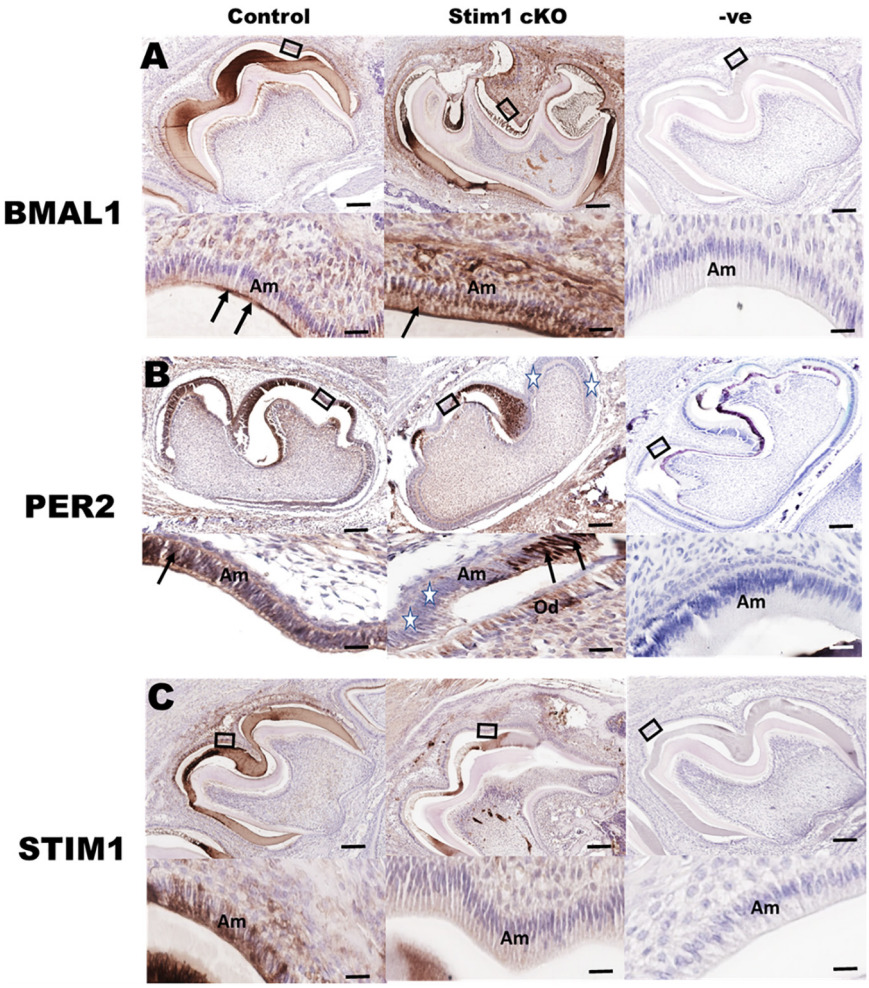

FIGURE 3 | Immunohistochemical validation of gene expression data. Representative images of mouse molar sections stained using specific antibodies against BMAL1 **(A)**, PER2 **(B)**, and STIM1 **(C)**. BMAL1 proteins levels are higher in the *Stim1* cKO group compared to control and is mainly localized in the apical cytoplasm (arrows) of the ameloblasts. PER2 expression is weaker in the *Stim1* cKO compared to control and is localized in the nucleus (arrows). Very weak STIM1 signal can be detected in *Stim1* cKO ameloblasts which confirms the validity of our experimental model. The rectangular areas are enlarged in the lower panel of each image. White stars label the cells expressing very low levels of *Per2*. Am, ameloblasts; Od, odontoblasts. Scale bars, 250 μm in upper panels, 50 μm in lower panels.

teeth in addition to mice postnatal teeth (Zheng et al., 2011, 2014). We and others have also shown that the expression levels and localization of their protein products in ameloblasts regularly alternates in a circadian manner (Lacruz et al., 2012a; Zheng et al., 2013). Preliminary *in vivo* and *vitro* analysis from our lab revealed that both genes may play a major role in regulating the expression of key enamel matrix proteins such as amelogenin, and proteases such as Kallikrein 4 (Klk4). Moreover, our preliminary *in vivo* analysis of *Per2* KO mice teeth showed abnormal enamel matrix formation associated with defective hypomineralized AI phenotype similar to AI observed in our *Stim1* cKO (unpublished data). All of the above-mentioned observations indicate that STIM1-caused dysregulation of the circadian clock network may lead to impaired enamel formation. Thus, the SOCE-mediated circadian disruption may be critical in the development of AI observed in patients with *STIM1/ORAI1* loss of function mutations.

Calcium signaling is particularly important in regulating the circadian expression of *Per1&2* genes as their promoters contain functional CREs (cAMP/Ca^{2+}-response elements) (Shim et al., 2007). *In vivo* and *in vitro* studies of the SCN showed that calcium influx induces the activity of Ca^{2+}/calmodulin-dependent protein kinase II (CaMKII), resulting in the activation of protein kinase A (PKA), and protein kinase C (PKC). These kinases then phosphorylate CREB in a circadian manner (Agostino et al., 2004; Hegazi et al., 2019). The phosphorylated CREB translocates into the nucleus where it recognizes the CRE of the Per genes promoters and induces their expression (Lee et al., 2010). Furthermore, it has been shown that SOCE is essential for activating CREB in multiple tissues including smooth muscles and immune cells (Avila-Medina et al., 2018; Martin-Romero et al., 2018). The fact that SOCE-deficient ameloblast showed significantly lowered levels of the *Per2* genes suggests that control of CREB activity may represent

one of the main mechanisms by which SOCE can directly affect the circadian TTFLs in ameloblasts, similar to the SCN and other cells (**Figure 4**). Indeed, other researchers have also postulated that SOCE may be one of the intracellular modulators that links calcium to the circadian clock both centrally and peripherally (Noguchi et al., 2012, 2017; O'Neill and Reddy, 2012). Additional studies are needed in ameloblasts to evaluate why SOCE disruption affected the *Per2* gene much more than *Per1*. Nevertheless, we postulate that *Per2* downregulation, which results in *Bmal1* upregulation, is one of the main molecular mechanisms involved in the *Stim1 cKO*-caused AI.

Another key finding from our work is the observation that *Stim1* cKO ameloblasts showed higher level of *Fbxl3* expression, a key component of the circadian clock. FBXL3 protein plays an important role in the negative feedback loop of the mammalian molecular circadian rhythm. In the nucleus, the FBXL3 protein targets the CRY2 proteins by ubiquitination to prevent them from inactivating BMAL1 (Huber et al., 2016). Moreover, FBXL3 plays a vital role in promoting Bmal1 transcription by inactivating the Bmal1 suppressor, REV-ERB alpha (Shi et al., 2013). Thus, upregulated levels of *Fbxl3* expression might also be one of the ways that lead to the over-expression of Bmal1 in *Stim1* cKO ameloblast.

The use of PCR arrays to investigate the genes that are differentially expressed in SOCE-deficient ameloblasts has brought forward genes that are also known to play a role in ameloblast differentiation and tooth morphogenesis, including *Tgf-β1* and *Mapk14*. TGF-β1 is a multi-functional growth factor with important roles in several biological processes, such as cellular proliferation and embryonic development, in addition to its role in the circadian clock signaling (Xu et al., 2018). Our RNA array and qRT-PCR analyses revealed that *Tgf-β1* is significantly downregulated in SOCE-deficient ameloblasts. Several previous studies had showed that SOCE plays an important role in regulating the TGF pathway activity in healthy and cancerous tissues (Chaudhari et al., 2017; Bhattacharya et al., 2018). In the context of amelogenesis, TGF-β1 is known to play a key role in the normal enamel development, and similar to STIM1 it appears to play an important role in regulating ameloblast function during enamel maturation through its interactions with Klk4 and matrix metalloprotease 20 (Kobayashi-Kinoshita et al., 2016). In fact, Cho et al. (2013) has shown that ameloblast specific deletion of its receptors has resulted in hypomature AI enamel phenotype with decreased mineral content concomitant

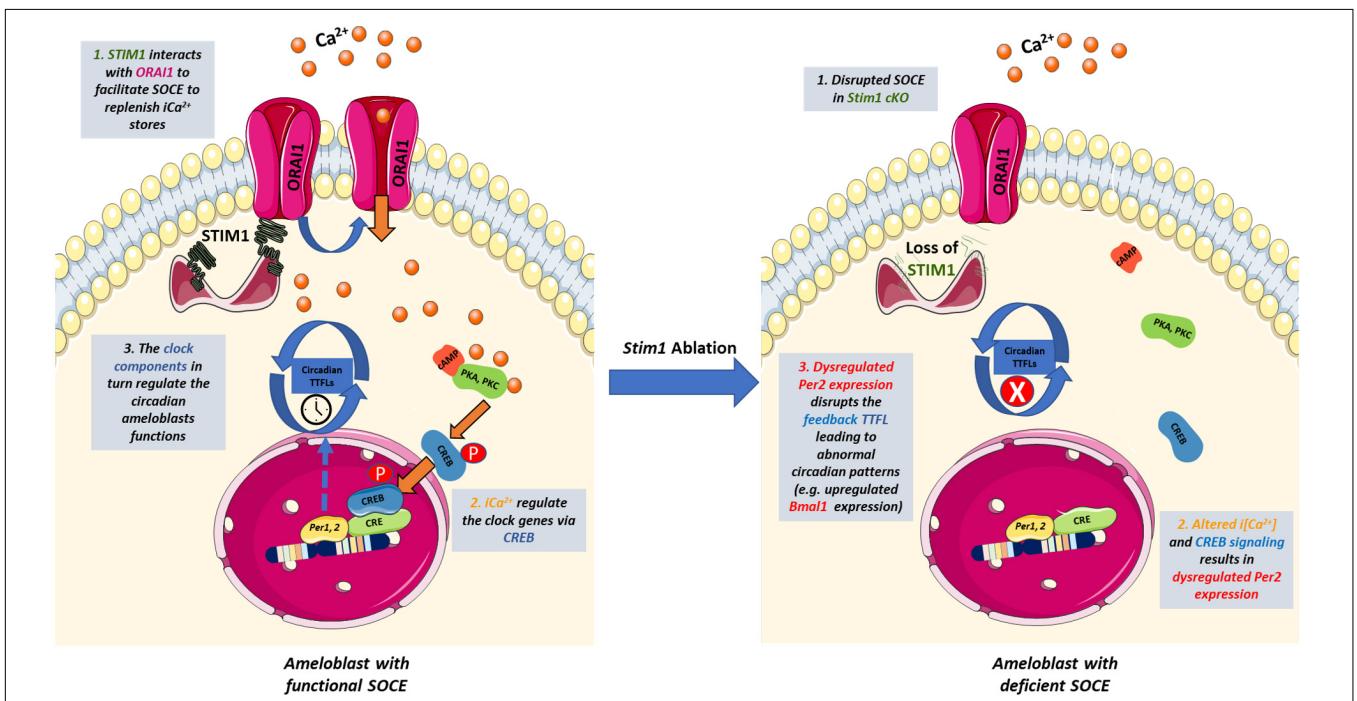

FIGURE 4 | The potential cross-talk between SOCE and the circadian clock in ameloblasts. Schematic representation summarizing how SOCE can potentially influence the ameloblasts' circadian clock based on our findings. Upon Ca^{2+} depletion in the ER, STIM1 binds to ORAI to facilitate Ca^{2+} entry and activate Ca^{2+}-dependent signal transduction. Calcium induces the activity of Ca^{2+}/calmodulin-dependent protein kinases which activate PKA and PKC that phosphorylate CREB in a circadian manner. The phosphorylated CREB translocate to the nucleus where it recognizes the cAMP Response Element in the promoter region of *Per1 & 2* and serves as a transcription factor. PER1 & 2 are core regulators of the mammalian circadian clock and participate in forming the autoregulatory TTFL. Disruption of SOCE in *Stim1 cKO* ameloblasts resulted in dysregulated expression of *Per2* that disrupts the TTFLs leading to abnormal circadian patterns including an upregulated *Bmal1* expression that maybe involved in the development of SOCE mediated AI. iCa^{2+}, intracellular calcium; TTFL, transcription translation feedback loop; PKA, protein Kinase A; PKC, protein Kinase C; CREB, cAMP response element-binding protein; STIM1, Stromal interaction molecule 1; P, Phosphate group. This figure was created with images adapted from Servier Medical Art by Servier. Original images are licensed under a Creative Commons Attribution 3.0 Unported License.

with increased attrition and thinner enamel crystallites. This phenotype is not unsimilar to the enamel phenotype observed in other *Stim1* cKO mice (Eckstein et al., 2017; Furukawa et al., 2017; Said et al., 2019), suggesting that TGF-β1 dysregulation might be partly involved in the development of *Stim1* deletion-caused AI. On the other hand, *Mapk14* expression was significantly upregulated in *Stim1* deficient ameloblasts. MAPK14 has been shown to regulate SOCE both indirectly (through TGF-β1 and NF-kappa) or directly by phosphorylating *Stim1* (Martin-Romero et al., 2018). In ameloblasts, MAPK14 has been shown to play a role in regulating early tooth morphogenesis and its ectodermal tissue deletion results in abnormally shaped dental cusps and a profoundly hypoplastic enamel layer (Greenblatt et al., 2015).

Additionally, the present RNA profile studies revealed that SOCE disruption altered the expression of other circadian transcription factors with currently unknown functions in amelogenesis. These include: transcription Factor AP-2 Alpha (TFA2PA), nuclear receptor subfamily 2 group F member 6 (NR2F6), and early growth response proteins 1&3 (EGR1, EGR3). TFA2PA is expressed in ectoderm and migrating neural crest cell lineages, and plays an important role in early craniofacial morphogenesis (Mitchell et al., 1991). Liu et al. (2015) showed that TFA2PA is highly expressed during the presecretory stage of amelogenesis, and suggested that it participates in the differentiation of pre-ameloblasts to secretory ameloblast. Similar to STIM1, both EGR1, and NR2F6 were shown to be highly expressed during the maturation stage, yet their exact roles in amelogenesis are poorly understood (Tsuchiya et al., 2009; Lacruz et al., 2011). Moreover, EGR1 is a major regulator of STIM1 and its expression is induced by TGF-β1 in the maturational ameloblasts which may explain why it is downregulated in *Stim1* cKO (Tsuchiya et al., 2009; Samakai et al., 2016). These preliminary findings and related hypotheses need further confirmation and will be part of future studies. Nevertheless, we can conclude that the apparent differential stage-specific regulation of circadian clock related genes (downregulation of *Tgf-β1*, *Egr1*, and *Nr2f6* which are expressed in maturation stage, and upregulation of *Mapk14* and *Tfa2pa* which are expressed in pre-secretory and secretory stage) in *Stim1* cKO teeth supports the idea of complex downstream effects of altered SOCE signaling in ameloblasts. Our data suggests that SOCE phenotypic and genotypic effects throughout amelogenesis may be produced by directly modulating downstream molecular signaling pathways and by contributing to the circadian clock system dysregulation observed in this model.

The essential role of calcium signaling in regulating the circadian clock has been demonstrated in several studies which have reported that changes in the intracellular $[Ca^{2+}]$ not only contribute directly to the timekeeping mechanism of the central and peripheral clocks, but also that the intracellular $[Ca^{2+}]$ is regulated by the circadian clock suggesting complex regulatory feedback mechanisms between the two systems (Honma and Honma, 2003; Lundkvist et al., 2005; Enoki et al., 2017; Martí Ruiz et al., 2018). Consistently, two studies by Noguchi et al. (2012, 2017) demonstrated how autonomous circadian oscillations in i$[Ca^{2+}]$ correlated with the autonomous rhythmicity of *PER2* expression in murine primary fibroblasts and the SCN neurons, and that both *PER2* and intracellular$[Ca^{2+}]$ rhythms were abolished in SCN cells deficient in Bmal1. In addition, Chen et al. (2016) reported that CLOCK-BMAL1 heterodimers regulate the expressions and functions of the cardiac L-type calcium channel which play an important role in the cardiac electrogenesis and arrhythmogenesis. Moreover, it was found that Ubiquitin-Specific Protease 2 (Usp2), which is a clock output effector, is involved in regulating bodily Ca^{2+} homeostasis *via* controlling the expression of the intestinal Ca^{2+} channels (Pouly et al., 2016). All the above suggests that an inverse regulation (i.e., the circadian clock regulates calcium homeostasis and rhythmicity) may also exist. However, most of the studies examining this correlation have been conducted in the SCN. The crosstalk between calcium signaling and circadian pathways in the peripheral clocks remain greatly understudied. Our report further contributes in understanding the chronobiology of circadian peripheral clocks and the links to intracellular $[Ca^{2+}]$ signaling. More studies are needed to examine the role of circadian clock in directing Ca^{2+} rhythmicity and signaling in ameloblasts.

In conclusion, in this work we analyzed the circadian gene profiles in the ameloblasts collected from a SOCE-deficient teeth. We uncovered how SOCE disruption resulted in the dysregulation of multiple circadian rhythm genes which may have a direct impact on certain aspects of *STIM1* AI. Our study provides further evidence that ameloblast activity is tightly controlled by several molecular and circadian pathways, and highlights the need to investigate their interactions more thoroughly to achieve a better understanding of amelogenesis. Future studies including additional functional assays are needed to further examine the potential molecular crosslinks between calcium dynamics and the circadian pathways in ameloblasts.

DATA AVAILABILITY STATEMENT

All datasets presented in this study are included in the article/**Supplementary Material**.

ETHICS STATEMENT

The animal study was reviewed and approved by University Animal Care Committee (UACC) of the University of Saskatchewan, Saskatoon, SK, Canada.

AUTHOR CONTRIBUTIONS

RS, SP, and PP conceived the study. RS performed the experimental procedures, data analysis, experimental designing, and manuscript writing. LL helped with the experimental procedures and data analysis, and provided scientific support. SP and PP provided scientific support

and contributed to the experimental design, data analysis, and manuscript writing. All authors read and approved the submitted version of the manuscript.

FUNDING

Funding is provided by NSERC Development Grant (RGPIN-2020-06025), University of Saskatchewan, College of Dentistry start-up funds and SHRF Establishment Grant to PP. University of Saskatchewan College of Medicine start-up funds to SP.

SUPPLEMENTARY MATERIAL

The Supplementary Material for this article can be found online at: https://www.frontiersin.org/articles/10.3389/fphys.2020.00920/full#supplementary-material

REFERENCES

Adeola, H. A., Papagerakis, S., and Papagerakis, P. (2019). Systems biology approaches and precision oral health: a circadian clock perspective. *Front. Physiol.* 10:399. doi: 10.3389/fphys.2019.00399

Agostino, P. V., Ferreyra, G. A., Murad, A. D., Watanabe, Y., and Golombek, D. A. (2004). Diurnal, circadian and photic regulation of calcium/calmodulin-dependent kinase II and neuronal nitric oxide synthase in the hamster suprachiasmatic nuclei. *Neurochem. Int.* 44, 617–625. doi: 10.1016/j.neuint.2003.09.005

Athanassiou-Papaefthymiou, M., Kim, D., Harbron, L., Papagerakis, S., Schnell, S., Harada, H., et al. (2011). Molecular and circadian controls of ameloblasts: regulation of ameloblast differentiation. *Eur. J. Oral Sci.* 119, 35–40. doi: 10.1111/j.1600-0722.2011.00918.x

Avila-Medina, J., Mayoral-Gonzalez, I., Dominguez-Rodriguez, A., Gallardo-Castillo, I., Ribas, J., Ordoñez, A., et al. (2018). The complex role of store operated calcium entry pathways and related proteins in the function of cardiac, skeletal and vascular smooth muscle cells. *Front. Physiol.* 9:257. doi: 10.3389/fphys.2018.00257

Bailleul-Forestier, I., Davideau, J. L., Papagerakis, P., Noble, I., Nessmann, C., Peuchmaur, M., et al. (1996). Immunolocalization of vitamin D receptor and calbindin-D28k in human tooth germ. *Pediatr. Res.* 39, 636–642. doi: 10.1203/00006450-199604000-00013

Bawden, J. W. (1989). Calcium transport during mineralization. *Anat. Rec.* 224, 226–233. doi: 10.1002/ar.1092240212

Berdal, A., Papagerakis, P., Hotton, D., Bailleul-Forestier, I., and Davideau, J. L. (1995). Ameloblasts and odontoblasts, target-cells for 1,25-dihydroxyvitamin D3: a review. *Int. J. Dev. Biol.* 39, 257–262.

Bhattacharya, A., Kumar, J., Hermanson, K., Sun, Y., Qureshi, H., Perley, D., et al. (2018). The calcium channel proteins ORAI3 and STIM1 mediate TGF-β induced Snai1 expression. *Oncotarget* 9, 29468–29483. doi: 10.18632/oncotarget.25672

Chaudhari, S., Li, W., Wang, Y., Jiang, H., Ma, Y., Davis, M. E., et al. (2017). Store-operated calcium entry suppressed the TGF-β1/Smad3 signaling pathway in glomerular mesangial cells. *Am. J. Physiol. Renal Physiol.* 313, F729–F739. doi: 10.1152/ajprenal.00483.2016

Chen, Y., Zhu, D., Yuan, J., Han, Z., Wang, Y., Qian, Z., et al. (2016). CLOCK-BMAL1 regulate the cardiac L-type calcium channel subunit CACNA1C through PI3K-Akt signaling pathway. *Can. J. Physiol. Pharmacol.* 94, 1023–1032. doi: 10.1139/cjpp-2015-0398

Cho, A., Haruyama, N., Hall, B., Danton, M. J. S., Zhang, L., Arany, P., et al. (2013). TGF-ß regulates enamel mineralization and maturation through KLK4 expression. *PLoS One* 8:e82267. doi: 10.1371/journal.pone.0082267

Eckstein, M., and Lacruz, R. S. (2018). CRAC channels in dental enamel cells. *Cell Calcium* 75, 14–20. doi: 10.1016/j.ceca.2018.07.012

Eckstein, M., Vaeth, M., Fornai, C., Vinu, M., Bromage, T. G., Nurbaeva, M. K., et al. (2017). Store-operated Ca2+ entry controls ameloblast cell function and enamel development. *JCI Insight* 2:e91166. doi: 10.1172/jci.insight.91166

Enoki, R., Ono, D., Kuroda, S., Honma, S., and Honma, K. (2017). Dual origins of the intracellular circadian calcium rhythm in the suprachiasmatic nucleus. *Sci. Rep.* 7, 1–8. doi: 10.1038/srep41733

Fahrner, M., Schindl, R., and Romanin, C. (2018). "Studies of structure-function and subunit composition of Orai/STIM channel," in *Calcium Entry Channels in Non-Excitable Cells*, eds J. A. Kozak and J. W. Putney (Boca Raton, FL: CRC Press).

Feske, S. (2019). CRAC channels and disease – from human CRAC channelopathies and animal models to novel drugs. *Cell Calcium* 80, 112–116. doi: 10.1016/j.ceca.2019.03.004

Furukawa, Y., Haruyama, N., Nikaido, M., Nakanishi, M., Ryu, N., Oh-Hora, M., et al. (2017). Stim1 regulates enamel mineralization and ameloblast modulation. *J. Dent. Res.* 96, 1422–1429. doi: 10.1177/0022034517719872

Greenblatt, M. B., Kim, J.-M., Oh, H., Park, K. H., Choo, M.-K., Sano, Y., et al. (2015). p38α MAPK Is required for tooth morphogenesis and enamel secretion. *J. Biol. Chem.* 290, 284–295. doi: 10.1074/jbc.M114.599274

Hastings, M. H., Maywood, E. S., and Brancaccio, M. (2018). Generation of circadian rhythms in the suprachiasmatic nucleus. *Nat. Rev. Neurosci.* 19, 453–469. doi: 10.1038/s41583-018-0026-z

Hegazi, S., Lowden, C., Rios Garcia, J., Cheng, A. H., Obrietan, K., Levine, J. D., et al. (2019). A symphony of signals: intercellular and intracellular signaling mechanisms underlying circadian timekeeping in mice and flies. *IJMS* 20:2363. doi: 10.3390/ijms20092363

Herzog, E. D., Hermanstyne, T., Smyllie, N. J., and Hastings, M. H. (2017). Regulating the suprachiasmatic nucleus (SCN) circadian clockwork: interplay between cell-autonomous and circuit-level mechanisms. *Cold Spring Harb. Perspect. Biol.* 9:a027706. doi: 10.1101/cshperspect.a027706

Honma, S., and Honma, K. (2003). The biological clock: Ca2+ links the pendulum to the hands. *Trends Neurosci.* 26, 650–653. doi: 10.1016/j.tins.2003.09.012

Hoth, M., and Niemeyer, B. A. (2013). The neglected CRAC proteins: Orai2, Orai3, and STIM2. *Curr. Top. Membr.* 71, 237–271. doi: 10.1016/B978-0-12-407870-3.00010-X

Houari, S., Babajko, S., Loiodice, S., Berdal, A., and Jedeon, K. (2018). Micro-dissection of enamel organ from mandibular incisor of rats exposed to environmental toxicants. *J. Vis. Exp.* 133:57081. doi: 10.3791/57081

Huang, D. W., Sherman, B. T., and Lempicki, R. A. (2009). Systematic and integrative analysis of large gene lists using DAVID bioinformatics resources. *Nat. Protoc.* 4, 44–57. doi: 10.1038/nprot.2008.211

Hubbard, M. J. (2000). Calcium transport across the dental enamel epithelium. *Crit. Rev. Oral Biol. Med.* 11, 437–466. doi: 10.1177/10454411000110040401

Huber, A.-L., Papp, S. J., Chan, A. B., Henriksson, E., Jordan, S. D., Kriebs, A., et al. (2016). CRY2 and FBXL3 cooperatively degrade c-MYC. *Mol. Cell* 64, 774–789. doi: 10.1016/j.molcel.2016.10.012

Janjiæ, K., and Agis, H. (2019). Chronodentistry: the role and potential of molecular clocks in oral medicine. *BMC Oral Health* 19:32. doi: 10.1186/s12903-019-0720-x

Kobayashi-Kinoshita, S., Yamakoshi, Y., Onuma, K., Yamamoto, R., and Asada, Y. (2016). TGF-β1 autocrine signalling and enamel matrix components. *Sci. Rep.* 6, 1–14. doi: 10.1038/srep33644

Lacruz, R. S. (2017). Enamel: molecular identity of its transepithelial ion transport system. *Cell Calcium* 65, 1–7. doi: 10.1016/j.ceca.2017.03.006

Lacruz, R. S., Hacia, J. G., Bromage, T. G., Boyde, A., Lei, Y., Xu, Y., et al. (2012a). The circadian clock modulates enamel development. *J. Biol. Rhythms* 27, 237–245. doi: 10.1177/0748730412442830

Lacruz, R. S., Smith, C. E., Bringas, P., Chen, Y.-B., Smith, S. M., Snead, M. L., et al. (2012b). Identification of novel candidate genes involved in mineralization of dental enamel by genome-wide transcript profiling. *J. Cell. Physiol.* 227, 2264–2275. doi: 10.1002/jcp.22965

Lacruz, R. S., Smith, C. E., Chen, Y.-B., Hubbard, M. J., Hacia, J. G., and Paine, M. L. (2011). Gene expression analysis of early and late maturation stage rat enamel organ. *Eur. J. Oral Sci.* 119, 149–157. doi: 10.1111/j.1600-0722.2011.00881.x

Lee, Y., Lee, J., Kwon, I., Nakajima, Y., Ohmiya, Y., Son, G. H., et al. (2010). Coactivation of the CLOCK–BMAL1 complex by CBP mediates resetting of the circadian clock. *J. Cell Sci.* 123, 3547–3557. doi: 10.1242/jcs.070300

Liu, C., Niu, Y., Zhou, X., Xu, X., Yang, Y., Zhang, Y., et al. (2015). Cell cycle control, DNA damage repair, and apoptosis-related pathways control pre-ameloblasts differentiation during tooth development. *BMC Genomics* 16:592. doi: 10.1186/s12864-015-1783-y

Lundkvist, G. B., Kwak, Y., Davis, E. K., Tei, H., and Block, G. D. (2005). A calcium flux is required for circadian rhythm generation in mammalian pacemaker neurons. *J. Neurosci.* 25, 7682–7686. doi: 10.1523/JNEUROSCI.2211-05.2005

Martí Ruiz, M. C., Hubbard, K. E., Gardner, M. J., Jung, H. J., Aubry, S., Hotta, C. T., et al. (2018). Circadian oscillations of cytosolic free calcium regulate the Arabidopsis circadian clock. *Nat. Plants* 4, 690–698. doi: 10.1038/s41477-018-0224-8

Martin-Romero, F. J., Pascual-Caro, C., Lopez-Guerrero, A., Espinosa-Bermejo, N., and Pozo-Guisado, E. (2018). "Regulation of calcium signaling by STIM1 and ORAI1," in *Calcium and Signal Transduction*, ed. J. N. Buchholz (London: Intech Open), doi: 10.5772/intechopen.78587

Mitchell, P. J., Timmons, P. M., Hébert, J. M., Rigby, P. W., and Tjian, R. (1991). Transcription factor AP-2 is expressed in neural crest cell lineages during mouse embryogenesis. *Genes Dev.* 5, 105–119. doi: 10.1101/gad.5.1.105

Noguchi, T., Leise, T. L., Kingsbury, N. J., Diemer, T., Wang, L. L., Henson, M. A., et al. (2017). Calcium circadian rhythmicity in the suprachiasmatic nucleus: cell autonomy and network modulation. *eNeuro* 4:ENEURO.0160-17.2017. doi: 10.1523/ENEURO.0160-17.2017

Noguchi, T., Wang, C. W., Pan, H., and Welsh, D. K. (2012). Fibroblast circadian rhythms of PER2 expression depend on membrane potential and intracellular calcium. *Chronobiol. Int.* 29, 653–664. doi: 10.3109/07420528.2012.679330

Nurbaeva, M. K., Eckstein, M., Concepcion, A. R., Smith, C. E., Srikanth, S., Paine, M. L., et al. (2015a). Dental enamel cells express functional SOCE channels. *Sci. Rep.* 5:15803. doi: 10.1038/srep15803

Nurbaeva, M. K., Eckstein, M., Feske, S., and Lacruz, R. S. (2017). Ca 2+ transport and signalling in enamel cells: calcium in enamel cells. *J. Physiol.* 595, 3015–3039. doi: 10.1113/JP272775

Nurbaeva, M. K., Eckstein, M., Snead, M. L., Feske, S., and Lacruz, R. S. (2015b). Store-operated Ca 2+ entry modulates the expression of enamel genes. *J. Dent. Res.* 94, 1471–1477. doi: 10.1177/0022034515598144

O'Neill, J. S., and Reddy, A. B. (2012). The essential role of cAMP/Ca2+ signalling in mammalian circadian timekeeping. *Biochem. Soc. Trans.* 40, 44–50. doi: 10.1042/BST20110691

Palacios-Muñoz, A., and Ewer, J. (2018). Calcium and cAMP directly modulate the speed of the *Drosophila* circadian clock. *PLoS Genet.* 14:e1007433. doi: 10.1371/journal.pgen.1007433

Papagerakis, S., Zheng, L., Schnell, S., Sartor, M. A., Somers, E., Marder, W., et al. (2014). The circadian clock in oral health and diseases. *J. Dent. Res.* 93, 27–35. doi: 10.1177/0022034513505768

Partch, C. L., Green, C. B., and Takahashi, J. S. (2014). Molecular architecture of the mammalian circadian clock. *Trends Cell Biol.* 24, 90–99. doi: 10.1016/j.tcb.2013.07.002

Pouly, D., Chenaux, S., Martin, V., Babis, M., Koch, R., Nagoshi, E., et al. (2016). USP2-45 is a circadian clock output effector regulating calcium absorption at the post-translational level. *PLoS One* 11:e0145155. doi: 10.1371/journal.pone.0145155

Prakriya, M., and Lewis, R. S. (2015). Store-operated calcium channels. *Physiol. Rev.* 95, 1383–1436. doi: 10.1152/physrev.00020.2014

Said, R., Zheng, L., Saunders, T., Zeidler, M., Papagerakis, S., and Papagerakis, P. (2019). Generation of amelx-iCre mice supports ameloblast-specific role for Stim1. *J. Dent. Res.* 98, 1002–1010. doi: 10.1177/0022034519858976

Samakai, E., Hooper, R., Martin, K. A., Shmurak, M., Zhang, Y., Kappes, D. J., et al. (2016). Novel STIM1—dependent control of Ca 2+ clearance regulates NFAT activity during T—cell activation. *FASEB J.* 30, 3878–3886. doi: 10.1096/fj.201600532R

Shi, G., Xing, L., Liu, Z., Qu, Z., Wu, X., Dong, Z., et al. (2013). Dual roles of FBXL3 in the mammalian circadian feedback loops are important for period determination and robustness of the clock. *Proc. Natl. Acad. Sci. U.S.A.* 110, 4750–4755. doi: 10.1073/pnas.1302560110

Shim, H. S., Kim, H., Lee, J., Son, G. H., Cho, S., Oh, T. H., et al. (2007). Rapid activation of CLOCK by Ca2+-dependent protein kinase C mediates resetting of the mammalian circadian clock. *EMBO Rep.* 8, 366–371. doi: 10.1038/sj.embor.7400920

Simmer, J. P., Papagerakis, P., Smith, C. E., Fisher, D. C., Rountrey, A. N., Zheng, L., et al. (2010). Regulation of dental enamel shape and hardness. *J. Dent. Res.* 89, 1024–1038. doi: 10.1177/0022034510375829

St. John, P. C., Hirota, T., Kay, S. A., and Doyle, F. J. (2014). Spatiotemporal separation of PER and CRY posttranslational regulation in the mammalian circadian clock. *Proc. Natl. Acad. Sci. U.S.A.* 111, 2040–2045. doi: 10.1073/pnas.1323618111

Takahashi, J. S. (2017). Transcriptional architecture of the mammalian circadian clock. *Nat. Rev. Genet.* 18, 164–179. doi: 10.1038/nrg.2016.150

Tonelli, F. M. P., Santos, A. K., Gomes, D. A., da Silva, S. L., Gomes, K. N., Ladeira, L. O., et al. (2012). Stem cells and calcium signaling. *Adv. Exp. Med. Biol.* 740, 891–916. doi: 10.1007/978-94-007-2888-2_40

Tsuchiya, M., Sharma, R., Tye, C. E., Sugiyama, T., and Bartlett, J. D. (2009). TGF-β1 expression is up-regulated in maturation stage enamel organ and may induce ameloblast apoptosis. *Eur. J. Oral Sci.* 117, 105–112. doi: 10.1111/j.1600-0722.2009.00612.x

Xu, X., Zheng, L., Yuan, Q., Zhen, G., Crane, J. L., Zhou, X., et al. (2018). Transforming growth factor-β in stem cells and tissue homeostasis. *Bone Res.* 6:2. doi: 10.1038/s41413-017-0005-4

Ye, R., Selby, C. P., Chiou, Y.-Y., Ozkan-Dagliyan, I., Gaddameedhi, S., and Sancar, A. (2014). Dual modes of CLOCK:BMAL1 inhibition mediated by cryptochrome and period proteins in the mammalian circadian clock. *Genes Dev.* 28, 1989–1998. doi: 10.1101/gad.249417.114

Zheng, L., Ehardt, L., McAlpin, B., About, I., Kim, D., Papagerakis, S., et al. (2014). The tick tock of odontogenesis. *Exp. Cell Res.* 325, 83–89. doi: 10.1016/j.yexcr.2014.02.007

Zheng, L., Papagerakis, S., Schnell, S. D., Hoogerwerf, W. A., and Papagerakis, P. (2011). Expression of clock proteins in developing tooth. *Gene Expr. Patterns* 11, 202–206. doi: 10.1016/j.gep.2010.12.002

Zheng, L., Seon, Y. J., Mourão, M. A., Schnell, S., Kim, D., Harada, H., et al. (2013). Circadian rhythms regulate amelogenesis. *Bone* 55, 158–165. doi: 10.1016/j.bone.2013.02.011

Zheng, L., Zinn, V., Lefkelidou, A., Taqi, N., Chatzistavrou, X., Balam, T., et al. (2015). Orai1 expression pattern in tooth and craniofacial ectodermal tissues and potential functions during ameloblast differentiation. *Dev. Dyn.* 244, 1249–1258. doi: 10.1002/dvdy.24307

Conflict of Interest: The authors declare that the research was conducted in the absence of any commercial or financial relationships that could be construed as a potential conflict of interest.

frontiers in Physiology

ORIGINAL RESEARCH
published: 24 August 2020
doi: 10.3389/fphys.2020.00996

Balance Between Tooth Size and Tooth Number Is Controlled by Hyaluronan

*Natalia Sánchez[1], María Constanza González-Ramírez[1], Esteban G. Contreras[2], Angélica Ubilla[1], Jingjing Li[3], Anyeli Valencia[1], Andrés Wilson[1], Jeremy B. A. Green[3], Abigail S. Tucker[3] and Marcia Gaete[1]**

[1]Department of Anatomy, Faculty of Medicine, Pontificia Universidad Católica de Chile, Santiago, Chile, [2]Faculty of Medicine, Universidad de Chile, Santiago, Chile, [3]Centre for Craniofacial and Regenerative Biology, King's College London, London, United Kingdom

OPEN ACCESS

Edited by:
Agnes Bloch-Zupan, Université de Strasbourg, France

Reviewed by:
Frederic Michon, University of Helsinki, Finland
Markku I. Tammi, University of Eastern Finland, Finland
Marianna Bei, Harvard Medical School, United States

***Correspondence:**
Marcia Gaete
mgaets@uc.cl

Specialty section:
This article was submitted to Craniofacial Biology and Dental Research, a section of the journal Frontiers in Physiology

Received: *27 April 2020*
Accepted: *22 July 2020*
Published: *24 August 2020*

Citation:
Sánchez N, González-Ramírez MC, Contreras EG, Ubilla A, Li J, Valencia A, Wilson A, Green JBA, Tucker AS and Gaete M (2020) Balance Between Tooth Size and Tooth Number Is Controlled by Hyaluronan. Front. Physiol. 11:996. doi: 10.3389/fphys.2020.00996

While the function of proteins and genes has been widely studied during vertebrate development, relatively little work has addressed the role of carbohydrates. Hyaluronan (HA), also known as hyaluronic acid, is an abundant carbohydrate in embryonic tissues and is the main structural component of the extracellular matrix of epithelial and mesenchymal cells. HA is able to absorb large quantities of water and can signal by binding to cell-surface receptors. During organ development and regeneration, HA has been shown to regulate cell proliferation, cell shape, and migration. Here, we have investigated the function of HA during molar tooth development in mice, in which, similar to humans, new molars sequentially bud off from a pre-existing molar. Using an *ex vivo* approach, we found that inhibiting HA synthesis in culture leads to a significant increase in proliferation and subsequent size of the developing molar, while the formation of sequential molars was inhibited. By cell shape analysis, we observed that inhibition of HA synthesis caused an elongation and reorientation of the major cell axes, indicating that disruption to cellular orientation and shape may underlie the observed phenotype. Lineage tracing demonstrated the retention of cells in the developing first molar (M1) at the expense of the generation of a second molar (M2). Our results highlight a novel role for HA in controlling proliferation, cell orientation, and migration in the developing tooth, impacting cellular decisions regarding tooth size and number.

Keywords: successional tooth development, cell orientation, organogenesis, activator-inhibitor, molar development

INTRODUCTION

During development, the extracellular matrix plays a crucial role in controlling the growth and size of diverse organs (Jafari et al., 2010; Walker et al., 2018). Carbohydrates are important components of this matrix; however, their role is poorly studied in developmental biology. Hyaluronan (HA), also known as hyaluronic acid, is a polymeric carbohydrate and a major component of the extracellular matrix. HA is distributed widely throughout the connective and

epithelial tissues and can absorb large quantities of water, regulating the swelling pressure for tissue rigidity and biomechanical integrity (Toole, 2001; Spicer and Tien, 2004). Apart from this structural role, HA can interact with cell-surface receptors and activate the HA signaling pathway. CD44 is the most common HA receptor and its activation regulates cell aggregation, proliferation, survival, and migration (Lee and Spicer, 2000; Bourguignon et al., 2007; Pure and Assoian, 2009; Senbanjo and Chellaiah, 2017; Chen et al., 2018). HA is particularly abundant in tissues that proliferate and grow during embryogenesis, regeneration, and carcinogenesis, as it provides the conditions for cell migration and proliferation, thereby promoting tissue remodeling (Chen and Abatangelo, 1999; Jiang et al., 2007; Contreras et al., 2009; Preston and Sherman, 2011).

HA is synthesized by hyaluronan synthases (HAS), which are located at the plasma membrane, and extrude HA into the extracellular space (Weigel, 2015; Baggenstoss et al., 2017). In mammals, there are three HAS. Among these, HAS1 and HAS2 synthesize high molecular weight (HMW) HA, while HAS3, the most active of the three enzymes, polymerizes low molecular weight (LMW) HA (Spicer and Nguyen, 1999; Itano and Kimata, 2002; Tammi et al., 2011; Vigetti et al., 2014). *HAS2* null mutant mice show cardiac defects and die at E9.5 (Camenisch et al., 2000), whereas *HAS1* and *HAS3* single or double mutations are viable (Bai et al., 2005; Kobayashi et al., 2010; Kessler et al., 2015). In these knockouts, HAS2 levels increase and appear to compensate for loss of *HAS1* and *HAS3* (Wang et al., 2014).

Tooth development is an excellent model to understand cellular dynamics (proliferation, cell movement, and cell shape, etc.) during embryogenesis. The autonomy of these processes enables explants to faithfully replicate normal development (Alfaqeeh and Tucker, 2013; Gaete et al., 2015). The formation of a tooth begins by an oral epithelium thickening called the dental placode, which then forms a bud (bud stage) while the subjacent mesenchyme condenses around it and the epithelium, transitions to form a cap shape (cap stage) and then a bell (bell stage), where histodifferentation starts. From the cap stage, the dental epithelium is divided into the outer dental epithelium, the stellate reticulum in the center, the stratum intermedium, and the inner dental epithelium. The inner dental epithelium forms the ameloblasts for enamel production, while the mesenchyme inside the enamel organ forms the dental papilla, from which the external layer forms odontoblast for dentin formation (Tucker and Sharpe, 2004; Nanci, 2017).

In humans and mice, a single molar dental placode gives rise to three successional molars in each jaw quadrant. At E13.5, the first molar (M1) has reached the bud stage with a molar "tail" starting to develop at the posterior edge of the M1 (Gaete et al., 2015). At E14.5, the second molar (M2) starts to develop within the molar tail. Finally, the third molar (M3) forms postnatally from the posterior edge of the M2 (Chlastakova et al., 2011). When the molar placode is dissected out and cultured *in vitro*, the molar dentition forms in its normal sequence, highlighting the fact that all three molars form from this primordium (Lumsden, 1979; Gaete et al., 2015).

HA and the components of the HA pathway are expressed in dental tissues during embryogenesis and decrease after birth, suggesting a role during tooth development (Felszeghy et al., 2000, 2001, 2005; Tien and Spicer, 2005; Yang et al., 2016). HA is present in the dental epithelium and basal membrane during the bell stage, and it is localized around secretory cellular projections in ameloblasts and odontoblasts (Felszeghy et al., 2000). HA is also observed in the intercellular spaces in the stellate reticulum of the dental organ as these intercellular spaces expand (Felszeghy et al., 2000). According to chromatographic analyses, HA is the main and largely the only glycosaminoglycan present in dissociated dental epithelium, whereas in the mesenchyme HA, heparan and chondroitin sulfate proteoglycans are present (Lau and Ruch, 1983). HAS1 and HAS2 are expressed in the dental epithelium and mesenchyme, but their expression decreases over time, while HAS3 is mainly detected in the core of the dental epithelium (Tien and Spicer, 2005; Morita et al., 2016; Yang et al., 2016) and its expression increases over time (Yang et al., 2016). CD44 is found in the oral epithelium, dental lamina, and stratum intermedium, and moderately in the stellate reticulum (Nakamura and Ozawa, 1997; Felszeghy et al., 2001).

Although the presence of HA and its related components have been described during tooth development, its role is unknown. It has been demonstrated that the general inhibition of the synthesis of gycosaminoglycans inhibits tooth development (Jiang et al., 2019), however the specific role of HA was not studied. Here, we evaluated the functional role of HA during successional molar development in the mouse, characterizing the expression of the components of the HA pathway at early stages of dental development and performing loss-of-function approaches by blocking HA synthesis in tooth germ culture using a chemical inhibitor. We show that, when the production of HA is inhibited, the budding of a new molar is blocked, and the first molar increases in size. These changes in size and number appear to be controlled by alterations in cell orientation and proliferation. HA, therefore, plays an unexpected and novel role in regulating the balance between tooth size and tooth number. These findings provide important insights into how organ size can be regulated.

MATERIALS AND METHODS

Animals and Explant Culture

All experimental procedures were performed following the requirements and approval of Pontificia Universidad Católica de Chile and the King's College London Ethics Committees. Mouse embryos were collected at E14.5 to perform cultures. Experiments were performed in wild type CD1 and/or C57BL/6J according to the availability of the strains. Figures show CD1 data. **Supplementary Figure S1** show C57BL/6J data. For cultures, we used the air-liquid interface method: dissected mandibular molar placodes were placed on top of transparent nucleopore filters (VWR) supported by metal grids at the surface of Advanced DMEM/F12 culture medium (Gibco®), supplemented with 1% penicillin/streptomycin (Gibco®) and 1% GlutaMAX®. These

cultures were incubated at 37°C/5% CO_2, and the medium was changed three times per week (Alfaqeeh et al., 2013; Gaete and Tucker, 2013; Gaete et al., 2015). The cultures were treated with 200 μM 4-methylumbelliferone (4-Mu; a chemical inhibitor for HA synthesis, Sigma-Aldrich M1381) from a of 200 mM stock solution in DMSO, while DMSO was added to control cultures. This concentration of 4-Mu has previously been shown to cause inhibition of tail regeneration in *Xenopus laevis* tadpoles (Contreras et al., 2009) and was chosen after a titration in our system. Experimental and control pairs were obtained using contralateral molar regions.

Whole Mount Immunofluorescence, F-Actin Staining and Fate Mapping

Whole-mount immunostaining was performed as described (Gaete and Tucker, 2013), with minor modifications: permeabilization and washes were performed using PBS-Tr 1% (1% Triton X-100 in 1X phosphate-buffered saline). The following antibodies and dilutions were used: anti-phospho-Histone H3 at 1:300 (Merck, 05-806) and CD44 1:25 (5D2-27 supernatant, Developmental Studies Hybridoma Bank). Alexa Fluor® 488 or 568 (Thermo Fisher) at 1:500 was used as secondary antibodies. For F-actin and DNA staining, fixed samples were washed in 1X PBS and incubated overnight at 4°C with Phalloidin Alexa Fluor 488 (Thermo Fisher) at 1:150 in 1% BSA in PBSTr 0.5% (0.5% Triton X-100 in 1X PBS). In all samples, DNA was stained with Hoechst 33342 dye (Sigma-Adrich), washed in PBS for 2 h, mounted with Fluoroshield™ (Sigma-Aldrich), and scanned using a Leica SP5 confocal microscope. For fate mapping, DiI [CellTracker CM-DiI (C7000, ThermoFisher)] was re-suspended in 100% ethanol, and dried crystals at the tip of a tungsten needle were placed into the molar region using a micromanipulator. The position of the DiI label was imaged during the culture period to follow cell movement.

Histology and *in situ* Hybridization

Samples were fixed in 4% PFA at 4°C, washed in 1X PBS/DEPC, incubated in methanol series, isopropanol, cleared in tetrahydronaphtalene, embedded in paraffin, and sectioned at 8 μm in a microtome. For histology, samples were rehydrated and stained with Mayer's hematoxylin, 1% alcian blue 8GX (Merck, 33864-99-2), and alcoholic eosin Y, dehydrated and mounted in mounting media (Cancer Diagnostics). For *in situ* hybridization, Has2 and Has3 plasmids that contain EGFP in their N-terminus were kindly provided by Dr. Markku Tammi, and originally came from Dr. Andrew Spicer, being completely functional as to hyaluronan synthesis (Rilla et al., 2005; Kultti et al., 2006). We amplified and subcloned the complementary DNA (cDNA) in pBluescript SK plasmid to generate HAS2 and HAS3 probes. Digoxigenin-labeled RNA probes were synthesized using T7, T3, and Sp6 RNA polymerases (Roche). 10 μm sections were rehydrated, permeabilized in 10 μg/ml proteinase K for 15 min, refixed in 4% PFA for 20 min, and incubated in hybridization solution: 1 μg/ml *HAS2*, or *HAS3* probes in hybridization buffer (50% formamide, 20 mM Tris/DEPC pH 7.5, 300 mM NaCl/DEPC, 5 mM EDTA/DEPC, 1x Denhardt's solution, 10% dextran sulfate, and 0.5 mg/ml tRNA) overnight at 65°C. Samples were washed in 50% formamide/2x SSC, 2x SSC, and 0.2x SSC, each wash performed twice for 30 min at 60°C. Then, sections were washed in Maleic Acid Buffer plus Tween (MABT) and blocked in blocking buffer: 10% of goat serum Gibco® and 1% Boehringer Blocking reagent (BBR), in MABT buffer for 2 h at room temperature and incubated with 1:1000 anti-DIG Alkaline Phosphatase antibody (Roche) in blocking buffer overnight at 4°C. Samples were washed four times in MABT buffer for 30 min and incubated twice in AP-Buffer (100 mM Tris-HCl pH 9.5, 50 mM MgCl2, 100 mM NaCl, and 0.1% Tween 20) for 10 min. The color reaction was developed using BM purple (Roche).

Hyaluronan Detection

For HA detection, paraffin sections, obtained as described above, were cleared and rehydrated to 1x PBS. Endogenous peroxidase was blocked using 0.3% H_2O_2 in cold methanol for 15 min on ice. Samples were incubated with 1:200 hyaluronic acid binding protein (HABP, Biotinylated, Merck) in 1% BSA at 4°C overnight. Then, samples were washed and incubated with ABC kit (Vectastain Elite Standard, Vector Labs) for 30 min at room temperature and revealed with DAB reaction (DAB substrate peroxidase kit, SK 4100, Vector Labs), dehydrated and mounted with mounting media (Cancer diagnostics). For fluorescent HA detection, whole fixed slices of tissue were fixed in 4% PFA, permeabilized 45 min in PBSTr 1% (1x PBS, 1%Triton X-100), incubated with 1x trypsin (Gibco®) on ice for 15 min, washed and blocked with 10% goat serum, 1% DMSO, and 1% Triton X-100 for 2 h at room temperature, and incubated with 1:100 HABP in the blocking solution overnight at 4°C. The samples were washed with PBSTr 1% and incubated with ABC kit for 1 h at room temperature, then the samples were incubated with 1:500 anti-streptavidin Alexa Fluor™ 488 (Thermo Fisher) and 1:1000 Hoechst overnight at 4°C. Finally, the samples were washed in PBSTr 1% and mounted with Fluoroshield™ (Sigma-Aldrich).

Image Capture, Processing, and Statistics

Slices and placodes cultures were photographed during the culture period using a Nikon SMZ18 Stereomicroscope. Immunofluorescence, fluorescence detection of HA, phospho-Histone H3 (pH3), and DiI labeling was scanned on a confocal microscope (Leica SP5 laser scanning confocal microscope). Images were processed using Fiji software and Adobe Photoshop CC. For CD44, autofluorescence subtraction was applied on Fiji. For live explant culture photography, Smart Sharpen filter was applied to eliminate Gaussian liquid effect. To obtain the area and growth rate of the cultures, the contour tooth germs or from the stereomicroscope images were delimited and the area calculated at different days using Fiji. A ratio between the enamel knot and the entire dental region was calculated. The shape and the absence of proliferation were used as a guide to observe the enamel knot and the total germ using

pH3 immunostained samples. The areas were plotted and analyzed by Student's *t*-test using GraphPad Prism 5 software. For growth measurements, sequential histological sections stained as described before, were photographed and the molar area was delimited, drawn, and filled using Adobe Photoshop CC and calculated using Fiji software. Volume was calculated as the area under the curve using GraphPad Prism 5 software. To obtain the mitotic index, the percentage of pH3 positive cells under total cells was calculated. To differentiate the anterior and posterior proliferation, the M1 was virtually divided in anterior and posterior half, pH3+ cells were calculated and area was measured finally, and pH3+ cells per area was determined. For cell density calculations, the total cells of the tooth germ were manually counted in four Z-level plane sections in four independent explants pairs (n = 8), in the entire germ, and divided by the area occupied in mm^2. No significant differences between the different zones of the tooth were found. Results were plotted and analyzed by Student's *t*-test using GraphPad Prism 5 software.

Cellular Shape and Orientation Analysis

Confetti transgenic mice that express fluorescent proteins after Cre excision were utilized to follow cell clones (Schepers et al., 2012). Pregnant female mice carrying R26R-CreER/Confetti embryos were injected with 1.5 mg tamoxifen at E13.5. This amount of tamoxifen was the minimum needed to obtain labeling of single cells or small clones at the end of the culture period. The treated embryos were collected at E14.5 and the molar region was cultured, treated with 4-Mu (200 μM) or DMSO as control for 2 days, then scanned using multiphoton microscopy (Zeiss 7MP). The images provided were analyzed by 3D segmentation and ellipsoid fitting method in the cell membrane expressed CFP using Fiji software and associated plug-ins, providing information to investigate cell clones, shape, volume, orientation, and major axis of four samples from three litters (total n = 33 cells per group). To determine the cell shape, ratios between R1/R2, R1/R3, or R2/R3 were obtained. The ratio of the radius of principal and secondary axes of ellipsoids ranging from 0.5 to 2, was calculated and values near to 1 indicate a rounded cell. The data were plotted and analyzed by Student's *t*-test using GraphPad Prism 5 software. To determine the axis orientation of the cell, the angle formed between the ellipsoid and the XY, XZ, and YZ planes of the molar was determined. The angles were plotted in a rose-type graph using Oriana4 software in categories of 15° each and statistical analysis to measure distribution of ordinal data was made using Mann-Whitney-Wilcoxon test.

RESULTS

Components of the Hyaluronan Pathway Are Expressed During Molar Placode Development

To understand the role of HA during molar development, we first analyzed the presence of HA in the molar region at E14.5 at the level of the first molar germ (M1; **Figures 1A,B**) and in the molar tail, a region posterior to the M1 where the successional molar 2 germ (M2) will develop (**Figures 1A,C**). For specific HA localization in the molar germ we used biotinylated HABP, which demonstrated that HA is present throughout the dental mesenchyme (**Figures 1D,E**). Within the epithelium, HA was present mainly in the stellate reticulum at the center of the M1 (**Figure 1D**) and weakly in the middle epithelium of the molar tail (**Figure 1E**). The stellate reticulum and middle epithelium are characterized by star-shaped cells surrounded by extensive intercellular spaces. The condensed dental mesenchyme stained less intensely than the rest of the mesenchyme (**Figures 1D,E**). Thus, HA was localized in the developing molar mesenchyme and in the core of the epithelium.

This result prompted us to identify where HA is synthesized in the molar placode in our system, following on from previous reports (Tien and Spicer, 2005; Morita et al., 2016). By *in situ* hybridization, we observed that the mRNA of *HAS2* and *HAS3* was expressed in the E14.5 M1. *HAS2* was detected in the lingual oral epithelium and weakly in the mesenchyme (**Figure 1F**). Within the epithelium, *HAS3* was expressed in the stellate reticulum, inner enamel epithelium, and enamel knot (**Figure 1H**), agreeing with previously reported expression patterns (Tien and Spicer, 2005). No expression of *HAS2* or *HAS3* was evident in the molar tail (**Figures 1G,I**). The HA receptor CD44 was detected in the more superficial epithelium connecting the M1 to the oral epithelium and in the middle dental epithelium of the molar tail by immunofluorescence (**Figures 1J–K'**). Thus, HA is widely expressed in the tooth, while HAS3 and CD44 have almost complementary expression in the inner enamel epithelium, while only CD44 is present in the epithelium of the molar tail.

Hyaluronan Synthesis Inhibition Increases the Size of the Developing Molar Germ, but Decreases the Formation of the Successional Molar

To assess the function of HA during molar formation, we performed explant cultures in the presence of 4-Mu, a chemical compound that specifically inhibits HA synthesis (Nakamura et al., 1995; Kakizaki et al., 2004). Molar placodes from E14.5 mouse embryo were dissected out and cultured in control medium (**Figures 2A–C**) or in the presence of 4-Mu (**Figures 2D–F**). A reduction of HA was observed in treated cultures (**Supplementary Figure S1**). After 2 days, the first and the second molar germ had formed in control cultures (**Figure 2B**), whereas in the 4-Mu treated cultures, the M1 appeared bigger than the control culture, while the M2 did not develop (**Figure 2E**). After 5 days of culture, a large M1 was observed in the 4-Mu treated group (**Figure 2F**) in comparison to control cultures (**Figure 2C**). The inhibition of the formation of the M2 was maintained after 5 days of culture (**Figure 2F**, arrowhead). We quantified the increase of the M1 area at different days post-culture. At 3d, the 4-Mu treated cultures started to grow more than controls, and at 5d appeared significantly larger than controls (**Figures 2G,H**).

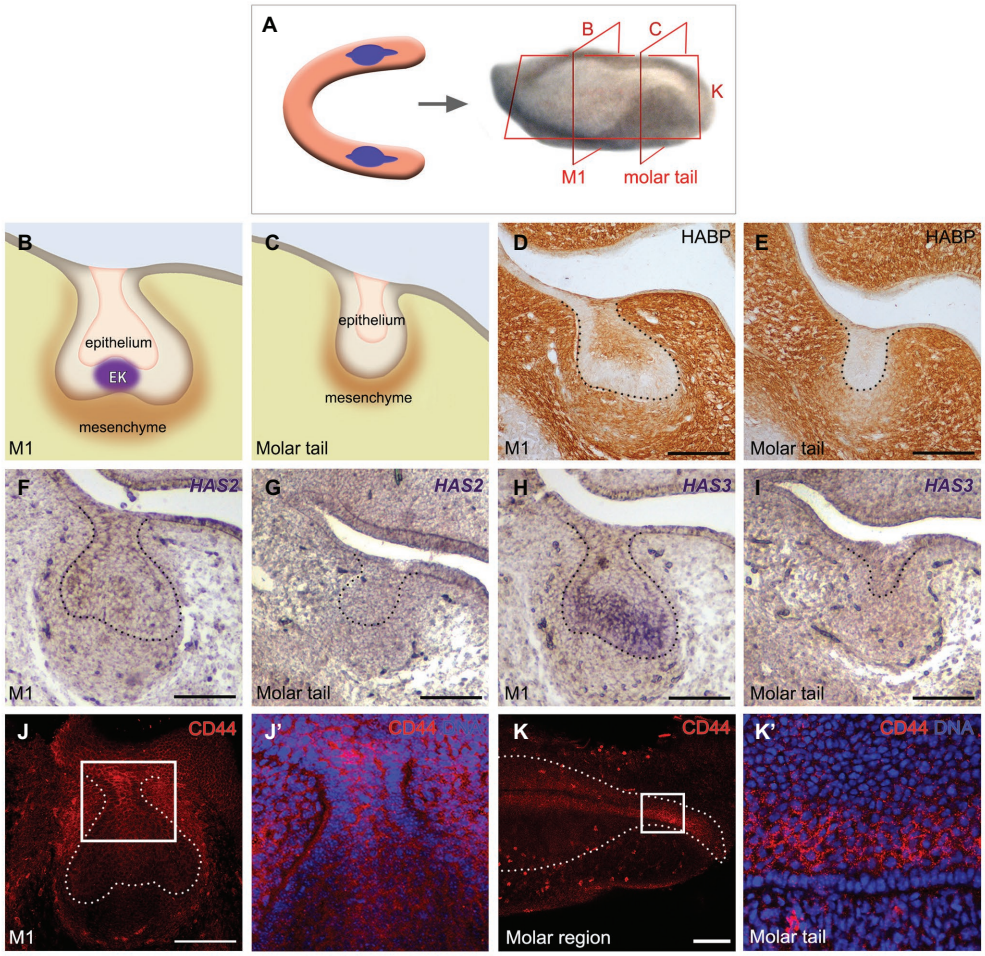

FIGURE 1 | Components of the hyaluronan (HA) pathway are detected in the molar germ. **(A–C)** Schematics of the **(A)** developing molar region and **(B)** a section at the level of **(B)** M1 and **(C)** the molar tail. **(D,E)** Detection of HA by hyaluronic acid binding protein (HABP) in the dental mesenchyme and epithelial core of the **(D)** molar and less intense in the **(E)** tail. **(F–I)** *In situ* hybridization of HA synthase 2 and 3 (*HAS2* and *HAS3*), **(F)** HAS2 is expressed in the lingual oral epithelium and weakly in the dental mesenchyme, whereas **(H)** HAS3 is detected mainly in the stellate reticulum, inner epithelium, and enamel knot. **(G,I)** No expression of *HAS2* or *HAS3* was evident in the molar tail. **(J,K)** CD44 immunofluorescence in a **(J)** frontal view of the molar region, including a **(J')** zoom of the region indicated in **(J)** and **(K)** in a sagittal view at M1 including a **(K')** zoom of the region indicated in **(K)**. CD44 is expressed in complementary regions together with *HAS3*. Scale bar: 100 μm.

At the end of the culture period, the molars were processed for volume analysis, confirming that 4-Mu treated M1 were significantly larger than controls (**Figures 2I,J**). Changes in the size of the molar could be related to a change in the size of the enamel knot. A ratio between the size of the enamel knot and the tooth germ was calculated in the cultured samples (**Supplementary Figure S2A**). We found non-significant differences in the relative size of the enamel knot between control and treated conditions after 2 days of culture, meaning that, as the molar germ grew in size, the enamel knot is also expanded in proportion. Moreover, *in situ* hybridization against *Shh* on explants cultured for 5 days, showed no difference in the pattern of expression (data not shown).

To analyze the molar succession, we quantified the number of samples that developed M2 at day 3 of culture in the presence of 4-Mu. We found that the formation of M2 occurred in less than 20% of the 4-Mu-treated cultures (n = 4/18), whereas the M2 was well-developed in the majority of control cultures after 3 days (n = 14/17; **Figures 2G,K**). Altogether, the use of a HA synthesis inhibitor produced an opposing phenotype among the molars: the developing M1 became bigger, while the formation of the M2 was inhibited.

4-Mu Treatment Increases Cell Proliferation of the Developing Molar

In order to find a cellular mechanism for the increase in size of M1 after HA synthesis inhibition, we investigated whether cell proliferation was altered after 4-Mu treatment. By immunofluorescence detection of the mitotic marker pH3, we observed an increase in the proportion of proliferating

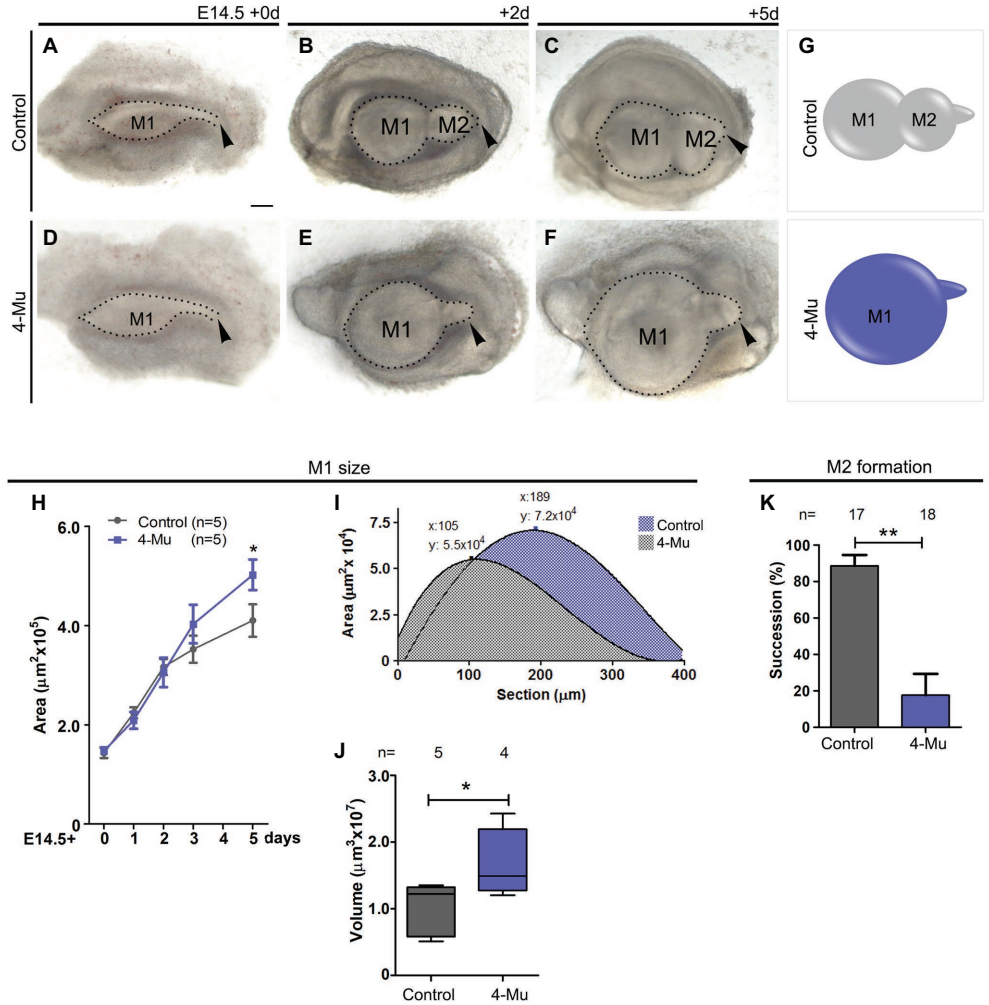

FIGURE 2 | Inhibition of hyaluronan synthase (HAS) generates a big tooth germ and impairs the formation of the second molar. **(A–F)** Molar placodes were dissected from an E14.5 embryo mandible and cultured in control **(A–C)** or 4-methylumbelliferone (4-Mu; **D–F**) media until 5 days. 4-Mu treated cultures show a bigger M1 and no M2 formation comparing to control culture. Arrowhead indicates the tail of the molar placode where the next tooth should be formed. **(G–J)** First molar growth in control and 4-Mu treated cultures. **(G)** Scheme indicating the M1, whose **(H)** area was measure showing that treated cultures, generate significant bigger teeth. **(I)** Area under the curve of M1 was calculated confirming the increase of volume of the 4-Mu treated placodes. **(J)** Box-plot of the M1 volume shows almost two times of increase in the volume of 4-Mu treated placodes. **(K)** M2 successional molar formation in percentage, showing a decrease of almost four times of the presence of M2 in 4-Mu treated culture. Scale bar: 100 µm. $^{*}p < 0.05$; $^{**}p < 0.01$.

cells in the dental organ and a significant increase in the mitotic index in 4-Mu treated cultures compared to controls (**Figures 3A–C**), while the cell density was conserved (**Figure 3D**). The distribution of the proliferation was similar in the anterior and posterior compartments when compared (**Supplementary Figure S2B**). These results indicate that the HA-inhibited M1 is bigger than controls because of an increased cell proliferation, but without affecting cell density ($n = 4$).

Hyaluronan Is Necessary to Conserve the Morphology of the Molar Tail

To determine whether the larger tooth germs generated by 4-Mu treatment had differences in histomorphology or organization of the tissues, we used conventional hemotoxylin-eosin and alcian blue staining. No key differences between the tissue of the control and the 4-Mu treated molar germs were observed (**Figures 4A–D**). As molar succession was impaired, we analyzed the morphology of the molar tail and its proliferation. Using F-actin and DNA staining, we observed that in the 4-Mu treated explants, the molar tail was thinner and with fewer layers in contrast to untreated explants, in which the tail was bigger, stratified and with a distinguishable middle epithelium (**Figures 4E–G** compare to **Figures 4H–J**, seen in 4/4 experimental samples, compared to 2/2 controls). However, tail proliferation was increased (**Supplementary Figure S2C**). In conclusion, loss of HA synthesis conserved the general morphology of the M1; however, it disrupted the size and structure of the tail.

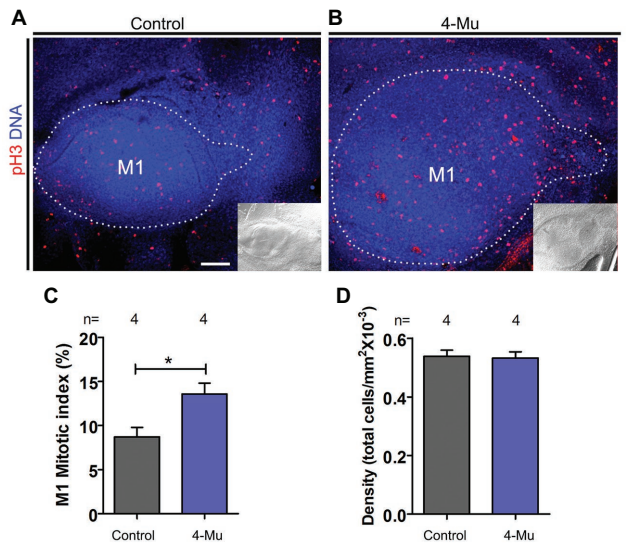

FIGURE 3 | Proliferation is increased in 4-Mu treated placodes. **(A,B)** Immunofluorescence of pH3 of **(A)** control and **(B)** 4-Mu treated placodes showing an increase of the proliferation in 4-Mu cultures. An inset of the DIC channel is included for a general view. **(C)** Mitotic index of M1 in control and 4-Mu treated cultures indicating a 5% of increase in 4-Mu cultures. **(D)** M1 cell density shows no difference between control and 4-Mu treated cultures. Scale bar: 100 μm. $^*p < 0.05$.

Altered Dental Cell Shape and Orientation Is Observed After Blocking Hyluronan Synthesis

After blocking HA synthesis, an increase in M1 cell proliferation and size occurred together with a formation of a smaller tail. This phenotype could be explained by a defect in cell orientation and movement. Therefore, we evaluated cell shape and orientation after treatment with 4-Mu. For this, we used Rosa26-Cre:Confetti transgenic embryos (Schepers et al., 2012) to trace cells in the molar placode. This transgenic mouse expresses fluorescent proteins after Cre excision. Pregnant female mice were injected with the minimum of tamoxifen to obtain single cell resolution *in vivo* and after 24 h, and the developing molars of their embryos were cultured in the presence of 4-Mu for 2 days (**Figures 5A,B**). We analyzed the plasma membrane fluorescent marker (CFP) in two planes to understand cellular shape and orientation (**Figure 5C**). We found that after 2 days of 4-Mu treatment, cells were significantly more elongated than cells in control cultures (**Figure 5D**). Additionally, the cells from 4-Mu explants displayed an orientation closely aligned toward the oral-aboral axis, while in control cultures cells were more rounded and oriented in the antero-posterior axis (**Figures 5F–I**, see schemes of the planes and cells in **Figures 5A–J**) with significant differences. Therefore, control M1 cells were mildly elongated in an axis toward the M2, while in the 4-Mu treated explants, cells were strongly elongated in an axis toward the top of the M1, losing their normal orientation (**Figure 5**, see summary in **Figure 5J**). Altogether, our results indicate defects in cell shape and orientation after impairing HA synthesis.

Hyaluronan Is Required for Cell Migration During Molar Development

Given that the M2 is formed at the tail region of the molar placode, we asked whether this phenotype is due to retention of some cells in the region of the first molar. To answer this question, we performed lineage-tracing experiments. We used DiI to label the M1 and the tail of the molar placode in three dots from anterior to posterior regions (**Figures 6A,D**, indicated by the yellow, green, and blue arrowhead, respectively) after 1d starting with E13.5 molar placodes. This timing allowed the tissue to stick to the filter for a precise labeling. We followed the labels and after 3–5 days in culture, observing that the dots were closer in the 4-Mu treated cultures compared to the control cultures, in which the dots were more separated and scattered within the molar tissue (**Figures 6A–F**). To quantify this, we divided the distance between the anterior dot and the middle dot after culture by the original distance at day 0. The middle dot (green arrow) was named the "isthmus spot," because it was located at the posterior edge of M1 and the beginning of the molar tail. As suggested by the images, the dots between the center of the M1, and the isthmus had moved significantly further apart when compared to the 4-Mu treated cultures (**Figure 6G**). In the displayed culture (**Figures 6A–F**), we observed that part of the isthmus spot that contributes to the second molar in the control, was recruited into the first molar (**Figures 6C,F**, green arrow). The isthmus spot fate was therefore followed throughout the culture period and the final position registered. In the treated cultures, approximately 90% of the samples retain the isthmus dot in M1 compared to approximately 40% in the controls (**Figure 6H**). This indicated a lack of movement of cells from the first molar into the second molar after the treatment with 4-Mu, resulting in cells that normally contributed to the second molar, were recruited into the first molar.

DISCUSSION

In this work, we studied the function of HA during successional molar development in mice. For this, the molar region was exposed to an inhibitor of HA synthesis when the M1 was at the cap stage and the M2 was forming from the tail of the M1. Interestingly, the phenotype that we observed between the two molar germs was paradoxical: the M1 continued its development and increased its size as M2 was arrested in its formation.

Our results indicate that the inhibition of HA synthesis caused an increase in the mitotic index of the M1 cells, explaining the size of the M1. The increase in proliferation after the incubation with 4-Mu in our system is at odds to the findings published in other systems, in which decreasing HA synthesis reduced cell proliferation (Contreras et al., 2009; Saito et al., 2013; Wang et al., 2015; Nagase et al., 2017; Ouyang et al., 2017). Similarly, this phenotype is in contrast to the reduced proliferation and molar size reported after inhibition of the synthesis of general glycosaminoglycans (Jiang et al., 2019). This suggests that the effect might be stage dependent, or that there is compensation from other glycosaminoglycans after HA inhibition.

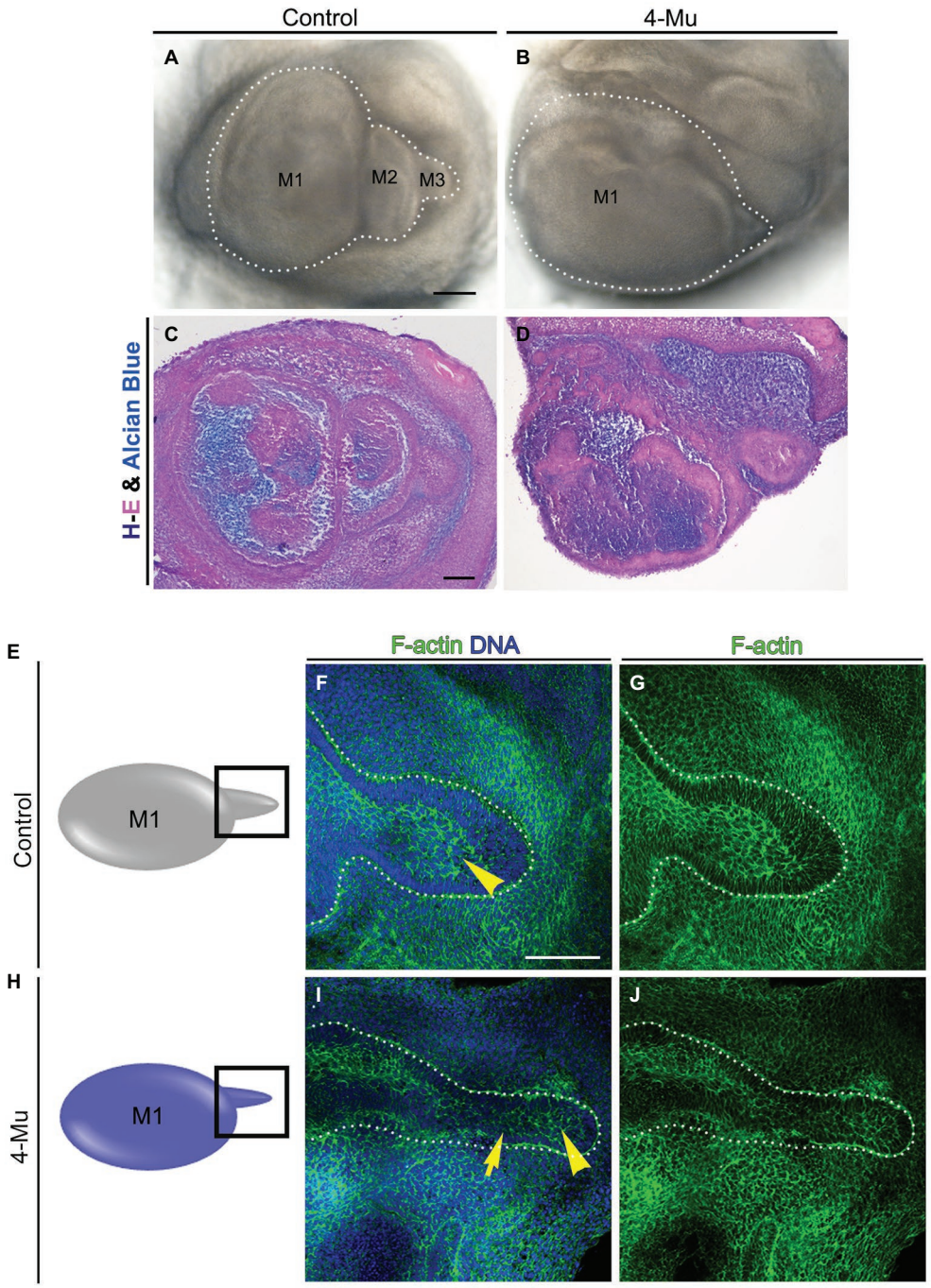

FIGURE 4 | Morphology of tooth germ is conserved in 4-Mu treated cultures, but not in the tail **(A,B)** molar placodes cultured by 5 days in **(A)** control or **(B)** 4-Mu conditions, showing the increase of size and the lack of succession in 4-Mu treated cultures. **(C,D)** Trichrome staining of molar placode sections showing no differences in morphology in **(C)** control or **(D)** 4-Mu cultures. **(E–J)** Morphology of molar tail in **(E–G)** control and **(H–J)** 4-Mu treated cultures visualized by F-actin and DNA staining showing a thinner and disorganized molar tail in 4-Mu cultures. The middle epithelium is not distinguishable in 4-Mu cultures (yellow arrowhead) and less stratification in the epithelium is observed (yellow arrow). Scale bar: 100 μm.

In the case of molar succession, the 4-Mu treated M1 was bigger, but the M1 tail was smaller than in control cultures. Interestingly, just before the phenotype appeared, cells of the first molar were more elongated but not in a direction toward the molar tail as in their control counterparts. This was correlated with the fact that cells in the posterior edge of the M1 (isthmus spot) did not migrate to be incorporated into the second molar. If the M2 is formed by contribution of cells from M1

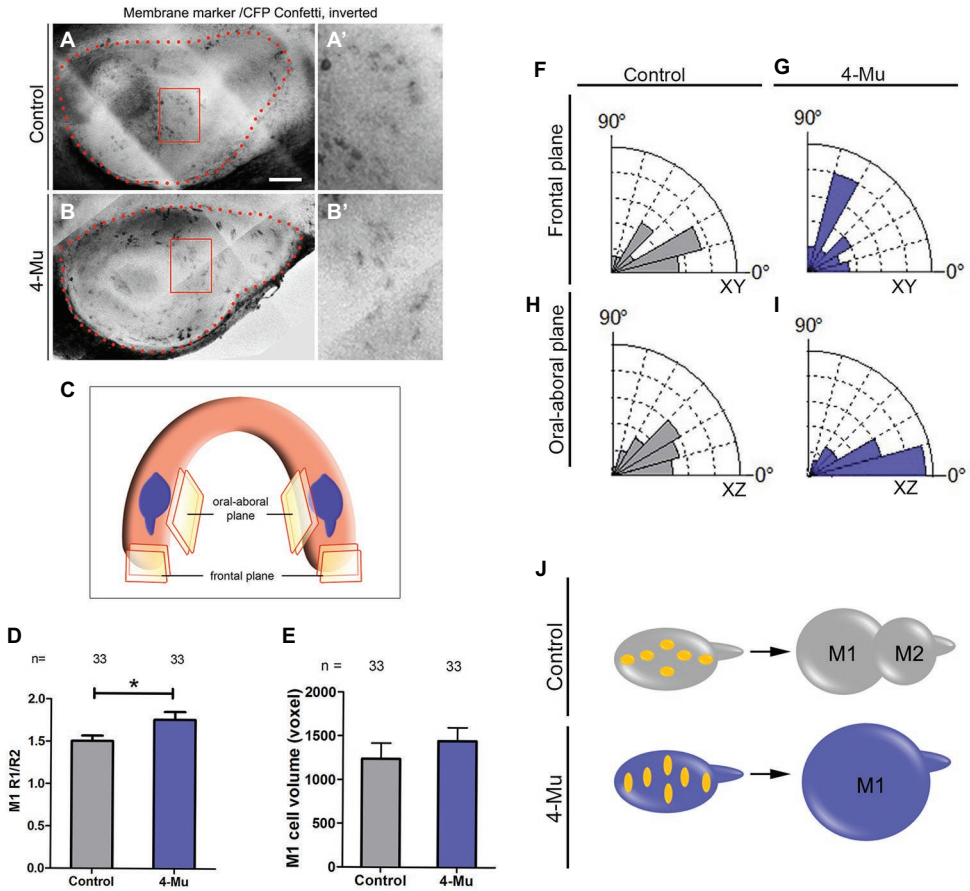

FIGURE 5 | 4-Mu treated cultures show more elongated and oral-aboral orientated cells compared to control. **(A,B)** Z-projection of CFP-label **(A,A')** control and **(B,B')** 4-Mu molar placodes analyzed. **(A',B')** are magnifications from **(A,B)**, respectively. **(C)** Mandible scheme showing the molar placodes and the orientation planes analyzed by multiphoton microscopy from Confetti mouse molars. CFP-label (cell membrane marker) was analyzed to determine **(D)** cell shape, **(E)** M1 cell volume, and **(F–I)** orientation in control and 4-Mu treated cultures. **(D)** Ratio between two radiuses of the cells showing that 4-Mu cultures have more elongated cells. **(E)** M1 cell volume showing no differences between control and 4-Mu treated samples. **(F–I)** Cell orientation in frontal plane of **(F)** control and **(G)** 4-Mu treated placodes and oral-aboral plane of **(H)** control and **(I)** 4-Mu cultures, indicating that 4-Mu cells were aligned toward the oral-aboral axis (see **A** for planes), while control cells were orientated in the antero-posterior axis. The significance of the distribution of the uncategorized angles was *XY and **XZ. **(J)** Scheme of cell shape and orientation in control and 4-Mu treated cultures. Scale bar: 100 μm. $^{*}p < 0.05$; $^{**}p < 0.01$.

(Juuri et al., 2013), therefore, after inhibition of HA synthesis, some cells that normally would have migrated to form the M2 have now been retained in the field of the M1. Thus, the M1 gets bigger at the expense of the M2 (see working model in **Figure 7**). Although this model can certainly explain the observed phenotype, our results do not discard the possibility of an arrest in the development of the M2, as a consequence of a direct effect of HA on M2 development, independent of the effect on M1 growth. From our experiments, it is important to understand that we cannot distinguish whether the development of M2 is just delayed by 4-Mu or if it remains completely blocked. Thus, HA levels could interfere with the activator-inhibitor model, with the consequence that when M1 grows larger, its field of inhibition also increases and M2 fails to form. Later, M2 cells could be far enough from this field of inhibition, reactivating M2 development. Limitations of the culture system prevent yet longer culture. *In vivo* analysis using kidney capsule-cultures or mouse models such as *HAS3* knockout could provide the necessary time to address those questions.

At the start of the culture period, HA was shown to be present in the tooth mesenchyme and in epithelial tissues with mesenchymal or myxoid morphology, such as the stellate reticulum and the middle epithelium of the tail. Both the stellate reticulum and the middle epithelium have been proposed to be a source of stem cells in the mouse incisor (Wang et al., 2007) and in polyphyodont models (Smith et al., 2009) and express the transcription factor Sox9 (Gaete et al., 2015). HA may play a key role in the function of this tissue and the formation of a new tooth during molar succession, in addition to tooth replacement. Additionally, HA is involved in epithelial-mesenchymal transformation (Camenisch et al., 2000), which can be an event necessary for the epithelial migration to form M2 in the molar succession.

HA could also have a role on the formation of primary enamel knot. Our 4-Mu incubations started relatively late to

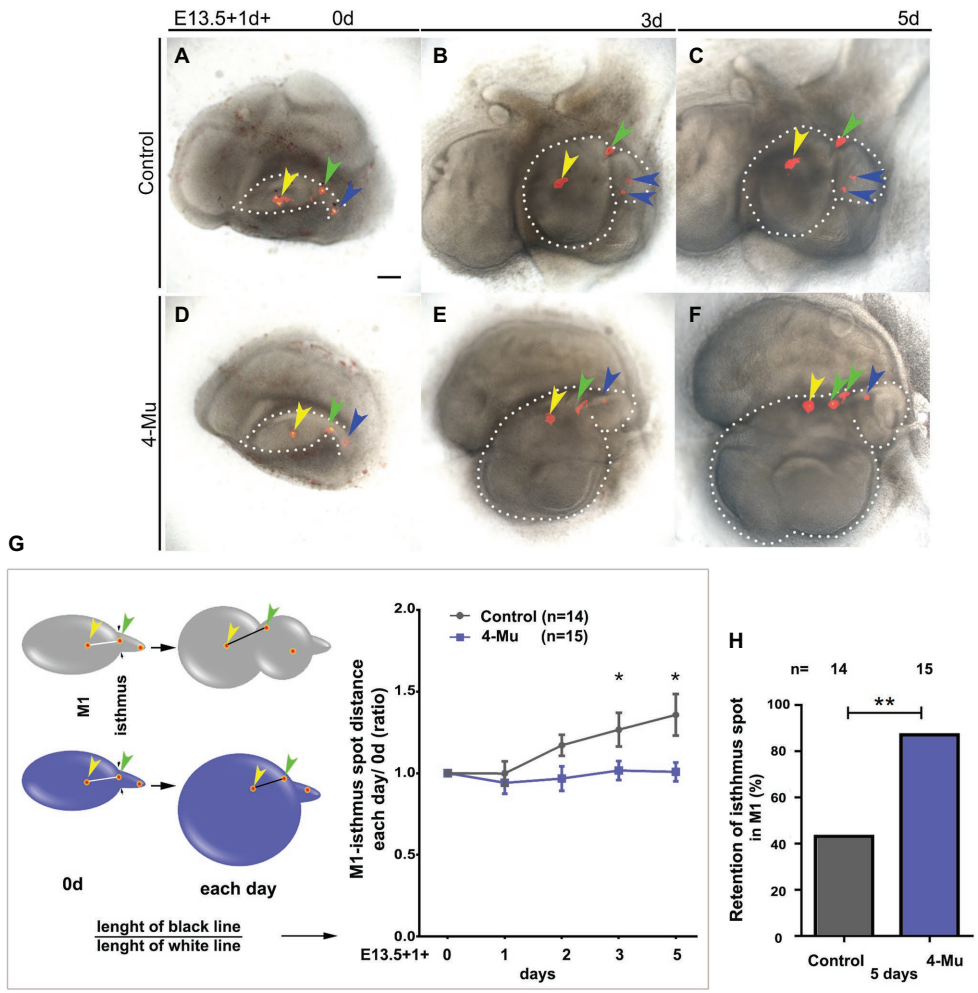

FIGURE 6 | Cell movement is affected in 4-Mu treated cultures. **(A–F)** DiI labeling was used to label three areas along the **(A–C)** control and **(D–F)** 4-Mu treated molar placode at E13.5 from anterior to posterior regions (yellow, green, and blue arrowhead, respectively). Placodes were cultured for up to 5 days and the position of the label followed. **(A,D)** day 0. **(B,E)** day 3. **(C,F)** day 5. **(G)** In 4-Mu cultures the label in the M1 and in the isthmus (middle label, indicated by the green arrowhead) retained a fairly constant relative position, while in controls comparable labels moved apart after 3–5 days in culture. **(H)** The isthmus label was retained in M1 in most of the 4-Mu treated cultures. Data based on $N = 14$ control and 15 treated placodes. Scale bar: 100 μm. $^{*}p < 0.05$; $^{**}p < 0.01$.

understand initial patterning of the enamel knot (E14.5); therefore, early experiments should be conducted to address this possibility. Importantly, our results indicated that as the molar grow in size the enamel knot also increase in size, which means that overall tooth patterning could be proportionally enlarged as the phenotype appears.

Regarding its signaling properties, it has been shown that HA plays an important role during embryonic development regulating cell migration, shape, and proliferation (Spicer and Tien, 2004). *HAS3* is the most active enzyme of the HAS family and polymerizes shorter HA chains (Itano et al., 1999; Itano and Kimata, 2002) that stimulates cell signaling, proliferation, and epithelial-to-mesenchymal transition in cancer models (Kultti et al., 2014; Kuo et al., 2017; Arasu et al., 2019). *HAS3* expression is higher in the dental epithelium than the mesenchyme, with the distribution of CD44 appearing complementary to *HAS3* in the dental epithelium. This suggests that CD44 may mediate HA signaling in adjacent locations. It has been proposed that HA is synthesized in cells in the epithelial dental lamina to produce a pericellular HA coat, which may be required for the proliferation and migration of cells in the dental lamina into the underlying mesenchyme (Felszeghy et al., 2000). In our model, the assembly and presence of a pericellular HA coat might facilitate the budding off for the successional molar formation.

The inhibition of HA synthesis did not impact the gross morphogenesis of the first molar, with normal formation of dental tissues. However, HA inhibition altered levels of proliferation and cell orientation. Interestingly, stimulated HA synthesis by HAS3 changes the cell polarization with aberrant mitotic spindle orientation in dividing cells that impact in epithelial thickness (Rilla et al., 2012).

Hydrogels can affect the diffusion of growth factors *in vitro* (Silva et al., 2009), and HA-CD44 interaction can affect the activation of growth factors in cancer (Misra et al., 2011).

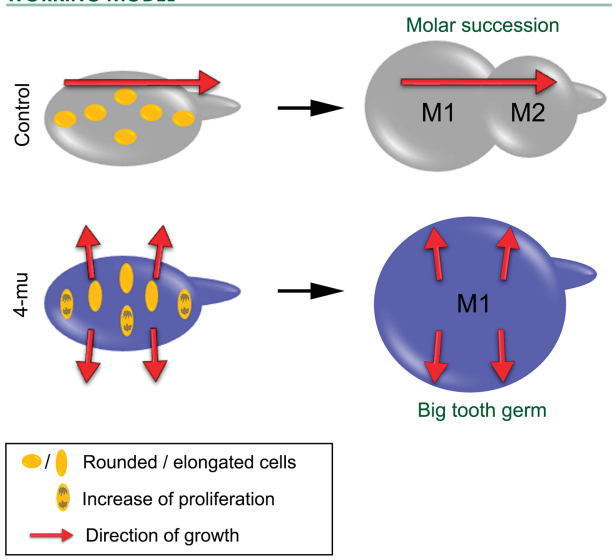

FIGURE 7 | Working model. Scheme of control and 4-Mu treated cultures *at initio* and after 5 days of treatment. M1 cells were mildly elongated in an axis toward the M2, however in the 4-Mu, cells were strongly elongated in an axis that follows the expansion of M1, which proliferates more than the control, resulting in a bigger M1 and impairment in the formation of the successional M2.

HA could have effects on the diffusion of both FGFs and Hhs during tooth development. Further investigation of these pathways, for example FGF targets, like Sprouty, and Hh targets such as Ptc and Gli, could be analyzed after 4-Mu treatment to address this question. This would allow us to clarify whether the phenotype observed was due to a change in signaling gradients or due to mechanical effects, which might drive cell rearrangement.

In this work, we considered that the effects of 4-Mu are due to the inhibition of HA-synthesis. 4-Mu is a highly specific inhibitor, and it is unlikely to affect any key pathways other than HA synthesis (Nakamura et al., 1995; Kakizaki et al., 2004; Kultti et al., 2009; Nagy et al., 2019). However, we cannot excluded the possibility that 4-Mu might be affecting other targets that control the sequential formation of molars. Having this in mind, any effects on alternative pathways could also be a consequence of the decrease in HA synthesis. Future directions analyzing the phenotype of *HAS* knockout animals would provide additional validation of the role of HA during molar formation.

It is known that the size and number of molar teeth that normally develop from the molar placode appears to be regulated by a system of positive signals from the mesenchyme and negative signals from the intermolar region (Kavanagh et al., 2007). The inhibitor model proposes M1 inhibits M2 development, and M2 inhibits M3. Thus, when the M2 primordium is removed from M1 in culture, the inhibitory signal is eliminated and M2 develops earlier than normal and reaches a greater size, depending on BMP signaling (Kavanagh et al., 2007). Hence, when a tooth reaches a given size the inhibition of the next tooth in the series is lost, allowing it to develop. This occurs efficiently when the original primordium is large (Cai et al., 2007).

In our model, it is important to understand whether the development of M2 is just delayed by 4-Mu or whether it remains completely blocked in late phases. HA could interfere with the activator-inhibitor model, with the consequence that when M1 grows larger, its field of inhibition also increases and the M2 fails to form, unless the cells are far enough away from this field to be reactivated. *In vivo* analysis using kidney capsule-cultures or mouse models, such as *HAS2/HAS3* knockout animals, would provide the necessary temporality to address such questions. Moreover, the involvement of HA synthesis could be supported by directly blocking the expression of *HAS2* and/or *HAS3*.

In summary, our results suggest that HA has a pivotal role during tooth development, regulating the size of the molar placode and influencing cell proliferation, shape, orientation, and movement of the cells. Hence, we believe that the role of polysaccharides needs to be revisited and further analysis performed in order to understand the participation of carbohydrates in tooth development and regeneration. The role of HA in the control of molar size is very interesting and provides a tool by which tooth size could be modulated during *ex-vivo* regenerative therapies.

DATA AVAILABILITY STATEMENT

The raw data supporting the conclusions of this article will be made available by the authors, without undue reservation.

ETHICS STATEMENT

The animal study was reviewed and approved by Comité Ético Científico para el Cuidado de Animales y Ambiente CEC-CAA, Pontificia Universidad Católica de Chile, ID number 181203001, CEBA 14024. Mouse work at King's College London followed Home Office guidelines, with the appropriate licenses and approvals for breeding of transgenic mice in place. Culling of mice followed approved schedule one methods.

AUTHOR CONTRIBUTIONS

NS: performed experiments, data analysis and figures. MG-R, AW, AU, and AV: performed experiments. EC: performed experiments, discussion of data and manuscript writing. JL: performed multiphoton imaging, analysis, and discussion of data. AT and JG: did experimental design, discussion of data and manuscript writing. MG performed experiments, did experimental design, data analysis, discussion of data, manuscript writing, and figures. All authors contributed to the article and approved the submitted version.

FUNDING

This work was funded by FONDECYT of Initiation into Research 11140303, CONICYT-Chile and Proyecto CONICYT Concurso

Redes Internacionales para Investigadores en Etapa Inicial, REDI170595. NS was funded by FONDECYT Postdoctorado N 3190798. EC was funded by FONDECYT Postdoctorado N 3160412. Biotechnology & Biological Sciences Research Council grant BB/P007325/1 funded to JG.

SUPPLEMENTARY MATERIAL

The Supplementary Material for this article can be found online at: https://www.frontiersin.org/articles/10.3389/fphys.2020.00996/full#supplementary-material.

SUPPLEMENTARY FIGURE S1 | HABP levels are decreased in the stellate reticulum after 4-Mu treatment. HABP levels were measured in different areas of control and 4-Mu treated placodes, showing a significant decrease of HABP detection in the stellate reticulum of 4-Mu treated germs. *$p < 0.05$ (Student's *t*-test for each tissue analyzed).

SUPPLEMENTARY FIGURE S2 | Enamel knot area and M1 anterior-posterior proliferation are conserved in control and 4-Mu dental organ, but tail proliferation is increased in 4-Mu treated samples. **(A)** Enamel knot (EK)/dental organ area ratio were calculated at day 2 of culture, showing no differences between control and 4-Mu samples. **(B)** M1 was virtually divided in anterior and posterior half and pH3+ cells was quantified, no-significant differences between anterior-posterior half were found in control or 4-Mu treated germs at 3 days. **(C)** Molar tail mitotic index was calculated, showing an increase of tail proliferation in 4-Mu treated samples compared to control. Student's *t*-test was performed. *$p < 0.05$.

REFERENCES

Alfaqeeh, S. A., Gaete, M., and Tucker, A. S. (2013). Interactions of the tooth and bone during development. *J. Dent. Res.* 92, 1129–1135. doi: 10.1177/0022034513510321

Alfaqeeh, S. A., and Tucker, A. S. (2013). The slice culture method for following development of tooth germs in explant culture. *J. Vis. Exp.* 81:e50824. doi: 10.3791/50824

Arasu, U. T., Deen, A. J., Pasonen-Seppanen, S., Heikkinen, S., Lalowski, M., Karna, R., et al. (2019). HAS3-induced extracellular vesicles from melanoma cells stimulate ihh mediated c-myc upregulation via the hedgehog signaling pathway in target cells. *Cell. Mol. Life Sci.* doi: 10.1007/s00018-019-03399-5 [Epub ahead of print]

Baggenstoss, B. A., Harris, E. N., Washburn, J. L., Medina, A. P., Nguyen, L., and Weigel, P. H. (2017). Hyaluronan synthase control of synthesis rate and hyaluronan product size are independent functions differentially affected by mutations in a conserved tandem b-x7-b motif. *Glycobiology* 27, 154–164. doi: 10.1093/glycob/cww089

Bai, K. J., Spicer, A. P., Mascarenhas, M. M., Yu, L., Ochoa, C. D., Garg, H. G., et al. (2005). The role of hyaluronan synthase 3 in ventilator-induced lung injury. *Am. J. Respir. Crit. Care Med.* 172, 92–98. doi: 10.1164/rccm.200405-652OC

Bourguignon, L. Y., Gilad, E., Peyrollier, K., Brightman, A., and Swanson, R. A. (2007). Hyaluronan-CD44 interaction stimulates rac1 signaling and pkn gamma kinase activation leading to cytoskeleton function and cell migration in astrocytes. *J. Neurochem.* 101, 1002–1017. doi: 10.1111/j.1471-4159.2007.04485.x

Cai, J., Cho, S. W., Kim, J. Y., Lee, M. J., Cha, Y. G., and Jung, H. S. (2007). Patterning the size and number of tooth and its cusps. *Dev. Biol.* 304, 499–507. doi: 10.1016/j.ydbio.2007.01.002

Camenisch, T. D., Spicer, A. P., Brehm-Gibson, T., Biesterfeldt, J., Augustine, M. L., Calabro, A., et al. (2000). Disruption of hyaluronan synthase-2 abrogates normal cardiac morphogenesis and hyaluronan-mediated transformation of epithelium to mesenchyme. *J. Clin. Invest.* 106, 349–360. doi: 10.1172/JCI10272

Chen, W. Y., and Abatangelo, G. (1999). Functions of hyaluronan in wound repair. *Wound Repair Regen.* 7, 79–89. doi: 10.1046/j.1524-475x.1999.00079.x

Chen, C., Zhao, S., Karnad, A., and Freeman, J. W. (2018). The biology and role of CD44 in cancer progression: therapeutic implications. *J. Hematol. Oncol.* 11:64. doi: 10.1186/s13045-018-0605-5

Chlastakova, I., Lungova, V., Wells, K., Tucker, A. S., Radlanski, R. J., Misek, I., et al. (2011). Morphogenesis and bone integration of the mouse mandibular third molar. *Eur. J. Oral Sci.* 119, 265–274. doi: 10.1111/j.1600-0722.2011.00838.x

Contreras, E. G., Gaete, M., Sanchez, N., Carrasco, H., and Larrain, J. (2009). Early requirement of hyaluronan for tail regeneration in xenopus tadpoles. *Development* 136, 2987–2996. doi: 10.1242/dev.035501

Felszeghy, S., Hyttinen, M., Tammi, R., Tammi, M., and Modis, L. (2000). Quantitative image analysis of hyaluronan expression in human tooth germs. *Eur. J. Oral Sci.* 108, 320–326. doi: 10.1034/j.1600-0722.2000.108004311.x

Felszeghy, S., Meszar, Z., Prehm, P., and Modis, L. (2005). The expression pattern of hyaluronan synthase during human tooth development. *Arch. Oral Biol.* 50, 175–179. doi: 10.1016/j.archoralbio.2004.10.010

Felszeghy, S., Modis, L., Tammi, M., and Tammi, R. (2001). The distribution pattern of the hyaluronan receptor CD44 during human tooth development. *Arch. Oral Biol.* 46, 939–945. doi: 10.1016/S0003-9969(01)00053-X

Gaete, M., Fons, J. M., Popa, E. M., Chatzeli, L., and Tucker, A. S. (2015). Epithelial topography for repetitive tooth formation. *Biol. Open* 4, 1625–1634. doi: 10.1242/bio.013672

Gaete, M., and Tucker, A. S. (2013). Organized emergence of multiple-generations of teeth in snakes is dysregulated by activation of wnt/beta-catenin signalling. *PLoS One* 8:e74484. doi: 10.1371/journal.pone.0074484

Itano, N., and Kimata, K. (2002). Mammalian hyaluronan synthases. *IUBMB Life* 54, 195–199. doi: 10.1080/15216540214929

Itano, N., Sawai, T., Yoshida, M., Lenas, P., Yamada, Y., Imagawa, M., et al. (1999). Three isoforms of mammalian hyaluronan synthases have distinct enzymatic properties. *J. Biol. Chem.* 274, 25085–25092. doi: 10.1074/jbc.274.35.25085

Jafari, G., Burghoorn, J., Kawano, T., Mathew, M., Morck, C., Axang, C., et al. (2010). Genetics of extracellular matrix remodeling during organ growth using the *Caenorhabditis elegans* pharynx model. *Genetics* 186, 969–982. doi: 10.1534/genetics.110.120519

Jiang, D., Liang, J., and Noble, P. W. (2007). Hyaluronan in tissue injury and repair. *Annu. Rev. Cell Dev. Biol.* 23, 435–461. doi: 10.1146/annurev.cellbio.23.090506.123337

Jiang, B., Xu, F., Li, L., Chen, W., Hong, S., and Chen, R. (2019). The inhibition of glycosaminoglycan incorporation influences the cell proliferation and cytodifferentiation in cultured embryonic mouse molars. *J. Mol. Histol.* 50, 11–19. doi: 10.1007/s10735-018-9803-2

Juuri, E., Jussila, M., Seidel, K., Holmes, S., Wu, P., Richman, J., et al. (2013). Sox2 marks epithelial competence to generate teeth in mammals and reptiles. *Development* 140, 1424–1432. doi: 10.1242/dev.089599

Kakizaki, I., Kojima, K., Takagaki, K., Endo, M., Kannagi, R., Ito, M., et al. (2004). A novel mechanism for the inhibition of hyaluronan biosynthesis by 4-methylumbelliferone. *J. Biol. Chem.* 279, 33281–33289. doi: 10.1074/jbc.M405918200

Kavanagh, K. D., Evans, A. R., and Jernvall, J. (2007). Predicting evolutionary patterns of mammalian teeth from development. *Nature* 449, 427–432. doi: 10.1038/nature06153

Kessler, S. P., Obery, D. R., and de la Motte, C. (2015). Hyaluronan synthase 3 null mice exhibit decreased intestinal inflammation and tissue damage in the dss-induced colitis model. *Int. J. Cell Biol.* 2015:745237. doi: 10.1155/2015/745237

Kobayashi, N., Miyoshi, S., Mikami, T., Koyama, H., Kitazawa, M., Takeoka, M., et al. (2010). Hyaluronan deficiency in tumor stroma impairs macrophage trafficking and tumor neovascularization. *Cancer Res.* 70, 7073–7083. doi: 10.1158/0008-5472.CAN-09-4687

Kultti, A., Pasonen-Seppanen, S., Jauhiainen, M., Rilla, K. J., Karna, R., Pyoria, E., et al. (2009). 4-methylumbelliferone inhibits hyaluronan synthesis by depletion of cellular UDP-glucuronic acid and downregulation of hyaluronan synthase 2 and 3. *Exp. Cell Res.* 315, 1914–1923. doi: 10.1016/j.yexcr.2009.03.002

Kultti, A., Rilla, K., Tiihonen, R., Spicer, A. P., Tammi, R. H., and Tammi, M. I. (2006). Hyaluronan synthesis induces microvillus-like cell surface protrusions. *J. Biol. Chem.* 281, 15821–15828. doi: 10.1074/jbc.M512840200

Kultti, A., Zhao, C., Singha, N. C., Zimmerman, S., Osgood, R. J., Symons, R., et al. (2014). Accumulation of extracellular hyaluronan by hyaluronan synthase 3 promotes tumor growth and modulates the pancreatic cancer microenvironment. *Biomed. Res. Int.* 2014:817613. doi: 10.1155/2014/817613

Kuo, Y. Z., Fang, W. Y., Huang, C. C., Tsai, S. T., Wang, Y. C., Yang, C. L., et al. (2017). Hyaluronan synthase 3 mediated oncogenic action through forming inter-regulation loop with tumor necrosis factor alpha in oral cancer. *Oncotarget* 8, 15563–15583. doi: 10.18632/oncotarget.14697

Lau, E. C., and Ruch, J. V. (1983). Glycosaminoglycans in embryonic mouse teeth and the dissociated dental constituents. *Differentiation* 23, 234–242. doi: 10.1111/j.1432-0436.1982.tb01288.x

Lee, J. Y., and Spicer, A. P. (2000). Hyaluronan: a multifunctional, megadalton, stealth molecule. *Curr. Opin. Cell Biol.* 12, 581–586. doi: 10.1016/S0955-0674(00)00135-6

Lumsden, A. G. (1979). Pattern formation in the molar dentition of the mouse. *J. Biol. Buccale* 7, 77–103.

Misra, S., Heldin, P., Hascall, V. C., Karamanos, N. K., Skandalis, S. S., Markwald, R. R., et al. (2011). Hyaluronan-CD44 interactions as potential targets for cancer therapy. *FEBS J.* 278, 1429–1443. doi: 10.1111/j.1742-4658.2011.08071.x

Morita, T., Fujikawa, K., Baba, O., and Shibata, S. (2016). An in situ hybridization study of hyaluronan synthase (has) mRNA in developing mouse molar and incisor tooth germs. *Gene Expr. Patterns* 21, 28–40. doi: 10.1016/j.gep.2016.06.002

Nagase, H., Kudo, D., Suto, A., Yoshida, E., Suto, S., Negishi, M., et al. (2017). 4-methylumbelliferone suppresses hyaluronan synthesis and tumor progression in scid mice intra-abdominally inoculated with pancreatic cancer cells. *Pancreas* 46, 190–197. doi: 10.1097/MPA.0000000000000741

Nagy, N., Gurevich, I., Kuipers, H. F., Ruppert, S. M., Marshall, P. L., Xie, B. J., et al. (2019). 4-methylumbelliferyl glucuronide contributes to hyaluronan synthesis inhibition. *J. Biol. Chem.* 294, 7864–7877. doi: 10.1074/jbc.RA118.006166

Nakamura, H., and Ozawa, H. (1997). Immunolocalization of CD44 and the ezrin-radixin-moesin (erm) family in the stratum intermedium and papillary layer of the mouse enamel organ. *J. Histochem. Cytochem.* 45, 1481–1492. doi: 10.1177/002215549704501105

Nakamura, T., Takagaki, K., Shibata, S., Tanaka, K., Higuchi, T., and Endo, M. (1995). Hyaluronic-acid-deficient extracellular matrix induced by addition of 4-methylumbelliferone to the medium of cultured human skin fibroblasts. *Biochem. Biophys. Res. Commun.* 208, 470–475. doi: 10.1006/bbrc.1995.1362

Nanci, A. (ed.) (2017). *Ten cate's oral histology: Development, structure, and function*. *9th Edn*. Elsevier.

Ouyang, X., Panetta, N. J., Talbott, M. D., Payumo, A. Y., Halluin, C., Longaker, M. T., et al. (2017). Hyaluronic acid synthesis is required for zebrafish tail fin regeneration. *PLoS One* 12:e0171898. doi: 10.1371/journal.pone.0171898

Preston, M., and Sherman, L. S. (2011). Neural stem cell niches: roles for the hyaluronan-based extracellular matrix. *Front. Biosci. (Schol. Ed.)* 3, 1165–1179. doi: 10.2741/218

Pure, E., and Assoian, R. K. (2009). Rheostatic signaling by CD44 and hyaluronan. *Cell. Signal.* 21, 651–655. doi: 10.1016/j.cellsig.2009.01.024

Rilla, K., Pasonen-Seppanen, S., Karna, R., Karjalainen, H. M., and Torronen, K., Koistinen, V., et al. (2012). HAS3-induced accumulation of hyaluronan in 3d mdck cultures results in mitotic spindle misorientation and disturbed organization of epithelium. *Histochem. Cell Biol.* 137, 153–164. doi: 10.1007/s00418-011-0896-x

Rilla, K., Siiskonen, H., Spicer, A. P., Hyttinen, J. M., Tammi, M. I., and Tammi, R. H. (2005). Plasma membrane residence of hyaluronan synthase is coupled to its enzymatic activity. *J Biol Chem*. 280, 31890–31897. doi: 10.1074/jbc.M504736200

Saito, T., Dai, T., and Asano, R. (2013). The hyaluronan synthesis inhibitor 4-methylumbelliferone exhibits antitumor effects against mesenchymal-like canine mammary tumor cells. *Oncol. Lett.* 5, 1068–1074. doi: 10.3892/ol.2013.1124

Schepers, A. G., Snippert, H. J., Stange, D. E., van den Born, M., van Es, J. H., van de Wetering, M., et al. (2012). Lineage tracing reveals lgr5+ stem cell activity in mouse intestinal adenomas. *Science* 337, 730–735. doi: 10.1126/science.1224676

Senbanjo, L. T., and Chellaiah, M. A. (2017). CD44: a multifunctional cell surface adhesion receptor is a regulator of progression and metastasis of cancer cells. *Front. Cell Dev. Biol.* 5:18. doi: 10.3389/fcell.2017.00018

Silva, A. K., Richard, C., Bessodes, M., Scherman, D., and Merten, O. W. (2009). Growth factor delivery approaches in hydrogels. *Biomacromolecules* 10, 9–18. doi: 10.1021/bm801103c

Smith, M. M., Fraser, G. J., and Mitsiadis, T. A. (2009). Dental lamina as source of odontogenic stem cells: evolutionary origins and developmental control of tooth generation in gnathostomes. *J. Exp. Zool. B Mol. Dev. Evol.* 312B, 260–280. doi: 10.1002/jez.b.21272

Spicer, A. P., and Nguyen, T. K. (1999). Mammalian hyaluronan synthases: investigation of functional relationships in vivo. *Biochem. Soc. Trans.* 27, 109–115. doi: 10.1042/bst0270109

Spicer, A. P., and Tien, J. Y. (2004). Hyaluronan and morphogenesis. *Birth Defects Res. C Embryo Today* 72, 89–108. doi: 10.1002/bdrc.20006

Tammi, R. H., Passi, A. G., Rilla, K., Karousou, E., Vigetti, D., Makkonen, K., et al. (2011). Transcriptional and post-translational regulation of hyaluronan synthesis. *FEBS J.* 278, 1419–1428. doi: 10.1111/j.1742-4658.2011.08070.x

Tien, J. Y., and Spicer, A. P. (2005). Three vertebrate hyaluronan synthases are expressed during mouse development in distinct spatial and temporal patterns. *Dev. Dyn.* 233, 130–141. doi: 10.1002/dvdy.20328

Toole, B. P. (2001). Hyaluronan in morphogenesis. *Semin. Cell Dev. Biol.* 12, 79–87. doi: 10.1006/scdb.2000.0244

Tucker, A., and Sharpe, P. (2004). The cutting-edge of mammalian development; how the embryo makes teeth. *Nat. Rev. Genet.* 5, 499–508. doi: 10.1038/nrg1380

Vigetti, D., Viola, M., Karousou, E., De Luca, G., and Passi, A. (2014). Metabolic control of hyaluronan synthases. *Matrix Biol.* 35, 8–13. doi: 10.1016/j.matbio.2013.10.002

Walker, C., Mojares, E., and Del Rio Hernandez, A. (2018). Role of extracellular matrix in development and cancer progression. *Int. J. Mol. Sci.* 19:3028. doi: 10.3390/ijms19103028

Wang, Y., Lauer, M. E., Anand, S., Mack, J. A., and Maytin, E. V. (2014). Hyaluronan synthase 2 protects skin fibroblasts against apoptosis induced by environmental stress. *J. Biol. Chem.* 289, 32253–32265. doi: 10.1074/jbc.M114.578377

Wang, X. P., Suomalainen, M., Felszeghy, S., Zelarayan, L. C., Alonso, M. T., Plikus, M. V., et al. (2007). An integrated gene regulatory network controls stem cell proliferation in teeth. *PLoS Biol.* 5:e159. doi: 10.1371/journal.pbio.0050159

Wang, R., Zhou, W., Wang, J., Liu, Y., Chen, Y., Jiang, S., et al. (2015). Role of hyaluronan and glucose on 4-methylumbelliferone-inhibited cell proliferation in breast carcinoma cells. *Anticancer Res.* 35, 4799–4805.

Weigel, P. H. (2015). Hyaluronan synthase: the mechanism of initiation at the reducing end and a pendulum model for polysaccharide translocation to the cell exterior. *Int. J. Cell Biol.* 2015:367579. doi: 10.1155/2015/367579

Yang, G., Jiang, B., Cai, W., Liu, S., and Zhao, S. (2016). Hyaluronan and hyaluronan synthases expression and localization in embryonic mouse molars. *J. Mol. Histol.* 47, 413–420. doi: 10.1007/s10735-016-9684-1

Conflict of Interest: The authors declare that the research was conducted in the absence of any commercial or financial relationships that could be construed as a potential conflict of interest.

frontiers in Physiology

ORIGINAL RESEARCH
published: 03 September 2020
doi: 10.3389/fphys.2020.01010

Expression Profiles of CircRNA and mRNA in Lacrimal Glands of AQP5$^{-/-}$ Mice With Primary Dry Eye

*Yaning Liu†, Guohu Di†, Shaohua Hu, Tianyu Zhao, Xinkai Xu, Xiaoyi Wang and Peng Chen**

Department of Human Anatomy, Histology and Embryology, School of Basic Medicine, Qingdao University, Qingdao, China

Purpose: This work aimed to identify differentially expressed circular RNAs (circRNAs) and elucidate their potential function in aquaporin 5 (AQP5) knockout (AQP5$^{-/-}$) mice with the primary dry eye phenotype.

Methods: A slit lamp examination was performed on AQP5$^{-/-}$ mice to assess corneal epithelial defects using fluorescein sodium staining. Hematoxylin–eosin staining and transmission electron microscopy analysis were performed to identify structural changes in lacrimal gland epithelial cells due to AQP5 deficiency. The expression profiles of circRNA and messenger RNA (mRNA) were determined by a microarray analysis. The selected circRNA was verified by quantitative real-time reverse transcription-polymerase chain reaction (qRT-PCR). Gene Ontology and Kyoto Encyclopedia of Genes and Genomes (KEGG) pathway enrichment analyses were performed to predict the biological functions and the potential pathways of parental genes involved in lacrimal gland epithelial cell changes. According to the bioinformatics analysis of identified circRNAs, we predicted a circRNA–miRNA–mRNA network of phagosomes.

Results: The AQP5$^{-/-}$ mice spontaneously exhibit dry eye symptoms, wherein the AQP5 deficiency changes the structure of lacrimal gland epithelial cells. The analysis revealed that, compared to AQP5$^{+/+}$ mice, 30 circRNAs in the lacrimal glands of AQP5$^{-/-}$ mice were differentially expressed (fold change $\geq$ 2.0, $p < 0.05$). Nine upregulated circRNAs were identified using qRT-PCR, and nine upregulated validated circRNAs, 40 altered microRNAs (miRNAs), and nine upregulated mRNAs were identified through a network analysis. The KEGG analysis showed that these nine target genes were expressed in phagosomes.

Conclusion: The AQP5$^{-/-}$ mice have primary and stable dry eye phenotypes from birth. We identified differently expressed circRNAs in the lacrimal glands of AQP5$^{-/-}$ and AQP5$^{+/+}$ mice, predicting a circRNA–miRNA–mRNA network of phagosomes. CircRNA likely plays an important role in lacrimal gland epithelial cell pathogenesis. Therefore, it is reasonable to use circRNA as a potential therapeutic agent for the treatment of dry eyes.

Keywords: AQP5, lacrimal gland, dry eye, circRNA, miRNA, mRNA

OPEN ACCESS

Edited by:
Maisa Hanna-Maija Seppala, King's College London, United Kingdom

Reviewed by:
Zhi Chen, Wuhan University, China
Harald Osmundsen, University of Oslo, Norway

****Correspondence:***
Peng Chen
chenpeng599205@126.com

† These authors have contributed equally to this work

Specialty section:
This article was submitted to Craniofacial Biology and Dental Research, a section of the journal Frontiers in Physiology

Received: *11 March 2020*
Accepted: *24 July 2020*
Published: *03 September 2020*

Citation:
Liu Y, Di G, Hu S, Zhao T, Xu X, Wang X and Chen P (2020) Expression Profiles of CircRNA and mRNA in Lacrimal Glands of AQP5$^{-/-}$ Mice With Primary Dry Eye. Front. Physiol. 11:1010. doi: 10.3389/fphys.2020.01010

INTRODUCTION

Dry eye is currently the most common eye disease except for ametropia, with a worldwide incidence of 5–34% (Messmer, 2015). The main pathophysiological mechanisms are tear film instability, increased tear permeability, ocular surface inflammation and injury, and neurosensory abnormalities (Craig et al., 2017). The current treatment strategies for dry eye include the use of artificial tears, administration of anti-inflammatory drugs, and surgery (Lemp and Foulks, 2007). However, the incidence of dry eye is still rising, emphasizing the urgent need to determine its pathogenesis and to develop effective treatment measures.

Aquaporin 5 (AQP5), a kind of aquaporin, is highly expressed in the corneal epithelium and lacrimal glands and is closely related to eye diseases (Raina et al., 1995; Takata et al., 2004). Compared with $AQP5^{+/+}$ mice, the lenses of $AQP5^{-/-}$ mice *in vitro* appear to be slightly turbid at high glucose concentrations, suggesting that AQP5 might maintain crystal transparency by regulating osmotic pressure (Sindhu Kumari and Varadaraj, 2013). AQP5 has also been shown to reduce saliva and airway mucus secretions and increase corneal thickness in experimental animals (Ma et al., 1999; Thiagarajah and Verkman, 2002). In addition, lack of AQP5 affects the migration and the proliferation of cells, leading to slow corneal healing (Kumari et al., 2018). One of the symptoms of dry eye is an epithelial defect in the cornea (Levin and Verkman, 2006). A previous study considered AQP5 level as an index of dry eye (Lin et al., 2019), and the occurrence of dry eye is believed to be accompanied by a decrease in AQP5 level. However, whether AQP5 deficiency can cause dry eye has not been proved yet.

Circular RNA (circRNA), as a specific and specific non-coding RNA, has a closed circular structure and is more stable than long non-coding RNAs (Jiang et al., 2018). A recent study has shown that circRNA molecules are rich in microRNA (miRNA) binding sites, which play the role of an miRNA sponge in cells, thus relieving the inhibition of miRNA on its target genes and increasing the expression levels of those target genes (Kulcheski et al., 2016). CircRNA might be a biomarker for primary Sjögren's syndrome, correlating with the primary Sjögren's syndrome etiology such as has-circRNA-001264, has-circRNA-104121, and has-circRNA-045355 (Su et al., 2019). Meanwhile, miR-146a and miR-155 have also been reported to be related to dry eye (Shi et al., 2014). Therefore, the expression and the clinical significance of circRNA in dry eye need to be studied.

In this study, we used aquaporin 5 knockout ($AQP5^{-/-}$) mice that exhibit dry eye characteristics and performed hematoxylin–eosin staining to determine structural changes in the lacrimal glands of these mice. We found that the lacrimal glands of $AQP5^{-/-}$ mice exhibited abnormal changes compared with those of $AQP5^{+/+}$ mice. The differential expression of circRNA was also found by high-throughput sequencing, and a circRNA–miRNA–mRNA network related to phagosomes was predicted. These data suggest that the lack of AQP5 may cause a differential expression of circRNA, which may, in turn, lead to the development of primary dry eye.

Abbreviations: AGO2, argonauute 2; AQP5, aquaporin 5; circRNA, circular RNA; GAPDH, glyceraldehyde 3-phosphate dehydrogenase; GO, Gene Ontology; KEGG, Kyoto Encyclopedia of Genes and Genomes; miRNA, microRNA; mRNA, messenger RNA; nt, nucleotides; qRT-PCR, quantitative real-time polymerase chain reaction; rRNAs, ribosomal RNA; RIP, RNA immunoprecipitation; SD, standard deviation.

MATERIALS AND METHODS

Animals

Using CRISPR/Cas9 technology, $AQP5^{-/-}$ mice were produced by the high-flux electric transfer of fertilized eggs from Cyagen Biosciences Inc. (Guangzhou, China). We used age-matched $AQP5^{+/+}$ and $AQP5^{-/-}$ mice for our study. All experimental and animal care procedures were followed according to the ARVO Statement for the Use of Animals in Ophthalmic and Vision Research, and the study was approved by the Animal Care and Use Committee of Qingdao University (Qingdao, China). Spontaneous defects of the corneal epithelium were visualized by instilling 0.25% fluorescein sodium and photographing under a slit lamp (66 Vision Tech. Co., Ltd., Suzhou, China).

Tear production was examined using the phenol red thread (Jingming) test as described previously (Stevenson et al., 2014). In brief, the thread was placed on the palpebral conjunctiva of the lower eyelid at one-third of the distance from the lateral canthus for 20 s. The length of the wet portion was measured in millimeters.

Hematoxylin–Eosin Staining and Transmission Electron Microscopy

$AQP5^{+/+}$ and $AQP5^{-/-}$ mice were sacrificed by cervical dislocation, and the lacrimal glands were removed for further use. The lacrimal glands were fixed in 10% buffered formalin and embedded in paraffin. Paraffin sections (4 μm) were produced using paraffin-embedded tissues. The sections were stained with hematoxylin–eosin and observed under a light microscope (Nikon Eclipse E100, Nikon, Japan). Samples of approximately 1 mm^3 were dissected from the lacrimal glands and subsequently fixed with electron microscope fixation fluid (Servicebio, G1102), post-fixed with 1% osmic acid in 0.1 mol/L phosphate buffer, dehydrated in a graded series of ethanol, and embedded in embedding agent (SPI, 90529-77-4). The specimens were cut into 60–80 nm sections by using an ultrathin microtome (Leica UC7, Leica). The sections were double-stained with uranium and lead and observed under a transmission electron microscope (HITACHI, HT7700).

Extraction and Separation of RNA Samples

According to the manufacturer's instructions (Lu et al., 2018), Trizol (Invitrogen, Carlsbad, CA, United States) was used to extract RNA from the lacrimal glands of both $AQP5^{+/+}$ and $AQP5^{-/-}$ mice, and the optical density ($OD_{260/280}$) value was determined by using a NanoDrop ND-2000 instrument (Thermo Fisher Scientific, Waltham, MA, United States) to measure the

RNA concentration. RNA integrity was determined by agarose gel electrophoresis.

High-Throughput Sequencing

High-throughput transcriptome sequencing and bioinformatics analysis were performed using Cloud-Seq Biotech (Shanghai, China). Specifically, total RNA was treated with a Ribo-Zero rRNA Removal kit (Illumina, San Diego, CA, United States) to remove ribosomal RNA (rRNA). An RNA library was constructed according to the manufacturer's instructions using the purified RNA samples and the TruSeq Stranded Total RNA Library Prep kit (Illumina, San Diego, CA, United States). The BioAnalyzer 2100 system was used for ensuring quality control and library quantification. Then, 10-pM libraries were denatured into single-stranded DNA molecules, captured on Illumina flow cells, amplified *in situ*, and clustered, and finally, 150 cycles of sequencing were performed on the Illumina HiSeq sequencer according to the manufacturer's instructions (Lu et al., 2018).

CircRNA Sequencing Analysis

The paired terminal readings were obtained from the Illumina HiSeq 4000 sequencer, and quality control was performed through Q30. High-quality reads were primarily screened by Cutadapt software (version 1.9.3) (Martin, 2011), and after performing 3′ adapter trimming, low-quality reads were removed. We used STAR software (version 2.5.1b) (Dobin et al., 2013) to map and align high-quality reads with the reference genome/transcriptome. Next, we selected some nucleotide sequences from the reads as anchor points and input the results into the DCC software (version 0.4.4) (Cheng et al., 2016) that eventually compared connected and unconnected reads to identify possible circRNAs. We used EdgeR software (version 3.16.5) (Robinson et al., 2010) to normalize the data and analyze the differential expression of the identified circRNAs.

Analysis of Differential CircRNAs and mRNAs

The differential expression of circRNAs and mRNAs between the $AQP5^{+/+}$ and the $AQP5^{-/-}$ mice groups was calculated using standardized readings. CircRNAs and mRNAs with a fold change of $\geq$2.0 and a $p < 0.05$ were considered to indicate a differential expression that was statistically significant.

Validation of Differentially Expressed CircRNAs, miRNAs, and mRNAs

The reliability of high-throughput RNA sequencing was verified by quantitative real-time reverse transcription-polymerase chain reaction (qRT-PCR). Among all the identified differentially expressed circRNAs and miRNAs, nine upregulated circRNAs and six upregulated mRNAs were selected for validation. Glyceraldehyde-3-phosphate dehydrogenase was used as a reference for standardization. Among all the identified differentially expressed miRNAs, four downregulated miRNAs were selected for validation. U6 was used as a reference for standardization. Total RNA was reverse-transcribed into complementary DNA using the PrimeScript RT kit (Perfect Real Time; Takara, Osaka, Japan), and qRT-PCR was performed using the Applied Biosystems 7500 Fast Real-Time PCR system. Three independent experiments were performed on all samples. The expression was determined using a threshold cycle, and the relative expression level was calculated using the $2^{-\Delta\Delta CT}$ method. The primers used for all the selected circRNAs are specified in **Table 1**. The primers for all the selected mRNAs are specified in **Table 2**. The primers used for miRNA reverse transcription are specified in **Table 3**. The primers for all the selected miRNAs used in qRT-PCR are specified in **Table 4**.

GO and KEGG Pathway Analyses

GO and KEGG were used to analyze genes related to differentially expressed circRNAs and mRNAs. GO analysis is divided into

TABLE 1 | The primers used in qRT-PCR.

Gene	Primer type	Primer sequence
chr5:147450653-147455188 +	Forward	CTTCGGTGCCCTCAACATCT
	Reverse	GGACTCTGTGAGACTCGCATC
chr6:143180587-143197565 +	Forward	AGGGCTTTGGCAGTGATGTC
	Reverse	TAGCAGGCGATGAGCTTGTT
chr9:3441055-3460131 +	Forward	TGGAATCTGATGAAGAATGGTCC
	Reverse	TGGCCCCCAACTTGTTCTTT
chr2:18284623-18294044-	Forward	TGACTGGCTGGAAAACAGGA
	Reverse	TCTAGCCAGTGCGTCTTCTT
chr5:90298540-90304065-	Forward	CGCTTGTTCTGCTGGGTACT
	Reverse	CAGCAGTGCCTGATAGAAGC
chr19:4342847-4394892-	Forward	GCCACTGCACAAGAAGTGTG
	Reverse	AGAAACCACTCCAGGGATGC
chr10:82492146-82492319-	Forward	CTGATTTTGCAGCCAATACACG
	Reverse	TCATTAGGGTCTGCAGTGGTT
chr14:74807474-74835775-	Forward	AGGACCAGGCAGAAGACTGT
	Reverse	GAGAGGCAGACCACACAGG
chr6:8537817-8582790 +	Forward	TCCCAGGATGGAAGTCCTTG
	Reverse	CCAGAGAAGAGGTTCGCCTT
GAPDH	Forward	AAGGTCATCCCAGAGCTGAA
	Reverse	CTGCTTCACCACCTTCTTGA

TABLE 2 | The primers used in qRT-PCR.

Gene	Primer type	Primer sequence
5430435G22Rik	Forward	GCTGCATTCCATTCCCTGAG
	Reverse	CCCTAGTGGCCAGTCATCAA
Rilp	Forward	CAGTGAGGATGAGGATGGCT
	Reverse	TCACCCCGATACCATAAGCC
Thbs1	Forward	TCTTCCTGGCTTCCTTGAGG
	Reverse	CTGGCCAGTGTTGTCTTTCC
Ncf1	Forward	GAAGACAAAGCGAGGTTGGG
	Reverse	TTCACCTGCGTAGTTGGGAT
Msr1	Forward	GAAAAGGGAGACAGAGGGCT
	Reverse	CCAGGGAAGCCAATTTGTCC
Tubb6	Forward	CAGCAGACCAGGGAGATCTC
	Reverse	AACTCTGATGGGGTGGGAAG
GAPDH	Forward	AAGGTCATCCCAGAGCTGAA
	Reverse	CTGCTTCACCACCTTCTTGA

TABLE 3 | The RT primers of miRNA used in reverse transcription.

Gene	Primer sequence
miR-135b-5p	GTCGTATCCAGTGCGTGTCGTGGAGTCGG CAATTGCACTGGATACGACTCACAT
miR-320-3p	GTCGTATCCAGTGCGTGTCGTGGAGTCGG CAATTGCACTGGATACGACTCGCCC
miR-135a-5p	GTCGTATCCAGTGCGTGTCGTGGAGTCG GCAATTGCACTGGATACGACTCACAT
miR-8104	GTCGTATCCAGTGCGTGTCGTGGAGTCGGCA ATTGCACTGGATACGACCGCTGC
miR-1950	GTCGTATCCAGTGCGTGTCGTGGAGTCGGCA ATTGCACTGGATACGACTGACCA
miR-3473f	GTCGTATCCAGTGCGTGTCGTGGAGTCGGC AATTGCACTGGATACGACCATCTC
miR-125a-3p	GTCGTATCCAGTGCGTGTCGTGGAGTCG GCAATTGCACTGGATACGACGGCTCC
U6	AACGCTTCACGAATTTGCGT

TABLE 4 | The primers used in qRT-PCR.

Gene	Primer type	Primer sequence
miR-135b-5p	Forward	GGGTATGGCTTTTCATTCCT
	Reverse	CAGTGCGTGTCGTGGAGT
miR-320-3p	Forward	GGGAAAAGCTGGGTTGAGA
	Reverse	CAGTGCGTGTCGTGGAGT
miR-135a-5p	Forward	GGGTATGGCTTTTTATTCCT
	Reverse	CAGTGCGTGTCGTGGAGT
miR-8104	Forward	GGGCAGGATGAGGTGGAGT
	Reverse	CAGTGCGTGTCGTGGAGT
miR-1950	Forward	GGGTCTGCATCTAAGGATA
	Reverse	CAGTGCGTGTCGTGGAGT
miR-3473f	Forward	GGGCAAATAGGACTGGA
	Reverse	CAGTGCGTGTCGTGGAGT
miR-125a-3p	Forward	GGGACAGGTGAGGTTCTTG
	Reverse	CAGTGCGTGTCGTGGAGT
U6	Forward	CTCGCTTCGGCAGCACA
	Reverse	AACGCTTCACGAATTTGCGT

three aspects: molecular function, biological process, and cell composition. We ranked the top 10 enriched GO terms according to the *p*-value. KEGG pathway analysis was used to analyze the possible biological functions of differentially expressed circRNA and mRNA.

Analysis of the CircRNA–miRNA–mRNA Network and Related Prediction

The miRNA binding sites and target mRNAs were predicted using proprietary software based on TargetScan (version 7.0) and MiRanda (version 3.3a). Based on the prediction results, we used the Cycloscape software (version 3.1.0) to construct a network map of circRNA–miRNA–mRNA.

RNA Immunoprecipitation–qPCR

RNA immunoprecipitation (RIP) analysis was performed using the EZ-Magna RIP RNA binding protein immunoprecipitation kit (Millipore, Billerica, MA, United States) and the RIP protocol. The lacrimal glands of $AQP5^{+/+}$ mice were cleaved and incubated with RIP buffer containing magnetic beads of anti-AGO2 antibody and immunoglobulin G (IgG, Abcam) as a negative control. To analyze the enrichment of circRNAs and mRNAs, qRT-PCR was performed to analyze the extracted RNA. The primers used for all the selected circRNAs and mRNAs are specified in **Tables 1**, **2**.

Data Analysis

The results were expressed as mean ± standard deviation (*SD*). All the experimental data were analyzed by GraphPad Prism 7.0 (GraphPad Software Inc., La Jolla, CA, United States). A $p < 0.05$ was considered as statistically significant. The data are representative of at least three experiments.

RESULTS

Dry-Eye-Like Characteristics Found in $AQP5^{-/-}$ Mice

In the course of our routine breeding of $AQP5^{-/-}$ mice, we found that these mice exhibited spontaneous dry eye symptoms. Under a slit lamp, a spontaneous punctate epithelial defect in the cornea of these mice could be observed (**Figure 1A**). Then, we used a phenol red cotton thread to measure tears in $AQP5^{-/-}$ mice by using $AQP5^{+/+}$ mice as control. The tear volume of $AQP5^{-/-}$ mice was significantly lesser than that of $AQP5^{+/+}$ mice (**Figure 1B**). However, there was no difference between the tear volume produced by male and female $AQP5^{-/-}$ mice (**Figure 1C**).

AQP5 Deficiency Changed the Structure of Epithelial Cells in Lacrimal Glands

Hematoxylin–eosin staining revealed that there were more vacuoles in the epithelial cells of the lacrimal glands of $AQP5^{-/-}$ mice than in those of $AQP5^{+/+}$ mice, and the arrangement of the acini was disordered in $AQP5^{-/-}$ mice than in $AQP5^{+/+}$ mice (**Figure 2A**). The specific observations in $AQP5^{-/-}$ mice were as follows: the number of acini decreased (**Figure 2BI**), the area of single acinus increased (**Figure 2BII**), and the number of epithelial cells decreased (**Figure 2BIII**), and at the same time, the number and the proportion of vacuoles in lacrimal gland epithelial cells per unit area increased significantly (**Figures 2BIV,V**).

To further study the structural changes in the epithelial cells of lacrimal glands, the lacrimal glands of both groups of mice were subjected to electron microscopy analysis. The results showed that compared with the epithelial cells of $AQP5^{+/+}$ mice, those of $AQP5^{-/-}$ mice were seriously damaged, the mitochondria were swollen and enlarged, a large number of mitochondrial cristae had disappeared, the membrane had disintegrated, some secretory granules were dissolved, the secretory granules were fused, the levels of autophagy bodies increased, the cell gap was enlarged, and the endoplasmic reticulum around the cell membrane had expanded (**Figure 2C**).

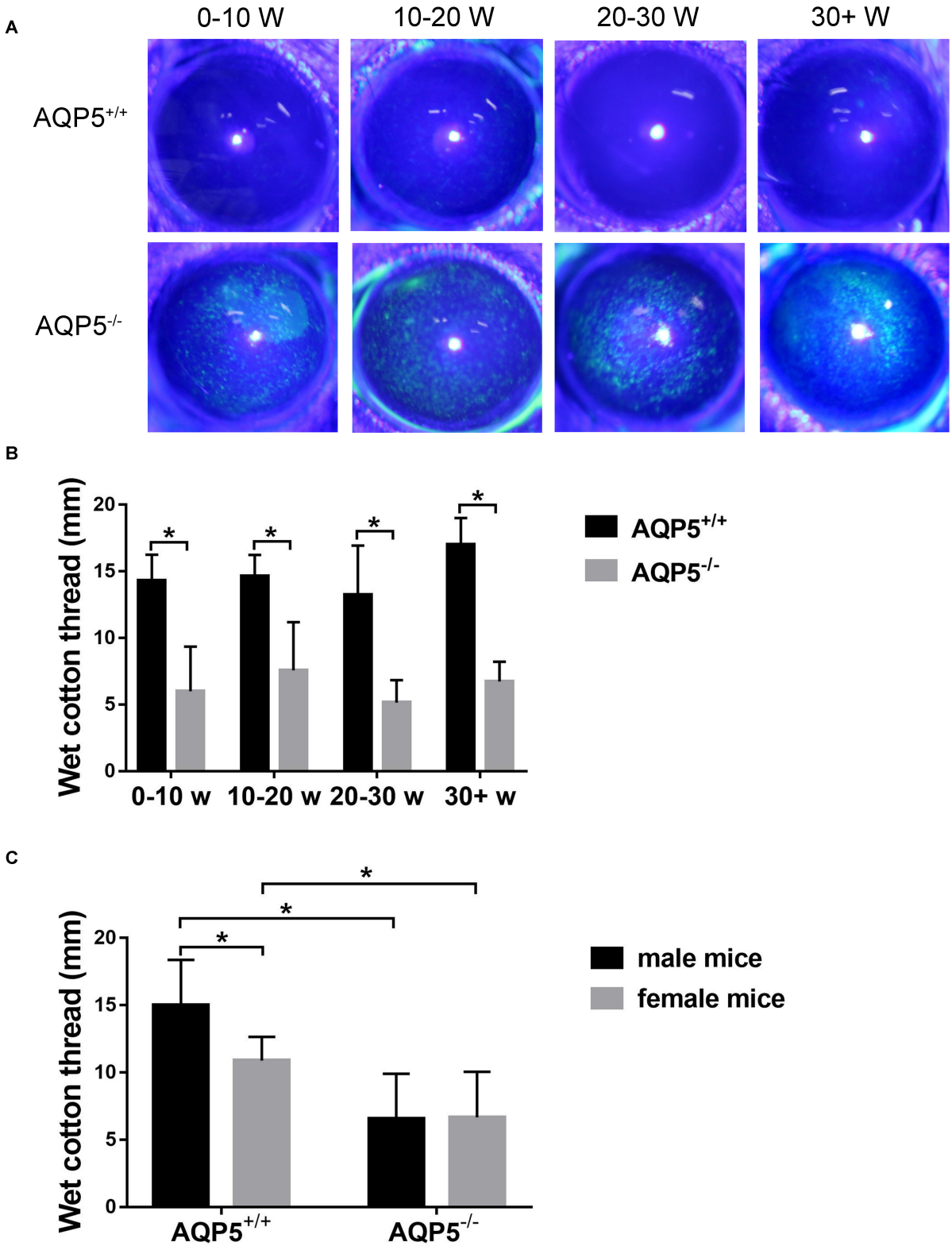

FIGURE 1 | Effect of AQP5 knockout on the tear secretion of mice. **(A)** The results of sodium fluorescein staining in the cornea of AQP5$^{+/+}$ mice and AQP5$^{-/-}$ mice at different ages. The staining point was a corneal defect. **(B,C)** The lacrimal secretion of AQP5$^{+/+}$ mice and AQP5$^{-/-}$ mice was measured using the phenol red cotton thread method. The wet length of phenol red cotton thread in mice of different ages **(B)** and genders **(C)**. The data are expressed as mean ± *SD* (n = 14 per group). *$p < 0.05$.

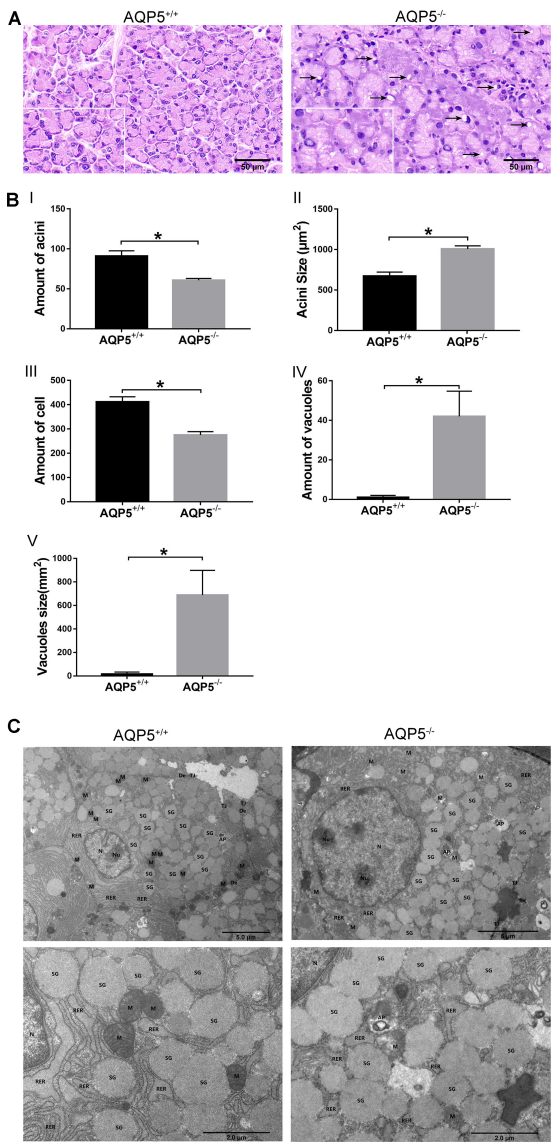

FIGURE 2 | Structural changes of lacrimal glands in AQP5$^{-/-}$ mice compared to AQP5$^{+/+}$ mice. **(A)** Hematoxylin–eosin staining of lacrimal glands from AQP5$^{+/+}$ mice and AQP5$^{-/-}$ mice. Arrows indicate vacuoles inside the cytoplasm of AQP5$^{-/-}$ acinar cells. **(B)** The number (I) and the area of single acini (II) in the unit area, the number of lacrimal gland epithelial cells in the unit area (III), and the number (IV) and area of vacuoles (V) in the unit area were compared between AQP5$^{-/-}$and AQP5$^{+/+}$mice. The data are expressed as mean ± *SD* (n = 6 per group). *$p < 0.05$. **(C)** Transmission electron microscopy of lacrimal glands from AQP5$^{+/+}$ mice and AQP5$^{-/-}$ mice. N, nuclei; Nu, nucleolus; M, mitochondrion; RER, rough endoplasmic reticulum; SG, secretory granule; TJ, tight junction; DE, desmosome; AP, autophagosome; triangles, intercellular space.

Overview of CircRNA Expression in Lacrimal Glands

To study the effect of AQP5 deficiency on lacrimal gland performance, we obtained lacrimal glands from AQP5$^{-/-}$ and AQP5$^{+/+}$ mice and sequenced their RNA with high throughput to determine the expression profile of circRNA in the glands. A total of 2,541 circRNAs were identified in the lacrimal glands of the two groups, 937 of which have not been reported before (**Figure 3A**).

Most circRNAs were located on chromosomes 1–19 (**Figure 3B**). There was a variety of catalogs of circRNAs, and most of them were exonic circRNAs (**Figure 3C**). The size of these circRNAs ranged from 82 nucleotides (nt) to more than 10,000 nt (**Figure 3D**). The overall average length was 2,824 nt.

Differential Expression of CircRNAs in the Lacrimal Glands of AQP5$^{-/-}$ and AQP5$^{+/+}$ Mice

Among the 2,541 identified circRNAs, 920 could only be detected in AQP5$^{+/+}$ mice, 948 could only be detected in AQP5$^{-/-}$ mice, and 673 could be detected in both types of mice (**Figure 4A**). Thirty circRNAs were differentially expressed in AQP5$^{-/-}$ mice compared to AQP5$^{+/+}$ mice, wherein nine of them were upregulated, while 21 were downregulated. Hierarchical clustering showed a distinguishable circRNA expression profile between AQP5$^{-/-}$ and AQP5$^{+/+}$ mice (**Figure 4B**).

To verify the high-throughput sequencing results, quantitative real-time polymerase chain reaction was performed for the nine upregulated circRNAs. The relative expression level of the nine circRNAs was consistent with that determined by high-throughput sequencing (**Figure 4C**).

Function of Differentially Expressed CircRNAs in the Lacrimal Glands of AQP5$^{-/-}$ and AQP5$^{+/+}$ Mice

To preferably understand the biological function of the differentially expressed circRNAs present in the lacrimal glands of AQP5$^{-/-}$ mice, we performed Gene Ontology (GO) and Kyoto Encyclopedia of Genes and Genomes (KEGG) pathway enrichment analyses. The GO terms mainly covered three areas: biological processes, cellular components, and molecular functions. We found that the most abundant GO terms in the upregulated circRNAs were RNA phosphodiester in the endoplasmic reticulum, cell surface furrow, and ribonuclease activity. According to the KEGG analysis, the pathway related to the upregulation of circRNAs was protein processing in the endoplasmic reticulum (**Figure 5A**).

In the downregulated circRNAs, the most abundant GO terms were positive regulation of cellular process, nuclear part, and high-voltage-gated calcium channel activity. The most relevant pathway of these circRNAs was the synaptic vesicle cycle (**Figure 5B**).

Differential Expression of mRNAs in the Lacrimal Glands of AQP5$^{-/-}$ and AQP5$^{+/+}$ Mice

By high-throughput analysis, 15,243 messenger RNAs (mRNAs) were detected in the lacrimal glands of both AQP5$^{-/-}$ and AQP5$^{+/+}$ mice. Among these mRNAs, 549 could only be detected in AQP5$^{+/+}$ mice, 325 could only be detected in

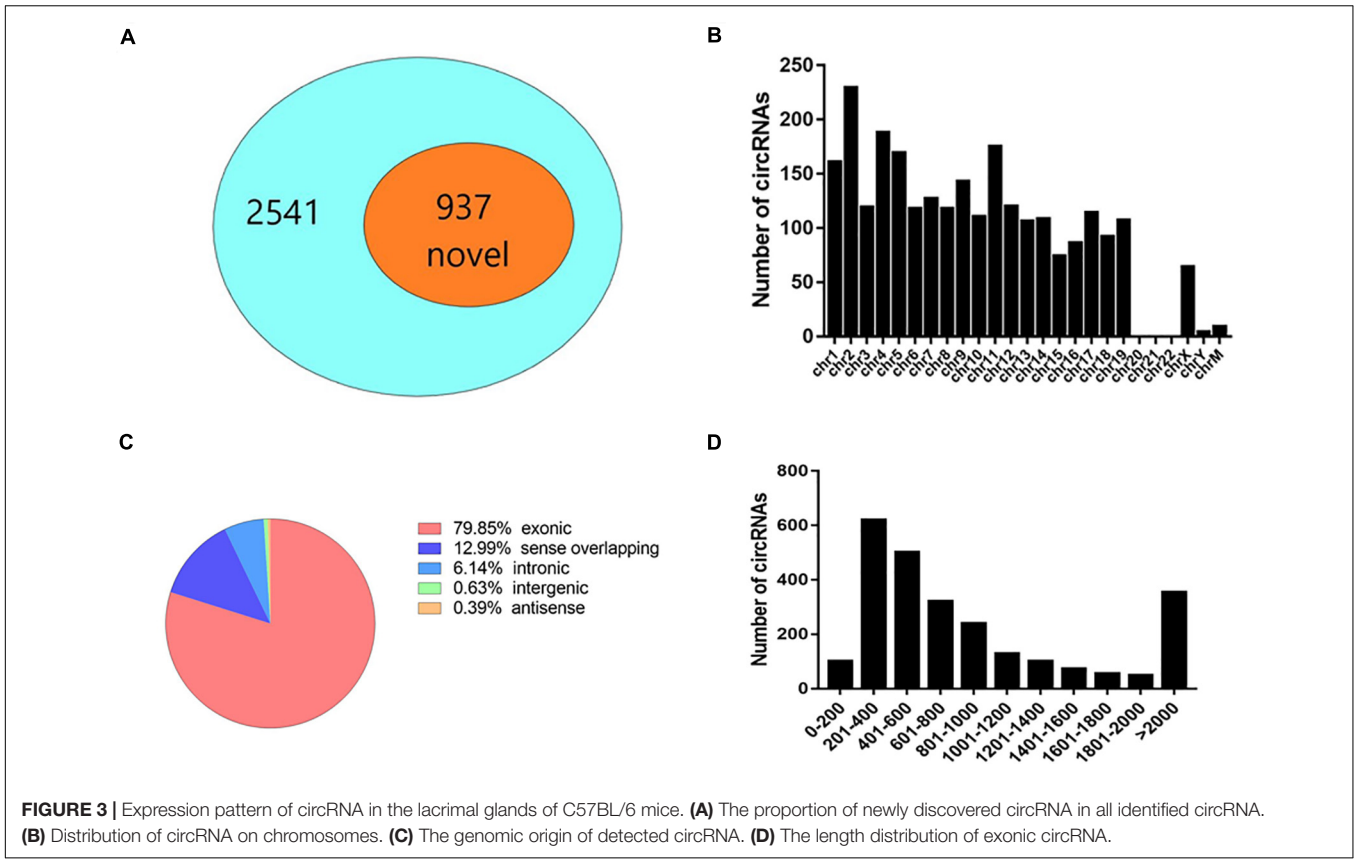

FIGURE 3 | Expression pattern of circRNA in the lacrimal glands of C57BL/6 mice. **(A)** The proportion of newly discovered circRNA in all identified circRNA. **(B)** Distribution of circRNA on chromosomes. **(C)** The genomic origin of detected circRNA. **(D)** The length distribution of exonic circRNA.

$AQP5^{-/-}$ mice, and 14,369 could be detected in both types of mice (**Figure 6A**). Compared to the mRNAs found in $AQP5^{+/+}$ mice, 515 mRNAs were differentially expressed in $AQP5^{-/-}$ mice, wherein 229 were upregulated and 286 were downregulated. Hierarchical clustering showed a distinguishable mRNA expression profile between $AQP5^{-/-}$ and $AQP5^{+/+}$ mice (**Figure 6B**).

To verify the high-throughput sequencing results, qRT-PCR was performed for the six upregulated mRNAs and four downregulated miRNAs. The relative expression levels of the six mRNAs (**Figure 6C**) and the four miRNAs (**Figure 6D**) were consistent with the sequencing results.

Function of Differentially Expressed mRNAs in the Lacrimal Glands of $AQP5^{-/-}$ and $AQP5^{+/+}$ Mice

We also performed GO and KEGG pathway analyses on the differentially expressed mRNAs to determine their biological function in the lacrimal glands of $AQP5^{-/-}$ mice. We found that the most abundant GO terms for the upregulated mRNAs were response to external stimulus, extracellular space, and glycosaminoglycan binding. According to the KEGG analysis, the pathway related to circRNA upregulation was phagosome (**Figure 7A**).

For the downregulated mRNAs, the most abundant GO terms were single-organism process, intracellular part, and metal ion binding. The most relevant pathway pertaining to the downregulated mRNAs was vitamin B6 metabolism (**Figure 7B**).

CircRNA–miRNA–mRNA Network Analysis

To further determine the mechanism(s) underlying the functions of the identified circRNAs, we constructed a ceRNA regulatory network of circRNA–miRNA–mRNA. We targeted miRNAs and mRNAs using miRNA target prediction software according to TargetScan and miRanda. The top five miRNAs associated with each circRNA were involved in the network. All the targeted mRNAs of each of the top five miRNAs matched with the upregulated mRNAs that were identified by mRNA sequencing.

The network was constructed by using nine upregulated validated circRNAs, 40 altered miRNAs, and nine upregulated mRNAs (**Figure 8**). In this complex network, one circRNA can associate with multiple miRNAs and one miRNA can regulate multiple mRNAs. According to the comparison with the database, these nine mRNAs and phagosome pathways are also closely related.

To further study the function of the previously identified circRNAs and verify the reliability of the predicted network of circRNA–miRNA–mRNA, RIP-qPCR was performed. As shown in **Figure 8**, compared with the IgG group (control), chr5:147450653-147455188 + (**Figure 8BI**) and chr9:3441055-3460131 + (**Figure 8BII**) can combine with the AGO2–miRNA complex, suggesting that chr5:147450653-147455188 + and

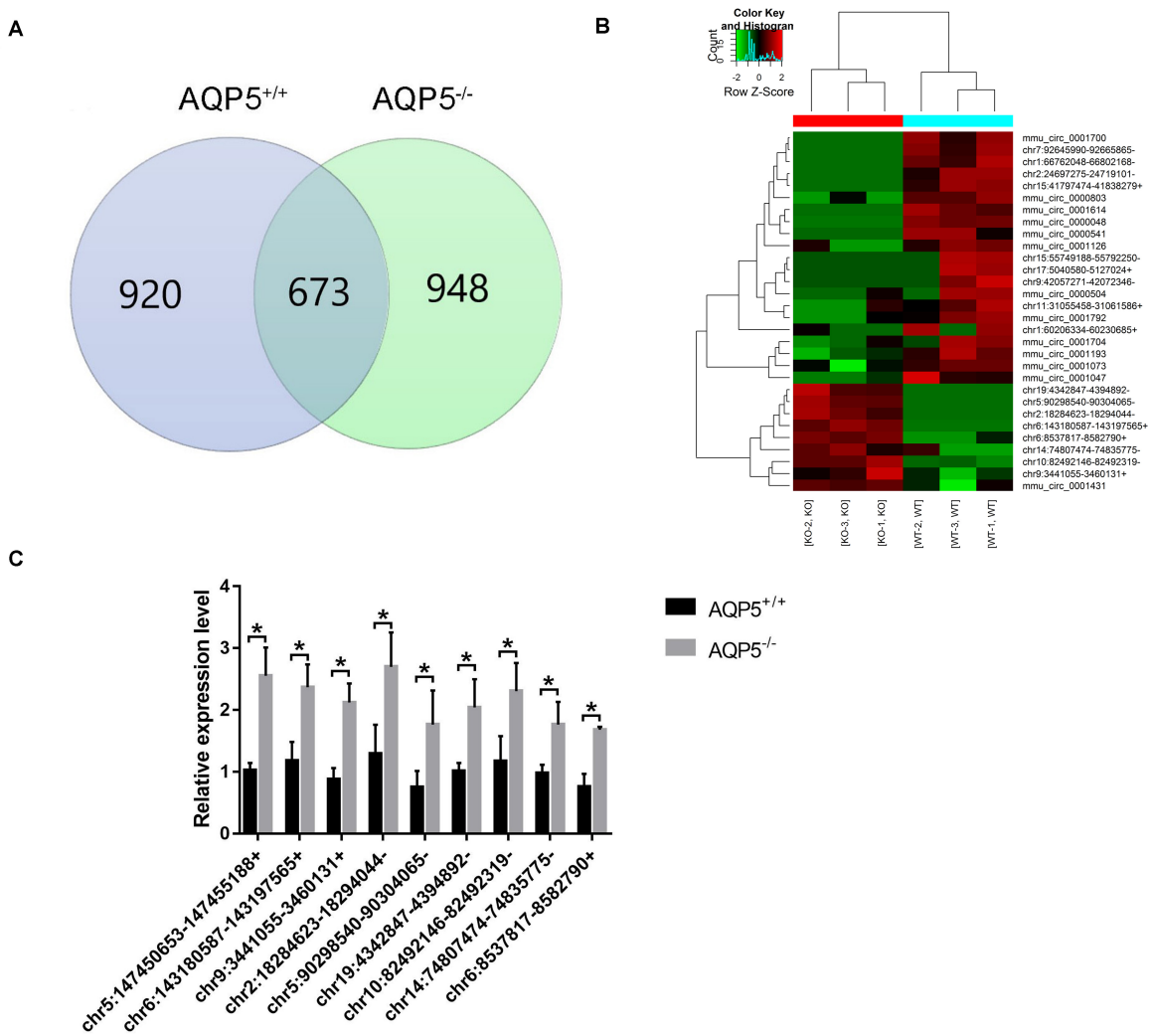

FIGURE 4 | Identification of differential expression circRNA after AQP5 knockout. **(A)** Venn diagram of differentially expressed circRNA; 673 circRNAs were detected in both mice. **(B)** Clustering graph. Hierarchical clustering displayed the circRNA expression profile of AQP5$^{+/+}$ mice (n = 3) vs. AQP5$^{+/+}$ mice (n = 3). **(C)** The expression of nine upregulated circRNAs in AQP5$^{+/+}$and AQP5$^{+/+}$ mice was detected by real-time fluorescence quantitative PCR. *$p < 0.05$.

chr9:3441055-3460131 + can combine with miRNA through a sponge mechanism. In addition, compared with the IgG group (control), 5430435G22Rik (**Figure 8BIII**) and Thbs1 (**Figure 8BIV**), identified in the previously predicted network graph, could also be detected, which indicates that our prediction is reliable.

DISCUSSION

Dry eye is a common chronic ocular surface disease caused by many factors such as reduced tear film stability, increase in tear osmolality, and ocular surface inflammation (Nelson et al., 2017). With changes in people's working environments and living habits, the incidence of dry eye is increasing annually, but there are few effective drugs to treat it. This lack of effective drugs is mainly related to the diverse physiological symptoms associated with dry eye in humans and the lack of corresponding animal models for studying these diverse symptoms in detail.

Previous studies have used animal models of dry eye by administering drugs to inhibit the secretion of tears or by removing the lacrimal or Harderian glands of mice (Gilbard et al., 1987; Viau et al., 2008; Fakih et al., 2019). However, these methods are too complex and cumbersome, the efficiency of the models is not stable, and the damage to the mice is greater. Therefore, selecting a simpler and more stable animal model of dry eye for studying its pathogenesis and for treatment drug screening is particularly important. In this study, we found that AQP5$^{-/-}$ mice naturally develop dry eye symptoms from birth, which makes them a stable, simple, and effective dry eye research animal model that can be used to study the pathogenesis of this condition. The AQP5 level has been considered to decrease with the occurrence of dry eye and is usually regarded as an indicator of dry eye in fundamental research (Wang et al., 2017).

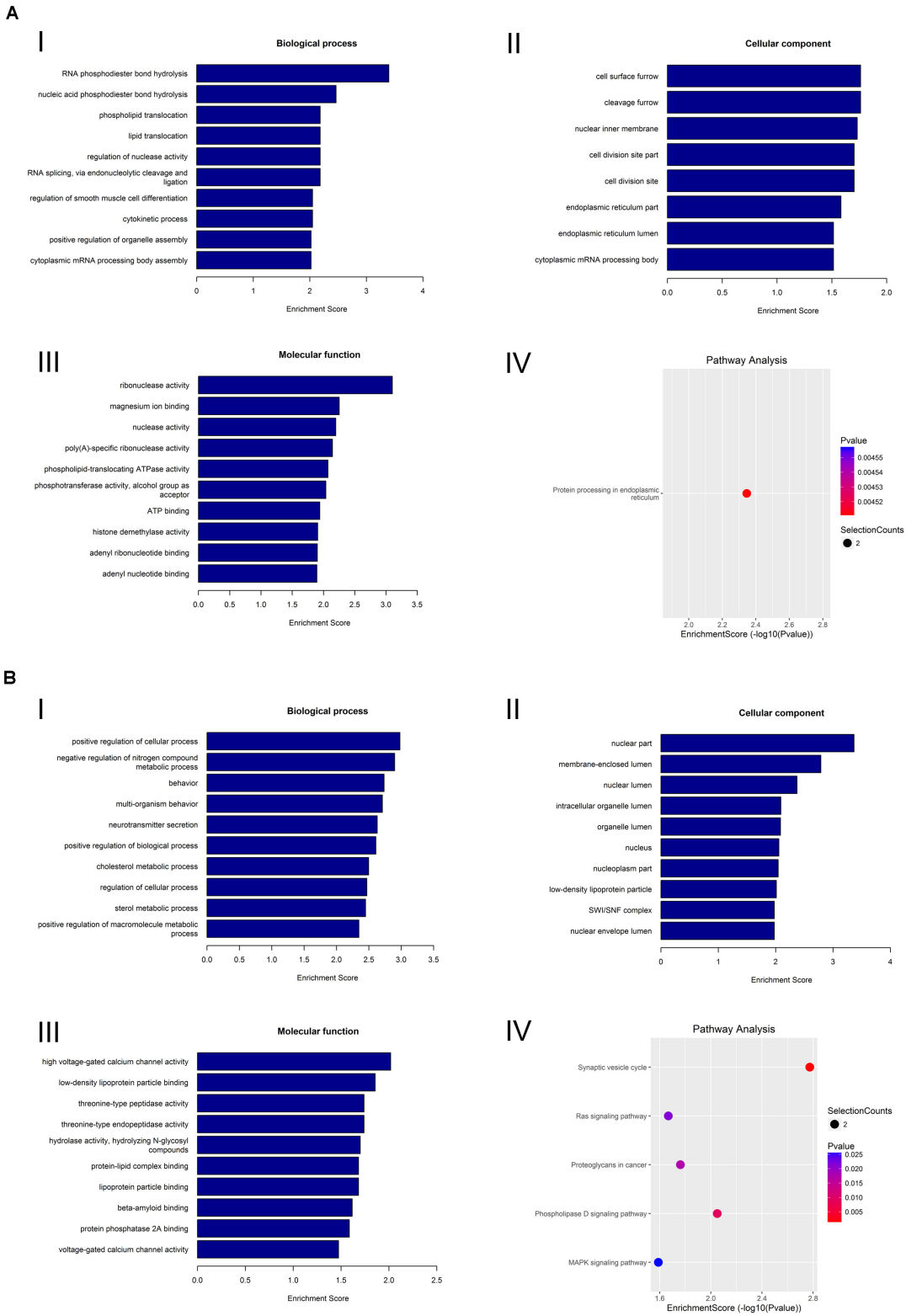

FIGURE 5 | GO analysis and KEGG analysis of circRNA. **(A)** GO analysis and KEGG analysis of upregulated circRNA. GO analysis identified (I) molecular functions, (II) biological processes, and (III) cellular components. (IV) Relevant pathways were identified for upregulated circRNA. **(B)** GO analysis and KEGG pathway analysis of downregulated circRNA. GO analysis identified (I) molecular functions, (II) biological processes, and (III) cellular components. (IV) Relevant pathways were identified for downregulated circRNA.

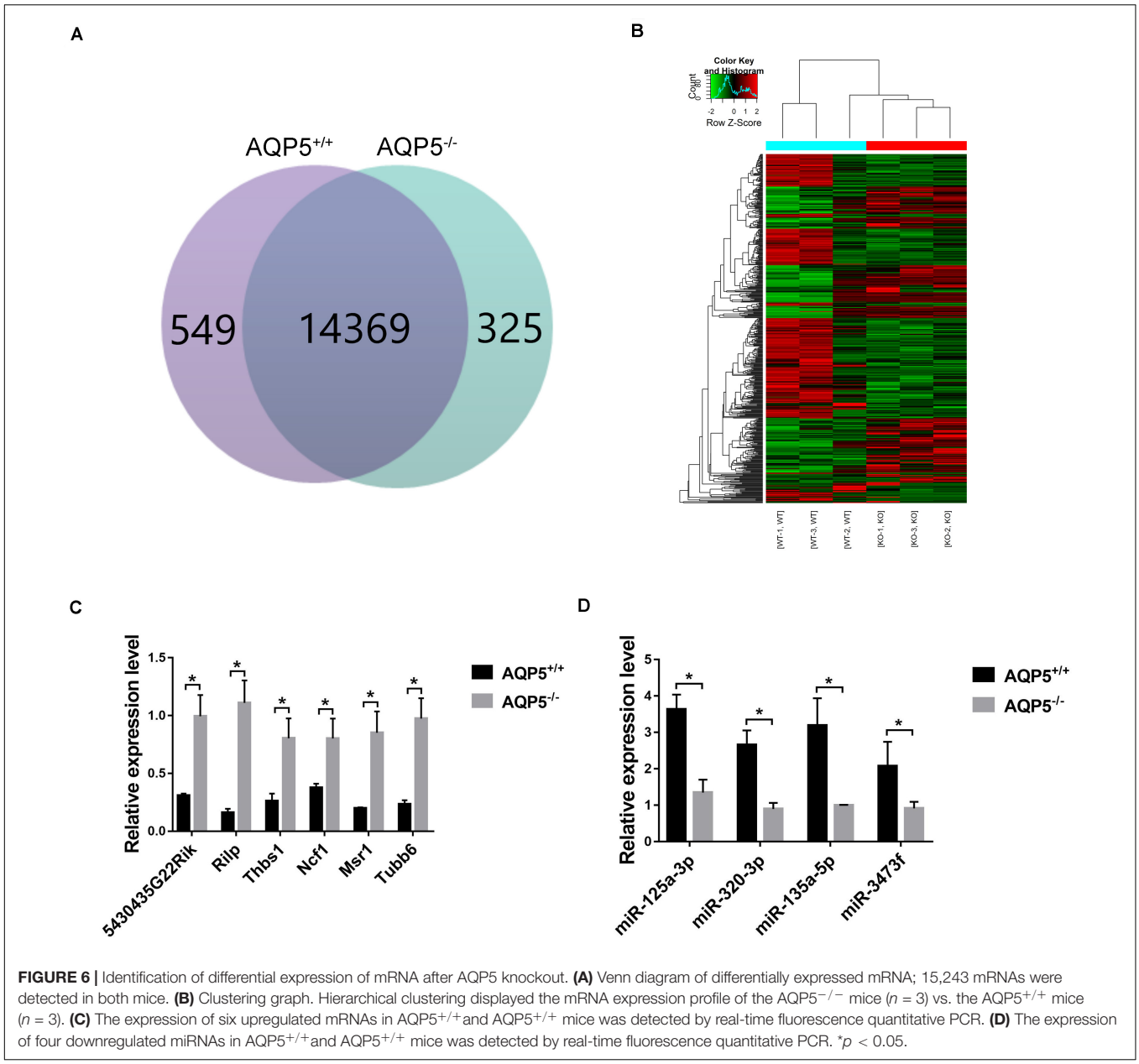

FIGURE 6 | Identification of differential expression of mRNA after AQP5 knockout. **(A)** Venn diagram of differentially expressed mRNA; 15,243 mRNAs were detected in both mice. **(B)** Clustering graph. Hierarchical clustering displayed the mRNA expression profile of the AQP5$^{-/-}$ mice (n = 3) vs. the AQP5$^{+/+}$ mice (n = 3). **(C)** The expression of six upregulated mRNAs in AQP5$^{+/+}$and AQP5$^{+/+}$ mice was detected by real-time fluorescence quantitative PCR. **(D)** The expression of four downregulated miRNAs in AQP5$^{+/+}$and AQP5$^{+/+}$ mice was detected by real-time fluorescence quantitative PCR. *$p < 0.05$.

However, whether dry eye occurs because of *AQP5* knockout has not been reported.

The occurrence of dry eye is usually related to age and gender; the incidence gradually increases with age, and women are more likely to develop dry eye than men (Kaštelan et al., 2013). However, in this study, we did not observe this phenomenon. AQP5$^{-/-}$ mice had dry eyes since birth, and no age- and gender-related trends were observed. This may be because the type of dry eye after AQP5 knockout is primary.

Hematoxylin–eosin staining of the lacrimal gland specimens of AQP5$^{-/-}$ mice revealed that the structure of the acini was disordered, and there were many changes in the vacuolation structure in the acini. The same phenomenon was observed in TSP$^{-/-}$ mice, a mouse model of Sjögren's syndrome (an autoimmune disease) (Bhattacharya et al., 2018). Electron microscopic observations revealed that a large number of mitochondrial cristae had disappeared, and there was an increase in the number of autophagosomes. These results suggest that the structural changes in the lacrimal gland epithelial cells of AQP5$^{-/-}$ mice may be related to autophagy.

As new non-coding RNAs, circRNAs play a key role in many ophthalmic diseases such as macular degeneration and corneal neovascularization (Liu et al., 2020; Wu et al., 2020). However, the role of circRNAs in dry eye and lacrimal gland development has not been studied before. Thus, to better understand the complex pathogenesis of dry eye, identification of comprehensive circRNA expression profiles in the lacrimal glands of AQP5$^{-/-}$ mice was critical. We identified 2,541 circRNAs, of which 937 were newly

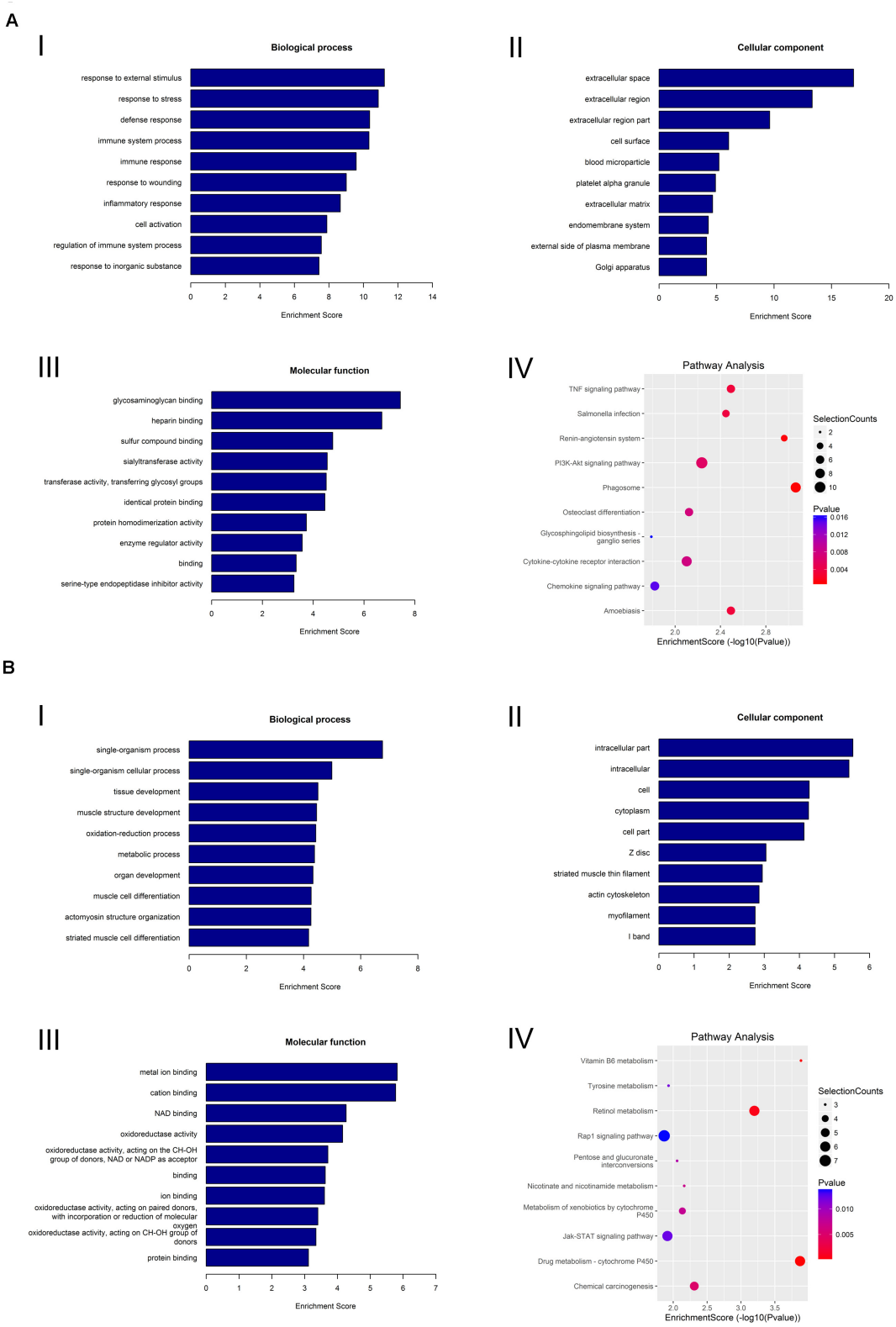

FIGURE 7 | GO analysis and KEGG pathway analysis of mRNA. **(A)** GO analysis and KEGG pathway analysis of upregulated mRNA. GO analysis identified (I) molecular functions, (II) biological processes, and (III) cellular components. (IV) Relevant pathways were identified for upregulated mRNA. **(B)** GO analysis and KEGG pathway analysis of downregulated mRNA. GO identified (I) molecular functions, (II) biological processes, and (III) cellular components. (IV) Relevant pathways were identified for downregulated mRNA.

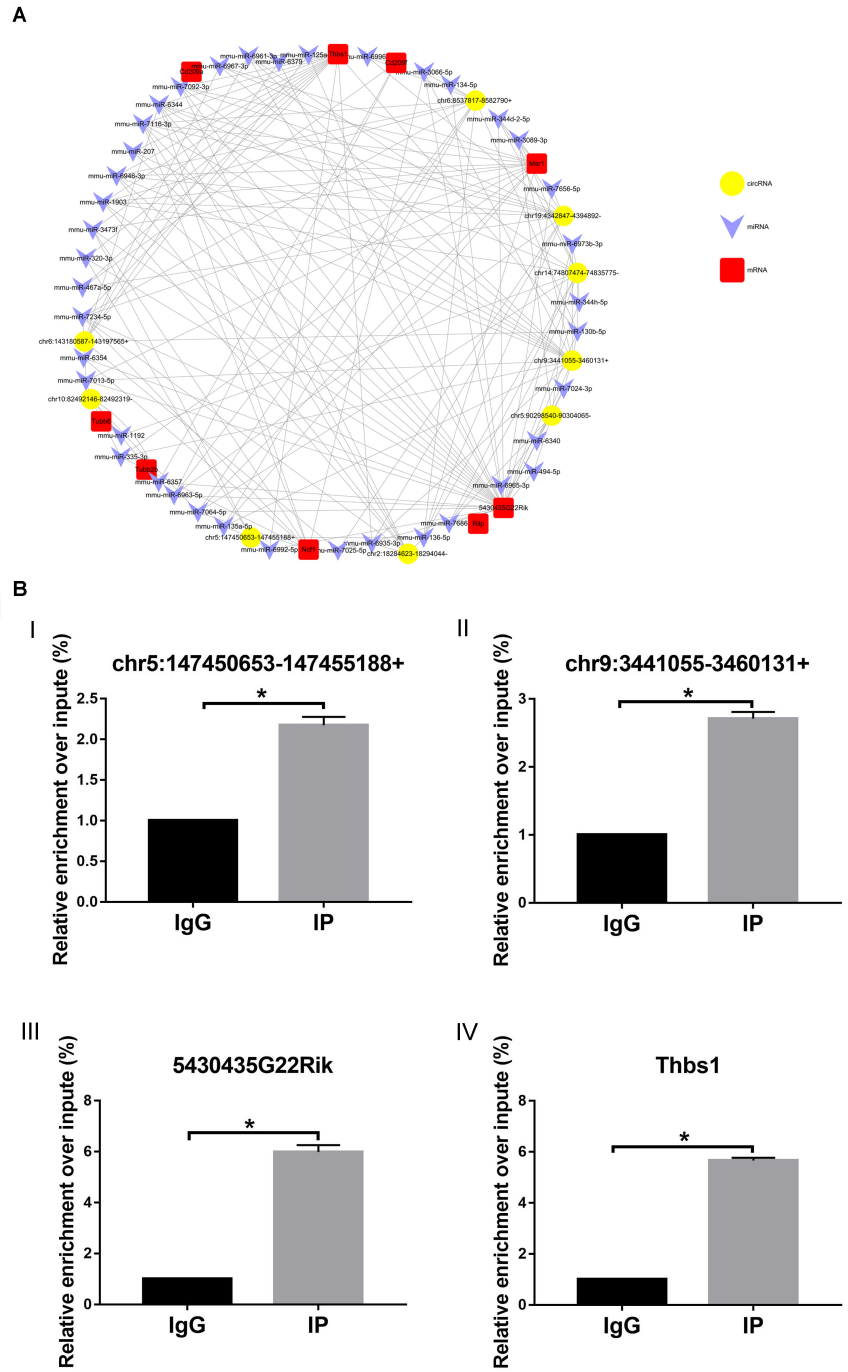

FIGURE 8 | circRNA–miRNA–mRNA network. **(A)** Circles represent circRNA, arrowhead represents miRNA, and squares represent mRNA. **(B)** RIP-qPCR detected (I) chr5:147450653-147455188+, (II) chr9:3441055-3460131+, (III) 5430435G22Rik, and (IV) Thbs1. IG, negative control immunoglobulin G group; IP, containing magnetic beads of anti-AGO2 antibody group. *$p < 0.05$.

identified. We also identified 30 differentially expressed circRNAs in the lacrimal glands of AQP5$^{-/-}$ mice compared with those of control mice. We selected nine upregulated circRNAs for validation. The qRT-PCR results were consistent with those of high-throughput sequencing, which proved the reliability of high-throughput sequencing.

In the circRNA–miRN–mRNA regulatory network or the ceRNA theory, circRNAs play the role of miRNA sponge and influence the expression of target mRNAs by competitive adsorption of miRNAs (Qi et al., 2015). We found the circRNA and the mRNA with the same trend by sequencing circRNA and mRNA and then find the circRNA and mRNA with the

same miRNA binding site by bioinformatics analysis. Only by meeting the above two conditions can the circRNA and mRNA be used to construct the circRNA–miRNA–mRNA regulatory network. Based on the nine validated upregulated circRNAs and the top five miRNAs predicted by using circRNAs, we predicted a circRNA–miRNA–mRNA network. In addition, by performing RIP-qPCR experiments, we proved that our predicted network is reliable. As a known member of the Argonaute protein family, Argonaute 2 (AGO2) can combine with miRNA to form the AGO2–miRNA complex (Zhang et al., 2020). This complex can be combined with circRNA *via* the sponge mechanism, which proves that chr5:147450653-147455188 + and chr9:3441055-3460131 + can play a role through sponge mechanism. In addition, the circRNAs and the mRNAs identified in our previously predicted network can also be detected by combining with the AGO2–miRNA complex, which shows that our network is reliable.

Interestingly, the target genes involved in this network are all related to phagosomes, according to the comparison with the database. These observations highly correlated with the results of our KEGG analysis of upregulated mRNA. Phagosomes, as a highly dynamic organelle, play an important role in innate and adaptive immunity as well as in tissue homeostasis (Dean et al., 2019). Our results indicate that the circRNA–miRNA–mRNA network predicted in our study is a network of phagosomes. What is more surprising is that our prediction is consistent with the structural changes in the lacrimal gland epithelial cells that we mentioned before. Therefore, these circRNAs may be involved in the regulatory networks and the pathways of phagosomes involved in the pathogenesis of dry eye. However, the regulatory mechanism of circRNAs is very complex; hence, it is necessary to further study the function and the mechanism of these circRNAs.

CONCLUSION

The present study demonstrates that (i) *AQP5* knockout can lead to primary dry eye development in mice (AQP5$^{-/-}$ mice have a stable dry eye phenotype since birth) and this phenotype may be produced by altering the structure of lacrimal glands, (ii) circRNA levels are significantly altered in the lacrimal glands of AQP5$^{-/-}$ mice, and (iii) the interactions of the circRNA–miRNA–mRNA network associated with phagosomes may regulate the expression of *AQP5* involved in the pathogenesis of dry eye.

DATA AVAILABILITY STATEMENT

The data of sequencing results for this study can be found in the GEO database (GSE149832). Please see https://www.ncbi.nlm.nih.gov/geo/query/acc.cgi?acc=GSE149832 for more details.

ETHICS STATEMENT

All experimental and animal care procedures followed the ARVO Statement for the Use of Animals in Ophthalmic and Vision Research and were approved by the Animal Care and Use Committee of Qingdao University (Qingdao, China).

AUTHOR CONTRIBUTIONS

GD and PC conceived and designed the study. YL, SH, XX, and XW performed the experiments. GD and TZ analyzed the data. YL and PC wrote the manuscript. All authors read and approved the final manuscript.

FUNDING

This work was supported by the National Natural Science Foundation of China (Grant No. 81970782), Shandong Provincial Natural Science Foundation (Grant No. ZR2018MH016), Qingdao Postdoctoral Application Research Project (Grant No. 40518060071), and China Postdoctoral Science Foundation (Grant No. 2017M612211). All the above funds are provided by the corresponding author (PC).

ACKNOWLEDGMENTS

We cordially thank Ms. Meifang Dai for assistance in data analysis and Editage (www.editage.com) for English language editing.

REFERENCES

Bhattacharya, S., García-Posadas, L., Hodges, R. R., Makarenkova, H. P., Masli, S., and Dartt, D. A. (2018). Alteration in nerves and neurotransmitter stimulation of lacrimal gland secretion in the TSP-1-/- mouse model of aqueous deficiency dry eye. *Mucosal Immunol.* 11, 1138–1148. doi: 10.1038/s41385-018-0002-y

Cheng, J., Metge, F., and Dieterich, C. (2016). Specific identification and quantification of circular RNAs from sequencing data. *Bioinformatics* 32, 1094–1096. doi: 10.1093/bioinformatics/btv656

Craig, J. P., Nichols, K. K., Akpek, E. K., Caffery, B., Dua, H. S., Joo, C.-K., et al. (2017). TFOS DEWS II definition and classification report. *Ocul. Surf.* 15, 276–283.

Dean, P., Heunis, T., Härtlova, A., and Trost, M. (2019). Regulation of phagosome functions by post-translational modifications: a new paradigm. *Curr. Opin. Chem. Biol.* 48, 73–80. doi: 10.1016/j.cbpa.2018.11.001

Dobin, A., Davis, C. A., Schlesinger, F., Drenkow, J., Zaleski, C., Jha, S., et al. (2013). STAR: ultrafast universal RNA-seq aligner. *Bioinformatics* 29, 15–21. doi: 10.1093/bioinformatics/bts635

Fakih, D., Zhao, Z., Nicolle, P., Reboussin, E., Joubert, F., Luzu, J., et al. (2019). Chronic dry eye induced corneal hypersensitivity, neuroinflammatory responses, and synaptic plasticity in the mouse trigeminal brainstem. *J. Neuroinflamm.* 16, 1–20.

Gilbard, J., Rossi, S. R., and Gray, K. L. (1987). A new rabbit model for keratoconjunctivitis sicca. *Invest. ophthalmol. Vis. Sci.* 28, 225–228.

Jiang, L.-H., Sun, D.-W., Hou, J.-C., and Ji, Z.-L. (2018). CircRNA: a novel type of biomarker for cancer. *Breast Cancer* 25, 1–7. doi: 10.1007/s12282-017-0793-9

Kaštelan, S., Tomić, M., Salopek-Rabatić, J., and Novak, B. (2013). Diagnostic procedures and management of dry eye. *Biomed Res. Int.* 2013:309723.

Kulcheski, F. R., Christoff, A. P., and Margis, R. (2016). Circular RNAs are miRNA sponges and can be used as a new class of biomarker. *J. Biotechnol.* 238, 42–51. doi: 10.1016/j.jbiotec.2016.09.011

Kumari, S. S., Varadaraj, M., Menon, A. G., and Varadaraj, K. (2018). Aquaporin 5 promotes corneal wound healing. *Exp. Eye Res.* 172, 152–158. doi: 10.1016/j.exer.2018.04.005

Lemp, M. A., and Foulks, G. N. (2007). The definition and classification of dry eye disease. *Ocul. Surf.* 5, 75–92. doi: 10.1016/s1542-0124(12)70081-2

Levin, M. H., and Verkman, A. (2006). Aquaporin-3-dependent cell migration and proliferation during corneal re-epithelialization. *Invest. Ophthalmol. Vis. Sci.* 47, 4365–4372.

Lin, H., Liu, Y., and Yiu, S. (2019). Three dimensional culture of potential epithelial progenitor cells in human lacrimal gland. *Transl. Vis. Sci. Technol.* 8, 32–32.

Liu, X., Zhang, L., Wang, J. H., Zeng, H., Zou, J., Tan, W., et al. (2020). Investigation of circRNA expression profiles and analysis of circRNA-miRNA-mRNA networks in an animal (Mouse) model of age-related macular degeneration. *Curr. Eye Res.* 6, 1–8. doi: 10.1080/02713683.2020.1722179

Lu, Q., Gong, W., Wang, J., Ji, K., Wang, Y., Xu, C., et al. (2018). Identification of circular RNAs altered in mouse jejuna after radiation. *Cell. Physiol. Biochem.* 47, 2558–2568. doi: 10.1159/000491652

Ma, T., Song, Y., Gillespie, A., Carlson, E. J., Epstein, C. J., and Verkman, A. S. (1999). Defective secretion of saliva in transgenic mice lacking aquaporin-5 water channels. *J. Biol. Chem.* 274, 20071–20074. doi: 10.1074/jbc.274.29.20071

Martin, M. (2011). Cutadapt removes adapter sequences from high-throughput sequencing reads. *EMBnet. J.* 17, 10–12.

Messmer, E. M. (2015). The pathophysiology, diagnosis, and treatment of dry eye disease. *Dtsch. Arztebl. Int.* 112, 71–81. doi: 10.3238/arztebl.2015.0071

Nelson, J. D., Craig, J. P., Akpek, E. K., Azar, D. T., Belmonte, C., Bron, A. J., et al. (2017). TFOS DEWS II introduction. *Ocul. Surf.* 15, 269–275.

Qi, X., Zhang, D. H., Wu, N., Xiao, J. H., Wang, X., and Ma, W. (2015). ceRNA in cancer: possible functions and clinical implications. *J. Med. Genet.* 52, 710–718. doi: 10.1136/jmedgenet-2015-103334

Raina, S., Preston, G. M., Guggino, W. B., and Agre, P. (1995). Molecular cloning and characterization of an aquaporin cDNA from salivary, lacrimal, and respiratory tissues. *J. Biol. Chem.* 270, 1908–1912. doi: 10.1074/jbc.270.4.1908

Robinson, M. D., McCarthy, D. J., and Smyth, G. K. (2010). edgeR: a bioconductor package for differential expression analysis of digital gene expression data. *Bioinformatics* 26, 139–140. doi: 10.1093/bioinformatics/btp616

Shi, H., Zheng, L. Y., Zhang, P., and Yu, C. Q. (2014). miR−146a and miR−155 expression in PBMC s from patients with Sjögren's syndrome. *J. Oral pathol. Med.* 43, 792–797. doi: 10.1111/jop.12187

Sindhu Kumari, S., and Varadaraj, K. (2013). Aquaporin 5 knockout mouse lens develops hyperglycemic cataract. *Biochem. Biophys. Res. Commun.* 441, 333–338. doi: 10.1016/j.bbrc.2013.10.058

Stevenson, W., Chen, Y., Lee, S.-M., Lee, H. S., Hua, J., Dohlman, T., et al. (2014). Extraorbital lacrimal gland excision: a reproducible model of severe aqueous tear-deficient dry eye disease. *Cornea* 33, 1336–1341. doi: 10.1097/ico.0000000000000264

Su, L.-C., Xu, W.-D., Liu, X.-Y., Fu, L., and Huang, A.-F. (2019). Altered expression of circular RNA in primary Sjögren's syndrome. *Clin. Rheumatol.* 38, 3425–3433. doi: 10.1007/s10067-019-04728-6

Takata, K., Matsuzaki, T., and Tajika, Y. (2004). Aquaporins: water channel proteins of the cell membrane. *Prog. Histochem. cytochem.* 39, 1–83. doi: 10.1016/j.proghi.2004.03.001

Thiagarajah, J. R., and Verkman, A. S. (2002). Aquaporin deletion in mice reduces corneal water permeability and delays restoration of transparency after swelling. *J. Biol. Chem.* 277, 19139–19144. doi: 10.1074/jbc.M202071200

Viau, S., Maire, M.-A., Pasquis, B., Grégoire, S., Fourgeux, C., Acar, N., et al. (2008). Time course of ocular surface and lacrimal gland changes in a new scopolamine-induced dry eye model. *Graefes Arch. Clin. Exp. Ophthalmol.* 246, 857–867. doi: 10.1007/s00417-008-0784-9

Wang, S.-Q., Wang, Y.-X., and Hua, H. (2017). Characteristics of labial gland mesenchymal stem cells of healthy individuals and patients with sjögren's syndrome: a preliminary study. *Stem Cell. Dev.* 26, 1171–1185. doi: 10.1089/scd.2017.0045

Wu, P., Zhang, D., Geng, Y., Li, R., and Zhang, Y. (2020). Circular RNA-ZNF609 regulates corneal neovascularization by acting as a sponge of miR-184. *Exp. Eye Res.* 192:107937. doi: 10.1016/j.exer.2020.107937

Zhang, X., Liu, X., Jing, Z., Bi, J., Li, Z., Liu, X., et al. (2020). The circINTS4/miR-146b/CARMA3 axis promotes tumorigenesis in bladder cancer. *Cancer Gene Ther.* 27, 189–202. doi: 10.1038/s41417-019-0085-y

Conflict of Interest: The authors declare that the research was conducted in the absence of any commercial or financial relationships that could be construed as a potential conflict of interest.

frontiers in Physiology

ORIGINAL RESEARCH
published: 02 October 2020
doi: 10.3389/fphys.2020.538835

Observation of the Epithelial Cell Behavior in the Nasal Septum During Primary Palate Closure in Mice

Sayuri Yamamoto[1], Hiroshi Kurosaka[1], Jiro Miura[2], Gozo Aoyama[1], Safiye Esra Sarper[1,3], Ayaka Oka[1], Toshihiro Inubushi[1], Kohei Nakatsugawa[1], Yu Usami[4], Satoru Toyosawa[4] and Takashi Yamashiro[1]**

[1] Department of Orthodontics and Dentofacial Orthopedics, Graduate School of Dentistry, Osaka University, Osaka, Japan, [2] Division for Interdisciplinary Dentistry, Dental Hospital, Osaka University, Osaka, Japan, [3] Department of Biological Sciences, Graduate School of Science, Osaka University, Osaka, Japan, [4] Department of Oral Pathology, Graduate School of Dentistry, Osaka University, Osaka, Japan

OPEN ACCESS

Edited by:
Maisa Hanna-Maija Seppala,
King's College London,
United Kingdom

Reviewed by:
Daniel Graf,
University of Alberta, Canada
Amel Gritli-Linde,
University of Gothenburg, Sweden
Timothy C. Cox,
University of Missouri–Kansas City,
United States

***Correspondence:**
Hiroshi Kurosaka
kurosaka@dent.osaka-u.ac.jp
Takashi Yamashiro
yamashiro@dent.osaka-u.ac.jp

Specialty section:
This article was submitted to Craniofacial Biology and Dental Research, a section of the journal Frontiers in Physiology

Received: 28 February 2020
Accepted: 10 September 2020
Published: 02 October 2020

Citation:
Yamamoto S, Kurosaka H, Miura J, Aoyama G, Sarper SE, Oka A, Inubushi T, Nakatsugawa K, Usami Y, Toyosawa S and Yamashiro T (2020) Observation of the Epithelial Cell Behavior in the Nasal Septum During Primary Palate Closure in Mice. Front. Physiol. 11:538835. doi: 10.3389/fphys.2020.538835

Epithelial fusion is critical in palatogenesis, and incomplete fusion results in various type of facial cleft, depending on the region that fails to fuse. In mammalian palatogenesis, the bilateral secondary palatal processes fuse in the middle of the face to form the secondary palate. Later, the dorsal side of the secondary palatal shelves fuses with the nasal septum to complete palatogenesis. Importantly, the anterior border of the secondary palatal shelf fuses with the primary palate, which is located at the anterior and ventral border of the nasal septum. While numerous studies have investigated the mechanism of fusion between secondary palatal shelves, very little is known about how the primary palate touches and fuses with the secondary palatal shelves. In this study, we investigate the possible epithelial cell behaviors on the surface of the primary palate using palatal explant cultures of *K14-GFP* mice. A time-lapse observation of the GFP-labeled epithelium and an SEM analysis revealed that the extrusion epithelium appeared at the region corresponding to the fusing area and expanded rostrally on the nasal septum surface in the absence of the secondary palatal processes. Unlike on the secondary palate surface, cellular migration and subsequent autonomous mesenchymal exposure were not evident on the nasal septum or the primary palate. TUNEL staining revealed that these extrusion epithelia were undergoing apoptosis. These findings indicated that extrusion with apoptosis was autonomously initiated at the presumptive region of the fusion without contact with the opposing secondary palate.

Keywords: nasal septum, cleft palate, live imaging, craniofacial abnormalities, epithelium, organ culture

INTRODUCTION

Palatal fusion is essential for obtaining tissue continuity of facial processes from different embryonic origins. The palate is derived from both the primary palate and the secondary palate. The secondary palate fuses with the nasal septum, which is continuous with the primary palate (Ferguson, 1988). The primary palate and nasal septum are derived from the ventral protrusion of the frontonasal process, whereas the secondary palate develops by the outgrowth of the bilateral maxillary process (Hilliard et al., 2005). Palatal fusion occurs at the midline of the secondary palate following bilateral

outgrowth of the maxillary process. Thereafter, in humans, the anterior and dorsal parts of the secondary palate fuse to the primary palate, and the posterior and dorsal portions of the secondary palate fuse with the nasal septum. On the other hand, in mice, fusion of the nasal septum to the palate only occurs in the most anterior region, and the posterior region would remain a common nasal passage (Ferguson, 1978; Yu et al., 2017). After these processes contact, the intervening epithelium between the growing shelves merges to form an epithelial seam, which must be removed to complete the fusion (Ferguson, 1988; Bush and Jiang, 2012). Most previous studies focused on palatal fusion between bilateral secondary palates; fewer studies have focused on the fusion between the secondary palate and the primary palate/nasal septum.

Multiple studies have demonstrated that the migrating epithelium plays major roles in removing the epithelial seam, while other cellular mechanisms, such as apoptosis and epithelial mesenchymal transformation, are unlikely to play a role—in a strict sense—in this process (Carette and Ferguson, 1992; Griffith and Hay, 1992; Shuler et al., 1992; Cuervo and Covarrubias, 2004; Jin and Ding, 2006; Kim et al., 2015). Among these mechanisms, cell migration was first showed by confocal imaging of Dil-labeled cells (Carette and Ferguson, 1992) and by *in vitro* chimeric culture experiments using *K14-Cre; R26R* mice (Jin and Ding, 2006). A recent time-lapse imaging study succeeded in directly capturing the dynamic migration of the fluorescently labeled medial edge epithelium of the secondary palate (Kim et al., 2015). On the other hand, in unpaired palatal shelf cultures (Takigawa and Shiota, 2004), where one side of the shelf is removed, the medial edge epithelium (MEE) disappears without contact to the opposing palatal shelf and consequent mesenchymal exposure could be observed. Interestingly, our recent time lapse observation revealed such autonomous epithelial disappearance in unpaired palatal shelf cultures, in which it was triggered by dynamic migration of the MEE (Aoyama et al., 2019). Furthermore, the region of mesenchymal exposure to epithelial migration never expanded anteriorly beyond between the first and second rugae in unpaired palatal shelf organ cultures (Charoenchaikorn et al., 2009), indicating that the fusion mechanism differs between the anterior and posterior palate at this boundary. Taken together, our time-lapse direct observation of the secondary palate surface clearly identified autonomous and intrinsic programmed events, even in the absence of the contact of the opposing process *in vitro*.

Along the anterior-posterior axis, palatogenesis is differentially regulated at the molecular level (Hilliard et al., 2005; Li and Ding, 2007). Several transcription factors and/or signaling molecules (e.g., *Msx1*, *Bmp4*, *Shh*, *Fgf10*, *Fgf7*, and *Shox2*) are specifically expressed in the anterior regions and some mutant mice also showed anterior cleft palate. Although a different gene mutation caused anterior-specific cleft palate, it was of interest that the posterior border of the anterior cleft is localized at the 1st rugae (Dudas et al., 2006; Xu et al., 2006; Lane et al., 2015; Sarper et al., 2018b, 2019). However, most of previous investigations have focused on palatal fusion of bilateral secondary palate, and mechanisms of fusion in the anterior region between the primary and secondary palate is still largely elusive.

We evaluated the cellular behavior of the epithelium on the primary palate and the nasal septum using *K14-GFP* mouse explant culture as a model (Vaezi et al., 2002). Time-lapse imaging and an SEM analysis demonstrated that epithelial extrusion appears specifically on the regions of palatal fusion and that these extruding cells expanded rostrally along the fusing regions. We also showed that these cells are undergoing apoptosis. Our findings have shown that this experimental model can be a unique tool for exploring the possible regulatory mechanism of apoptosis that occurs in palatal fusion between the primary and secondary palate.

RESULTS

SEM Observation of Cultured Mouse Nasal Septum

The secondary palatal process starts to fuse at the midline on E14.5, and then the anterior-most region of the secondary palate further fuses with the primary palate. At a similar developmental stage, the secondary palate also anterodorsally fuses with the nasal septum (Bush and Jiang, 2012). In order to investigate the detailed surface morphology of the anterior nasal septum during fusion with the secondary palate, we used a scanning electron microscope (SEM) to assess cultured maxillary complex explants. A dashed line in the **Figure 1A** schematic shows the plane of dissection for exposing the nasal septum during maxillary explant culture. Different embryonic time points were selected to observe stage-specific events of nasal septum development. At E14.5, the surface of the nasal septum showed a somewhat smooth surface (**Figures 1B,E**). Even after 12 h (**Figures 1C,F**) and 24 h (**Figures 1D,G**) of culture, the surface morphology of the nasal septum did not show noticeable differences. However, when we started culturing the explant from E15.0 (**Figures 1H,K**), extruding epithelial cells could be observed after 12 h of explant culture at the presumptive fusion site of the nasal septum and the secondary palate (**Figures 1I,L**) and also remained after 24 h of culture (**Figures 1J,M**). These results indicate that the nasal septum epithelium exhibits protrusive extruding behavior during the process of fusion with the secondary palatal shelves.

The explants were approximately 1500 μm in width, 1000 μm in length, and 700 μm in thickness (**Supplementary Figure 3**). Previous reports using a similar size of maxillary complex for organ culture showed certain cellular events that recapitulate the *in vivo* situation (Shiota et al., 1990; Takigawa and Shiota, 2004).

Induction of Extruding Cells on the Epithelial Surface of Primary Palate Explants of K14-GFP Mice

In order to further investigate the behavior of epithelial cells of the developing nasal septum, transgenic mice that carry GFP under the promoter of *Keratin14* (*K14*) were used (**Figure 2A**) (Vaezi et al., 2002). Primary palate explants, including the nasal septum, were dissected at E15.0. The bilateral secondary palatal processes were further removed as the presumptive region of fusion could be directly visualized using a fluorescence

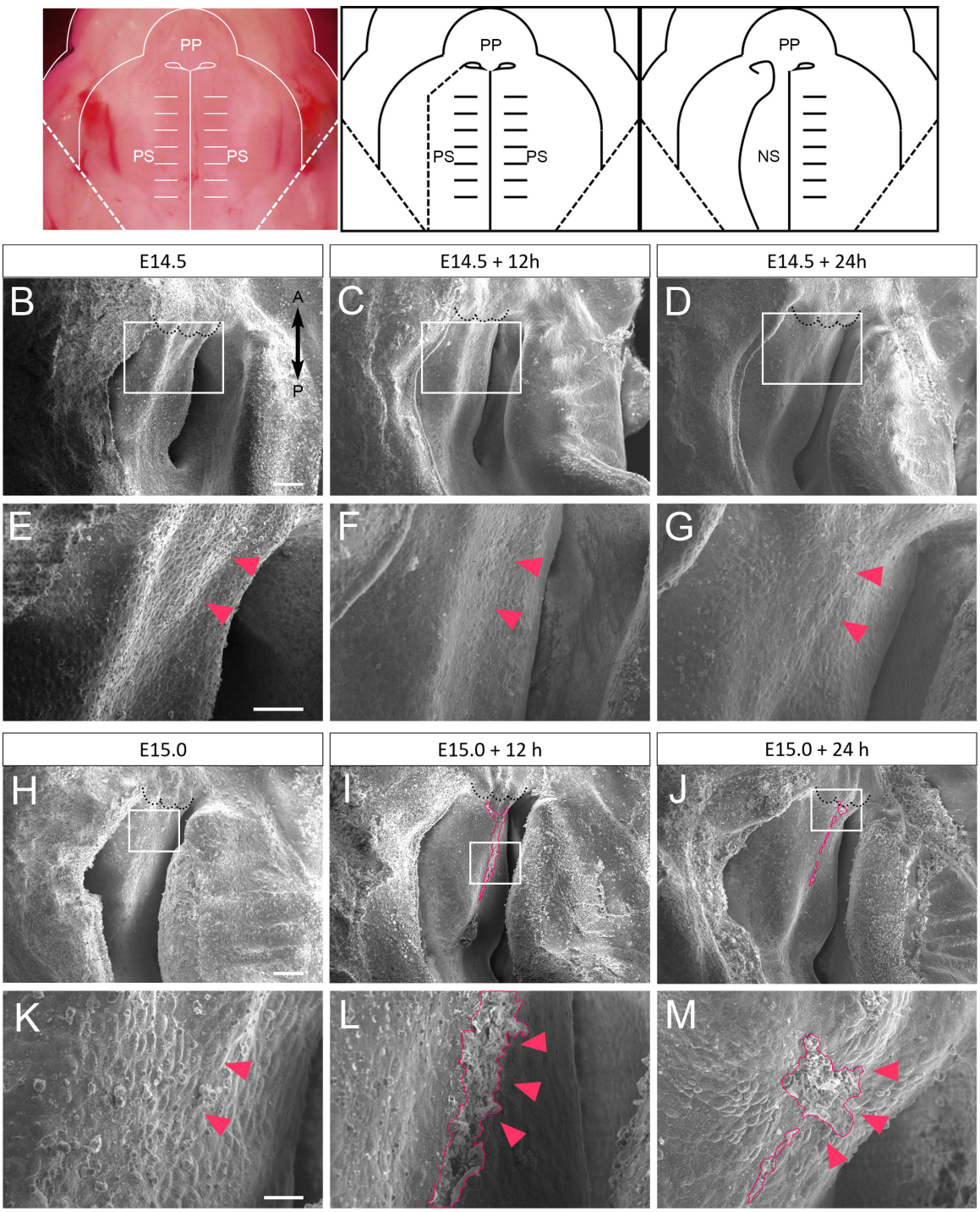

FIGURE 1 | SEM observation of mouse nasal septum explants. **(A)** A schematic of the removal of the explants from the right palatal shelf from each maxilla. **(B–G)** Occlusal views of the WT mouse nasal septum at E14.5 **(B,E)**, after 12 h of culture **(C,F)**, and after 24 h of culture **(D,G)**. **(E–G)** Higher magnification views in the region indicated by white boxes in **B–D**. No protrusion of epithelial cells of the nasal septum occurred (red arrowheads). **(H–M)** Occlusal views of the WT mouse nasal septum at E15.0 **(H,K)**, after 12 h of culture **(I,L)**, and after 24 h of culture **(J,M)**. **(K–M)** Higher magnification views in the region indicated by white boxes in **H–J**. Protrusion of epithelial cells of the nasal septum occurred (red area, red arrowheads). Black dotted lines in **B–D** and **H–J** indicate the posterior border of the primary palate. A, anterior; P, posterior; PP, primary palate; PS, secondary palate; NS, nasal septum. Scale bars: **B** 100 μm (**B–D** same magnification); **E** 50 μm (**E–G** same magnification); **H** 100 μm (**H–J** same magnification); **K** 20 μm (**K–M** same magnification).

microscope (**Figure 2B**). These dissected explants were captured at 12 and 24 h after culture. The uniform expression of GFP covering the nasal septum could be observed immediately after dissection (**Figures 2C,F**). After 12 h of culture, GFP-positive epithelium was gathered at the anterior and median nasal septum. Interestingly, accumulated GFP signaling could be detected in the region in which cellular protrusion was observed by SEM (**Figures 2D,G**). This accumulated GFP signaling remained after 24 h of culture (**Figures 2E,H**). These results indicate that the epithelial protrusion that was detected by SEM was caused by the behavior of the epithelial cells of the developing nasal septum.

Live Imaging of Epithelial Cells of Nasal Septum Explants

In order to assess the dynamism of the nasal septum epithelium during the fusion of nasal septum and the secondary palate, we used a live imaging technique. In this analysis, GFP-positive epithelium showed movement that gathered at the anterior and median nasal septum from 3 to 8 h of culture (**Figures 3A–D**). The converging cells showed a strong GFP signal. However, after that, dynamic cell migration did not occur until 24 h of culture and did not show the mesenchymal exposure that had been observed at the secondary palatal shelves (**Figures 3E–H** and **Supplementary Movies 1**, **2**). Furthermore, the epithelial migration in the nasal septum was significantly shorter than that in the secondary palate (**Supplementary Figure 1**), indicating that the behavior of the epithelial cells of the nasal septum is distinguished from that of the secondary palate MEE under organ culture conditions, suggesting that different mechanisms underlie the removal of epithelial cells in each tissue.

TUNEL Staining in Sections of Cultured Nasal Septum of K14-GFP Mice

In order to explore the cellular mechanism of nasal septum epithelium removal, we performed whole mount TUNEL staining to detect apoptotic cells during nasal septum development, since apoptosis is known to be one of the mechanisms by which the secondary palate MEE is removed. A small number of apoptotic cells could be seen at the nasal septum immediately after dissection at E15.0 (**Figure 4A**). An increased number of apoptotic cells at the anterior and median nasal septum were detected after 12 and 24 h of culture (**Figures 4B,C**). From the detailed observation of histological sections at the plane of the nasal septum and secondary palate fusion, we also detected apoptotic GFP-positive epithelial cells that showed extruding behavior (**Figures 4D–I**). The shape of the cells outside of the epithelium was round and differed from that of epidermal cells that have cell–cell adhesion. The region in which apoptosis was detected in this experiment corresponded to the region of the extruding epithelial cells that was observed in the SEM analysis. Hematoxylin and eosin staining of histological sections using cultured nasal septum showed a thickened epithelium (**Figures 4J–L**), which also corresponds to the region of strong GFP signaling in **Figures 2**, **3**. We also confirmed that the *in vivo* epithelial cell death in the nasal septum increased during the fusion process between the nasal septum and secondary palate (**Supplementary Figure 4**). These results indicate that the cellular behaviors in our explant organ culture model were at least partially recapitulated the normal developmental process.

Nasal Septum Phenotypes of *K14-Cre/Runx1*$^{fl/fl}$ Mice

From our previous results, the epithelial-specific elimination of Runx1 is known to be exhibited at the anterior cleft palate (Sarper et al., 2018a,b). It is also known that fewer TUNEL-positive cells were detected on the unfused epithelium in *Runx1* mutants (Sarper et al., 2018b). We did not detect a significant reduction in the area of protruded cells in the cultured nasal septum of *K14-Cre/Runx1*$^{fl/fl}$ mice in comparison to the control group (**Figure 5**). While the statistical test did not support significance, there is a trend toward a reduced protruded area in *K14-Cre/Runx1*$^{fl/fl}$ mice that might become significant with a larger sample size. Furthermore, in *K14-Cre/Runx1*$^{fl/fl}$ maxillary complex cultures, the nasal septum epithelium showed a significant reduction in apoptosis in comparison with the control (**Supplementary Figure 5**).

Taken together, it is indicated that proper apoptotic behavior in the developing nasal septum is important for fusion with the secondary palate.

DISCUSSION

A time lapse observation of tissue explants *in vitro* provides solid evidence of cellular behavior (Bush and Jiang, 2012; Aoyama et al., 2019). Our time-lapse observation found that the epithelial extrusion of the nasal septum appeared at the presumptive region of palatal fusion and that this extruding region expanded in the rostral direction along the presumptive area of fusion. A TUNEL analysis demonstrated that these extruding cells were undergoing apoptosis. Since the secondary palatal process was removed, fusion does not occur at the primary and secondary palate junction in our culture system. The present findings indicated that extruding with apoptosis was initiated without contacting the secondary palatal shelf.

Our present findings demonstrated that cellular mechanisms in the initiation of palatal fusion differ between the primary/secondary palate junction and the bilateral secondary palate process junction. Apoptosis in palatal fusion is evident, both at the primary/secondary palate junction and at the bilateral secondary palate process junction; however, present results using live imaging of the GFP-labeled epithelium together with the maxillary explant culture system clarified the different initial cellular behavior between these junctions. Since the extrusion occurs at the specific region of the presumptive region of fusion, without contact with the opposing tissue, apoptosis would be initiated as an intrinsically programmed event at the primary/secondary palate junction. On the other hand, our previous *in vitro* study demonstrated that dynamic migration rather than apoptosis is initiated at the medial edge epithelium and that it is visible later on the secondary palate (Aoyama et al., 2019). The lack of influence of the opposing

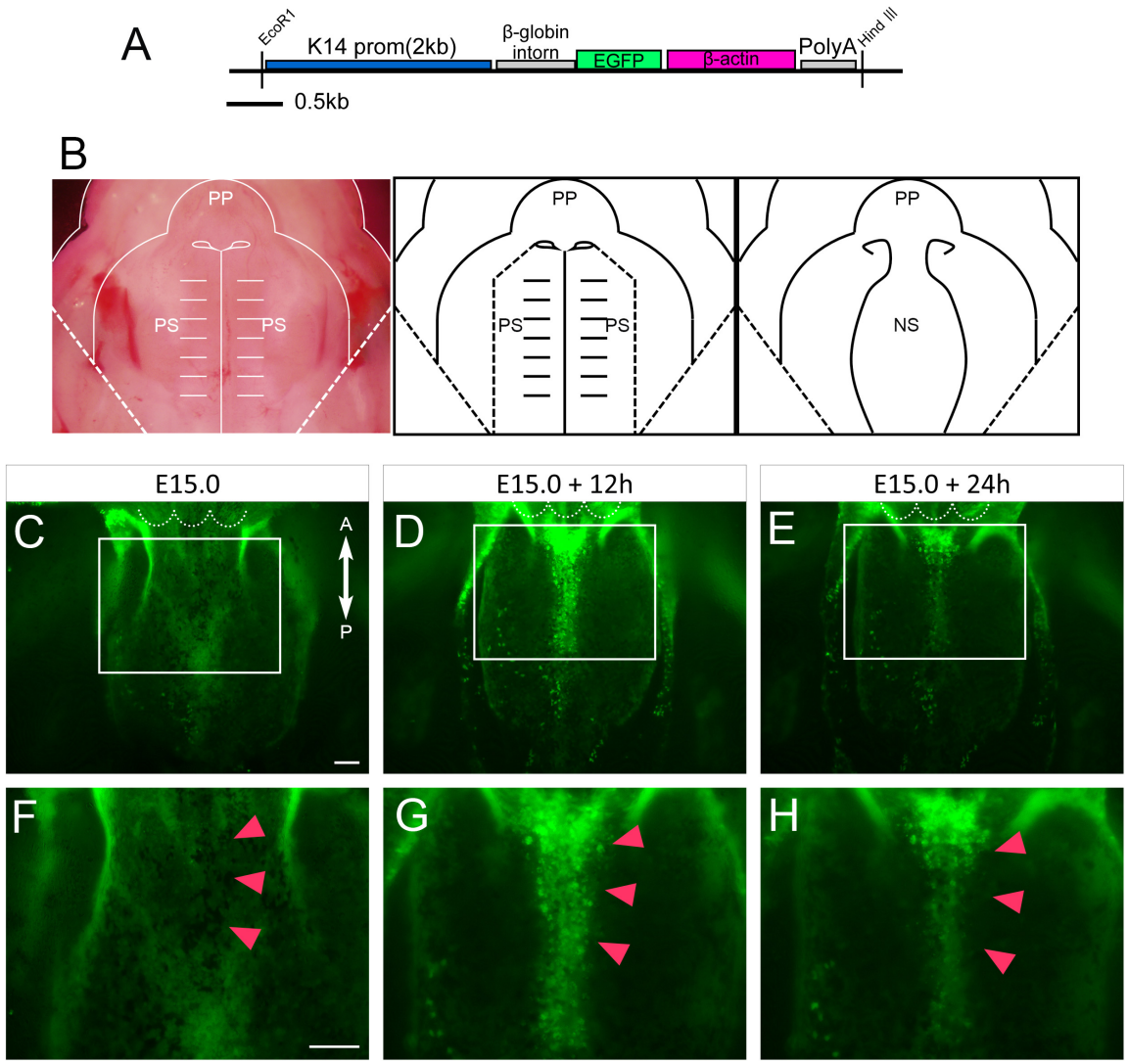

FIGURE 2 | An anatomical analysis of the nasal septum of the *K14-GFP* mouse during 12 h culture. **(A)** The K14-GFP transgene construct. **(B)** A schematic of the removal of the explants from both palatal shelves from each maxilla. **(C–H)** Fluorescence microscopic image showing oral views of the nasal septum at different developmental stages. At E15.0 **(C,F)**, after 12 h of culture **(D,G)**, after 24 h of culture **(E,H)**. GFP-positive epithelium was gathered at the anterior and median nasal septum (red arrowheads). **(F–H)** Higher magnification views in the region indicated by white boxes in **C–E**. Red arrowheads in **F–H** indicate the center of the developing nasal septum. White dotted lines in **C–E** indicate the posterior border of the primary palate. A, anterior; P, posterior; PP, primary palate; PS, secondary palate; NS, nasal septum. Scale bars: **C** 100 μm (**C–E** same magnification); **F** 100 μm (**F–H** same magnification).

secondary palate is a limitation of this model; thus, it might not reflect the environment of fusion *in vivo*. However, our *in vitro* experimental models, with future pharmaceutical and genetic manipulations, could provide a potential tool to further investigate the initial cellular and molecular events of the palatal fusion and the difference in these events between the primary/secondary junction and the bilateral secondary palatal process. The limitations of this experimental method include the artifacts of explant culture. We confirmed continuous mesenchymal cell proliferation in maxillary complex cultures, which proves that this culture condition at least partially recapitulates the developmental process *in vivo* (**Supplementary Figure 2**). We also need to keep in mind that the fusion method for the nasal septum and secondary palate varies among species. For example, the mouse nasal septum only fuses with the secondary palate at the anterior-most point and leaves a common nasal passage, while the human nasal septum fuses along its entire length (Ferguson, 1978; Yu et al., 2017).

Our study demonstrated that apoptosis was initiated at the presumptive region of fusion as a programmed event at the primary/secondary palate junction. However, the functional significance of apoptosis remains controversial (Honarpour et al., 2001; Jin and Ding, 2006). The present and previous findings suggest that the induction of extrusion is critical for the fusion of facial processes and that it can be inhibited by *Runx1* depletion (Martínez-Alvarez et al., 2000; Takigawa and Shiota, 2004, 2007;

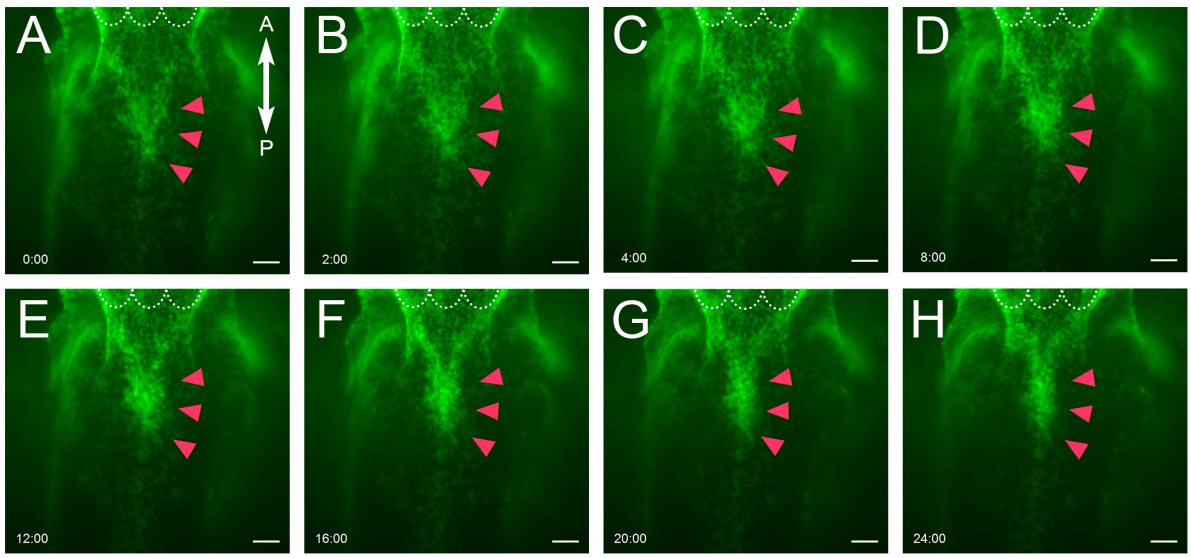

FIGURE 3 | Live imaging of epithelial cells of nasal septum explants. **(A–H)** Epithelial cell movement captured by live imaging in the nasal septum explant model. At E15.0 **(A)**, after 2 h of culture **(B)**, 4 h of culture **(C)**, 8 h of culture **(D)**, 12 h of culture **(E)**, 16 h of culture **(F)**, 20 h of culture **(G)**, 24 h of culture **(H)**. The GFP-positive epithelium was slightly gathered at the anterior and median nasal septum (red arrowheads). White dotted lines indicate the posterior border of primary palate. A, anterior; P, posterior. Scale bars: 100 μm.

Charoenchaikorn et al., 2009; Hu et al., 2015). Importantly, our previous report showed that the excision of *Runx1* in epithelial tissues takes place at the beginning of explant culture (Sarper et al., 2018a,b, 2019).

In Runx1 mutant mice, the anterior cleft palate is associated with reduced apoptosis and retained periderm, at the boundary between the primary and secondary palate junction. In these mutants, the expression of Tgfb3, a critical regulator of apoptosis, was significantly disturbed and TGFB3 protein rescued the formation of the anterior cleft (Sarper et al., 2018a,b, 2019). The molecular mechanism through which apoptosis is initiated remains unclear; however, the reduced induction of extrusion is associated with a reduction in the expression of *Tgfb3*. Of note, *Tgfb3* is widely expressed in the anterior palate; thus, the *Tgfb3* expression alone does not explain the region-specific induction of apoptosis and extrusion, suggesting that some other molecule is also involved in this regulatory process.

CONCLUSION

The cellular and molecular mechanisms underlying nasal septum and secondary palate fusion are not completely understood. Our time-lapse observation using isolated primary palate explants combined with an SEM analysis revealed that the epithelial extrusion was initiated at the presumptive region of fusion. We also detected significant differences in the epithelial behavior between the fusing nasal septum and secondary palate. Our new experimental system could become a potential tool to further investigate the initial cellular and molecular events of palatal fusion and how these events differ between the primary/secondary palate junction and the bilateral secondary palatal process.

MATERIALS AND METHODS

Animals

We utilized transgenic mice which express GFP under the control of the Cytokeratin-14 promoter (*K14-GFP*) (Vaezi et al., 2002) (**Figure 2A**). Mature female mice of C57BL/6J (CLEA, Tokyo, Japan) were mated with a *K14-GFP* male mouse. The day on which a vaginal plug was found was defined as embryonic day (E) 0.5. GFP expression was confirmed by the green fluorescent glow of the skin. For generating *K14-Cre/Runx1*$^{fl/fl}$ mice, *K14-Cre/Runx1*$^{fl/+}$ male mice were bred with *Runx1*$^{fl/fl}$ female mice. Genotyping was performed using the genome DNA extracted from individual tail and conventional polymerase chain reaction (PCR), as previously described (Sarper et al., 2018b). The littermates that did not carry the *K14-Cre/Runx1*$^{fl/fl}$ genotype were used as control animals. All of the animal experiments were performed in accordance with the guidelines of the Animal Care and Use Committee of the Osaka University Graduate School of Dentistry, Osaka, Japan. The protocol was recognized by the Committee on the Ethics of Animal Experiments of Osaka University Graduate School of Dentistry (permit number: 26-017-0, 26-004-0).

Nasal Septum Explant Cultures

To evaluate the cellular behavior of nasal septum epithelium, we dissected the primary palate from E14.5 and E15.0 *K14-GFP* embryos for subsequent organ culturing and live imaging (Charoenchaikorn et al., 2009).

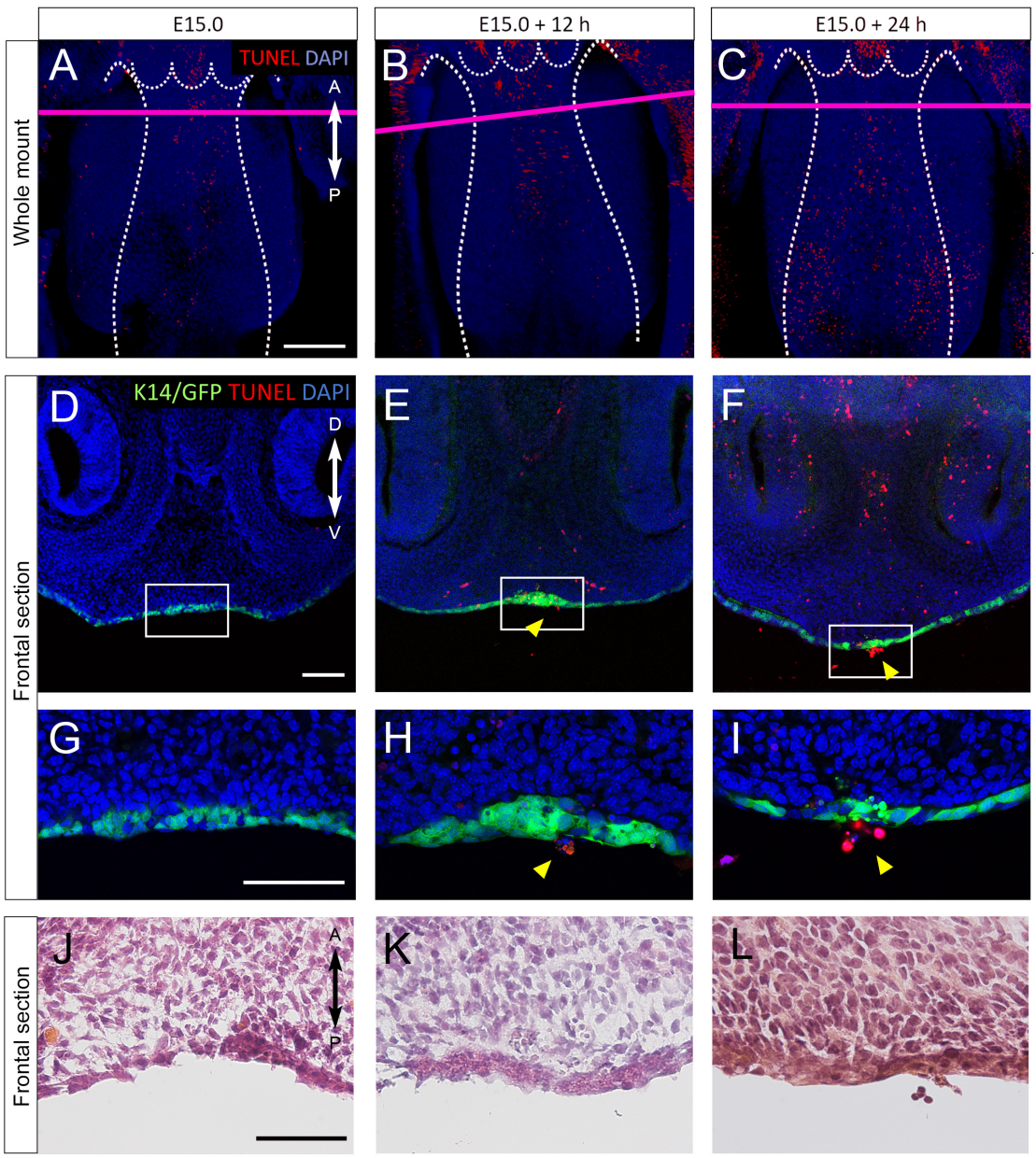

FIGURE 4 | (A–I) TUNEL staining of sections of cultured nasal septum of *K14-GFP* mice. **(A–C)** A fluorescence microscopic image showing oral views of the nasal septum at E15.0 **(A)**, after 12 h of culture **(B)**, after 24 h of culture **(C)**. A, anterior; P, posterior. Scale bars: **A** 200 μm (**A–C** same magnification). **(D–I)** The frontal sections. **D–I** are from the area indicated by the red line in **A–C**. **(D–I)** Fluorescence microscopic images showing frontal views of the nasal septum at E15.0 **(D,G)**, after 12 h of culture **(E,H)**, after 24 h of culture **(F,I)**. **(G–I)** Higher magnification views in the region indicated by white boxes in **D–F**. Protrusion of epithelial cells of the nasal septum occurred (yellow arrowheads). **(J–L)** Hematoxylin and eosin staining images showing equivalent position of **G–I**. D, dorsal; V, ventral. Scale bars: **D** 100 μm (**D–F** same magnification); **G** 100 μm (**G–I** same magnification); **J** 50 μm (**J–L** same magnification).

A rolling culture system (Ikemoto Scientific technology, Kanagawa, Japan) was utilized for organ culture, as previously described (Takigawa and Shiota, 2004). Dissected primary palate specimens were incubated in BGJb medium (Gibco@ Life Technologies) at 37℃ in the glass bottle with a rotation speed of 25–30 rpm, in an atmosphere containing 50% O_2, 5% CO_2, and 45% N_2 using a standard incubator for 12 or 24 h. The BGJb medium contains 0.2 mg/L D-Calcium pantothenate and 555.0 mg/L calcium lactate as calcium content.

For live imaging and the quantitative analysis, we removed both palatal shelves (**Figure 2B**). The nasal septum was cultured in a glass-bottomed dish (Matsunami, Osaka, Japan) with medium containing 0.6% low melting agarose (Wako Osaka, Japan). Explants were cultured and GFP was monitored

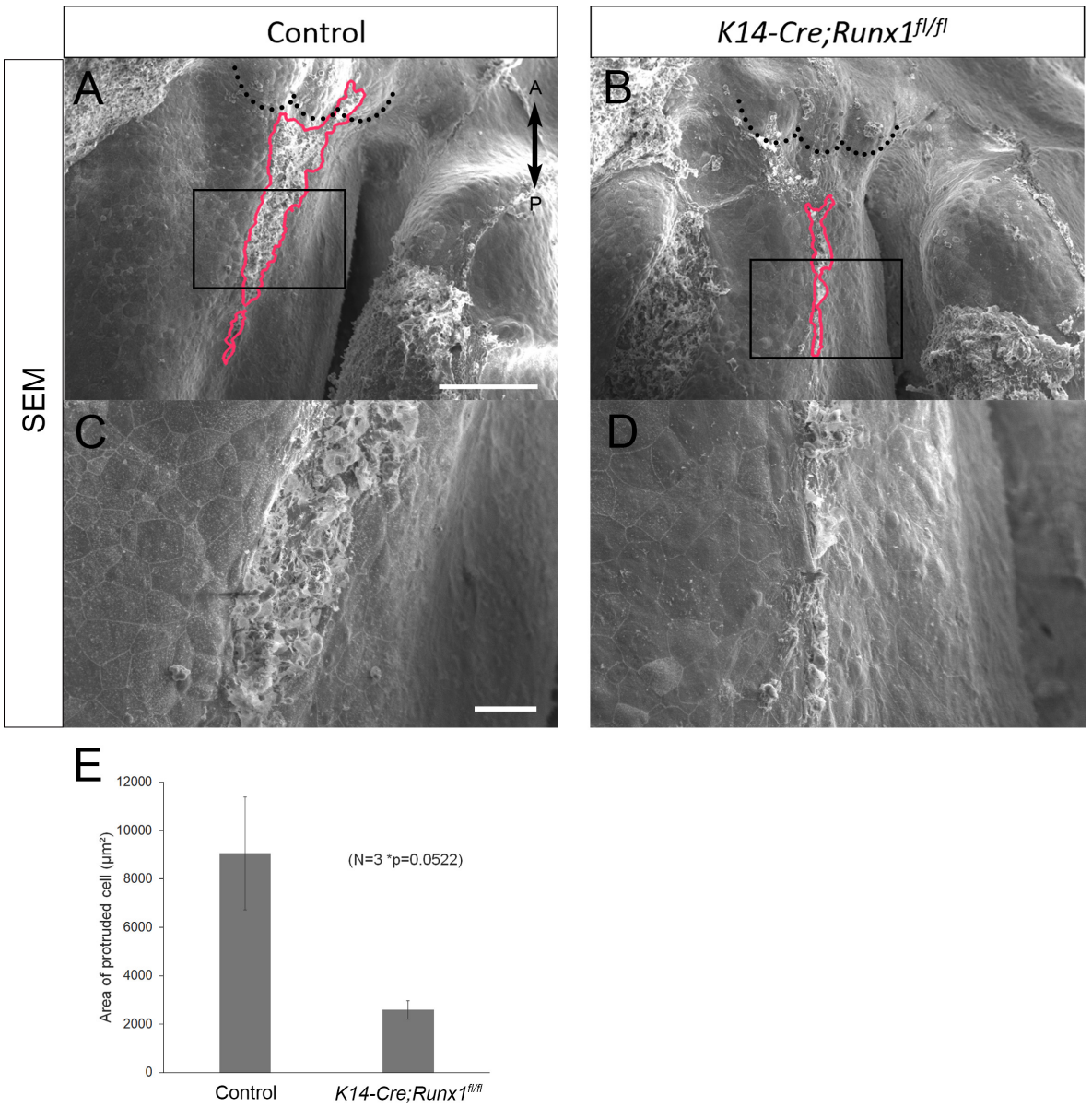

FIGURE 5 | Nasal septum phenotypes of *K14-Cre/Runx1*$^{fl/fl}$ mice. **(A,B)** Occlusal views of the control and *K14-Cre/Runx1*$^{fl/fl}$ mouse nasal septum at E15.0, after 12 h of culture. The area of epithelial protrusion in *K14-Cre/Runx1*$^{fl/fl}$ mice was narrower than that in control mice (red line). **(C,D)** Higher magnification views of **(A,B)**. Black dotted lines in **A** and **B** indicate the posterior border of the primary palate. A, anterior; P, posterior. Scale bars: **A** 1000 μm (**A,B** same magnification); **C** 20 μm (**C**, **D** same magnification). **(E)** The area of epithelial protrusion was slightly reduced in *K14-Cre/Runx1*$^{fl/fl}$ mice. *p = 0.0522, Student's t-test, n = 3.

using an all-in-one fluorescence microscope (BZ-X700, Keyence, Osaka, Japan).

Imaging

(1) The morphological analysis by scanning electron microscope

The nasal septum was fixed in 2% glutaraldehyde and 2% paraformaldehyde in PBS with 100 nM Hepes for 6 h at 4℃. After washing with PBS, the explants were treated with 1% osmium tetraoxide for 1 h at room temperature (RT). Graded ethanol solution was used to dehydrate the samples. Explants were mounted on a specimen holder with carbon adhesion tape followed by platinum coating. All explants were examined by an SEM (JSM-6390LV, JEOL, Tokyo, Japan) with the secondary electron emission mode and accelerating voltages of 10 kV. The magnifications used were × 120, × 250, and × 800.

(2) Chronological analysis

All fluorescence images of explant cultures were captured by an all-in-one fluorescence microscope (BZ-X700, Keyence,

Osaka, Japan) with filters for GFP channel (excitation: 475 nm, emission: 525 nm).

(3) Live imaging of primary palate cultures

Live imaging of explant cultures was performed using an all-in-one fluorescence microscope (BZ-X700, Keyence, Osaka, Japan), equipped with filters for GFP (excitation: 475 nm, emission: 525 nm) channel. The instrument was controlled by the BZ Viewer version 1.0 software program (Keyence, Osaka, Japan). Live images were captured with either ×10 0.45 NA objective lens or a ×20 0.75 NA objective lens to collect 26 Z-stacks (10.0 μm/step). The migration length of the epithelial cells was analyzed using 30 GFP-positive epithelial cells in the nasal septum and secondary palatal shelf, as previously described (Aoyama et al., 2019).

(4) TUNEL staining

Maxillary explants were fixed in 4% paraformaldehyde with 0.1 M sodium phosphate buffer (pH 7.4) overnight at 4℃. Whole-mount TUNEL staining was performed using fixed E15.0 palates and cultured palates. Histological sections of primary palate were produced as previously described. Frontal frozen sections (20 μm) were prepared from samples. The explants and sections were processed for a terminal deoxynucleotidyl transferase-mediated deoxyuridine triphosphate (dUTP) nick end labeling (TUNEL) assay using an In Situ Cell Death Detection Kit TMR Red (Roche Applied Science, IN, United States) according to manufacturer's protocol. Finally, nuclear staining was performed using DAPI solution (Wako Pure Chemical Industries, Osaka, Japan).

DATA AVAILABILITY STATEMENT

All datasets generated for this study are included in the article/**Supplementary Material**.

ETHICS STATEMENT

The animal study was reviewed and approved by the Committee on the Ethics of Animal Experiments of Osaka University Graduate School of Dentistry.

AUTHOR CONTRIBUTIONS

SY performed the experiments and wrote the manuscript. HK funded the study, performed the experiments, and wrote the manuscript. JM, GA, SS, AO, TI, KN, and YU performed the experiments. ST provided technical support and conceptual advice. TY supervised the experimental analysis, edited the manuscript, and supplied funds. All authors discussed the results and implications and commented on the manuscript at all stages.

FUNDING

This work was supported by Grants-In-Aid for Scientific Research Program from the Japan Society for the Promotion of Science (#19H03858 to HK and #17K19754 to TY).

SUPPLEMENTARY MATERIAL

The Supplementary Material for this article can be found online at: https://www.frontiersin.org/articles/10.3389/fphys.2020.538835/full#supplementary-material

Supplementary Movie 1 | Live imaging of the epithelial cells of nasal septum explants. Scale bar: 100 μm. Images were captured every 15 min for 24 h.

Supplementary Movie 2 | Live imaging of the epithelial cells of secondary palate explants. Scale bar: 100 μm. Images were captured every 10 min for 8 h.

Supplementary Figure 1 | The migration length was significantly increased in the secondary palate. *$p < 0.05$, Student's *t*-test, $n = 30$.

Supplementary Figure 2 | The E-cadherin and PHH3 expression in the nasal septum. D, dorsal; V, ventral. Scale bars: 100 μm.

Supplementary Figure 3 | The size of the cultured tissue at E 15.0. The approximate width is 1500 μm. The approximate length is 1000 μm. The approximate thickness is 700 μm. A, anterior; P, posterior. Scale bars: **A** 500 μm (**A**, **B** same magnification).

Supplementary Figure 4 | TUNEL staining of the frontal section of the nasal septum at E14.5 and E15.5. D, dorsal; V, ventral. Scale bars: **A** 50 μm (**A**, **B** same magnification). **(C)** The numbers of TUNEL-positive cells were significantly increased at E15.5. *$p < 0.05$, Student's *t*-test, $n = 3$.

Supplementary Figure 5 | TUNEL staining of the frontal section of the control and *K14-Cre/Runx1*$^{fl/fl}$ mouse nasal septum. D, dorsal; V, ventral. Scale bars: **A** 50 μm (**A**, **B** same magnification). **(C)** The numbers of TUNEL-positive cells were significantly decreased at *K14-Cre/Runx1*$^{fl/fl}$ mouse. *$p < 0.05$, Student's *t*-test, $n = 3$.

REFERENCES

Aoyama, G., Kurosaka, H., Oka, A., Nakatsugawa, K., Yamamoto, S., Sarper, S. E., et al. (2019). Observation of dynamic cellular migration of the medial edge epithelium of the palatal shelf. *Front. Physiol.* 10:698. doi: 10.3389/fphys.2019.00698

Bush, J. O., and Jiang, R. (2012). Palatogenesis: morphogenetic and molecular mechanisms of secondary palate development. *Development* 139, 231–243. doi: 10.1242/dev.067082

Carette, M. J., and Ferguson, M. W. (1992). The fate of medial edge epithelial cells during palatal fusion in vitro: an analysis by dii labelling and confocal microscopy. *Development* 114, 379–388.

Charoenchaikorn, K., Yokomizo, T., Rice, D. P., Honjo, T., Matsuzaki, K., Shintaku, Y., et al. (2009). Runx1 is involved in the fusion of the primary and the secondary palatal shelves. *Dev. Biol.* 326, 392–402. doi: 10.1016/j.ydbio.2008.10.018

Cuervo, R., and Covarrubias, L. (2004). Death is the major fate of medial edge epithelial cells and the cause of basal lamina degradation during palatogenesis. *Development* 131, 15–24. doi: 10.1242/dev.00907

Dudas, M., Kim, J., Li, W. Y., Nagy, A., Larsson, J., Karlsson, S., et al. (2006). Epithelial and ectomesenchymal role of the type i tgf-beta receptor alk5 during

facial morphogenesis and palatal fusion. *Dev. Biol.* 296, 298–314. doi: 10.1016/j.ydbio.2006.05.030

Ferguson, M. W. (1978). Palatal shelf elevation in the wistar rat fetus. *J. Anat.* 125(Pt 3), 555–577.

Ferguson, M. W. (1988). Palate development. *Development.* 103, 41–60.

Griffith, C. M., and Hay, E. D. (1992). Epithelial-mesenchymal transformation during palatal fusion: carboxyfluorescein traces cells at light and electron microscopic levels. *Development* 116, 1087–1099.

Hilliard, S. A., Yu, L., Gu, S., Zhang, Z., and Chen, Y. P. (2005). Regional regulation of palatal growth and patterning along the anterior-posterior axis in mice. *J. Anat.* 207, 655–667. doi: 10.1111/j.1469-7580.2005.00474.x

Honarpour, N., Gilbert, S. L., Lahn, B. T., Wang, X., and Herz, J. (2001). Apaf-1 deficiency and neural tube closure defects are found in fog mice. *Proc. Natl. Acad. Sci. U.S.A.* 98, 9683–9687. doi: 10.1073/pnas.171283198

Hu, L., Liu, J., Li, Z., Ozturk, F., Gurumurthy, C., Romano, R. A., et al. (2015). Tgfβ3 regulates periderm removal through δnp63 in the developing palate. *J. Cell Physiol.* 230, 1212–1225. doi: 10.1002/jcp.24856

Jin, J. Z., and Ding, J. (2006). Analysis of cell migration, transdifferentiation and apoptosis during mouse secondary palate fusion. *Development* 133, 3341–3347. doi: 10.1242/dev.02520

Kim, S., Lewis, A. E., Singh, V., Ma, X., Adelstein, R., and Bush, J. O. (2015). Convergence and extrusion are required for normal fusion of the mammalian secondary palate. *PLoS Biol.* 13:e1002122. doi: 10.1371/journal.pbio.1002122

Lane, J., Yumoto, K., Azhar, M., Ninomiya-Tsuji, J., Inagaki, M., Hu, Y., et al. (2015). Tak1, smad4 and trim33 redundantly mediate tgf-β3 signaling during palate development. *Dev. Biol.* 398, 231–241. doi: 10.1016/j.ydbio.2014.12.006

Li, Q., and Ding, J. (2007). Gene expression analysis reveals that formation of the mouse anterior secondary palate involves recruitment of cells from the posterior side. *Int. J. Dev. Biol.* 51, 167–172. doi: 10.1387/ijdb.062212ql

Martínez-Alvarez, C., Bonelli, R., Tudela, C., Gato, A., Mena, J., O'Kane, S., et al. (2000). Bulging medial edge epithelial cells and palatal fusion. *Int. J. Dev. Biol.* 44, 331–335.

Sarper, S. E., Inubushi, T., Kurosaka, H., Ono Minagi, H., Kuremoto, K. I., Sakai, T., et al. (2018a). Runx1-stat3 signaling regulates the epithelial stem cells in continuously growing incisors. *Sci. Rep.* 8:10906.

Sarper, S. E., Inubushi, T., Kurosaka, H., Ono Minagi, H., Murata, Y., Kuremoto, K. I., et al. (2019). Anterior cleft palate due to cbfb deficiency and its rescue by folic acid. *Dis. Model. Mech.* 12:dmm038851. doi: 10.1242/dmm.038851

Sarper, S. E., Kurosaka, H., Inubushi, T., Ono Minagi, H., Kuremoto, K. I., Sakai, T., et al. (2018b). Runx1-stat3-tgfb3 signaling network regulating the anterior palatal development. *Sci. Rep.* 8, 11208.

Shiota, K., Kosazuma, T., Klug, S., and Neubert, D. (1990). Development of the fetal mouse palate in suspension organ culture. *Acta Anat. (Basel)* 137, 59–64. doi: 10.1159/000146859

Shuler, C. F., Halpern, D. E., Guo, Y., and Sank, A. C. (1992). Medial edge epithelium fate traced by cell lineage analysis during epithelial-mesenchymal transformation in vivo. *Dev. Biol.* 154, 318–330. doi: 10.1016/0012-1606(92)90071-n

Takigawa, T., and Shiota, K. (2004). Terminal differentiation of palatal medial edge epithelial cells in vitro is not necessarily dependent on palatal shelf contact and midline epithelial seam formation. *Int. J. Dev. Biol.* 48, 307–317. doi: 10.1387/ijdb.041840tt

Takigawa, T., and Shiota, K. (2007). Amniotic fluid induces rapid epithelialization in the experimentally ruptured fetal mouse palate–implications for fetal wound healing. *Int. J. Dev. Biol.* 51, 67–77. doi: 10.1387/ijdb.062216tt

Vaezi, A., Bauer, C., Vasioukhin, V., and Fuchs, E. (2002). Actin cable dynamics and rho/rock orchestrate a polarized cytoskeletal architecture in the early steps of assembling a stratified epithelium. *Dev. Cell* 3, 367–381. doi: 10.1016/s1534-5807(02)00259-9

Xu, X., Han, J., Ito, Y., Bringas, P., Urata, M. M., and Chai, Y. (2006). Cell autonomous requirement for tgfbr2 in the disappearance of medial edge epithelium during palatal fusion. *Dev. Biol.* 297, 238–248. doi: 10.1016/j.ydbio.2006.05.014

Yu, K., Deng, M., Naluai-Cecchini, T., Glass, I. A., and Cox, T. C. (2017). Differences in oral structure and tissue interactions during mouse vs. Human palatogenesis: implications for the translation of findings from mice. *Front. Physiol.* 8:154. doi: 10.3389/fphys.2017.00154

Conflict of Interest: The authors declare that the research was conducted in the absence of any commercial or financial relationships that could be construed as a potential conflict of interest.

frontiers in Physiology

ORIGINAL RESEARCH
published: 26 October 2020
doi: 10.3389/fphys.2020.582610

An *Msx2-Sp6-Follistatin* Pathway Operates During Late Stages of Tooth Development to Control Amelogenesis

*Intan Ruspita[1,2†], Pragnya Das[1,3†], Yan Xia[1], Sarah Kelangi[4,5], Keiko Miyoshi[6], Takafumi Noma[7], Malcolm L. Snead[8], Rena N. D'Souza[9] and Marianna Bei[4,5]**

[1] Center for Regenerative and Developmental Biology, The Forsyth Institute, Cambridge, MA, United States, [2] Department of Prosthodontics, Universitas Gadjah Mada, Yogyakarta, Indonesia, [3] Division of Neonatology, Cooper University Hospital, Camden, NJ, United States, [4] Center for Engineering in Medicine, Department of Surgery, Massachusetts General Hospital and Harvard Medical School, Boston, MA, United States, [5] Shriners Hospital for Children, Boston, MA, United States, [6] Department of Molecular Biology, Institute of Biomedical Sciences, Tokushima University, Tokushima, Japan, [7] Faculty of Human Life Studies, Hiroshima Jogakuin University, Hiroshima, Japan, [8] Center for Craniofacial Molecular Biology, Herman Ostrow School of Dentistry of USC, University of Southern California, Los Angeles, CA, United States, [9] University of Utah, Salt Lake City, UT, United States

OPEN ACCESS

Edited by:
Abigail Saffron Tucker, King's College London, United Kingdom

Reviewed by:
Thomas G. H. Diekwisch, Texas A&M University, United States
Javier Catón, Universidad Complutense de Madrid, Spain

***Correspondence:**
Marianna Bei
mbei@partners.org;
mbei@mgh.harvard.edu

[†] These authors have contributed equally to this work

Specialty section:
This article was submitted to Craniofacial Biology and Dental Research, a section of the journal Frontiers in Physiology

Received: 12 July 2020
Accepted: 28 September 2020
Published: 26 October 2020

Citation:
Ruspita I, Das P, Xia Y, Kelangi S, Miyoshi K, Noma T, Snead ML, D'Souza RN and Bei M (2020) An Msx2-Sp6-Follistatin Pathway Operates During Late Stages of Tooth Development to Control Amelogenesis. Front. Physiol. 11:582610. doi: 10.3389/fphys.2020.582610

Background: Ameloblasts are epithelially derived cells responsible for enamel formation through a process known as amelogenesis. Amongst the several transcription factors that are expressed during amelogenesis, both *Msx2* and *Sp6* transcription factors play important role. *Msx2* and *Sp6* mouse mutants, exhibit similar amelogenesis defects, namely enamel hypoplasia, while humans with amelogenesis imperfecta (AI) carry mutations in the human homologues of MSX2 or SP6 genes. These across species similarities in function indicate that these two transcription factors may reside in the same developmental pathway. In this paper, we test whether they work in a coordinated manner to exert their effect during amelogenesis.

Methods: Two different dental epithelial cell lines, the mouse LS8 and the rat G5 were used for either overexpression or silencing of *Msx2* or *Sp6* or both. *Msx2* mutant mouse embryos or pups were used for *in vivo* studies. *In situ* hybridization, semi-quantitative and quantitative real time PCR were employed to study gene expression pattern. *MatInspector* was used to identify several potential putative *Msx2* binding sites upstream of the murine *Sp6* promoter region. Chromatin Immunoprecipitation (chIP) was used to confirm the binding of *Msx2* to *Sp6* promoter at the putative sites.

Results: Using the above methods we identified that (i) *Msx2* and *Sp6* exhibit overlapping expression in secretory ameloblasts, (ii) *Sp6* expression is reduced in the *Msx2* mouse mutant secretoty ameloblasts, and (iii) that *Msx2,* like *Sp6* inhibits *follistatin* expression. Specifically, our *loss-of* function studies by silencing *Msx2* and/or *Sp6* in mouse dental epithelial (LS8) cells showed significant downregulation of *Sp6* but upregulation of *Fst* expression. Transient transfection of *Msx2* overexpression plasmid,

up-regulated *Sp6* and downregulated *Fst* expression. Additionally, using *MatInspector,* we identified several potential putative *Msx2* binding sites, 3.5 kb upstream of the murine *Sp6* promoter region. By chIP, we confirmed the binding of *Msx2* to *Sp6* promoter at these sites, thus suggesting that *Sp6* is a direct target of *Msx2*.

Conclusion: Collectively, these results show that *Sp6* and *Msx2* work in a concerted manner to form part of a network of transcription factors that operate during later stages of tooth development controlling ameloblast life cycle and amelogenesis.

Keywords: *Msx2*, *Sp6*, *follistatin*, dental epithelial cells, *in situ* hybridization, chromatin immunoprecipitation

INTRODUCTION

The development of teeth depends on cell interactions between epithelium and mesenchyme that leads to the differentiation of cells derived from mesenchyme into odontoblasts and of cells derived from epithelium into ameloblasts (Kollar and Lumsden, 1979; Thesleff and Nieminen, 2005). The process of epithelial cells differentiating into functional ameloblasts is time-dependent and through this process several morphologic changes occur known as: (i) *the inductive stage* (pre-ameloblasts); (ii) *the initial-secretory stage*; (iii) *the secretory stage*; and (iv) the *maturation stage* (Nanci, 2007). Pre-secretory, secretory, and mature ameloblasts express several proteins, including secreted proteins, enzymes, signaling molecules, cell–cell adhesion molecules, and transcription factors (reviewed in Wright et al., 2000, 2015; Aldred et al., 2003; Wright, 2006; Hu et al., 2008; Nakamura et al., 2008; Bei, 2009a,b; Bartlett, 2013; Habelitz, 2015; Shin et al., 2020).

Studies in animal models and humans have shown that Msx2 and Sp6 transcription factors play important role during amelogenesis. Specifically, in mice lacking the homeobox gene *Msx2* "the ameloblasts reach the secretory stage of their differentiation process, but only sparse amounts of enamel matrix are deposited" (Satokata et al., 2000; Bei et al., 2004; Babajko et al., 2014). In a case of syndromic amelogenesis imperfecta (AI) sequence analysis of the human homolog of MSX2 gene identified a missense mutation of T447C, further indicating the important role of *Msx2* during amelogenesis (Suda et al., 2006). Expression studies have also indicated that Msx2 is required for the expression of important secreted proteins and cell-cell adhesion molecules for amelogenesis, such as *laminin 5 alpha 3*, *amelogenin*, and *enamelin* (Bei et al., 2004; Ruspita et al., 2008; Molla et al., 2010).

Specificity protein 6 (*Sp6*) is another transcription factor that, like *Msx2*, is expressed by secretory ameloblasts and when its function is eliminated in mice amelogenesis is affected. The *Sp6* mutant mice among other phenotypes exhibit enamel hypoplasia (Nakamura et al., 2008; Utami et al., 2011). Recently, in a Caucasian family with autosomal dominant hypoplastic AI, a missense protein change, p.(Ala273Lys), is identified in *SP6*, the gene encoding the SP6 transcription factor (Smith et al., 2020). The authors have also "identified a potential SP6 binding motif in the *AMBN* proximal promoter sequence and showed that wild-type (WT) SP6 binds more strongly to it than the mutant protein," further indicating the important role of Sp6 in amelogenesis (Smith et al., 2020). Earlier studies indicate that *Sp6* promotes amelogenesis *in vitro* through inhibition of *follistatin* (*Fst*) gene which is a soluble extracellular inhibitor of TGFβ superfamily and is involved in differentiation of secretory ameloblasts during tooth development (Ruspita et al., 2008). In addition, "overexpression of *follistatin* in the dental epithelium inhibits ameloblast differentiation in transgenic mouse incisors, whereas in *follistatin* knockout mice, ameloblasts differentiate ectopically on the lingual enamel-free surface" (Wang et al., 2004).

Based on the above, the role of *Msx2* and *Sp6* genes in amelogenesis is important. Here, we study the interplay between *Msx2, Sp6*, and *Fst* and we show that (i) *Sp6* expression is reduced in the *Msx2* mouse mutant secretoty ameloblasts, (ii) *Msx2,* like *Sp6* inhibits *follistatin* expression *in vitro*, (iii) *Sp6* and *follistatin* are early response genes whose expression is under the control of Msx2, and that (iv) Msx2 binds to *Sp6* promoter *in vitro,* suggesting that *Sp6* is a direct target of *Msx2*. These results raise the possibility that these transcription factors interact closely with each other and within a common molecular cascade.

MATERIALS AND METHODS

Cell Culture

Two different dental epithelial cell lines were used in the present study – the rat dental epithelial cell line (G5), generously provided by Dr. Takafumi Noma, Dental School of Tokushima University, Japan and the mouse dental epithelial cell line (LS8) kindly provided by Dr. Malcolm Snead, USC, CA, United States. Both cell lines were maintained in high-glucose Dulbecco's modified Eagle's medium (Gibco, Grand Island, NY, United States), containing 100 U/ml penicillin, 100 mg/ml streptomycin, and 10% fetal bovine serum (Gibco, Grand Island, NY, United States) at 37°C in 5% CO_2 humidified atmosphere following the standard protocols (Ruspita et al., 2008; Chang et al., 2017)

Gain-of-Function and Loss-of-Function Studies

For overexpression of *Msx2*, LS8, and G5 cells were transfected with pCMVtag2-Flag-*Msx2*, and then cultured for 48–72 h following which total RNA was isolated from the cells using Trizol (Qiagen, MD, United States). An empty vector (pCMVtag2) served as a negative control for gain-of-function studies.

For loss of function of *Msx2*, commercially available small interfering RNA for *Msx2* (*Msx2*-siRNA) was purchased from Santa Cruz Biotechnology (Santa Cruz, CA, United States). We used the following oligonucliotides, sense sequence 5′CAGCUCUCUGAACCUUAC 3′ (sc-43947). As negative control we used a scramble sequence that will not lead to the specific degradation of any known cellular mRNA: sense scramble control 5′UUCUCCGAACGUGUCACG 3′ (sc-37007). To prepare lipid-siRNA complexes, the siRNA (80 pmol) in 100 μl of transfection medium (sc-36868) and 5 μl of siRNA transfection reagent (sc-29528) in 100 μl of transfection medium were combined, incubated for 30 min at 25°C, and then diluted with 800 μl of transfection medium. Cells were rinsed once with serum-free DMEM/F12, and 1000 μl of lipid-siRNA mixture-described above-was applied per well. After incubation for 6 h at 37°C in a humidified 5% CO_2 cell chamber, an additional 1 ml of 20% FBS in DMEM/F12 was added per well, and lipofection was allowed to continue overnight. The following day, lipofection media was aspirated, and transfected monolayer cells refed with fresh 10% FBS in DMEM/F12. After 48 and 72 h, total cellular RNA was harvested for reverse-transcriptase-polymerase chain reaction (RT-PCR) analysis. For lentiviral (ShRNA) gene knock down assay, we obtained plasmids containing the sequences for *Msx2*-shRNA, *Sp6-shRNA* and non-target scramble shRNA from Sigma Aldrich (St. Louis, MO, United States). LS8 cells were seeded into six-well culture plates and cultured in DMEM/F12 containing 10% fetal bovine serum without antibiotic. Upon 80% confluency, cells were infected with lentiviruses with a MOI (multiplicity of infection) = 5 and selected for stable integration with 1 μg/ml puromycin.

Time Dependent Assay

LS8 cells were transfected with pCMVtag2-Flag-*Msx2* (Invitrogen, United States) and then cultured for up to 48 h. The cells were harvested at 4 and 16 h for RNA isolation and subjected to real time qPCR analysis to check for expression of *Sp6* and *Fst*.

RNA Extraction and Reverse-Transcriptase-Polymerase Chain Reaction

Total RNA was isolated from cultured cells after the desired time points using the standard procedure by TRIZOL (Qiagen) method. First-strand cDNA was generated from 1 μg of total RNA using quantitect, RT kit (Qiagen, Valencia, CA, United States) in total of 20 μl according to the manufacturer's instructions. Semi-quantitative PCR was performed on 1 μl of RT product in 20 μl of reaction mixture to check for expression of *Msx2, Sp6*, and *Fst*. *Gapdh* was used as the loading control. The PCR products were analyzed on 1.5% agarose gel. The primer sequences are listed in **Supplementary Table 1**.

Real-Time Quantitative PCR

For real-time quantitative PCR, total RNA from was isolated from cultured cells after the desired time points using the standard procedure by TRIZOL (Qiagen) method and reverse transcriptions were performed using qScript cDNA synthesis kit (Quanta Biosciences, Gaithersburg, MD, United States). Quantitative PCR was carried out in LightCycler and LightCycler-Faststart DNA Master SYBR Green I (Roche Diagnostics, Switzerland). The expression level of each sample was normalized to glyceraldehyde-3phosphate dehydrogenase (GAPDH) mRNA expression. The primer sequences are listed in **Supplementary Table 1**.

Mice and Genotyping

All animal studies and experimental procedures were conducted in accordance to the guidelines for the care and use of laboratory animals by the Forsyth Institute, Cambridge, MA and Massahusetts General Hospital, Boston, MA. Embryos and postnatal pups (E18.5, P1 and P3) were collected from matings of *Msx2* heterozygous animals maintained in BALB/c background. The day of plug discovery was designated as embryonic day 0.5 (E0.5). Genotyping was performed as previously described (Bei et al., 2004). Age matched wildtype pups and/or embryos served as the appropriate controls.

In situ Hybridization

Embryonic Day 18.5 embryos and postnatal animals (P1, P3) were collected and heads decapitated for making coronal and sagittal sections. E18.5, P1 and P3 samples were immediately fixed in 4% paraformadehyde. All samples were then dehydrated through graded ethanol series, embedded in paraffin, sectioned at 8 μm and processed for in situ hybridization (ISH), as previously described (Bei and Maas, 1998). Murine *Sp6* and *Fst* antisense probes were purchased from IDT (IA, United States) and labeled with DIG-UTP (Roche) following the manufacturer's instructions. The sense probes for both genes were used as a negative control. *In situ* hybridization was performed as previously described (Bei et al., 2004)

Chromatin Immunoprecipitation Assay

Chromatin immunoprecipitation (chIP) was performed using the EZ-Magna chip kit (Millipore, Billerica, MA, United States) according to the manufacturer's instructions. Forty-eight hours after transfection with pCMV-FLAG-*Msx2* expression plasmid, LS8 cells were fixed and crosslinked with 1% (v/v) formaldehyde at 37°C for 10 min. Crosslinking was stopped by adding glycine to a final concentration of 125 mM, followed by washing with cold PBS. After sonication chromatin was incubated with magnetic beads conjugated to either 1 μg of monoclonal anti-Flag antibody (Sigma) or 1 μg of normal rabbit IgG (Sigma) antibody. Immunoprecipitated chromatin was reverse crosslinked and washed before DNA extraction. Polymerase A was used as a positive control while IgG was used as the negative control. Finally, the immunoprecipitated DNA and the corresponding non-immunoprecipitated DNA (input) was subjected to PCR using different set of forward and reverse primers, specific for the different putative binding regions, and analyzed on 1.5% agarose gel. The primers used for the different putative binding sites are listed in **Supplementary Table 1**.

In silico Analysis of Promoter Binding Sites

UCSC MatInspector software was used to predict the putative promoter binding regions for Msx2. Primers were designed from these predicted regions for chIP followed by PCR amplification using these primers, using Primer 3 database.

Imaging and Densitometric Quantification

The imaging for ISH was done using Olympus microscope while densitometric quantification of semi-quantitative RT-PCR bands were done using ImageJ (NIH, version 5).

Statistics

Each cell culture experiment was replicated three times. For ISH, a minimum of 3–4 mice pups were used. Statistics was done using one-way ANOVA or students *t*-tailed test, wherever applicable using GraphPad prism (version 7, CA). *P* value of <0.05 was considered statistically significant.

RESULTS

Msx2 Differentially Regulates the Expression of Genes Involved in Amelogenesis

There are several genes known to be involved in amelogenesis (Bei, 2009b; Wright et al., 2015). To test whether *Msx2* regulates the expression of some of these genes, we performed semi-quantitative RT-PCR after overexpressing *Msx2* in LS8 (**Figure 1**) and G5 cells (data not shown). The ameloblast-like cell LS8 cell line, derived from murine EO epithelium, and the G5 cell line, derived from rat dental epithelial derived ameloblast-lineage clone, both, constitute ideal cell systems to test gene regulation for the following reasons. (Chen et al., 1992; Xu et al., 2006; Abe et al., 2007; Ruspita et al., 2008). The LS8 and G5 "cells express many of the genes specific for amelogenesis, such as *ameloblastin*, *amelogenin*, and *enamelin*, at sufficiently high levels, they have been used for many *in vitro* studies of amelogenesis, including gene promoter analysis and LS8 cells, in particular, produce an enamel extracellular matrix that is similar to authentic enamel after treatment with peptide amphiphiles" (Zhou et al., 2000; Huang et al., 2008). After overexpressing *Msx2* in both cells lines, we show that the expression of *Sp6*, *Sp3*, *Sprouty 2*, *Connexin 43*, *Wnt3*, *Tgfb1* and *Enam* (*enamelin*), *Laminin 5 alpha 3* (*lama3*), as well as *Msx2* itself, is up-regulated in the *Msx2* overexpressing cells. In contrast, the expression of *Tbx1*, *Amel* (*amelogenin*), *Fst* (*Follistatin*) is downregulated in the *Msx2* overexpressing cells, while *Ambn* (*ameloblastin*) expression is partially diminished, almost not affected (**Figure 1**). These results further confirm previous results where we and others showed that *Msx2* is required for the regulation of *Lama3*, *Amel, Enam* and *Ambn* gene expression (Zhou et al., 2000; Bei et al., 2004; Ruspita et al., 2008; Molla et al., 2010; Bei, unpublished). We also show for the first time that *Msx2* is required for the regulation of *Sp6*, *Sp3*, *Sprouty 2*, *Connexin 43*, *Wnt3*, *Tgfb1*, *Tbx1*, and *Fst* (*Follistatin*) gene expression. For the purposes of this study, we will focus on *Sp6* and *Fst* regulation, only.

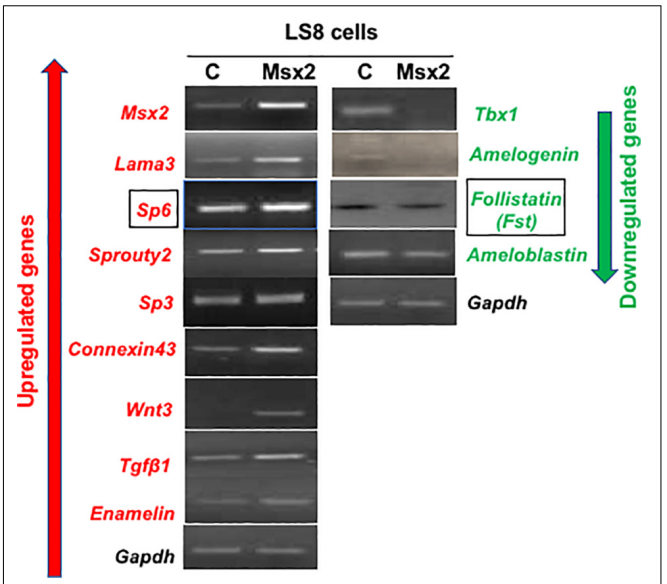

FIGURE 1 | Screening of representative genes involved in amelogenesis: LS8 cells were transfected with pCMVtag2-Flag-*Msx2* then cultured for 48 h. Total RNA was isolated from the cells and subjected to reverse transcription PCR analysis. Upregulated genes are shown in red while downregulated ones are shown in green. The expression of *Sp6*, *Sp3*, *Sprouty 2*, *Connexin 43*, *Wnt3*, *Tgfb1* and *Enam* (*enamelin*), *Laminin 5 alpha 3* (*lama3*), as well as *Msx2* itself, is up-regulated in the *Msx2* overexpressing cells. In contrast, the expression of *Tbx1*, *Amel* (*amelogenin*), *Fst* (*Follistatin*) is downregulated in the *Msx2* overexpressing cells, while *Ambn* (*ameloblastin*) expression is partially diminished, almost not affected. *Gapdh* is the housekeeping gene. C, cells transfected with control vector only; Msx2, cells are transfected with pCMVtag2-Flag-Msx2.

The Expression of *Sp6* and *Fst* Is Modulated Early in Response to *Msx2*

The previous results indicate that *Sp6* expression is up-regulated while *Fst* expression is downregulated, upon *Msx2* overexpression. To determine the kinetics of *Sp6* and *Fst* (*Follistatin*) gene expression, we performed a time dependent assay to ascertain whether their expression is modulated early in response to *Msx2* upregulation (**Figure 2**). LS8 cells were transfected with *Msx2* over-expression plasmid for two time points, 4 and 16 hours. Total RNA was isolated from the cells and subjected to qPCR analysis. *Sp6* and *Fst* could be detected as early as 4h after transfection by real time qPCR (**Figure 2**). By 16 h, there was a significant increase in the expression of *Sp6* (**Figure 2A**) with a corresponding decrease of *Fst* expression (**Figure 2B**). We have not seen any significant response earlier than 4 h, thus these results indicate that both *Sp6* and *follistatin* are secondary early response genes to *Msx2* (response after 4 h of *Msx2* overexpression). These experiments have not been performed in the presence of the protein synthesis inhibitor, cycloheximide and thus, we do not know whether the secondary

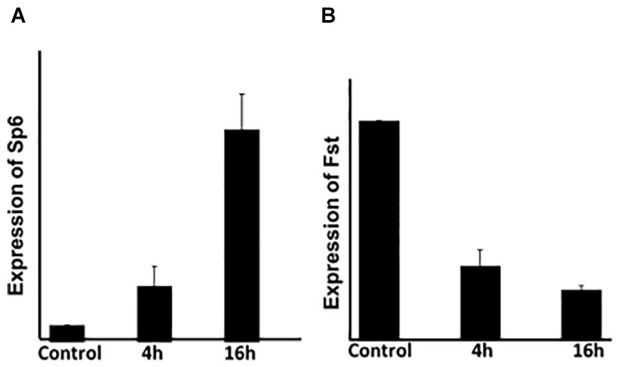

FIGURE 2 | The expression of *Sp6* and *Fst* is modulated early in response to *Msx2:* LS8 cells were transfected with *Msx2* over-expression plasmid for two time points, 4 and 16 h. Total RNA was isolated from the cells and subjected to qPCR analysis. **(A)** *Sp6* and **(B)** *Fst* could be detected as early as 4h after transfection by real time qPCR. By 16 h, there was a significant increase in the expression of *Sp6* **(A)** with a corresponding decrease of *Fst* expression **(B)**. *Gapdh* is the normalizing gene. C, cells transfected with control vector only. The experiment was conducted three times in replicates of 3. $^{**}p \leq 0.005$.

response of *Sp6* and *Fst* genes require *de novo* protein synthesis for transcription.

Loss of Function of *Msx2* and *Sp6* in LS8 Ameloblast-Derived Cells

We have shown that overexpression of *Msx2* in both LS8 (**Figures 2**, **3A**) and G5 cells (**Figure 3A**) leads to a significant increase of *Msx2* in both cell lines-indicating that the transfection efficiency is quite successful-with concomitant increase of *Sp6* and decrease of *Fst* expressions (**Figure 3A**). To test whether the opposite holds true, we tested the effects of acute knockdown of Msx2 in LS8 ameloblast-derived cells, and compared to what happens in development where Msx2 is permanently absent in the *Msx2*-null mice (**Figure 4**). For the knock down experiment, we used siRNA technology in LS8 cells (**Figure 3B**). After 48 and 72 h transfection the cells were subjected to RT-PCR. We found that upon silencing of *Msx2*, *Sp6* was downregulated while *Fst* expression was upregulated, further suggesting that *Sp6* requires Msx2 for its expression and that Msx2 inhibits *Fst* expression (**Figure 3B**). In addition, we used lentiviral shRNA mediated approach to assess the direct effects of silencing *Msx2* and *Sp6* genes. Specifically, the LS8 cells were infected with mouse Msx2shRNA, or Sp6shRNA or both lentiviral transduction particles. qPCR shows that (i) Msx2shRNA or Sp6shRNA lentiviral transduction particles alone effectively reduce each other's expression in LS8 cells, while they increase expression of *Fst* compared to control shRNA treated cells; (ii) that both Msx2shRNA plus Sp6shRNA lentiviral transduction particles abolished *Sp6* and *Msx2* expression in LS8 cells and increased *Fst* expression comparing with control shRNA treated cells (**Figure 3C**).

The loss of function along with the gain of function results show for the first time that Msx2 is required for *Sp6* expression and that Sp6 is required for *Msx2* expression. This result suggests that these two transcription factors may interact at the molecular level to control each other's transcriptional output. We also show that Msx2 inhibits *Fst* expression and confirmed that Sp6 inhibits *Fst* expression (Ruspita et al., 2008). In addition, we show that Msx2 and Sp6 act synergistically to control the level of *Fst* inhibition, since when we silenced both Msx2 and Sp6, at the same time, the inhibition of *Fst* was less robust compared to silencing by *Msx2* or *Sp6* alone. The latter result is of particular interest as it suggests that the synergistic interaction of Msx2 with Sp6 may alleviate each other's inhibitory effect on *Fst* by allowing one, or more than one, transcription activators to exert their function and thus regulating *Fst*'s gene dosage.

Msx2 Is Essential for *Sp6* Gene Expression During Late Tooth Development

To determine whether *Msx2* is required for *Sp6* regulation and whether this requirement is associated with the defect in amelogenesis, *in situ* hybridization was performed in wild type and *Msx2* deficient mouse molar tooth germs at E.18.5, postnatal day 1 (P1) and postnatal day 3 (P3) (**Figure 4**). *Msx2* is expressed at very low levels by pre-ameloblasts (E18.5-P1) but is highly expressed in secretory ameloblasts (P3) (MacKenzie et al., 1992; Gritli-Linde et al., 2002; Bei et al., 2004; Bei, 2009a,b). Partial diminution of *Sp6* expression is observed in *Msx2* deficient tooth germs at P1 compared to wild type (**Figures 4A,B**). In contrast, a dramatic reduction of *Sp6* expression, is observed in *Msx2* deficient ameloblasts compared to wild type at P3, when ameloblasts are at their secretory stage (**Figures 4C,D**). This result indicates that *Sp6* requires *Msx2* for its expression in the secretory stage ameloblasts, and is consistent with the *in vitro* loss and gain of function studies.

Follistatin (Fst) starts to be co-expressed with *Msx2* at the early bell stage of tooth development. Although it seems to be expressed widely in the dental epithelial organ, its expression is more concentrated in the inner enamel epithelium (iee). As development proceeds however, and the inner enamel epithelium cells become pre-secretory ameloblasts and, later on, secretory ameloblasts, *Fst* ceases to be expressed (Wang et al., 2004; Bei, 2009b). In the absence of *Msx2*, *follistatin* is expressed throughout the dental epithelium at the bell stage and its expression is increased in the inner dental epithelium (data not shown). This result is consistent with the *in vitro* loss of function and gain of function studies.

Msx2 Directly Binds to *Msx2* Recognition Sites on the *Sp6* Promoter

The loss and/or gain-of-function studies along with the *in vivo* experiments using the *Msx2* mouse mutants revealed that Msx2 is required for the expression of *Sp6* in the secretory ameloblasts, during amelogenesis. Computational sequence analysis of the nucleotides in the proximal 3.5 kb of the murine *Sp6* promoter region revealed the presence of 6 fully conserved Msx2 binding sites upstream from the transcription initiation site in the mouse (**Supplementary Figure 1**). To determine whether Msx2 binds to any of these sites and, therefore, directly

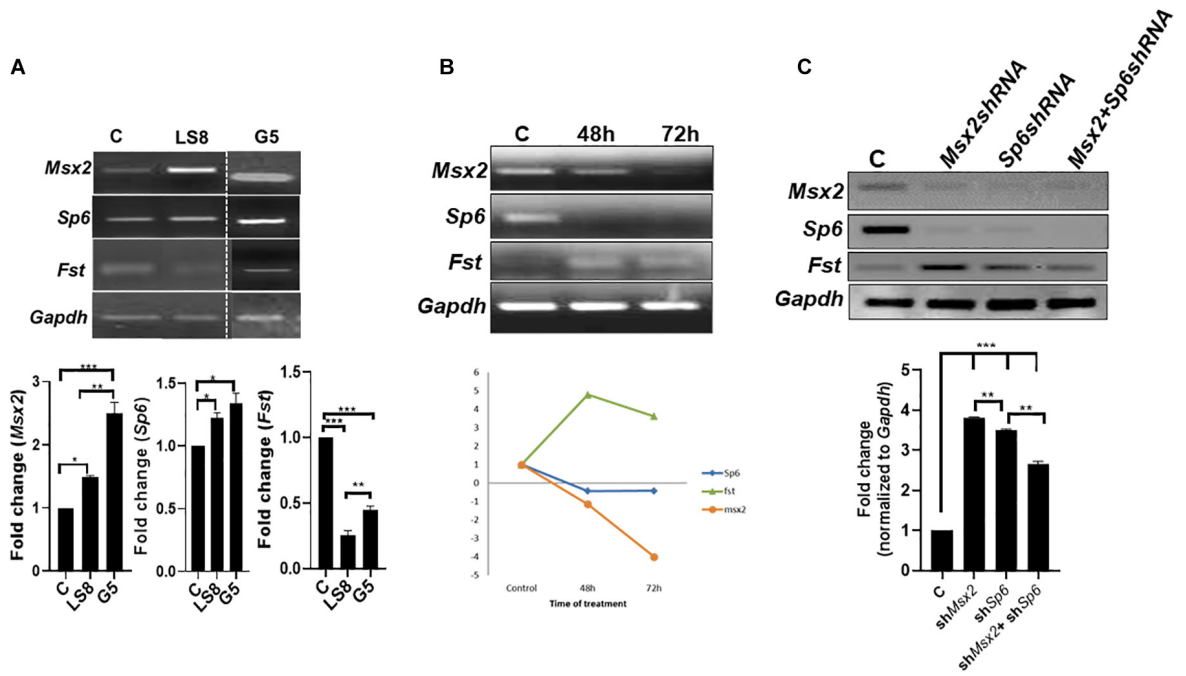

FIGURE 3 | Loss of function of *Msx2* and *Sp6* in LS8 ameloblast-derived cells: **(A)** Both LS8 and G5 cells were overexpressed with *Msx2* over-expression plasmid. Representative RT-PCR showing *Sp6* is upregulated whereas *Fst* is downregulated in both cell lines after *Msx2* overexpression. Bottom panel shows densitometric quantification of the bands. **(B)** The knockdown of *Msx2* with siRNA relative to scrambled control shows downregulation of *Msx2* and *Sp6* and upregulation of *Fst*, in 48 and 72 h. RT-PCR results were normalized to *Gapdh* that served as an internal control and expression levels were relative to scrambled controls. $^{**}P < 0.01$. Bottom panel shows a graph describing the trend of genes' expression. **(C)** Lentiviral (ShRNA) gene knockdown assay, where *Msx2*-shRNA and *Sp6*-shRNA, and non-target-shRNA infected LS8 cells further confirm the siRNA results. qPCR results were normalized to *Gapdh*. Bottom panel shows densitometric quantification of the bands. Experiments were done in triplicates. $^{**}p \leq 0.005$; $^{***}p \leq 0.0001$.

regulates *Sp6*, chromatin immuno-precipitation was performed with exogenously expressed Msx2-FLAG. Immunoprecipitated chromatin fragments (IP samples) and non-immunoprecipitated samples (1% input) were subjected to PCR analysis using specific primers spanning the six binding sites. PCR amplifications showed that Msx2 binds directly to four out of six sites carrying the conserved motif (TAAT) in the endogenous promoter of the mouse *Sp6* gene (**Supplementary Figure S1**). This result demonstrates that Msx2 binds directly to the proximal *Sp6* promoter *in vitro*.

In sum, we show that (i) *Msx2* and *Sp6* exhibit overlapping expression in secretory ameloblasts; (ii) they regulate each other's expression; (iii) *Msx2,* like *Sp6* alone or in coordination with *Sp6* inhibits *follistatin* expression; and (iv) *Msx2* binds directly to *Sp6* promoter, suggesting that *Sp6* is a direct target of *Msx2*.

Collectively, these results raise the possibility that the *Sp6* and *Msx2* transcription factors interact closely with each other and work in a concerted manner within a common molecular cascade to form part of a network of transcription factors that control ameloblast life cycle and amelogenesis.

DISCUSSION

Of the several transcription factors, *Msx2* and *Sp6* constitute key players of amelogenesis. Both, *Msx2* and *Sp6* mouse mutants, exhibit enamel hypoplasia, while humans with AI carry mutations in the human homologues of MSX2 or SP6 genes (Satokata et al., 2000; Bei et al., 2004; Suda et al., 2006; Nakamura et al., 2008; Utami et al., 2011; Babajko et al., 2014; Smith et al., 2020). These similarities in function indicate that these two transcription factors may reside in the same developmental pathway.

In this paper, we show that Msx2 and Sp6 transcription factors reside in the same developmental pathway and that they work in a coordinated manner to regulate the expression of *follistatin* (*Fst*), a signaling molecule that also controls enamel formation (Wang et al., 2004).

Msx2 and Sp6 Transcription Factors Require Each Other to Exert Their Function

Our gain of function, loss of function, time dependent assay and *in vivo* data demonstrate that *Sp6* requires Msx2 for its expression (**Figure 5**). Our loss of function experiments indicate that *Msx2* also requires Sp6 for its expression, indicating that these two genes reside in the same genetic pathway and that these two transcription factors may interact at the molecular level to control each other's transcriptional output (**Figure 5**). Characterization of *Sp6* promoter for Msx2 binding sites revealed six putative Msx2 binding sites and our ChIP experiments

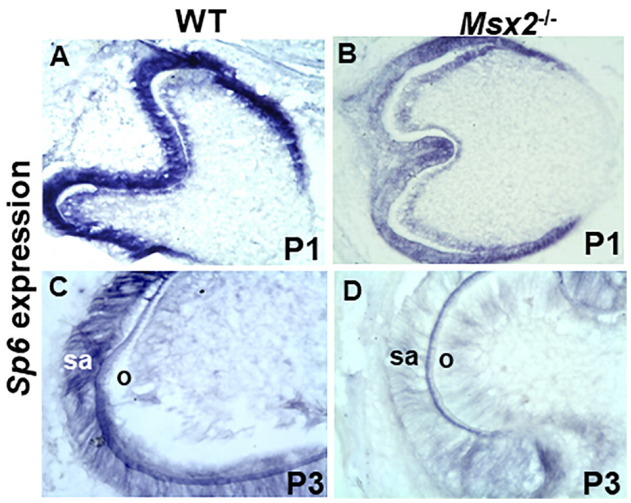

FIGURE 4 | Msx2 is essential for *Sp6* gene expression during late stage tooth development: In situ hybridization analyses of transcripts in wild type **(A,C)** and *Msx2* deficient **(B,D)** first lower molar teeth at postnatal day P1 **(A,B)** and postnatal day P3 **(C,D)**. Expression of *Sp6* is reduced **(B)** relative to wild type **(A)**. In contrast, a dramatic reduction of *Sp6* expression, is observed in *Msx2* deficient ameloblasts **(D)** compared to wild type at P3 **(C)**. sa, secretory ameloblasts. Scale: X400 ($N = 4$).

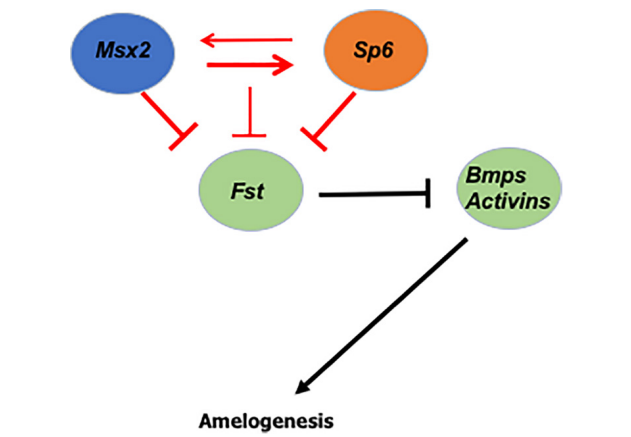

FIGURE 5 | Predicted model of Msx2 and Sp6 function during amelogenesis: We show that the two transcription factors *Msx2* and *Sp6* regulate each other's expression (red arrows) and that *Msx2* binds directly to *Sp6* promoter (thick red arrow), suggesting that *Sp6* is a direct target of *Msx2*. In addition, we show that *Msx2* alone, like *Sp6* (thick red inhibition lines) inhibits *follistatin* expression. In coordination with *Sp6* (thin red inhibition line) the inhibition of *follistatin* expression is less robust. Collectively, these results raise the possibility that the *Sp6* and *Msx2* transcription factors interact closely with each other and work in a concerted manner to form part of a network that controls ameloblast life cycle and amelogenesis, in a cell autonomous manner.

provided evidence that Msx2 binds directly to *Sp6* promoter to four out of six sites, suggesting that *Sp6* is a direct target for Msx2 and that Msx2 may promote *Sp6* expression directly acting as an activator of *Sp6* expression (**Figure 5**). Msx1 and Msx2 transcription factors are known to act as repressors (Catron et al., 1993, 1995; Zhang et al., 1997), but, consistent to our results recent findings in other developmental systems demonstrate that *Msx1* and *Msx2* may act as transcriptional activators, as well (Duval et al., 2014).

The fact that Msx2 binds directly to the *Sp6* promoter does not rule out the possibility that these two transcription factors may interact with each other physically and/or *in vivo* via a protein–protein interaction mechanism. Consistent with this idea, we have shown that Msx2 interacts *in vitro* and *in vivo* with another member of the Sp family of transcription factors, the Sp3 (Zhao et al., 2013). Interstingly, *Sp3* homozygous null mice, like *Sp6* null mice, exhibit a hypoplastic phenotype in both, dentine and enamel matrices (Bouwman et al., 2000).

Another interesting finding is that Msx2 seems to regulate its own expression. The gain of function experiments indicate that Msx2 is required for its own expression. This is consistent with other studies showing that Msx2 auto-regulates its promoter and simultaneously represses *Dlx2* transcription factor activation in LS8 ameloblast-like cells (Diamond et al., 2006). Here, we show that Msx2 is required for its own expression potentially via an autoregulation mechanism to activate the *Sp6* transcription factor. As transcription factors are known to operate sometimes through a feed-forward positive autoregulation mechanism, we can hypothesize that in this case Msx2 activates expression of *Sp6*, followed potentially by auto-regulatory binding to maintain expression of both genes at a certain level for specific time. To our knowledge, it is not known whether Sp6 operates through an auto-regulatory mechanism, like Msx2 does. Considering, however, that transfection of *Sp6* promoted dental epithelial cell differentiation into ameloblasts, by controlling the rate of proliferation of inner enamel epithelium (Nakamura et al., 2008; Ruspita et al., 2008), it would be interesting to see in the future, whether these two transcription factors sustain each other's expression through positive autoregulation. Positive autoregulation is a process where a transcription factor either directly or indirectly activates its own expression, resulting in continuation of transcription in the absence of the factors that started its expression.

Follistatin Expression Is Inhibited by, Both, Msx2 and Sp6 to Promote Amelogenesis

In vivo studies have clearly demonstrated that "*Follistatin* is essential for enamel-free area formation by preventing ameloblast differentiation" (Wang et al., 2004). "Overexpression of *follistatin*, a BMP inhibitor, in the epithelium abrogates ameloblast differentiation. The K14-*follistatin* mice lack enamel, the ameloblasts fail to form and they do not express enamel specific markers" (Wang et al., 2004). In contrast, in the *follistatin* knockout mice, functional ameloblasts differentiated on the normally enamel-free surface (Wang et al., 2004). In addition, "experiments on cultured tooth explants suggest that the mechanism by which *follistatin* prevents ameloblast differentiation is by inhibiting the ameloblast-inducing activity of BMP4 from the underlying odontoblasts. Thus, *follistatin*

controls ameloblast differentiation in a cell-autonomous manner by integrating the effect of a non-cell-autonomous signal, that of BMP4 from odontoblasts" (Wang et al., 2004).

In the secretory ameloblasts, it is known that Sp6 inhibits *Fst* expression (Ruspita et al., 2008). Here, we show for the first time that, like Sp6, Msx2 inhibits *Fst* expression in the secretory ameloblasts and confirmed the previous result by Ruspita et al. (2008). In addition, we show that Msx2 and Sp6 act synergistically to control the level of *Fst* inhibition, since when we silenced both Msx2 and Sp6, at the same time, the inhibition of *Fst* was less robust compared to silencing by *Msx2* or *Sp6* alone (**Figure 5**). The latter result is of particular interest as it suggests that Msx2's synergistic interaction with Sp6 may alleviate each other's inhibitory effect on *Fst* by allowing a third or other transcription activators to exert their function and thus regulating *follistatin's* final gene dosage (**Figure 5**).

A Cell Autonomous Pathway of *Msx2*, *Sp6*, and *Fst* Operate to Ensure Enamel Formation

As mentioned above, the role of *follistatin* in preventing enamel to be formed by inhibiting the ameloblast-inducing activity of BMP4 from the underlying odontoblasts is well known (Wang et al., 2004). What this paper shows, is that Msx2 and Sp6 transcription factors coordinately function by regulating each other's expression to ensure that the expression of *follistatin* is inhibited and that ameloblasts secrete enamel (**Figure 5**). *Follistatin* is expressed in the inner enamel epithelium to ensure proliferation of the cells and it does so by inhibiting the ameloblast-inducing activity of BMP4 from the underlying odontoblasts (Wang et al., 2004; Bei, 2009b). For enamel to be formed, *follistatin* needs to cease to be expressed, so that BMP4 from underlying odontoblasts is able to induce enamel formation. Thus, controlling the timing of *follistatin's* switch, from on to off, is extremely important. In light of our recent findings, we propose that Msx2 and Sp6's coordinated action controls either the cease of *follistatin's* expression or the reduction of its level in order to promote enamel deposition, in a cell autonomous manner (**Figure 5**).

DATA AVAILABILITY STATEMENT

The raw data supporting the conclusions of this article will be made available by the authors, without undue reservation.

ETHICS STATEMENT

The animal study was reviewed and approved by The Forsyth Institute and Massachusetts General Hospital Boston, Boston MA, United States.

AUTHOR CONTRIBUTIONS

IR and MB contributed to the concept and design of the study. IR, PD, YX, and MB contributed to the acquisition of data. IR, PD, SK, and MB prepared the figures. IR, PD, RD'S, and MB contributed to the data analysis and interpretation. IR, PD, and MB wrote the manuscript. IR, PD, MS, TN, RD'S, and MB contributed to the editing and the critical revision for intellectual content. All authors have approved the final version of the submitted manuscript.

FUNDING

This study was supported by funds from NIH [grants R01DE027255-01S1 (subcontract), R21DE028091], to MB and (grant R01DE027255), to RD'S. The funders had no role in study design, data collection and analysis, decision to publish, or preparation of the manuscript.

SUPPLEMENTARY MATERIAL

The Supplementary Material for this article can be found online at: https://www.frontiersin.org/articles/10.3389/fphys.2020.582610/full#supplementary-material

Supplementary Figure 1 | Msx2 directly binds to *Msx2* recognition sites on the *Sp6* promoter: *In silico* model showing six potential *Msx2* binding sites (F1-R1: -1317 to -1323; F2-R2: -1731 to -1736; F3-R3: -1881 to 1886; F4-R4: -2109 to -2114, -2119 to -2124, -2141 to -2146; F5-R5: -2487 to -2493; F6-R6, position -2827 to -2833) on the *Sp6* promoter using MatInspector. The different binding sites are represented by green ellipses. Primers were designed from different promoter regions (blue arrows). After chromatin immunoprecipitation, samples from LS8 cells transfected with pCMV-Msx2-FLAG were PCR amplified; the binding region was directly amplified prior to immunoprecipitation (1% Input) and specifically amplified in the immunoprecipitated sample (anti-FLAG). (right panel). No amplification was detected in the normal mouse serum IgG-immuno precipitated sample (IgG; negative control). Pol A is the positive control. Band in the input lane shows endogenous binding while band in the sample lane shows binding after specific immunoprecipitation with FLAG tagged antibody after overexpression. The results show that *Msx2* binds only to four out of six predicted regions in the *Sp6* promoter.

REFERENCES

Abe, K., Miyoshi, K., Muto, T., Ruspita, I., Horiguchi, T., Nagata, T., et al. (2007). Establishment and characterization of rat dental epithelial derived ameloblast-lineage clones. *J Biosci Bioeng* 103, 479–485. doi: 10.1263/jbb.103.479

Aldred, M. J., Savarirayan, R., and Crawford, P. J. (2003). Amelogenesis imperfecta: a classification and catalogue for the 21st century. *Oral Dis* 9, 19–23. doi: 10.1034/j.1601-0825.2003.00843.x

Babajko, S., De La Dure-Molla, M., Jedeon, K., and Berdal, A. (2014). MSX2 in ameloblast cell fate and activity. *Front Physiol* 5:510. doi: 10.3389/fphys.2014.00510

Bartlett, J. D. (2013). Dental enamel development: proteinases and their enamel matrix substrates. *ISRN Dent* 2013:684607.

Bei, M. (2009a). Molecular genetics of ameloblast cell lineage. *J Exp Zool B Mol Dev Evol* 312B, 437–444. doi: 10.1002/jez.b.21261

Bei, M. (2009b). Molecular genetics of tooth development. *Curr. Opin. Genet. Dev* 19, 504–510. doi: 10.1016/j.gde.2009.09.002

Bei, M., and Maas, R. (1998). FGFS and BMP4 induce both Msx1-independent and Msx1-dependent signaling pathways in early tooth development. *Development* 125, 4325–4333.

Bei, M., Stowell, S., and Maas, R. (2004). Msx2 controls ameloblast terminal differentiation. *Dev. Dyn.* 231, 758–765. doi: 10.1002/dvdy.20182

Bouwman, P., Gollner, H., Elasser, H. P., Eckhoff, G., Karis, A., Grosveld, F., et al. (2000). Transcription factor Sp3 is essential for post-natal survival and late tooth development. *EMBO J.* 19, 655–661. doi: 10.1093/emboj/19.4.655

Catron, K. M., Iler, N., and Abate, C. (1993). Nucleotides flanking a conserved TAAT core dictate the DNA binding specificity of three murine homeodomain proteins. *Mol. Cell. Biol.* 13, 2354–2365. doi: 10.1128/mcb.13.4.2354

Catron, K. M., Zhang, H., Marshall, S. C., Inostroza, J. A., Wilson, J. M., and Abate, C. (1995). Transcriptional repression by Msx-1 does not require homeodomain DNA-binding sites. *Mol. Cell. Biol.* 15, 861–871. doi: 10.1128/mcb.15.2.861

Chang, H., Wang, Y., Liu, H., Nan, X., Wong, S., Peng, S., et al. (2017). Mutant Runx2 regulates amelogenesis and osteogenesis through a miR-185-5p-Dlx2 axis. *Cell Death Dis* 8:3221.

Chen, L. S., Couwenhoven, R. I., Hsu, D., Luo, W., and Snead, M. L. (1992). Maintenance of amelogenin gene expression by transformed epithelial cells of mouse enamel organ. *Arch. Oral. Biol.* 37, 771–778. doi: 10.1016/0003-9969(92)90110-t

Diamond, E., Amen, M., Hu, Q., Espinoza, H. M., and Amendt, B. A. (2006). Functional interactions between Dlx2 and lymphoid enhancer factor regulate *Msx2*. *Nucleic Acids Res.* 34, 5951–5965. doi: 10.1093/nar/gkl689

Duval, N., Daubas, P., Bourcier de Carbon, C., St Cloment, C., Tinevez, J. Y., Lopes, M., et al. (2014). Msx1 and Msx2 act as essential activators of *Atoh1* expression in the murine spinal cord. *Development* 141, 1726–1736. doi: 10.1242/dev.099002

Gritli-Linde, A., Bei, M., Maas, R., Zhang, X. M., Linde, A., and Mcmahon, A. P. (2002). Shh signaling within the dental epithelium is necessary for cell proliferation, growth and polarization. *Development* 129, 5323–5337. doi: 10.1242/dev.00100

Habelitz, S. (2015). Materials engineering by ameloblasts. *J. Dent. Res.* 94, 759–767. doi: 10.1177/0022034515577963

Hu, J. C., Hu, Y., Smith, C. E., Mckee, M. D., Wright, J. T., Yamakoshi, Y., et al. (2008). Enamel defects and ameloblast-specific expression in Enam knock-out/lacz knock-in mice. *J. Biol. Chem.* 283, 10858–10871.

Huang, Z., Sargeant, T. D., Hulvat, J. F., Mata, A., Bringas, P. Jr., Koh, C. Y., et al. (2008). Bioactive nanofibers instruct cells to proliferate and differentiate during enamel regeneration. *J. Bone. Miner. Res.* 23, 1995–2006. doi: 10.1359/jbmr.080705

Kollar, E. J., and Lumsden, A. G. (1979). Tooth morphogenesis: the role of the innervation during induction and pattern formation. *J Biol Buccale* 7, 49–60.

MacKenzie, A., Ferguson, M. W., and Sharpe, P. T. (1992). Expression patterns of the homeobox gene, Hox-8, in the mouse embryo suggest a role in specifying tooth initiation and shape. *Development* 115, 403–420.

Molla, M., Descroix, V., Aioub, M., Simon, S., Castaneda, B., Hotton, D., et al. (2010). Enamel protein regulation and dental and periodontal physiopathology in MSX2 mutant mice. *Am. J. Pathol.* 177, 2516–2526. doi: 10.2353/ajpath.2010.091224

Nakamura, T., De Vega, S., Fukumoto, S., Jimenez, L., Unda, F., and Yamada, Y. (2008). Transcription factor epiprofin is essential for tooth morphogenesis by regulating epithelial cell fate and tooth number. *J. Biol. Chem.* 283, 4825–4833. doi: 10.1074/jbc.m708388200

Nanci, A. (2007). *Development, Structure, and Function. Ten Cate's Oral Histology*. St.Louis, MO: Mosby Inc.

Ruspita, I., Miyoshi, K., Muto, T., Abe, K., Horiguchi, T., and Noma, T. (2008). Sp6 downregulation of follistatin gene expression in ameloblasts. *J. Med. Invest.* 55, 87–98. doi: 10.2152/jmi.55.87

Satokata, I., Ma, L., Ohshima, H., Bei, M., Woo, I., Nishizawa, K., et al. (2000). Msx2 deficiency in mice causes pleiotropic defects in bone growth and ectodermal organ formation. *Nat. Genet.* 24, 391–395. doi: 10.1038/74231

Shin, N. Y., Yamazaki, H., Beniash, E., Yang, X., Margolis, S. S., Pugach, M. K., et al. (2020). Amelogenin phosphorylation regulates tooth enamel formation by stabilizing a transient amorphous mineral precursor. *J. Biol. Chem.* 295, 1943–1959. doi: 10.1074/jbc.ra119.010506

Smith, C. E. L., Whitehouse, L. L. E., Poulter, J. A., Wilkinson Hewitt, L., Nadat, F., Jackson, B. R., et al. (2020). A missense variant in specificity protein 6 (SP6) is associated with amelogenesis imperfecta. *Hum. Mol. Genet.* 29, 1417–1425. doi: 10.1093/hmg/ddaa041

Suda, N., Kitahara, Y., and Ohyama, K. (2006). A case of amelogenesis imperfecta, cleft lip and palate and polycystic kidney disease. *Orthod. Craniofac. Res.* 9, 52–56. doi: 10.1111/j.1601-6343.2006.00337.x

Thesleff, I. A., and Nieminen, P. (2005). *Tooth Induction*. Chichester: John Wiley & Sons Ltd.

Utami, T. W., Miyoshi, K., Hagita, H., Yanuaryska, R. D., Horiguchi, T., and Noma, T. (2011). Possible linkage of SP6 transcriptional activity with amelogenesis by protein stabilization. *J Biomed Biotechnol* 2011:320987.

Wang, X. P., Suomalainen, M., Jorgez, C. J., Matzuk, M. M., Werner, S., and Thesleff, I. (2004). Follistatin regulates enamel patterning in mouse incisors by asymmetrically inhibiting BMP signaling and ameloblast differentiation. *Dev. Cell* 7, 719–730. doi: 10.1016/j.devcel.2004.09.012

Wright, J. T. (2006). The molecular etiologies and associated phenotypes of amelogenesis imperfecta. *Am J Med Genet A* 140, 2547–2555. doi: 10.1002/ajmg.a.31358

Wright, J. T., Carrion, I. A., and Morris, C. (2015). The molecular basis of hereditary enamel. *J Dent Res.* 94, 52–61. doi: 10.1177/0022034514556708

Wright, J. T., Hart, P. S., Aldred, M. J., Seow, K., Crawford, P. J., Hong, S. P., et al. (2000). Identification of CCAAT/enhancer-binding protein alpha as a transactivator of the mouse amelogenin gene. *J. Biol. Chem.* 275, 12273–12280. doi: 10.1074/jbc.275.16.12273

Xu, L., Harada, H., Yokohama-Tamaki, T., Matsumoto, S., Tanaka, J., and Taniguchi, A. (2006). Reuptake of extracellular amelogenin by dental epithelial cells results in increased levels of amelogenin MRNA through enhanced MRNA stabilization. *J. Biol. Chem.* 281, 2257–2262. doi: 10.1074/jbc.m507695200

Zhang, H., Hu, G., Wang, H., Sciavolino, P., Iler, N., Shen, M. M., et al. (1997). Heterodimerization of Msx and Dlx homeoproteins results in functional antagonism. *Mol. Cell. Biol.* 17, 2920–2932. doi: 10.1128/mcb.17.5.2920

Zhao, M., Gupta, V., Raj, L., Roussel, M., and Bei, M. (2013). A network of transcription factors operates during early tooth morphogenesis. *Mol. Cell Biol.* 33, 3099–3112. doi: 10.1128/MCB.00524-13

Zhou, Y. L., Lei, Y., and Snead, M. L. (2000). Functional antagonism between Msx2 and CCAAT/enhancer-binding protein alpha in regulating the mouse amelogenin gene expression is mediated by protein-protein interaction. *J. Biol. Chem.* 275, 29066–29075.

Conflict of Interest: The authors declare that the research was conducted in the absence of any commercial or financial relationships that could be construed as a potential conflict of interest.

frontiers in Physiology

ORIGINAL RESEARCH
published: 19 November 2020
doi: 10.3389/fphys.2020.573214

Phenotypic and Genotypic Features of Thai Patients With Nonsyndromic Tooth Agenesis and *WNT10A* Variants

Charinya Kanchanasevee[1], Kanokwan Sriwattanapong[2], Thanakorn Theerapanon[2], Sermporn Thaweesapphithak[3], Wanna Chetruengchai[4,5], Thantrira Porntaveetus[2] and Vorasuk Shotelersuk[4,5]*

[1] Geriatric Dentistry and Special Patients Care International Program, Faculty of Dentistry, Chulalongkorn University, Bangkok, Thailand, [2] Genomics and Precision Dentistry Research Unit, Department of Physiology, Faculty of Dentistry, Chulalongkorn University, Bangkok, Thailand, [3] Center of Excellence for Regenerative Dentistry, Faculty of Dentistry, Chulalongkorn University, Bangkok, Thailand, [4] Center of Excellence for Medical Genomics, Medical Genomics Cluster, Department of Pediatrics, Faculty of Medicine, Chulalongkorn University, Bangkok, Thailand, [5] Excellence Center for Genomics and Precision Medicine, King Chulalongkorn Memorial Hospital, Thai Red Cross Society, Bangkok, Thailand

OPEN ACCESS

Edited by:
Maisa Hanna-Maija Seppala, King's College London, United Kingdom

Reviewed by:
Dong Han, Peking University Hospital of Stomatology, China
Mushriq Abid, University of Baghdad, Iraq

***Correspondence:**
Thantrira Porntaveetus
thantrira.p@chula.ac.th
orcid.org/0000-0003-0145-9801

Specialty section:
This article was submitted to Craniofacial Biology and Dental Research, a section of the journal Frontiers in Physiology

Received: *16 June 2020*
Accepted: *27 October 2020*
Published: *19 November 2020*

Citation:
Kanchanasevee C, Sriwattanapong K, Theerapanon T, Thaweesapphithak S, Chetruengchai W, Porntaveetus T and Shotelersuk V (2020) Phenotypic and Genotypic Features of Thai Patients With Nonsyndromic Tooth Agenesis and WNT10A Variants. Front. Physiol. 11:573214. doi: 10.3389/fphys.2020.573214

Tooth agenesis is one of the most common orodental anomalies that demonstrate phenotypic and genotypic heterogeneity with a prevalence of 2.5%–7%. Mutations in *WNT10A* have been proposed to be the most common cause of nonsyndromic tooth agenesis (NSTA). The aim of this study was to characterize the dental features and genetic variants of NSTA in a Thai population. We recruited 13 unrelated patients with NSTA who attended the Faculty of Dentistry, Chulalongkorn University, Thailand, from 2017 to 2019. All 13 underwent whole exome sequencing that identified likely pathogenic genetic variants, all in *WNT10A*, in five patients. All five patients had second premolar agenesis, while three also had absent or peg-shaped upper lateral incisors. Patient 1 possessed a novel heterozygous duplication, c.916_918dupAAC (p.Asn306dup) in *WNT10A.* Patients 2 and 3 harbored a heterozygous and homozygous c.637G > A (p.Gly213Ser) in *WNT10A*, respectively. Patients 4 possessed a heterozygous c.511C > T (p.Arg171Cys) in *WNT10A*. Patient 5 harbored a homozygous c.511C > T (p.Arg171Cys) in *WNT10A* and a novel heterozygous c.413A > T (p.Asn138Ile) in *EDARADD*, suggesting digenic inheritance. We recruited another 18 family members of these five patients. Out of 23 participants, homozygous *WNT10A* variants were identified in 2 patients and heterozygous variants in 17 individuals. Both homozygous patients had NSTA. Eight out of 17 heterozygous individuals (8/17) had NSTA or a peg-shaped lateral incisor, indicating a 47% penetrance of the heterozygous variants or 53% (10/19) penetrance of either homozygous or heterozygous variants in *WNT10A*. The frequencies of the c.511C > T in our in-house 1,876 Thai exome database, Asian populations, and non-Asian populations were 0.016, 0.005–0.033, and 0.001, respectively; while those of the c.637G > A were 0.016, 0.004–0.029, and 0.000, respectively. In conclusion, our study reports two novel variants with one each in *WNT10A* and *EDARADD*, expanding the genotypic spectra of NSTA. Second premolar

agenesis is a common phenotype in affected individuals with variants in *WNT10A*; however, its penetrance is incomplete. Lastly, the different frequencies of *WNT10A* variants, c.511C > T and c.637G > A, in diverse populations might contribute to the prevalence range of NSTA between continents.

Keywords: hypodontia, oligodontia, nonsynonymous, homozygous, heterozygous, ectoderm

INTRODUCTION

Tooth agenesis is the most common developmental dental anomaly in humans with a prevalence between 2.5 and 7% (Polder et al., 2004; Khalaf et al., 2014). Missing less than 6 teeth is called hypodontia, agenesis of 6 or more teeth is called oligodontia, and the complete absence of teeth is called anodontia. Multiple signaling pathways, including bone morphogenic protein, fibroblast growth factor, sonic hedgehog, and wingless (WNT), play important roles in the epithelial-mesenchymal interactions during tooth development. WNT/β-catenin signaling is involved from the early to late stages of tooth formation (Liu et al., 2008; Porntaveetus et al., 2012; Intarak et al., 2018). Among *WNT* family members, mutations in *WNT10A* (OMIM *606268) are predominantly related to tooth agenesis (TA) involving both nonsyndromic/isolated/selective tooth agenesis (NSTA/STHAG4, MIM #150400) and syndromic tooth agenesis, such as odontoonychodermal dysplasia (MIM #257980) and Schopf-Schulz-Passarge syndrome (MIM #224750).

Population-based studies have revealed that 28%–62% of tooth agenesis patients have with *WNT10A* variants (van den Boogaard et al., 2012; Mostowska et al., 2013; Arzoo et al., 2014). Heterozygous, homozygous, and compound heterozygous forms of *WNT10A* were associated with NSTA with phenotypic heterogeneity. Using *WNT10A* target sequencing, significantly elevated frequencies of *WNT10A* variants were observed in the tooth agenesis group compared with the control group (Song et al., 2014; Machida et al., 2017). Biallelic *WNT10A* variants were proposed to be a pathogenic factor for tooth agenesis with complete penetrance, while a single allelic variant, presenting in a significantly higher frequency in tooth agenesis patients, was considered to be a predisposing factor for tooth agenesis with reduced penetrance (Mues et al., 2014; Guazzarotti et al., 2018). These findings prompted us to investigate the dental phenotype and genotype in Thai patients with NSTA and determine the allele frequencies of *WNT10A* in Thais compared with Asian and non-Asian populations.

MATERIALS AND METHODS

Subject Enrollment

The study protocol was approved by the Institutional Review Board (HREC-DCU 2018-091), Faculty of Dentistry, Chulalongkorn University and complied with the Declaration of Helsinki. Written informed consents were obtained prior to the patients' participation in this study. Thirteen unrelated patients with NSTA who attended the Faculty of Dentistry, Chulalongkorn University, Thailand between January 2017 and March 2019 and their family member were recruited. Clinical and radiographic examinations, dental history, and intraoral photographs of the probands were used to assess tooth agenesis. The size and shape of the remaining teeth were also observed. The patients did not have any signs or symptoms related to ectodermal organ defects, e.g. intolerance to heat, dry skin, abnormal sweating, sparse hair, or brittle nails (Bergendal et al., 2006). The dental phenotypes of the probands' family members were obtained from clinical and radiographic examinations, dental records, or participant interviews.

Mutation Analyses

Genomic DNA extracted from peripheral blood leukocytes was subjected to mutation analysis using whole exome sequencing (WES) (Porntaveetus et al., 2018). Briefly, genomic DNA was captured using a SureSelect Human All Exon version 4 kit (Agilent Technologies, Santa Clara, CA, United States) and sequenced using Hiseq2000 (Macrogen, Seoul, South Korea). The sequences were aligned to the human genome reference sequence[1] using the Burrows-Wheeler Aligner[2]. Downstream processing was performed with SAMtools[3] and annotated against the dbSNP and 1000 Genomes. After quality filtering, the variants were screened using the genes listed in HP: 0009804 (reduced number of teeth) in Human Phenotype Ontology (Köhler et al., 2018). All calls with a coverage < 10×, minor allele frequency > 5% in the 1000 Genomes Project, Genome Aggregation Database (gnomAD[4]), and our in-house database of 1,876 Thai exomes; non-coding variants; and synonymous exonic variants were filtered out. The identified variants were confirmed by Sanger sequencing (**Supplementary Table 1**). The alignment and conservation of amino acid residues were generated by Clustal Omega (Madeira et al., 2019).

Allele frequencies of *WNT10A* variants were screened with multiple variant databases comprising the Genome Aggregation Database (gnomAD), GenomeAsia100K consortium, Northeast Asian Reference Database (NARD), Han Chinese genome project (PGG.Han), 4.7K Japanese individual genome variation (4.7KJPN), Human Genetic Variation Database (HGVD), Korean Variant Archive (KOVA), and our in-house database, last access on June 3, 2020.

Bioinformatics tools consisting of PolyPhen-2 (Adzhubei et al., 2010), SIFT (Kumar et al., 2009), MutationTaster

[1]UCSC Genome Browser, hg19
[2]http://bio-bwa.sourceforge.net/
[3]samtools.sourceforge.net/
[4]gnomad.broadinstitute.org

FIGURE 1 | Family pedigrees and genetic variants. Arrow indicates the proband. Tooth phenotypes of the participants were determined either by the dentist or reported by the participants. W+/+, homozygous *WNT10A* variant; W+/-, heterozygous *WNT10A* variant; W+/+, wild-type *WNT10A* variant; E+/+, homozygous *EDARADD* variant; E+/-, heterozygous *EDARADD* variant; E+/+, wild-type *EDARADD* variant.

(Schwarz et al., 2014), and CADD (Rentzsch et al., 2018) were used to predict each variant's pathogenicity.

RESULTS

We performed WES for 13 unrelated patients with NSTA during 2017–2019 and detected variants related to tooth agenesis (HP: 0009804) in five patients. All five patients (Patients 1–5) possessed variants in *WNT10A* (NM_025216.3). We then recruited 18 additional family members of these 5 index patients, characterized their dental phenotype, and performed Sanger sequencing (**Figure 1** and **Supplementary Figure 1**).

Patient 1, a 16-year-old female, lacked nine permanent teeth, all premolars and the lower right first molar. The lower left second molar was extracted due to pulp necrosis. Oral examination revealed that she had peg-shaped upper lateral incisors, severely hypoplastic edentulous ridges, anterior deep bite, and malocclusion. WES identified that the patient possessed a novel heterozygous duplication, c.916_918dupAAC (p.Asn306dup), in *WNT10A* (ClinVar SCV001335264). This variant was detected in the patient's mother and grandmother who had NSTA, and in the unaffected half aunt.

Patient 2, a 27-year-old female, had 6 missing teeth, 4 upper premolars, and 2 lower third molars. The known heterozygous missense mutation, c.637G > A (p.Gly213Ser), in *WNT10A* was identified in the patient, and in the patient's father and two sisters who reported no missing teeth. The mothers had biallelic wild-type alleles.

Patient 3, a 28-year-old male, had 12 missing teeth comprising an upper right canine, 3 first premolars, 4 second premolars, and 4 third molars. The homozygous mutation, c.637G > A (p.Gly213Ser), in *WNT10A* was identified in the patient. The *WNT10A* heterozygous c.637G > A (p.Gly213Ser) variant was

detected in the patient's older sister who was missing her 4 second premolars, and the younger sister, father, and mother who did not have any teeth missing.

Patient 4, a 31-year-old female, was missing her 2 lower second premolars and peg-shaped upper lateral incisors. Her deciduous lower right and left second molars were retained. Four third molars were previously extracted. The known heterozygous missense variant, c.511C > T (p.Arg171Cys), in *WNT10A* was detected in the patient, and in the patient's older sister and mother who did not have tooth agenesis. The father possessed wild-type alleles.

Patient 5, a 34-year-old male, had agenesis of 8 permanent teeth, 2 upper lateral incisors, 2 right second premolars, and 4 third molars. He had implant replacements at the upper right lateral incisor and lower right second premolar. The homozygous missense variant, c.511C > T (p.Arg171Cys) in *WNT10A* and a novel heterozygous missense variant, c.413A > T (p.Asn138Ile), in *EDARADD* (Clinvar SCV001335265) was identified in the patient. The heterozygous *WNT10A* c.511C > T variant was also detected in the patient's older sister who was missing two upper lateral incisors and two lower third molars and the mother who had peg-shaped upper lateral incisors. The heterozygous *EDARADD* c.413A > T variant was present in the patient's older brother, but not in the sister and mother.

In Patients 1–5, the number of missing teeth was between 2 and 12 or between 2 and 9 teeth (excluding the third molars). An absent second premolar or peg-shaped upper lateral incisor was frequently observed in the patients (**Table 1**).

We used several bioinformatic tools to predict the pathogenicity of the variants. We found that the *WNT10A* c.511C > T (p.Arg171Cys) was predicted to be deleterious (CADD: 25.6), deleterious (SIFT: 0.0), possibly damaging (PolyPhen-2: 0.93), and disease causing (MutationTaster). The *WNT10A* c.637G > A (p.Gly213Ser) was predicted to be deleterious (CADD: 27.2), deleterious (SIFT: 0.0), probably damaging (PolyPhen-2: 1.0), and disease causing (MutationTaster). Furthermore, the *EDARADD* c.413A > T (p.Asn138Ile) was predicted to be deleterious (CADD: 27.3), deleterious (SIFT: 0.0), possibly damaging (PolyPhen: 1.0), and disease causing (MutationTaster).

The amino acid residues; p.Arg171, p.Gly213, and p.Asn306 in WNT10A, and p.Asn128 in EDARADD are conserved among multiple species (**Supplementary Figure 2**). According to the ACMG standards and guidelines, the *WNT10A* c.511C > T and c.637G > A and the *EDARADD* c.413A > T variants are considered to be likely pathogenic, while the *WNT10A* c.916_918dupAAC variant is considered as uncertain significance (Richards et al., 2015).

Eighteen members of the five index patients' families (23 total) were included. Out of the 23 participants, the homozygous *WNT10A* variants were identified in 2 patients (3.II.2 and 5.II.3) and the heterozygous variants in 17 individuals. Both homozygous patients had nonsyndromic tooth agenesis (NSTA). Eight (1.I.2, 1.II.2, 1.III.1, 2.II.1, 3.II.1, 4.II.2, 5.I.2, and 5.II.2) out of 17 heterozygous individuals (8/17) had NSTA or a peg-shaped lateral incisor, indicating a 47% penetrance of the heterozygous variants, or a 53% (10/19) penetrance of either homozygous or heterozygous variants in *WNT10A*.

We screened the frequencies of the *WNT10A* c.511C > T and c.637G > A variants in multiple variant databases comprising the Genome Aggregation Database (gnomAD), GenomeAsia100K consortium, Northeast Asian Reference Database (NARD), Han Chinese genome project (PGG.Han), 4.7K Japanese individual genome variation (4.7KJPN), Human Genetic Variation Database (HGVD), Korean Variant Archive (KOVA), and our in-house database. The allele frequencies of *WNT10A* c.511C > T and c.637G > A in Asian populations was between 0.005 and 0.033 and between 0.004 and 0.029, respectively. In our in-house database (ThWES) of 1,876 Thai exomes, the frequency of c.511C > T variant was 0.016 and that of c.637G > A variant was 0.016, which were in the Asian population ranges. In contrast, the frequency of the c.511C > T variant was 0.001 and that of the c.637G > A variant was and 0.000 in non-Asian populations (**Table 2**). These results indicate that the WNT10A c.511C > T and c.637G > A variants are common and concentrated in Asian populations compared with non-Asian populations.

DISCUSSION

In this study, we identified five index patients having NSTA and variants in *WNT10A*. Eighteen more family members were included. The number of missing teeth observed ranged from 2 to 12 teeth or 2 to 9 teeth, excluding third molars. *WNT10A* is the most common variant associated with NSTA (van den Boogaard et al., 2012; Mostowska et al., 2013; Arzoo et al., 2014). Here, we identified that all five patients possessed *WNT10A* variants. The novel heterozygous duplication, c.916_918dupAAC (p.Asn306dup), was identified in Patient 1. The heterozygous state of c.637G > A (p.Gly213Ser) variant was detected in Patient 2 and its homozygous state in Patient 3. The heterozygous state of c.511C > T (p.Arg171Cys) variant was detected in Patient 4 and its homozygous state was detected in Patient 5. The novel heterozygous c.413A > T (p.Asn138Ile) in *EDARADD* was observed in Patient 5.

The relationship between the heterozygous *WNT10A* variants (c.511C > T and c.637G > A) and NSTA was characterized in large well-phenotyped population cohorts (Song et al., 2014; Machida et al., 2017). Both variants were significantly associated with tooth agenesis compared with healthy control individuals. In other studies, the variants were shown to cause tooth agenesis with incomplete penetrance (He et al., 2013; Plaisancié et al., 2013; Kantaputra et al., 2014). Biallelic *WNT10A* variants were proposed to be the pathogenic factor for tooth agenesis with complete penetrance, while single allelic variants, presenting with a significantly higher frequency in tooth agenesis patients, were considered to be a predisposing factor for tooth agenesis with reduced penetrance (Mues et al., 2014; Guazzarotti et al., 2018). In addition, the phenotypic spectrum of *WNT10A* mutations was shown to be dose-dependent with variable expressivity, including within the same family (Park et al., 2019). Patients with biallelic *WNT10A* mutations had severe tooth agenesis,

TABLE 1 | The identified *WNT10A* variants in subjects with tooth agenesis or peg-shaped upper lateral incisors.

Family	Patient	Dental arch	Tooth															Number of missing teeth (excluding 3rd molars)	Mode	Mutation	Amino acid change
			8	7	6	5	4	3	2	1	1	2	3	4	5	6	7	8				
1	Patient 1	Upper				●	●		□			□		●	●							
		Lower			●	●	●							●	●		x		9	Het	c.916_918dup	p.Asn360dup
2	Patient 2	Upper				●	●							●	●							
		Lower	●															●	6 (4)	Het	c.637G > A	p.Gly213Ser
3	Patient 3	Upper	●			●	●	●						●	●			●				
		Lower	●			●								●	●			●	12 (8)	Homo	c.637G > A	p.Gly213Ser
	Patient 3's older sister	Upper				●									●							
		Lower	□			□								□	□			□	2	Het	c.637G > A	p.Gly213Ser
4	Patient 4	Upper							□			□										
		Lower				●									●				2	Het	c.511C > T	p.Arg171Cys
5	Patient 5[a]	Upper	●			●			■			■						●				
	(II.3)	Lower	●			●												●	8 (4)	Homo	c.511C > T	p.Arg171Cys
	Patient 5's sister	Upper							■			■										
	(II.2)	Lower	■			□												●	4 (2)	Het	c.511C > T	p.Arg171Cys
	Patient 5's mother	Upper							□			□										
	(I.2)	Lower																	0	Het	c.511C > T	p.Arg171Cys

1, central incisor; 2, lateral incisor; 3, canine; 4, first premolar; 5, second premolar; 6, first molar; 7, second molar; 8, third molar.; ●, missing tooth; ■, missing upper lateral incisor; □, peg-shaped upper lateral incisors; x, extraction; NA, not available; Het, heterozygous; Homo, homozygous.

[a]*The heterozygous missense variant, c.413A > T (p.Asn138Ile), in EDARADD was also found in Patient 5.*

TABLE 2 | Allele frequencies and details of *WNT10A* c.511C > T (p.Arg171Cys) and c.637G > A (p.Gly213Ser) variants.

Database	rs116998555 c.511C > T (p.Arg171Cys)				rs147680216 c.637G > A (p.Gly213Ser)			
	Allele count	**Allele number**	**Number of homozygotes**	**Allele frequency**	**Allele count**	**Allele number**	**Number of homozygotes**	**Allele frequency**
gnomAD (v2.1.1 and v3)								
East Asian	370	23084	3	0.016	657	22960	16	**0.029**
Non-East Asian	335	402864	1	0.001	22	400838	0	0.000
South Asian	51	33652	1	0.002	4	33616	0	0.000
African	32	67004	0	0.001	3	66550	0	0.000
Ashkenazi Jewish	0	13692	0	0.000	0	13646	0	0.000
European (Finnish)	13	35558	0	0.000	0	35046	0	0.000
European (non-Finnish)	223	193594	0	0.001	4	192768	0	0.000
Latino	6	49094	0	0.000	3	48994	0	0.000
Other	10	10270	0	0.001	8	10218	0	0.001
Total	705	425948	4	0.002	679	423798	16	0.002
GenomeAsia 100K								
Southeast Asia	4	692	0	0.006	3	692	0	**0.004**
Northeast Asia	5	702	0	0.007	10	702	0	0.014
South Asia	7	1448	0	**0.005**	0	1448	0	0.000
Other	0	636	0	0.000	0	636	0	0.000
Total	16	3478	0	0.005	13	3478	0	0.004
Northeast Asian Reference Database (NARD)	35	3558	NA	0.010	51	3558	NA	0.014
Han Chinese genome project (PGG.Han)	3596	107232	NA	**0.033**	1161	108146	NA	0.011
4.7K JPN (4,773 Japanese individuals)	NA	NA	NA	0.010	NA	NA	NA	0.015
HGVD (3,248 Japanese individuals)	36	2412	0	0.015	35	2388	0	0.015
Korean Variant Archive (KOVA) (1,055 healthy Korean individuals)	NA	NA	NA	0.019	NA	NA	NA	0.019
ThWES 1876 (In-house database of 1,876 Thai individuals)	58	3752	4	0.016	59	3752	0	0.016

JPN, Japanese individual genome variation; genomAD, Genome Aggregation Database; HGVD, Human Genetic Variation Database; NA, not available. Bold numbers indicate maximum and minimum allele frequencies in the column.

while heterozygous patients were either unaffected or had a mild tooth phenotype.

In our study, Patient 3 (3.II.2) and Patient 5 (5.II.3), who harbor the homozygous *WNT10A* c.637G > A and c.511C > T variants, respectively, have tooth agenesis and their phenotypes are more severe than the heterozygous individuals with the same variant. In our cohort, the heterozygous c.511C > T and c.637G > A variants demonstrated incomplete penetrance, which is consistent with previous reports. The evidence mentioned above suggests that the heterozygous *WNT10A* c.511C > T or c.637G > A allele can be a contributing factor for NSTA with low penetrance, while biallelic variants are associated with greater clinical severity. However, there might be other genetic or environmental factors influencing the phenotypic expression of NSTA patients.

Mutations in *EDARADD* (OMIM* 606603) are associated with autosomal dominant ectodermal dysplasia 11A (MIM# 614940) (Bal et al., 2007; Cluzeau et al., 2011) and autosomal recessive ectodermal dysplasia 11B (MIM# 614941) (Chaudhary et al., 2016). The *EDARADD* c.413A > T (p.Asn138Ile) variant identified in Patient 5 is located in the death domain that interacts with EDAR. The homozygous and heterozygous mutations in the EDAR death domain cause hypohidrotic ectodermal dysplasia (MIM #614940, #614941) with low penetrance (Bal et al., 2007; Cluzeau et al., 2011). To the best of our knowledge, only one heterozygous *EDARADD* variant, c.308C > T, p.Ser103Phe, was identified in patients with NSTA. The allelic frequency of the *EDARRADD* c.308C > T variant is found in up to 2% of a healthy population according to the dbSNP database. However, this variant has been associated with NSTA, but with low penetrance and variable expressivity. (Bergendal et al., 2011; Arte et al., 2013; Barbato et al., 2018; Martínez-Romero et al., 2019). Although the heterozygous *EDARADD* c.413A > T mutation was detected in the patient and his unaffected brother, it was not in his affected sister or mother.

Interestingly, the digenic heterozygous variants of *WNT10A* and other genes in the EDA pathway, including *EDA, EDAR,* and *EDARADD*, have been found in several patients with NSTA (Arte et al., 2013; He et al., 2013; Barbato et al., 2018; Martínez-Romero et al., 2019). The WNT and EDA pathways are suggested to play complementary roles during tooth development (Yu et al., 2019). In Family 5, the *WNT10A* c.511C > T variant was present in the homozygous state in the patient (8 missing teeth), in the heterozygous state in the sister (4 missing teeth) and proband's mother (peg-shaped lateral incisors), and not detected in the proband's brother (unaffected). Therefore, the role of the *WNT10A* variant in this family may be because its homozygous state is associated with more severe NSTA than those with the heterozygous variant, and the heterozygous variant shows incomplete penetrance. Moreover, the coexistence and variable penetrance of *WNT10A* and *EDARADD* variants may modulate the final phenotype of Patient 5.

Tooth agenesis is one of the most common anomalies in human development. Its prevalence in the general population is 2.5–7% (Polder et al., 2004). Mutations in *WNT10A* are the most frequently found variants associated with NSTA in several populations studied to date (van den Boogaard et al., 2012; Mostowska et al., 2013; Song et al., 2014; Tardieu et al., 2017). In particular, the *WNT10A* c.511C > T and c.637G > A variants are predominant in Asian populations compared with Europeans (Song et al., 2014; Machida et al., 2017). According to multiple genetic databases, we observed the allele frequencies of *WNT10A* c.511C > T and c.637G > A variants in Asian populations up to 0.033 and 0.029, respectively, compared with those in non-Asians, which are 0.000–0.001. The frequencies of the c.511C > T and c.637G > A variants in our in-house database of 1,876 Thai exomes are 0.016, which are in the range of Asian populations, including Japanese, Chinese, and Koreans. These results indicate that these two variants are relatively common in Asian populations. The difference in *WNT10A* allele frequencies among different ethnic groups may also partly explain the diverse prevalence of tooth agenesis on different continents (Khalaf et al., 2014).

The number and location of missing teeth are associated with mutations in specific genes (Al-Ani et al., 2017). A genotype-phenotype correlation study revealed that the second premolars were the most common missing teeth found in patient with *WNT10A* variants (Arzoo et al., 2014). All five patients in our study had agenesis of the second premolars, suggesting that *WNT10A* variants might be responsible for the absence of second premolars with high penetrance. Mutations in *WNT10A* have also been proposed to cause agenesis or microdontia of the upper lateral incisors (Kantaputra et al., 2014; Mostowska et al., 2015). Absent upper lateral incisors was observed in Patient 5 and his sister, and peg-shaped upper lateral incisors were found in Patient 1, Patient 4, and Patient 5's mother who had the heterozygous *WNT10A* variants.

CONCLUSION

In conclusion, this study reports a novel in-frame duplication, c.916_918dupAAC (p.Asn306dup), in *WNT10A* and a novel heterozygous missense variant, c.413A > T (p.Asn138Ile), in *EDARADD,* expanding the genotypic spectrum related to NSTA. The heterozygous *WNT10A* c.511C > T and c.637G > A variants demonstrate incomplete penetrance. Both variants are more common in Asian populations compared with non-Asians, which might explain the diverse prevalence of NSTA in various continents.

DATA AVAILABILITY STATEMENT

The datasets presented in this study can be found in online repositories. The names of the repository/repositories and accession number(s) can be found in the article/**Supplementary Material**.

ETHICS STATEMENT

The studies involving human participants were reviewed and approved by the Institutional Review Board (HREC-DCU 2018-091), Faculty of Dentistry, Chulalongkorn University and were

complied with the Declaration of Helsinki. Written informed consent to participate in this study was provided by the participants' legal guardian/next of kin. Written informed consent was also obtained from the individual(s), and minor(s)' legal guardian/next of kin, for the publication of any potentially identifiable images or data included in this article.

AUTHOR CONTRIBUTIONS

CK and TT contributed to the data acquisition and drafting of the manuscript. KS, ST, and WC contributed to the analysis and interpretation of the results. TP contributed to the study conception and design and drafting of the manuscript. VS contributed to the conception and data analysis. All authors revised and approved the submitted version.

FUNDING

This project was funded by the National Research Council of Thailand, Global partnership CU-C16F630029, Health Systems Research Institute, Thailand Research Fund (MRG6280001 and DPG6180001), and Faculty Research Grant (DRF64013) Faculty of Dentistry, Chulalongkorn University. KS is supported by Ratchadapisek Somphot Fund for Postdoctoral Fellowship, Chulalongkorn University. ST is supported by the 100th Anniversary Chulalongkorn University Fund for Doctoral Scholarship and The 90th Anniversary Chulalongkorn University Fund (Ratchadaphiseksomphot Endowment Fund).

ACKNOWLEDGMENTS

We thank Nut Pusuntisumpun, Adisa Suthirathikul, and Athipong Boonchanawiwat for their kind assistance with specimen collection, and Dr. Kevin A. Tompkins for the language revision of the manuscript.

SUPPLEMENTARY MATERIAL

The Supplementary Material for this article can be found online at: https://www.frontiersin.org/articles/10.3389/fphys.2020.573214/full#supplementary-material

Supplementary Figure 1 | Clinical and radiographic features of the patients. *indicates missing tooth.

Supplementary Figure 2 | Schematic diagrams of the *WNT10A* and *EDARADD* genes and proteins showing the identified *WNT10A* variants c.916_918dupAAC (p.Asn306dup), c.637G > A (p.Gly213Ser), and c.511C > T (p.Arg171Cys).

Supplementary Table 1 | Primers for Sanger sequencing.

REFERENCES

Adzhubei, I. A., Schmidt, S., Peshkin, L., Ramensky, V. E., Gerasimova, A., Bork, P., et al. (2010). A method and server for predicting damaging missense mutations. *Nat. Methods* 7, 248–249. doi: 10.1038/nmeth0410-248

Al-Ani, A. H., Antoun, J. S., Thomson, W. M., Merriman, T. R., and Farella, M. (2017). Hypodontia: an update on its etiology, classification, and clinical management. *BioMed Res. Int.* 2017:9378325. doi: 10.1155/2017/9378325

Arte, S., Parmanen, S., Pirinen, S., Alaluusua, S., and Nieminen, P. (2013). Candidate gene analysis of tooth agenesis identifies novel mutations in six genes and suggests significant role for WNT and EDA signaling and allele combinations. *PLoS One* 8:e73705. doi: 10.1371/journal.pone.0073705

Arzoo, P. S., Klar, J., Bergendal, B., Norderyd, J., and Dahl, N. (2014). WNT10A mutations account for $\frac{1}{2}$ of population-based isolated oligodontia and show phenotypic correlations. *Am. J. Med. Genet. A* 164a, 353–359. doi: 10.1002/ajmg.a.36243

Bal, E., Baala, L., Cluzeau, C., El Kerch, F., Ouldim, K., Hadj-Rabia, S., et al. (2007). Autosomal dominant anhidrotic ectodermal dysplasias at the EDARADD locus. *Hum. Mut.* 28, 703–709. doi: 10.1002/humu.20500

Barbato, E., Traversa, A., Guarnieri, R., Giovannetti, A., Genovesi, M. L., Magliozzi, M. R., et al. (2018). Whole exome sequencing in an Italian family with isolated maxillary canine agenesis and canine eruption anomalies. *Arch. Oral. Biol.* 91, 96–102. doi: 10.1016/j.archoralbio.2018.04.011

Bergendal, B., Klar, J., Stecksén-Blicks, C., Norderyd, J., and Dahl, N. (2011). Isolated oligodontia associated with mutations in EDARADD. AXIN2, MSX1, and PAX9 genes. *Am. J. Med. Genet. A* 155, 1616–1622. doi: 10.1002/ajmg.a.34045

Bergendal, B., Norderyd, J., Bågesund, M., and Holst, A. (2006). Signs and symptoms from ectodermal organs in young Swedish individuals with oligodontia. *Int. J. Paediatr. Dent.* 16, 320–326. doi: 10.1111/j.1365-263X.2006.00741.x

Chaudhary, A. K., Girisha, K. M., and Bashyam, M. D. (2016). A novel EDARADD 5'-splice site mutation resulting in activation of two alternate cryptic 5'-splice sites causes autosomal recessive hypohidrotic ectodermal dysplasia. *Am. J. Med. Genet. A* 170, 1639–1641. doi: 10.1002/ajmg.a.37607

Cluzeau, C., Hadj-Rabia, S., Jambou, M., Mansour, S., Guigue, P., Masmoudi, S., et al. (2011). Only four genes (EDA1, EDAR, EDARADD, and WNT10A) account for 90% of hypohidrotic/anhidrotic ectodermal dysplasia cases. *Hum. Mut.* 32, 70–72. doi: 10.1002/humu.21384

Guazzarotti, L., Tadini, G., Mancini, G. E., Sani, I., Pisanelli, S., Galderisi, F., et al. (2018). WNT10A gene is the second molecular candidate in a cohort of young Italian subjects with ectodermal derivative impairment (EDI). *Clin. Genet.* 93, 693–698. doi: 10.1111/cge.13147

He, H., Han, D., Feng, H., Qu, H., Song, S., Bai, B., et al. (2013). Involvement of and interaction between WNT10A and EDA mutations in tooth agenesis cases in the Chinese population. *PLoS One* 8:e80393. doi: 10.1371/journal.pone.0080393

Intarak, N., Theerapanon, T., Srijunbarl, A., Suphapeetiporn, K., Porntaveetus, T., and Shotelersuk, V. (2018). Novel compound heterozygous mutations in KREMEN1 confirm it as a disease gene for ectodermal dysplasia. *Br. J. Dermatol.* 179, 758–760. doi: 10.1111/bjd.16541

Kantaputra, P., Kaewgahya, M., and Kantaputra, W. (2014). WNT10A mutations also associated with agenesis of the maxillary permanent canines, a separate entity. *Am. J. Med. Genet. A* 164, 360–363. doi: 10.1002/ajmg.a.36280

Khalaf, K., Miskelly, J., Voge, E., and Macfarlane, T. V. (2014). Prevalence of hypodontia and associated factors: a systematic review and meta-analysis. *J. Orthod.* 41, 299–316.

Köhler, S., Carmody, L., Vasilevsky, N., Jacobsen, J. O. B., Danis, D., Gourdine, J.-P., et al. (2018). Expansion of the human phenotype ontology (HPO) knowledge base and resources. *Nucleic Acids Res.* 47, D1018–D1027. doi: 10.1093/nar/gky1105

Kumar, P., Henikoff, S., and Ng, P. C. (2009). Predicting the effects of coding non-synonymous variants on protein function using the SIFT algorithm. *Nat. Protoc.* 4, 1073–1081. doi: 10.1038/nprot.2009.86

Liu, F., Chu, E. Y., Watt, B., Zhang, Y., Gallant, N. M., Andl, T., et al. (2008). Wnt/β-catenin signaling directs multiple stages of tooth morphogenesis. *Dev. Biol.* 313, 210–224. doi: 10.1016/j.ydbio.2007.10.016

Machida, J., Goto, H., Tatematsu, T., Shibata, A., Miyachi, H., Takahashi, K., et al. (2017). WNT10A variants isolated from Japanese patients with congenital tooth agenesis. *Hum. Genome Var.* 4:17047. doi: 10.1038/hgv.2017.47

Madeira, F., Park, Y. M., Lee, J., Buso, N., Gur, T., Madhusoodanan, N., et al. (2019). The EMBL-EBI search and sequence analysis tools APIs in 2019. *Nucleic Acids Res.* 47, W636–W641. doi: 10.1093/nar/gkz268

Martínez-Romero, M. C., Ballesta-Martínez, M. J., López-González, V., Sánchez-Soler, M. J., Serrano-Antón, A. T., Barreda-Sánchez, M., et al. (2019). EDA, EDAR, EDARADD and WNT10A allelic variants in patients with ectodermal derivative impairment in the Spanish population. *Orphanet J. Rare Dis.* 14:281. doi: 10.1186/s13023-019-1251-x

Mostowska, A., Biedziak, B., Zadurska, M., Dunin-Wilczynska, I., Lianeri, M., and Jagodzinski, P. P. (2013). Nucleotide variants of genes encoding components of the Wnt signalling pathway and the risk of non-syndromic tooth agenesis. *Clin. Genet.* 84, 429–440. doi: 10.1111/cge.12061

Mostowska, A., Biedziak, B., Zadurska, M., Matuszewska-Trojan, S., and Jagodziński, P. P. (2015). WNT10A coding variants and maxillary lateral incisor agenesis with associated dental anomalies. *Eur. J. Oral Sci.* 123, 1–8. doi: 10.1111/eos.12165

Mues, G., Bonds, J., Xiang, L., Vieira, A. R., Seymen, F., Klein, O., et al. (2014). The WNT10A gene in ectodermal dysplasias and selective tooth agenesis. *Am. J. Med. Genet. A* 164A, 2455–2460. doi: 10.1002/ajmg.a.36520

Park, H., Song, J.-S., Shin, T. J., Hyun, H.-K., Kim, Y.-J., and Kim, J.-W. (2019). WNT10A mutations causing oligodontia. *Arch. Oral. Biol.* 103, 8–11. doi: 10.1016/j.archoralbio.2019.05.007

Plaisancié, J., Bailleul-Forestier, I., Gaston, V., Vaysse, F., Lacombe, D., Holder-Espinasse, M., et al. (2013). Mutations in WNT10A are frequently involved in oligodontia associated with minor signs of ectodermal dysplasia. *Am. J. Med. Genet. A* 161, 671–678. doi: 10.1002/ajmg.a.35747

Polder, B. J., Van't Hof, M. A., Van der Linden, F. P. G. M., and Kuijpers-Jagtman, A. M. (2004). A meta-analysis of the prevalence of dental agenesis of permanent teeth. *Am. J. Med. Genet. A* 32, 217–226. doi: 10.1111/j.1600-0528.2004.00158.x

Porntaveetus, T., Abid, M. F., Theerapanon, T., Srichomthong, C., Ohazama, A., Kawasaki, K., et al. (2018). Expanding the oro-dental and mutational spectra of kabuki syndrome and expression of KMT2D and KDM6A in human tooth germs. *Int. J. Biol. Sci.* 14, 381–389. doi: 10.7150/ijbs.23517

Porntaveetus, T., Ohazama, A., Choi, H. Y., Herz, J., and Sharpe, P. T. (2012). Wnt signaling in the murine diastema. *Eur. J. Orthod.* 34, 518–524. doi: 10.1093/ejo/cjr049

Rentzsch, P., Witten, D., Cooper, G. M., Shendure, J., and Kircher, M. (2018). CADD: predicting the deleteriousness of variants throughout the human genome. *Nucleic Acids Res.* 47, D886–D894. doi: 10.1093/nar/gky1016

Richards, S., Aziz, N., Bale, S., Bick, D., Das, S., Gastier-Foster, J., et al. (2015). Standards and guidelines for the interpretation of sequence variants: a joint consensus recommendation of the American College of medical genetics and genomics and the association for molecular pathology. *Genet. Med.* 17, 405–423. doi: 10.1038/gim.2015.30

Schwarz, J. M., Cooper, D. N., Schuelke, M., and Seelow, D. (2014). MutationTaster2: mutation prediction for the deep-sequencing age. *Nat. Methods* 11, 361–362. doi: 10.1038/nmeth.2890

Song, S., Zhao, R., He, H., Zhang, J., Feng, H., and Lin, L. (2014). WNT10A variants are associated with non-syndromic tooth agenesis in the general population. *Hum. Genet.* 133, 117–124. doi: 10.1007/s00439-013-1360-x

Tardieu, C., Jung, S., Niederreither, K., Prasad, M., Hadj-Rabia, S., Philip, N., et al. (2017). Dental and extra-oral clinical features in 41 patients with WNT10A gene mutations: a multicentric genotype–phenotype study. *Clin. Genet.* 92, 477–486. doi: 10.1111/cge.12972

van den Boogaard, M. J., Créton, M., Bronkhorst, Y., van der Hout, A., Hennekam, E., Lindhout, D., et al. (2012). Mutations in WNT10A are present in more than half of isolated hypodontia cases. *J. Med. Genet.* 49, 327–331. doi: 10.1136/jmedgenet-2012-100750

Yu, M., Wong, S.-W., Han, D., and Cai, T. (2019). Genetic analysis: wnt and other pathways in nonsyndromic tooth agenesis. *Oral. Dis.* 25, 646–651. doi: 10.1111/odi.12931

Conflict of Interest: The authors declare that the research was conducted in the absence of any commercial or financial relationships that could be construed as a potential conflict of interest.

The reviewer MA declared a past co-authorship with the authors TT and TP to the handling editor.

frontiers in Physiology

BRIEF RESEARCH REPORT
published: 26 November 2020
doi: 10.3389/fphys.2020.581843

Pax9's Interaction With the Ectodysplasin Signaling Pathway During the Patterning of Dentition

*Shihai Jia[1], Jeremie D. Oliver[1,2], Emma C. Turner[3], Maranda Renouard[4], Marianna Bei[5], J. T. Wright[6] and Rena N. D'Souza[1,2,7]**

[1] School of Dentistry, University of Utah Health, Salt Lake City, UT, United States, [2] Department of Biomedical Engineering, College of Engineering, The University of Utah, Salt Lake City, UT, United States, [3] Dental School, Faculty of Health and Medical Sciences, The University of Western Australia, Perth, WA, Australia, [4] College of Pharmacy, University of Utah Health, Salt Lake City, UT, United States, [5] Massachusetts General Hospital, Harvard Medical School, Boston, MA, United States, [6] Adams School of Dentistry, The University of North Carolina at Chapel Hill, Chapel Hill, NC, United States, [7] Department of Neurobiology and Anatomy, Pathology, and Surgery, The University of Utah, Salt Lake City, UT, United States

OPEN ACCESS

Edited by:
Abigail Saffron Tucker, King's College London, United Kingdom

Reviewed by:
Anne Poliard, Université Paris Descartes, France
Brad A. Amendt, The University of Iowa, United States

***Correspondence:**
Rena N. D'Souza
Rena.DSouza@hsc.utah.edu

Specialty section:
This article was submitted to Craniofacial Biology and Dental Research, a section of the journal Frontiers in Physiology

Received: *09 July 2020*
Accepted: *05 November 2020*
Published: *26 November 2020*

Citation:
Jia S, Oliver JD, Turner EC, Renouard M, Bei M, Wright JT and D'Souza RN (2020) Pax9's Interaction With the Ectodysplasin Signaling Pathway During the Patterning of Dentition. Front. Physiol. 11:581843. doi: 10.3389/fphys.2020.581843

In these studies, we explored for the first time the molecular relationship between the paired-domain-containing transcription factor, *Pax9*, and the ectodysplasin (*Eda*) signaling pathway during mouse incisor formation. Mice that were deficient in both *Pax9* and *Eda* were generated, and the status of dentition analyzed in all progeny using gross evaluation and histomorphometric means. When compared to wildtype controls, $Pax9^{+/-}Eda^{-/-}$ mice lack mandibular incisors. Interestingly, *Fgf* and *Shh* signaling are down-regulated while *Bmp4* and *Lef1* appear unaffected. These findings suggest that *Pax9*-dependent signaling involves the *Eda* pathway and that this genetic relationship is important for mandibular incisor development. Studies of records of humans affected by mutations in *PAX9* lead to the congenital absence of posterior dentition but interestingly involve agenesis of mandibular central incisors. The latter phenotype is exhibited by individuals with *EDA* or *EDAR* mutations. Thus, it is likely that *PAX9*, in addition to playing a role in the formation of more complex dentition, is also involved with *EDA* signaling in the initiation of odontogenesis within the incisal domain.

Keywords: tooth development, signaling interaction, patterning, incisor development, *Pax9*, ectodysplasin pathway

INTRODUCTION

The formation of mammalian dentition is a remarkable developmental process and a valuable model for studying epithelial–mesenchymal signaling interactions that control patterning morphogenesis. Much of our understanding about the patterning of dentition comes from mouse studies. The use of transgenesis, gene targeting, expression analyses, functional tooth recombination, as well as bead implantation assays have advanced our knowledge about the patterning of the murine dentition. What has emerged is the realization that tooth development involves a complex series of genetic interactions between growth factors, transcription factors, signal receptors, and diffusible morphogens that interact within five critical pathways, namely, bone morphogenetic protein (Bmp), wingless-integrated site (Wnt), fibroblast growth factor (Fgf), sonic

hedgehog (Shh), and ectodysplasin (Eda) (Lan et al., 2014; Balic and Thesleff, 2015; Huang et al., 2019).

That the patterning of dentition is under strict genetic control is best underscored by the condition of human tooth agenesis, a common inherited disorder that affects over 20% of the population. Classified as genetically and phenotypically heterogeneous, tooth agenesis most commonly affects third molars, mandibular second premolars, maxillary lateral incisors, and maxillary second premolars (Kapadia et al., 2007; Nieminen, 2009; Ye and Attaie, 2016; Williams and Letra, 2018). These commonly missing teeth represent the most distal members of each tooth family and fail to develop due to a disruption in normal signaling. This suggests that distinct distal-proximal morphogenetic gradients are involved in guiding the patterning of human dentition.

The appearance of tooth placodes marks the onset of odontogenesis and the formation of incisiform and molariform fields that develop when the inductive potential from dental epithelium is transferred to underlying mesenchyme (Jarvinen et al., 2018; Balic, 2019). This was proven in elegant recombination experiments where bud-staged molar mesenchyme was shown to fully transform non-dental epithelium to form teeth (Mina and Kollar, 1987; Lumsden, 1988). Systems biology approaches that integrated data from genome-wide expression profiling, bioinformatics, and *in vivo* genetic models show that canonical Wnt signals are the primary drivers of tooth signaling interactions (O'Connell et al., 2012). *Lef1*, a nuclear mediator of Wnt signaling, associates with β-catenin and activates Wnt-responsive genes. The molecular relationship between Wnt and Eda signaling pathways is well established in tooth development as *Eda* is down-regulated in $Lef1^{-/-}$ tooth organs that are arrested at the bud stage and Wnt6 can induce *Eda* expression in a *Lef1*-dependent manner (Laurikkala et al., 2001). Multiple lines of evidence further converge to support the hypothesis that the interactions between signaling pathways, rather than the intrinsic functions of transcription factors alone, dictate how the patterning of dentition is orchestrated.

Several studies point to the importance of the homeodomain-containing transcription factor, *Pax9*, as a key mediator of the odontogenic potential in the mesenchyme (Neubuser et al., 1997; Peters et al., 1998; Jernvall and Thesleff, 2000; Kapadia et al., 2006; Ogawa et al., 2006; Chen et al., 2009). Although *Pax9*-dependent signaling in tooth mesenchyme involves a partnership with *Msx1* and the up-regulation of *Bmp4* expression, its relationship with other key pathways is not well understood. These studies explored for the first time the relationship of *Pax9* with the Eda signaling pathway during the formation of mouse dentition. Through the use of mouse genetics, we demonstrate that *Pax9*-dependent signaling is functionally integrated with Eda signaling during mandibular incisor development. Disruptions in this molecular relationship lead to downregulation of other signaling molecules. We also report on the findings of our long-term human genetic studies that show that mutations in *PAX9,* while dominantly affecting posterior dentition, often involve mandibular central incisors. The latter, we observe is a common occurrence in individuals with mutations in *EDA* or *EDAR*. Taken together, our results indicate that *Pax9*-mediated signaling involves the Eda pathway, impacting the initiation of odontogenesis within the mandibular incisiform field.

MATERIALS AND METHODS

Mouse Strains

All animal procedures were approved by the Institutional Animal Care and Use Committee (IACUC) at the University of Utah (Protocol #19-12012). $Pax9^{+/-}$ mice were provided by Dr. Rulang Jiang (Cincinnati Children's Hospital), and $Eda^{+/-}$ mice (# 000314) were purchased from Jackson laboratory. Mouse colonies were maintained in the *C57BL/6* background, and 2–8-month-old females were used for intercross mating.

Histology Analysis

For the whole-mount overview of mandibles and maxillae, 2-month-old mouse heads were removed using fine forceps under a stereomicroscope. Mandibles were carefully dissected after removal of the tongue, and images were taken through a stereomicroscope (Zeiss Stemi 508).

For H&E staining, whole heads were fixed in 4% paraformaldehyde (PFA) in PBS overnight and processed through serial gradients of ethanol and xylene for paraffin embedding. 7 μm-thick sagittal sections were stained with H&E and evaluated under a digital microscope (EVOS).

In situ Hybridizations

Sagittal paraffin sections of E13.5 and E14 embryos using digoxigenin-labeled RNA probes (1 μg/ml) as described previously (Jia et al., 2017). Embryo heads were fixed in 4% PFA in PBS overnight then processed through serial ethanol and xylene for paraffin embedding. 7 μm-thick sagittal sections were hybridized with digoxigenin-labeled antisense RNA probes (1 μg/ml) to *Bmp4*, *Fgf3*, *Lef1*, and *Shh* as described previously. An anti-digoxigenin-AP antibody (11093274910, ROCHE, 1:1000) was used to detect the labeled probe. Comparable images were taken with a digital microscope (EVOS). At least three biological replicates were used to establish the reproducibility of results.

Tooth Germ Dissections and Real-Time Reverse Transcription (RT)-PCR Analyses

The embryos heads were harvested at E13.5 in cold PBS. After the lower jaw and brain were removed under a dissecting microscope, the incisors were carefully dissected using fine forceps and stored individually at −80°C for total RNA extraction. After genotyping, 3 pairs of incisors were pooled and total RNA was extracted using the RNeasy Micro Kit (Qiagen). First-strand cDNA was synthesized using the SuperScript First-Strand Synthesis System IV (Thermo Fisher Scientific). Quantitative reverse transcription (RT)-PCRs were performed using the SYBR Green^{ER} qPCR Supermix (Thermo Fisher Scientific). A list of gene-specific primers is provided in **Supplementary Table S1**. For each sample,

the relative levels of target mRNAs were normalized to *Gapdh* using the standard curve method (Zhou et al., 2013). Three sets of biological replicates were analyzed for each gene.

Clinical Findings From Human Genetic Studies

Patients were identified and evaluated after approval was obtained from the Committee for the Protection of Human Subjects, University of Texas Health Science Center at Houston. Consent to participate (including a release of dental records) was obtained from a parental guardian, in the case of minors. Patient records are secured at the University of Utah and analyzed for these studies under HIPAA policies and without any personal identifiers. Medical and dental records of patients diagnosed with mutations in *PAX9* and *EDAR* were studied along with radiographs and photographs. Patterns of tooth agenesis were noted, and records were selected to illustrate mandibular incisor agenesis in two individuals with mutations in *PAX9* and *EDAR*, respectively.

RESULTS

Pax9$^{+/-}$*Eda*$^{-/-}$ Compound Mutant Mice Exhibited Fewer Molars and Missing Mandibular Incisors

Pax9$^{+/-}$ and *Eda*$^{+/-}$ mice exhibited normal dentition with no disruptions in the size, shape, and number of teeth. To begin to assess whether *Pax9* and *Eda* genetically interact during tooth development, *Pax9*$^{+/-}$*Eda*$^{-/-}$ mice were generated through a series of breeding. As shown in **Figures 1A,D**, *Pax9*$^{+/-}$*Eda*$^{+/+}$ mice had a full complement of six molars (3 + 3) and two incisors in each mandible and maxilla, respectively. The 2-month-old *Pax9*$^{+/+}$*Eda*$^{-/-}$ mice (**Figures 1B,E**) had smaller molars with shallower cusps (as reported earlier) with six molars (3 + 3) and two incisors present in each mandible and maxilla analyzed. The compound mutant *Pax9*$^{+/-}$*Eda*$^{-/-}$ mice exhibited missing third molars in both the mandible and maxilla, as well as missing mandibular incisors (**Figures 1C,F,G**). These data suggest that *Pax9* and *Eda*-dependent signaling pathway genes share a genetic interaction in controlling the molar number and the formation of mandibular incisors.

Mandibular Incisor Development in *Pax9*$^{+/-}$*Eda*$^{-/-}$ Compound Mutants

We examined embryos from E13.5 to P0, and found that at E13.5, the mandibular incisors formed bud-shape tooth germs in *Pax9*$^{+/-}$*Eda*$^{+/+}$, *Pax9*$^{+/+}$*Eda*$^{-/-}$, and *Pax9*$^{+/-}$*Eda*$^{-/-}$ compound mutant mice (**Figures 2A,E,I**). At E14.5, the cervical loops of *Pax9*$^{+/-}$*Eda*$^{+/+}$ and *Pax9*$^{+/+}$*Eda*$^{-/-}$ mandibular incisors were well formed, whereas the cervical loops of *Pax9*$^{+/-}$*Eda*$^{-/-}$ compound mutant mandibular incisors appeared under-developed (**Figures 2B,F,J**). At P0, mandibular incisors showed asymmetric cervical loops at E17.5 and well-differentiated tooth organ layers in *Pax9*$^{+/-}$*Eda*$^{+/+}$ and *Pax9*$^{+/+}$*Eda*$^{-/-}$ mandible (**Figures 2C,D,G,H**). In contrast, the mandibular incisors in *Pax9*$^{+/-}$*Eda*$^{-/-}$ compound mutant exhibited residue of retarded tooth germs (**Figures 2K,L**).

The Activity of *Fgf* and *Shh* Signaling Was Reduced in *Pax9*$^{+/-}$*Eda*$^{-/-}$ Mandibular Incisors

To investigate the potential interactions between *Pax9* and the Eda/r signaling pathway, we analyzed the expression patterns of *Bmp4*, *Fgf3*, *Lef1*, and *Shh* in E13.5 and E14.0 *Eda*$^{+/-}$, *Eda*$^{-/-}$, and *Pax9*$^{+/-}$*Eda*$^{-/-}$ incisor organs. Results of *in situ* hybridization indicate that the patterns of *Bmp4* and *Lef1* expression seen in both *Eda*$^{+/-}$ and *Eda*$^{-/-}$ incisor organs resembled that visible in *Pax9*$^{+/-}$*Eda*$^{-/-}$ embryos (**Figures 3A–L**). The expression level of *Bmp4* and *Lef1* was not significantly reduced in the *Pax9*$^{+/-}$*Eda*$^{-/-}$ mandibular incisors confirmed by quantitative RT-PCR (**Figure 3M**). In contrast, the expression pattern of *Fgf3* and *Shh* appeared down-regulated in *Pax9*$^{+/-}$*Eda*$^{-/-}$ incisors in comparison to that evident in both *Eda*$^{+/-}$ and *Eda*$^{-/-}$ samples (**Figures 3N–Y**). Quantitative RT-PCR revealed that the expression of *Fgf3* in the *Pax9*$^{+/-}$*Eda*$^{-/-}$ mandibular incisor was significantly reduced in comparison to that in the *Eda*$^{+/-}$ samples; and the expression of *Shh* in the *Pax9*$^{+/-}$*Eda*$^{-/-}$ mandibular incisor was significantly reduced compared with that in both *Eda*$^{+/-}$ and *Eda*$^{-/-}$ samples (**Figure 3Z**).

Patterns of Missing Teeth in Individuals With *PAX9* and *EDAR* Mutations

Mutations in *PAX9* result in a pattern of tooth agenesis that dominantly involves permanent maxillary and mandibular first, second, and third molars along with second premolars. However, agenesis of mandibular central incisors are often associated with missing molars and premolars, as shown in **Figure 4B**, and as previously reported by our group (Goldenberg et al., 2000; Stockton et al., 2000; Frazier-Bowers et al., 2002a,b). A sibling with an unaffected *PAX9* gene shows a normal complement of permanent teeth (**Figure 4A**). For individuals with mutations in *EDA* or *EDAR*, tooth agenesis is more severe and mixed, typically including maxillary and central incisors while frequently involving mandibular central incisors (**Figures 4C,D**).

DISCUSSION

The patterning of dentition is a complex and unique developmental process involving multiple genes that control the precise shape, size, number, and position of teeth. While the past decades have advanced our understanding of the transcription factors that are involved, relatively little is known about their interactions with downstream effectors within the Bmp, Fgf, Wnt, Eda, and Shh pathways. Here, we sought to understand the relationship between *Pax9*, a key transcription factor in dental mesenchyme, and the Eda signaling pathway during the development of the dentition. Previous studies indicate that *Pax9* regulates both Wnt and Bmp signaling pathways and Eda signaling has been reported linked with

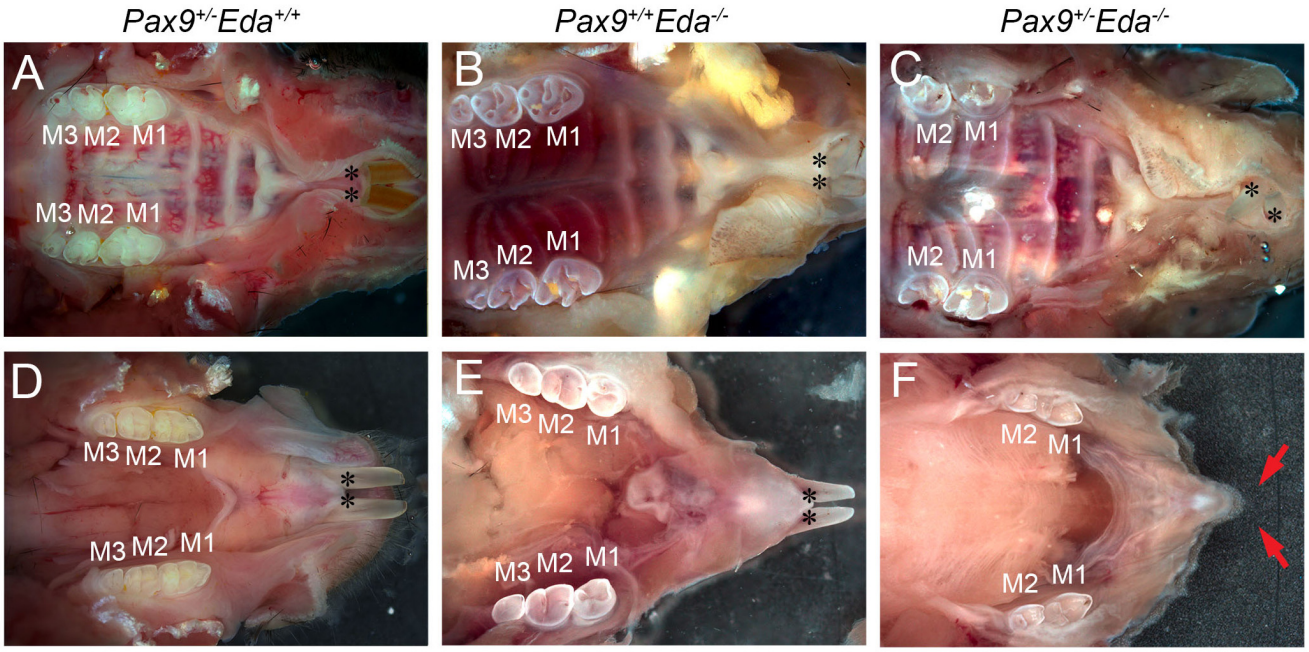

G

Genotype	Mice (n)	Molar		Incisor	
		Max(L+R)	Mand(L+R)	Max	Mand
Pax9$^{+/-}$*Eda*$^{+/+}$	10	3+3	3+3	2	2
Pax9$^{+/+}$*Eda*$^{-/-}$	18	3+3	3+3	2	2
Pax9$^{+/-}$*Eda*$^{-/-}$	13	2+2	2+2	2	0 (10) 1 (3)

FIGURE 1 | Missing teeth in *Pax9*$^{+/-}$*Eda*$^{-/-}$ compound mutant mice. **(A–C)** Whole-mount view of maxillary teeth in 2-month-old mice. **(A)** *Pax9*$^{+/-}$*Eda*$^{+/+}$ mice showed six molars (3 + 3) and two incisors. **(B)** *Pax9*$^{+/+}$*Eda*$^{-/-}$ mice showed six molars (3 + 3) with fewer cusps and two incisors. **(C)** *Pax9*$^{+/-}$*Eda*$^{-/-}$ mice showed four molars (2 + 2) and two incisors. **(D–F)** Whole-mount view of mandibular teeth in 2-month-old mice. **(D)** *Pax9*$^{+/-}$*Eda*$^{+/+}$ mice showed two incisors and six molars (3 + 3). **(E)** *Pax9*$^{+/+}$*Eda*$^{-/-}$ mice showed two incisors and six molars (3 + 3) with smaller size and fewer cusps. **(F)** *Pax9*$^{+/-}$*Eda*$^{-/-}$ mice showed missing incisors and four molars (2 + 2) with smaller size and fewer cusps. **(G)** Summary of teeth phenotype in *Pax9*$^{+/-}$*Eda*$^{-/-}$ compound mutants. Red arrows pointed to the space of missing incisors. M1, M2, and M3 are first, second, and third molar, respectively. Black * presents incisors. Max, maxillary; Mand, mandible.

Wnt signaling (Peters et al., 1998; Laurikkala et al., 2001; Zhang et al., 2009; O'Connell et al., 2012; Voutilainen et al., 2015). Our studies show, for the first time, that *Pax9*-dependent signaling is functionally integrated with Eda signaling during odontogenesis. A mouse genetic model deficient in both *Pax9* and *Eda* shows a consistent lack of maxillary and mandibular third molar development. Interestingly, mandibular incisor organs are arrested, a phenotypic change that suggests regionally specific interactions between *Pax9*-dependent signaling and the Eda pathway. In order to fully elucidate the nature of Pax9's relationship with Eda signaling, further experiments such as chromatin immunoprecipitation (ChIP) or electrophoretic mobility shift assay (EMSA) are needed. Our mouse data align with observations from our human genetic analyses of individuals with mutations in *PAX9* and *EDA/R* genes that show agenesis of mandibular central incisors. Taken together, these results underscore the need for further studies that will elucidate the relationship of *Pax9* with other signaling molecules that direct key epithelial–mesenchymal interactions in tooth development.

As reported earlier, *Eda*$^{-/-}$ mice exhibit mild defects in dentition that include fewer and shallower cusps in molars, hypoplasia, and agenesis of maxillary and mandibular third molars in 20% of animals studied. These studies also showed that decreased levels of Eda signaling did not affect incisor development (Pispa et al., 1999; Parveen et al., 2019). Without exception, all of the 13 *Pax9*$^{+/-}$*Eda*$^{-/-}$ mice studied showed maxillary and mandibular third molar agenesis with an overall reduction in size and cuspal morphology of residual first and second molars. *Pax9*$^{+/-}$ mice have a full complement of teeth while *Pax9*$^{-/-}$ mice consistently lack all molars (Kist et al., 2005; Mitsui et al., 2014). Furthermore, permanent molars are the dominant tooth group affected in individuals with mutations in *PAX9* (Goldenberg et al., 2000; Stockton et al.,

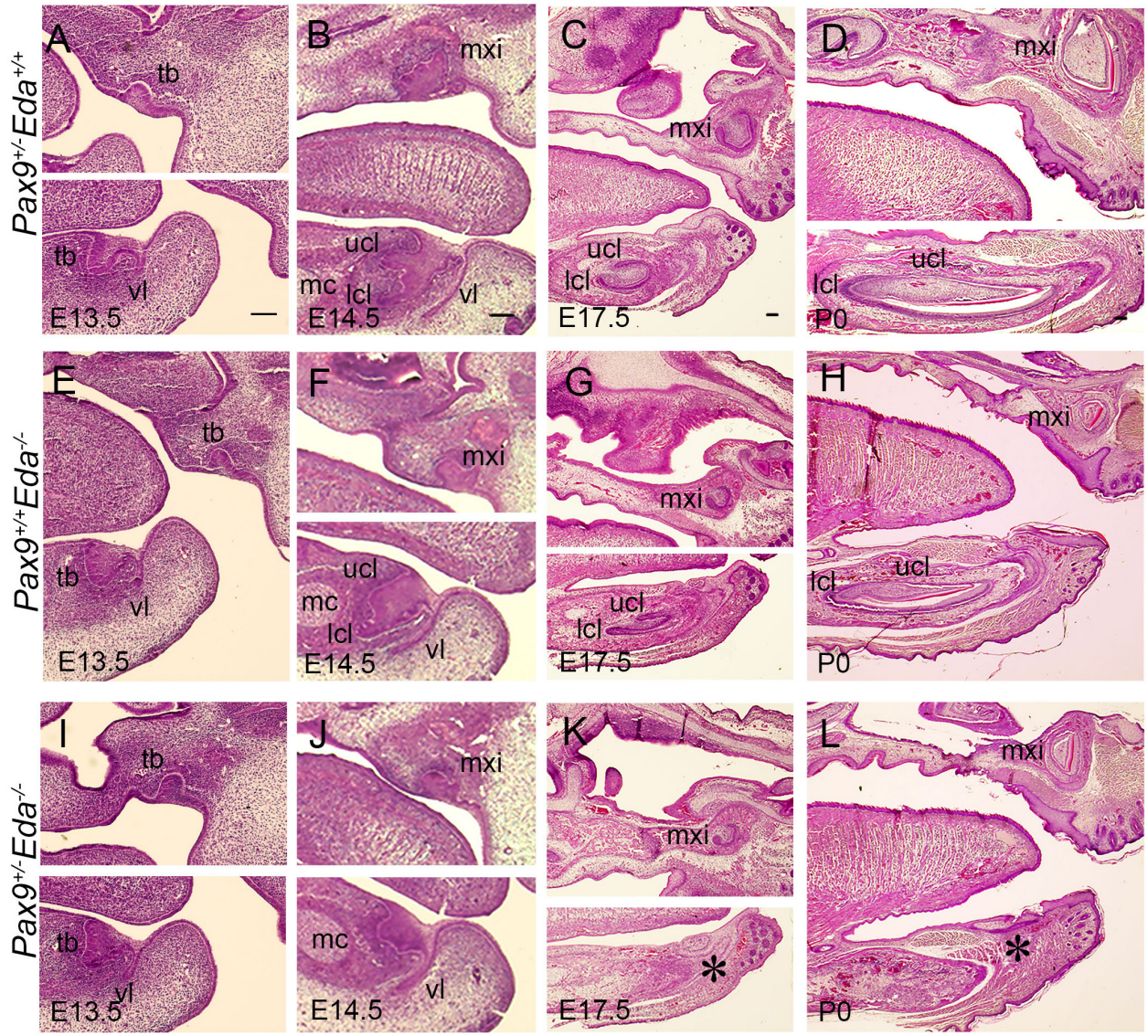

FIGURE 2 | Incisor developmental defects in the *Pax9*$^{+/-}$*Eda*$^{-/-}$ compound mutant embryos. Hematoxylin and eosin-stained (HE) sagittal sections through the developing incisor tooth germs. The *Pax9*$^{+/-}$*Eda*$^{+/+}$, *Pax9*$^{+/+}$*Eda*$^{-/-}$, and *Pax9*$^{+/-}$*Eda*$^{-/-}$ compound mutants at E13.5 **(A,E,I)**, E14.5 **(B,F,J)**, E17.5 **(C,G,K)**, and P0 **(D,H,L)**, respectively, are shown. Scale bar presented 100 μm, * indicates the region of missing incisor. lcl, lower cervical loop; mc, Meckel's cartilage; mxi, maxillary incisor; tb, tooth bud; ucl, upper cervical loop, vl, vestibular lamina.

2000; Frazier-Bowers et al., 2002a). Therefore, it is likely that the combinatorial reduction of *Pax9* and Eda signaling in *Pax9*$^{+/-}$*Eda*$^{-/-}$ mice has an additive effect on maxillary and mandibular molar development.

Pax9$^{+/-}$*Eda*$^{-/-}$ mice also exhibited a mandibular incisor phenotype as 10 of 13 embryos studied lacked lower incisors while in three of 13 embryos only a single mandibular incisor was present. In mouse genetic models disruptions in *Pitx2*, *BCL11B* and Wnt, Fgf, Bmp, and Wnt signaling pathway genes result in incisor organ agenesis or hypoplasia (Lin et al., 1999; Lu et al., 1999; Millar et al., 2003; Golonzhka et al., 2009; Yang et al., 2013; Yu et al., 2020). Furthermore, supernumerary incisors arise in mice lacking *Spry2/4*, *Sostdc1*, and *Lrp4* (Ohazama et al., 2008; Munne et al., 2009; Charles et al., 2011). In these models, both maxillary and mandibular incisors were affected as compared to mice where the up-regulation of NF-κB activity and the reduction of *Fam20B* selectively affect mandibular vs. maxillary incisors, respectively (Wang et al., 2013; Tian et al., 2015). Our quantitative RT-PCR and *in situ* hybridization data revealed that the expression of *Fgf3* in the *Pax9*$^{+/-}$*Eda*$^{-/-}$ mandibular incisor was significantly reduced in comparison to that in the *Eda*$^{+/-}$ samples. Whereas, in comparison to the *Eda*$^{+/-}$ samples, the expression of *Fgf3* was reduced in the *Eda*$^{-/-}$ incisors, but we found $p > 0.05$ with statistic analysis (**Figure 3Z**). Previous studies showed that *Fgf3*, *Fgf10*, and *Fgf20* were related to tooth development, both *Fgf3* and

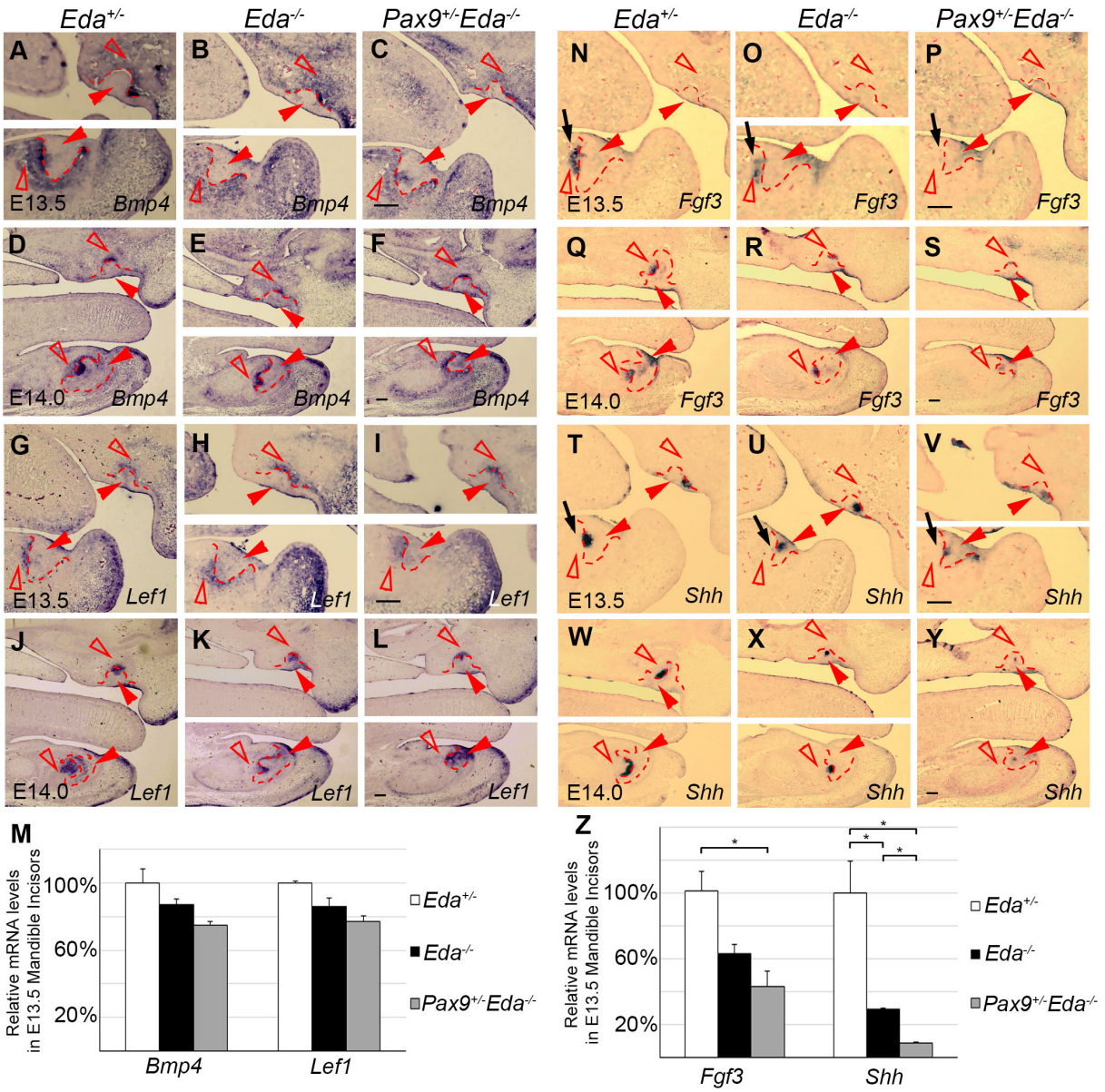

FIGURE 3 | Comparison of incisor molecular marker expression in E13.5 and E14.0 tooth germs. The mRNA expression of *Bmp4* and *Lef1* were shown in $Eda^{+/-}$, $Eda^{-/-}$, and $Pax9^{+/-}Eda^{-/-}$ mutants by *in situ* hybridization at E13.5 **(A–C,G–H)**, as well as at E14.0 **(D–F,G–L)**. The expression of *Fgf3* and *Shh* was shown in $Eda^{+/-}$, $Eda^{-/-}$, and $Pax9^{+/-}Eda^{-/-}$ mutants by *in situ* hybridization at E13.5 **(N–P,T–V)**, as well as at E14.0 **(Q–S,W–Y)**. Scale bar presented 100 μm, black arrows indicate mandibular incisor tooth germ. Red solid arrowheads indicate dental epithelia and red open arrowheads indicate dental mesenchyme. Red dashed lines indicate the boundary of incisor tooth germ mesenchyme and epithelia. **(M,Z)** The relative mRNA levels of *Bmp4*, *Lef1*, *Fgf3*, and *Shh* were analyzed by quantitative RT-PCR using the microdissected E13.5 mandibular incisors ($n = 3$). Error bars indicate SEM, $^*P < 0.01$.

Fgf10 were down-regulated in $Pax9^{+/-}Msx1^{+/-}$ embryos with missing mandibular incisors; and treatment with Fgf10 partially rescued the cusp defect in $Eda^{-/-}$ mouse (Pispa et al., 1999; Nakatomi et al., 2010). The expression of *Fgf20* was reduced in the developing $Eda^{-/-}$ incisors, while the *Fgf20* null mice had normal incisors (Häärä et al., 2012). Taken together, the Fgf signaling activity was reduced in $Eda^{-/-}$ tooth germs but appear adequate for regulating tooth formation; in $Pax9^{+/-}Eda^{-/-}$ mandibles, the level of Fgf signaling was reduced to a certain level that appears inadequate for the normal development of mandibular incisors. Furthermore, the expression of *Shh* in the $Pax9^{+/-}Eda^{-/-}$ mandibular incisor was significantly reduced compared with that in both $Eda^{+/-}$ and $Eda^{-/-}$ samples (**Figure 3Z**). The marker gene analysis indicates that both Fgf and Shh signaling pathways were involved in the genetic interaction between *Pax9* and *Eda* during mandibular incisor formation. These data when viewed in the light of our findings suggest that a distinct cadre of genetic interactions are involved in the

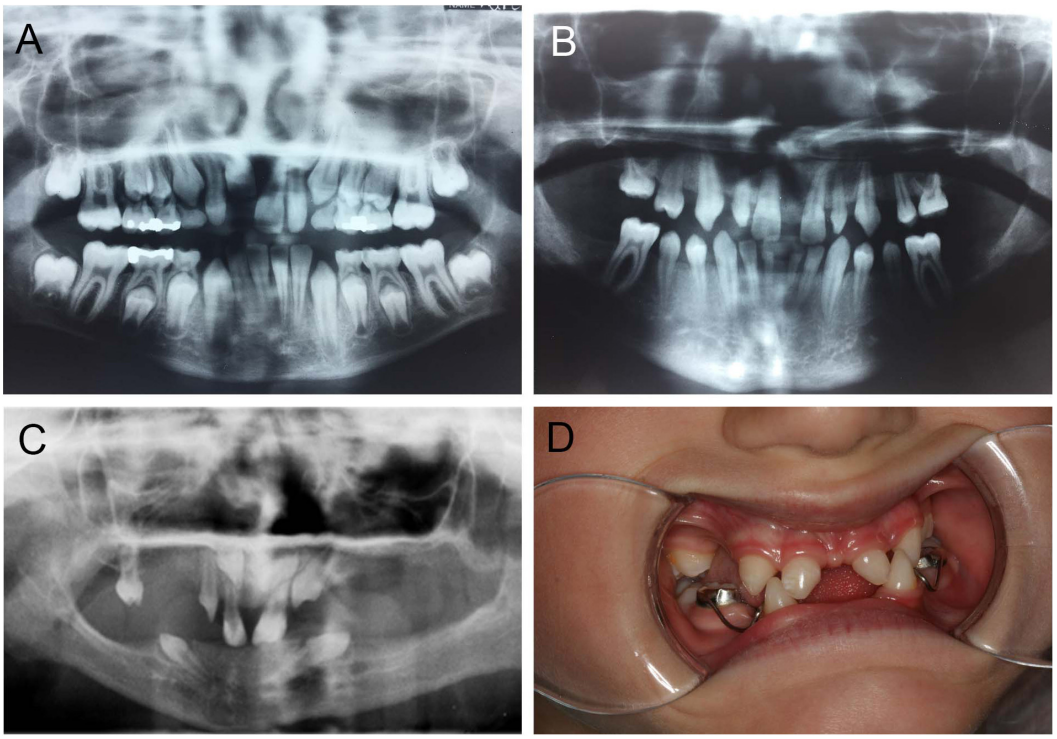

FIGURE 4 | Abnormal tooth appearance, including agenesis of mandibular central incisors, premolars, and molars in a *PAX9* mutant patient **(B)** compared to an unaffected sibling with normal permanent dentition **(A)**; 5-year-old patient with a confirmed mutation of *EDA* gene (XLHED), no permanent teeth in the mandible and only primary canines (never erupted), conical incisors, canines, and one molar noted in the maxilla **(C)**; female patient with autosomal recessive (AR) HED, missing mandibular incisors, and first primary molars, as well as maxillary lateral incisors and first primary molars **(D)**.

formation of mandibular incisors, whose initiation signifies the earliest zone of odontogenic induction in the mandibular arch.

As described by Nakatomi et al. (2010), *Pax9* and *Msx1* double heterozygous mutant mice show a consistent lack of mandibular incisors, a phenotype that is not evident in single mutant strains. Arrested $Pax9^{+/-}Msx1^{+/-}$ mandibular incisor organs show a marked reduction in *Fgf3* and *Fgf10* expression within dental mesenchyme as well as reduced expression of *Shh* and *Bmp2* in the dental epithelium. Our earlier biochemical analyses had first demonstrated that *Pax9* interacts synergistically with *Msx1* (Ogawa et al., 2006), so it is likely that this partnership plays a key role in driving key signaling interactions between dental mesenchyme and epithelium during the transition from the bud to the cap stage of development. Whether Eda signaling pathway genes are down-regulated in $Pax9^{+/-}Msx1^{+/-}$ mandibular incisor organs offers a valuable direction for future studies. Our findings that signaling pathway genes are differentially affected in $Pax9^{+/-}Eda^{-/-}$ mandibular incisor organs also warrant further investigation. In $Pax9^{+/-}Eda^{-/-}$ maxillary incisors, *Shh* expression was slightly changed suggesting that the level of *Shh* was enough to induce the formation of maxillary incisors. Since the expression of *Bmp4* remained unaffected in dental mesenchyme of $Pax9^{+/-}Eda^{-/-}$ compound mandibular incisors, it is possible that the haploinsufficiency of *Pax9* did not compromise *Bmp4* expression in the developing incisor mesenchyme. Although it was reported that Wnt signaling pathway mediator *Lef1* was down-regulated in the skin of *Tabby* mice (Durmowicz et al., 2002), our data showed that the expression of *Lef1* was not affected in $Pax9^{+/-}Eda^{-/-}$ compound mutant, which matched the regulatory hierarchy that *Eda* was downstream of *Lef1* in the tooth organ (Laurikkala et al., 2001).

Patterns of tooth agenesis in humans provide valuable clues about the important roles that transcription factors in modulating epithelial–mesenchymal signaling during tooth development. As one of the best-studied genes, *PAX9*, is largely viewed as important for the patterning of human dentition. Our group's clinical observations and that of others have documented that mutations in *PAX9* consistently result in a pattern of tooth agenesis that involves posterior dentition, namely, molars and premolars. Intriguing is the finding that individuals with mutations in *PAX9* often miss mandibular central incisors, the least patterned tooth in human dentition. While patients affected with mutations in *EDA* or *EDAR* lack posterior and anterior teeth in both arches, mandibular incisors are most often missing, a pattern of tooth agenesis that resembles that seen in individuals with mutations in *WNT10A* (Mues et al., 2014). Taken together, these data suggest that each tooth family (incisiform and cuspform/molariform) arises from distinct morphogenetic gradients or fields created by the differential actions of transcription factors and signaling

pathways. However, the initiation of odontogenesis within each field is spatially regulated by unique molecular relationships such as for mandibular incisors where Pax9-dependent signaling and the Eda pathway appear to play an important role.

DATA AVAILABILITY STATEMENT

The original contributions presented in the study are included in the article/**Supplementary Material**. Further inquiries can be directed to the corresponding author.

ETHICS STATEMENT

The studies involving human participants were reviewed and approved by the Committee for the Protection of Human Subjects, University of Texas Health Science Center at Houston. Written informed consent to participate in this study was provided by the participants' legal guardian/next of kin. The animal study was reviewed and approved by the Institutional Animal Care and Use Committee (IACUC) at the University of Utah (Protocol #19-12012). Written informed consent was obtained from the individual(s), and minor(s)' legal guardian/next of kin, for the publication of any potentially identifiable images or data included in this article.

AUTHOR CONTRIBUTIONS

SHJ and RD'S contributed to the research design, data acquisition, and analyses, as well as the writing of the manuscript. JO contributed to the writing of the manuscript. ET and MR contributed to the mouse genetic data acquisition. MB contributed to the mouse genetic data analysis. JW contributed to the data acquisition for the medical and dental records of the patient. Each author gave final approval and agreed to be accountable for all aspects of the work, ensuring integrity and accuracy. All authors contributed to the article and approved the submitted version.

FUNDING

The following grants from the National Institutes of Health/National Institute of Dental and Craniofacial Research have supported this research: DE019471, DE019471-ARRA supplement, to RD'S, DE027255 to RD'S and SHJ, DE027355 supplement to MB. A fellowship was awarded to JO from the Ole and Marty Jensen Endowment Fund.

ACKNOWLEDGMENTS

We thank Dr. Pascal Schneider for valuable feedback and advice throughout the project, the technical assistance of Greg Pratt.

SUPPLEMENTARY MATERIAL

The Supplementary Material for this article can be found online at: https://www.frontiersin.org/articles/10.3389/fphys.2020.581843/full#supplementary-material

REFERENCES

Balic, A. (2019). Concise review: cellular and molecular mechanisms regulation of tooth initiation. *Stem Cells* 37, 26–32. doi: 10.1002/stem.2917

Balic, A., and Thesleff, I. (2015). Tissue interactions regulating tooth development and renewal. *Curr. Top. Dev. Biol.* 115, 157–186. doi: 10.1016/bs.ctdb.2015.07.006

Charles, C., Hovorakova, M., Ahn, Y., Lyons, D. B., Marangoni, P., Churava, S., et al. (2011). Regulation of tooth number by fine-tuning levels of receptor-tyrosine kinase signaling. *Development* 138, 4063–4073. doi: 10.1242/dev.069195

Chen, J., Lan, Y., Baek, J. A., Gao, Y., and Jiang, R. (2009). Wnt/beta-catenin signaling plays an essential role in activation of odontogenic mesenchyme during early tooth development. *Dev. Biol.* 334, 174–185. doi: 10.1016/j.ydbio.2009.07.015

Durmowicz, M. C., Cui, C. Y., and Schlessinger, D. (2002). The EDA gene is a target of, but does not regulate Wnt signaling. *Gene* 285, 203–211. doi: 10.1016/s0378-1119(02)00407-9

Frazier-Bowers, S. A., Guo, D. C., Cavender, A., Xue, L., Evans, B., King, T., et al. (2002a). A novel mutation in human PAX9 causes molar oligodontia. *J. Dent. Res.* 81, 129–133. doi: 10.1177/154405910208100209

Frazier-Bowers, S. A., Scott, M. R., Cavender, A., Mensah, J., and D'Souza, R. N. (2002b). Mutational analysis of families affected with molar oligodontia. *Connect. Tissue Res.* 43, 296–300. doi: 10.1080/03008200290000961

Goldenberg, M., Das, P., Messersmith, M., Stockton, D. W., Patel, P. I., and D'Souza, R. N. (2000). Clinical, radiographic, and genetic evaluation of a novel form of autosomal-dominant oligodontia. *J. Dent. Res.* 79, 1469–1475. doi: 10.1177/00220345000790070701

Golonzhka, O., Metzger, D., Bornert, J. M., Bay, B. K., Gross, M. K., Kioussi, C., et al. (2009). Ctip2/Bcl11b controls ameloblast formation during mammalian odontogenesis. *Proc. Natl. Acad. Sci. U.S.A.* 106, 4278–4283. doi: 10.1073/pnas.0900568106

Häärä, O., Harjunmaa, E., Lindfors, P. H., Huh, S., FliniauxS, I., Åberg, T., et al. (2012). Ectodysplasin regulates activator-inhibitor balance in murine tooth development through Fgf20 signaling. *Development* 139, 3189–3199. doi: 10.1242/dev.079558

Huang, X., Wang, F., Zhao, C., Yang, S., Cheng, Q., Tang, Y., et al. (2019). Dentinogenesis and tooth-alveolar bone complex defects in BMP9/GDF2 knockout mice. *Stem Cells Dev.* 28, 683–694. doi: 10.1089/scd.2018.0230

Jarvinen, E., Shimomura-Kuroki, J., Balic, A., Jussila, M., and Thesleff, I. (2018). Mesenchymal Wnt/beta-catenin signaling limits tooth number. *Development* 145:dev158048. doi: 10.1242/dev.158048

Jernvall, J., and Thesleff, I. (2000). Reiterative signaling and patterning during mammalian tooth morphogenesis. *Mech. Dev.* 92, 19–29. doi: 10.1016/s0925-4773(99)00322-6

Jia, S., Zhou, J., Fanelli, C., Wee, Y., Bonds, J., Schneider, P., et al. (2017). Small-molecule Wnt agonists correct cleft palates in Pax9 mutant mice in utero. *Development* 144, 3819–3828. doi: 10.1242/dev.157750

Kapadia, H., Frazier-Bowers, S., Ogawa, T., and D'Souza, R. N. (2006). Molecular characterization of a novel PAX9 missense mutation causing posterior tooth agenesis. *Eur. J. Hum. Genet.* 14, 403–409. doi: 10.1038/sj.ejhg.5201574

Kapadia, H., Mues, G., and D'Souza, R. (2007). Genes affecting tooth morphogenesis. *Orthod. Craniofac. Res.* 10, 237–244. doi: 10.1111/j.1601-6343.2007.00407.x

Kist, R., Watson, M., Wang, X., Cairns, P., Miles, C., Reid, D. J., et al. (2005). Reduction of Pax9 gene dosage in an allelic series of mouse mutants causes

hypodontia and oligodontia. *Hum. Mol. Genet.* 14, 3605–3617. doi: 10.1093/hmg/ddi388

Lan, Y., Jia, S., and Jiang, R. (2014). Molecular patterning of the mammalian dentition. *Semin. Cell Dev. Biol.* 2, 61–70. doi: 10.1016/j.semcdb.2013.12.003

Laurikkala, J., Mikkola, M., Mustonen, T., Aberg, T., Koppinen, P., Pispa, J., et al. (2001). TNF signaling via the ligand-receptor pair ectodysplasin and edar controls the function of epithelial signaling centers and is regulated by Wnt and activin during tooth organogenesis. *Dev. Biol.* 229, 443–455. doi: 10.1006/dbio.2000.9955

Lin, C. R., Kioussi, C., O'Connell, S., Briata, P., Szeto, D., Liu, F., et al. (1999). Pitx2 regulates lung asymmetry, cardiac positioning and pituitary and tooth morphogenesis. *Nature* 401, 279–282. doi: 10.1038/45803

Lu, M. F., Pressman, C., Dyer, R., Johnson, R. L., and Martin, J. F. (1999). Function of Rieger syndrome gene in left-right asymmetry and craniofacial development. *Nature* 401, 276–278. doi: 10.1038/45797

Lumsden, A. G. (1988). Spatial organization of the epithelium and the role of neural crest cells in the initiation of the mammalian tooth germ. *Development* 103(Suppl.), 155–169.

Millar, S. E., Koyama, E., Reddy, S. T., Andl, T., Gaddapara, T., Piddington, R., et al. (2003). Over- and ectopic expression of Wnt3 causes progressive loss of ameloblasts in postnatal mouse incisor teeth. *Connect. Tissue Res.* 44(Suppl. 1), 124–129. doi: 10.1080/713713645

Mina, M., and Kollar, E. J. (1987). The induction of odontogenesis in non-dental mesenchyme combined with early murine mandibular arch epithelium. *Arch. Oral Biol.* 32, 123–127. doi: 10.1016/0003-9969(87)90055-0

Mitsui, S. N., Yasue, A., Masuda, K., Watanabe, K., Horiuchi, S., Imoto, I., et al. (2014). Novel PAX9 mutations cause non-syndromic tooth agenesis. *J. Dent. Res.* 93, 245–249. doi: 10.1177/0022034513519801

Mues, G., Bonds, J., Xiang, L., Vieira, A. R., Seymen, F., Klein, O., et al. (2014). The WNT10A gene in ectodermal dysplasias and selective tooth agenesis. *Am. J. Med. Genet. A* 164A, 2455–2460. doi: 10.1002/ajmg.a.36520

Munne, P. M., Tummers, M., Jarvinen, E., Thesleff, I., and Jernvall, J. (2009). Tinkering with the inductive mesenchyme: Sostdc1 uncovers the role of dental mesenchyme in limiting tooth induction. *Development* 136, 393–402. doi: 10.1242/dev.025064

Nakatomi, M., Wang, X., Key, D., Lund, J. J., Turbe-Doan, A., Kist, R., et al. (2010). Genetic interactions between Pax9 and Msx1 regulate lip development and several stages of tooth morphogenesis. *Dev. Biol.* 340, 438–449. doi: 10.1016/j.ydbio.2010.01.031

Neubuser, A., Peters, H., Balling, R., and Martin, G. R. (1997). Antagonistic interactions between FGF and BMP signaling pathways: a mechanism for positioning the sites of tooth formation. *Cell* 90, 247–255. doi: 10.1016/s0092-8674(00)80333-5

Nieminen, P. (2009). Genetic basis of tooth agenesis. *J. Exp. Zool. B Mol. Dev. Evol.* 312B, 320–342. doi: 10.1002/jez.b.21277

O'Connell, D. J., Ho, J. W., Mammoto, T., Turbe-Doan, A., O'Connell, J. T., Haseley, P. S., et al. (2012). A Wnt-bmp feedback circuit controls intertissue signaling dynamics in tooth organogenesis. *Sci. Signal.* 5:ra4. doi: 10.1126/scisignal.2002414

Ogawa, T., Kapadia, H., Feng, J. Q., Raghow, R., Peters, H., and D'Souza, R. N. (2006). Functional consequences of interactions between Pax9 and Msx1 genes in normal and abnormal tooth development. *J. Biol. Chem.* 281, 18363–18369. doi: 10.1074/jbc.m601543200

Ohazama, A., Johnson, E. B., Ota, M. S., Choi, H. Y., Porntaveetus, T., Oommen, S., et al. (2008). Lrp4 modulates extracellular integration of cell signaling pathways in development. *PLoS One* 3:e4092. doi: 10.1371/journal.pone.0004092

Parveen, A., Khan, S. A., Mirza, M. U., Bashir, H., Arshad, F., Iqbal, M., et al. (2019). Deleterious variants in WNT10A, EDAR, and EDA causing isolated and syndromic tooth agenesis: a structural perspective from molecular dynamics simulations. *Int. J. Mol. Sci.* 20:5282. doi: 10.3390/ijms20215282

Peters, H., Neubuser, A., Kratochwil, K., and Balling, R. (1998). Pax9-deficient mice lack pharyngeal pouch derivatives and teeth and exhibit craniofacial and limb abnormalities. *Genes Dev.* 12, 2735–2747. doi: 10.1101/gad.12.17.2735

Pispa, J., Jung, H. S., Jernvall, J., Kettunen, P., Mustonen, T., Tabata, M. J., et al. (1999). Cusp patterning defect in Tabby mouse teeth and its partial rescue by FGF. *Dev. Biol.* 216, 521–534. doi: 10.1006/dbio.1999.9514

Stockton, D. W., Das, P., Goldenberg, M., D'Souza, R. N., and Patel, P. I. (2000). Mutation of PAX9 is associated with oligodontia. *Nat. Genet.* 24, 18–19. doi: 10.1038/71634

Tian, Y., Ma, P., Liu, C., Yang, X., Crawford, D. M., Yan, W., et al. (2015). Inactivation of Fam20B in the dental epithelium of mice leads to supernumerary incisors. *Eur. J. Oral Sci.* 123, 396–402. doi: 10.1111/eos.12222

Voutilainen, M., Lindfors, P. H., Trela, E., Lonnblad, D., Shirokova, V., Elo, T., et al. (2015). Ectodysplasin/NF-κB promotes mammary cell fate via Wnt/β-catenin pathway. *PLoS Genet.* 11:e1005676. doi: 10.1371/journal.pgen.1005676

Wang, Y., Yan, M., Yu, Y., Wu, J., Yu, J., and Fan, Z. (2013). Estrogen deficiency inhibits the odonto/osteogenic differentiation of dental pulp stem cells via activation of the NF-kappaB pathway. *Cell Tissue Res.* 352, 551–559. doi: 10.1007/s00441-013-1604-z

Williams, M. A., and Letra, A. (2018). The changing landscape in the genetic etiology of human tooth agenesis. *Genes* 9:255. doi: 10.3390/genes9050255

Yang, Z., Hai, B., Qin, L., Ti, X., Shangguan, L., Zhao, Y., et al. (2013). Cessation of epithelial Bmp signaling switches the differentiation of crown epithelia to the root lineage in a beta-catenin-dependent manner. *Mol. Cell. Biol.* 33, 4732–4744. doi: 10.1128/mcb.00456-13

Ye, X., and Attaie, A. B. (2016). Genetic basis of nonsyndromic and syndromic tooth agenesis. *J. Pediatr. Genet.* 5, 198–208. doi: 10.1055/s-0036-1592421

Yu, W., Sun, Z., Sweat, Y., Sweat, M., Venugopalan, S. R., Eliason, S., et al. (2020). Pitx2-Sox2-Lef1 interactions specify progenitor oral/dental epithelial cell signaling centers. *Development* 147:dev186023. doi: 10.1242/dev.186023

Zhang, Y., Tomann, P., Andl, T., Gallant, N. M., Huelsken, J., Jerchow, B., et al. (2009). Reciprocal requirements for eda/edar/nf-kappab and wnt/beta-catenin signaling pathways in hair follicle induction. *Dev. Cell* 17, 49–61. doi: 10.1016/j.devcel.2009.05.011

Zhou, J., Gao, Y., Lan, Y., Jia, S., and Jiang, R. (2013). Pax9 regulates a molecular network involving Bmp4, Fgf10, Shh signaling and the Osr2 transcription factor to control palate morphogenesis. *Development* 140, 4709–4718. doi: 10.1242/dev.099028

Conflict of Interest: The authors declare that the research was conducted in the absence of any commercial or financial relationships that could be construed as a potential conflict of interest.

frontiers in Physiology

ORIGINAL RESEARCH
published: 04 May 2021
doi: 10.3389/fphys.2021.576816

Tooth Removal in the Leopard Gecko and the *de novo* Formation of Replacement Teeth

*Kirstin S. Brink†, Joaquín Ignacio Henríquez, Theresa M. Grieco†, Jesus Rodolfo Martin del Campo, Katherine Fu and Joy M. Richman**

Department of Oral Health Sciences, Life Sciences Institute, University of British Columbia, Vancouver, BC, Canada

OPEN ACCESS

Edited by:
Maisa Hanna-Maija Seppala, King's College London, United Kingdom

Reviewed by:
Hidemitsu Harada, Iwate Medical University, Japan
Nicolas Di-Poi, University of Helsinki, Finland

****Correspondence:***
Joy M. Richman
richman@dentistry.ubc.ca

†Present address:
Kirstin S. Brink, Department of Geological Sciences, University of Manitoba, Winnipeg, MB, Canada
Theresa M. Grieco, STEMCELL Technologies, Vancouver, BC, Canada

Specialty section:
This article was submitted to Craniofacial Biology and Dental Research, a section of the journal Frontiers in Physiology

Received: *27 June 2020*
Accepted: *25 March 2021*
Published: *04 May 2021*

Citation:
Brink KS, Henríquez JI, Grieco TM, Martin del Campo JR, Fu K and Richman JM (2021) Tooth Removal in the Leopard Gecko and the de novo Formation of Replacement Teeth. Front. Physiol. 12:576816. doi: 10.3389/fphys.2021.576816

Many reptiles are able to continuously replace their teeth through life, an ability attributed to the existence of epithelial stem cells. Tooth replacement occurs in a spatially and temporally regulated manner, suggesting the involvement of diffusible factors, potentially over long distances. Here, we locally disrupted tooth replacement in the leopard gecko (*Eublepharis macularius*) and followed the recovery of the dentition. We looked at the effects on local patterning and functionally tested whether putative epithelial stem cells can give rise to multiple cell types in the enamel organs of new teeth. Second generation teeth with enamel and dentine were removed from adult geckos. The dental lamina was either left intact or disrupted in order to interfere with local patterning cues. The dentition began to reform by 1 month and was nearly recovered by 2–3 months as shown in μCT scans and eruption of teeth labeled with fluorescent markers. Microscopic analysis showed that the dental lamina was fully healed by 1 month. The deepest parts of the dental lamina retained odontogenic identity as shown by PITX2 staining. A pulse-chase was carried out to label cells that were stimulated to enter the cell cycle and then would carry BrdU forward into subsequent tooth generations. Initially we labeled 70–78% of PCNA cells with BrdU. After a 1-month chase, the percentage of BrdU + PCNA labeled cells in the dental lamina had dropped to 10%, consistent with the dilution of the label. There was also a population of single, BrdU-labeled cells present up to 2 months post surgery. These BrdU-labeled cells were almost entirely located in the dental lamina and were the likely progenitor/stem cells because they had not entered the cell cycle. In contrast fragmented BrdU was seen in the PCNA-positive, proliferating enamel organs. Homeostasis and recovery of the gecko dentition was therefore mediated by a stable population of epithelial stem cells in the dental lamina.

Keywords: reptile, pulse-chase, label-retaining cell, dentition, polyphyodont, successional teeth, adult tissue stem cells, dental epithelium

INTRODUCTION

Polyphyodonty, or life-long tooth replacement, is a developmental process shared by most non-mammalian vertebrates. In polyphyodont reptiles, it has been well documented that replacement occurs in waves that pass from the back to the front of the mouth in alternating tooth positions (Edmund, 1960, 1962; Cooper, 1966; Kline and Cullum, 1984; Kline and Cullum, 1985;

Fastnacht, 2008; Grieco and Richman, 2018; Hanai and Tsuihiji, 2019). One key component of the expression of these jaw-level replacement waves is that each tooth position cycles on a temporally delayed schedule from adjacent positions. An examination of tooth replacement in young leopard geckos demonstrated that patterning is initiated *in ovo* and continuous in post-hatching animals, pointing to some conserved mechanisms at the patterning level in adults (Grieco and Richman, 2018). However, the mechanisms behind this cyclical tooth replacement are still not well understood.

Many studies have investigated potential mechanisms for the establishment of this alternating wave replacement pattern in polyphyodont animals. In fish, there is strong evidence for signals that originate with an initiator tooth at the front of the jaw and pattern the tooth row or rows (Huysseune et al., 2012; Gibert et al., 2019; Sadier et al., 2020). This mechanism has also been suggested for reptiles, however, it has not been tested (Edmund, 1969). Other potential mechanisms proposed for reptiles include a reaction-diffusion model or 'zone of inhibition' model that creates spacing between teeth that change through growth, creating an emergent alternating replacement pattern (Osborn, 1970, 1971; Westergaard and Ferguson, 1987; Murray and Kulesa, 1996; Fraser et al., 2008). These models have all been proposed based on examination of tooth initiation in embryos, and so it is still not known how patterns of tooth cycling are maintained in adults.

Tooth replacement in polyphyodont reptiles can be partially explained by the persistence of dental epithelium throughout life (Handrigan et al., 2010; Wu et al., 2013; Salomies et al., 2019; Brink et al., 2020). In reptiles the dental lamina may either be continuous around the jaws as in lizards and snakes, or be focal islands of epithelial cells next to the functional tooth as in crocodilians. In contrast, in most mammals, the dental epithelium undergoes apoptosis prenatally (Buchtova et al., 2012) and only a few cells posterior to the terminal tooth in the arch or in the periodontal ligament persist after birth. In the leopard gecko, tooth development begins at the most aboral end (furthest away from the oral cavity) or free-end of the dental lamina. The early bud passes through typical stages of tooth development (bud, cap, bell, histodifferentiation, eruption) ultimately emerging into the oral cavity. The dental lamina connects the functional tooth to the underlying replacement teeth at each tooth position. The dental lamina continues to grow on the lingual side of the youngest tooth to form the successional lamina. Each new tooth buds from the successional lamina and the cycle begins again. The ectomesenchyme condenses around the bud, and both tissues interact, to undergo morphogenesis and histodifferentiation (Handrigan et al., 2010; Handrigan and Richman, 2011).

The dental lamina is the likely source of epithelial stem cells in polyphyodont reptiles (Handrigan et al., 2010; Wu et al., 2013). Previous work in leopard geckos found that the majority of label-retaining cells (putative stem cells) were located on the lingual side of the dental lamina, approximately half-way between the successional lamina and the oral cavity (Handrigan et al., 2010). Label-retaining cells were not observed streaming into the generational teeth but instead appeared to be quiescent and isolated from other BrdU-positive cells. However, putative stem cells may have other niches close to the oral epithelium, as shown in the bearded dragon (Salomies et al., 2019). Label-retaining cells were present in low numbers in the successional lamina of the bearded dragon (Salomies et al., 2019) and iguana (Brink et al., 2020) but were only seen in the dental lamina bulge (successional lamina) of the American alligator in the pre-initiation stage of tooth development (Wu et al., 2013). The differences in proximity to the successional teeth and scarcity of these label-retaining cells means that there are still important questions to address regarding the fates (or roles) of these putative stem cells in development of the next generation of teeth.

Previously, there were studies that attempted to stimulate tooth replacement by removing functional teeth. In alligators, an increase in proliferation was observed in the dental lamina bulge (Wu et al., 2013). This response in the deepest part of the dental lamina could have led to the early differentiation of the successional lamina, however long term follow up was not included in this study (Wu et al., 2013). In the green iguana, teeth were also initiated earlier than expected after extraction of functional teeth (Brink et al., 2020). However, after early initiation, the timing of the tooth cycle was not affected. Because these iguana studies focused on individual functional teeth at different positions around the mouth, they could not provide information on the relationships between adjacent teeth or mechanisms contributing to jaw-wide patterning. Therefore, it is still not understood how disruptions to odontogenic tissues and developing replacement teeth affect the timing and patterning of replacement in the context of the most prevalent models for tooth replacement.

In this study, we aimed to track the effect of the removal of second generation teeth and damage to the dental lamina on the development of subsequent tooth generations using the leopard gecko, which has a known tooth shedding cycle length (Grieco and Richman, 2018) and populations of label-retaining cells in the dental lamina (Handrigan et al., 2010). We ask whether or not the removal of the second generation teeth will affect the patterning of neighboring teeth, whether or not the purported stem cells from the dental lamina (distant from the location of the next tooth bud) give rise to the next tooth generation, and whether or not the dental lamina cells can give rise to ameloblasts, stellate reticulum, and outer enamel epithelium of the enamel organs. We hypothesized that teeth would regenerate after healing of the dental lamina, but that patterning would be disrupted due to removal of signaling between adjacent teeth within the surgical area. We also hypothesized that epithelial stem cells from the dental lamina would contribute to all layers of the enamel organ in the newly formed teeth. Our results show that patterning is not greatly affected following removal of second generation teeth, and that the process of tooth regeneration is robust in the gecko since non-proliferative, dental epithelial progenitor cells

are maintained in the dental lamina. In addition, cells derived from the original labeled dental lamina contributed to all layers of the enamel organ.

MATERIALS AND METHODS

Survival Surgeries on Adult Geckos

All animal procedures were approved by the UBC Animal Care Committee (ethics protocol A15-0242). The colony of leopard geckos is housed in a dedicated facility with 12 h light-dark cycles and heated cages. Animals were raised from hatching or purchased from retail stores. Eighteen geckos (15 female and 3 male) ranging in age from 2 months to 1-year post-hatching and weighing 13–75 g were subjected to oral surgeries. Some individuals were used for experiments at multiple time points in the maxillae and mandibles (**Supplementary Table 1**). Survival surgeries were carried out in an animal surgical suite with an isofluorane vaporizer, O_2 mixer, scavenger system for the gas and fluorescence stereomicroscope (MZFLIII).

Geckos were given 0.2 mg/kg meloxicam orally and 15 mg/kg calcein (Sigma-Aldrich, cat no. C0875), via intraperitoneal injection 24 h before the surgery. The fluorescent calcein label is rapidly incorporated into mineralizing enamel, dentine and bone. Animals were induced with a mixture of 5% isoflurane/O_2 gas under continuous flow and intramuscular injections of 20 mg/kg alfaxalone were delivered bilaterally into the epaxial muscles. Local anesthetic was administered into the palate or mandible prior to surgery via injection (0.5% lidocaine, 7 mg/kg maximum dose).

Quadrants of the mouth were divided into different treatment regions ranging from 10 to 20 teeth: (1) enucleation (surgical removal) of developing second generation teeth containing mineralized tissue while leaving the non-mineralized, third generation bud stage teeth, (2) enucleation of second generation teeth plus curetting the surrounding tissues, thereby removing and/or displacing those tissues and non-mineralized third generation bud stage teeth, and (3) sham surgical areas, where the lingual mucosa was cut next to the teeth and retracted lingually with minimal damage to adjacent tissues (**Figures 1B–H**). Adjacent control, non-manipulated regions were also studied to assess the normal patterns of patterning and proliferation.

Iridectomy scissors were inserted into the marginal mucosa lingual to the functional teeth (**Figure 1B**). The mucosa was retracted with a blunt instrument (Dycal applicator, dental instrument) to view developing second generation teeth containing calcein (GFP filter set; **Figure 1C**). Third generation teeth were not visible because they were not mineralized. Several sites were treated in one animal (**Figure 1D**). In the experimental regions, mineralized, unerupted teeth were removed using #5 fine forceps with (enucleation + curettage) or without (enucleation) disruption of the dental epithelium (**Figures 1E–G**). For curettage, a spoon excavator (dental instrument) was moved anterior-posteriorly under the mucosa to tear and shift the position of the dental lamina. Affi-Gel blue beads (BioRad) were implanted at each end of the incision to mark the surgical area in subsequent histological analysis. Photographs were taken using a fluorescent and brightfield stereo microscope before and after surgery. One week before euthanization, six animals were administered 90 mg/kg of xylenol orange (Sigma-Aldrich, cat. No. 398187) through intraperitoneal injection to label teeth that mineralized after surgery (**Figure 2A**).

BrdU Pulse-Chase Experiment

Animals were administered 50 mg/kg Bromo-deoxyuridine (BrdU, Cat no. B5002, Sigma-Aldrich) intraperitoneally once a day for 4 consecutive days, beginning 3 days after surgery. Animals were euthanized as described at time zero (right after the 4-day pulse or 1 week post surgery), 3 weeks post BrdU (1 month post surgery), and 7 weeks post BrdU (8 weeks post-surgery).

μCT Scanning

Following euthanasia with isoflurane, gecko heads were fixed in 4% paraformaldehyde for at least 24 h at 4°C, rinsed in saline, embedded in 2% agarose, and dehydrated into 70% ethanol. Skulls were μCT scanned in the Centre for High Throughput Phenogenomics (CHTP) at the University of British Columbia on a Scanco Medical μCT100 at a resolution of 17 μm. A mandible from 1 animal was treated in a 0.7% Phosphotungstic Acid (PTA)-Methanol solution for 7 days in order to increase the radio-contrast of its soft tissues, following Metscher (2009). The mandible was μCT scanned at the Central European Institute of Technology (CEITEC) at Brno University of Technology on a GE phoenix v| tome| x m at a resolution of 4 μm. PTA staining is incompatible with histological or molecular analyses. All maxillary specimens were reserved for molecular studies.

Histology and Immunofluorescence Staining

After standard μCT scanning, the gecko maxilla and mandible pieces were divided into segments using landmarks recorded during surgery. Pieces were decalcified in 14% EDTA for at least 3 months at room temperature on a shaker prior to processing into paraffin wax. To determine the areas where surgery had been carried out, test slides were made. Every 10th section throughout the block was stained with Hematoxylin and Eosin. Selected 7 μm sections from multiple blocks were placed on slides so that the staining conditions were equivalent for a variety of treatments. Multiple replicates of teeth were put across several slides, further validating the results (**Supplementary Table 2**).

Sections were deparaffinized and rehydrated to water. Antigen retrieval for all immunostaining was performed using Diva Decloaker (Biocare #DV2004MX). For combination BrdU and PCNA staining, sections were pretreated with 0.1% Triton-X in PBS for 10 min and then blocked in 10% goat serum, 0.1% Triton-X in PBS for 30 min. Anti-BrdU (G3G4 clone, Developmental Studies Hybridoma Bank, mouse 1:20) and anti-PCNA (Proliferating Cell Nuclear Antigen, rabbit polyclonal, Abcam, #18197, 1:1000) were mixed together in blocking solution and incubated overnight at 4°C.

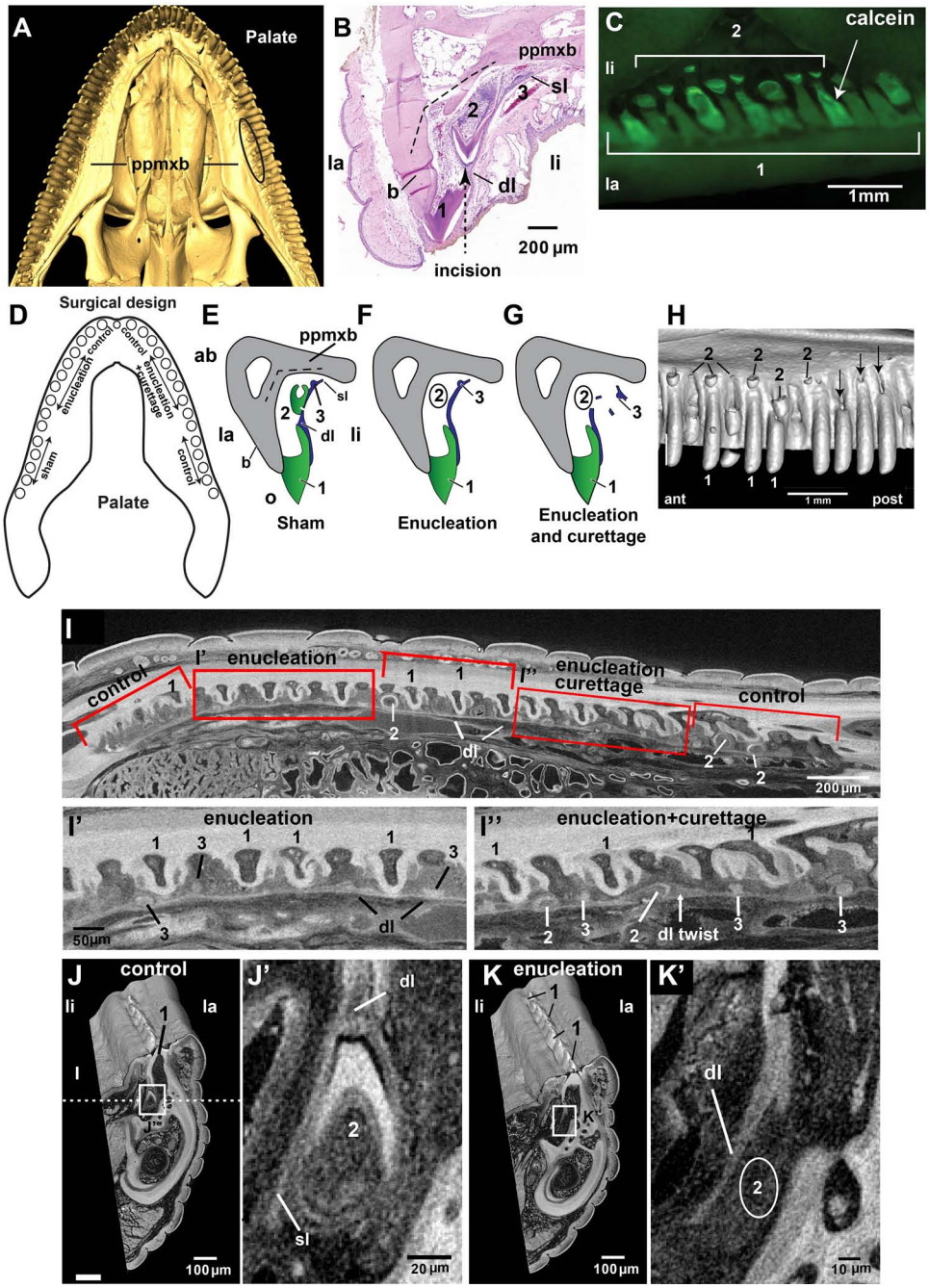

FIGURE 1 | The polyphyodont leopard gecko model. **(A)** µCT scan of leopard gecko maxilla showing replacement teeth close to the angle between the dental and palatal processes of the maxillary bone (oval outline). The mineralized replacement teeth are found around the arch at different stages of development. **(B)** Hematoxylin and Eosin-stained section of the leopard gecko maxilla, transverse plane. The mineralized first generation or functional tooth is connected to the second generation and third generation teeth by a dental lamina. The incision made lingual to the 1st generation tooth exposes the second generation tooth (dashed line with arrowhead). The projection of the palatine process of the maxillary bone is shown by the angled dashed line. This is anatomical reference for where to expect new teeth to form. **(C)** Calcein-labeled teeth at the time of surgery. The mucosa has been incised and retracted to show the labeled, unerupted second generation teeth. **(D)** Experimental design for tooth removal surgeries in the maxilla, which involves multiple sites of 10 teeth each. Third generation teeth form close to the palatine process of the maxillary bone. **(E)** Schematic to show the sham surgical control, with the oral mucosa cut and retracted but teeth and soft tissues not disturbed. **(F)** Enucleation involves removal of the second generation tooth (2 inside a circle) while leaving the dental lamina and third generation teeth in place. **(G)** enucleation with curettage, comprising removal of second generation teeth (2 inside a circle) and curettage of dental tissues, damaging the dental and successional laminae. **(H)** Lingual view of a region of a µCT scan showing the specificity of the surgery. A group of teeth have been removed posteriorly while the anterior second generation teeth remain undisturbed. **(I–K')** Contrast-enhanced µCT scan of a 1-week post-surgery mandible. Several regions were treated in one

(Continued)

FIGURE 1 | Continued
quadrant to maximize information obtained from this specimen. **(I')** Enucleation surgical area in frontal view showing third generation replacement teeth present and a straight dental lamina. **(I")** Enucleation with curettage surgical area in frontal view showing the missing and displaced replacement teeth as well as a thicker dental lamina that may be twisted. **(J,J')** Transverse slice through the control area showing a second generation tooth and dental lamina. Dashed line indicates plane of section in **(I–I")**. **(K,K')** Transverse slice through the enucleated area showing the absent second generation tooth plus remaining dental lamina. Key: 1- functional, 1st generation tooth; 2- second generation replacement tooth; 3- third generation replacement tooth; ab, aboral; ant, anterior; b, bone; dl, dental lamina; dl twist, twisted dental lamina; la, labial; li, lingual; o, oral; post, posterior; ppmxb, palatine process of maxillary bone; sl, successional lamina.

For PITX2, Keratin, and SOX2 staining sections were blocked in 5% bovine serum, 0.1% Tween-20 in TBS for 1 h at room temperature. Tissues were incubated overnight at 4°C in primary antibodies diluted in blocking serum (sheep polyclonal anti-PITX2, R&D Systems, #AF7388, 1:500; anti-SOX2, rabbit polyclonal, Abcam # 97959, 1:1000; rabbit anti Pan-Keratin, Dako, cat no. Z062201-2, 1:500).

Secondary antibodies were applied for 1 h at room temperature (all diluted 1:250, Life Technologies, Alexa Fluor 647 donkey anti-sheep, #A-21488; Alexa Fluor 488 goat anti-mouse, #A11029; Cy5 goat anti-rabbit, #A10523). Nuclei were counterstained in Hoescht 33258 (Sigma, 10 μg/ml) for 30 min. Slides were mounted with Prolong Gold (Invitrogen #P36934). Fluorescence imaging was conducted using a 20X objective on a Panoramic MIDI II slide scanner with 488, Cy5, and DAPI filter sets (3D Histech Ltd., Hungary). Images were captured with CaseViewer software v.2.4.0.119028 (3D Histech Ltd., Hungary).

Proliferation Analysis

We used CaseViewer software to count BrdU-, PCNA- and Hoechst-stained nuclei in the dental laminae. By turning on and off the channels, dual-labeled nuclei could be confirmed. The total number of green, red or dual-labeled cells was divided by the number of Hoechst-stained cells in that specimen to give the percent label for that dental lamina. Care was taken to space apart the paraffin sections by at least 250 microns (the width of a functional tooth) so that teeth from different families were being analyzed. These teeth rather than the animals were considered individual biological replicates. Teeth for each of the experimental conditions (enucleated, enucleation + curettage, sham or control) were combined from three animals (**Supplementary Table 2**). We compared percent label at two time points (Time zero and 1 month) as well as between the four treatments using two-way ANOVA (**Supplementary Tables 3A–D**). Statistical analyses were carried out using GraphPad Prism 9.0.2.

For animals euthanized at 2 months, few labeled cells were present, therefore we did not calculate percentages (**Supplementary Table 4**). Instead, we determined the raw number of labeled cells in different regions of the enamel organ (inner enamel epithelium, outer enamel epithelium, and stellate reticulum) and the dental lamina of bud or cap stage teeth (**Supplementary Table 4**).

TUNEL Assay

Apoptosis was assessed by TUNEL analysis using the ApopTag Apoptosis Kit (Millipore #S7111) and was detected using fluorescein-tagged anti-digoxigenin antibody as described previously (Hosseini-Farahabadi et al., 2013). A qualitative assessment of presence of TUNEL-positive cells was carried out.

RESULTS

Our goal in this study was to challenge the adult gecko dentition by purposely disrupting tooth replacement, thus initiating a healing response. We left functional teeth in place and instead removed or enucleated the unerupted, partly mineralized (second generation) replacement teeth in select regions of the jaw of the leopard gecko (**Figure 1**). The aim was to leave the dental lamina behind plus or minus immature third generation teeth (non-mineralized bud or early cap stage). In more advanced cap stage teeth, the successional lamina may be present. The aim was to test the regenerative capacity of the dental epithelium inside the jaws.

The adult leopard gecko has approximately 40 functional teeth in each quadrant (**Figure 1A**) and in the maxilla each functional tooth is connected to two successional teeth via a dental epithelial lamina (**Figure 1B**). The second generation, mineralized, unerupted teeth are nestled at the inflection between the dental and palatine processes of the maxillary bone (**Figure 1A**) and are at various stages of crown formation (**Figure 1A**). In addition, each family contains a tooth in bud or early cap stage prior to cytodifferentiation (third generation) that is visible only in histology (**Figure 1B**). The successional lamina is connected to the outer enamel epithelium of the second generation tooth and continues to initiate the third generation of teeth (**Figure 1B**). For direct visualization of second generation teeth during surgery, we injected calcein which was rapidly taken up in the dentine and enamel caps (**Figure 1C**). The three treatments – sham, enucleation and enucleation, and curettage (**Figures 1D–G**) – started with an incision lingual to the functional tooth (**Figure 1B**). This incision gave direct access to second generation teeth (**Figure 1C**). We confirmed that teeth were removed using conventional μCT scans for all specimens that were subsequently used for histology (**Figure 1H**). One mandibular quadrant was treated with the two surgeries, fixed after 1 week, then stained with phosphotungstic acid prior to scanning at high resolution (**Figures 1I–K'**). Mineralized second generation replacement teeth are still present in the control areas (**Figures 1I,J,J'**). However, in the enucleated areas, second generation replacement teeth were successfully removed (**Figures 1K,K'**), and soft tissues with third generation teeth are still present (**Figures 1I–I"**). Buds are evenly spaced in the enucleated area, while in the enucleated area with curettage, some buds are bunched together at the edges of the treatment site and

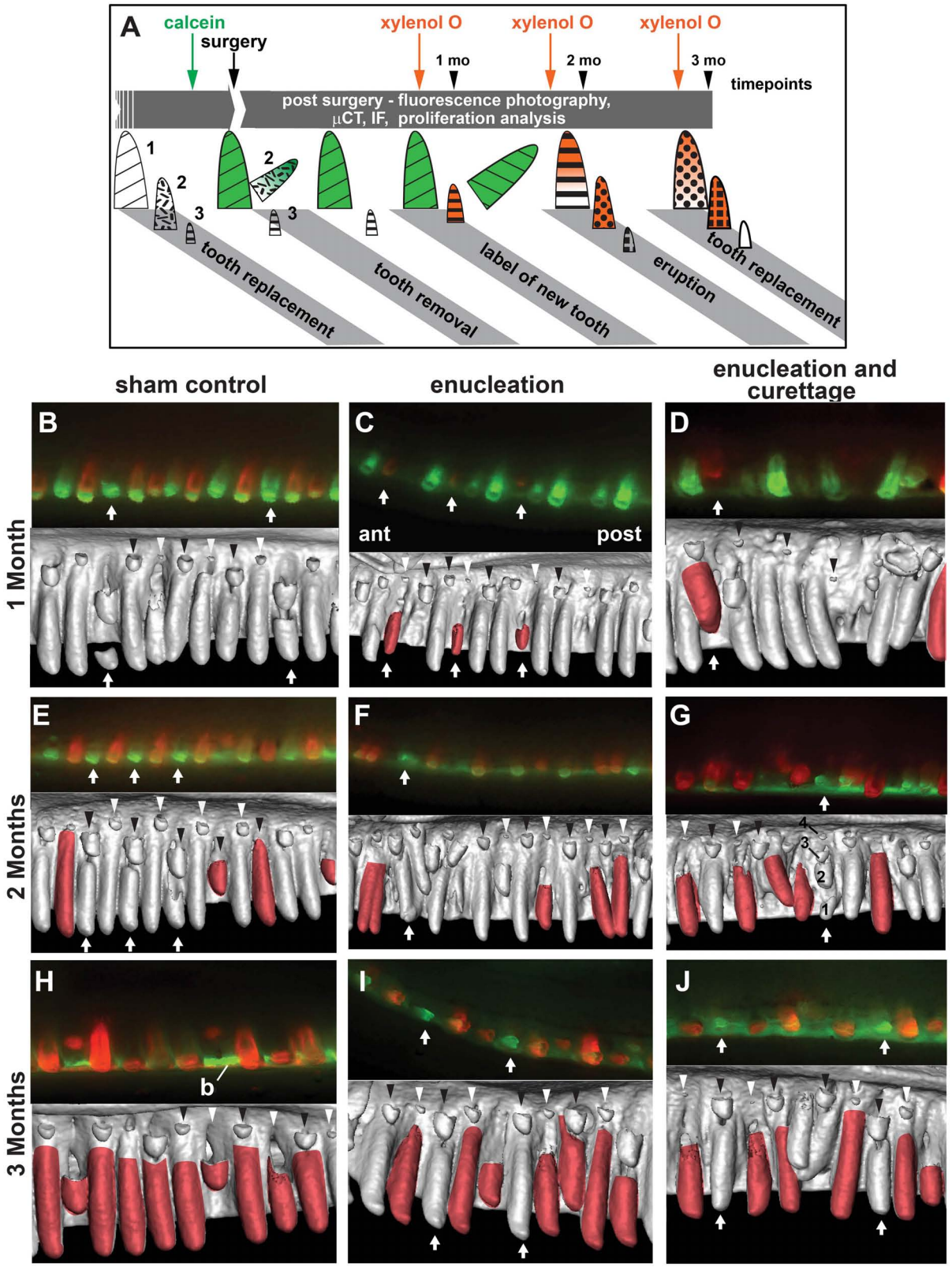

FIGURE 2 | Tooth regeneration dynamics. **(A)** Schematic of the experiment starting on the left. Calcein was administered once, 24 h before second generation tooth removal. Functional teeth and second generation teeth are labeled green. Third generation teeth are not mineralized and do not take up the label. Xylenol orange was

(Continued)

FIGURE 2 | Continued
administered 1 week prior to the 1, 2, and 3 months timepoints (euthanization). Orange teeth are mineralized after the surgery. Fill patterns correspond to specific tooth generations. **(B–J)** Top half of each panel are fluorescent images taken after fixation with all soft tissues present. Signal is partially obscured by the mucosa. The fluorescent orange teeth were matched up to the equivalent teeth in the μCT images (bottom half) and only teeth with exclusive orange label were false colored. Black and white arrowheads indicate replacement waves or incipient replacement waves in alternating tooth positions. **(B)** Sham control – Most teeth are double labeled with green tips and an orange base with the exception of two teeth that are green only and are about to be replaced with orange teeth (arrows). **(C)** Enucleation – three teeth are completely orange and are newly erupting (arrows). **(D)** Enucleation with curettage – A newly-erupting, orange tooth is visible (arrow). **(E)** At 2 months post-surgery in the sham control, many teeth are double labeled and several erupted teeth are exclusively orange. The green teeth will soon be replaced (arrows). **(F,G)** 2 months following enucleation or enucleation and curettage, double-labeled teeth are present, exclusively orange teeth are present, and occasional green teeth are still present (arrows). The μCT scans show some third generation teeth are out-of-place. In **(G)**, one tooth position has 3 successional teeth (arrow). **(H)** At 3 months post-surgery in the sham control, all teeth are orange, indicating that they have all been replaced since the surgery. The visible green is in the underlying jawbone. **(I,J)** After enucleation or enucleation and curettage some of the original green teeth have been retained in the mouth longer than expected when compared to controls (arrows). The μCT scans show third generation teeth are initiating in a somewhat normal alternating pattern. Key: ant, anterior; b, bone; post, posterior.

the dental lamina is thicker and therefore likely to be twisted (**Figure 1I"**).

Recovery of Normal Patterns of Tooth Replacement by 3 Months

Next, we followed the recovery of the dentition. Animals were injected with calcein 24 h before surgery and were injected with xylenol orange 1 week before euthanization to label teeth that were formed *de novo* post-surgery (**Figure 2A**). After 1 month, the control areas contained mainly teeth with a double label (green tip and orange base). The dual label indicated that these teeth were present prior to the surgery (green) and had added new dentine since the surgery (orange). In the subsequent μCT scan of the matched region, second generation teeth are visible in an alternating wave pattern of small and large teeth, increasing in size toward the back of the jaw (**Figure 2B**, black and white arrowheads). When compared to the μCT scan, the green teeth are about to be replaced and were not actively mineralizing (**Figure 2B**, arrows). In both treated areas, new teeth labeled with xylenol orange were superficial enough to make them visible through the mucosa (**Figures 2C,D**, white arrows). Enucleation and curettage interfered with the patterning of *de novo* tooth formation (**Figure 2D**, black arrowheads) more severely than enucleation alone (**Figure 2C**, black and white arrowheads). In addition, teeth are crowded together and oriented abnormally, suggesting that tooth initiation and development were occurring in displaced tissues (**Figure 2D**).

By 2 months post-treatment, the control areas show more exclusively orange teeth, indicating they were newly formed since the calcein was administered. Several teeth are still double-labeled and some show only a green calcein-label, indicating that they are no longer actively mineralizing and will soon be replaced (arrows, **Figure 2E**). The erupted teeth retaining the green label are in tooth positions alternating with orange teeth, and when matched with the developing replacement teeth, waves can be seen in alternating tooth positions increasing in size toward the back of the jaw (**Figure 2E**, black and white arrowheads). Disruptions to normal eruption patterns are still evident in the regions where teeth were removed (arrows, **Figures 2F,G**). In the enucleated treatment, newly mineralizing teeth appear in an alternating pattern of large and small teeth (**Figure 3F**, black and white arrowheads), but do not show a clear pattern of gradual size increase in alternating positions, as seen in the sham control (**Figure 2E**). In the enucleation with curettage treatment area (**Figure 2G**), one tooth position shows one functional tooth about to be shed containing green label only, and three partially mineralized replacement teeth following it (white arrow).

Three months post-treatment, every tooth in the sham control is labeled orange, indicating that all teeth have been replaced (**Figure 2H**). The jawbone is still labeled green (**Figure 2H**). In the treated areas, teeth are retained that contain a green label only, longer than would be expected when compared to the sham control (**Figures 2I,J**, arrows). Newly mineralizing teeth in both areas show a pattern of alternating tooth sizes approaching the pattern observed in sham control regions (**Figures 2I,J**, black and white arrowheads).

Cellular Responses to Removal of Unerupted, Second Generation Teeth

We demonstrated that after removing the second generation teeth gradual recovery occurred. Next, we examined the tissue-level response. Using a TUNEL assay, cell death is present in the dental lamina and the surrounding mesenchyme 3 days post-surgery in enucleated areas (**Supplementary Figures 1A,B**). By 7 days post-surgery, there are small amounts of cell death in the mesenchyme but no TUNEL-positive cells in the epithelium (**Supplementary Figures 1D,E**). The sham control teeth did not have any TUNEL-positive cells. The cell debris was cleared by 1 week.

Next, we examined proliferation using PCNA to determine whether the pattern of proliferating cells in the dental epithelium and adjacent mesenchyme was changed by the surgery. The normal pattern of PCNA labeling in bell stage teeth is to have high proliferation in the mesenchyme, cervical loops and successional lamina (Handrigan et al., 2010). The dental lamina typically has much lower proliferation (**Figures 3A–A"**). Cap and bud stage teeth are 100% labeled with PCNA. During the first 24 h after removal of the second generation tooth the dental lamina retained PCNA-positive cells near the aboral end (**Figures 3B–C"**). Tearing of the dental lamina did not affect the pattern (**Figure 3C"**). The sham control appeared to have increased PCNA staining in the dental lamina at 72 h compared to 24 h (**Figures 3D–D"**). The clearest change between 24 and 72 h

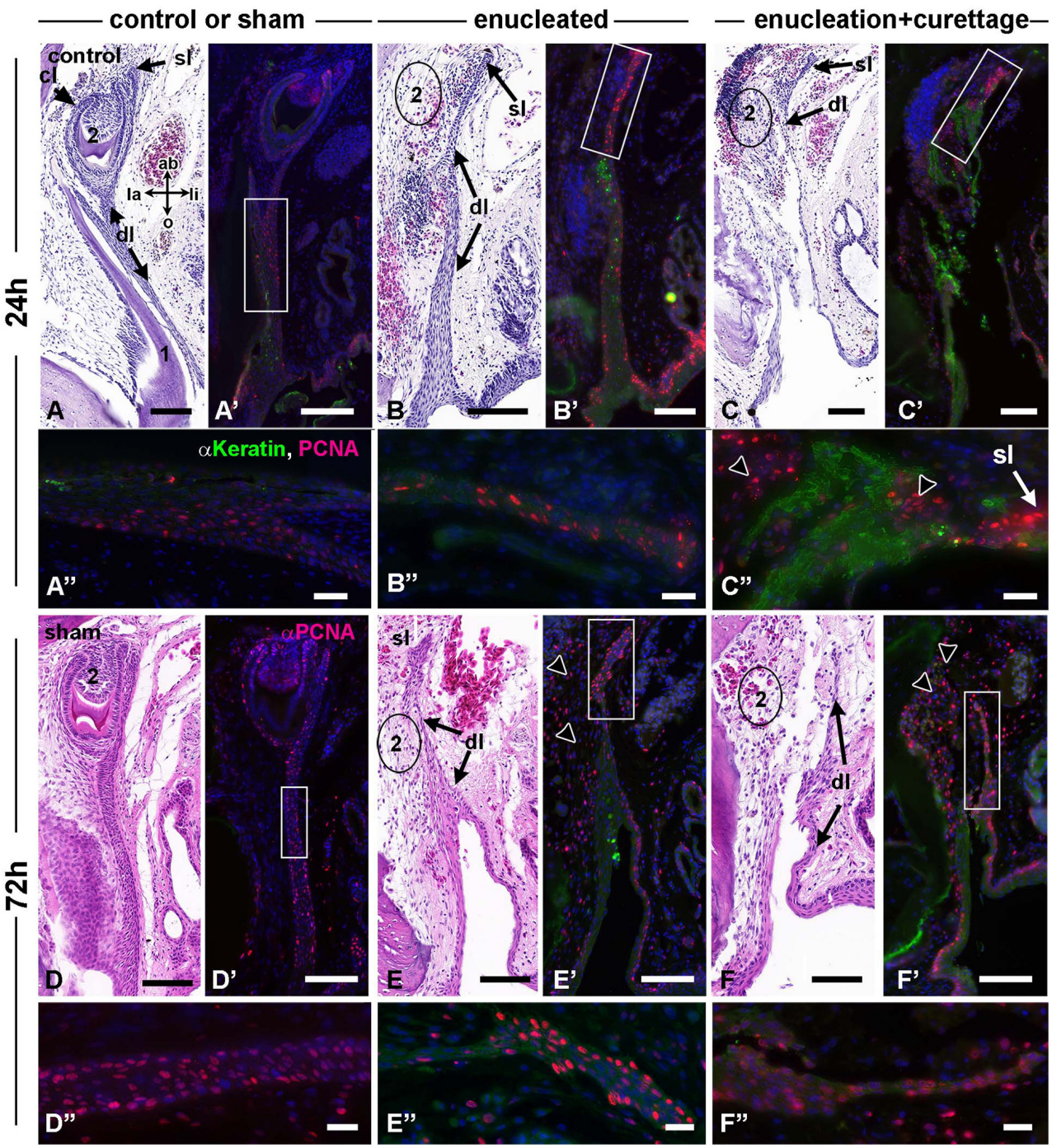

FIGURE 3 | Gecko dental surgical outcomes, 24–72 h. Histological sections stained with H and E and near-adjacent sections stained with PCNA antibody and pan-cytokeratin antibody (Except for **D–D"**). **(A–A")** The second generation tooth is in advanced bell stage with dentine and enamel deposited. PCNA positive cells are present in the cervical loops, successional lamina, and dental lamina. Anti-cytokeratin labels the epithelium. **(B–B")** Removal of second generation teeth leaves a space where the tooth used to be (2 with circle around it). The dental lamina is largely intact with proliferating cells concentrated in the successional lamina. **(C–C")** enucleation and curettage caused tears in the dental lamina. There are shreds of cytokeratin-positive epithelium present **(C',C")**. Proliferation is mainly limited to the presumptive successional lamina (black arrowheads, **C"**). After 72 h, healing has begun. **(D–D")** Sham treated teeth are present and differentiating in the expected location. The dental lamina has many PCNA positive cells **(D")**. **(E–E")** The remaining dental lamina continues to have higher proliferation at the aboral tip **(E")**. There are also large numbers of proliferating mesenchymal cells (black arrowheads). **(F–F")** Torn dental lamina is starting to heal and there is high proliferation in the epithelium as well as mesenchyme (black arrowheads). Key: ab, aboral; cl, cervical loop; dl, dental lamina; la, labial; li, lingual; o, oral; sl, successional lamina. Scale bars = 100 μm for low power **(A–F')** and 20 microns for high power images **(A"–F")**.

was the increase in PCNA label in the mesenchyme in the area where the second generation tooth had been removed (**Figures 3E',F'**). The most aboral extension of the dental lamina continued to express PCNA (**Figures 3E",F"**). After 1-week, proliferation in the sham controls was similar to unmanipulated dental tissues (**Figures 4A–A"**). Mesenchymal proliferation was increased next to the location where the second generation teeth were removed (**Figures 4B–B"**). In areas where the dental lamina was torn, proliferation was noted near the edges of the epithelium (**Figures 4C–C"**).

Two weeks after surgery, sham controls continued to have strong signal in the second generation teeth mainly in the cervical loops and successional lamina (**Figures 4D–D"**). The mesenchymal response had changed and there was very little PCNA staining next to the dental lamina (**Figures 4E',E"**). New bone was visible on the dental process of the maxillary bone (**Figures 4E,F**). The dental lamina continued to express PCNA near the aboral end and occasionally new tooth buds could be seen (**Figures 4F–F"**). The dental lamina was torn in some locations following curettage (**Figures 4F–F"** and **Supplementary Figures 2D,E**) but this did not affect proliferation near the aboral tip of the dental lamina. Other phenotypes in the dental lamina are observed following surgical disruption. These include cysts forming within the dental lamina (**Supplementary Figures 2A–C**), tearing or truncation of the dental lamina (**Supplementary Figures 2D,E**), thickening or twisting of the dental lamina (**Supplementary Figure 2F**), and rotation of developing teeth (**Supplementary Figures 2G,H**). In summary, after tooth removal in the non-curetted regions, the dental lamina remains full-length, extending to the palatine process of the maxillary bone or lingual process of the dentary (**Figures 3B,E** and **Supplementary Figure 2A,B**). There was no evidence of retraction of the dental epithelium in the sham surgical sites. We did not have a specific marker for the successional lamina but it seemed likely that that plucking of the mineralized tooth likely brings with it any attached successional lamina (as in **Figures 4A,D**).

We then examined expression of PITX2, a marker of odontogenic potential, in normal tooth development and in tissues with dysmorphic dental laminae. In control tissues, PITX2 protein is expressed in the enamel organ, cervical loops, and successional laminae of developing teeth at all stages (**Figures 5A–A"**). In contrast, in the other regions of the dental lamina there were very few positive cells (10% of cells in the oral third were PITX2 positive, $N = 22$ as compared to 60% of cells close to the tooth, $n = 35$). Immediately after surgery, there is little expression of PITX2 in the torn dental lamina (**Figures 5B–B"**), except for the most aboral extension in some cases (**Figures 5C–C"**). At 1 week, a similar low level of signal was seen in the oral portions of the shortened dental lamina (**Figures 5D–D"**). By 2 weeks, only pieces of dental lamina that were located close to the typical position of the third generation tooth bud showed initiation of new teeth, even though shortened oral portions had some cells with PITX2 expression (**Figures 5E–F"'**). Thus, dental identity was maintained in the aboral dental epithelia even though spatial information may have been scrambled. We hypothesized that epithelial-mesenchymal interactions needed to initiate teeth are only supported in specific locations deep in the jaw mesenchyme.

We examined a second label of dental epithelium and one that identifies putative stem cells. SOX2 marks progenitor cells in some mammals (Juuri et al., 2012) and reptiles (Juuri et al., 2013; Kim et al., 2020), sharks (Martin et al., 2016), and bearded dragon (Salomies et al., 2019). Unlike these other animals, and unlike expression detected in embryonic geckos (Juuri et al., 2013) or juvenile geckos (Kim et al., 2020), there was no SOX2 antibody staining in the tooth bud or successional lamina (**Supplementary Figure 3B** in this 1 week mandibular control section). The differences between our studies may be related to the ages of the animals. Animals used for SOX2 staining here were adults and not juveniles or embryos. There is minimal expression in the dental lamina, with light staining of some nuclei near the oral cavity. There is strong staining in the taste buds, showing that the antibody did cross-react with gecko SOX2 protein (**Supplementary Figure 3C**). The SOX2-positive cells in the taste buds were complementary to PCNA-positive cells (**Supplementary Figure 3C**), as reported previously in the mouse (Castillo-Azofeifa et al., 2018). Similarly, in the tooth there is no overlap between PCNA-positive and SOX2-positive cells. There are some regions of the dental lamina where overlapping staining is visible (**Supplementary Figures 3E,E'**).

We also examined the expression of SOX2 1–2 weeks post surgery (**Supplementary Figures 4A–H"**). There are similar patterns of staining 1 week after surgery consisting of light SOX2 staining in nuclei of the central and oral portion of the dental lamina (**Supplementary Figures 4A–D"**). After 2 weeks we identified SOX2-positive cells in the oral portion of the dental lamina and sometimes in the aboral dental lamina. These qualitative observations do not support a change in the number or location of SOX2-positive cells after surgery. These animals were not labeled with BrdU so no direct comparison between SOX2-positive and BrdU-positive cells is possible.

BrdU Pulse-Chase of Dental Epithelial Cells to Trace the Progeny of Label-Retaining Cells

In order to determine whether previously purported stem cells in the dental lamina (Handrigan et al., 2010) give rise to new teeth, we performed a BrdU pulse-chase analysis (**Figures 6–9**). Based on the time-course of PCNA expression, proliferation in the dental lamina was highest 3–7 days after surgery (**Figure 3**). Therefore, we began injecting BrdU 3 days post-surgery and continued for 4 days. We anticipated that we would label putative stem cells that may have been activated in response to the injury. We analyzed multiple teeth across three different animals (**Supplementary Table 2**).

Time Zero, Normal Proliferation Patterns and the Maximum Incorporation of BrdU

One gecko was immediately euthanized after the 4-day BrdU pulse (7 days post surgery, Animal 9) to determine the maximum proportion of labeled cells at time 0 under different treatment

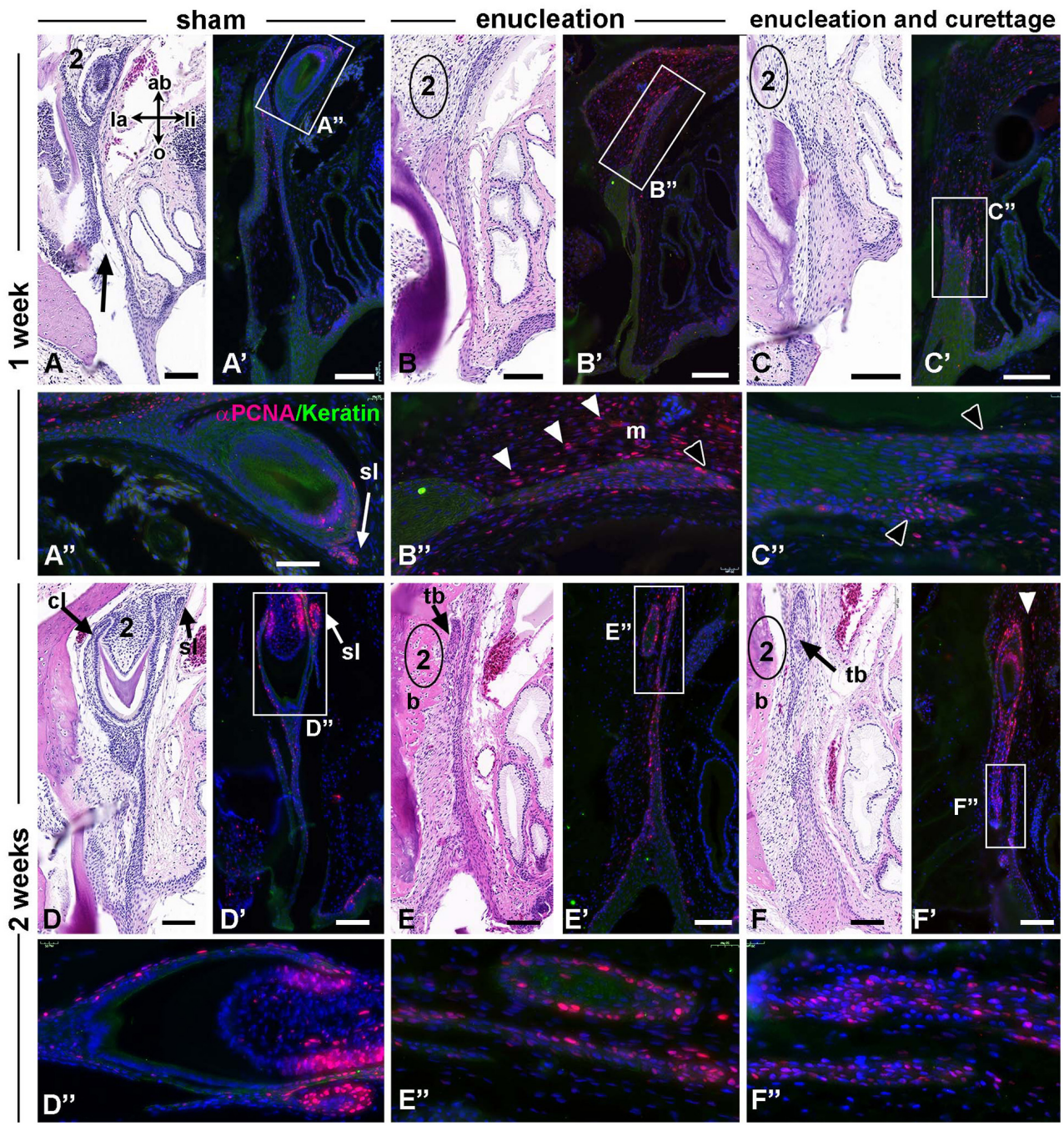

FIGURE 4 | Gecko dental surgical outcomes, 1–2 weeks. Histological sections stained with H and E and near-adjacent sections stained with PCNA antibody and pan-cytokeratin antibody. **(A–A")** In sham controls, the PCNA positive cells were present in the successional lamina. There is no PCNA staining in the mesenchyme surrounding the tooth or between the dental lamina and bone. Tearing of the dental lamina is still present from the original incision (black arrow). **(B–B")** The area where the tooth was removed is shown in **(B)** and mesenchyme in this area has increased PCNA staining (arrowheads **B',B"**). Strong PCNA staining in the free end of the dental lamina is also present (**B"**, black arrowhead). **(C–C")** The dental lamina is truncated and the cells closest to the torn edge are PCNA positive (arrowheads). **(D–D")** By 2 weeks the healing of the sham controls is complete and normal PCNA staining is present in the cervical loops and successional lamina. **(E—F')** In enucleation and enucleation + curettage treatments teeth are beginning to develop at the aboral end. Bone apposition has occurred in the site of tooth removal. The dental epithelium is PCNA positive. Cells in the dental lamina are also positive and this is not affected by local separations of the oral and aboral sections of the dental lamina **(F")**. Mesenchymal proliferation is present around the tooth buds (white arrowheads). Key: 2, second generation tooth; ab, aboral; b – bone apposition; cl, cervical loop; dl, dental lamina; la, labial; li, lingual; m, mesenchyme; o, oral; sl, successional lamina; tb, tooth bud. Scale bars = 100 μm for low power images and 50 μm for **(A"–F")**. Bar in **(A")** applies to all others.

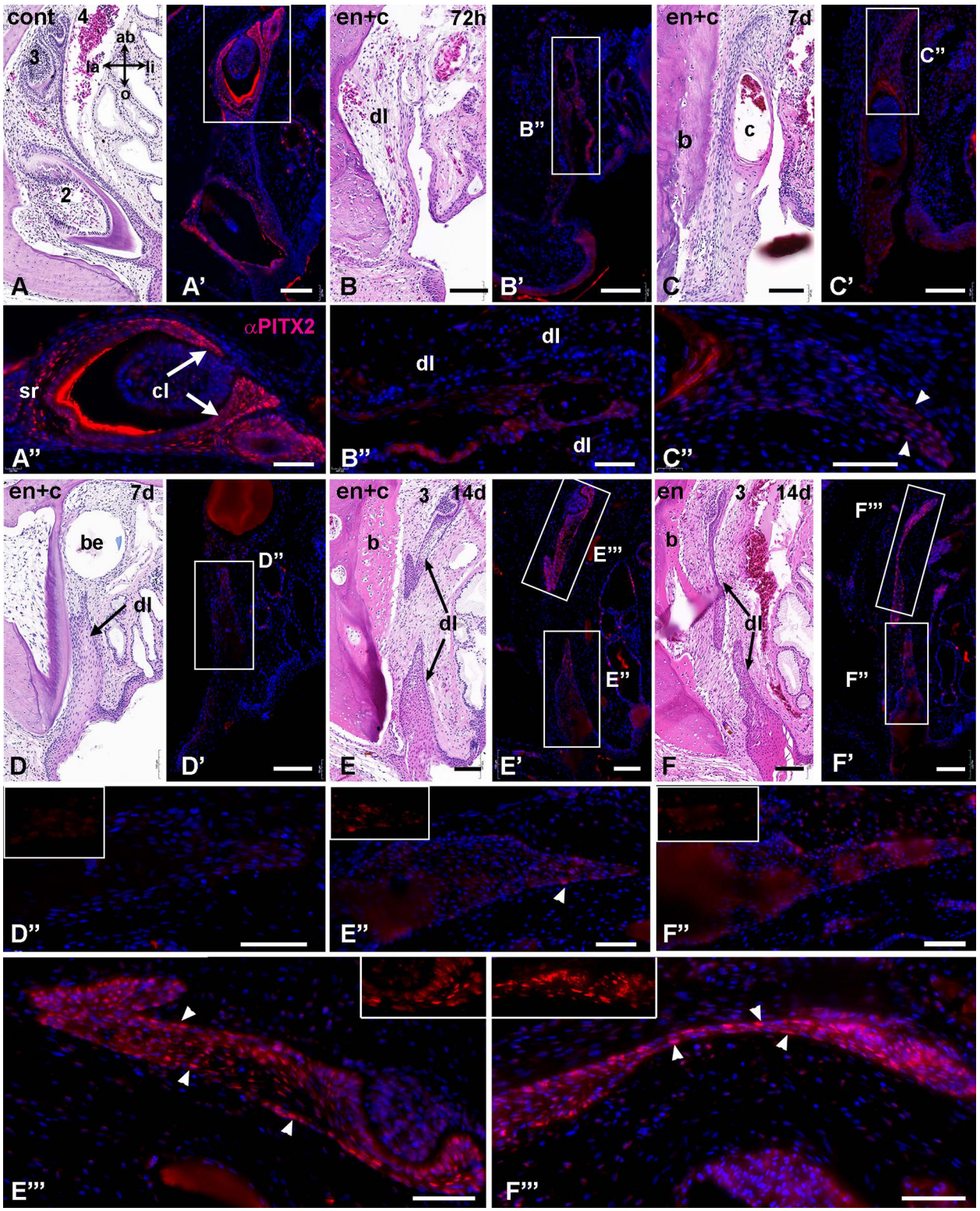

FIGURE 5 | Expression of PITX2 in non-treated and treated dental epithelium. Transverse sections are stained with H and E and near-adjacent sections stained with anti-PITX2 antibody (red) and Hoechst nuclear stain (blue). **(A–A")** Premaxillary tooth family with three successional teeth. The dental epithelium of the enamel organs is PITX2-positive. **(B–B")** 72 h after the surgery, the dental lamina retains weak PITX2 staining. **(C–C")** By 7 days the dental laminae have cysts in some locations. PITX2 nuclear staining is only visible at the most aboral end (**C"**, arrowheads). **(D–D")** One week post surgery, In areas where the dental lamina is short, there is

(Continued)

FIGURE 5 | Continued
very weak nuclear staining of PITX2 (**D"** and inset shows PITX2 channel). This section includes the bead which marks the start of the surgical site. **(E–E"')** Two weeks after enucleation and curettage, bone apposition is present close to where the tooth was removed. There is a separation between oral and aboral sections of the dental lamina. The oral portion has a few cells near the torn edge with PITX2 staining (**E"** and inset). In the aboral dental lamina a tooth bud is beginning to form from the remnants of dental lamina and strong nuclear staining is visible (**E"'**, arrowheads and inset). **(F–F"')**. There is separation between oral and aboral sections of the dental lamina. The strongest nuclear staining is in the nascent tooth bud and aboral end of the dental lamina (arrowheads in **F"'** and inset). Key: 2, second generation tooth; 3, third generation tooth; 4, fourth generation tooth; ab, aboral; b, bone; be, bead; c, cyst; cl, cervical loop; cont, control; dl, dental lamina; en, enucleation; e + c, enucleation and curettage; la, labial; li, lingual; sl, successional lamina; sr, stellate reticulum. Scale bars = 100 μm for low magnifications and 50 μm for high magnifications **(A"–F",E"',F"')**.

conditions (**Figures 6**, **7** and **Supplementary Tables 1, 2**). We also examined 2 other animals with PCNA labeling only (Animals 5 and 11, **Supplementary Tables 1, 2**). PCNA would be present in cells that were in late G1, S, and G2 to M transition phase (Kurki et al., 1986) and this label represents the normal proliferation in the tissue at that moment in time. In contrast, BrdU had been sequentially added to the animals over 4 days. Therefore, cells entering S phase on any of the 4 days would be cumulatively labeled. There is insufficient time to dilute the original BrdU label between days 1 and 4.

We were particularly interested to know whether the surgery had caused normally quiescent dental lamina cells to divide and take up BrdU. In the control regions there were less than 20% of dental lamina cells that were BrdU-positive with or without PCNA label (BrdU +/- PCNA; **Figures 6A**, **7A–A"** and **Supplementary Table 3A**). In contrast, in the treated regions, approximately 50% of dental lamina cells were labeled with BrdU +/- PCNA (**Figures 6A**, **7B–C"**). This level of incorporation was significantly higher than the controls (**Figures 6A**, $P < 0.01$, **Supplementary Table 3A**). These results suggest that the retraction of the mucosa in the shams stimulates incorporation of BrdU. We also assessed the number of cells that just had BrdU label at time 0 (**Supplementary Table 2**, and **Supplementary Figure 5**). These are cells that are not in the cell cycle as shown by lack of PCNA staining. The BrdU-positive cells may have been stimulated to divide immediately after the surgery but prior to euthanasia the cells had entered G0 or early G1 and hence were PCNA negative (Kurki et al., 1986).

In the control and sham control regions, all terminally differentiated, post-mitotic ameloblasts that were present before the surgery were unlabeled (**Figure 5B'**). The calcein label visible in the mineralized dentine or enamel distinguishes teeth that were present at the time of the surgery (**Figure 5B'**).

The percentage of PCNA labeling in the dental lamina represents cells in the cell cycle at the time of euthanasia. There was no difference across the treatments and controls at time 0 (**Figures 6B**, **7A"'–C"'** and **Supplementary Table 3B**). From these data we cannot rule out a change in the basal level of proliferation compared to an animal that did not have surgery.

We then calculated how efficiently we had labeled cells that were in the cell cycle with BrdU. At first, we looked at the proportion of dual-labeled cells out of the entire population of cells in the dental lamina (BrdU + PCNA labeled, **Figure 6C**). There were significantly more cells labeled compared to control dental laminae (**Supplementary Tables 3A,C** and **Figures 6C**, **7B",C"**). In a related analysis, the proportion of BrdU + PCNA labeled cells out of all the PCNA positive cells was higher (70–78%, **Figure 6D** and **Supplementary Tables 3A,D**) than in control dental laminae. In summary, we had identified a population of single-labeled, BrdU-positive cells in the dental lamina that were not in the cell cycle. These could therefore be putative progenitor or stem cells. The surgery did not affect the proportion of these slower-dividing cells. However, the surgery did significantly increase the number of BrdU-labeled cells entering the cell cycle (BrdU + PCNA).

One-Month Post-surgery

We examined three animals 3 months after surgery (**Figure 8** and **Supplementary Figure 6**). By 1 month post-surgery it was hard to find torn dental laminae therefore it appears that they had healed completely (**Supplementary Figures 2G,H,5D,E**). We are unable to determine whether healing occurred from dental lamina growing in from the edges of the defect, whether there was aboral growth of the shorter, torn dental lamina, or a mixture of both. Typically an erupted tooth will remain in place for approximately 5–8 weeks while it is in function (**Figures 2E,H**; Grieco and Richman, 2018). Then the second generation tooth erupts and 4 weeks elapse before the third generation tooth erupts (**Figure 2H**). Thus, 1 month after removing the second generation teeth we estimate that third generation teeth have likely progressed to cytodifferentiation. There will be some teeth that formed since the surgery that were not initially present. These would have reached cap stage but no ameloblasts would have differentiated. In sham or non-manipulated controls, we would see the second generation tooth has formed the full crown and is resorbing the 1st generation tooth.

The BrdU label serves two purposes 1-month post-surgery. The first is to differentiate putative stem cells from transit amplifying cells in the dental lamina. The most slowly dividing, undifferentiated dental lamina cells will retain most of the single BrdU label (the nucleus will be filled with the fluorescence signal) and importantly, will not be labeled with PCNA. The dental lamina cells that are dual labeled with fragmented BrdU and with PCNA are likely to be transit amplifying cells. The second purpose is to differentiate between three types of teeth: (1) those that formed from an existing tooth bud present at the time of surgery, (2) those that intiated immediately after surgery, and (3) those that were formed *de novo* several weeks after surgery from remaining dental lamina. The presence of terminally differentiated, post-mitotic unlabeled ameloblasts combined with the calcein label (visible under UV illumination of the sections) indicates the first tooth type, a tooth bud that was present and partially differentiated prior to conducting the surgery. The second type of tooth will have ameloblasts that are fully labeled

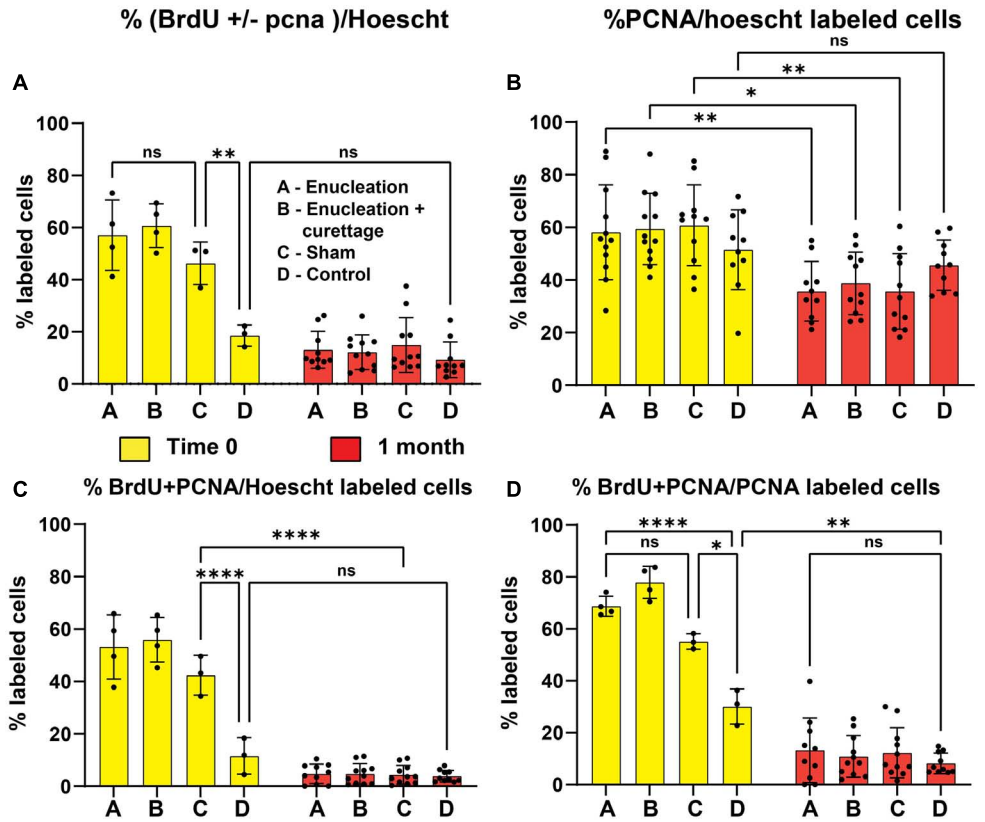

FIGURE 6 | Proliferation in the dental lamina following a pulse-chase. **(A)** The incorporation of BrdU +/- PCNA relative to the total number of cells in the dental lamina was significantly higher in the treated and sham control compared to the non-manipulated controls at time 0. At 1 month there were no significant differences between the types of manipulation. In addition, the number of labeled cells was the same in controls as at time zero. **(B)** PCNA labeling was significantly higher in the time 0 relative to the 1-month post-surgery dental lamina with the exception of control dental laminae. **(C)** At time 0, dual labeled cells were present in significantly higher proportions between the controls and all experimentally treated tissues. There was no significant difference between the percentage of dual labeled cells at time 0 and 1 month in the controls. Other treated tissues had significantly lower labeling at 1 month compared to time 0. **(D)** The proportion of BrdU + PCNA/PCNA cells was very high in the treated tissues at time 0 compared to controls. In addition, there were higher numbers of labeled cells in controls at time 0 compared to 1 month post-chase. Asterisks: $^{*}P < 0.05$, $^{**}P < 0.01$, $^{***}P < 0.001$, $^{****}P < 0.0001$.

with BrdU but became post-mitotic almost immediately after surgery. The *de novo* or third type of teeth will have reached cap or bud stage, will be strongly labeled with PCNA, and will have a proportion of cells also labeled with fragmented BrdU. Note that xylenol orange was present in the specimens but was not retained following processing for histology.

In non-manipulated controls, large second generation teeth were present in the expected location. As predicted, the majority of ameloblasts did not pick up the BrdU because they were post mitotic (**Figure 8A** and **Supplementary Figure 6A**) however the least mature ameloblasts were labeled and then ceased dividing (**Figure 8A"** and **Supplementary Figure 6A"**). Third generation teeth were present ranging from bud to bell stage. In bud stage teeth there were very few BrdU positive cells (**Figure 8A'**). The dental lamina was very weakly labeled (**Figure 8A"**). The same pattern was observed in sham controls (**Figure 8B**). Third generation teeth that were present at the time of surgery could easily be distinguished by the presence of calcein label and the heavily labeled, secretory ameloblasts (**Figures 8B,B'** and **Supplementary Figures 6B,B'**). Tooth buds in the sham areas that had not been present originally were labeled in all areas of the enamel organ (**Figures 8C,C'** and **Supplementary Figures 6C,C'**). In the areas where second generation teeth were removed, the most aboral teeth close to the palatine process of the maxillary bone were in bud or cap stage (**Figures 8D–E'**). These teeth were lightly labeled with fragmented BrdU in the inner enamel epithelium which was also PCNA positive (**Figures 8D–E'**). These dual labeled cells in the least mature teeth raised the possibility that the original BrdU labeled cells in the dental lamina gave rise to all the layers of the enamel organ of the new teeth.

Transit amplifying cells are the first progeny of a stem cell to form after an asymmetric cell division. As such, transit amplifying cells should retain much of the original BrdU label and be in close proximity to the stem cell niche (Yu and Klein, 2020). The dental laminae of sham controls and treated teeth had label retaining cells plus several transit amplifying cells close by (**Figures 8B"–E"**).

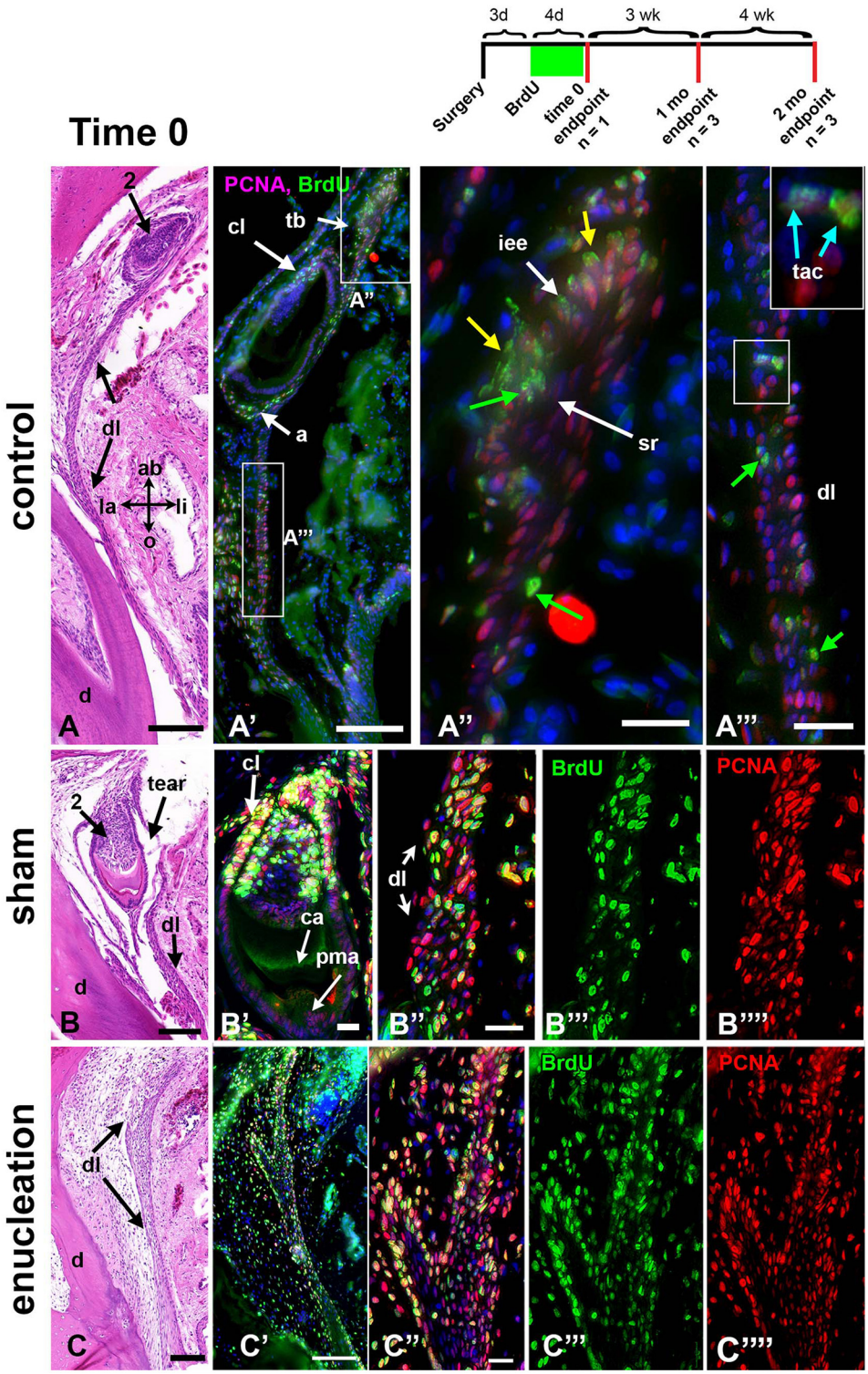

FIGURE 7 | Maximum labeling from 4-day pulse of BrdU – time 0. The experimental paradigm is illustrated above. Three days post-surgery the BrdU pulse begins and carries on for 4 days. Animals are euthanized after the pulse at time 0, 1, or 2 months. Sections were stained with H and E and near-adjacent sections were used for dual labeling with BrdU (green) and PCNA (red). **(A–A"')** Control, non-manipulated maxillary tooth after a 4-day pulse of BrdU. The ameloblasts that were proliferating took up the label **(A')** as did the cervical loops and successional lamina **(A")**. The least mature tooth bud is captured in the near-adjacent fluorescent section **(A")**. Much of the inner enamel epithelium is dual labeled (yellow arrows). Almost no BrdU is taken up in the stellate reticulum. **(A"')** The dental lamina is mainly labeled with PCNA but a few cells labeled only with BrdU are also present (green arrows). There are also some dual-labeled transit amplifying cells

(Continued)

FIGURE 7 | Continued
(blue arrows). The red spot is non-specific stain. **(B–B"")** A sham tooth that was undergoing cytodifferentiation at the time of the label. **(B')** The original calcein label is visible. Post-mitotic ameloblasts were unlabeled whereas the cervical loops and successional lamina were heavily labeled. **(B")** The dental lamina contained many more BrdU positive cells than the control **(B"')** and many of the cells were dual labeled with PCNA (compare **B"' to B""**). **(C–C"")** Removal of a tooth has resulted in strong labeling of BrdU throughout the dental lamina. Split channels show that many of the PCNA cells are co-labeled with BrdU. Key: 2, second generation tooth; a, ameloblasts; ab, aboral; ca, calcein; cl, cervical loop; d, dentine of first generation tooth; dl, dental lamina; iee, inner enamel epithelium; la, labial; li, lingual; pma, post-mitotic ameloblast; o, oral; sl, successional lamina; sr, stellate reticulum; tac, transit amplifying cell; tb, tooth bud. Scale bars = 100 μm in **(A,A',B,C,C')**. All other bars = 20 μm.

Our quantification of proliferation in the dental lamina at 1 month across three animals found that percentage of BrdU +/- PCNA labeled cells and other related calculations had significantly dropped compared to time zero (**Figures 6A,C**, **8A–E"**). There was no significant difference in the control teeth between time 0 and 1 month (**Figures 6A,C**, **8A"** and **Supplementary Table 4A**). Interestingly there was no significant difference in the proportion of exclusively BrdU-labeled cells between time 0 and 1 month (**Supplementary Figure 5**). The numbers varied quite a lot between sections so statistical significance was not reached (**Supplementary Table 2** and **Supplementary Figure 5**). Nevertheless, in the majority of sections, the dental lamina had retained quite a few putative stem cells (**Figures 8B"–D",E'**). The proportion of BrdU + PCNA/PCNA cells dropped significantly between time 0 and 1 month (**Figure 6D**). A part of the difference was due to the decrease in overall BrdU labeling at 1 month (**Figure 6B**). The PCNA data from the dental lamina suggests that at time 0 the animal did respond to the surgery by an overall increase in proliferation (possibly a general stress-response) but that by 1 month, homeostasis was restored. The level of PCNA labeling seen in the controls at time 0 was not significantly different than controls at 1 month and therefore represents the typical level of proliferating cells in the dental lamina.

The teeth that were present in bell stage at the time of surgery, no matter what the type of treatment, often had calcein labeling but ameloblasts at the cusp tip were unlabeled because they were post-mitotic (**Figures 8A,C**). Teeth that were in cap or early bell stage at the time of surgery had taken up BrdU in the ameloblasts and then stopped dividing (**Figure 8B'**). As predicted, teeth that were either not present or in early bud stage had progressed either to bud or cap stage but not to bell stage. The enamel organs and successional laminae of these teeth had strong PCNA labeling but also there were some BrdU positive cells present (**Figures 8A',C'–E'**). A similar pattern of staining in the successional lamina (strong PCNA with a minority of cells labeled with BrdU) was reported by others (Kim et al., 2020). We did not quantify the proportion of dual labeled cells in the teeth at 1 month post surgery because it was highly variable.

Two Months Post-surgery

We examined three animals, 2 months after surgery. Regrettably, two of the animals did not have sufficient penetration of the fixative so the majority of teeth originated from 1 animal (**Figures 9A–E""**, **Supplementary Figures 7A–B"'**, and **Supplementary Table 4**).

Based on the timing of tooth succession, by 8 weeks the tooth buds that were in bud or cap stage at the time of surgery would have reached position #2 and would have entered late bell or histodifferentiation stage (**Figures 9A–E**). Tooth buds that were not present at the time of surgery would be in early cap stage (**Figures 9A,B,D**). The bell stage teeth whether in control or treated tissues had BrdU in the inner enamel epithelium (**Figures 9A",B",E"**). There were also fragments of BrdU present in the outer enamel epithelium (**Figures 9A",B"',C"–E"**). The bud stage teeth that were not present at the time of surgery contained labeled cells in the outer and inner enamel epithelium, the majority of which were dual labeled (**Figures 9D",E"'** and **Supplementary Figures 7A",B"**). The frequent presence of BrdU +/- PCNA cells within the dental lamina after removal of second generation teeth and the presence of fragmented BrdU in the new tooth buds suggests that the dental lamina is contributing to the next generation of teeth. The dental lamina retained BrdU-positive cells in all treated and control tissues (**Supplementary Table 4** and **Figures 9C"',D"',E""**). There were cells labeled with PCNA and BrdU and based on their location in the dental lamina, they could be transit amplifying cells. A proportion of dental lamina cells were only labeled with BrdU and these are likely the undifferentiated, slowly dividing progenitor cells.

DISCUSSION

This study transiently disrupted tooth replacement in adult geckos by selectively removing the unerupted, second generation mineralized teeth. The healing of the dental lamina and resumption of tooth replacement is a robust process and was approaching normal patterns by 3 months. Although there were parts of the dental lamina that were torn and the successional lamina was disrupted, the dental lamina retained odontogenic identity, healed, and *de novo* tooth formation occurred. We also present the first data comparing normal and healing dental laminae in adult animals. We also determined that even though teeth were initially forming much closer than normal to each other in disrupted dental and successional laminae, there was no inhibition of development. Once the subsequent generation of teeth initiated, teeth form as independent units in the correct position, deep in the jaws, based on local epithelial-mesenchymal signaling.

Replacement Timing and Patterning of the Adult Gecko Dentition Is Controlled by Local Rather Than Regional Factors

Our work partially tested the hypothesis that in the adult reptile dentition there are diffusible signals acting between tooth families going over long distances in the jaw to set up the tooth replacement pattern (Edmund, 1969). Work on other animal

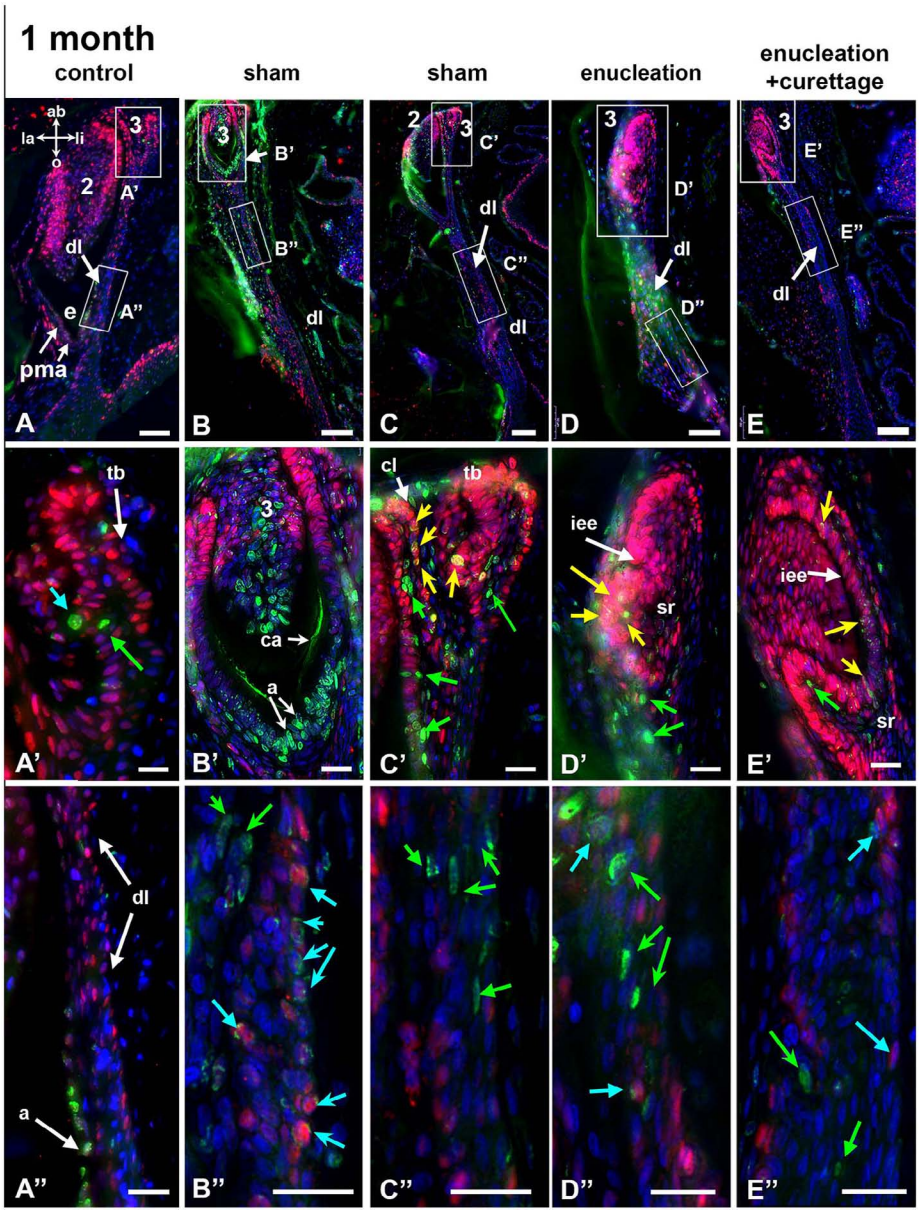

FIGURE 8 | BrdU label retention after 1 month and co-labeling with PCNA. Five teeth **(A–E)** sampled from different regions of the same animal. BrdU is green, PCNA is red, and nuclei are blue. Axes in A apply to all panels. **(A–A")** A tooth family with BrdU retained in some cells within the third generation tooth bud **(A')**. Most of the dental lamina is labeled with PCNA but not BrdU **(A")**. The ameloblasts formed at the time the label was administered have taken up BrdU **(A")**. **(B–B")** The second generation tooth bud has been labeled with calcein and the ameloblasts are labeled with BrdU. The newest enamel is deposited between the calcein label and cusp tip. The majority of BrdU has been trapped in the post-mitotic ameloblasts and therefore this tooth is about 1 month old. The dental lamina contains many dual-labeled cells that are transit amplifying cells (blue arrows). Several label-retaining cells are only labeled with BrdU (green arrows). **(C–C")** Many BrdU-labeled cells (green arrows) and dual-labeled cells (yellow arrows) are in the new tooth bud and cervical loop of the second generation tooth. The dental lamina is also labeled with BrdU **(C")**. **(D–D")** A new tooth bud that was not present at the time of surgery. There are dual labeled cells in the inner enamel epithelium and stellate reticulum (yellow arrows, **D'**). The dental lamina has multiple BrdU cells (green arrows) and several adjacent transit amplifying cells (blue arrows). **(E–E")** A third generation tooth bud that has labeled cells in the inner enamel epithelium (**E'**, yellow arrows). The dental lamina has interstitial BrdU labeled cells and a few transit amplifying cells (blue arrows). Key: 2, second generation tooth; 3, third generation tooth; a, ameloblasts; ab, aboral; ca, calcein; cl, cervical loop; dl, dental lamina; e, enamel; iee, inner enamel epithelium; la, labial; li, lingual; o, oral; pma; post-mitotic ameloblast; sr, stellate reticulum; tb, tooth bud. Scale bars = 20 μm for **(A'–E")**, 50 μm for **(A,D)** and 100 μm for **(B,C,E)**.

models suggested that there is a zone of inhibition between nearby teeth, in cichlids (Fraser et al., 2008) and in denticles of shark skin (Cooper et al., 2018) that establish patterning. In our enucleation experiments, mineralizing teeth were removed, but the dental lamina, successional lamina, and any bud-stage teeth that did not show fluorescently labeled mineralizing tissue were

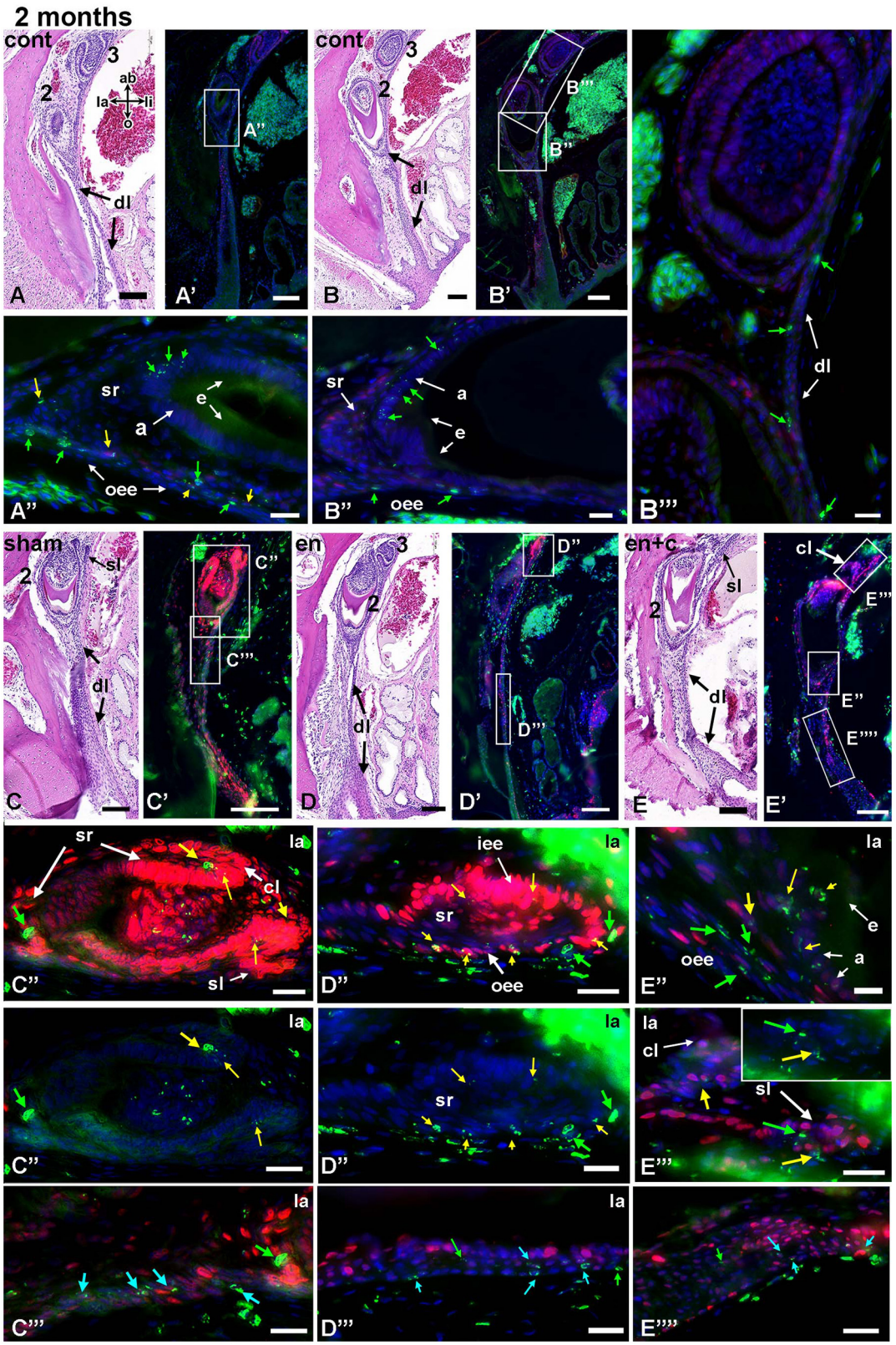

FIGURE 9 | BrdU label retention after 2 months and co-labeling with PCNA. Transverse sections of teeth from different regions of the maxilla stained with H and E. Near-adjacent sections were used for immunofluorescence staining. **(A–B''')** Second generation teeth have retained fragments of BrdU in the nuclei of the

(Continued)

FIGURE 9 | Continued
post-mitotic ameloblasts. **(B"')** Label-retaining cells are present in the dental lamina between the second and third generation teeth (green arrows). **(C–C"')** A differentiating tooth has BrdU-retaining cells in the stellate reticulum (green arrows). Dual labeled cells are scattered in the cervical loops. **(C"')** In the dental lamina there are several BrdU and transit amplifying cells (blue arrows). **(D–D"')** A tooth family with a second generation tooth that was in bud stage at the time of surgery. The newest tooth bud derived from the successional lamina of the second generation tooth and contains dual labeled cells in the inner and outer enamel epithelium. The dental lamina continues to harbor lightly labeled, BrdU-positive cells (green arrows, **D"'**). **(E–E"")** A tooth in bell stage that has just started to deposit enamel matrix. Fragments of BrdU are in the ameloblasts and outer enamel epithelial cells. This tooth was in early bud stage during the original surgery. The successional lamina which arose since the surgery contains BrdU labeled cells (green arrows). Key: 2, second generation tooth; 3, third generation tooth; a, ameloblasts; ab, aboral; cl, cervical loop; cont, control; dl, dental lamina; en, enamel matrix; iee, inner enamel epithelium; la, labial; li, lingual; o, oral; oee, outer enamel epithelium; sl, successional lamina; sr, stellate reticulum. Scale bars = 100 μm for low magnification views and 20 μm for **(A'–E"')**.

left in the jaw. This explains the quick recovery in which teeth that had already initiated maintained the timing and patterning of subsequent tooth initiation. In the curetted treatment sites, some tooth buds were pushed close together or twisted into different positions, yet still continued to develop even though the implied zone of inhibition was disrupted. This suggests that, if present in reptiles, the zone of inhibition is more important pre-initiation for spacing the dentition but less important once teeth begin differentiation. We acknowledge that other experiments are needed to determine what would happen to the pattern of initiation if all the third generation teeth were removed in a localized region.

We noted at two weeks post-surgery that teeth initiated only in the most aboral sections of the dental lamina. The instructive signals to begin tooth formation may lie either in the mesenchyme or epithelium. Currently we lack markers of odontogenic mesenchyme and have no method of separating the two tissues *in vivo*. Potential molecules that may be involved in local patterning in the reptile dentition were reported in a study on the bearded dragon (Salomies et al., 2019). These authors performed bulk RNA sequencing specifically on the successional lamina and surrounding mesenchyme using tissues isolated with laser capture microdissection. Some candidate mesenchymal genes were presented but many of these are not annotated. More bioinformatics work needs to be done to find potential instructive signaling pathways involved in tooth induction in adult reptiles.

Signals From Unerupted Teeth May Be Needed to Correctly Time Tooth Shedding

Our data suggest that the dental lamina contains the information to correctly pattern newly initiating teeth, and signals are not emanating from the second generation tooth. However, the second generation tooth may be required for the resorption of the functional tooth. We found that the functional tooth was retained in the mouth for longer than expected and was not replaced until a replacement tooth was present to resorb it. The importance of tooth resorption in maintaining tooth cycle timing has also been shown in studies where the functional tooth was broken, but not removed, in fish (Huysseune et al., 2012) and iguanas (Brink et al., 2020). The timing of tooth replacement in iguanas was not affected by breakage of the tooth crown, since the base still needed to be resorbed before being shed. The gecko teeth appear to require signals from the replacement tooth to initiate resorption of the functional teeth.

Timing of Initiation of Replacement Teeth Is Not Accelerated Following Tooth Enucleation

Besides affecting tooth resorption, our data do not show evidence for earlier initiation of teeth after enucleation of replacement teeth. Tooth buds that were present at the time of surgery developed normally after the treatment, as shown by the presence of small mineralized teeth in μCT scans. A similar presence of third generation teeth in early stages of histodifferentiation was seen in histology. Perhaps the best evidence for a lack of acceleration in the rate of tooth development is in the PCNA data. After 1 month there was a decrease rather than an increase in PCNA labeling in the dental lamina across all conditions including controls. The teeth themselves are labeled with PCNA in a similar pattern at time 0, 1, and 2 months. The new teeth, once they initiate morphogenesis, are highly proliferative and this is not dependent on whether second generation teeth were removed.

Our results differ from results in the alligator, where removal of a functional tooth triggered proliferation and initiation of new teeth earlier than expected (Wu et al., 2013). The long-term effect of tooth removal in alligators has yet to be reported. Thus, it is not known whether the proliferation ultimately affects the formation of teeth or whether the same group of cells becomes quiescent for a period of time. In the green iguana, proliferation of the successional lamina occurs only when a tooth initiates, so there are much longer periods of quiescence between initiation events than in the leopard gecko (Brink et al., 2020). In the gecko, there is always a new tooth budding at most tooth positions and all successional laminae are proliferating as shown by PCNA labeling. This readiness to form new teeth may explain the more rapid turn over of teeth in the gecko compared to the iguana (4–5 weeks in geckos, Grieco and Richman, 2018; compared to 10–20 weeks in iguana, Brink et al., 2020).

BrdU-PCNA Labeling Distinguishes Putative Stem Cells From Their Progeny by Location and BrdU Fragmentation

The retention of BrdU label was first reported in the dental lamina, close to the second generation teeth (Handrigan et al., 2010). In that study there was retention of labeled cells in the undifferentiated dental lamina and in the outer enamel epithelium of differentiating teeth. It was also previously reported that there was uptake of BrdU in ameloblasts that were about to differentiate and become post-mitotic (Handrigan et al., 2010).

In the present study, we combined PCNA and BrdU labeling, which added to the story. First, with higher resolution, we were able to see that the retention of BrdU varies in quality (extent of fragmentation) and quantity (number of cells) according to the location and stage of differentiation of the tooth buds. Second, we could distinguish cells that were carrying BrdU that had likely entered G0 from those that had entered the cell cycle (BrdU + PCNA). In the previous study, cell counts included BrdU +/- PCNA labeled cells. Some of the cells were likely transit amplifying cells and not exclusively BrdU label-retaining cells. In the previous study it was hypothesized that there would be progeny of the transit amplifying cells in the new tooth buds, ultimately contributing to the different layers of the enamel organ. Here we found that removal of second generation teeth allowed us to separate the contributions of label-retaining cells in the dental lamina from those that may be present within the tooth itself.

Two Interpretations of BrdU-Labeled Cells – Dedifferentiation Versus Stem/Progenitor Cells

A recent study has suggested that under conditions of chemical ablation, the partially differentiated cells of the inner enamel epithelium in the mouse incisor may revert to progenitor cells (Sharir et al., 2019). This idea that tissues can regenerate even if the local stem cell population is almost depleted has been demonstrated in the intestine and other organs (Gola and Fuchs, 2021; Shivdasani et al., 2021).

We feel it is unlikely that BrdU-positive cells in the dental lamina of the gecko were terminally differentiated and then in response to injury had dedifferentiated into progenitor cells. For the first part of the hypothesis to be true, the dental lamina would need to have characteristics of a differentiated epithelium. There are no signs of stratification as in oral non-keratinized epithelia (Groeger and Meyle, 2019). Since the epithelial cells near the basement membrane are proliferative and undifferentiated in all stratified epithelia (Gola and Fuchs, 2021), any post-mitotic, terminally differentiated cells would be confined to the center of the dental lamina. However, in the gecko and bearded dragon, BrdU-positive cells are located close to the basement membrane often nearby to dual labeled cells. In a study from a different lab (Kim et al., 2020) sections of the leopard gecko dentition were stained with antibodies to the basement membrane protein laminin5. The expression in the successional lamina was diffuse and did not form a distinct outline of the epithelium as in the mouse. This is consistent with the successional lamina not being a differentiated epithelium. The structure of the basement membrane around the dental lamina has yet to be examined. The dental lamina does not serve a barrier function like other oral epithelia and thus does not need specialized cell junctions at the surface. In addition, we showed that the expression of PITX2 is restricted to epithelia that are committed to an odontogenic lineage, whereas most of the dental lamina has lower numbers of PITX2-positive cells. Had dedifferentiation been a major mechanism in the formation of new teeth, we would have seen loss of PITX2 staining in the aboral parts of the dental lamina.

The concept that the dental epithelium had dedifferentiated would be supported by an increase in stem cell marker expression. However, SOX2 is not expressed in most of the gecko dental lamina where BrdU-labeled cells were often found. In addition, there was no increased signal for SOX2 following surgery. Further co-localization experiments will be done to verify the expression of SOX2 and other stem cell markers with respect to the label-retaining cells in the gecko.

It is interesting that immediately following injury, there was an increase in the number of BrdU + PCNA cells. This suggests that the surgery had stimulated more cells that were originally quiescent to enter the cell cycle. However, the number of BrdU-only labeled cells did not change between the original time 0 and 1 month. The gecko dentition must have a means to maintain a minimum number of stem cells throughout life.

Dual Labeling With PCNA and BrdU Separates Transit Amplifying Cells From Adult Tissue Stem Cells

The transit amplifying cells play an important role in regenerating the dentition. The traditional view is that transit amplifying cells are close to the stem cells but lack the markers of epithelial stem cells such as Lgr5 and Sox2 (Binder et al., 2019). Transit amplifying cells are also proliferative (Yu and Klein, 2020). The strongest evidence that these dual labeled cells in the dental lamina are TA cells comes from the surgical design of the study and the fact that only dental lamina or immature tooth buds were left after removal of second generation teeth. The remaining tooth buds, seen at 1 month of age as cap stage teeth, were highly proliferative and contained fragmented BrdU. In contrast, the main location with nuclei that were fully labeled with BrdU was the dental lamina.

In the present study we were able to accurately identify nuclei that either had pure BrdU label, pure PCNA label, or both. The dual-labeled cells were present in many different locations in the dental epithelium but based on the work of others in the mouse incisor (Harada et al., 1999) and hair follicle (Hsu et al., 2014; Yang et al., 2017), only those dual labeled cells close to the stem cell niche should be considered as transit amplifying cells. In contrast, the undifferentiated epithelial cells (not ameloblasts) that were solely labeled with BrdU were almost always located in the dental lamina, except for a few occurrences in the stellate reticulum. These BrdU-labeled cells were likely the equivalent of adult tissue stem cells found at the base of hair follicles (Yang et al., 2017; Gola and Fuchs, 2021).

Our work does not identify a consistent labio-lingual pattern where previously we reported that most of the BrdU-labeled cells were on the lingual surface of the dental lamina (Handrigan et al., 2010). We attribute this difference to the fact that we sampled many more teeth in the present study and our imaging techniques were more advanced. In addition, some of the lingual cells in the previous study would have been dual labeled but were not identified as such.

Our new model is that some of the transit amplifying cells located in the dental lamina move or are displaced toward the budding teeth. Indeed, we often found clusters of dual-labeled cells very close to the tooth within the dental

lamina. The movement of cells from the oral to aboral parts of the dental lamina was also observed in the bearded dragon (Salomies et al., 2019). This directional flow of cells in the dental lamina may direct tooth budding to deeper rather than superficial regions of the jaw.

There are very few models in which to study adult dental stem cells, with the exception of the mouse incisor and teeth in certain reptiles. The mouse has the obvious advantage of being able to perform lineage tracing with genetic markers. The proxy for lineage tracing used here was the extent of dilution of the BrdU label and location of the progeny. We showed that BrdU-labeled cells resident in the dental lamina are generally more fully labeled with BrdU than the highly fragmented BrdU-labeled cells in the tooth germs. Thus BrdU-labeled cells can maintain a subset of progeny with less frequent cell divisions while other subsets are dividing more rapidly and giving rise to the teeth. These BrdU-labeled cells appear to be multipotent. The adult leopard gecko does have desirable properties for understanding dental epithelial stem cells. There is continuous tooth replacement in more than 40 tooth positions per quadrant so there are robust mechanisms to maintain tissue homeostasis amenable to experimental studies. We tested whether removing sections of the dental lamina in a targeted manner (curettage) would delay tooth formation. Remarkably, the integrity of the dental lamina was restored between 2 weeks and 1 month after surgery. There was no delay in forming the replacement teeth as shown on μCT scans. We attribute the rapid healing to the persistence of stem cells in the dental lamina remnants. We predict that a more severe treatment such as chemical ablation (Sharir et al., 2019) may give different results. Taking the normal propensity of the dental lamina to maintain homeostasis, together with the ability of the dental lamina to heal easily and the retention of single BrdU-labeled cells over several months, our data support the idea that the dental lamina houses the dental epithelial stem cell population.

DATA AVAILABILITY STATEMENT

The raw data supporting the conclusions of this article will be made available by the authors, without undue reservation.

ETHICS STATEMENT

The animal study was reviewed and approved by University of British Columbia Animal Care Committee.

AUTHOR CONTRIBUTIONS

KB and JMR: conceptualization, execution of experiments, analysis of data, and drafted the manuscript. TG: conceptualization, execution of experiments, analysis of data, and edited the manuscript. JIH: edited the manuscript, immunostaining, analysis of cell proliferation. JIH and JRMC: proliferation analysis. KF: immunostaining. All authors contributed to the article and approved the submitted version.

FUNDING

This experimental work was funded by NSERC grant RGPIN-2016-05477 and NIH grant 5R21DE026839-02 to JMR. Funding for the gecko surgical suite was from NSERC grant RTI-2016-00117 to JMR. KB was funded by a Killam Postdoctoral Fellowship, a Michael Smith Foundation for Health Research Postdoctoral Trainee Award, and an NSERC Banting Postdoctoral Fellowship. TG was funded by an NIH F32 Individual Postdoctoral Fellowship F32DE024948.

ACKNOWLEDGMENTS

For assistance with histology, we thank the following undergraduate Worklearn students: Jen Cooper, Kaylin Ho, Queenie Li, Bayan Noureddine, and Felar Yu. For help with experiments and fruitful discussions, we thank members of the JMR lab, Thomas Bertin, and Sid Vora. For assistance with animal care, we thank the veterinarians and staff at the Centre for Comparative Medicine, UBC. We acknowledge the Centre for High-Throughput Phenogenomics at UBC for conventional μCT scans of the geckos and Tomas Zikmund at CEITEC, Brno, Czech Republic for the contrast-enhanced PTA scan of the gecko jaw.

SUPPLEMENTARY MATERIAL

The Supplementary Material for this article can be found online at: https://www.frontiersin.org/articles/10.3389/fphys.2021.576816/full#supplementary-material

REFERENCES

Binder, M., Chmielarz, P., McKinnon, P. J., Biggs, L. C., Thesleff, I., and Balic, A. (2019). Functionally Distinctive Ptch Receptors Establish Multimodal Hedgehog Signaling in the Tooth Epithelial Stem Cell Niche. *Stem Cells* 37, 1238–1248. doi: 10.1002/stem.3042

Brink, K. S., Wu, P., Chuong, C. M., and Richman, J. M. (2020). The Effects of Premature Tooth Extraction and Damage on Replacement Timing in the Green Iguana. *Integr. Comp Biol.* 60, 581–593. doi: 10.1093/icb/icaa099

Buchtova, M., Stembirek, J., Glocova, K., Matalova, E., and Tucker, A. S. (2012). Early regression of the dental lamina underlies the development of diphyodont dentitions. *J. Dent Res.* 91, 491–498. doi: 10.1177/0022034512442896

Castillo-Azofeifa, D., Seidel, K., Gross, L., Golden, E. J., Jacquez, B., Klein, O. D., et al. (2018). SOX2 regulation by hedgehog signaling controls adult lingual epithelium homeostasis. *Development* 145:164889.

Cooper, J. S. (1966). Tooth Replacement in Slow Worm (Anguis Fragilis). *J. Zool.* 150:235. doi: 10.1111/j.1469-7998.1966.tb03006.x

Cooper, R. L., Thiery, A. P., Fletcher, A. G., Delbarre, D. J., Rasch, L. J., and Fraser, G. J. (2018). An ancient Turing-like patterning mechanism regulates skin denticle development in sharks. *Sci. Adv.* 4:eaau5484. doi: 10.1126/sciadv.aau5484

Edmund, A. G. (1960). Tooth replacement phenomena in the lower vertebrates. *Contribut. Life Sci. Div.* 52, 1–190.

Edmund, A. G. (1962). Sequence and rate of tooth replacement in the Crocodilia. *Contribut. Life Sci. Div.* 56, 7–42.

Edmund, A. G. (1969). "Dentition," in *Biology of the Reptilia, . Morphology A*, eds C. Gans, A. Bellaris, and T. Parsons (London: Academic Press), 117–200.

Fastnacht, M. (2008). Tooth replacement pattern of Coloborhynchus robustus (Pterosauria) from the Lower Cretaceous of Brazil. *J. Morphol.* 269, 332–348. doi: 10.1002/jmor.10591

Fraser, G. J., Bloomquist, R. F., and Streelman, J. T. (2008). A periodic pattern generator for dental diversity. *BMC Biol.* 6:32. doi: 10.1186/1741-7007-6-32

Gibert, Y., Samarut, E., Ellis, M. K., Jackman, W. R., and Laudet, V. (2019). The first formed tooth serves as a signalling centre to induce the formation of the dental row in zebrafish. *Proc. R Soc. B Biol. Sci.* 286:0401. doi: 10.1098/rspb.2019.0401

Gola, A., and Fuchs, E. (2021). Environmental control of lineage plasticity and stem cell memory. *Curr. Opin. Cell Biol.* 69, 88–95. doi: 10.1016/j.ceb.2020.12.015

Grieco, T. M., and Richman, J. M. (2018). Coordination of bilateral tooth replacement in the juvenile gecko is continuous with in ovo patterning. *Evol. Dev.* 20, 51–64. doi: 10.1111/ede.12247

Groeger, S., and Meyle, J. (2019). Oral Mucosal Epithelial Cells. *Front. Immunol.* 10:208. doi: 10.3389/fimmu.2019.00208

Hanai, T., and Tsuihiji, T. (2019). Description of Tooth Ontogeny and Replacement Patterns in a Juvenile Tarbosaurus bataar (Dinosauria: Theropoda) Using CT-Scan Data. *Anat. Rec.* 302, 1210–1225. doi: 10.1002/ar.24014

Handrigan, G. R., Leung, K. J., and Richman, J. M. (2010). Identification of putative dental epithelial stem cells in a lizard with life-long tooth replacement. *Dev.* 137, 3545–3549. doi: 10.1242/dev.052415

Handrigan, G. R., and Richman, J. M. (2011). Unicuspid and bicuspid tooth crown formation in squamates. *J. Exp. Zool. B Mol. Dev. Evol.* 316, 598–608. doi: 10.1002/jez.b.21438

Harada, H., Kettunen, P., Jung, H. S., Mustonen, T., Wang, Y. A., and Thesleff, I. (1999). Localization of putative stem cells in dental epithelium and their association with Notch and FGF signaling. *J. Cell Biol.* 147, 105–120. doi: 10.1083/jcb.147.1.105

Hosseini-Farahabadi, S., Geetha-Loganathan, P., Fu, K., Nimmagadda, S., Yang, H. J., and Richman, J. M. (2013). Dual functions for WNT5A during cartilage development and in disease. *Matrix Biol.* 32, 252–264. doi: 10.1016/j.matbio.2013.02.005

Hsu, Y. C., Li, L., and Fuchs, E. (2014). Transit-amplifying cells orchestrate stem cell activity and tissue regeneration. *Cell* 157, 935–949. doi: 10.1016/j.cell.2014.02.057

Huysseune, A., Vandenplas, S., De Groeve, B., Fjelldal, P. G., and Hansen, T. (2012). The pattern of the lower jaw dentition in farmed Atlantic salmon (Salmo salar): a tool to study mechanisms of tooth replacement? *J. Appl. Ichthyol.* 28, 330–335. doi: 10.1111/j.1439-0426.2012.02002.x

Juuri, E., Jussila, M., Seidel, K., Holmes, S., Wu, P., Richman, J., et al. (2013). Sox2 marks epithelial competence to generate teeth in mammals and reptiles. *Dev.* 140, 1424–1432. doi: 10.1242/dev.089599

Juuri, E., Saito, K., Ahtiainen, L., Seidel, K., Tummers, M., Hochedlinger, K., et al. (2012). Sox2+ stem cells contribute to all epithelial lineages of the tooth via Sfrp5+ progenitors. *Dev. Cell* 23, 317–328. doi: 10.1016/j.devcel.2012.05.012

Kim, E. J., Jung, S. Y., Wu, Z., Zhang, S., and Jung, H. S. (2020). Sox2 maintains epithelial cell proliferation in the successional dental lamina. *Cell Prolif.* 53:e12729. doi: 10.1111/cpr.12729

Kline, L. W., and Cullum, D. (1984). A Long-Term Study of the Tooth Replacement Phenomenon in the Young Green Iguana, Iguana-Iguana. *J. Herpetol.* 18, 176–185. doi: 10.2307/1563746

Kline, L. W., and Cullum, D. R. (1985). Tooth Replacement and Growth in the Young Green Iguana, Iguana-Iguana. *J. Morphol.* 186, 265–269. doi: 10.1002/jmor.1051860303

Kurki, P., Vanderlaan, M., Dolbeare, F., Gray, J., and Tan, E. M. (1986). Expression of Proliferating Cell Nuclear Antigen (Pcna)/Cyclin during the Cell-Cycle. *Exp. Cell Res.* 166, 209–219. doi: 10.1016/0014-4827(86)90520-3

Martin, K. J., Rasch, L. J., Cooper, R. L., Metscher, B. D., Johanson, Z., and Fraser, G. J. (2016). Sox2+ progenitors in sharks link taste development with the evolution of regenerative teeth from denticles. *Proc. Natl. Acad. Sci. U S A* 113, 14769–14774. doi: 10.1073/pnas.1612354113

Metscher, B. D. (2009). MicroCT for developmental biology: a versatile tool for high-contrast 3D imaging at histological resolutions. *Dev. Dyn.* 238, 632–640. doi: 10.1002/dvdy.21857

Murray, J. D., and Kulesa, P. M. (1996). On a dynamic reaction-diffusion mechanism: The spatial patterning of teeth primordia in the alligator. *J. Chem. Soc. -Faraday Transact.* 92, 2927–2932. doi: 10.1039/ft9969202927

Osborn, J. W. (1970). New approach to Zahnreihen. *Nature* 225, 343–346. doi: 10.1038/225343a0

Osborn, J. W. (1971). The ontogeny of tooth succession in Lacerta vivipara Jacquin (1787). *Proc. R Soc. Lond. B Biol. Sci.* 179, 261–289. doi: 10.1098/rspb.1971.0097

Sadier, A., Jackman, W. R., Laudet, V., and Gibert, Y. (2020). The Vertebrate Tooth Row: Is It Initiated by a Single Organizing Tooth? *Bioessays* 42:1900229. doi: 10.1002/bies.201900229

Salomies, L., Eymann, J., Khan, I., and Di-Poi, N. (2019). The alternative regenerative strategy of bearded dragon unveils the key processes underlying vertebrate tooth renewal. *Elife* 8:47702. doi: 10.7554/eLife.47702

Sharir, A., Marangoni, P., Zilionis, R., Wan, M., Wald, T., Hu, J. K., et al. (2019). A large pool of actively cycling progenitors orchestrates self-renewal and injury repair of an ectodermal appendage. *Nat. Cell Biol.* 21, 1102–1112. doi: 10.1038/s41556-019-0378-2

Shivdasani, R. A., Clevers, H., and de Sauvage, F. J. (2021). Tissue regeneration: Reserve or reverse? *Science* 371, 784–786. doi: 10.1126/science.abb6848

Westergaard, B., and Ferguson, M. W. J. (1987). Development of the Dentition in Alligator-Mississippiensis. Later Development in the Lower Jaws of Embryos, Hatchlings and Young Juveniles. *J. Zool.* 212, 191–222. doi: 10.1111/j.1469-7998.1987.tb05984.x

Wu, P., Wu, X., Jiang, T.-X., Elsey, R. M., Temple, B. L., Divers, S. J., et al. (2013). Specialized stem cell niche enables repetitive renewal of alligator teeth. *Proc. Natl. Acad. Sci. U S A* 110, E2009–E2018.

Yang, H., Adam, R. C., Ge, Y., Hua, Z. L., and Fuchs, E. (2017). Epithelial-Mesenchymal Micro-niches Govern Stem Cell Lineage Choices. *Cell* 48:e413. doi: 10.1016/j.cell.2017.03.038

Yu, T., and Klein, O. D. (2020). Molecular and cellular mechanisms of tooth development, homeostasis and repair. *Development* 147:184754. doi: 10.1242/dev.184754

Conflict of Interest: TG is currently employed by the company STEMCELL Technologies. All lab work performed by TG was prior to employment at STEMCELL Technologies. STEMCELL Technologies has no financial or experimental contribution to this work.

The remaining authors declare that the research was conducted in the absence of any commercial or financial relationships that could be construed as a potential conflict of interest.

Advantages of publishing in Frontiers

OPEN ACCESS
Articles are free to read for greatest visibility and readership

FAST PUBLICATION
Around 90 days from submission to decision

HIGH QUALITY PEER-REVIEW
Rigorous, collaborative, and constructive peer-review

TRANSPARENT PEER-REVIEW
Editors and reviewers acknowledged by name on published articles

Frontiers
Avenue du Tribunal-Fédéral 34
1005 Lausanne | Switzerland

Visit us: www.frontiersin.org
Contact us: frontiersin.org/about/contact

REPRODUCIBILITY OF RESEARCH
Support open data and methods to enhance research reproducibility

DIGITAL PUBLISHING
Articles designed for optimal readership across devices

FOLLOW US
@frontiersin

IMPACT METRICS
Advanced article metrics track visibility across digital media

EXTENSIVE PROMOTION
Marketing and promotion of impactful research

LOOP RESEARCH NETWORK
Our network increases your article's readership